FACULTAD DE CIENCIAS
Departamento de Química Inorgánica

New Alkaline-Earth Polymeric Frameworks as green materials for sorption and heterogeneous catalysis

MEMORIA

Para aspirar al grado de

DOCTOR EN CIENCIAS QUÍMICAS

Ana Eva Platero Prats

Instituto de Ciencia de Materiales de Madrid (CSIC)
Madrid - 2011

Ana Eva Platero Prats

New Alkaline-Earth Polymeric Frameworks as green materials for sorption and heterogeneous catalysis

MEMORIA

para aspirar al grado de

DOCTOR EN CIENCIAS QUIMICAS

Dirigida por:

Prof. Dr. Enrique Gutiérrez Puebla

Dr. Natalia Snejko

Instituto de Ciencia de Materiales de Madrid (ICMM-CSIC)

UNIVERSIDAD AUTÓNOMA DE MADRID
Facultad de Ciencias
Departamento de Química Inorgánica
Año 2011

Summary

Metal-Organic Frameworks (or MOFs) are porous organic-inorganic crystalline materials in which the metallic centers are joined through organic ligands *via* coordination bonds to give frameworks with different dimensionalities. Thus, through the wide choice of metals, and the unlimited choice and design of ligands, a broad range of **properties** (magnetic, electric, optical, and catalytic, among others) might be rationally incorporated into such materials.

The increasing number of MOFs reported in the last years has offered a rich variety of new structural types to materials science. In this sense, **Crystallography** has played an important role, not only in the structure determination of novel materials, but also in the process of finding consistent strategies to classify them, then to point out possible structural tendencies and, as a result of the former, to possibly predict structures in the design of new materials. In this context, the role of new **topological approaches** in the crystal chemistry is becoming more and more important.

The work presented in this thesis is focused on the obtaining of new MOFs using **alkaline-earth elements** as metal centers. The use of alkaline-earth metals to synthesize new MOFs remains a scientific challenge, mainly due to the inherent difficulties concerning their formation/crystallization and the variable coordination environments that these elements exhibit. In spite of all this, the development of alkaline-earth MOFs could represent a comparatively cheap, nontoxic and green alternative to conventional MOFs.

Concerning the organic ligands used in this work, two different ligand functionalities have been evaluated: carboxylate and sulfonate groups.

With regard to carboxylate ligands, flexible dipodal linkers have been considered to obtain new alkaline-earth MOFs. The used linker 4,4'-hexafluoroisopropylidene)*bis*(benzoic) acid (**$H_2L_{(1)}$**) has been utilized before in our research group to synthesize both transition metals and rare-earth elements MOFs. These previous studies have shown that this flexibility can induce interesting materials phenomena like polymorphism, as well as the formation of a wide variety of networks with unexpected topologies. Continuing in this way, the role that play nonbinding $-CF_3$

groups present in $\mathbf{H_2L_{(1)}}$ in the formation of some selected frameworks has been studied, compared to its counterpart with nonbinding –H groups (diphenylmethane-4,4'-dicarboxylic acid, $\mathbf{H_2L_{(2)}}$). It is worth highlighting that most of the materials obtained using these linkers have shown a good performance as heterogeneous catalysts in hydrogenation and hydrosilylation reactions under mild conditions. In addition, a flexible calcium MOF with selective sorption properties (both in liquid and gas phases) has been obtained using $\mathbf{H_2L_{(1)}}$. This material exhibits a reversible phase transition related to the remove/uptake of guest molecules that has been studied in detail. These results are presented in **Chapter 4**.

Continuing with the flexible dicarboxylate $\mathbf{H_2L_{(1)}}$ ligand, in the case of Mg, an exhaustive study was performed to elucidate the effect of the introduction of nitrogenated chelating ancillary ligands in the formation of different supramolecular frameworks. Additionally, computational studies were performed to show the relative energy for the five obtained networks, allowing a better understanding of the processes that govern the formation of these Mg MOFs. These results are presented in **Chapter 5**.

Finally, the other part of this work is based on the use of an anthraquinone derivate of disulfonate ligand (anthraquinone-2,6-disulfonate, **2,6-AQDS**) to obtain new alkaline-earth MOFs. This rigid disulfonate linker has been before proved in our research group to be a suitable linker to obtain materials with high thermal stability. Moreover, as sulfonate groups can exhibit a wide variety of coordination modes, the use of this ligand can also lead to the formation of different alkaline-earth coordination environments. In this sense, novel materials with Mg, Ca, Sr and Ba have been successfully synthesized and tested as heterogeneous catalysts in hydrogenation and hydrosilylation reactions. These results are presented in **Chapter 6**.

Resumen

Los **Metal-Organic Frameworks** (o MOFs) son materiales organo-inorgánicos cristalinos y porosos en los que centros metálicos coordinan con ligandos para dar lugar a estructuras con redes de diferente dimensionalidad. Teniendo en cuenta tanto el gran número de centros metálicos que pueden ser utilizados, así como el casi ilimitado potencial del diseño de nuevos ligandos orgánicos, una amplia variedad de propiedades (magnéticas, eléctricas, ópticas y catalíticas, entre otras) pueden ser introducidas racionalmente en dichos materiales.

Así, el cada vez mayor número de nuevos MOFs publicados durante los últimos años, ha provisto a la Ciencia de Materiales de una gran variedad de nuevos tipos estructurales. En este sentido, la Cristalografía ha jugado un papel crucial, no sólo en cuanto a la determinación estructural de nuevos materiales, sino también en el proceso de clasificación, establecimiento de tendencias y, gracias a ello, la posible predicción de estructuras hacia el diseño de nuevos materiales. En este contexto, el uso de enfoques topológicos en la Cristaloquímica está siendo cada vez más extendido.

El trabajo presentado en esta tesis se centra en la obtención de nuevos MOFs usando elementos alcalinotérreos como centros metálicos. El uso de metales alcalinotérreos para sintetizar nuevos MOFs se considera un reto científico, debido tanto a las dificultades que presentan estos metales en los procesos de formación/cristalización, como a la variabilidad en sus entornos de coordinación. A pesar de todo esto, el desarrollo de MOFs alcalinotérreos podría representar una alternativa barata, no-tóxica y *verde* a los MOFs convencionales.

Respecto a los ligandos orgánicos utilizados en este trabajo, se han estudiado el uso de dos funcionaliades distintas: grupos carboxilato y sulfonato.

En cuanto a los ligandos carboxilatos, se ha estudiado la obtención de nuevos MOFs alcalinotérreos basados en ligandos flexibles de tipo dipodal. Así, uno de los ligandos utilizados ha sido el 4,4'-hexafluoroisopropylidene)*bis*(benzoic) acid (**$H_2L_{(1)}$**), el cual ha sido anteriormente estudiado en nuestro grupo de investigación para la síntesis de MOFs basados tanto en metales de transición como en tierras raras. Estos estudios previos mostraron que la flexibilidad que posee este ligando puede dar lugar a

interesantes fenómenos en materiales como es el caso del polimorfismo, así como a la formación de una gran variedad de redes con topologías poco frecuentes. Siguiendo con esta vía de trabajo, en esta tesis se ha estudiado el papel que juegan los grupos sustituyentes no coordinantes en estos ligandos, comparando el comportamiento de $\mathbf{H_2L_{(1)}}$ (grupos -CF_3) con su homólogo con grupos –H (diphenylmethane-4,4'-dicarboxylic acid, $\mathbf{H_2L_{(2)}}$), para la obtención de diferentes redes. Cabe destacar que la mayoría de los compuestos derivados de estos ligandos han mostrado interesante propiedades como catalizadores heterogéneos en procesos de hidrogenación e hidrosililación. Además, se ha sintetizado un MOF de calcio flexible basado en $\mathbf{H_2L_{(1)}}$ con interesantes propiedades en procesos de sorción selectiva, tanto en fase gas como en liquida. Este material presenta una transición de fase reversible relacionada con la pérdida/absorción de moléculas huésped que se ha estudiado de manera detallada. Estos resultados se presentan en el **Capítulo 4**.

Siguiendo con el ligando dicarboxilato flexible $\mathbf{H_2L_{(1)}}$, en el caso de Mg, se ha llevado a cabo un estudio exhaustivo con el objetivo de elucidar el efecto que tiene la introducción de ligandos nitrogenados auxiliares de tipo quelato en la formación de diferentes redes supramoleculares. Este trabajo se ha completado con estudios computacionales, con el objetivo de determinar las energías relativas de las redes obtenidas, permitiendo así una mayor comprensión de los procesos que gobiernan la formación de estos MOFs de Mg. Estos resultados se presentan en el **Capítulo 5**.

Finalmente, se ha explorado el uso de un ligando disulfonato derivado de la molécula antraquinona (anthraquinone-2,6-disulfonate, **2,6-AQDS)**, para la obtención de nuevos MOFs alcalinotérreos. El uso de este ligando rígido ha dado lugar anteriormente a materiales con alta estabilidad térmica en nuestro grupo de investigación. Además, debido a los diferentes modos de coordinación de los grupos sulfonato, el uso de **2,6-AQDS** puede dar lugar a diferentes entornos de coordinación. En este sentido, se ha conseguido sintetizar nuevos MOFs basados en **2,6-AQDS** para Mg, Ca, Sr y Ba. Además, estos materiales han sido evaluados como catalizadores heterogéneos en procesos de hidrogenación e hidrosililación. Estos resultados se presentan en el **Capítulo 6**.

CONTENTS

Chapter 1

Introduction

1.1.

Metal-Organic Frameworks Materials

1.1.1. Background

At the end of the last century, solid state chemistry and materials science provided fascinating solids that gave rise to significant advances in solid state science: high T_c superconductors[1,2] in the 1980s and fullerenes[3] and giant magneto resistive materials[4] in the 1990s. In addition to these new important families of materials, the domain of porous solids is historically much older.

The past decade has seen a number of significant breakthroughs in the design of novel porous materials, driven by the rapid growth of emerging applications, such as energy conversion and storage, environmentally friendly catalysis and drug delivery.[5,6] This growth was firstly represented by zeolites, alumino- and gallophosphates. In these materials the frameworks are purely inorganic, and the porosity is generated by the use of the organic molecules which act as templates. More recently, a new class of porous hybrid organic-inorganic materials appeared. In them, the metallic centers are joined through organic ligands *via* coordination bonds to give rise to one-dimensional (1D), two-dimensional (2D) or three-dimensional (3D) frameworks.[7] This kind of compounds has been named in different ways: *metal-organic frameworks*, *coordination polymers*, *hybrid organic-inorganic materials* and *organic zeolite analogues*. Even though an obvious overlap can be often observed in the literature, each term carries its own connotation regarding which compounds it encompasses. In this sense, some elegant attempts have been made in order to elucidate their definitions.[8,9]

The term *coordination polymer* is undoubtedly the most nebulous; it simply signifies the extended connection of metal and ligand monomers through coordination bonds with no regard towards the final structure or morphology. However, the use of the term *metal-organic framework* implies the following attributes: strong bonding providing robustness, linking units that are available for modification by organic synthesis, and a geometrically well-defined structure. The latter property further implies

that these solids should be highly crystalline, an important criterion for the precise establishment of structure-properties relationships.

1.1.2. Synthesis through design

The interest in this new class of materials arises from the high versatility that they offer, with many potential applications coming from their inherent properties. This versatility is due to the wide range of possibilities that the combination of two main components of the MOFs offers: the metallic centers (connectors) and the organic ligands (linkers). In principle, through the wide choice of metals, and the unlimited choice and design of ligands, a broad range of properties (magnetic, electric, optical, and catalytic, among others) might be rationally incorporated into such materials.

Concerning the rational MOF synthesis, several considerations must be taken into account. On one hand, the building blocks must be carefully chosen as their properties can be retained and exhibited by the product material. On the other hand, it is worth highlighting that the building units connectivity determines largely the properties of a MOF (for instance, acentricity for non-linear optical applications or the presence of large channels). Consequently, MOF synthesis not only requires the selection and/or preparation of the desired modules, but also a good knowledge about how they will be assembled in the final solid.

In this sense, one important consequence that arises from the ever-increasing collection of crystalline structures of MOFs materials, is the opportunity to search for trends in connectivity, and to identify the principles that govern the design of MOFs: that is, to *predict* structures.

In order to aid in this prediction process, the concept of secondary building units (SBUs), which is used to describe conceptual fragment of zeolites, is adopted. In the field of MOFs, the number of SBUs and their geometries are varied, and the control of the synthesis conditions can allow obtaining them. In most of the cases, these SBUs are formed by aggregates of metal atoms with geometrically well-defined coordination environments. The successful design of rigid frameworks based on SBUs is the basis for both the *Scale Chemistry*[10] and the *Reticular Chemistry*.[11]

1.1.3. Linkers nature: variety is the spice of life

The organic constituents (ligands) represent an important point to be discussed. Generally speaking, linkers in MOFs are multidentate organic molecules that act as spacers between metallic centers. One important point regarding the linker nature is the type of **functional groups** present in the ligand molecule, which are the linkage points to the metal ions.

- Traditionally, **cyano-** and **amino-** derivatives have been extensively employed, with nitrogen atoms coordinated to metal centers. Even more extensively used are the **carboxylate** (-CO_2) functional groups, which coordinate to metal centers *via* their oxygen atoms. Between these two types of functional groups, some differences that derive from their inherent chemical properties can be highlighted. Probably the most important one lies in the variety of **coordination modes** than can exhibit the carboxylate groups (**Figure 1.1**), instead of the η^1 coordination mode typically found in cyano- and amino-derivates. In addition, another interesting feature of carboxylate groups concerns their **geometry**: the C-CO_2 bond adopts different torsion angles when the oxygen atoms are coordinated to metal centers.

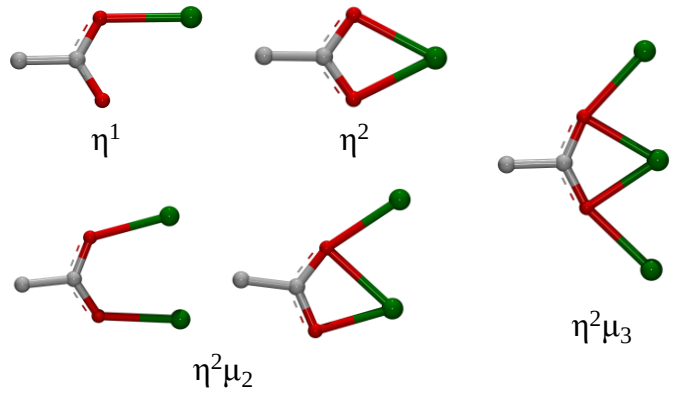

Figure 1.1. Depiction of coordination modes that can exhibit carboxylate groups. In the case of $\eta^2\mu_2$, both the bridge (left) and chelate-bridge (right) modes are shown.

- The third main group is based on **phosphonate** ligands; there are three points that have likely hindered broader proliferation of their study as MOFs linkers, relative to carboxylate. The first is the predisposition of molecular metal phosphonates to a dense layered motif that makes forming porous materials a challenge. The second reason is that the growth of single crystals with phosphonates is more difficult as they

often precipitate rapidly as less ordered, insoluble phases. The final point is that, again relative to other studied ligating groups (cyano- and amino-groups, carboxylates), the coordination chemistry of phosphonates is less predictable owing to possible coordination modes and three possible states of protonation.

- Another candidate is the **sulfonate** group (-SO_3). Sulfonate groups have been studied considerably less than other classes of functional groups but for different reasons than those explained for phosphonates.[12] On one hand, coordination ability of sulfonate anions is relatively low. This fact facilitates the formation of crystalline products but, oftentimes, the networks are not sufficiently robust to sustain permanent pores. On the other hand, and as it occurs in the case of phosphonates, the spherical ligating ability of a sulfonate does again make *a priori* coordination predictions a challenge, giving rise to a high number of possible **coordination modes** (**Figure 1.2**).

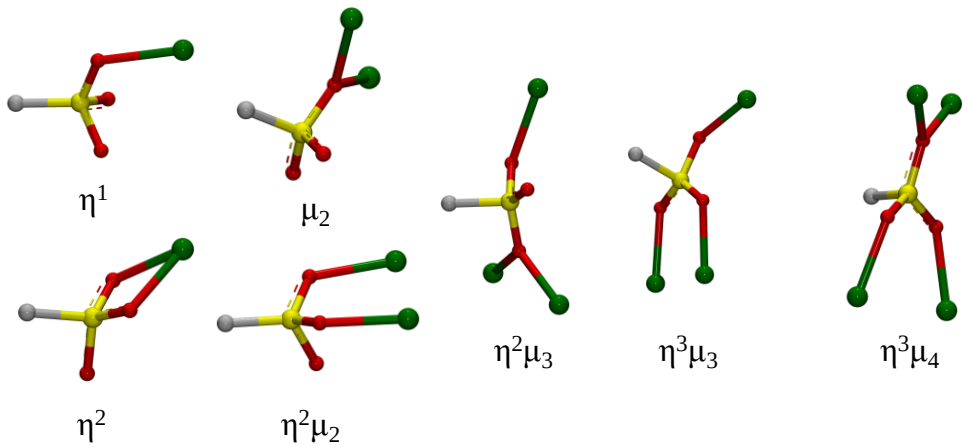

Figure 1.2. Representation of some possible coordination modes that can exhibit sulfonate groups.

- Finally, it is worth mentioning that there are also examples of MOFs based on ligands having mixed functional groups, as well as examples in which more than one type of ligands are employed (for instance, pyridine derivatives and carboxylate ligands).

An additional important point regarding the linker nature is its **geometry**, which has an obvious influence on the obtaining of interesting porous frameworks. This is probably one of the aspects concerning MOFs design on which organic chemistry has had more influence.

- One of the most accepted MOFs synthetic strategy is probably the use of **longer linkers** that can allow the presence of larger pores in the framework (**Figure 1.3**). However, due to the fact that long linker nets frequently give rise to interpenetrated frameworks, the anticipated pores size can be considerably reduced.

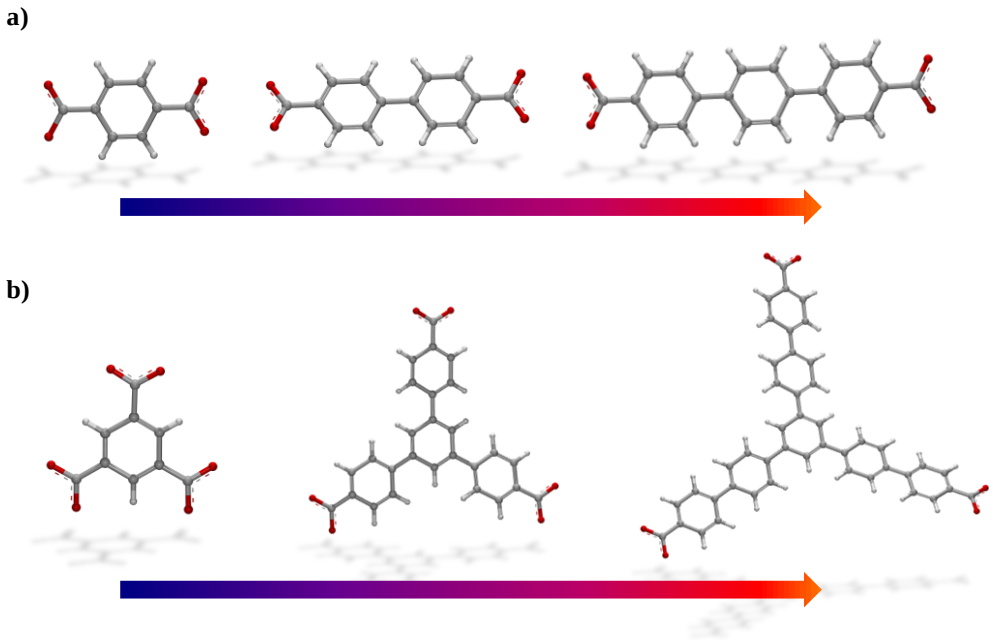

Figure 1.3. 1,4-benzedicarboxylate **(a)** and 1,3,5-benzenetricarboxylate **(b)**, and two longer linkers that can be derived from each one of these ligands.

- Another potential strategy to design new MOFs is the use of **flexible** ligands (**Figure 1.4**). This is an interesting point to be considered, mainly due to the fact that this flexibility can induce exciting materials phenomena, like polymorphism and reversible phase transitions. In addition, as the geometrical conformation of the linker can be modified by controlling the synthesis conditions, a wide variety of structural types based on the same or related ligands can be obtained.

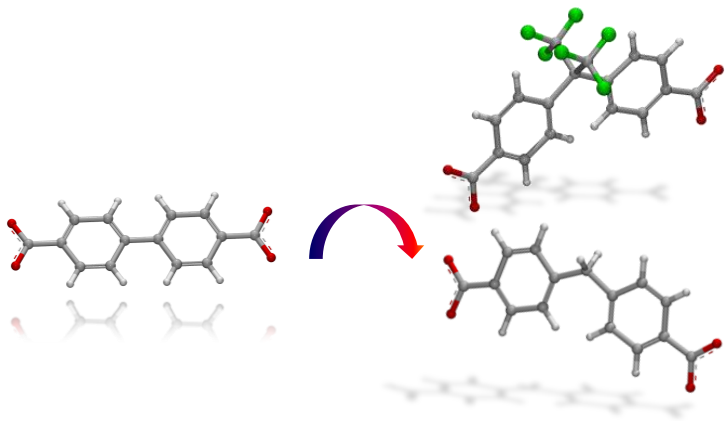

Figure 1.4. Depiction of the biphenyldicarboxylate, which is a typical rigid linker used in the MOFs synthesis, together with two related flexible ligands that have been used in this thesis (4,4'-hexafluoroisopropylidene)bis(benzoate) (right up) and diphenylmethane-4,4'-dicarboxylate) (right down).

1.1.4. Alkaline-Earth MOFs

The metal centers must undoubtedly be considered as important building constituents in MOFs, due to the fact that they transfer their chemical and physical inherent properties to the final material.

By far, **transition metals** are the most employed in the synthesis of MOFs. The well-defined coordination environments that exhibit these metals make them more suitable for their use in rational synthesis of these materials. More recently, synthetic efforts have been made in order to obtain MOFs containing **rare-earth elements**. These elements, which have been considered for long time as unsuitable due to their variable coordination environments, have given rise to interesting materials which possess unexpected optical and catalytic properties.[13,14] Certainly, the successful demonstration of the fact that other non-conventional metals can be used to synthesize MOFs opened up new horizons in this field.

One of the main disadvantages related to rare-earth elements is their relatively high price. In this sense, other "*low cost*" possibilities have to be considered. However, the use of **alkaline-earth metals** to synthesize new MOFs remains still a scientific challenge. Several reasons can explain the small number of alkaline-earth MOFs that are reported up to the moment: on one hand, the inherent difficulties concerning the formation and crystallization of alkaline-earth MOFs;[15]on the other hand, as it occurred

with rare-earth elements, their variable coordination environments make it more difficult a rational design. In spite of all this, alkaline-earth MOFs could represent a comparatively cheap, nontoxic and green alternative to conventional MOFs.

During the last years, it seems that the use of alkaline-earth metals to prepare MOFs have attracted the interest of scientific community, above all in the case of calcium and magnesium elements. However, the number of alkaline-earth MOFs reported in the literature still remains very limited.[16-28] In order to emphasize the small number of obtained alkaline-earth MOFs, we performed a detailed search in the Cambridge Structural Database (CSD) to find the 3D alkaline-earth frameworks reported up to the moment. The main results are discussed in the following.

The first conclusion that can be drawn from this exhaustive search is the small number of 3D alkaline-earth frameworks published up to the moment: 66 (Ba), 35(Sr), 40(Ca) and 40(Mg) (**Figure 1.5**). In order to do not get lost in numbers, these analyses were focussed on frameworks with dicarboxylate and disulfonate ligands, as those are the kinds of ligands that have been used in this work.

Alkaline-Earth dicarboxylates. In **Figure 1.5a** there are shown all the alkaline-earth containing crystal structures found in the CSD which possess 3D networks. Among these structures, and for each alkaline-earth metal, those frameworks whose organic component is only based on C, H and O were selected (**Figure 1.5b**). Finally, among the few structures found for barium (20), strontium(10), calcium(17) and Mg(19), those exclusively based on dicarboxylate ligands were finally chosen and studied more in detail (**Figure1.5c**).

Concerning these dicarboxylate alkaline-earth frameworks, although the majority is based on aliphatic ligands, some nice examples should be highlighted. Firstly, it is worth mentioning the barium 1,4-benzedicarboxylate crystal structure reported in 1998 by Williams *et al.*[29] Nevertheless, the most interesting examples probably come from calcium and magnesium metals. In the case of Ca, Férey and co-workers reported two frameworks obtained using 2,6-naphthalenedicarboxylate and 4,4'-biphenyldicarboxylate ligands.[26] Finally, regarding magnesium, although the corresponding crystal structure using 4,4'-biphenyldicarboxylate[30] ligand has been reported, some more detailed works have derived from the use of the well-known 1,4-benzedicarboxylate ligand.[18,31]

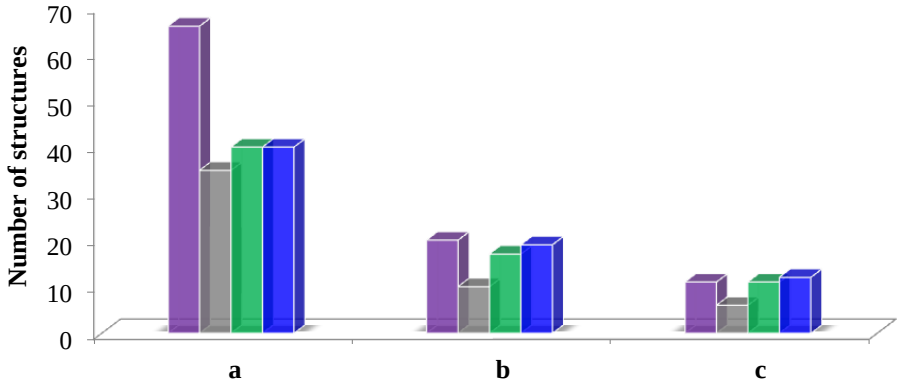

Figure 1.5. a) 3D Alkaline-Earth based frameworks reported in the literature and **b)** those based on the corresponding metal and C, H and O elements. **c)** Alkaline-Earth dicarboxylate frameworks. (Barium: violet, Strontium: grey, Calcium: green and Magnesium: blue).

Alkaline-Earth disulfonates. Another part of the work carried out in this thesis consists of the obtaining of new alkaline-earth MOFs using disulfonate linker. Although the number of alkaline earth dicarboxylates is quite limited, even less examples of networks based on sulfonate ligation have been reported.[32-36] Emphasizing this fact, few systematic works have shown that in the case of sulfonates ligands, alkaline and alkaline-earth ions, being hard metal ions, remain highly hydrated and typically produce zero or one-dimensional structures.[33,34]

The same kind of analysis above discussed, was also carried out for the disulfonate based materials reported in the literature up to moment. Firstly, in **Figure 1.6a** there are shown all the alkaline-earth structures which possess 3D networks reported in the literature. Among these structures, and for each alkaline-earth metal, only those networks based on C, H, O and S elements and the corresponding alkaline-earth metal ion were selected (**Figure 1.6b**). It is worth mentioning that, in the case of magnesium, no structures are reported with this chemical composition. Finally, among the few structures found for barium (8), strontium (3) and calcium (1), those only based on disulfonate ligands were selected and studied in detail (**Figure 1.6c**). On one hand, note that in the case of calcium no disulfonates compounds with 3D networks have been reported up to the moment. Among these works, it is worth highlighting the works of Cai *et al.*[32,36] in which the authors present a systematic work showing the coordination nature of 1,5-naphthalenedisulfonate ligand (1,5-NDS) with different Group 1 and Group 2 metals. In these studies, different frameworks have been reported based on Ba^{+2}, and Sr^{+2} ions. The authors also showed the tendency to form solvated

metal centers species in the case of Mg^{+2} and, therefore, zero dimensional compounds.[32] Thus, even though there are other examples in the use of ligands with both sulfonate and hydroxyl or carboxylate groups,[33,34] the 1,5-NDS ligand represents the unique linker used, up to the moment, to synthesize alkaline-earth disulfonate frameworks.

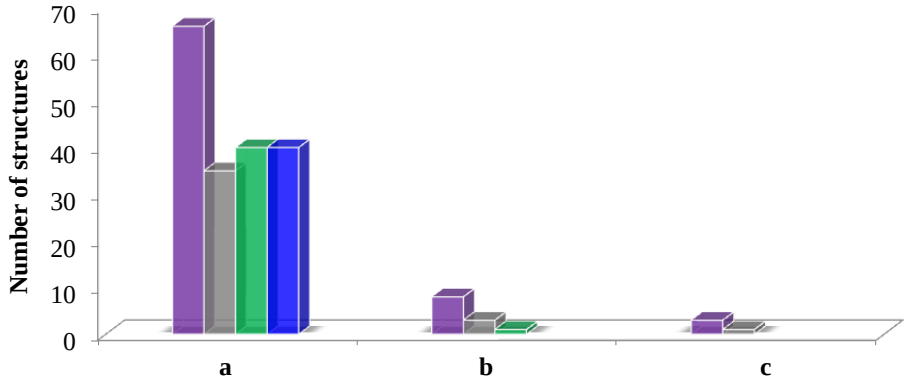

Figure 1.6. a) 3D Alkaline-Earth based frameworks reported in the literature and **b)** those based on the corresponding metal and C, H, O and S elements. **c)** Alkaline-Earth disulfonate frameworks. (Barium: violet, Strontium: grey, Calcium: green and Magnesium: blue).

1.1.5. MOFs as heterogeneous catalysts

MOFs share advantages and some inconveniences of molecular and solid state catalysts. In this sense, the existence of porosity in these materials together with their relative **structural analogy with zeolites** (uniform pores and cavity sizes), can explain the efforts that the scientific community have made during the last years to demonstrate the potential application of MOFs as heterogeneous catalysts.

In spite of similarities between MOFs and zeolites, they also differ in important features. Nevertheless, it is probably in their differences, where the catalytic interest of MOFs lies in. Firstly, as MOFs´ composition includes organic linkers, they can be synthesised in much greater **chemical variety** than zeolites. However, particularly the presence of this organic component makes the MOFs chemical stability lower than that of zeolites. Secondly, the limited **thermal stability** observed in some MOFs, which is based on the strong metal-ligand interactions present in these materials, is significantly lower and cannot be compared with that of purely inorganic zeolites.

Taking into account the above mentioned considerations, nowadays it is difficult to imagine that the performance of MOFs can surpass or even be close to that

of zeolites in typical catalytic applications, like oil refining and petrochemical processes. However, MOFs can compete or even overcome the activity of zeolites in **liquid-phase reactions**, particularly those under mild conditions. It is worth highlighting the use of MOFs in **high-value-added reactions** (production of fine chemicals, delicate molecules, individual enantiomers), that can be accomplished under these conditions.

The catalytic activity observed in MOFs can be related to three different components: the metal center, the organic ligand and the pore system. Concerning those reactions in which the metallic component play a catalytic role, some of the main catalytic processes in which the use of MOFs has been investigated are: *hydrogenation reactions*, *oxidation of organic substances*, *CO oxidation to* CO_2, *carbonyl cyanosilylation*, *hydrodesulfuration* and *photocatalysis*.[37,38]

Regarding to the **hydrogenation** reactions, which are among the catalytic processes studied in this thesis, some results reported in the literature have to be mentioned. Firstly, some earlier works have proved the catalytic performance of an indium MOF in the hydrogenation of nitroaromatic compounds such as the 2-methylnitro-naphthalene substrate, under mild conditions (313 K, 4 atm H_2).[39] Some years later, the use of a Pd-MOF as heterogeneous catalyst in the hydrogenation of 1-octene was also demonstrated under similar conditions (308 K, 2 atm H_2).[40] Certainly, these results showing the good catalytic behaviour of some MOFs, open an alternative to traditional precious metal-based hydrogenation catalysts.

Additionally, other way to obtain catalytically active MOFs is *via* a post-synthesis modification. Thus, IRMOF-3[41] can be treated with an Au(III) salt producing an Au(III) complex wall lined MOF, which has been tested with good conversion in 1,3-butadiene hydrogenation reaction under rather mild conditions (1 atm H_2, 403 K).[42]

1.1.6. Selective gas adsorption and separation in MOFs

Currently, industrial methods for selective gas adsorption rely heavily on cryogenic as well as membrane- and adsorption-based techniques. In adsorption-based separation, commonly used adsorbents include zeolites, molecular sieves, carbon nanotubes, aluminosilicates and silica gel. All materials for selective gas adsorption are chosen based on two main criteria: **(1)** the **adsorption capacity** of the adsorbent and **(2)** the **selectivity** of the adsorbent for an adsorbate. In this context, MOFs are very

promising candidates for selective gas adsorption, which can give rise to their use in gas purification processes.

The numerous works reported during the last years in selective gas adsorption and separation using MOFs[43,44] have allowed to jump into processes of industrial interest. Thus, the research in this field is currently rather focussed on useful gas separations like the separation of alkanes with similar size and from different stream gases. In this context, it is worth highlighting the work reported by Chen *et al.* in which a Zn-MOF is used to separate the components of such alkanes mixture.[45]

More recently, other interesting application such as the separation of CO_2 and CH_4 gases was reported by Couch *et al.* using amino-functionalized aluminium MOF, for which the high affinity of CO_2 molecules for amino groups was proved.[46]

1.2.

Topological analyses in Crystal Chemistry

1.2.1. Background

The increasing number of networked species reported in the last years offers a rich variety of new structural types. More particularly in the field of MOFs, due to the great number of crystal structures reported in the last decades, there is a needed to find consistent strategies to classify them, then to point out possible structural tendencies and, as a result of the former, to possibly predict structures in the design of new materials.

In this context, the role of new topological approaches in the crystal chemistry is becoming more and more used, compared to traditional geometrical methods. While geometrical models represent the crystal structure as a set of points allocated in the space, **topological approaches** take also into account the system of chemical bonds. This system can be naturally described by an infinite periodic graph, which is the theoretical basis of the topological part of modern crystal chemistry.

1.2.2. Simplification process

A correct topological analysis of a given structure lies in the rational simplification of its framework in order to avoid misinterpretations. In fact, this is probably the most important (and interesting) point concerning the topological analyses. The **simplification process** consists of removing all unnecessary elements that have no topological relevance, thus leaving only the essentials, represented by nodes and links.

Rod Packing. Most of the dicarboxylate MOFs exhibit complicated metal-carboxylate chains, which are not trivial to simplify. Certainly, the simplification process of a metallic chain can become subjective and therefore, can give rise to different nets for a given framework. In order to avoid this confusion, O'Keeffe and Yaghi proposed[47] an elegant way to clarify this phenomenon in MOFs describing the metal-carboxylate units as rods which are linked among them *via* the organic units. This is called *rod-packing*. Probably the nicest point that can be found in this work, in which details of the rod simplification process for some typical networks are given, is the consideration of these rods as the inorganic SBUs.

1.2.3. Topological classification of networks

A brief summary of the specific topological terminology used in this thesis is presented in Appendix. More detailed set of definitions is given by Delgado-Friedrichs and O'Keeffe.[48]

One of the main problems that have appeared in the topological simplification of nets lies in the fact that the same net is described with several names and symbols. This problem has increased in the last years, since more and more frameworks appear every day in the literature. In the following, the generally accepted *criteria* used in a variety of structural contexts are explained.

Three-letters code. O'Keeffe and co-workers proposed[49,50] the use of a lower-case three-letters code. In fact, the need of using a universal nomenclature lies in the fact that some networks have been described with many names and symbols during the last years. Note the case of the **srs** net, which is observed for the Si atoms arrangement in the $SrSi_2$ structure. This net has been called (10,3)-a, Laves net, Y*, 3/10/c1, or labyrinth graph of the gyroid surface. The suggested lower-case three-letters code nomenclature is designed in line with the widely accepted upper-case three-letter codes employed for zeolites.[51]

Point Symbol. The assignment of the local topology for 2D or 3D nets is based on the analysis of the *cycles* at the angles of a node. Any two edges at a node define an angle, and with *n*-connected nodes there are [*n*(*n*-1)/2] such angles in a 3D net (but only *n* in a 2D simple layer),[52] for each of which we can find a large number of different circuits of different sizes. A *n*-connected node can be identified by a **Point Symbol**(PS), of the form $A^a.B^b.C^c$..., in which A < B < C < ... and a + b + c ... = *n*(*n*–1)/2, that represents the sizes (A, B, C...) and numbers (a, b, c...) of the "shortest circuits" contained at each angle. Thus for the 4-connected diamond net (**dia**) and for the 6-connected primitive cubic lattice (**pcu**), the PS are 6^6 and $4^{12}.6^3$, respectively (**Figure 1.7**). For multinodal nets, the corresponding PS is grouped according to the multiplicity of the node in the unit cell.

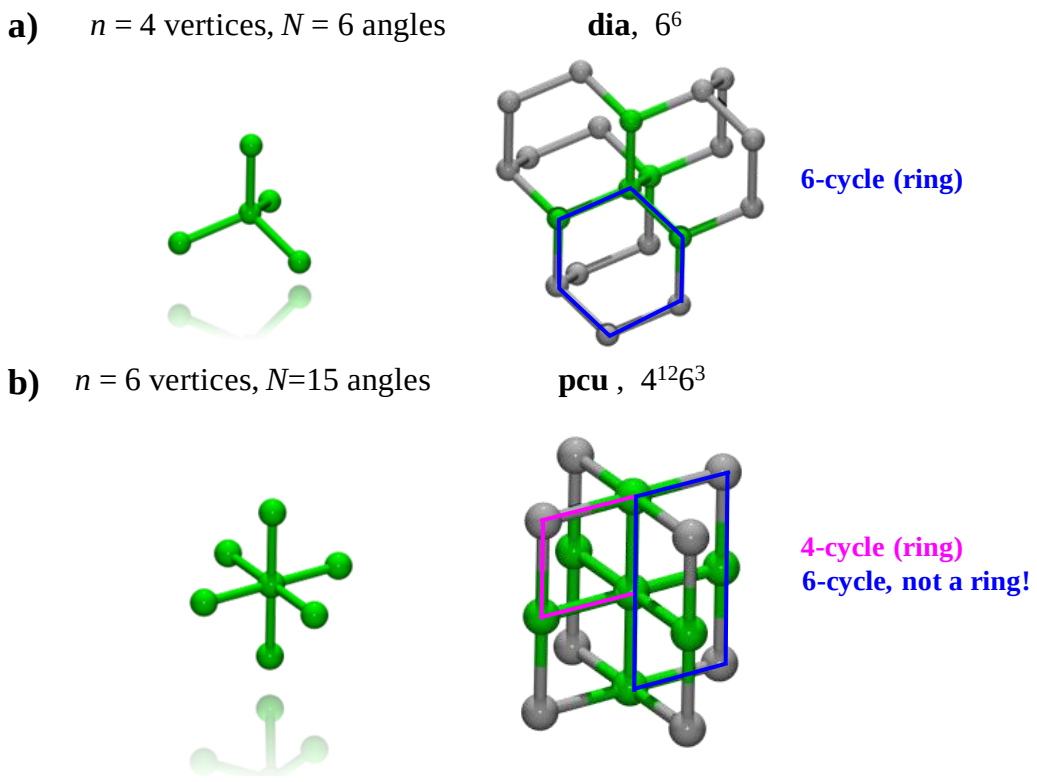

Figure 1.7. Depiction of the Point Symbol definitions for: **a) dia** net and **b) pcu** net.

Vertex Symbol and Coordination Sequence. The PS is extensively used, but it is not sufficient to identify a net. In fact, it was Wells who early pointed out the

ambiguity of this classification.[53-55] Some well-known nets such as the **srs** and **ths**, which describe the arrangement of Si atoms in $SrSi_2$ and $ThSi_2$ phases, respectively, have the same PS: 10^3. In this context and to distinguish nets with the same PS, the concept of **Vertex Symbol** (VS) was introduced. The VS is described as $A_a.B_b.C_c...$, in which A < B < C < ... and a + b + c ... = $n(n–1)/2$, that represents the sizes (A, B, C...) and numbers (a, b, c...) of the "smallest ring" at an angle.

Thus, taking up again the 3-connected nets above mentioned, the **srs** net has five 10-rings at each angle and therefore its VS is $10_5.10_5.10_5$. However, in the case of the **ths** net, with two, four and four 10-rings at each angle, the VS is $10^2.10^4.10^4$. In the case of 4-connected nets there are six angles at a node. The diamond net (**dia**) with two 6-rings at each angle has VS = $6_2.6_2.6_2.6_2.6_2.6_2$. However, not all the angles of a 4-connected net necessarily possess rings. When there is not a ring an asterisk is inserted in the VS. Thus for the 4–connected **cds** net the Vertex Symbol is $6.6.6.6.6_2.*$.

The main problem that lies in the use of the VS concerns the analyses of nets with higher connectivity. Due to the fact that the number of angles increases as the square of the coordination number, the VS representation easily becomes something unmanageable. For instance, the VS for the 6-coordinated **pcu** net is 4.4.4.4.4.4.4.4.4.4.4.*.*.*.*.

Unfortunately, the VS is not sufficient either to identify a net. For example **dia** and **lon** nets have the same VS = $6_2.6_2.6_2.6_2.6_2.6_2$ and, therefore, other descriptors must be considered. It is then necessary to define the *Coordination Sequence* (CS(k))[56] of a node, which is defined as a sequence of numbers in which the k^{th} term is the number of nodes in "shell" k that are connected to nodes in "shell" k – 1. It is worth mentioning that CS is usually computed up to k = 10.

An appropriate way of unequivocal classification of nets consists of the assignment of both the VS and CS for each node of a net. This can be computationally performed using *TOPOS 4.0 Pro* software,[57] which gives VS and CS for each crystallographycally independent nodes of a net.

1.2.4. Tiling

The tile description of nets is based on the combinatorial *tiling theory*.[58,59] The tiles are generalized polyhedra (cages), which generate the entire structure when packed together. For each periodic net there are many possible tilings but a unique type called *natural tiling*.[60-63] For instance, the natural tiling for a **pcu** net can be described as the packing of cubes with eight vertices and six faces formed by four-membered rings (*natural tile*) which can be symbolized as [4^6] (**Figure 1.8**).

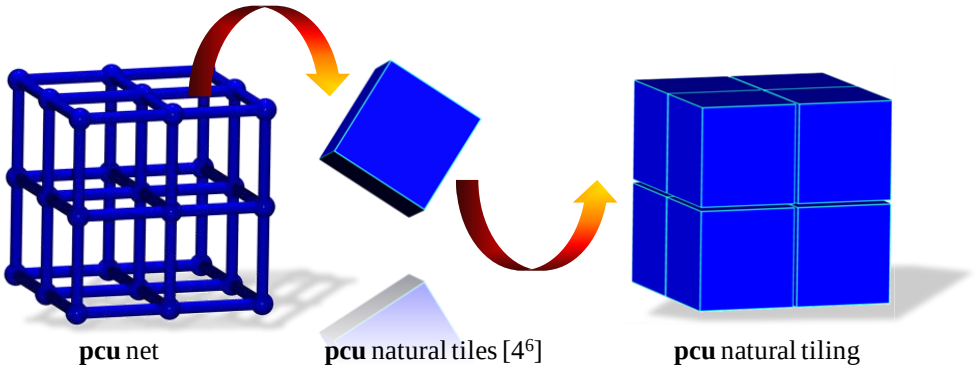

Figure 1.8. Depiction of the two different kinds to topologically described a **pcu** net, showing both the net and the tiling.

References

1. Michel, C.; Raveau, B. *Rev. Chim. Miner.*, **1984**, *21*, 407.

2. Bednorz, A.; Müller, Z. *Physik*, **1986**, *B64*, 187.

3. Kroto, H. *Nature*, **1987**, *329*, 529.

4. Rao, C. N. R.; Raveau, B. In *Colossal magneto Resistance, Charge Ordering and Related Properties of Rare Earth Manganese Oxides*, World Scientific: Singapore, **1998**.

5. Cheetham, A. K.; Férey, G.; Loiseau, T. *Angew. Chem. Int. Ed.*, **1999**, *38(22)*, 3268.

6. Corma, A. *Chem. Rev.*, **1995**, *95(3)*, 559.

7. Dutta, S.; Georgiev, I. G.; MacGillivray, L. R. In *Metal-Organic Frameworks. Design and Application*, John Wiley & Sons, Inc., Hoboken, New Jersey, **2010**.

8. Férey, G. *Chem. Mater.*, **2001,** *13(10)*, 3084.

9. Janiak, C. *Dalton Trans.*, **2003**, (*14)*, 2781.

10. Férey, G. *J. Solid State Chem.*, **2000**, *152*, 37.

11. Yaghi, O. M.; O'Keeffe, M.; Ockwig, N. W.; Chae, H. K.; Eddaoudi, M.; Kim, J. *Nature*, **2003**, *423*, 705.

12. Shimizu, G.K.H.; Vaidhyanathan, R.; Taylor, J.M. *Chem. Soc. Rev.*, **2009**, *38*, 1430.

13. Gándara, F.; Andrés, A. d.; Gómez-Lor, B.; Gutiérrez-Puebla, E.; Iglesias, M.; Monge, M. A.; Proserpio, D. M.; Snejko, N. *Cryst. Growth Des.*, **2008**, *8(2)*, 378.

14. Gándara, F.; Puebla, E. G.; Iglesias, M.; Proserpio, D. M.; Snejko, N.; Monge, M. Á. *Chem. Mater.*, **2009**, *21(4)*, 655.

15. Fromm, K. M. *Coord. Chem. Rev.*, **2008**, *252*, 856.

16. Dincă, M.; Long, J. R.*J. Am. Chem. Soc.*, **2005**, *127(26)*, *9376*.

17. Rood, J. A.; Noll, B. C.; Henderson, K. W. *Inorg. Chem.*, **2006**, *45(14)*, 5521.

18. Davies, R. P.; Less, R. J.; Lickiss, P. D.; White, A. J. P. *Dalton Trans.*, **2007**, *(24)*, 2528.

19. Senkovska, I.; Fritsch, J.; Kaskel, S. *Eur. J. Inorg. Chem.*, **2007**, *(35)*, 5475.

20. Dietzel, P. D. C.; Blom, R.; Fjellvåg, H. *Eur. J. Inorg. Chem.*, **2008**, *(23)*, 3624.

21. Rossin, A.; Ienco, A.; Costantino, F.; Montini, T.; Di Credico, B.; Caporali, M.; Gonsalvi, L.; Fornasiero, P.; Peruzzini, M. *Cryst. Growth Des.*, **2008**, *8*(9), 3302.

22. Mallick, A.; Saha, S.; Pachfule, P.; Roy, S.; Banerjee, R. *Inorg. Chem.*, **2011**, *50(4)*, 1392.

23. deLill, D. T.; Bozzuto, D. J.; Cahill, C. L. *Dalton Trans.*, **2005**, *(12)*, 2111.

24. Birkedal Nielsen, R. K.; Kongshaug, K. O.; Fjellvåg, H. *Solid State Sci.*, **2006**, 8(10), 1237.

25. Volkringer, C.; Loiseau, T.; Férey, G.; Warren, J. E.; Wragg, D. S.; Morris, R. E. *Solid State Sci.*, **2007**, *9*, 455.

26. Volkringer, C.; Marrot, J.; Férey, G.; Loiseau, T. *Cryst. Growth Des.*, **2008**, *8(2)*, 685.

27. Williams, C. A.; Blake, A. J.; Wilson, C.; Hubberstey, P.; Schröder, M. *Cryst. Growth Des.*, **2008**, *8(3)*, 911.

28. Miller, S. R.; Horcajada, P.; Serre, C. *CrystEngComm*, **2010**, *13(6)*, 1894.

29. Lo, S. M. F.; Chui, S. S. Y.; Williams, I. D. *Acta Crystallogr.*, **1998**, *C54(12)*, 1846.

30. Liu, H. K.; Peng, X. W.; Lin C. H. *Acta Crystallogr.*, **2009**, *E65*, m237.

31. Kaduk, J. A. *Acta Crystallogr.*, **2002**, *B58(5)*, 815.

32. Cai, J.; Chen, C.-H.; Liao, C.-Z.; Feng, X.-L.; Chen, X.-M. *ActaCrystallogr.*, **2001**, *B57*(4), 520.

33. Côté,A.C.; Shimizu, G.K.H. *Chem. Eur. J.*, **2003**, *9 (21)*, 5361.

34. Kennedy, A. R.; Kirkhouse, J. B. A.; McCarney, K. M.; Puissegur, O.; Smith, W. E.; Staunton, E.; Teat, S. J.; Cherryman, J. C.; James, R. *Chem. Eur. J.*, **2004**, *10(18)*, 4606.

35. Huo, L.-H.; Gao, S.; Xu, S.-X.; Zhao, H.; Ng, S. W. *Acta Crystallogr.*, **2004**, *E60(9)*, m1240.

36. Gao, S.; Zhu, Z.-B.; Huo, L.-H.; Ng, S. W. *Acta Crystallogr.*, **2005**, *E61(3)*, m528.

37. Lee, J.; Farha, O. K.; Roberts, J.; Scheidt, K. A.; Nguyen, S. T.; Hupp, J. T. *Chem. Soc. Rev.*, **2009**, *38(5)*, 1450.

38. Corma, A.; García, H.; Llabrés i Xamena, F. X. *Chem. Rev.*, **2010**, *110(8)*, 4606.

39. Gómez-Lor, B.; Gutiérrez-Puebla, E.; Iglesias, M.; Monge, M. A.; Ruiz-Valero, C.; Snejko, N. *Inorg. Chem.*, **2002**, *41(9)*, 2429.

40. Llabrés i Xamena, F. X.; Abad, A.; Corma, A.; Garcia, H. *J. Catal.*, **2007**, *250(2)*, 294.

41. Eddaoudi, M.; Kim, J.; Rosi, N.; Vodak, D.; Wachter, J.; O'Keeffe, M.; Yaghi, O. *Science*, **2002**, *295*, 469.

42. Zhang, X.; Llabrés i Xamena, F. X.; Corma, A. *J. Catal.*, **2009**, *265(2)*, 155.

43. Ma, S.; Wang, X.-S.; Collier, C. D.; Manis, E. S.; Zhou, H.-C. *Inorg. Chem.*, **2007**, *46(21)*, 8499.

44. Dincă, M.; Yu, A. F.; Long, J. R. *J. Am. Chem. Soc.*, **2006**, *128(27)*, 8904.

45. Chen, B.; Liang, C.; Yang, J.; Contreras, D. S.; Clancy, Y. L.; Lobkovsky, E. B.; Yaghi, O. M.; Dai, S. *Angew. Chem. Int. Ed.*, **2006**, *45(9)*, 1390.

46. Couck, S.; Denayer, J. F. M.; Baron, G. V.; Rémy, T.; Gascon, J.; Kapteijn, F. *J. Am. Chem. Soc.*, **2009**, *131(18)*, 6326.

47. Rosi, N. L.; Kim, J.; Eddaoudi, M.; Chen, B.; O'Keeffe, M.; Yaghi, O. M. *J. Am. Chem. Soc.*, **2005**, *127*(5), 1504.

48. Delgado-Friedrichs, O.; O'Keeffe, M. *J. Solid State Chem.*, **2005**, *178*, 2480.

49. Delgado Friedrichs, O.; O'Keeffe, M.; Yaghi, O. M. *Acta Crystallogr.*, **2003**, *A59*, 22.

50. Delgado Friedrichs, O.; O'Keeffe, M.; Yaghi, O. M. *Acta Crystallogr.*, **2003**, *A59*, 515.

51. Baerlocher, C.; Meier, W. M.; Olsen, D. H. *Atlas of Zeolite Framework Types*, Elsevier, Amsterdam, **2001**

52. O'Keeffe, M.; Hyde, B. G. *Phil. Trans. R. Soc. London*, **1980**, *295A*, 553.

53. Wells, A.F. *Three-dimensional Nets and Polyhedra*, Wiley, New York, **1977**.

54. Wells, A.F. *Further Studies of Three-dimensional Nets*, ACA monograph 8, **1979**.

55. Wells, A. F. *Structural Inorganic Chemistry*, 5th ed., Oxford University Press: Oxford, **1984.**

56. O'Keeffe, M.; Hyde, B. G. *Crystal Structures I: Patterns and Symmetry*, Washington, Mineral. Soc. Am. **1996**.

57. Blatov, V. A. *IUCr CompComm Newsletter*, **2006**, *7*, 4.

58. Delgado-Friedrichs, O.; Dress, A. W. M.; Huson, D. H.; Klinowsky, J.; Mackay, A. L. *Nature*, **1999**, *400*, 644.

59. O'Keeffe, M. *Nature*, **1999**, *400*, 617.

60. Delgado Friedrichs, O.; O'Keeffe, M.; Yaghi, O. M. *Acta Crystallogr.*, **2003**, *A59*, 22.

61. Delgado Friedrichs, O.; O'Keeffe, M.; Yaghi, O. M. *Acta Crystallogr.*, **2003**, *A59*, 515.

62. Delgado Friedrichs, O.; O'Keeffe, M.; Yaghi, O. M. *Solid State Sci.*, **2003**, *5*, 73.

63. Delgado Friedrichs, O.; O'Keeffe, M. *Acta Crystallogr.*, **2005**, *A61*, 358.

Chapter 2

Objectives

The objective of the present work is the **preparation of new alkaline-earth metal-organic frameworks and testing them as green materials for sorption and heterogeneous catalysis**. In order to achieve this general objective, the following points are included:

1. Search for new structural types with alkaline-earth elements as metal centers.

1.1. **Systems to explore:**

- **Alkaline-earth element / H_2L / ancillary ligand** system. With the aim of study the effect of these linkers in the framework formation, two different strategies are used:
  - Use of different flexible dicarboxylate linkers (H_2L), with water and some organics as ancillary ligands.
  - Use of flexible dicarboxylate linkers (H_2L) with chelating ancillary ligands.
- **Alkaline-earth element / disulfonate ligand** system, in order to obtain different coordination environments of the alkaline-earth elements.

1.2. **Structural studies** of the obtained compounds are performed to determine the novelty of the materials. In order to achieve this objective:

- Firstly, the bulk sample is analysed using Powder X-Ray Diffraction technique to determine the presence of unknown crystalline phases.
- In those cases for which unknown crystalline phases appear, the search for the obtaining of single-crystals suitable for X-Ray diffraction experiments is carried out. This technique allows the determination of the crystal structure of a novel compound.

2. Topological analyses of the obtained frameworks in order to:

2.1. Determine the novelty of the topological nets of the obtained new compounds.

2.2. Provide knowledge on new topologies.

2.3. Rationalize the design and preparation of new MOFs.

3. Preparation of the novel obtained compounds as pure phases and in a good yield in order to test them in various applications.

In order to achieve this objective, a systematic optimisation of the synthesis procedures has to be performed and the purity of the bulk sample is evaluated by X-Ray Powder Diffraction. Once the compound is synthesised as a pure crystalline phase, the material is characterized by additional techniques like elemental analysis, thermal gravimetric analyses and infrared spectroscopy.

4. Evaluation of the potential applications of the novel obtained materials.

The novel obtained materials are evaluated in heterogeneous catalysis and/or sorption of liquids and gases with the purpose of establishing structure-composition-properties relationships.

5. Study of structure-properties relationships to rationalize the design of novel MOFs

Taking into account both the results obtained in the evaluation of the potential applications, and the structural and topological features of the obtained materials, and once established the structure-properties relationships, the design of other MOFs with improved properties is accomplished.

Chapter 3

Techniques and Synthesis procedures

3.1.

Introduction

This chapter deals with a description of the experimental techniques used during the development of this research to characterize the synthesised materials. In the first part some general techniques used for a general characterization of the materials are presented (a more specific description is used for X-Ray diffraction techniques). This is then followed by a description of some more specific techniques used to study the applications of some of the compounds. Finally, an explanation of the synthesis procedures and Elemental Analyses characterization of all the compounds obtained during this thesis is presented.

3.2.

Physical Techniques

3.2.1. General Techniques

Elemental Analyses. Elemental Analyses (C, H, N, S) were performed on a CNHS Elemental Analyzer PERKIN ELMER 2400.

Fourier-Transform Infrared Spectroscopy (FTIR). Spectra were recorded from KBr pellets in the range 4000-400 cm^{-1} on a Nicolet FT-IR 20SXC spectrometer. In the case of the variable temperature experiments, the IR spectra were recorded in the range 1900-1000 cm^{-1} on a Perkin-Elmer Spectrometer with an increasing temperature rate of 2 $^{o}C \cdot min^{-1}$.

Thermogravimetric Analyses. Thermogravimetric analyses (TGA) were performed using a SEIKO model EXSTAR 6300 apparatus in the temperature range between 25 and 1000 °C in N_2 (flow of 50 ml·min^{-1}).

Differential Scanning Calorimetry (DSC). DSC measurements were performed at atmospheric pressure using a Perkin-Elmer DSC-7 calorimeter. For that purpose, the sample was placed in sealed aluminium capsules, and this was heated at 2 °C·min^{-1} until melting.

3.2.2. X-Ray Diffraction Techniques

How did all begin?

More than one century ago, in 1895, **Wilhelm Conrad Röntgen** (1845-1923), a German scientist from the University of Würzburg, discovered the X-rays and won for that discovery the first Nobel Prize in Physics (1901). Certainly, this discovery revolutionized the old field of Crystallography, which up to that moment was only dedicated to study the morphology of minerals. The interaction of X-rays with crystals shows us that X-rays are electromagnetic waves with a wavelength of about 10^{-10} meters and that the internal structure of crystals is regular, arranged in three-dimensional networks, with separations of that order.

Historically speaking, the true revolution arrived with another German scientist, **Max von Laue** (1879-1960), who trying to demonstrate the ondulatory nature of X-rays, discovered the phenomenon of X-ray diffraction by crystals. Laue demonstrated the nature of this new radiation by putting a crystal of the mineral Blenda in front of an X-ray source, obtaining the confirmation of his hypothesis and demonstrating both the ondulatory nature of this radiation and the periodic nature of crystals. The process by which the X-ray radiation, without changing its wavelength, is converted through interference by the lattice to a vast number of observable "reflections" with characteristic directions in the space is called X-ray diffraction. Laue received the Nobel Prize in Physics in 1914.

However, those who really benefited from the discovery of X-Rays radiation were the British Braggs (father and son), **William H. Bragg** (1862-1942) and **William L. Bragg** (1890-1971), who in 1915 received together the Nobel Prize in Physics for demonstrating the usefulness of the phenomenon discovered by von Laue for obtaining the internal structure of crystals. Father and son were able to explain the phenomenon

of X-ray diffraction in crystals through crystallographic planes acting as special mirrors for X-rays (*Bragg's Law*), and showed that the crystals of substances such as sodium chloride do not contain molecules of NaCl, but simply ions of Na+ and Cl-, both regularly ordered. These ideas revolutionized the field of the Theoretical Chemistry and caused the birth of a new science: X-ray Crystallography.

3.2.2.1. Single-Crystal X-Ray Diffraction

The solution of a crystal structure involves the determination of the precise spatial arrangements of all the atoms in a chemical compound in its crystalline state. In order to describe the structure of a crystal, it is only necessary to know the simplest repeating motif and the lengths and directions of the three vectors which together describe its repetition in space. The smallest repeating volume of the lattice is called the *unit cell*. It is characterized by three lattice constants *a*, *b*, *c* (the lengths of the basis vectors) and by the three angles which separate these vectors from one another. The positions of the atoms are described in terms of the crystallographic axes defined by the three basis vectors. The process in which the positions of all the atoms are correctly determined involves several steps.

The first step is naturally the obtaining of a suitable crystal. The development of a crystal depends on the relative rates of nucleation and growth. A rate of nucleation larger than the rate of growth results in the formation of agglomerates of small crystallites. On the other hand, a too rapid rate of growth may result in the inclusion of many faults in the crystal. For a new compound, the optimum conditions for the growth of a crystal cannot readily be predicted. When single crystals are obtained, one of them is selected. The quality of the collected data depends highly on the quality of the crystal, and therefore the selection of the appropriate single crystal must be carefully made. The crystals are usually selected with the help of an optical microscope. An ideal crystal must be free of defects, with well defined faces and edges. The use of polarized light helps to discard multiple crystals (individual parts normally extinguish at different angles when rotated) and to reveal the presence of cracks in a crystal (they appear as bright lines against the dark background). The size of the crystal is also important. To ensure a good statistics in the diffracted X-rays, one or two hundred micrometers are desired in every one of the crystal dimension. Once the best available single crystal has been selected, it is mounted on the extreme of a glass fiber, fixed with contact adhesive; typically two-component glue is employed for this purpose. The glass fiber has been

previously attached to a metal base, adapted to be mounted on a goniometer head. In the case of experiments performed at low temperatures, the single crystals are often mounted on a polyimide micromount (MiTeGen) with perfluoropolyether oil.

When the crystal has been selected and mounted, the subsequent study will be carried out with the single crystal diffractometer. It is worth highlighting that during the development of the work presented in this thesis, three different equipments were used. The technical specifications for each of them are presented in the following:

- A Bruker-Siemens Smart CCD difractometer with a 3 circles goniometer. This difractometer is equipped with a normal focus, 4 kW sealed tube X-ray source with a primary monochromator, using the Mo Kα radiation, λ = 0.71069 Å. A charge coupled device (CCD) area detector is used to collect the diffracted reflections.
- A Bruker four circle kappa-diffractometer equipped with, a Cu INCOATEC microsource operated at 30W power (45kV, 0.60 mA) to generated Cu Kα radiation (λ= 1.54178 Å), and a Bruker AXIOM area detector (microgap technology) (**Figure 2.1**).
- A Bruker four circle kappa-diffractometer equipped with a Cu INCOATEC microsource operated at 30W power (45kV, 0.60 mA) to generate Cu Kα radiation (λ= 1.54178 Å), and a Bruker APEXII area detector.

The preliminary study of the crystal includes a partial exploration of the reciprocal space. It usually takes less than one hour, and gives us an estimation of the quality of the crystal, determining if the whole data collection is being carried out. With the crystal correctly centered, the unit cell parameters and their orientation to the goniometer axes will be determined. This late is given by the orientation matrix, which is a 3x3 matrix which gives the components of the three reciprocal axes in the three directions of the goniometer's axial system. A random search for reflections is made, and an indexing program defines a lattice onto which all the observed reflections will fit. Indexing programs are based on a peak search for scattering vectors over the first exposures. On the basis of the differences between these vectors, reciprocal base vectors are sought, which can describe all found peaks as reciprocal lattice points. A reduced cell is then obtained for that originally found, and the corresponding orientation matrix is determined.

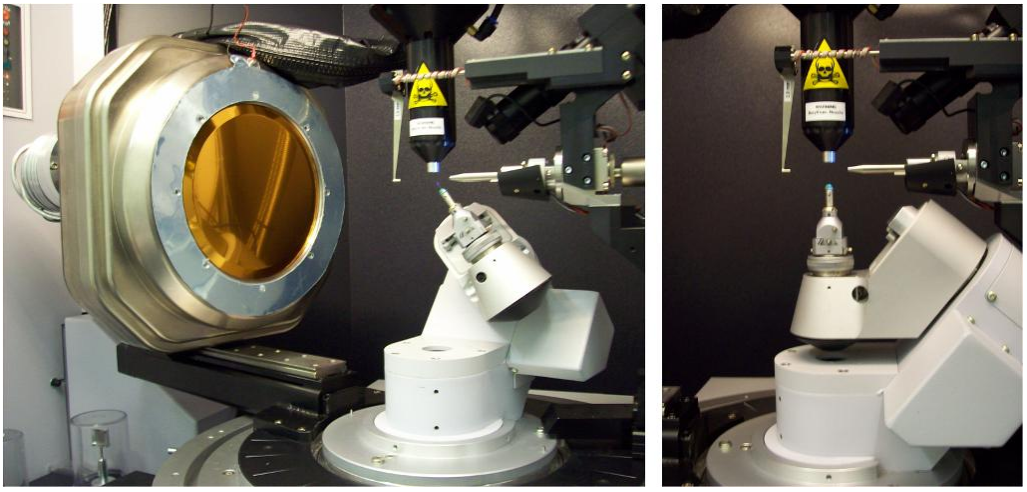

Figure 3.1. **Left)** Bruker four circle kappa-diffractometer equipped with a Bruker AXIOM area detector employed during the work here presented. **Right)** Detail of the four circle kappa goniometer.

If the cell parameters are not known and the crystal is of quality enough, a complete data collection is carried out. This consists of successive exposures of the crystal to the incident radiation at a rotation angle range. The angle range is selected based upon the symmetry of the crystal, and it must content at least one full set of independent data for the relevant Laue group. The data collection takes several hours, depending on the exposure time and the size of the observed portion of the Ewald sphere.

After the data collection is over, the intensities of the observed reflexions are integrated in the volume of the observed reciprocal space, in the predicted positions calculated with the orientation matrix. This is made with the SAINT program,[1] and to obtain high quality output data, a good accuracy in the orientation matrix is necessary, as well as non-displacing of the crystal from the goniometer centre during the data collection. The data integration is a feedback process, and the orientation matrix and the geometrical parameters of the diffractometer are also refined while the process is going on. The observed intensities are corrected with the polarization and Lorentz factors, and the Miller indices are assigned. Finally, a semiempirical absorption correction based on equivalent reflections is made, using the SADABS[2] software.

The final data set includes the cell parameters and the intensity data given as square structure factors F^2hkl. This set of data will be used for the structure solution and refinement. The software package SHELXTL 6.10[3] includes programs for the structure

solution and refinement of crystal structures from X-ray diffraction data. Using this software, and after the space group determination, Direct Methods are used to the initial phase assignment, and a first model is obtained. This initial model is refined, and the subsequent Fourier syntheses give the electronic density maps in which the atoms are located. The structure is refined with a full-matrix least square refinement on square structure factors, F^2, initially with isotropic thermal factors. Once all the non hydrogen atoms are located, a refinement is made with anisotropic thermal factors. The hydrogen atoms are finally located on the residual electronic density maps or geometrically calculated.

After the solution of the crystal structure and once the positions for all the atoms are known, the graphical representations are made with software like XSHELL (included in the SHELXTL package)[3] or ATOMS.[4]

The experimental details corresponding to the single-crystal X-Ray Diffraction measurements performed to solve the structure of the compounds presented in this thesis are described in Appendix.

3.2.2.2. X-Ray Powder Diffraction

X-ray Powder diffraction (XRPD) technique allows the analysis of the crystalline phases of a microcrystalline sample. Each crystalline phase exhibits a characteristic powder pattern, in which the 2θ positions of the diffracted peaks depend on the unit cell parameters and the space group, and their relative intensities are function of the composition and atomic positions. They are also influenced by others factors such as textural features of the microcrystalline samples. Knowing a crystal structure, its powder pattern can be simulated, and then compared with the experimental pattern to determine the purity of the samples. During the development of this research, XRPD has been used as routine characterization technique, since it allows the purity testing of the prepared compounds.

However, the potential applications of XRPD technique go beyond the simple identification of phases. In fact, since powerful mathematical methods have been recently developed in order to extract the intensities from a XRPD pattern, this technique can be also used to determine the crystal structure of unknown materials.

In the following, the different methodologies used with XRPD data during the development of the work presented in this thesis are carefully explained:

Rietveld refinement. The Rietveld method[5] was first developed for the refinement of crystalline structures using neutron diffraction data. Its use has been extended to the field of X-ray diffraction, and it is employed in, for example, the refinement of crystalline structures, the quantitative analysis of mixed crystalline phases or estimation of the size and shape of crystallites. The refinement of a crystalline structure by the Rietveld method consists of the minimization of the differences between an experimental powder pattern and one simulated with a structural model and with parameters that allows the distribution of the reflexions intensities in the whole pattern. The function to be minimized is $s_y = \sum w_i |y_i(0)-y_i(c)|^2$, where $y_i(0)$ and $y_i(c)$ are the observed and calculated intensities for each i point, and w_i is the assigned weight to each point. The calculated intensities are a function of two types of parameters: the atomic and the global parameters. The first ones allow the calculation of the intensity of the reflections, and they include the lattice parameters, space group, atomic positions, thermal agitation parameters and occupancy factors for the atoms in each crystalline phase. On the other hand, the global parameters affect the whole pattern, and allow the distribution of the reflections intensities in each point of the pattern. These parameters include: the scale factor of the pattern, the background function, zero displacement, peaks shape parameters, scale factor for each crystalline phase and preferred orientation parameters.

The Rietveld method is widely used to check the purity of a bulk sample for those compounds whose crystal structure was before solved, typically by single-crystal X-Ray Diffraction. The Rietveld refinements presented in this thesis have been performed using the Materials Studio software[6] package.

Pawley refinement. A revolution came with the Pawley method described in a paper entitled *Unit-cell refinement from powder diffraction scans*.[7] The main purpose of this method consists of refining cell parameters from the whole pattern; in addition, the possibility to use the extracted intensities as the starting point for the application of direct methods is available. As well as for the Rietveld method, the Pawley method was not recognized as a revolution for a long time. In the Pawley method, profiles are analytical, their width is constrained to follow a Caglioti law with the three refinable parameters U, V, W as defined in most of the Rietveld-derived softwares. The main difference with the Rietveld method is that the intensities are considered as refinable parameters. Slack constraints were introduced for stabilization of the intensities of those reflections overlapping too much. So, the reflection positions are constrained by the cell knowledge. Moreover, the cell parameters can be also refined during this process.

As in the case of Rietveld method, the Pawley method is also widely used to check the purity of a known crystalline phase. Above all in the case of the compounds presented in this thesis (*metal-organic frameworks*), some features make difficult the use of Rietveld method as a routine methodology to purity checking. First of all, these compounds use to exhibit XRPD patterns with clear peak overlapping and a lack of reflections at high Bragg angles. Moreover, since the asymmetric units of this kind of compounds are often composed by a high number of low scattering atoms (mainly due to the tendency to use complex organic molecules as linkers). These two features make more difficult the use of Rietveld methodologies to purity checking purposes. The Pawley refinements presented in this thesis have been carried out using the Materials Studio software[6] package.

Structure solving. In order to obtain a structural model from XRPD data, the pattern is firstly indexed using DICVOL04 program[8,9]. Then, after studying in detail the systemic absences, the corresponding space group is determined. With this principal information, a Pawley refinement procedure[7] is performed to refine the cell and peak profile parameters, as well as those of the background, peak asymmetry and zero shift. Then, a crystal structure model can be obtained using the direct-space global optimization algorithms implemented in computer program *Fox*.[10,11] When a reasonable structural model is obtained with *Fox*, Rietveld refinement[5] with energy optimization is employed to accurate this initial model, using the Materials Studio software.[6] This kind of methodology incorporates a description of potential energy in conjunction with the R_{wp} in the Rietveld refinement process, optimizing a combined figure of merit. This method tries to balance matching the simulated pattern with experimental diffraction data and minimizing the potential energy of the structure. The corresponding Rietveld refinement with energy optimization (*Pareto optimization*) was performed using the Reflex module of Materials Studio.[6] These Rietveld refinements are carried out in this step of the structure solving by considering molecules as rigid bodies (*rigid-body* methodology). Then, subsequent Rietveld refinements are performed using only gradually relaxed constraints (for instance, some torsion angles can be relaxed). Finally, hydrogen atoms are geometrically situated to complete the structural model.

Experimental details. The experimental powder patterns of the compounds presented in this thesis have been collected in a Bruker-AXS d8 advance diffractometer, equipped with a rapid detector (*lynxeye* detector), operating with the $CuK\alpha_{1,2}$ radiation (λ=0.15418 nm), at 40 kV and 30 mA (**Figure 2.2**). The powder patterns were collected in a 2θ range of 5-40 º, with a step size of 0.02º, and at exposure time of 1 s. Variable

temperature measurements were performed with a Philips X'Pert diffractometer in the θ–θ mode using nickel-filtered CuK$\alpha_{1,2}$ radiation. To perform in situ XRPD thermodiffraction studies, the diffractometer was equipped with an Anton-Paar chamber. The sample was dispersed on the steel sample holder and heated slowly to 100 ºC under vacuum. The powder patterns were collected in a 2θ range of 4-40 º, with a step size of 0.028º, and at exposure time of 1 s. The heating rate between temperatures was 2 ºC·min^{-1}.

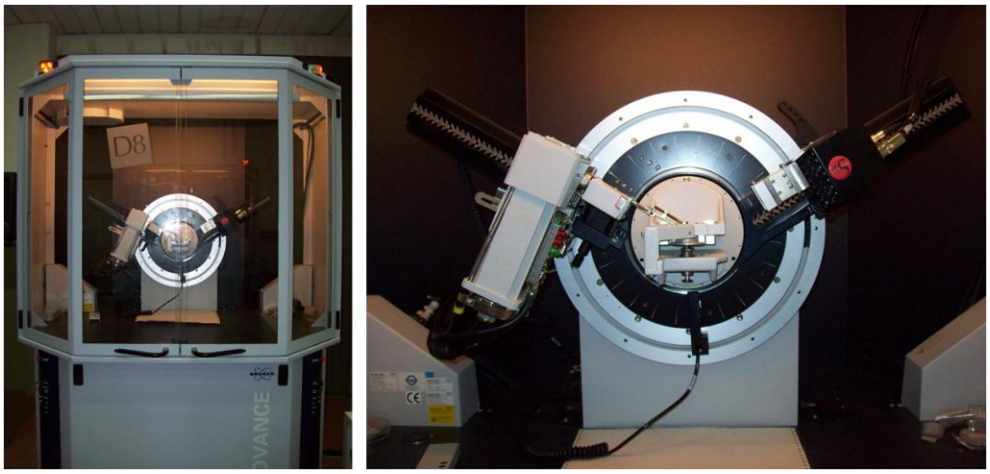

Figure 3.2. Bruker-AXS d8 advance diffractometer equipped with a rapid detector (lynxeye) used in this thesis.

3.2.3. Topological Analyses

The topological analyses of the materials presented in this thesis were performed using TOPOS software.[12] For those nets that have an equilibrium placement with no vertex collisions, it was possible to idealize them in their maximum symmetry embedding using *Systre* software.[13] In some cases, a natural or quasi-natural tilling can be described. For that purposed, the local program *3dt*, which utilizes the so-called Delaney-Dress symbols[14] to find embedding suitable illustrations for an idealised net was used.

3.2.4. Temperature Variable Optical Microscopy

The TVOM experiments presented in this thesis were carried out using a Linkam THMSG-600 stage mounted to a Nikon Eclipse 50iPol Microscope. The

sample was placed on a 7-mm quartz-cover slip, and encased within a pure Ag lid so that it was heated from all sides, ensuring a uniform temperature. The equipment also consists of LNP liquid nitrogen cooling system and a TMS94 temperature controller. Images were captured with the before mentioned Nikon Digital Camera DXM1200F and the NIS-Elements Software.

3.2.5. DFT Calculations

The periodic DFT calculations presented in this thesis were performed using a plane wave basis set and the VASP package.[15,16] The initial unit cell parameter and atom positions were taken from the experimental single crystal and powder X-ray analyses. The data obtained were then fully optimized by using the PW91 implementation of the GGA exchange correlation function[17,18] through the spin-interpolation formula of Vosko–Wilk–Nusair.[19,20] The effect of the core electrons on the valence electron density was described by the projector augmented wave method[21] implemented by Kresse and Joubert.[22] The valence one-electron Kohn–Sham states have been expanded on a plane wave basis with a cutoff of 415 eV for the kinetic energy. The total energy threshold defining self-consistency of the electron density was set to 10^{-4} eV. The convergence criterion for structural optimization was set to less than 103 eV, for the difference of total energy from consecutive geometries. Thus, forces on all atoms were ensured to be less than 0.3 $eVnm^{-1}$. A Gaussian smearing technique with a 0.2 eV width has been applied to enhance convergence. However, all energies presented in the following have been obtained by extrapolating to zero smearing (0 K). Integration in the reciprocal space was carried out by using the Monkhorst–Pack[23] sampling of the Brillouin zone. Several meshes of special k points were used to obtain the desired accuracy in the calculated energies.

3.2.6. Catalytic Experiments and Gas Chromatography

Many of the materials obtained during the development of this research work have been evaluated as heterogeneous catalysts, testing their activity in two different types of catalytic tests:

- **Hydrogenation of alkenes.** In a typical hydrogenation batch experiment in a Parr reactor (**Figure 2.3**), catalytic tests were performed using 1% mol catalyst, at

different temperatures (depending on the studied catalyst) using toluene as solvent. Thus, 10 mg of the catalyst and the corresponding amount of alkene substrate were added to 40 ml of toluene. After temperature adjustment, the pressure of H_2 was maintained at 5 atm. Specific details on catalytic experiments carried out are given in the corresponding chapter.

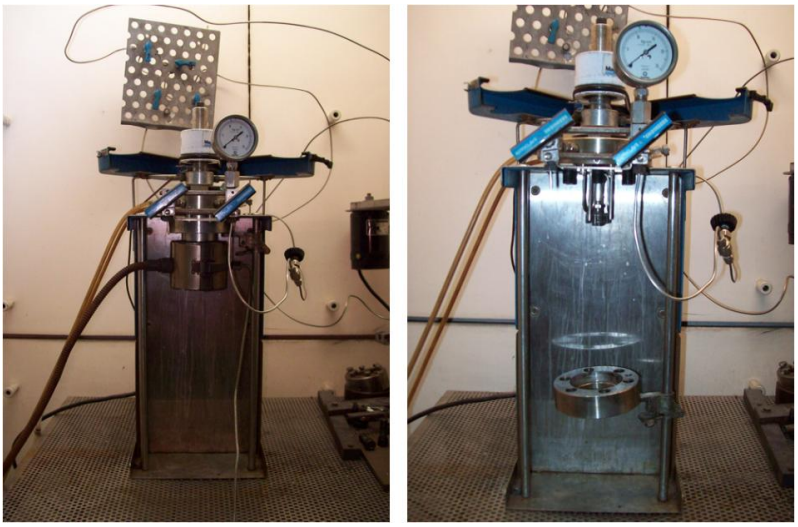

Figure 2.3. Parr reactor used in alkenes hydrogenation catalytic tests during the development of this work.

- Hydrosilylation of carbonyl and alkenes Hydrosilylation tests were carried out with a ratio carbonyl:silane (1:2) or alkene:silane (3:1), and catalyst (10% mol) in dry toluene (1 ml) at 363 K under inert atmosphere (N_2). Thus, 10 mg of the catalyst and the corresponding amount of silane and the carbonyl or alkene substrate were added to 1 ml of toluene under inert atmosphere. Specific details on catalytic experiments carried out are given in the corresponding chapter.

For both studied catalytic processes, the grade of conversion achieved at a selected period of time is measured by gas chromatography (GC). With the GC technique, compounds that can be vaporized without decomposition are analyzed and the different components of a mixture are separated. The compounds in gaseous form are carried by an inert gas, like helium or N_2, in what is known as mobile phase. This phase is transported through a stationary phase, which usually is a microscopic layer of liquid or polymer on an inert solid support, inside a column. The compounds interact with the stationary phase, and each different compound elute at a different time, known as a retention time. The GC experiments of this work have been carried out employing

a KONIK HRGC 40000B chromatograph equipped with a KONIK Quadrupole MSQ12 mass detector and a KAP-120212 column. TOF (Turn Over Frequency) values were calculated from first reaction run data points in the batch experiments (after 15 minutes of reaction).

3.2.7. Solvent sorption experiments

Part of the work presented in this thesis consists of the evaluation of the selective sorption properties of the obtained materials using common solvents: acetone, isopropyl alcohol, acetonitrile, toluene, 1-butanol, n-hexane, isooctane, benzene and cyclohexane.

In a typical procedure, a series of post-synthesis treatments were performed to evaluate the solvent sorption properties:

- **Activation**. In a typical procedure, 50 mg of sample is dried under vacuum at 383 K during 3 hours, in order to remove the extra framework species.

- **Solvent sorption experiments**. Then, the dry sample is dispersed in various common solvents in a glass holder and vigorously stirred for 4 h at 298 K. The sample is then isolated by centrifugation, and air-dried.

- **Structural and thermogravimetric studies.** First, XRPD measurements are performed on the sample after sorption experiments in order to evaluate the possible structural transformations after sorption experiments. Then, TGA-MS is performed to study the desorption process of solvent molecules from pores.

3.2.8. N_2 adsorption-desorption isotherms

Textural properties were determined by N_2 adsorption-desorption at 77 K using an Autosorb-1 series (Quantachrome Corp.) equipment. Before adsorption measurements the sample was degassed at 383K. Adsorption isotherms were obtained in relative pressure range of 10^{-6} to 1 atm. Apparent surface area values were calculated using the data points on the adsorption branch of the N_2 isotherm on the range P/P_0 = 0.1-0.3.

3.2.9. Gas adsorption experiments

The gas adsorption experiments were performed using a Hiden Isochema (Warrington, UK) Intelligent Gravimetric Analyzer (IGA) equipped with a micro-gram balance and two barotron pressure transducers in the ranges 0-2 mbar and 0-10 bar were used to monitor the pressure. The microbalance had a long-term stability of ± 1 μg with a weighing resolution of 0.2 μg. These measurements were carried out using high purity gases. The gas entrance was made using a BRONKHORST mass flow controller. All isotherms were measured to 1 bar at 304 K. The sample was outgassed under high vacuum at 403 K prior to the admission of any gas into the system. The buoyancy effects were corrected as a function of temperature taking into account the void volume of the cell determined with He gas at 77 K, assuming that the amount of He adsorbed is negligible. The saturation amount was calculated by fitting of the pressure as a function of the amount of gas adsorbed by means of the Sips equation:

$$\theta = \frac{n}{m} = \left(\frac{b. \cdot P^{\frac{1}{c}}}{1 + b. \cdot P^{\frac{1}{c}}} \right)$$

where n = moles adsorbed
m = moles adsorbed at saturation
P = pressure
b and c = constants

3.3.

Synthesis procedures

In this section the optimized synthesis conditions to obtain the compounds presented in this thesis are explained, together with the Elemental Analyses characterization. The descriptions of the synthesis are presented in the order in which the compounds appear in the thesis.

3.3.1. Synthesis of $H_2L_{(1)}$ based AEPFs

(Chapter 4.1)

Synthesis of Ca-AEPF-1. A solution of 4,4'-(hexafluoroisopropylidene)*bis*(benzoic acid) ($H_2L_{(1)}$, from now on) (400 mg, 1 mmol) in acetone (9 mL) was added under continuous stirring to a solution of $Ca(CH_3CO_2)_2{\cdot}H_2O$ (178 mg, 1 mmol) in distilled water (10 ml). The resulting mixture was stirred at room temperature for 5 minutes, and then placed in a Teflon-lined steel autoclave, which is sealed in a preheated oven at 170 ºC, and then heated for 3 days. The autoclave was allowed to cool to room temperature and the product was filtered and washed with distilled water (3x10 ml) and acetone (3x5 ml). The pure product was obtained in a yield of 70%. Elemental Analyses (C, H) found (calculated) for **Ca-AEPF-1**: C, 47.30 (48.34)% and H, 2.85 (2.24)%.

Synthesis of Ca-AEPF-6. A mixture of $H_2L_{(1)}$ (200 mg, 0.5 mmol), $Ca(CH_3CO_2)_2{\cdot}H_2O$ (90 mg, 0.5 mmol) and 5 ml of DEF was stirred at room temperature for 5 minutes. The resulting mixture was placed in a Teflon-lined steel autoclave, which was sealed and places in a preheated oven at 150 ºC, and then heated for 20 hours. The autoclave was allowed to cool to room temperature and the product was filtered and washed with distilled water (5x10 ml) and acetone (1x5 ml). The pure product was obtained in a yield of 25%. Elemental Analyses (C, H, N) found (calculated) for **AEPF-6**: C, 48.42 (48.34)%, H, 3.38 (3.30)% and N, 2.65 (2.71)%.

Synthesis of Ca-AEPF-7. A mixture of $H_2L_{(1)}$ (100 mg, 0.25 mmol), $Ca(NO_3)_2{\cdot}6\ H_2O$ (60 mg, 0.25 mmol), 1 ml of pyridine and 10 ml of distilled water was stirred at room temperature for 5 minutes. The resulting mixture was placed in a Teflon-lined steel

autoclave, which was sealed and placed in a preheated oven at 180 ºC, and then heated for 3 hours. The autoclave was allowed to cool to room temperature and the product was filtered and washed with distilled water (3x10 ml) and acetone (3x5 ml). The pure product was obtained in a yield of ~75%. Elemental Analyses (C, H, N) found (calculated) for **Ca-AEPF-7**: C, 49.25 (49.21)%, H, 2.92 (2.98)% and N, 2.50 (2.61)%.

Synthesis of Mg-AEPF-8. A mixture of $H_2L_{(1)}$ (200 mg, 0.5 mmol), $Mg(CH_3CO_2)_2{\cdot}4H_2O$ (107 mg, 0.5 mmol) and 5 ml of DEF was stirred at room temperature for 5 minutes. The resulting mixture was placed in a Teflon-lined steel autoclave, which was sealed and placed in a preheated oven at 150 ºC, and then heated for 1 hour. The autoclave was allowed to cool to room temperature and the product was filtered. Crystalline **Mg-AEPF-8** was obtained following this synthesis procedure, although it could not be synthesized as a unique phase.

Synthesis of Mg-AEPF-9. A mixture of $H_2L_{(1)}$ (200 mg, 0.5 mmol), $Mg(CH_3CO_2)_2{\cdot}4H_2O$ (107 mg, 0.5 mmol) and 10 ml of DEF was stirred at room temperature for 5 minutes. The resulting mixture was placed in a Teflon-lined steel autoclave, which was sealed and placed in a preheated oven at 180 ºC, and then heated for 15 hour. The autoclave was allowed to cool to room temperature and the product was filtered and washed with acetone (3x5 ml). Crystalline **Mg-AEPF-9** was obtained following this synthesis procedure, although it could not be synthesized as a unique phase.

Synthesis of Sr-AEPF-10. A mixture of $H_2L_{(1)}$ (400 mg, 1 mmol), $Sr(CH_3CO_2)_2{\cdot}$(255 mg, 1 mmol), 9 ml of n-hexane and 10 ml of distilled water was stirred at room temperature for 30 minutes. The resulting mixture was placed in a Teflon-lined steel autoclave, which was sealed and placed in a preheated oven at 170 ºC, and then heated for 3 days. The autoclave was allowed to cool to room temperature and the product was filtered and washed with distilled water (3x10 ml) and acetone (3x5 ml). Crystalline **Sr-AEPF-10** was obtained following this synthesis procedure, although it could not be synthesized as a unique phase.

3.3.2. Synthesis of $H_2L_{(2)}$ based AEPFs

(Chapter 4.2)

Synthesis of Mg-AEPF-11. A mixture of diphenylmethane-4,4'-dicarboxylic acid ($H_2L_{(2)}$, from now on) (200 mg, 0.75 mmol), $Mg(CH_3CO_2)_2{\cdot}4H_2O$ (160 mg, 0.75 mmol) and 5 ml of DEF was stirred at room temperature for 5 minutes. Then, propane-1-amine (0.5 ml) was added to the mixture, which was stirred for 5 minutes more. The resulting mixture was placed in a Teflon-lined steel autoclave, which was sealed and placed in a preheated oven at 150 ºC, and then heated for 60 hours. The autoclave was allowed to cool to room temperature and the product was filtered and washed with acetone (3x5 ml). The pure product was obtained in a yield of ~60%. Elemental Analyses (C, H, N) found (calculated) for **Mg-AEPF-11**: C, 62.17 (63.81)%, H, 4.50 (4.71)% and N, 1.98 (2.13)%.

Synthesis of Mg-AEPF-12. A mixture of $H_2L_{(2)}$ (200 mg, 0.75 mmol), $Mg(CH_3CO_2)_2{\cdot}4H_2O$ (160 mg, 0.75 mmol) and 5 ml of DMF was stirred at room temperature for 5 minutes. Then, n-propylamine (0.5 ml) was added to the mixture, which was stirred for 5 minutes more. The resulting mixture was placed in a Teflon-lined steel autoclave, which was sealed and placed in a preheated oven at 150 ºC, and then heated for 60 hours. The autoclave was allowed to cool to room temperature and the product was filtered and washed with acetone (3x5 ml). The pure product was obtained in a yield of ~60%. Elemental Analyses (C, H, N) found (calculated) for **Mg-AEPF-12**: C, 61.42 (62.17)%, H, 4.77 (4.88)% and N, 1.98 (2.07)%.

Synthesis of AEPF-13. A mixture of $H_2L_{(2)}$ (100 mg, 0.25 mmol), the corresponding inorganic salt ($Ca(CH_3CO_2)_2{\cdot}H_2O$ (72 mg, 0.4 mmol) or $Sr(CH_3CO_2)_2{\cdot}$(102 mg, 0.4 mmol)) and 10 ml of distilled water was stirred at room temperature for 5 minutes. Then, n-propylamine (0,5 ml) was added to the mixture, which was stirred for 5 minutes more. The resulting mixture was placed in a Teflon-lined steel autoclave, which was sealed and placed in a preheated oven at 170 ºC, and then heated for 12 hours. The autoclave was allowed to cool to room temperature and the product was filtered and washed with distilled water (3x10 ml) and acetone (3x5 ml). The pure products were obtained in a yield of ~45% for both **Ca-AEPF-13** and **Sr-APEF-13** compounds. Elemental Analyses (C, H) found (calculated) for **Ca-AEPF-13**: C, 57.42 (57.69)% and H, 3.69 (3.85)%. Elemental Analyses (C, H) found (calculated) for **Sr-AEPF-13**: C, 49.29 (50.02)% and H, 3.16 (3.33)%.

3.3.3. Synthesis of $H_2L_{(1)}$ and ancillary chelating ligands based AEPFs (Chapter 5)

Synthesis of Mg-α-AEPF-14. A mixture of $H_2L_{(1)}$ (100 mg, 0.25 mmol), phen (46 mg, 0.25 mmol) and $Mg(CH_3CO_2)_2{\cdot}4H_2O$ (50 mg, 0.25 mmol) and 15 ml of distilled water was stirred at room temperature for 5 minutes. The resulting mixture was placed in a Teflon-lined steel autoclave, which was sealed and placed in a preheated oven at 160 ºC, and then heated for 1 hour. The autoclave was allowed to cool to room temperature and the product was filtered and washed with acetone (3x5 ml). The pure product was obtained in a yield of ~45%. Elemental Analyses (C, H, N) found (calculated) for **Mg-α-AEPF-14**: C, 52.31 (52.19)%, H, 3.52 (3.60)% and N, 4.10 (4.20)%.

Synthesis of Mg-β-AEPF-14. A mixture of $H_2L_{(1)}$ (100 mg, 0.25 mmol), phen (46 mg, 0.25 mmol) and $Mg(CH_3CO_2)_2{\cdot}4H_2O$ (50 mg, 0.25 mmol), 5 ml of acetone and 10 ml of distilled water was stirred at room temperature for 5 minutes. The resulting mixture was placed in a Teflon-lined steel autoclave, which was sealed and heated at 200 ºC with 5 $ºC{\cdot}min^{-1}$ and then heated for 5 days. The autoclave was allowed to cool to room temperature and the product was filtered and washed with distilled water (3x10 ml). The pure product was obtained in a yield of ~65%. Elemental Analyses (C, H, N) found (calculated) for **Mg-β-AEPF-14**: C, 52.71 (52.19)%, H, 3.59 (3.60)% and N, 4.25 (4.20)%.

Synthesis of Mg-AEPF-15. A mixture of $H_2L_{(1)}$ (100 mg, 0.25 mmol), phen (46 mg, 0.25 mmol) and $Mg(CH_3CO_2)_2{\cdot}4H_2O$ (50 mg, 0.25 mmol) and 15 ml of distilled water was stirred at room temperature for 5 minutes. The resulting mixture was placed in a Teflon-lined steel autoclave, which was sealed and placed in a preheated oven at 170 ºC, and then heated for 1 hour. The autoclave was allowed to cool to room temperature and the product was filtered and washed with distilled water (3x10 ml). Crystalline **Mg-AEPF-15** was obtained following this synthesis procedure, although it could not be synthesized as a unique phase.

Synthesis of Mg-AEPF-16. A mixture of $H_2L_{(1)}$ (100 mg, 0.25 mmol), phen (46 mg, 0.25 mmol) and $Mg(CH_3CO_2)_2{\cdot}4H_2O$ (50 mg, 0.25 mmol) and 15 ml of distilled water was stirred at room temperature for 5 minutes. Then, the pH of the mixture was adjusted to 7 using a NaOH 0.1 M solution and stirred for 5 minutes more. The resulting mixture was placed in a Teflon-lined steel autoclave, which was sealed and placed in a preheated oven at 180 ºC, and then heated for 5 days. The autoclave was allowed to cool to room temperature and the product was filtered and washed with

distilled water (3x10 ml). The pure product was obtained in a yield of ~70%. Elemental Analyses (C, H, N) found (calculated) for **Mg-AEPF-16**: C, 55.21 (55.17)%, H, 3.22 (3.17)% and N, 4.72 (4.44)%.

Synthesis of Mg-AEPF-17. A mixture of $H_2L_{(1)}$ (100 mg, 0.25 mmol), phen (46 mg, 0.25 mmol) and $Mg(CH_3CO_2)_2{\cdot}4H_2O$ (50 mg, 0.25 mmol), 0.7 ml of acetone and 14.3 ml of distilled water was stirred at room temperature for 5 minutes. The resulting mixture was placed in a Teflon-lined steel autoclave, which was sealed and heated at 200 ºC with 5 ºC min^{-1}) and then heated for 5 days. The autoclave was allowed to cool to room temperature and the product was filtered and washed with distilled water (3x10 ml). The pure product was obtained in a yield of ~53%. Elemental Analyses (C, H, N) found (calculated) for **Mg-AEPF-17**: C, 55.42 (56.79)%, H, 3.07 (2.94)% and N, 4.46 (4.57)%.

3.3.4. Synthesis of 2,6-AQDS based AEPFs

(Chapter 6)

Synthesis of Mg-AEPF-2. A mixture of 2,6-AQDS (100 mg, 0.24 mmol), $Mg(CH_3CO_2)_2{\cdot}4H_2O$ (51 mg, 0.24 mmol), 5 ml of 1-butanol and distilled water was stirred at room temperature for 5 minutes. The resulting mixture was placed in a Teflon-lined steel autoclave, which was sealed and placed in a preheated oven at 170 ºC, and then heated for 3 days. The autoclave was allowed to cool to room temperature and the product was filtered and washed with distilled water (3x10 ml) and acetone (3x5 ml). The pure product was obtained in a yield of ~65%. Elemental Analyses (C, H, S) found (calculated) for **Mg-AEPF-2**: C, 38.69 (39.41)%, H, 2.46 (2.35)% and S, 14.49 (15.03)%.

Synthesis of Ca-AEPF-3. A mixture of 2,6-AQDS (100 mg, 0.24 mmol), $Ca(CH_3CO_2)_2{\cdot}4H_2O$ (43 mg, 0.24 mmol), 5 ml of 1-butanol and distilled water was stirred at room temperature for 5 minutes. The resulting mixture was placed in a Teflon-lined steel autoclave, which was sealed and placed in a preheated oven at 170 ºC, and then heated for 3 days. The autoclave was allowed to cool to room temperature and the product was filtered and washed with distilled water (3x10 ml) and acetone (3x5 ml). The pure product was obtained in a yield of ~70%. Elemental Analyses (C, H, S) found (calculated) for **Ca-AEPF-3**: C, 41.43 (41.37)%, H, 1.46 (1.48)% and S, 15.02 (15.78)%.

Synthesis of Sr-AEPF-4. A mixture of 2,6-AQDS (100 mg, 0.24 mmol), $Sr(CH_3CO_2)_2$ (61 mg, 0.24 mmol), 5 ml of 1-butanol and distilled water was stirred at room temperature for 5 minutes. The resulting mixture was placed in a Teflon-lined steel autoclave, which was sealed and placed in a preheated oven at 170 ºC, and then heated for 3 days. The autoclave was allowed to cool to room temperature and the product was filtered and washed with distilled water (3x10 ml) and acetone (3x5 ml). The pure product was obtained in a yield of ~62%. Elemental Analyses (C, H, S) found (calculated) for **Sr-AEPF-4**: C, 35.49 (35.63)%, H, 1.73 (1.70)% and S, 13.25 (13.56)%.

Synthesis of Ba-AEPF-5. A mixture of 2,6-AQDS (100 mg, 0.24 mmol), $Ba(CH_3CO_2)_2$ (61 mg, 0.24 mmol), 5 ml of 1-butanol and distilled water was stirred at room temperature for 5 minutes. The resulting mixture was placed in a Teflon-lined steel autoclave, which was sealed and placed in a preheated oven at 170 ºC, and then heated for 3 days. The autoclave was allowed to cool to room temperature and the product was filtered and washed with distilled water (3x10 ml) and acetone (3x5 ml). The pure product was obtained in a yield of ~62%. Elemental Analyses (C, H, S) found (calculated) for **Ba-AEPF-5**: C, 33.38 (33.38)%, H, 1.23 (1.19)% and S, 12.25 (12.71)%.

References

1. *SAINTplus package*. Bruker AXS Inc., Madison, Wisconsin, USA, **2007**.
2. Sheldrick, G. M. *SADABS program integrated in SAINTplus package*. Bruker AXS Inc., Madison, Wisconsin, USA.
3. *SHELXTL package*. Bruker AXS Inc., Madison, Wisconsin, USA, **2006**.
4. Dowty, E. *ATOMS v. 5.10 software*, **2000**.
5. Rietveld, H. M. *J. Appl. Crystallogr.*, **1969**, *2*, 65.
6. Materials Studio Modelling 4.4, http://www.accelerys.com/mstudio/ms_modeling.
7. Pawley, G. S. *J. Appl. Cryst.*, **1981**, *14*, 357.
8. Lour, D.; Louer, M. J. *J. Appl. Crystallogr.*, **1972**, *5*, 271.
9. Boultif, A.; Louer, D. *J. Appl. Crystallogr.*, **1991**, *24*, 987.
10. Favre-Nicolin, V.; Cerny, R. *J. Appl. Crystallogr.*, **2002**, *35*, 734.
11. Fox, *Free Objects for Crystallography software*, http://objcryst.sourceforge.net.
12. Blatov, V.A. *IUCr Comput. Comm. Newslett.* **2006**, 7, 4, see also: http://www.topos.ssu.samara.ru.
13. Delgado–Friedrichs, O.; O'Keeffe, M. *Acta. Crystallogr.*, **2003**, *B59*, 351.
14. Delgado–Friedrichs, O.; Dress, A. W. M.; Huson, D. H.; Klinowsky, J.; Mackay, A. L. *Nature (London)*, **1999**. *400*, 644.
15. Kresse, G.; Furthmller, J. *Comput. Mater. Sci.* **1996**, *6*, 15.
16. Kresse, g.; Hafner, J. *Phys. Rev. B*, **1993**, *47*, 558.
17. Perdew, J. P.; Wang, Y. *Phys. Rev. B*, **1992**, *45*, 13244.
18. Perdew, J. P.; Chevary, J. A.; Vosko, S. H.; Jackson, K. A.; Pederson, M. R.; Singh, D. J.; Fiolhais, C. *Phys. Rev. B*, **1992**, *46*, 6671.

19. Zhang, Y.; Yang, W. *Phys. Rev. Lett.*, **1998**, *80*, 890.

20. Vosko, S. H.; Wilk, L.; Nusair, M. *Can. J. Phys.*, **1980**, *58*, 1200.

21. Blöchl, P. E. *Phys. Rev. B*, **1994**, *50*, 17953.

22. Kresse, G.; Joubert, D. *Phys. Rev. B*, **1999**, *59*, 1758.

23. Monkhorst, H. J.; Pack, J. D. *Phys. Rev. B*, **1976**, *13*, 5188.

Chapter 4

Role of the non-binding substituent groups in flexible ligands

4,4'-(hexafluoroisopropylidene)*bis*(benzoic acid) ($H_2L_{(1)}$)

Diphenylmethane-4,4'-dicarboxylic acid ($H_2L_{(2)}$)

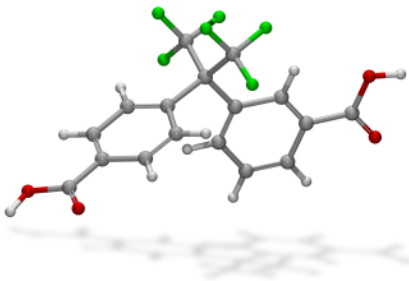

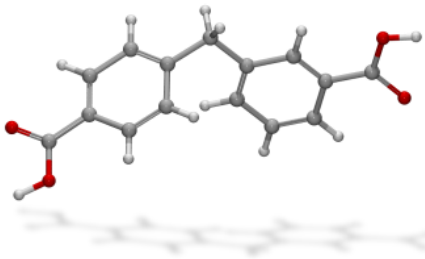

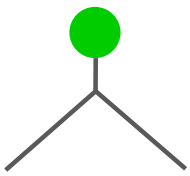

$H_2L_{(1)}$

$H_2L_{(2)}$

Abstract

Eleven new compounds based on alkaline-earth ions and 4,4'-(hexafluoroisopropylidene)*bis*(benzoic acid) ($H_2L_{(1)}$) (**Chapter 4.1**) and diphenylmethane-4,4'-dicarboxylic acid (**Chapter 4.2**) have been successfully synthesised under hydro- and solvothermal conditions. These materials belong to ten structural types. For some of the materials presented in this chapter their potential applications in heterogeneous catalysis and gas sorption were also evaluated.

4.1.

Introduction

Regarding to MOFs design, the choice of the ligand largely dictates the kind of framework that can be obtained. In this sense, the use of flexible ligands to synthesise new MOFs is an interesting synthetic strategy to be considered, mainly due to the fact that this flexibility can induce exciting materials phenomena, like polymorphism[1] or reversible phase transitions. In addition, as the geometrical conformation of the linker can be modified by controlling the synthesis conditions,[2] a wide variety of structural types based on the same or related ligands can be obtained. In this context, dipodal building blocks of the $X_2M(\text{-}Q\text{-}CO_2H)_2$ type offer a wide variety of flexible ligands to design new MOFs.[3]

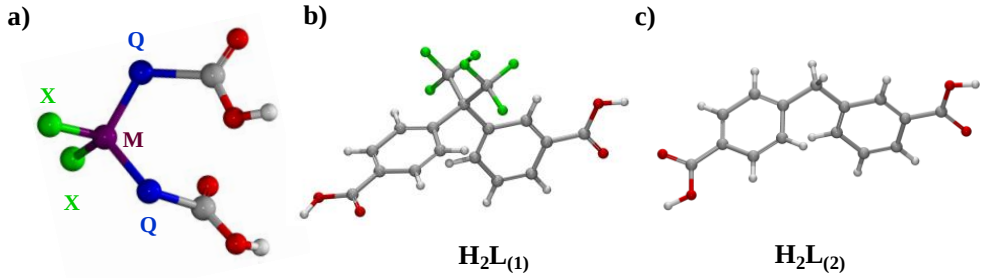

Figure 4.1. a) Dipodal linker of the $X_2M(\text{-}Q\text{-}CO_2H)_2$ type, **b)** 4,4'-(hexafluoroisopropylidene)*bis*(benzoic acid) ($H_2L_{(1)}$) and **c)** diphenylmethane-4,4'-dicarboxylic acid ($H_2L_{(2)}$).

The core atom of these dipodal ligands (M) can be silicon, carbon or sulfur atoms. The spacer groups Q are those that can expand the size of the organic ligand, for instance, benzene rings. Regarding to non-binding X substituents, a wide variety of functional groups can be considered. It is worth mentioning that these non-binding groups may be positioned either away from or into any void within the MOF framework. Consequently, they play a strategic role in the design of these porous materials. In this study, two different types of dipodal flexible ligands were used. While for both ligands the M is a carbon atom and the Q is a benzene group, they differ in the non-binding X substituents: $\text{-}CF_3$ groups in 4,4'-(hexafluoroisopropylidene)*bis*(benzoic acid) ($H_2L_{(1)}$); and –H atoms in diphenylmethane-4,4'-dicarboxylic acid ($H_2L_{(2)}$).

Chapter 4.1

4,4'-(hexafluoroisopropylidene)*bis*(benzoic acid) ($H_2L_{(1)}$)

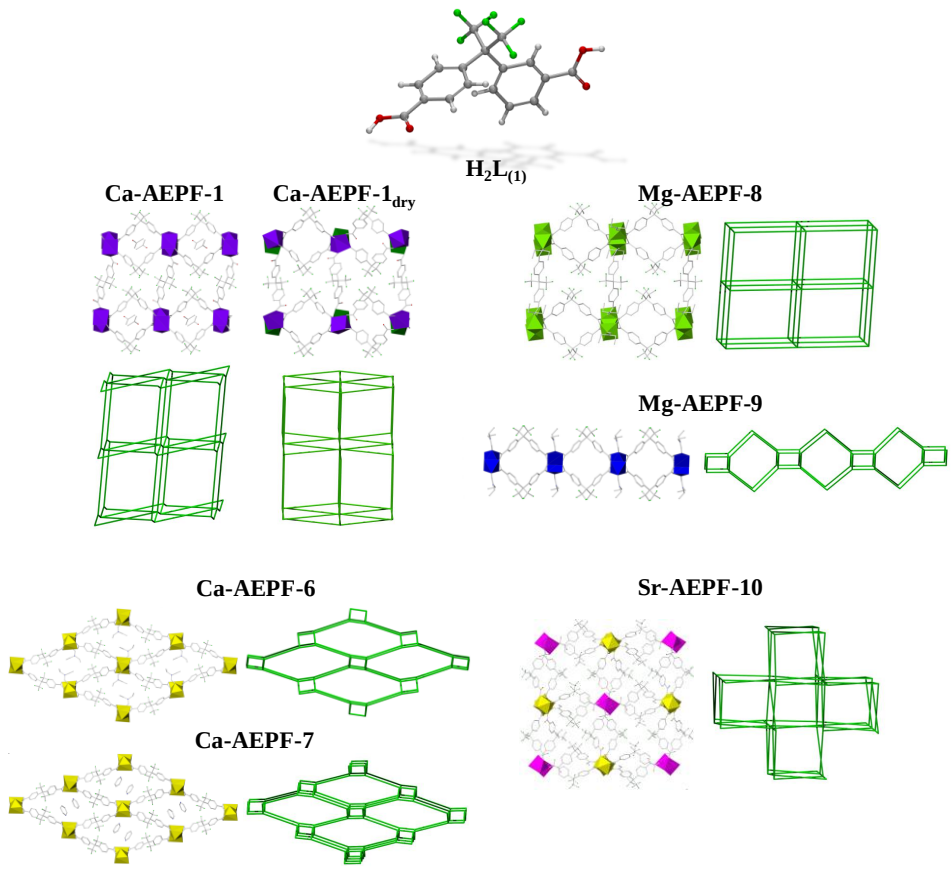

Abstract

Seven new compounds based on alkaline-earth ions and 4,4'-(hexafluoroisopropylidene)*bis*(benzoic acid) ($H_2L_{(1)}$) have been synthesised under solvothermal conditions. These novel materials belong to seven different structural types: **AEPF-1** and **AEPF-1**$_{dry}$ (Ca), **AEPF-6** (Ca), **AEPF-7** (Ca), **AEPF-8** (Mg), **AEPF-9** (Mg) and **AEPF-10** (Sr). The flexible **AEPF-1** material, which presents a reversible phase transition related to the loss of guest molecules, has been proved to be a good candidate for sorption and catalytic applications.

4.1.1.

Ca-AEPF-1 and Ca-AEPF-1_{dry}

In this section, we present a calcium MOF based on the $H_2L_{(1)}$ linker (4,4'-(hexafluoroisopropylidene)*bis*(benzoic acid)), named **AEPF-1**. This **AEPF** material exhibits a structural transformation that takes place by a *crystal-to-crystal transformation* (that is, without the formation of an amorphous phase during the transformation), accompanied by the loss of the single crystal integrity. For that reason, powder diffraction methods and computational studies were applied to determine the structure of the guest-free phase (**AEPF-1_{dry}**).

The work presented in this section is covered under the patent: A. E. Platero-Prats, E. Gutiérrez-Puebla, Á. Monge, N. Snejko, M. Iglesias, B. Gómez-Lor, V. A. de la Peña-O'Shea, *ES1641.453*, **2009**. The results of structural and topological studies as well as the liquid sorption properties have been published in *Chemistry - A European Journal*, **2010**, *16 (38)*, 11632; the catalytic studies have been published in *ChemCatChem*, **2010**, *2*, 147.

4.1.1.1.

AEPF-1: structural and topological description

The reaction between $H_2L_{(1)}$ and calcium acetate hydrate under the optimized solvothermal conditions, using a suitable combination of acetone (Me_2CO, from now on) and water as solvent mixture, gives rise to the **$[Ca(L_{(1)})(H_2L_{(1)})_{0.5}(H_2O)]\cdot 0.5\,Me_2CO$** compound (**AEPF-1**) (*see* Chapter 2, *Synthesis procedures*). This compound crystallizes in the monoclinic crystal system (*P2/n* space group). The cell parameters determined for this structure are: a = 18.7363(9) Å, b = 7.5101(4) Å, c = 20.807(1) Å, β = 104.041(2)º, V = 2840.3(2) $Å^3$. The main crystallographic and refinement data for **AEPF-1** are shown in **Table 4.1.1** and the ORTEP representation of its asymmetric unit is shown in **Figure 4.1.1**.

Table 4.1.1. Crystallographic and refinement data for **AEPF-1**.

Identification code	AEPF-1
Empirical formula	$C_{27}\ H_{15}\ Ca\ F_9\ O_{7.5}$
Formula weight	670.19
Temperature	123(2) K
Wavelength	1.54178 Å
Crystal system	Monoclinic
Space group	*P2/n*
Unit cell dimensions	a = 18.7363(9) Å α = 90° b = 7.5101(4) Å β = 104.041(2)° c = 20.807(1) Å γ = 90°
Volume	2840.3(2) $Å^3$
Z	4
Density (calculated)	1.568 Mg/m^3
Absorption coefficient	2.887 mm^{-1}
F(000)	1352
Crystal size	0.14 x 0.10 x 0.10 mm^3
Theta range for data collection	4.87 to 58.91°
Index ranges	-19<=h<=19, -8<=k<=5, -21<=l<=21
Reflections collected	10792
Independent reflections	3659 [R(int) = 0.0408]
Completeness to theta = 58.91°	89.4%
Absorption correction	Semi-empirical from equivalents
Max. and min. Transmission	0.7611 and 0.6880
Refinement method	Full-matrix least-squares on F^2
Data / restraints / parameters	3659 / 2 / 460
Goodness-of-fit on F^2	1.109
Final R indices [I>2sigma(I)]	R_1 = 0.0387, wR_2 = 0.1106
R indices (all data)	R_1 = 0.0432, wR_2 = 0.1129
Largest diff. peak and hole	0.523 and -0.271 e.$Å^{-3}$

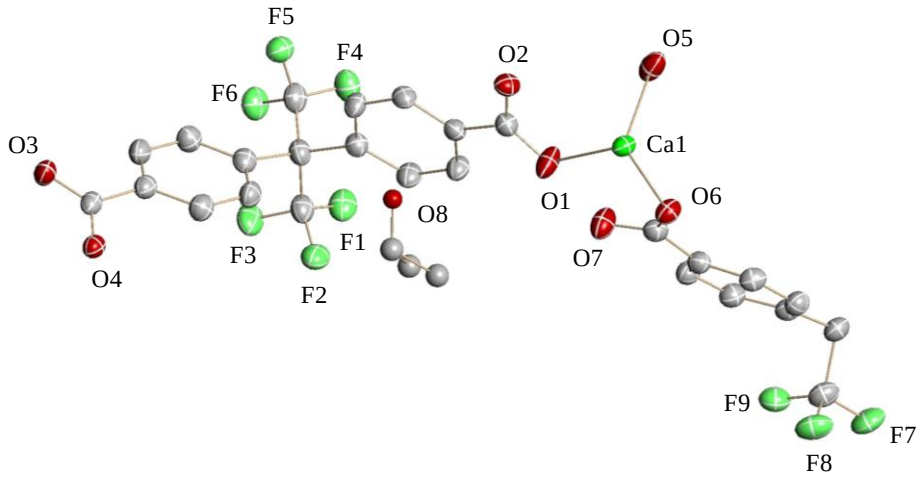

Figure 4.1.1. ORTEP representation of **AEPF-1** asymmetric unit. Ellipsoids are displayed at the 50% probability level. Hydrogen atoms were omitted for clarity.

Concerning the coordination environment of metal centres in **AEPF-1**, Ca^{+2} ions are hepta-coordinated to three oxygen atoms coming from a chelate-bridge $L_{(1)}^{-2}$ carboxylate group, two oxygen atoms from a bridge $L_{(1)}^{-2}$ carboxylate group, one oxygen atom coming from a $H_2L_{(1)}$ carbonyl group and one oxygen atom of a coordinated water molecule. This coordination environment gives rise to the formation of CaO_7 monocapped octahedra (**Figure 4.1.2a**), with an average Ca-O distance of ~2.41 Å (**Table 4.1.2**), which can be considered as the inorganic primary building units (PBUs).

Analysing more thoroughly the Ca-O distances in the CaO_7 polyhedra, some differences can be emphasized. On one hand, in the case of chelate-bridge carboxylate groups, two kinds of Ca-O distances are determined: a shorter bond corresponding to the bridge mode (~2.38 Å), and a larger one for chelate mode (~2.49 Å). On the other hand, those carboxylate groups that bond in a bridge mode, exhibit an average Ca-O bond distance of ~2.33 Å, which is slightly shorter than the distances described for chelate-bridge carboxylate groups. Finally, regarding the groups bonding in a η^1 coordination mode ($H_2L_{(1)}$ carbonyl groups and coordination water molecules), the Ca-O distance corresponding to carbonyl group is larger than that of water molecules.

Table 4.1.2. Interatomic distances in the coordination sphere of the CaO_7 polyhedra in **AEPF-1**.

Bond	Distance (Å)
Ca(1)-O(1)c	2.367(2)
Ca(1)-O(2)[1]c	2.298(2)
Ca(1)-O(3)[2]c	2.438(2)
Ca(1)-O(4)[2]c	2.545(2)
Ca(1)-O(4)[3]c	2.382(2)
Ca(1)-O(5)w	2.409(2)
Ca(1)-O(6)co	2.437(2)

Symmetry transformations used to generate equivalent atoms:
[1] -x,-y,-z+1 [3] x-1/2,-y,z-1/2
[2] -x+1/2,y+1,-z+3/2

Oc: oxygen atom coming from a carboxylate group. Oco: oxygen atom coming from a carbonyl group. Ow: oxygen atom coming from a water molecule.

The inorganic PBUs determined in **AEPF-1** are forming Ca_2O_{12} edge-sharing dimeric units, *via* the chelate-bridge carboxylate groups (**Figure 4.1.2b-1.2c)**. These dimeric units, which can be considered as the inorganic secondary building units (SBUs), are connected by the organic linker *via* the bridge carboxylate groups, giving rise to Ca_2O_{12} edge-sharing dimeric unit chains parallel to the *b* direction (**Figure 4.1.2b)**.

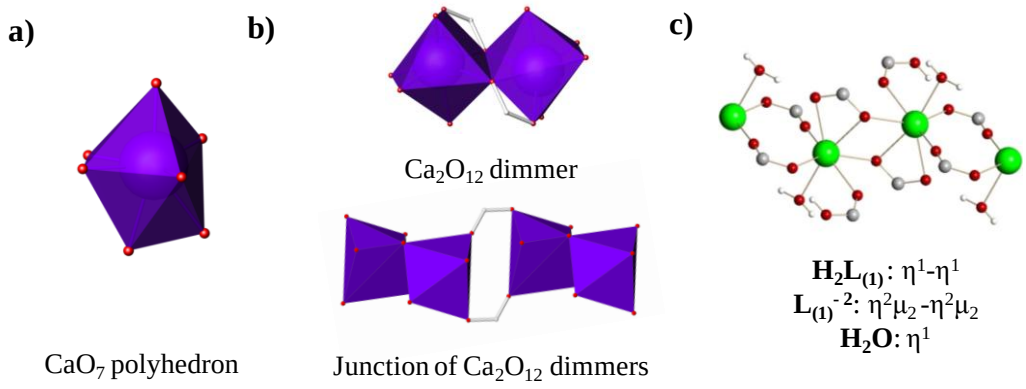

Figure 4.1.2. a) Inorganic PBUs in **AEPF-1**, **b**) detail of the Ca_2O_{12} dimmer and the junction among Ca_2O_{12} dimmers forming chains and **c)** coordination modes of the organic linkers and water molecules.

The inorganic chains described in **AEPF-1** are linked among them in two different ways. On one hand, these chains are joint through the whole deprotonated linker $L_{(1)}^{-2}$, which acts in a $\eta^2\mu_2$-$\eta^2\mu_2$ coordination mode (**Figure 4.1.2c**), forming layers with square-shaped channels. This kind of channels has been before described in other materials based on this ligand (named **A**-type channels,[1] from now on) (**Figure 4.1.3a**). On the other hand, the chains are also linked along the [0 0 1] direction through the protonated linker $H_2L_{(1)}$, that acts in a η^1-η^1 coordination mode (**Figure 4.1.2c**). In **Figure 4.1.3**, different polyhedral views along the crystallographic axes are depicted, evidencing the three-dimensional framework with square-shaped channels determined in **AEPF-1**.

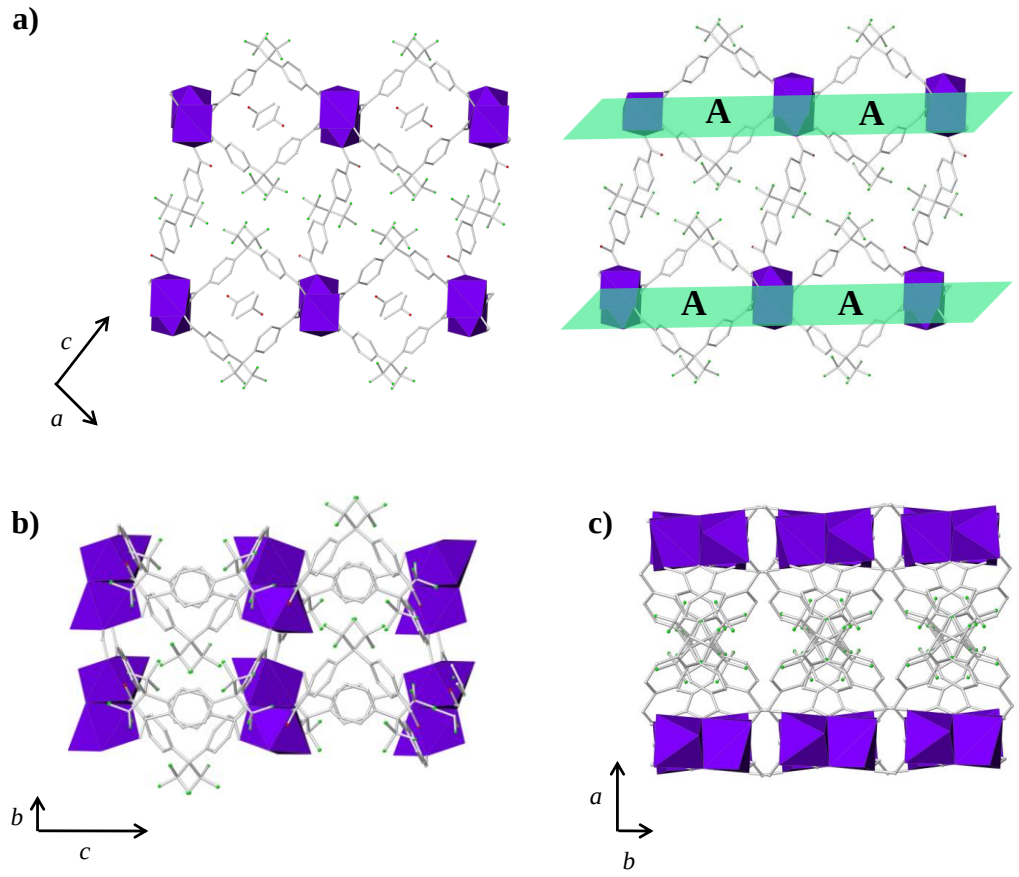

Figure 4.1.3. a) AEPF-1 polyhedral view, showing the square-shaped channels layers that can be described in this compound**. b**) Polyhedral representation along the *a* axis and **c)** along the *c* axis. Me_2CO molecules were omitted in **a)** (right), **b)** and **c)** for clarity.

The presence of supramolecular interactions in **AEPF-1** was also analysed mainly due to the presence of both water molecules and carboxylic groups that can establish hydrogen bonds. Thus, two kinds of different strong hydrogen bonds were determined and their main geometrical values are shown in Table **4.1.3**. The strongest hydrogen bond is determined between $H_2L_{(1)}$ carboxylic groups and bridge $L_{(1)}^{-2}$ carboxylate groups (O(7)···O(1)). As it is shown in **Figure 4.1.4**, this interaction can be favoured due to the distortion found in the CaO_7 polyhedra (**Figure 4.1.2a**). Moreover, the coordination water molecules act as donors of one hydrogen bond, that is established with chelate-bridge $L_{(1)}^{-2}$ carboxylate groups (O(5)···O(3)). In contrast to the other hydrogen bond before described, this one is present between the Ca_2O_{12} dimmeric units that form the inorganic chains in **AEPF-1** (**Figure 4.1.4**).

Table 4.1.3. Distances and angles of hydrogen bonds found in **AEPF-1** compound.

D-H···A[1]	D-H[2]	H···A[3]	D···A[4]	<D-H···A[5]
O(5)w-H(5A)w ··· O(3)c[1]	0.96(2)	1.76(2)	2.692(3)	164(4)
O(7)co-H(7A)co ··· O(1)c	0.86(4)	1.69(5)	2.539(3)	169(4)
Symmetry operators codes				
[1] x-1/2, -y-1, z-1/2				

D: donor atom, A: acceptor atom. [1]Names of donor, hydrogen and acceptor atoms involved in the hydrogen bond. [2] Distance D – A. [3]Distances H – A. [4]Distance D – A. [5] Angle D – H – A.

Oc: oxygen atom coming from a carboxylate group. Oco: oxygen atom coming from a carboxylic group. Hco: hydrogen atom coming from a carboxylic group. Ow: oxygen atom coming from a water molecule. Hw: hydrogen atom coming from a water molecule.

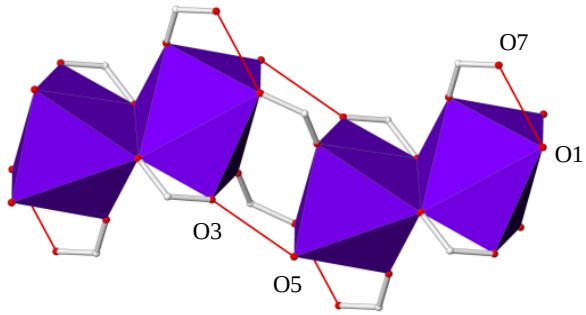

Figure 4.1.4. Polyhedral representation of two dimmeric units found in **AEPF-1**, showing in red the hydrogen bond interaction determined in this compound.

To consider topological features of **AEPF-1**, the crucial point is the simplification of the dimmeric unit chains that run along the *b* axis. In this case, after carefully analysing the net, the Ca(1) centers were chosen as unique nodes using

TOPOS[4] (**Figure 4.1.5a**). Thus, the **AEPF-1** net can be described as uninodal penta-connected, exhibiting an **hxg-d-5-*Pbcn*** topology (Point Symbol (6^{10})). The main simplification points, as well as the decorated and the final simplified nets for **AEPF-1**, are shown in **Figure 4.1.5**.

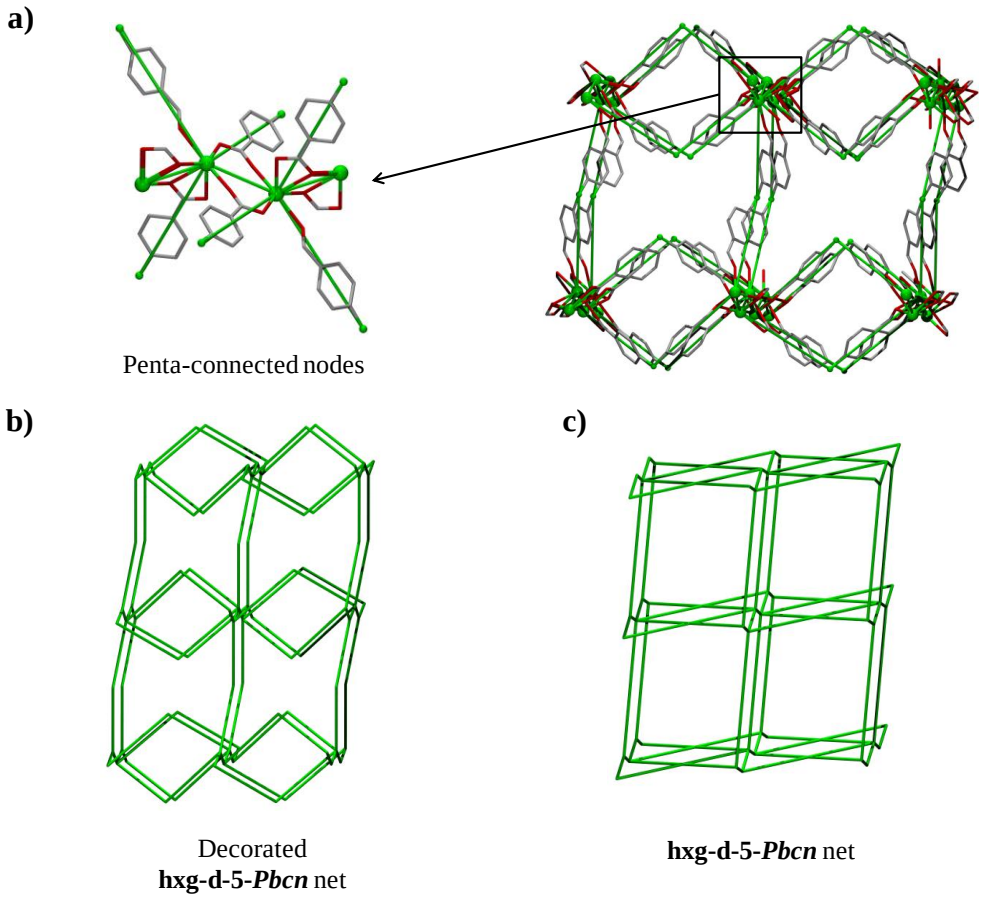

Figure 4.1.5. a) Topological simplifications performed to describe the penta-coordinated nodes in **AEPF-1**. Hydrogen atoms and $-CF_3$ groups were omitted for clarity. **b)** Decorated and simplified **hxg-d-5-*Pbcn*** net.

In addition, a topological study was performed to analyse the way in which the linker generates the **A**-type square shaped channels in **AEPF-1**. Thus, as it is shown in **Figure 4.1.6**, in this material the connections of metallic chains *via* $L_{(1)}^{-2}$ linker is made in an edge-crossing way.

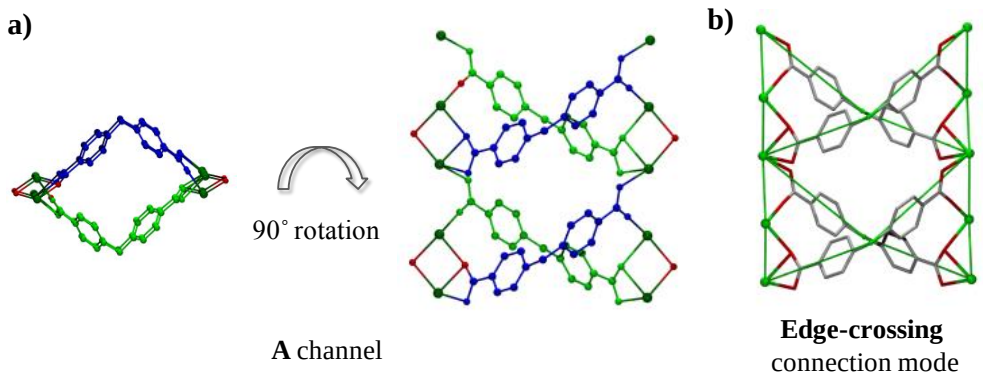

Figure 4.1.6. a) Different projections of the square shaped channels in **AEPF-1**. **b)** Detail of the real net together with the decorated **hxg-d-5-*Pbcn*** net, showing the edge-crossing connection mode of the linker. Hydrogen atoms and $-CF_3$ groups were omitted for clarity.

4.1.1.2.

Study of AEPF-1 activation

Taking into account the information coming from the structural resolution of this calcium MOF, two characteristics are noteworthy. On one hand, it has a porous structure, possessing cavities with an accessible free space of V=157 $Å^3$ and a pore size diameter of 6.9 Å (calculated with PLATON,[5] taking into account the van der Waals radii). On the other hand, **AEPF-1** contains acetone as guest molecules which are held inside pores through soft interactions, and can be removed by heating. Hence, the reversible uptake–release behaviour of guest molecules in **AEPF-1** would demonstrate the potential application of this material as an absorber, or as an organic-molecule sensor. Up to the moment, such studies have been reported for transition metal based MOFs,[6] but not for alkaline-earth metal MOFs

To investigate the potential application of this material for sorption, a detailed study of **AEPF-1** activation processes was performed following the loss of guest molecules from its pores, as follows: A thermal study of **AEPF-1** was carefully performed in the temperature range 20–200 ºC by using thermal gravimetric analysis (TGA) combined with mass spectrometry (TGA-MS) and differential scanning calorimetry (DSC). Within the temperature range explored, the weight loss was attributed to **1)** physisorbed water and acetone molecules (up to 75 ºC), and **2)** guest molecules from pores (up to 200 ºC), corresponding to two acetone molecules per unit

cell (**Figure 4.1.7**). Above this temperature, the material is stable up to 400 ºC. A change in the weight loss rate was observed at around 75 ºC. This weight loss rate reflects the departure of acetone from pores. This departure continues up to around 105 ºC (T_c), where the weight loss rate changes again. These results are in accordance with recent studies,[7] which show a two-step departure of acetone molecules that could be associated with structural changes in the framework. Furthermore, DSC has been used as a complementary tool to explore the energetic processes involved in the acetone departure from the pores in **AEPF-1** (**Figure 4.1.7**). A single peak centred at 105 ºC (T_c) is observed. This process is composed of two simultaneous steps: first, acetone loss from the pores; and second, structural changes in the **AEPF-1** framework.[8]

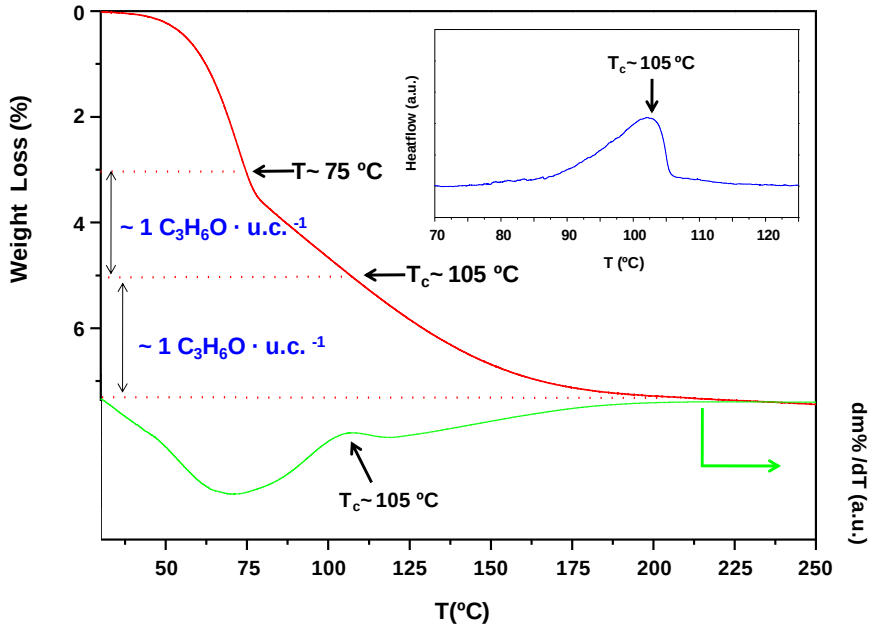

Figure 4.1.7. TGA profile (up) and its resulting derivative (down) for **AEPF-1**. DSC profile is shown in a detail inside the figure.

To determine the intrinsic energy involved in the guest removal process, a series of computational studies was performed by using the **AEPF-1** atomic coordinates determined by single-crystal XRD. All structural models were optimized by using plane wave density functional calculations (PWDF) (*see* Chapter 2, *Techniques*). Geometry optimization of **AEPF-1** converged to the same structure as determined by X-ray crystallography, which confirms the accuracy of the calculation method. These

theoretical calculations allowed the guest desorption apparent energy to be estimated at 25.5 kJ·mol^{-1}.[9]

Taking into account the results of the activation process of **AEPF-1**, a detailed structural study was performed to elucidate the effect on the crystal structure on the guest removal process. This entailed a series of experiments using variable-temperature optical microscopy (VTOM), variable temperature diffuse reflectance Fourier-transform infrared spectroscopy (VT-DRIFTS) and X-ray powder thermodiffraction (XRPTD).

Variable temperature optical microscopy (VTOM)

To study the variations in crystallinity accompanying the guest removal process in **AEPF-1**, VTOM experiments were performed (*see* the Chapter 2, *Techniques*). Thus, a single crystal of **AEPF-1** was heated from room temperature to 150 ºC (**Figure 4.1.8**). At around 75 ºC the crystal began to decay, which corresponds to removal of guest molecules from the pores (**Figure 4.1.8b**), as described above. Subsequent temperature increase to 105 ºC causes the total loss of single-crystal integrity, although the crystal retains its shape (**Figure 4.1.8f**), giving rise to a microcrystalline sample. These results confirm that possible structural changes related to the guest removal process cannot be followed by single-crystal diffraction studies for **AEPF-1**.

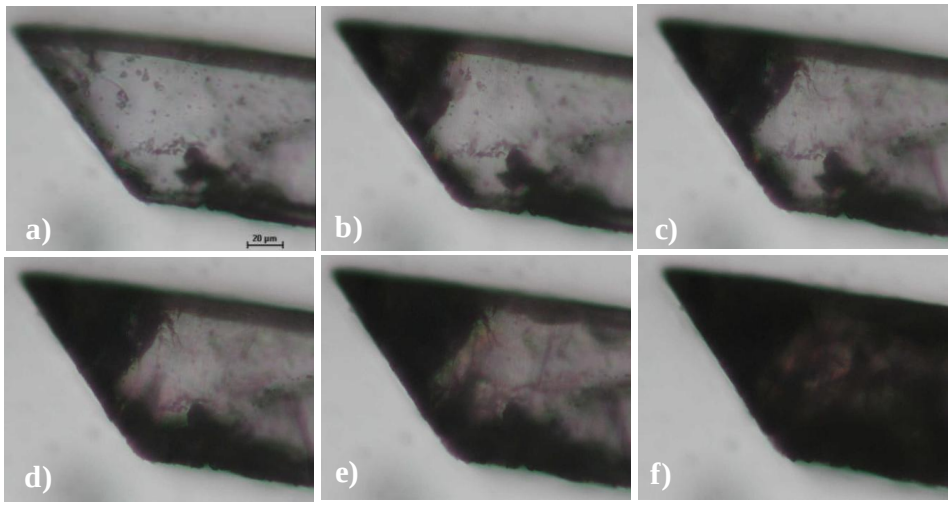

Figure 4.1.8. Optical microphotographs of a single crystal of **AEPF-1** at **a)** room temperature, **b)** 75 ºC, **c)** 82 ºC, **d)** 90 ºC, **e)** 97 ºC and **f)** 105 ºC.

X-ray powder thermodiffraction (XRPTD)

To accurately follow the structural changes accompanying the acetone removal process in **AEPF-1**, XRPTD experiments were performed (*see* the Chapter 2, *Techniques*). These studies show that when the temperature reaches 75 ºC, new peaks corresponding to an unknown crystalline phase (named **AEPF-1$_{dry}$**) appear together with those peaks associated with the **AEPF-1** phase. As the temperature is further increased, the intensity of the **AEPF-1** peaks decreases, whereas that of the **AEPF-1$_{dry}$** peaks increases; these two phases coexist up to 95 ºC. Finally, at temperatures above 100 ºC only the peaks of the **AEPF-1$_{dry}$** phase could be observed. These experiments confirm that the host material exhibits a structural transformation due to the loss of guest molecules (**Figures 4.1.9A-4.1.9B**), which gives rise to **AEPF-1$_{dry}$** with formula $[CaC_{25.5}F_9O_7H_{15}]_\infty$, as determined by elemental analysis (*see* the Chapter 2, *Synthesis Procedures*).

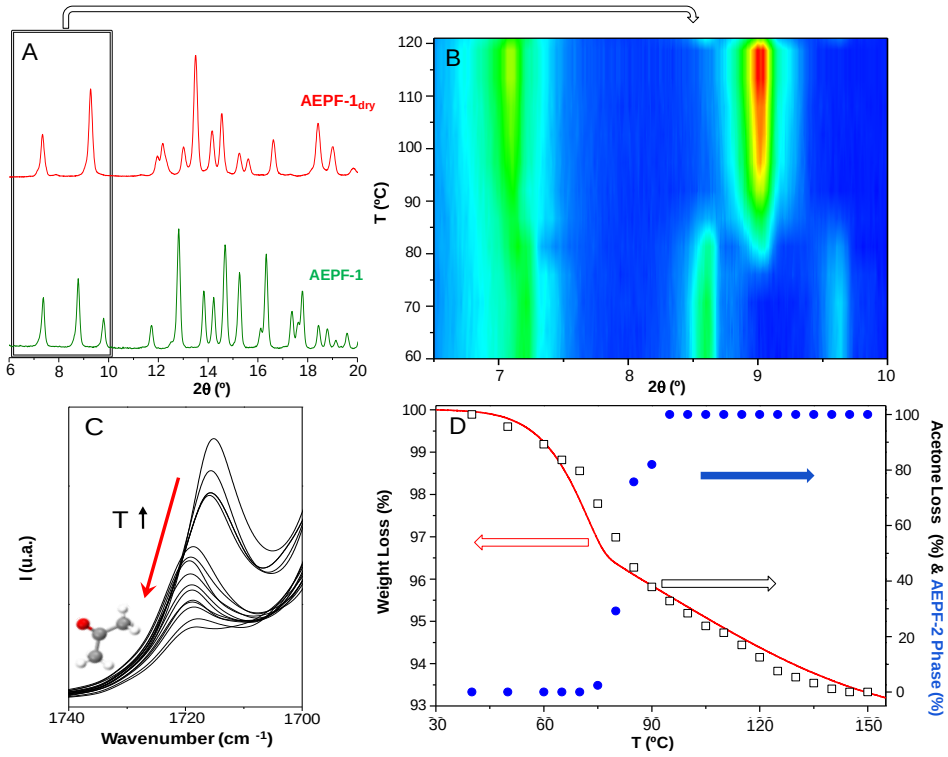

Figure 4.1.9. A) XRPD patterns of **AEPF-1** (red) and **AEPF-1$_{dry}$** (green). **B)** XRPTD experiments that show the transformation of **AEPF-1** to **AEPF-1$_{dry}$** increases with the temperature. **C)** Change in the IR spectrum of **AEPF-1** versus temperature, in the region of υ_{CO} for free acetone, due to the acetone loss. **D)** Plot of the ratio of **AEPF-1$_{dry}$** (blue), acetone loss (black), and weight loss (red) versus temperature.

Variable temperature diffuse reflectance Fourier-transform infrared Spectroscopy (VT-DRIFTS)

VT-DRIFTS studies were carried out at temperatures up to 130 ºC (*see* Chapter 2, *Techniques*). At room temperature, typical υ_{CO} vibrations corresponding to the carbonyl groups of free acetone (present in the pores of the framework) are determined at 1715 cm^{-1}. As the temperature is raised, a slight blue shift of the acetone band is observed (1720 cm^{-1}), while its intensity decreases (**Figure 4.1.9c**). Finally, above 120 ºC, no band corresponding to acetone is found. This variation was used to calculate the loss of acetone in **AEPF-1** (**Figure 4.1.9c**).

In **Figure 4.1.10**, the IR spectra performed at room temperature and 120 ºC are shown. Thus, at room temperature (**Figure 4.1.10a**), the bands corresponding to the υ_{CO} vibrations of the carbonyl and carboxylate groups in **AEPF-1** were determined at ~1685 (η^1 mode, **1**), ~1610(1595) (chelate-bridge $\eta^2\mu_2$ mode, **2**), and ~1560(1550) cm^{-1} (bridge $\eta^2\mu_2$ mode, **3**), which is consistent with the coordination modes of the carboxylate groups determined by single-crystal XRD. Upon increasing the temperature (**Figure 4.1.10b**), the bands in this range are detected at: ~1680 (**4**), 1660 (**5**), 1610 (**6**), and 1565 cm^{-1} (**7**). These results confirm that structural changes in **AEPF-1** take place during guest removal.

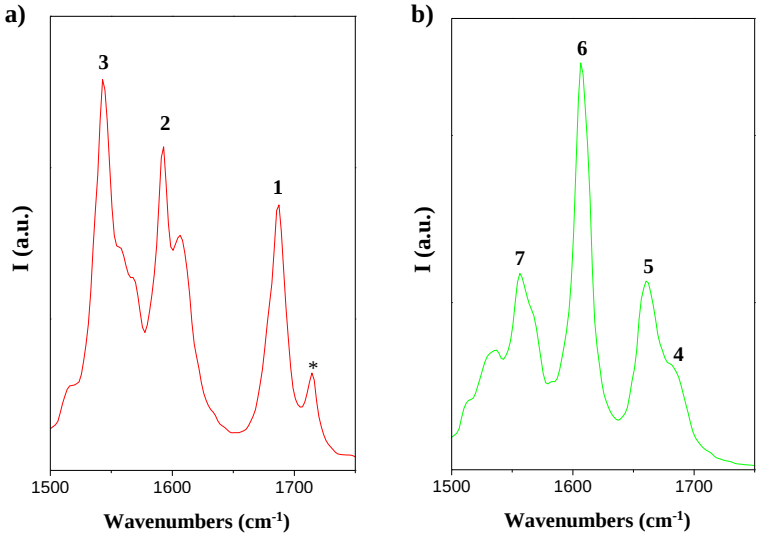

Figure 4.1.10. a) FT-IR Spectrum of **AEPF-1**, performed at room temperature, corresponding to carboxylate group modes region. The three different coordination modes of carboxylate groups are indicated. *A band at 1715 cm^{-1} corresponding to acetone from pores is observed. **b)** FT-IR Spectrum of **AEPF-1$_{dry}$**, performed at 120 ºC. The new coordination modes of carboxylate groups are indicated.

To summarize the variable temperature studies results, a plot of the ratio of **AEPF-1$_{dry}$** (calculated from XRPD data), the acetone loss (calculated from IR data), and the weight loss (calculated from TGA data) versus temperature are shown in **Figure 4.1.9D**. A clear relationship between the weight loss due to acetone removal and the phase transition from **AEPF-1** to **AEPF-1$_{dry}$** is determined.

4.1.1.3.

Structure determination of AEPF-1$_{dry}$

Since guest removal caused single-crystal decay, the structure of **AEPF-1$_{dry}$** was determined by XRPD and computational methods. The XRPD pattern of **AEPF-1$_{dry}$** shows clear peak overlap and a lack of peaks at high Bragg angles. Nevertheless, the pattern was indexed by using the DICVOL04 program[10,11] in an orthorhombic unit cell with cell parameters: a = 31.55 Å, b = 24.64 Å, c = 7.37 Å and V = 5731.7 Å^3 (figures of merit M_{20}= 10, F_{20}= 24). However, after carefully studying the systematic absences, the monoclinic system was chosen with β angle close to 90º and the space group was determined to be *P2/c* (Z=4). A matrix transformation was then applied to obtain the correct monoclinic unit cell with cell parameters: a = 24.64 Å, b = 7.37 Å, c = 31.55 Å, and β = 90º.

First, a Pawley profile fitting procedure,[12] which employed the Materials Studio software,[13] was used to refine the cell and peak-profile parameters, as well as those of the background, peak asymmetry, and zero shift. Then, a crystal structure model could be obtained by using the direct space global optimization algorithms implemented in the computer program FOX.[14-15] Since the unit cell volume of **AEPF-1$_{dry}$** ($V_{AEPF\text{-}1dry}$) is approximately twice of that of the unit cell volume of **AEPF-1** ($V_{AEPF\text{-}1}$), a valid chemical model consisting of two **AEPF-1** asymmetric units was used. The best of the **AEPF-1$_{dry}$** models generated by FOX was then optimized by Rietveld refinement[16] (considering molecules as rigid bodies) with energy optimization (Pareto optimization), using the Reflex module of the Materials Studio software. This method tries to balance matching the simulated pattern with the experimental diffraction data and then to minimize the potential energy of the structure.

Then, subsequent Rietveld refinements were performed by using only gradually relaxed constraints (some torsion angles were relaxed) to keep the model chemically sensible. Finally, hydrogen atoms were geometrically situated to complete the model. Refinement of this model converged with the R values R_{wp} = 0.186 and R_p = 0.263. Finally, to determine a chemically consistent structure of the dry phase PWDF calculations were carried out (*see* Chapter 2, *Techniques*). The initial coordinates of **AEPF-1$_{dry}$** were taken from the final refined structural model obtained by XRPD.

A structure minimization calculation was performed in the space group *P1* by keeping the cell parameters fixed. The newly obtained structural model was then optimized, as mentioned above, by using Rietveld methodology. Refinement of this model converged with R values R_{wp} = 0.115 and R_p = 0.156. The final refined cell parameters are: a = 24.644(7) Å, b = 7.382(3) Å, and c = 31.578(4) Å, with β = 90.17(3) º. This study has given rise to a structural model of the **AEPF-1** dry phase that is chemically consistent and consistent with the crystal structure, despite the complexity of the structure. Rietveld refinement profile for **AEPF-1$_{dry}$** is shown in **Figure 4.1.11**. Details of the unit cell and the refinement of **AEPF-1$_{dry}$** are given in **Table 4.1.4**.

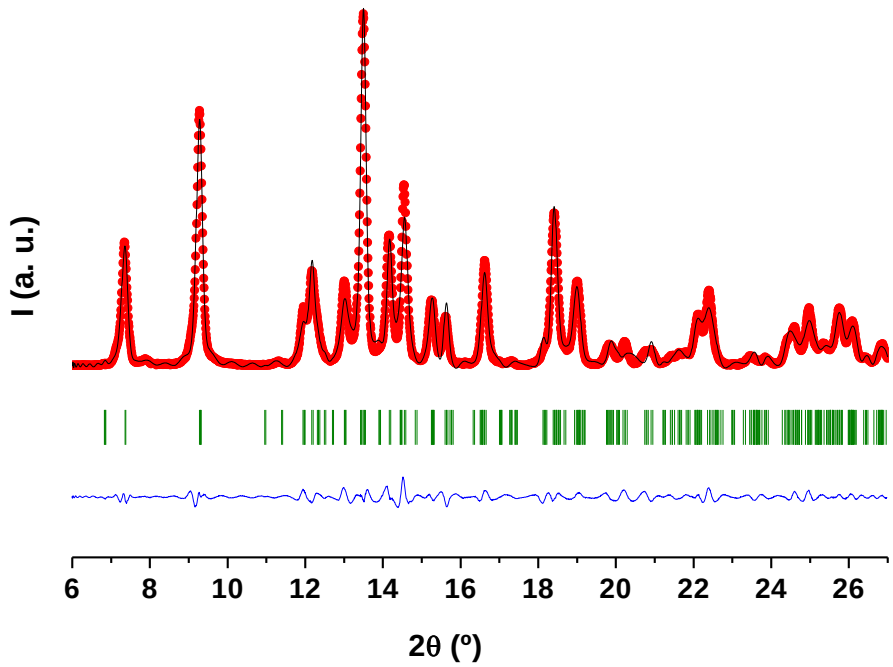

Figure 4.1.11. Rietveld refinement profile for **AEPF-1$_{dry}$**. Experimental data (red), simulated pattern (black) and difference (blue); observed reflections (green).

Table 4.1.4. Crystal data and structure refinement values for **AEPF-1$_{dry}$**.

Compound	AEPF-1$_{dry}$
Empirical formula	$C_{51}\ H_{30}\ Ca_2\ F_{18}\ O_{14}$
Formula weight	1288.91
Wavelength	1.542476 Å
Crystal system	Monoclinic
Space group	*P2 /c*
Unit cell dimensions	a = 24.644(7) Å α = 90˚
	b= 7.382(3)Å β = 90.17(3)˚
	c = 31.578(4) Å γ = 90˚
Volume	5744.7(2) Å^3
Z	4
Profile Function	Pseudo-Voigt
U	3.03(17)
V	-0.74(4)
W	0.066(3)
NA	0.68(4)
NB	-0.008(3)
Zero Point	0.2061(8)
Asymmetry correction	Finger-Cox-Jephcoat
H/L	0.01717 (3)
S/L	0.01665 (3)
Rwp	0.115
Rp	0.156

4.1.1.4.

AEPF-1$_{dry}$: structural and topological description

As it was before explained, the **AEPF-1$_{dry}$** compound (**[Ca(L$_{(1)}$)(H$_2$L$_{(1)}$)$_{0.5}$(H$_2$O)]**) crystallizes in the monoclinic crystal system (*P2/c* space group). The cell parameters determined for this structure are: a = 24.644(7) Å, b = 7.382(3) Å, c = 31.578(4) Å, β = 90.17(3) º and V = 5744.7(2) Å^3. The **AEPF-1$_{dry}$** asymmetric unit is shown in **Figure 4.1.12**.

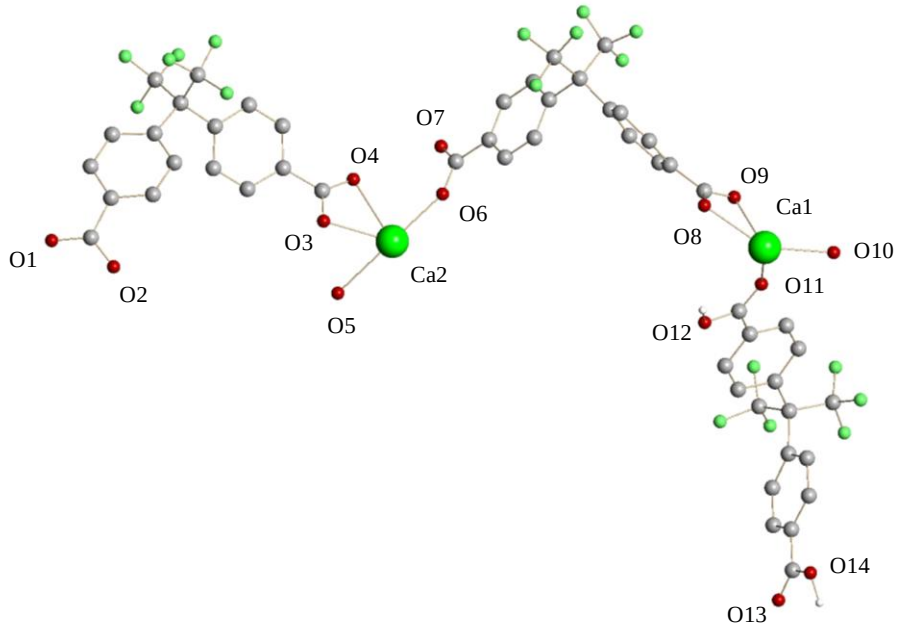

Figure 4.1.12. Representation of **AEPF-1$_{dry}$** asymmetric unit. Hydrogen atoms were omitted for clarity.

The structural model of **AEPF-1$_{dry}$** contains two independent calcium atoms: one is hepta-coordinated, and forms a CaO_7 monocapped octahedron, as it does in **AEPF-1** compound; however, the other calcium center is hexa-coordinated, forming a CaO_6 monocapped trigonal bipyramidal distorted polyhedron. These polyhedra can be considered as the inorganic PBUs in this material (**Figure 4.1.13a**).

Concerning the CaO_6 polyhedra, their vertices are occupied by three oxygen atoms from two different chelate-bridge $L_{(1)}^{-2}$ carboxylate groups, one oxygen atom of a bridge $L_{(1)}^{-2}$ carboxylate group, one oxygen atom from a $H_2L_{(1)}$ carbonyl group and one oxygen from a water molecule. In the case of CaO_7 polyhedra, an additional oxygen atom coming from a $L_{(1)}^{-2}$ carboxylate group which acts in a η^1 coordination mode is determined. The average Ca-O distance is the same for the two polyhedra (~2.43Å) (**Table 4.1.5**).

Table 4.1.5. Interatomic distances in the coordination sphere of the CaO_7 polyhedra for Ca(1) and CaO_6 polyhedra for Ca(2) in **AEPF-1$_{dry}$**.

Ca(1)

Bond	Distance (Å)
Ca(1)-O(1)c	2.443
Ca(1)-O(4)c	2.369
Ca(1)-O(7)c	2.442
Ca(1)-O(8)c	2.465
Ca(1)-O(9)c	2.484
Ca(1)-O(10)w	2.385
Ca(1)-O(11)co	2.397

Ca(2)

Bond	Distance (Å)
Ca(1)-O(3)c	2.411
Ca(1)-O(4)c	2.606
Ca(1)-O(5)w	2.518
Ca(1)-O(6)c	2.282
Ca(1)-O(9)c	2.484
Ca(1)-O(13)co	2.256

Oc: oxygen atom coming from a carboxylate group. Oco: oxygen atom coming from a carbonyl group. Ow: oxygen atom coming from a water molecule.

It is remarkable that the coordination modes of $L_{(1)}^{-2}$ carboxylate groups **AEPF-1$_{dry}$** ($\eta^2\mu_2$ (chelate bridge), $\eta^2\mu_2$ (bridge), and η^1 (monodentate)) are different from those determined in **AEPF-1** ($\eta^2\mu_2$ (chelate-bridge) and $\eta^2\mu_2$ (bridge)). This difference gives rise to the presence of two independent $L_{(1)}^{-2}$ forms in **AEPF-1$_{dry}$** asymmetric unit: **i)** the **A** form, which coordinates in a $\eta^2\mu_2$ (bridge)-$\eta^2\mu_2$ (chelate-bridge) and **ii)** the **B** form, which coordinates in a η^1-$\eta^2\mu_2$ (chelate bridge) (**Figure 4.1.13b**).

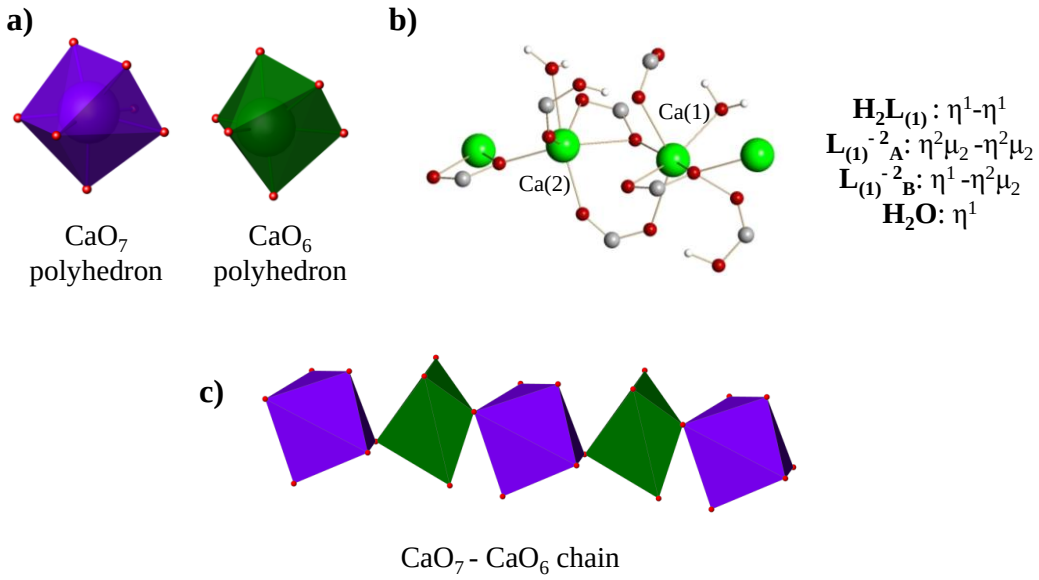

Figure 4.1.13. a) Inorganic PBUs in **AEPF-1$_{dry}$**, **b)** coordination modes of the organic linkers and water molecules in this compound and **c**) detail of the CaO_6-CaO_7 chain that run along the *b* axis.

The CaO_6 and CaO_7 polyhedra form vertex-sharing chains along the *b* axis (**Figure 4.1.13c**), through the $L_{(1)}^{-2}$ carboxylate groups. The junction of these inorganic chains is made in two different ways. On one hand, as it occurs in the case of **AEPF-1** compound, the chains are linked through the whole deprotonated linker, forming layers with square-shaped channels perpendicular to *c* axis. However, as in **AEPF-1$_{dry}$** there are two independent deprotonated ligands which exhibit different coordination modes ($L_{(1)}{}^{-2}{}_A$ and $L_{(1)}{}^{-2}{}_B$), two types of channels are determined (named **A'** and **A''**) (**Figure 4.1.14a**). On the other hand, the chains are also joint along the [0 0 1] direction through the protonated $H_2L_{(1)}$ linker, giving rise to a three-dimensional net. In **Figure 4.1.14**, different polyhedral views along the crystallographic axes are depicted.

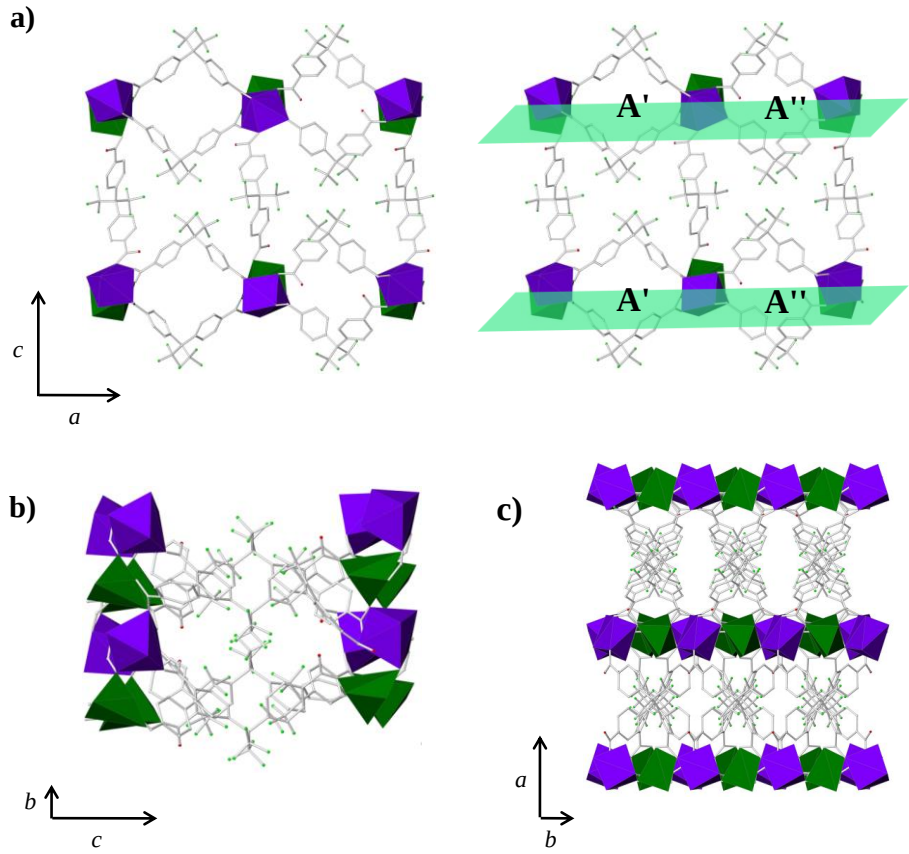

Figure 4.1.14. a) AEPF-1$_{dry}$ polyhedral view, showing the square-shaped channels layers**. b**) Polyhedral representation along the *a* axis and **c)** along the *c* axis.

The presence of supramolecular interactions in **AEPF-1$_{dry}$** was analysed in detail. It is worth mentioning that, due to the fact that all hydrogen atoms were geometrically calculated, the presence of hydrogen bonds interactions is based on the O···O distances. Thus, four different strong hydrogen bonds were determined and their main geometrical values are shown in **Table 1.1.6**. On one hand, two different types of hydrogen bonds are determined in the CaO_7 polyhedra: one strong between a bridge $L_{(1)}^{-2}$ carboxylate group and the $H_2L_{(1)}$ linker (O(7)···O(12)), and one weak among the non-bonded oxygen atoms from monodenated $L_{(1)}^{-2}$ carboxylate groups and the coordinated water molecules (O(2)···O(10)) (**Figure 4.1.15**). Furthermore, two additional weak hydrogen bonds are present among the CaO_6 and CaO_7 polyhedra along the inorganic chains: one bond between a chelate-bridge $L_{(1)}^{-2}$ carboxylate group and

one coordination water molecule (O(10)···O(3)); and the other one is determined among the bonded oxygen atoms from monodentated $L_{(1)}^{-2}$ carboxylate groups and the $H_2L_{(1)}$ linkers (O(14)···O(1)) (**Figure 4.1.15**).

Table 4.1.6. Distances and angles of hydrogen bonds found in **AEPF-1$_{dry}$** compound.

D-H···A[1]	D-H[2]	H···A[3]	D···A[4]	<D-H···A[5]
O(10)w-H(102)w ··· O(2)c	0.99	1.78	2.688	151
O(10)w-H(103)w ··· O(3)c	0.99	1.83	2.768	158
O(12)co-H(104)co ··· O(7)c	1.05	1.45	2.490	169
O(14)co-H(105)co ··· O(1)c	1.05	1.59	2.617	167

D: donor atom, A: acceptor atom. [1]Names of donor, hydrogen and acceptor atoms involved in the hydrogen bond. [2] Distance D – A. [3]Distances H – A. [4]Distance D – A. [5] Angle D – H – A.

Oc: oxygen atom coming from a carboxylate group. Oco: oxygen atom coming from a carboxylic group. Hco: hydrogen atom coming from a carboxylic group. Ow: oxygen atom coming from a water molecule. Hw: hydrogen atom coming from a water molecule.

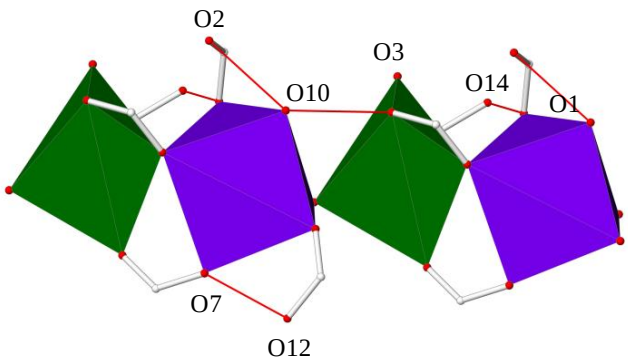

Figure 4.1.15. Polyhedral representation of the inorganic chains found in **AEPF-1$_{dry}$**, showing in red the hydrogen bond interactions determined in this compound.

To consider topological features of **AEPF-1$_{dry}$**, as it occurs in **AEPF-1** net, the crucial point is the simplification of the inorganic chains. In this case, the calcium centers were chosen as penta-cooridnated nodes using TOPOS[4] (**Figure 4.1.16a**). Even though there are two crystallographically independent calcium centers in **AEPF-1$_{dry}$**, it is worth mentioning that they become equivalent from the topological point of view, giving a uninodal net. Thus, the net for this compound is uninodal penta-conneted, exhibiting a **5/4/o13** topology (Point Symbol ($4^4.6^6$)). The main simplifications points, as well as the decorated and the final simplified nets for **AEPF-1**, are shown in **Figure 4.1.16**.

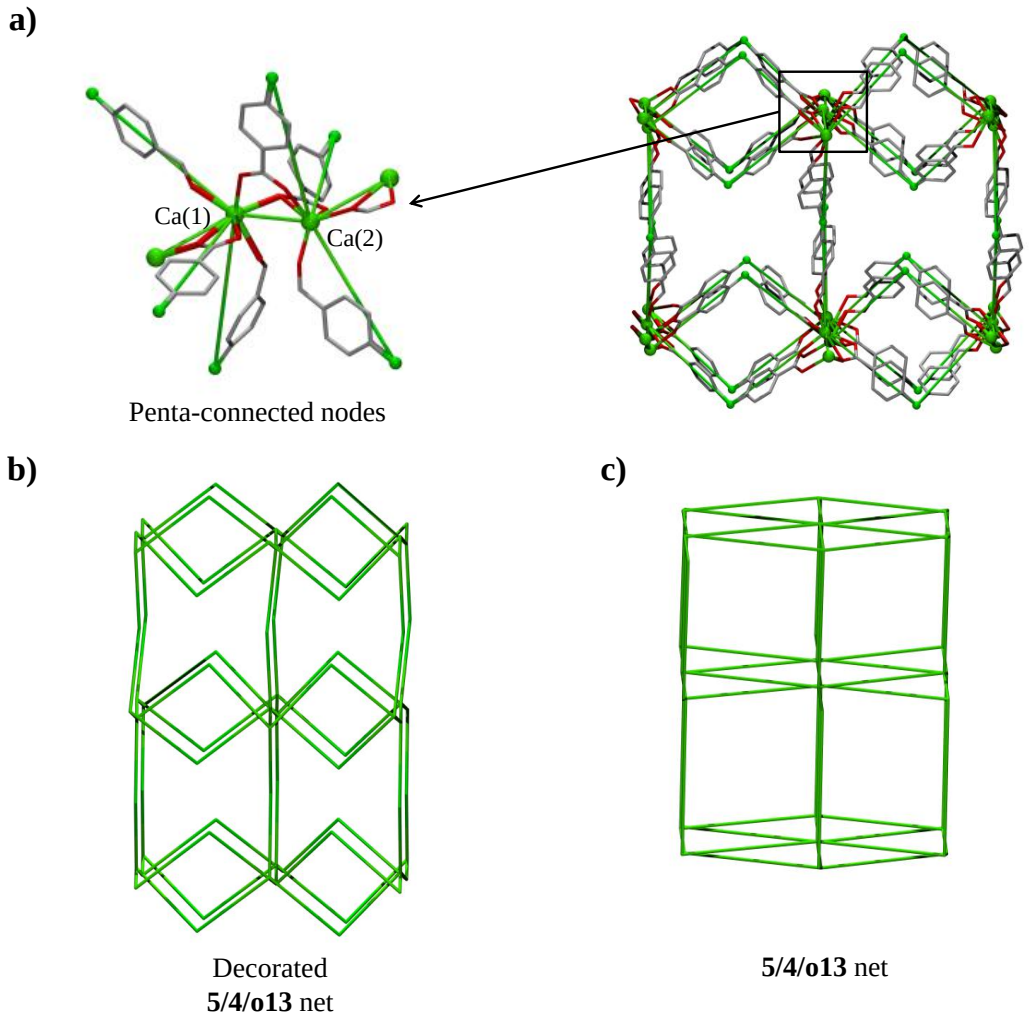

Figure 4.1.16. a) Topological simplifications performed to describe the penta-coordinated nodes in **AEPF-1$_{dry}$**. Hydrogen atoms and –CF_3 groups were omitted for clarity. **b)** Decorated and simplified **5/4/o13** net.

As it was done before for **AEPF-1**, a topological study was performed to analyse the way in which the linker generates the **A'**- and **A''**-type square shaped channels[1] in **AEPF-1$_{dry}$**. Thus, as it is shown in **Figure 4.1.17**, in this material the connections of metallic chains *via* $L_{(1)}^{-2}$ linkers is made in a similar edge-crossing way for the two types of channels.

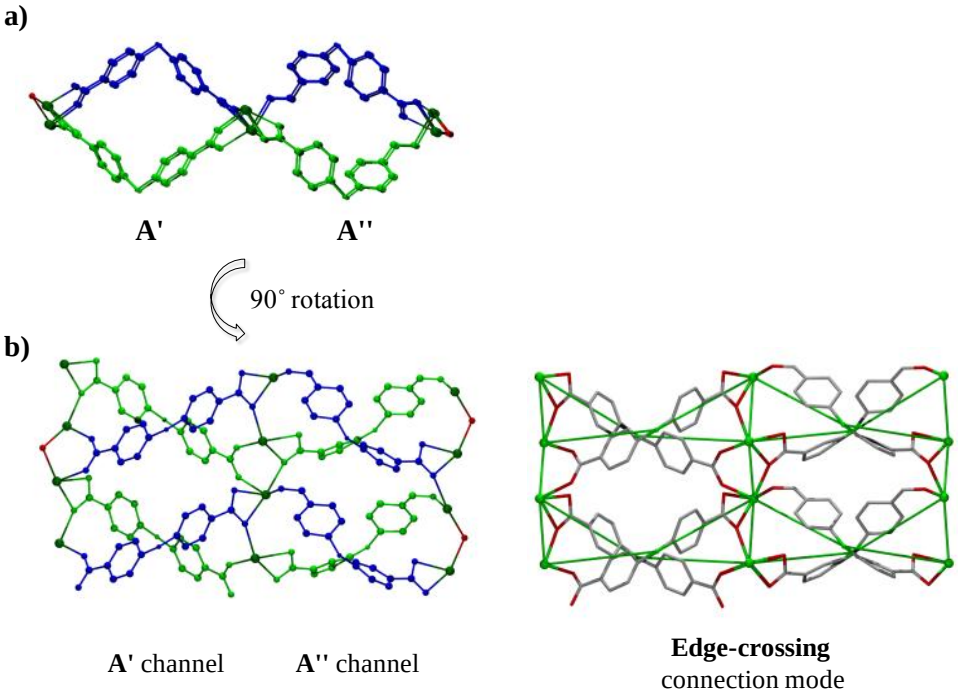

Figure 4.1.17. a) The two types of square shaped channels in **AEPF-1$_{dry}$** are depicted. **b)** Detail of the real net together with the decorated **5/4/o13** net, showing the edge-crossing connection mode of the linker. Hydrogen atoms and $-CF_3$ groups were omitted for clarity.

4.1.1.5.

AEPF-1 and AEPF-1$_{dry}$: comparative studies

Structural and topological features

Concerning the phase transition from **AEPF-1** to **AEPF-1$_{dry}$**, it is worth highlighting that the loss of acetone molecules involves changes in the conformation of the organic linker. Thus, in order to compare both structures, the conformation of the ligand was analysed by describing some geometrical parameters (**θ** angle, **ω** dihedral angle and **d** distance) (**Figure 4.1.18**). Their values for **AEPF-1** and **AEPF-1$_{dry}$** nets are shown in **Table 4.1.7**.

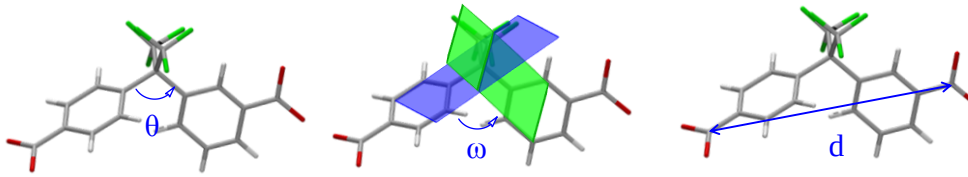

Figure 4.1.18. Definition of **θ** angle, **ω** dihedral angle and **d** distance used to describe the linker conformation.

Table 4.1.7. θ angle, **ω** dihedral angle and **d** distance values determined for the linker in **AEPF-1** and **AEPF-1$_{dry}$** compounds.

AEPF-1			
Linker	**θ (º)**	**ω (º)**	**d (Å)**
$H_2L_{(1)}$	109.30	63.02	8.752
$L_{(1)}^{-2}$	111.14	69.82	9.502

AEPF-1$_{dry}$			
Linker	**θ (º)**	**ω (º)**	**d (Å)**
$H_2L_{(1)}$	107.35	74.97	8.961
$L_{(1)}^{-2}{}_A$	110.37	74.86	9.693
$L_{(1)}^{-2}{}_B$	109.55	44.57	8.794

After analysing the linker conformation for both structures, several conclusions can be drawn. Concerning the protonated ligand molecules ($H_2L_{(1)}$), which join the square shaped channels layers, they exhibit only one conformation for each compound. Thus, while for **AEPF-1** compound the $H_2L_{(1)}$ ligand shows a higher **θ** angle value, in the case of **AEPF-1$_{dry}$**, it exhibits higher values for **ω** dihedral angle and **d** distance. However, despite of these differences, it can be concluded that the $H_2L_{(1)}$ conformation is quite similar both for **AEPF-1** and **AEPF-1$_{dry}$**.

Concerning the deprotonated linker forms ($L_{(1)}^{-2}$), which are directly implied in the formation of the square-shaped channels, in **AEPF-1** compound only one conformation is found (giving **A** channels). However, for **AEFP-1$_{dry}$**, deprotonated linker has alternating conformations along the *a* direction (**A'** and **A''** channels). Comparing the conformations of $L_{(1)}^{-2}$ in both structures, it is worth mentioning that the $L_{(1)}^{-2}{}_A$ linker (**A'** channels) exhibits a similar conformation to that found in **AEFP-1** (**A**

channels). In contrast, the conformation of $L_{(1)}{}^{-2}{}_{B}$ linker (**A''** channels) is markedly different, with a very low **ω** value, together with a **d** distance similar to $H_2L_{(1)}$ form.

Taking into account these structural analyses, a mechanism that explains the changes in the channels during the guest removal can be proposed (**Figure 4.1.19**). Thus, it can be suggested that, when a guest molecule enters into a fully open **A'** channel (**Figure 4.1.19b**), a conformational change occurs, giving the **A**-type partially open channel (**Figure 41.19a**) and opening the closed channel **A''** (**Figure 4.1.19b**), which would be then accessible to other guest molecules. These changes could thus facilitate the migration of each guest molecule to the neighbouring unit cell along the channel. Propagation of this process could effectively pump the solvent molecules along the channels throughout the crystal.

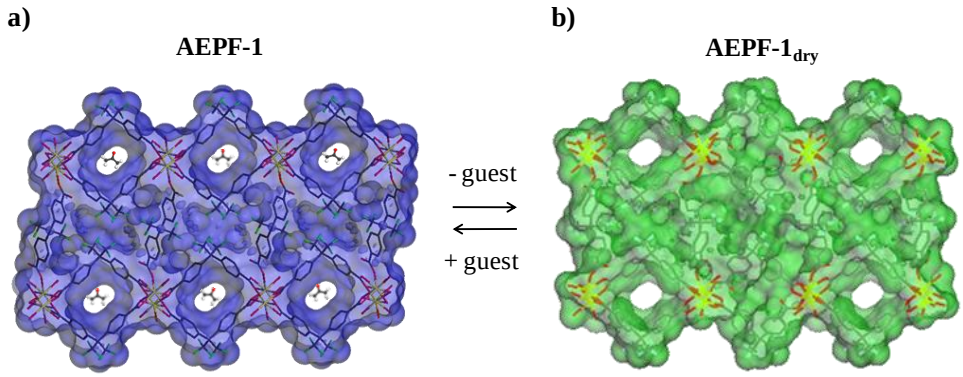

Figure 4.1.19. Connolly surface representation (effectively the inverse of the solvent-accessible surface) for: **a) AEPF-1** and **b) AEPF-1$_{dry}$** materials.

Computational studies

In addition to the diffraction experiments, a computational study was also performed to determine the energetic balance between the intrinsic stability of **AEPF-1** and the new **AEPF-1$_{dry}$** phase. As discussed above, PWDF calculations predicted an accurate 3D structure for **AEPF-1$_{dry}$**. As it was assumed for the structure determination of **AEPF-1$_{dry}$**, due to the fact that the unit cell volume of **AEPF-1$_{dry}$** ($V_{AEPF\text{-}1dry}$) is approximately twice that of **AEPF-1** ($V_{AEPF\text{-}1}$), the starting configuration of **AEPF-1** was based on a new cell twice as big as the original unit cell. This calculation showed that **AEPF-1** is thermodynamically more stable than **AEPF-1$_{dry}$**, with estimated energy required for the phase transition ($E_{AEPF\text{-}1}$-$E_{AEPF\text{-}1dry}$) of 283.9 kJ·mol^{-1}.

4.1.1.6.

AEPF-1 phase recovery

The structural analyses described above show that the transformation of **AEPF-1** into **AEPF-1$_{dry}$** with the loss of acetone guests leads to a new 3D structure. The next step was to investigate the reversibility of this process. Treatment of **AEPF-1$_{dry}$** in acetone at room temperature for 2 h gave the recovered phase named **AEPF-1'**. This shows that **AEPF-1$_{dry}$** can reabsorb acetone guests. To confirm the phase transition, the bulk samples were analyzed by XRPD. As it is shown in **Figure 4.1.20**, **AEPF-1'** shows a pattern closely resembling to that of **AEPF-1**, in accordance with the reversibility of the phase transition. The differences in relative intensities observed for the Bragg peak centred at 7.28 can be attributed to preferential adsorption of acetone molecules through the plane (101) in **AEPF-1'** (**Figure 4.1.20**). Further evidence for readsorption of the guest was obtained by TGA-MS. The TGA curve of **AEPF-1'** shows a weight loss of around 5.6 wt% from 75 to 200 ºC, which corresponds to the loss of 2.5 acetone molecules per unit cell.

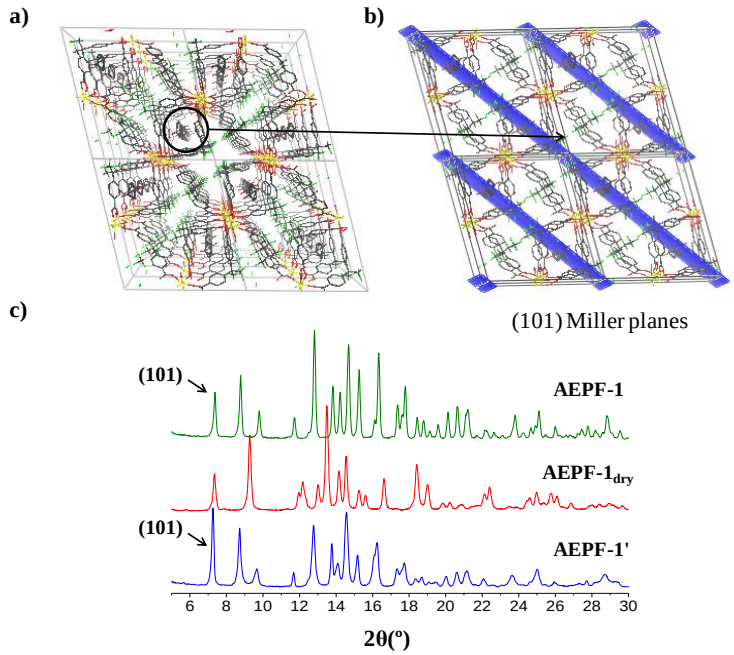

Figure 4.1.20. **a) AEPF-1** net representation. **b)** (101) Miller plane representation in **AEPF-1**. **c)** Comparison of the X-ray patterns of **AEPF-1**, **AEPF-1$_{dry}$**, and **AEPF-1'**.

4.1.1.7.

Adsorption by immersion in organic solvents

To investigate whether or not **AEPF-1$_{dry}$** can act as an absorber of other than acetone organic solvents, experiments were performed by suspending **AEPF-1$_{dry}$** samples in a number of different liquids with different polarity and molecular size/shape (acetone, acetonitrile, 1-butanol, isopropyl alcohol, toluene, benzene, n-hexane, and isooctane). All these solvents possess a molecular volume that is lower than the pore volume (157 Å^3), and should theoretically fit into the cavities of **AEPF-1** (**Table 4.1.8**). **AEPF-1$_{dry}$** samples were suspended in each solvent at room temperature for 2 h and then dried in air (see the Chapter 2, Experimental Section). TGA-MS was used to evaluate the presence of solvent guest molecules after the treatment (**Figure 4.1.21a**). These studies showed that **AEPF-1$_{dry}$** exhibits a huge adsorption capacity in the cases of acetonitrile, acetone, and 1-butanol (ca. 90, ca. 70, and ca. 62 mol% adsortion, respectively). Note that the isopropyl alcohol, which presents a higher molecular volume, presents a lower adsorption value (41 mol%). However, the 1-butanol is strongly absorbed despite its high molecular volume probably due to its linear shape (**Table 4.1.8**).

The aromatic solvents (benzene and toluene) were less adsorbed (**Figure 4.1.21a**). The nonpolar aliphatic organic solvents (n-hexane, isooctane) were not adsorbed at all. These experiments demonstrated the selectivity of **AEPF-1$_{dry}$** for small polar organic solvent molecules. The opposite behaviour, with selective adsorption of nonpolar organic solvents, was previously reported for a Cu-based MOF.[17,18]

XRPD was used to check the recovery of the **AEPF-1'** phase for **AEPF-1$_{dry}$** samples after the treatment. The XRPD patterns corresponding to samples immersed in each solvent are depicted in Figure **4.1.21c-4.1.21d**. For polar organic solvents complete recovery of **AEPF-1**' is observed (**Figure 4.1.21c**), whereas the sorption behaviour for aromatic solvents clearly entails a partial phase conversion (**Figure 4.1.21d**).

Table 4.1.8. Sorption properties of **AEPF-1$_{dry}$** at 25 ºC.

Solvent	Molecular volume [a] (Å^3)	Sorption (molar %)	Sorption (wt %)	Solvent molecules per unit cell
Toluene	91	16	2.2	1.4[b]
Benzene	81	22	2.7	2.3[b]
Isopropyl alcohol	64	41	3.8	1.6
1-Butanol	79	62	7.1	2.5
Acetone	57	70	6.2	2.8
Acetonitrile	26	90	5.7	3.6

[a] Approximate volume for each molecule calculated from the van der Waals surface. [b] Number of solvent molecules per unit cell of **AEPF-1** according to XRPD data.

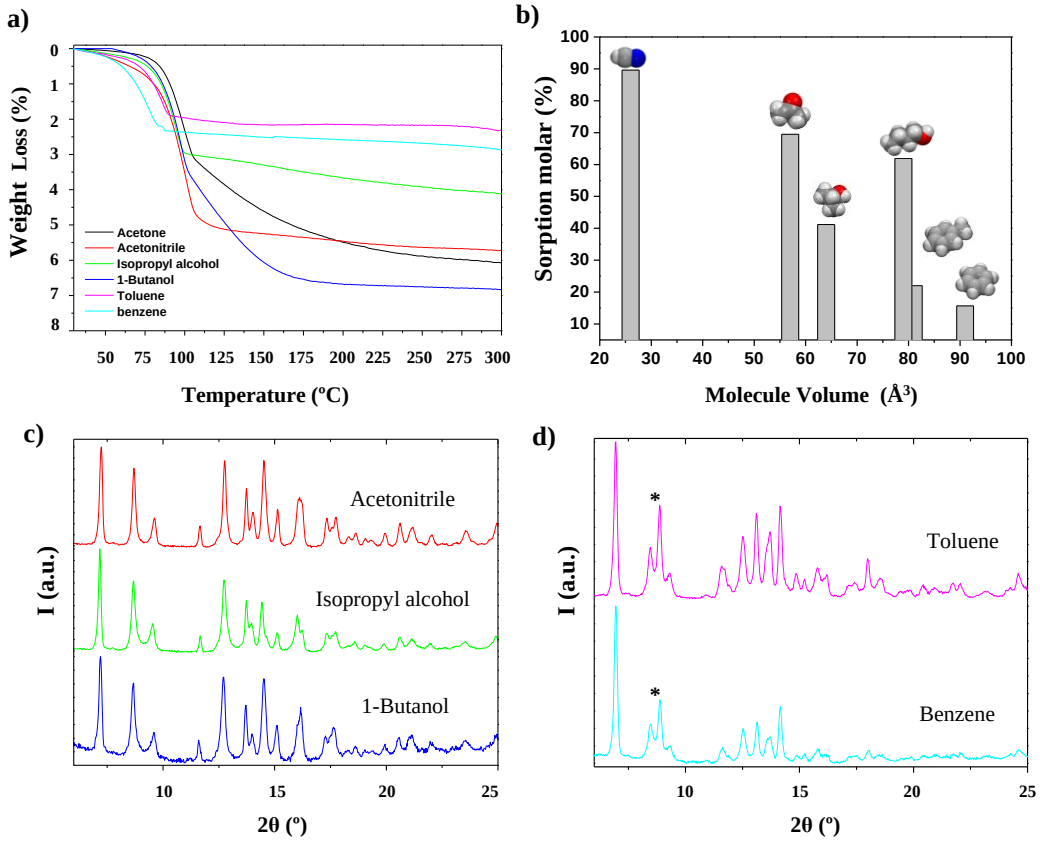

Figure 4.1.21. a) TGA for **AEPF-1$_{dry}$** samples after each sorption treatment. **b)** Plot of molar sorption for each solvent (calculated from TGA-MS) versus molecular volume. **c)** Comparison of the X-ray patterns for samples after sorption of polar organic solvents and **d)** of aromatic solvents. * denotes the most intense diffraction peak of **AEPF-1$_{dry}$**.

A profile fitting of XRPD data for each **AEPF-1'** sample was performed to determine the structural changes produced in the organic solvent sorption experiments. Pawley refinement profiles and the refinements values are shown in **Tables 4.1.9-4.1.12** and **Figure 4.1.22-4.1.25**.

Table 4.1.9. Crystal Data and structure refinement values for **AEPF-1'**, after immersion in acetone.

Compound	AEPF-1' after immersion in acetone
Crystal system	Monoclinic
Space group	*P2/n*
Unit cell dimensions	a = 18.890(3) Å α = 90˚
	b= 7.576(1) Å β = 104.423(7)˚
	c = 20.936(3) Å γ = 90˚
Profile Function	Pseudo-Voigt
U	0.7(3)
V	0.04(6)
W	0.014(3)
NA	0.86(5)
NB	-0.009(3)
Zero Point	-0.011(2)
Rwp	0.0681
Rp	0.0503

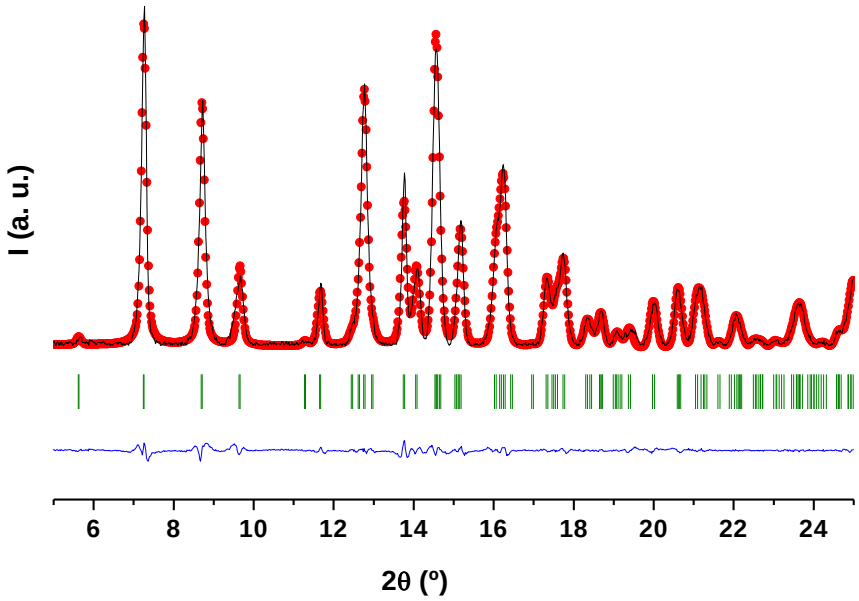

Figure 4.1.22. Pawley refinement for **AEPF-1'** sample after immersion in acetone. Experimental data (red), simulated patter (black) and difference (blue); observed reflections (green).

Table 4.1.10. Crystal Data and structure refinement values for **AEPF-1'**, after immersion in acetonitrile.

Compound	AEPF-1' after immersion in acetonitrile	
Crystal system	Monoclinic	
Space group	*P2/n*	
Unit cell dimensions	a = 18.928(2) Å	α = 90˚
	b= 7.5745(4) Å	β = 104.326(6)˚
	c = 20.908(2) Å	γ = 90˚
Profile Function	Pseudo-Voigt	
U	1.1(2)	
V	-0.18(4)	
W	0.032(2)	
NA	0.53(4)	
NB	0.014(3)	
Zero Point	-0.036(1)	
Rwp	0.0571	
Rp	0.0427	

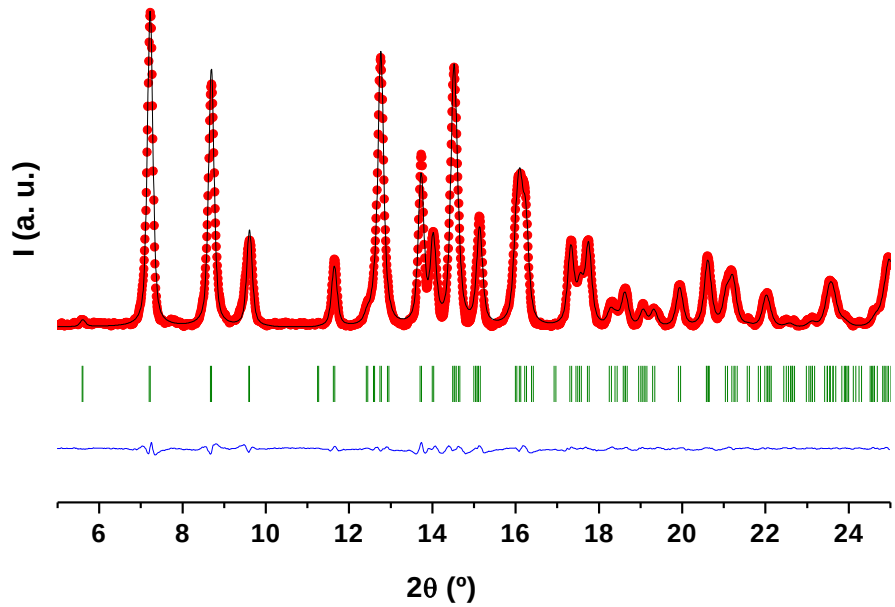

Figure 4.1.23. Pawley refinement for **AEPF-1'** sample after immersion in acetonitrile. Experimental data (red), simulated patter (black) and difference (blue); observed reflections (green).

Table 4.1.11. Crystal Data and structure refinement values for **AEPF-1'**, after immersion in isopropyl alcohol.

Compound	AEPF-1' after immersion in isopropyl alcohol	
Crystal system	Monoclinic	
Space group	*P2/n*	
Unit cell dimensions	a = 19.000(3) Å	α = 90˚
	b = 7.542(1) Å	β = 104.16(1)˚
	c = 20.872(4) Å	γ = 90˚
Profile Function	Pseudo-Voigt	
U	0.6(4)	
V	0.09(8)	
W	0.010(4)	
NA	0.83(6)	
NB	0.004(5)	
Zero Point	-0.071(2)	
Rwp	0.0704	
Rp	0.0521	

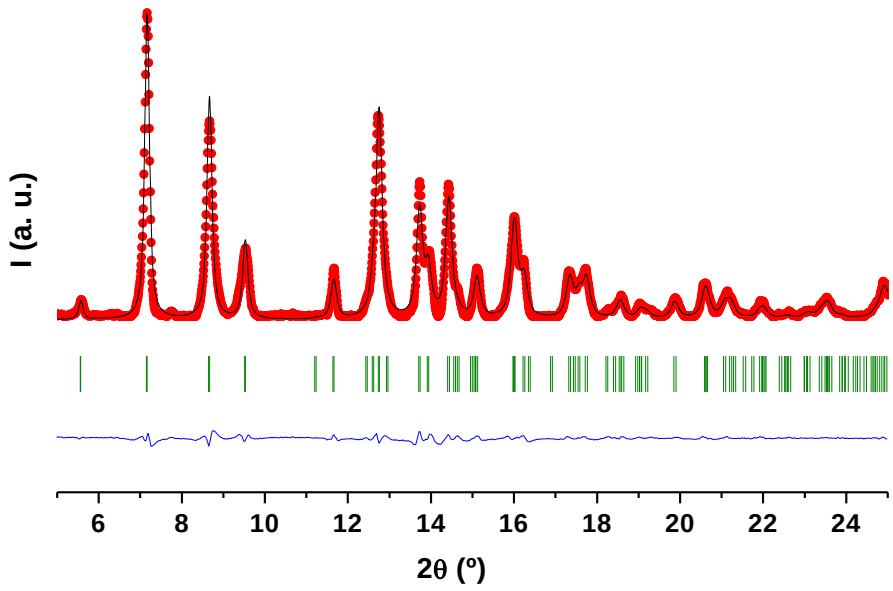

Figure 4.1.24. Pawley refinement for **AEPF-1'** sample after immersion in isopropyl alcohol. Experimental data (red), simulated patter (black) and difference (blue); observed reflections (green).

Table 4.1.12. Crystal Data and structure refinement values for **AEPF-1'**, after immersion in 1-butanol.

Compound	AEPF-1' after immersion in 1-butanol	
Crystal system	Monoclinic	
Space group	*P2/n*	
Unit cell dimensions	a = 18.921(4) Å	α = 90˚
	b= 7.572(1) Å	β = 104.49(1)˚
	c = 20.926(4) Å	γ = 90˚
Profile Function	Pseudo-Voigt	
U	1.4(3)	
V	-0.23(7)	
W	0.034(4)	
NA	1.00(6)	
NB	-0.016(5)	
Zero Point	-0.074(5)	
Rwp	0.0402	
Rp	0.0310	

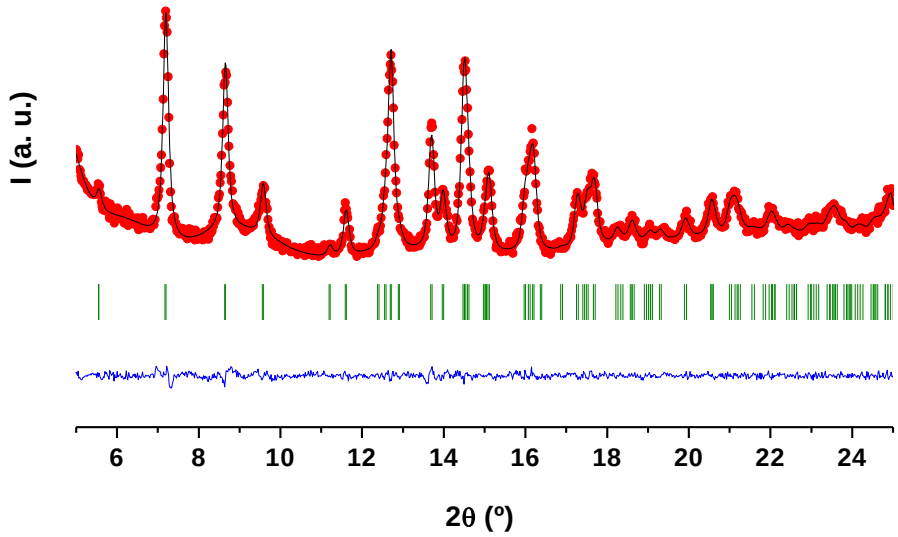

Figure 4.1.25. Pawley refinement for **AEPF-1'** sample after immersion in 1-butanol. Experimental data (red), simulated patter (black) and difference (blue); observed reflections (green).

4.1.1.8.

Selective adsorption by immersion in mixtures of organic solvents

The selective adsorption behaviour of **AEPF-1$_{dry}$** and **AEPF-1'** was examined in four equimolar mixtures of organic solvents: **A)** acetone/acetonitrile, **B)** acetone/1-butanol, **C)** acetone/toluene, and **D)** acetone/hexane. TGA-MS analyses were performed on **AEPF-1$_{dry}$** samples after immersion treatments to evaluate the selectivity of the adsorption process (**Figure 4.1.26**). For the mixture **A**, the thermogravimetric profile of **AEPF-1'** shows a weight loss of around 6.1 wt% up to 250 ºC, which corresponds to the loss of 2.60 acetone molecules and 0.40 acetonitrile molecules per unit cell. For the mixture **B**, the sample shows a weight loss of around 5.9 wt% up to 250 ºC, which corresponds to the loss of 2.10 acetone molecules and 0.50 1-butanol molecules per unit cell. For the mixture **C**, **AEPF-1'** shows a weight loss of around 5.4 wt% up to 275 ºC, which corresponds to the loss of 2.48 acetone molecules and 0.05 toluene molecules per unit cell. Finally, for the mixture **D**, only acetone adsorption is observed, with a weight loss of around 4.9 wt% , which corresponds to the loss of 2.19 acetone molecules per unit cell.

XRPD was used to examine the recovery of all samples of **AEPF-1'** (**Tables 4.1.13-4.1.15** and **Figure 4.1.27-4.1.29**), which showed that **AEPF-1$_{dry}$** not only selectively adsorbs polar organic solvents, but can also selectively separate organic solvents according to their size, shape, or polarity. Such behaviour could be important for potential applications of this Ca-based MOF as an adsorbent and/or sensor of organic compounds.

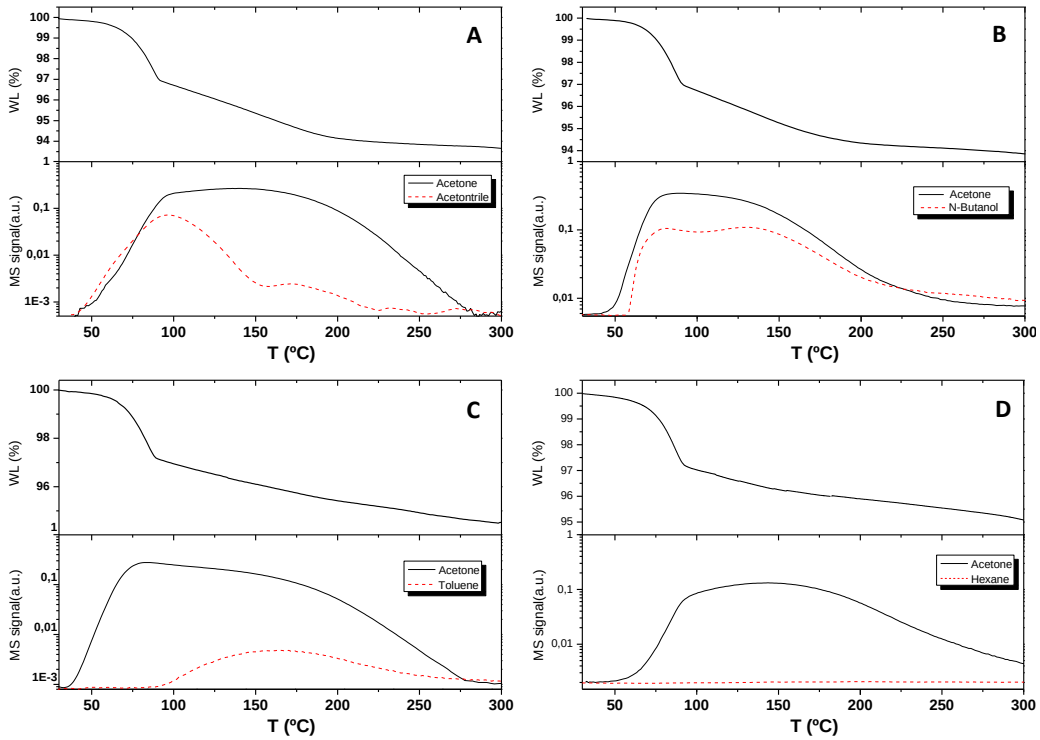

Figure 4.1.26. TGA-MS for solvent mixtures: **A)** acetone/acetonitrile, **B)** acetone /1-butanol, **C)** acetone/toluene, and **D)** acetone /hexane. WL=weight loss.

Table 4.1.13. Crystal Data and structure refinement values for **AEPF-1'** sample, after immersion in an acetone/acetonitrile mixture.

Compound	AEPF-1' after immersion in an acetone / acetonitrile
Crystal system	Monoclinic
Space group	*P2/n*
Unit cell dimensions	a = 18.900(1) Å α = 90˚ b = 7.5550(5) Å β = 104.473(4)˚ c = 20.887(2) Å γ = 90˚
Profile Function	Pseudo-Voigt
U	2.8(2)
V	-0.42(4)
W	0.061(2)
NA	0.86(2)
NB	-0.013(1)
Zero Point	-0.0065(8)
Rwp	0.0325
Rp	0.0211

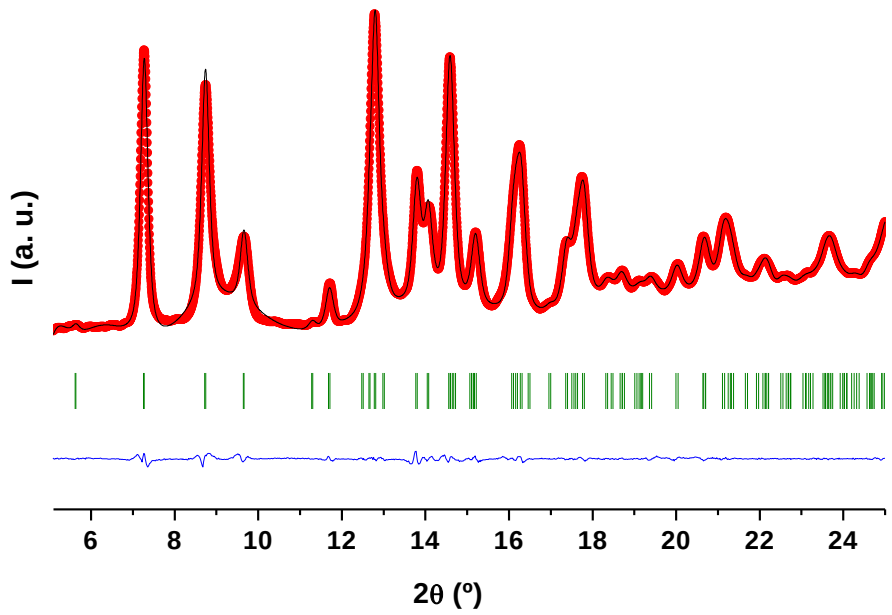

Figure 4.1.27. Pawley refinement for **AEPF-1'** sample after immersion an acetone/acetonitrile mixture. Experimental data (red), simulated patter (black) and difference (blue); observed reflections (green).

Table 4.1.14. Crystal Data and structure refinement values for **AEPF-1'** sample, after immersion in an acetone/1-butanol mixture.

Compound	AEPF-1' after immersion in an acetone / 1-butanol mixture
Crystal system	Monoclinic
Space group	*P2/n*
Unit cell dimensions	a = 18.930(1) Å α = 90˚
	b = 7.5490(4) Å β = 104.318(4)˚
	c = 20.897(1) Å γ = 90˚
Profile Function	Pseudo-Voigt
U	1.7(1)
V	-0.22(3)
W	0.034(4)
NA	1.00(2)
NB	-0.012(2)
Zero Point	-0.0134(7)
Rwp	0.0546
Rp	0.0376

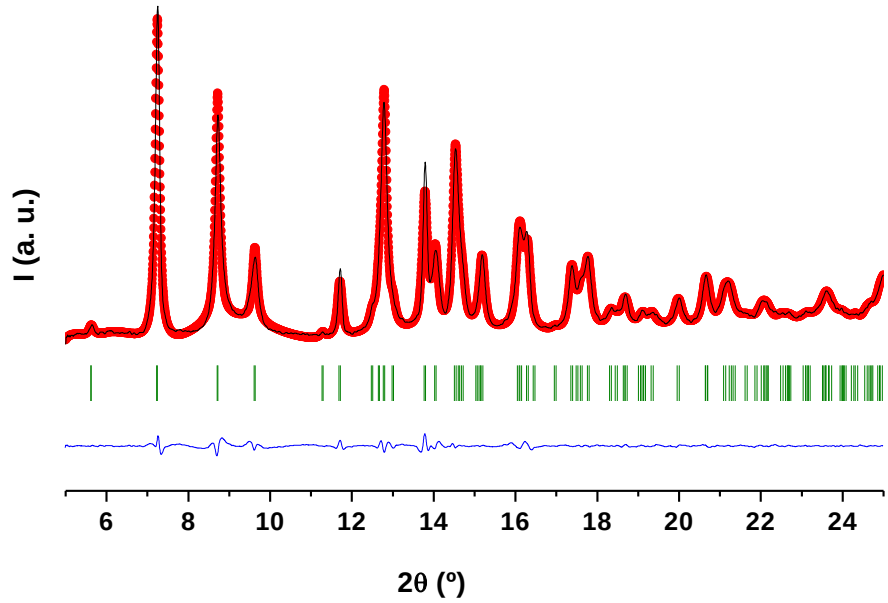

Figure 4.1.28. Pawley refinement for **AEPF-1'** sample after immersion an acetone/1-butanol mixture. Experimental data (red), simulated patter (black) and difference (blue); observed reflections (green).

Table 4.1.15. Crystal Data and structure refinement values for **AEPF-1'** sample, after immersion in an acetone/toluene mixture.

Compound	**AEPF-1' after immersion in an acetone / toluene mixture**
Space group	Monoclinic *P2/n*
Unit cell dimensions	a = 18.955(2)Å α = 90˚ b= 7.5348(6) Å β = 104.293(4)˚ c = 20.880(3) Å γ = 90˚
Profile Function	Pseudo-Voigt
U	0.6(2)
V	0.09(3)
W	0.011(2)
NA	0.88(2)
NB	-0.003(2)
Zero Point	0.0104(8)
Rwp	0.0677
Rp	0.0473

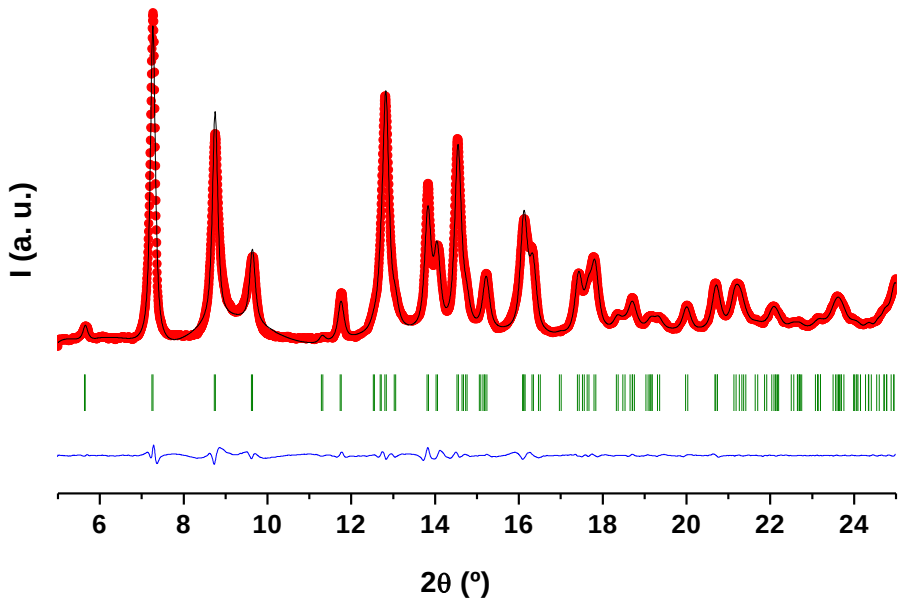

Figure 4.1.29. Pawley refinement for **AEPF-1'** sample after immersion an acetone/toluene mixture. Experimental data (red), simulated patter (black) and difference (blue); observed reflections (green).

4.1.1.9.

AEPF-1: A green calcium catalyst

The use of the $H_2L_{(1)}$ ligand as dicarboxylate linker has given rise to the obtaining of a flexible calcium MOF named **AEPF-1**, which shows selective adsorption behaviour of organic compounds based on their size, shape and polarity. The application of **AEPF-1** as heterogeneous catalysts was also explored in two reactions: **hydrogenation of alkenes** and **hydrosilylation of alkenes and ketones**

4.1.1.9.1. Hydrogenation of alkenes

Catalytic tests. The catalytic properties of **Ca-AEPF-1** presented in this chapter were investigated for the hydrogenation of alkenes using styrene as substrate model under mild conditions (*see* Chapter 2 and **Scheme 4.1.1**).

Scheme 4.1.1. Scheme reaction of styrene reduction with H_2.

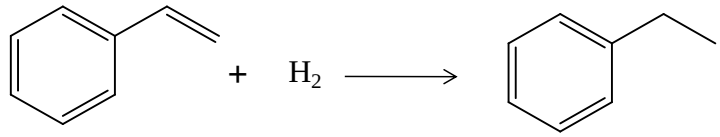

The performance of **Ca-AEPF-1** as heterogeneous catalyst was tested for the hydrogenation of styrene to form ethyl benzene at 373 K, 5 atm H_2, using toluene as solvent and 1 mol% catalyst. Hydrogenation was completed, with 100% selectivity, after 2 h without the formation of by products. Finally, in order to compare the catalytic activity of **Ca-AEPF-1** to that of a calcium salt, the styrene hydrogenation test was performed under the same conditions with calcium acetate monohydrate as catalyst. **Figure 4.1.30** shows a comparison between the catalytic performance of **AEPF-1** and the calcium salt.

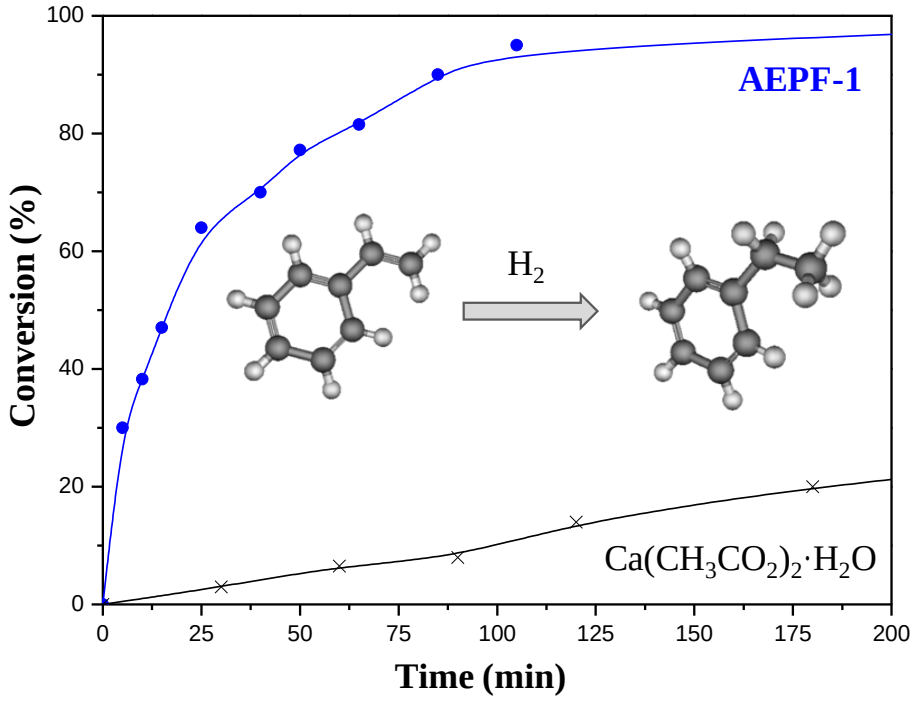

Figure 4.1.30. Kinetic profile for the hydrogenation of styrene with H_2 in toluene at 373 K: Comparison between the performances of **AEPF-1** and calcium acetate monohydrate.

By comparing the results of **AEPF-1** catalytic studies with those of recently reported calcium complexes in solution[19-20] or supported[21], we can conclude that the use of **AEPF-1** as catalyst results in total conversion with 100% selectivity to the hydrogenated product in 2 h, by using 1 mol% of catalyst at 373 K and 5 atm H_2, whereas the reported homogeneous catalyst[19,20] reached 100% conversion with 80% selectivity towards the alkane after 15 h with 5 mol% of catalyst at 293 K and 20 atm H_2.

Apparent activation energy (E_a). In order to study this catalytic behaviour, kinetics experiments were carried out to determine the apparent activation energy under the above described conditions (1 mol% catalyst and 5 atm H_2), using different temperatures (373 K, 358 K, 343 K and 313 K) (**Table 4.1.16**). Thus, taking into account the Arrhenius equation, the apparent E_a can be expressed as:

$$E_a = -RTlnv$$

where

E_a: Apparent activation energy ($J \cdot mol^{-1}$)
R: 8.314 $J \cdot K \cdot mol^{-1}$
T: Temperature (K)
v: Reaction rate

the E_a values for styrene hydrogenation using **Ca-AEPF-1** as catalyst is ~8.8 $cal \cdot mol^{-1}$.

Table 4.1.16. Hydrogenation of styrene with H_2 using **AEPF-1** as catalyst, under the described conditions.

T (K)	Time (h)	Conversion (%)[a]	TOF (h^{-1})[b]
313	4	50	82
343	4	52	164
358	4	55	201
373	2	100	254

[a] Yield of ethylbenzene based on styrene conversion (in all cases 100% selectivity was achieved). [b] TOF calculated at maximum rate.

Substrate selectivity. In a next step, to determine the influence of the substrate size and shape and their effect on the catalytic behaviour of **AEPF-1**, experiments were performed using a bulkier alkene (α-methylstyrene) (**Scheme 4.1.2**), affording a lower yield (60%) after 2 h, but again giving 100% selectivity (**Figure 4.1.31**). Although a

significant part of the reaction may have taken place in the external surface, these experiments highlighted the shape selectivity of **AEPF-1**.

Scheme 4.1.2. Scheme reaction of α-methylstyrene reduction with H_2.

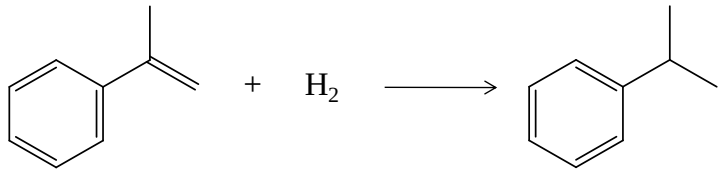

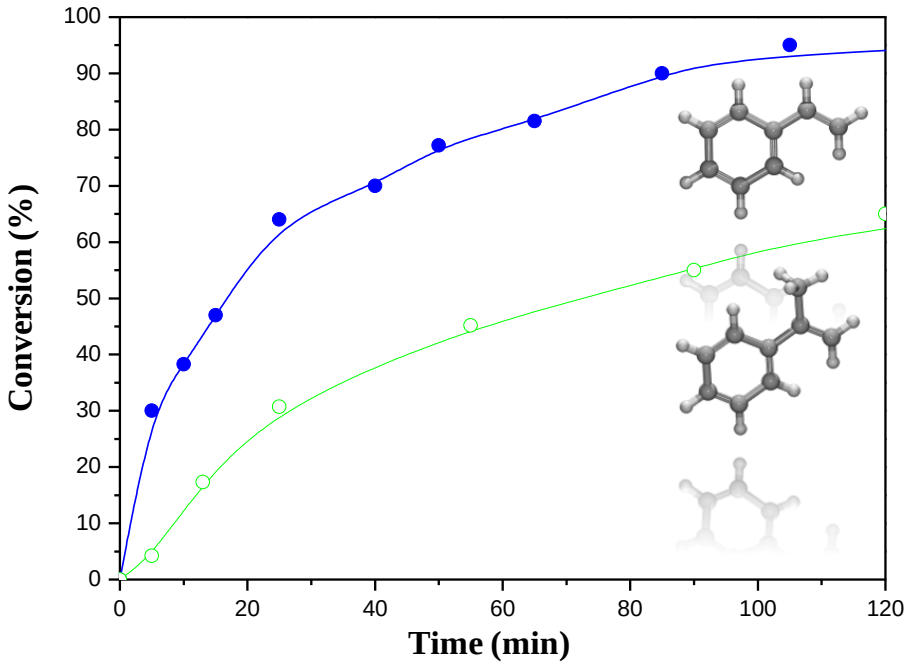

Figure 4.1.31. Substrate size experiments carried out with **AEPF-1** as catalyst: styrene (blue) and α-methylstyrene (green).

Proposed mechanism. A mechanism for the calcium MOF-mediated hydrogenation, based on the H_2 heterolytic cleavage (**Scheme 4.1.3**), could be analogous to that reported for transition metals.[22] The catalytic behaviour of **AEPF-1** could be favoured by the hepta-coordinated Ca environment, which aids coordination of the substrate and hydride formation, by increasing the calcium coordination number to eight. Furthermore, the acidity of **AEPF-1**, introduced by the protonated ligand, makes it easier the heterolytic cleavage of the hydrogen molecule.

Scheme 4.1.3. Proposed catalytic cycle for styrene hydrogenation in the presence of **AEPF-1** based on the heterolytic cleavage of H_2.

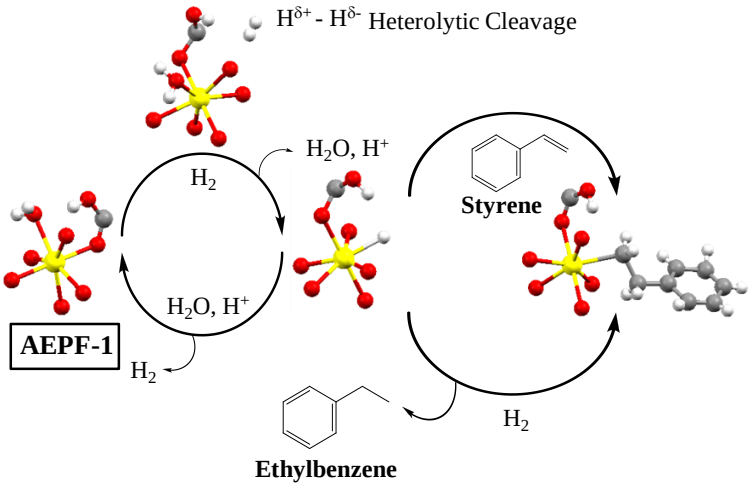

Recycling experiments. To investigate the lifetime, heterogeneity and the stability of **AEPF-1** in styrene hydrogenation, recycling experiments were performed employing the same catalyst in three consecutive reaction cycles. A minor decrease in the catalytic activity was observed after the first run (**Figure 4.1.32**), but after three more runs the catalytic activity remains constant.

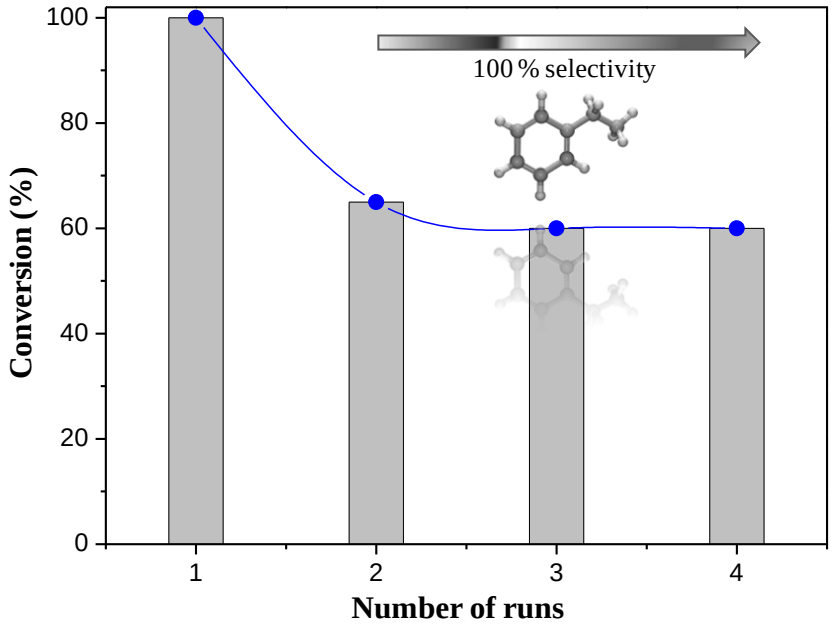

Figure 4.1.32. Recycling experiments carried out for styrene hydrogenation with **AEPF-1**, showing 100% of selectivity to ethylbenzene.

In addition, in order to determine whether or not leaching of active sites from **AEPF-1** takes place, the same reaction was performed during 15 min; at this point the catalyst was removed by hot filtration and the evolution of product formation was followed maintaining the same reaction conditions (**Scheme 4.1.4**). No further reaction occurs after the catalyst removing from solution, what demonstrates the absence of actives sites leaching (**Figure 4.1.33**).

Scheme 4.1.4. Scheme of hot filtration experiment.

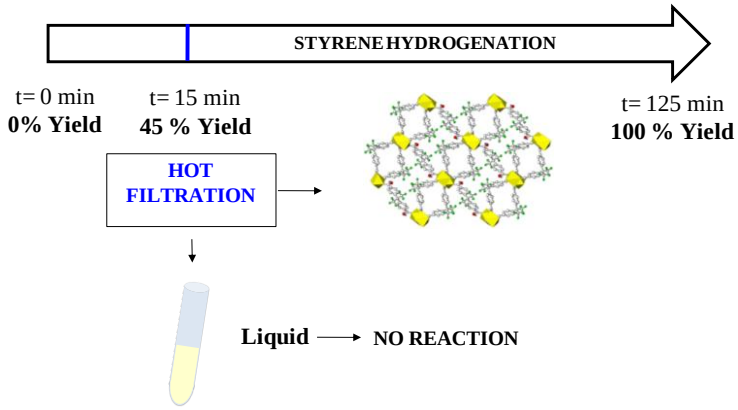

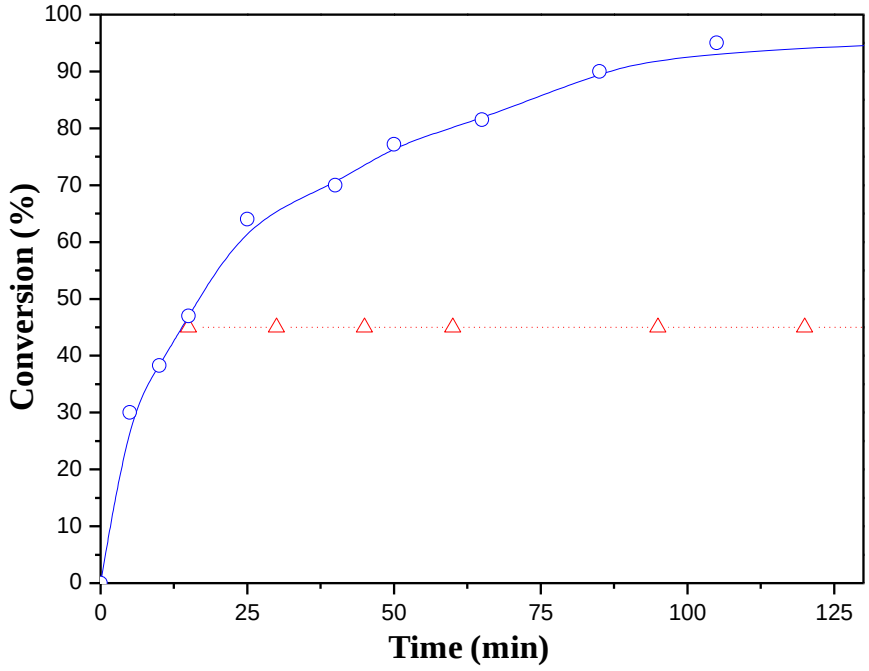

Figure 4.1.33. Hot filtration experiment carried out for styrene hydrogenation. No further reaction takes place removing the catalysts from solution (red).

Catalysts robustness. The catalysts employed in styrene hydrogenation were recovered by centrifugation, washed with toluene, and then characterized by X-ray powder diffraction to detect possible structural changes in **AEPF-1** after reaction. Comparison of the XRPD patterns before and after the recycling experiments confirms the robustness of **AEPF-1** in the studied conditions (**Figure 4.1.34**).

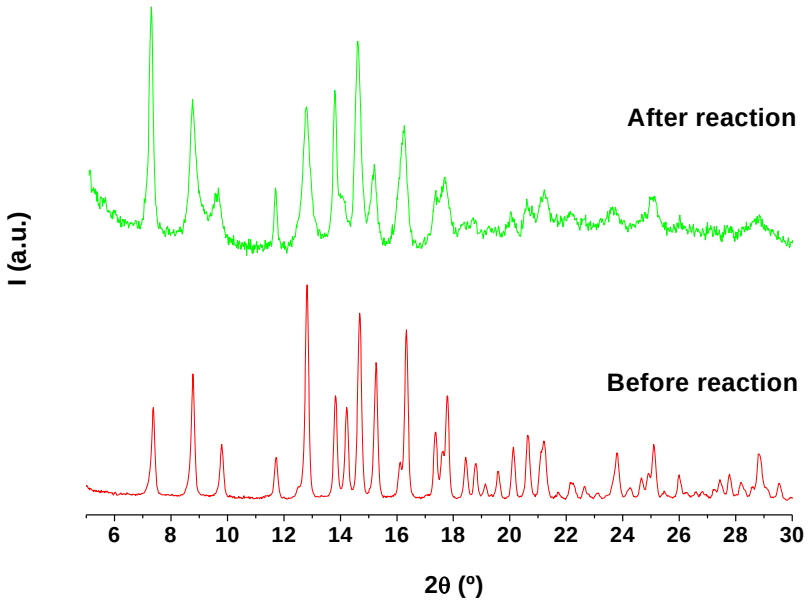

Figure 4.1.34. Comparison of the experimental XRPD pattern of **Ca-AEPF-1** after hydrogenation recycling experiments (green) with the pattern of the fresh sample before reaction (red).

4.1.1.9.2. Hydrosilylation of ketones and alkenes

Catalytic tests. Ca-AEPF-1 compound was also tested as heterogeneous catalyst in the hydrosilylation of benzaldehyde, acetophenone and styrene with diphenylsilane (*see* Chapter 2, *Techniques* and **Schemes 4.1.5-4.1.6**).

Scheme 4.1.5. Hydrosilylation of a carbonyl compound with diphenylsilane.

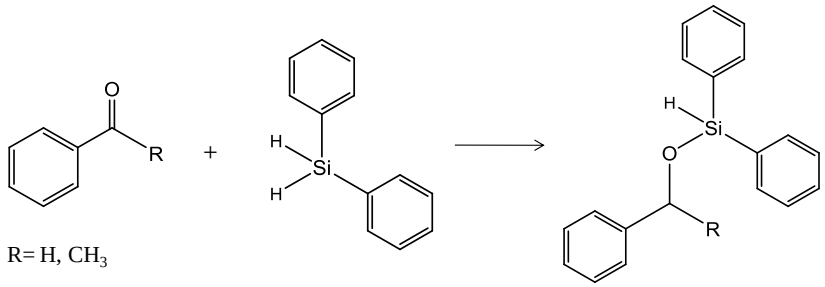

Scheme 4.1.6. Hydrosilylation of styrene with diphenylsilane.

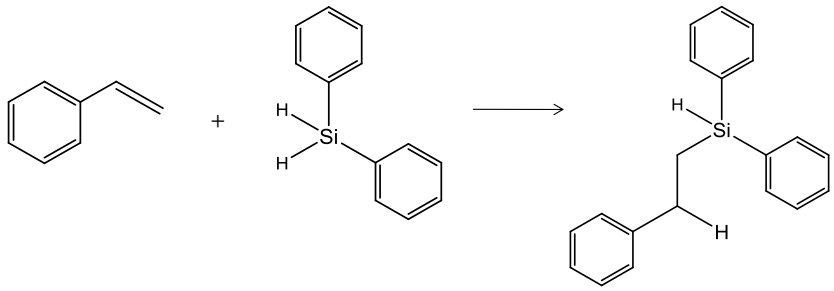

Hydrosilylation reactions were carried out with a ratio alkenes:diphenylsilane (3:1) and carbonyl:diphenylsilane (1:2), and **AEPF-1** (10 mol%) in toluene at 363 K under a nitrogen atmosphere. Results are shown in **Table 4.1.17** and **Figure 4.1.35**.

Table 4.1.17. Hydrosilylation reactions performed with **AEPF-1** as catalyst in toluene, at 363 K, using 10 mol% catalyst.

Substrate	Time (h)	Conversion (%)	TOF (h^{-1})
Benzaldehyde	10	97	1.3
Acetophenone	22	67	0.5
Styrene	22	92	2.5

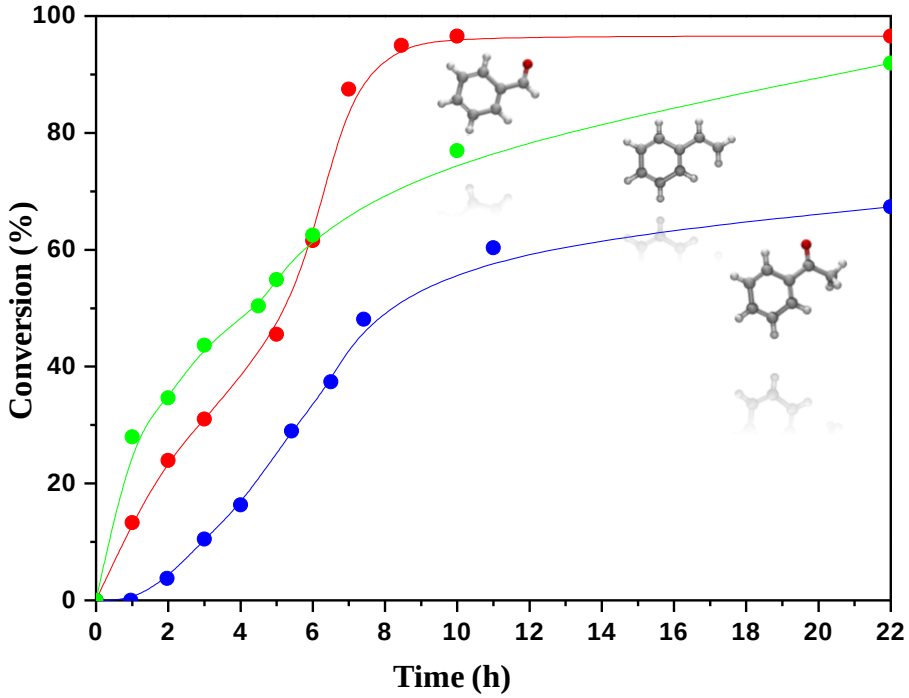

Figure 4.1.35. Kinetic profiles for benzaldehyde (red), acetophenone (blue) and styrene (green) hydrosilylation with diphenylsilane using **Ca-AEPF-1** as catalyst.

As it is shown in **Figure 4.1.35**, concerning the carbonyl compounds, the best result was obtained for the bezaldehyde hydrosilylation, for which the silylated product yield was 97% (TOF= 1.3 h^{-1}). In the case of acetophenone, the catalytic activity was clearly lower (yield 67% after 22 hours, TOF= 0.5 h^{-1}). In the reaction of styrene, the yield for the corresponding silylated product was 92% after 22 hours (TOF= 2.5 h^{-1}). It is worth mentioning that the styrene hydrosilylation leads to a 100% yield of the linear silane.

By comparing **AEPF-1** catalytic performance results with those of recently reported silica-supported calcium complex[21] for the hydrosilylation of styrene, the existence of soluble calcium species and a lack of evidence whether catalysis proceeded in a homogeneous or heterogeneous mode have been reported. **AEPF-1**, thanks to its stable robust structure with all of the active calcium centers forming part of the framework, acts as a purely heterogeneous catalyst, which has been proved by experiments that demonstrated an absence of both active site leaching and catalyst deactivation.

4.1.1.10.

Gas sorption studies

In order to evaluate the potential applications of **AEPF-1** in gas adsorption, the specific surface area was determined obtaining N_2 adsorption-desorption isotherms at 77 K (*see* Chapter 2, *Techniques*). A BET surface area of 201 $m^2 \cdot g^{-1}$, was calculated for **AEPF-1** by using the data points on the adsorption branch of the N_2 isotherm the range P/P_0 = 0.1-0.3.

Finally, in order to complete the absorption properties studies of this system, and to confirm the relation between pore structure and adsorption affinity with different kind of gases, several adsorption isotherms were obtained using gravimetric gas sorption technique (*see* Chapter 2, *Techniques*). The gas absorption isotherms at 304 K of different gases (CH_4, CO_2, H_2) are depicted in the **Fig. 4.1.36**. The H_2 adsorption shows an uptake of just 0.27 $mmol \cdot g^{-1}$ (0.05 wt%) at P/P_0 = 1, while the adsorption amount of CH_4 and CO_2 are 0.40 $mmol \cdot g^{-1}$ (0.64 wt%) and 0.76 $mmol \cdot g^{-1}$ (3.35 wt%), respectively. All these isotherms were fit to Sips equation in order to predict the saturation amount, which values are 0.33 $mmol \cdot g^{-1}$, 0.75 $mmol \cdot g^{-1}$ and 0.84 $mmol \cdot g^{-1}$ for H_2, CH_4 and CO_2, respectively.

These results show that gas adsorption through **AEPF-1** pores does not depend on the size of adsorbed molecules, but could be related with adsorption energy, being the lowest for H_2. This fact could explain the reactivity of H_2 molecule in this system, which favours the hydrogenation processes.

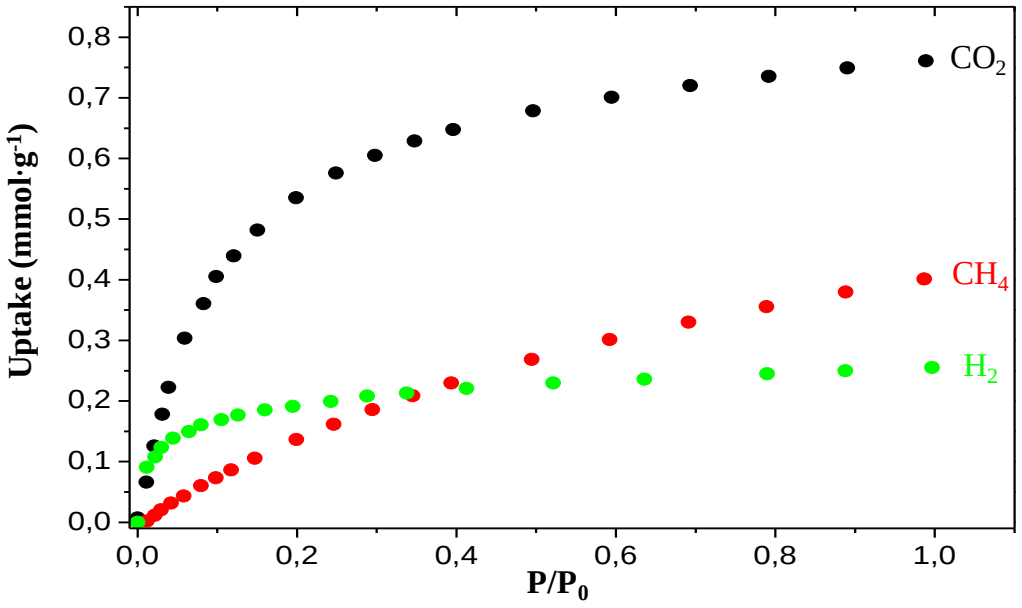

Figure 4.1.36. Gravimetric gas sorption isotherms for the uptake of H_2 (green), CH_4 (red) and CO_2 (black) at 304 K.

4.1.2.

Ca-AEPF-6 and Ca-AEPF-7

Continuing with the preparation of calcium MOFs based on the $H_2L_{(1)}$ ligand, different synthesis conditions to those used to synthesize **AEPF-1** were investigated. Thus, two different strategies were used to obtained novel calcium materials with larger pores and the results are presented in this chapter. Firstly, the use of an organic molecule (diethylformamide, DEF from now on) as solvent that can coordinate to Ca centers in a η^1 coordination mode (replacing the role of coordinated water molecules), and favouring the formation of an open-framework was studied (**AEPF-6**). In addition, the use of an organic molecule (pyridine, Py from now on) that can play the role of template was also investigated, being the novel **AEPF-7** compound obtained.

4.1.2.1.

Ca-AEPF-6

4.1.2.1.1. Structural and topological description

The reaction between $H_2L_{(1)}$ and calcium acetate hydrate under the optimized solvothermal conditions, using DEF as solvent, gives rise to the **[Ca($L_{(1)}$)(DEF)]** compound (**AEPF-6**) (*see* Chapter 2, *Synthesis procedures*). This compound crystallizes in the orthorhombic crystal system (*Pna2₁* space group). The cell parameters determined for this structure are: a = 27.3060(5) Å, b = 12.3117(3) Å, c = 6.9896(1) Å and V = 2349.79(8) Å^3. The ORTEP representation of **AEPF-6** asymmetric unit is shown in **Figure 4.1.37** and the main crystallographic and refinement data for this compound are shown in **Table 4.1.18**.

Table 4.1.18. Crystallographic and refinement data for **AEPF-6**.

Identification code	AEPF-6
Empirical formula	$C_{22}\ H_{19}\ F_6\ Ca\ N\ O_5$
Formula weight	515.69
Temperature	296(2) K
Wavelength	1.54178 Å
Crystal system	Orthorhombic
Space group	$Pna2_1$
Unit cell dimensions	a = 27.3060(5) Å α = 90° b = 12.3117(3) Å β = 90° c = 6.9896(1) Å γ = 90°
Volume	2349.79(8) $Å^3$
Z	4
Density (calculated)	1.458 Mg/m^3
Absorption coefficient	1.410 mm^{-1}
F(000)	1056
Crystal size	0.20 x 0.10 x 0.10 mm^3
Theta range for data collection	3.24 to 58.77°
Index ranges	-30<=h<=29, -13<=k<=13, -7<=l<=5
Reflections collected	22089
Independent reflections	2708 [R(int) = 0.0331]
Completeness to theta = 58.77°	99.7%
Absorption correction	Semi-empirical from equivalents
Max. and min. Transmission	0.7495 and 0.5798
Refinement method	Full-matrix least-squares on F^2
Data / restraints / parameters	2708 / 1 / 318
Goodness-of-fit on F^2	1.053
Final R indices [I>2sigma(I)]	R_1 = 0.0334, wR_2 = 0.0893
R indices (all data)	R_1 = 0.0352, wR_2 = 0.0906
Absolute structure parameter	0.02(1)
Extinction coefficient	0.0018(2)
Largest diff. peak and hole	0.350 and -0.249 e.$Å^{-3}$

In **AEPF-6**, Ca^{+2} ions are octa-coordinated to two oxygen atoms coming from a DEF μ^2 carbonyl group and six oxygen atoms coming from $L_{(1)}^{-2}$ chelate-bridge carboxylate groups of four different ligands, forming CaO_8 bicapped trigonal prisms

(**Figure 4.1.38a**). These polyhedra, which can be considered as the inorganic PBUs, have an average Ca-O distance of ~2.47 Å (**Table 4.1.19**). In the case of carboxylate groups, two kinds of Ca-O distances are determined: a shorter bond corresponding to the bridge mode (~2.34 Å) and a larger one for the chelate one (~2.50 Å). In the case of DEF μ^2 carbonyl groups, an average Ca-O distance of ~2.53 Å is determined, being quite similar to that of chelate $L_{(1)}^{-2}$ oxygen atoms.

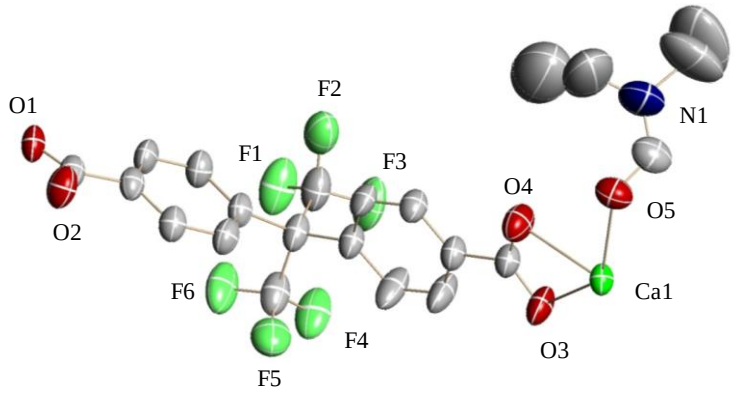

Figure 4.1.37. ORTEP representation of **AEPF-6** asymmetric unit. Ellipsoids are displayed at the 50% probability level. Hydrogen atoms were omitted for clarity.

Table 4.1.19. Interatomic distances in the coordination sphere of the CaO_8 polyhedra in **AEPF-6**.

Bond	Distance (Å)
Ca(1)-O(1)[1]c	2.332(2)
Ca(1)-O(1)[2]c	2.475(2)
Ca(1)-O(2)[2]c	2.513(2)
Ca(1)-O(3)c	2.565(2)
Ca(1)-O(3)[3]c	2.341(2)
Ca(1)-O(4)c	2.452(2)
Ca(1)-O(5)d	2.525(2)
Ca(1)-O(5)[4]d	2.541(2)

Symmetry transformations used to generate equivalent atoms:

[1] -x+1/2,y-1/2,z-1/2 [3] -x,-y,z-1/2

[2] x-1/2,-y+1/2,z [4] -x,-y,z+1/2

Oc: oxygen atom coming from a carboxylate group. Od: oxygen atom coming from a DEF molecule.

As it is shown in **Figure 4.1.38**, the CaO_8 polyhedra determined in **AEPF-6** form infinite sharing-faces chains that run along the *c* axis (**Figure 4.1.38b**). These inorganic chains are joint *via* the $L_{(1)}^{-2}$ linkers, which act in a $\eta^2\mu_2$-$\eta^2\mu_2$ coordination mode (**Figure 4.1.38c**).

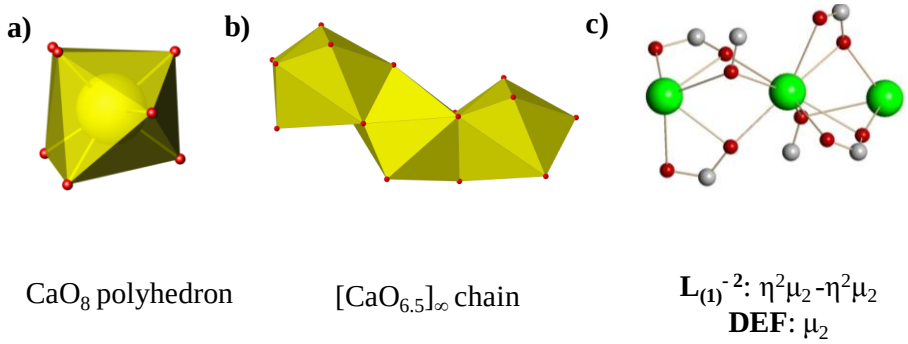

Figure 4.1.38. a) Inorganic PBUs in **AEPF-6**, **b)** detail of the CaO_8 sharing-faces chains that run along the *c* axis and **c)** coordination mode of $L_{(1)}^{-2}$ linker and DEF molecules.

In **Figure 4.1.39**, different polyhedral views along the crystallographic axes are depicted, evidencing the three-dimensional covalent framework determined in **AEPF-6**. As it is shown in **Figure 4.1.39a**, the presence of rhombic shaped channels is determined in this structure, which are going to be discussed in detail in the following. The potential solvent accessible voids in the crystal structure of **AEPF-6** were calculated using PLATON software[5] (SOLV mode). However, due to the presence of the DEF coordinated molecules, this material does not possess any accessible voids.

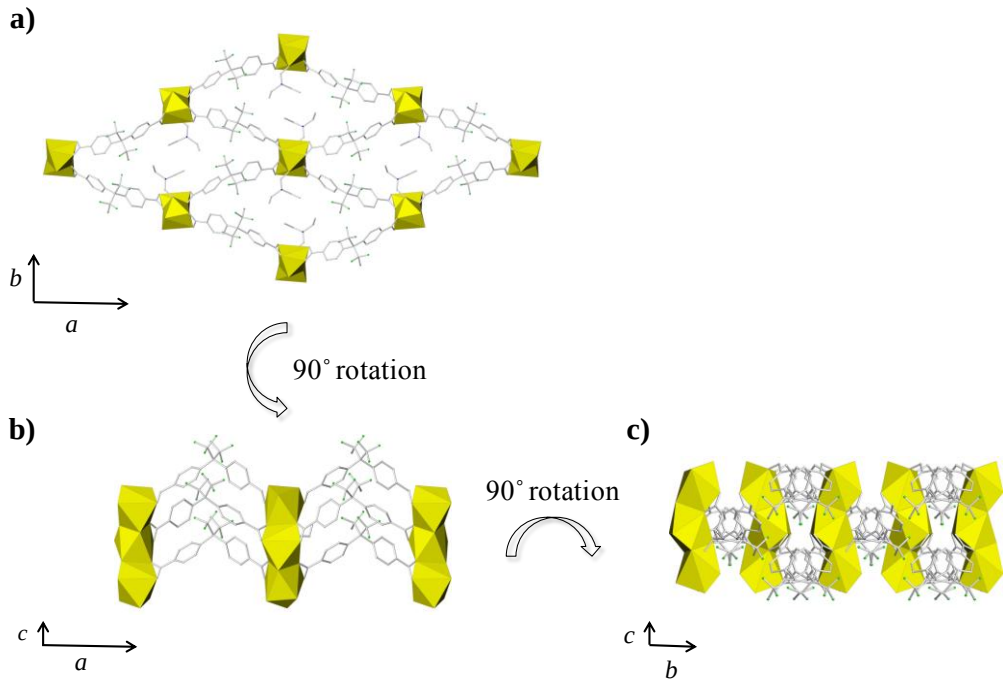

Figure 4.1.39. Polyhedral representation of **AEPF-6** net along the: **a)** *c* axis, **b)** *b* axis and **c)** *a* axis.

In order to analyse the flexibility of the ligand, an analysis of linker conformation was carried out for **AEPF-6** (the same as for **AEPF-1** and **AEPF-1$_{dry}$,** see **Table 4.1.7**), studying the three geometrical parameters **θ**, **ω** and **d** (**Figure 4.1.18**). In **Table 4.1.20**, their values for this structure are listed. It is worth mentioning that, in comparison with the linker conformations determined in **AEPF-1** and **AEPF-1$_{dry}$**, the **d** distance for the ligand in **AEPF-6** compound is markedly longer, which may explain the formation of large rhombic channels.

Table 4.1.20. θ angle, **ω** dihedral angle **d** distance values in **AEPF-6** compound for the $L_{(1)}^{-2}$ linker.

θ (º)	ω (º)	d (Å)
113.38	69.40	9.896

To describe the topological features in this material, the inorganic chains found in **AEPF-6** consisting of CaO_8 sharing-faces polyhedra, were simplified as rods using TOPOS,[4] taking into account the previously mentioned work of Yaghi and O'Keeffe.[23] Thus, the inorganic SBU in **AEPF-6** can be defined as these infinite $(\text{-O-Ca-})_\infty$ rods

with carboxylate O atoms completing the octa-coordination around Ca atoms to result in infinite rods of CaO_8 bicapped sharing-faces trigonal prisms. In **Figure 4.1.40** the topological simplifications performed in the CaO_8 chains to build the inorganic SBU are shown.

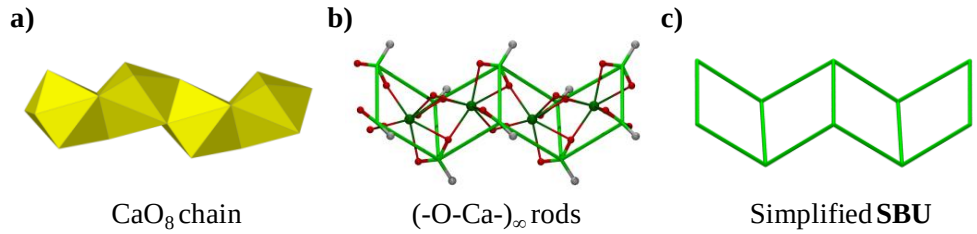

Figure 4.1.40. a) CaO_8 polyhedra chain. **b)** Topological simplifications performed to describe the $(\text{-O-Ca-})_\infty$ rods as the inorganic SBUs. **c)** Simplified inorganic SBU.

Considering the topological simplifications above mentioned, the **AEPF-6** net can be described as rods of quadrangles linked by sharing opposite edges (ladders). These ladders are linked with the rungs parallel to form a **sra** uninodal 4-connected net (point symbol $(4^2.6^3.8)$). It is worth highlighting that this net exhibits the same topology to that determined for ABW framework type in zeolites. The main simplification points, as well as the decorated and final simplified nets for **AEPF-6**, are shown in **Figure 4.1.41.**

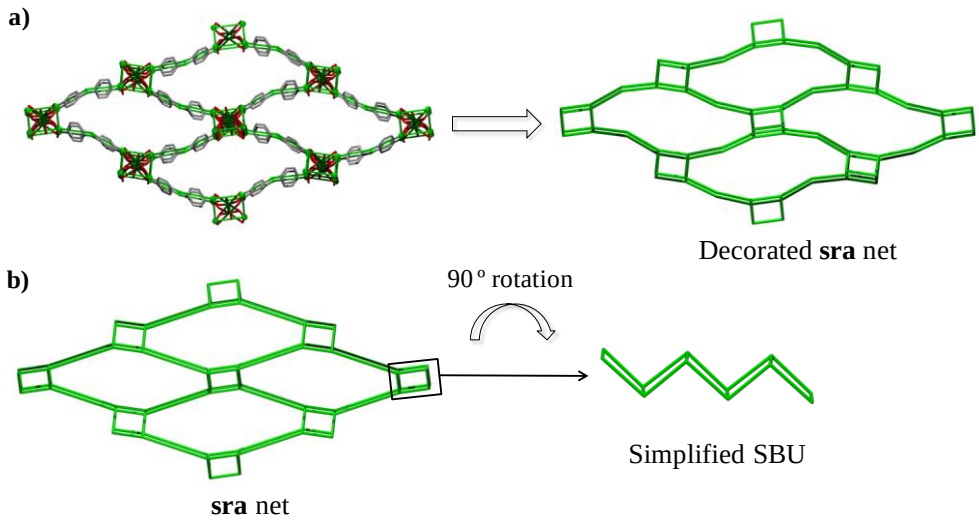

Figure 4.1.41. a) Depiction of the **AEPF-6** real net together with the decorated **sra** net. Hydrogen atoms and $-CF_3$ groups were omitted for clarity. **b)** Simplified **sra** net described in **AEPF-6** and detail of the simplified inorganic SBU.

Moreover, thanks to the topological studies performed in **AEPF-6** net, it was also possible to analyse the connection of the chains through the $L_{(1)}^{-2}$ organic linker. Thus, as it is depicted in **Figure 4.1.42**, the connection of the inorganic chains *via* de $L_{(1)}^{-2}$ ligands is made in a parallel way, being the channels thus of **B**-type.[1]

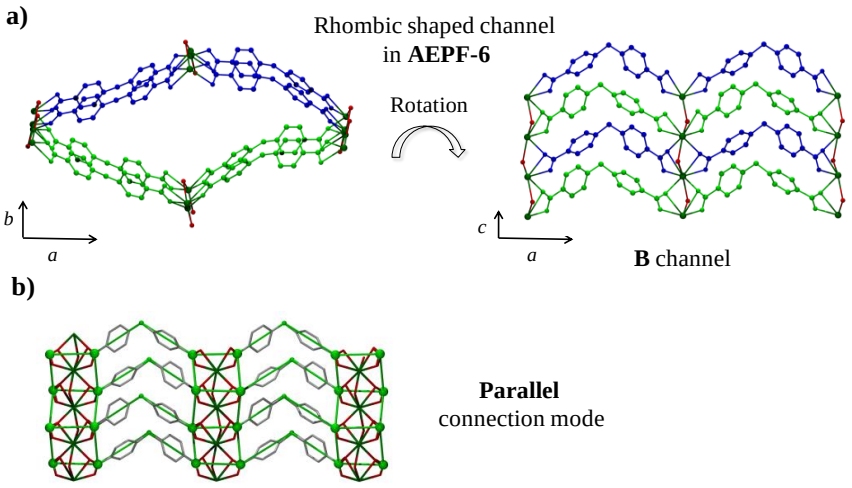

Figure 4.1.42. a) Different projections of the rhombic shaped channels in **AEPF-6**. **b)** Detail of the real net together with the decorated **sra** net, showing the parallel connection mode of the linker. Hydrogen atoms and $–CF_3$ groups were omitted for clarity.

4.1.2.1.2. Characterization

X-Ray Powder Diffraction

X-ray powder diffraction is a powerful technique to check the univocal presence of a desired crystalline phase together with the purity of the bulk sample, as it was before demonstrated in the case of **AEPF-1** and **AEPF-1$_{dry}$**. These are essential points that must be considered to subsequently evaluate the properties of the material. In addition, the use of Pawley refinement[12] procedures, implemented in Materials Studio[13] software, allows the determination of other experimental parameters as those related with the zero shift, the peak profile and the peak asymmetry, among others. Therefore, and due to the high crystallinity that exhibit **AEPF-6** samples, this kind of structural analysis was also performed to study this material. In the following, both the

Pawley refinement profile and the main refinement values for **Ca-AEPF-6** bulk sample are shown in **Table 4.1.21** and **Figure 4.1.43**.

Table 4.1.21. Crystal Data and Pawley profile refinement values for **AEPF-6**.

Compound	AEPF-6	
Crystal system	Orthorhombic	
Space group	$Pna2_1$	
Unit cell dimensions	a= 27.296(5) Å	α = 90˚
	b= 12.299(2) Å	β = 90˚
	c= 6.980(1) Å	γ = 90˚
Profile Function	Pseudo-Voigt	
U	0.74(5)	
V	-0.18(1)	
W	0.0255(6)	
NA	0.93(1)	
NB	-0.023(1)	
Zero Point	0.019(4)	
Asymmetry correction	Finger-Cox-Jephcoat	
H/L	0.0037(1)	
S/L	0.006(4)	
Rwp	0.0494	
Rp	0.1087	

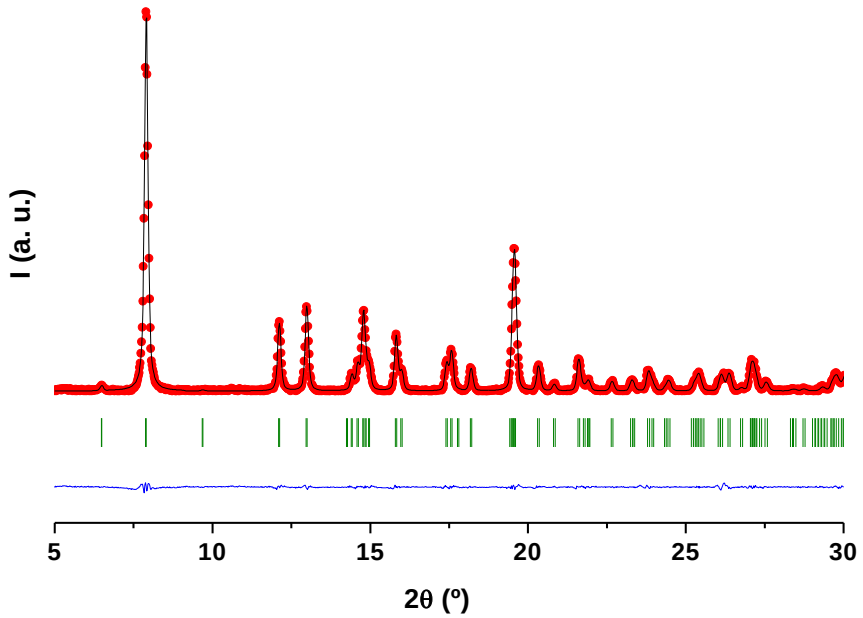

Figure 4.1.43. Pawley refinement for **AEPF-6**, showing the obtaining of the compound as a pure phase. Experimental data (red), simulated pattern (black) and difference (blue); observed reflections (green).

Infrared Spectroscopy

Infrared (IR) spectrum of **Ca-AEPF-6** shows the presence of bands in the -CO_2^- stretching mode zone (at ~1700-1500 (υ_{as}) and ~1500-1300 (υ_s) cm^{-1}), which correspond to the presence of carboxylate groups. Additional bands are determined in the region corresponding to –CH stretching mode zone (~3000 cm^{-1}).

In the first studied region (~4000-2500 cm^{-1}, **Figure 4.1.44a**), a broad band centred at ~3435 cm^{-1} is observed, which can be explained by the contribution of -OH stretching mode corresponding to physisorbed water molecules. Well defined multiple weak bands are determined between ~3085-2875 cm^{-1} associated to –CH stretching mode of DEF molecules and the organic linker.

Detail of IR spectrum of the region corresponding to CO_2^- and C=O stretching mode zone is given in **Figure 4.1.44b**. Thus, for **Ca-AEPF-6**, CO_2^- stretching mode bands were observed at ~1615, ~1605 and ~1555 (υ_{as}); at ~1415 and ~1400 cm^{-1} (υ_s). An intense band centred at ~1640 cm^{-1} is determined, which can be assigned to -C=O stretching mode corresponding to carbonyl groups of DEF molecules coordinated to Ca^{+2} ions.

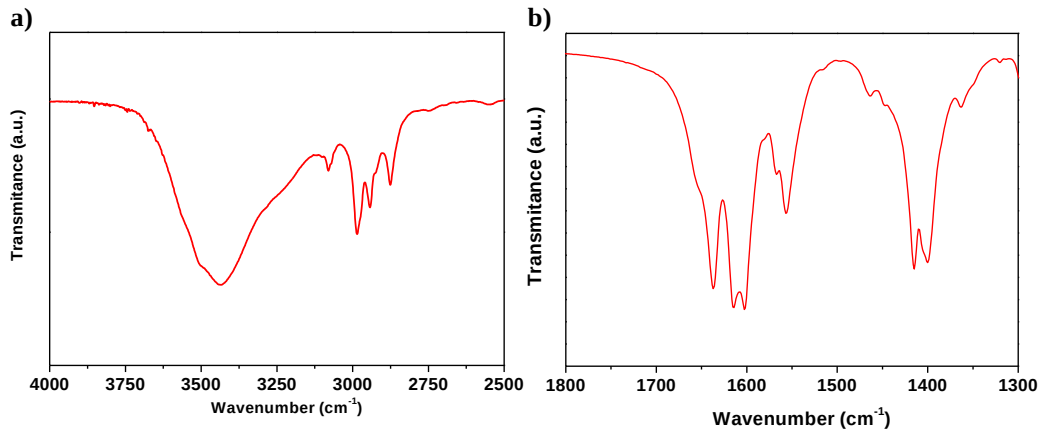

Figure 4.1.44. Details of IR spectrum for **Ca-AEPF-6** in the: **a)**-OH and –CH stretching mode zone (4000-2500 cm^{-1}) and **b)** –C=O and -CO_2^- stretching mode zone (1800-1300 cm^{-1}).

Thermal Gravimetric Analyses

Thermal Gravimetric Analyses (TGA) curve for **Ca-AEPF-6** performed under N_2 is shown in **Figure 4.1.45.**

TGA profile for this compound shows a first weight loss of ~ 1.7% between ~ 30-220 ºC, consistent with the loss of physisorbed DEF and water molecules. The second weight loss of ~ 19.7% between ~ 220-480 ºC is consistent with the removal of the coordinated DEF molecules (calc. 19.5%). After these two initial weight losses of ~21.3%, the product gradually decomposes until a final weight loss of 65.3%, which indicates the partial loss of the organic linker $L_{(1)}^{-2}$ (~80.4% decomposition) (the decomposition percentage for organic linker was calculated considering CaF_2 as the main residue). CaF_2 phase was identified as a main residue by XRPD using the Joint Committee on Powder Diffraction Standards files (JCPDS file No. 03-1088).

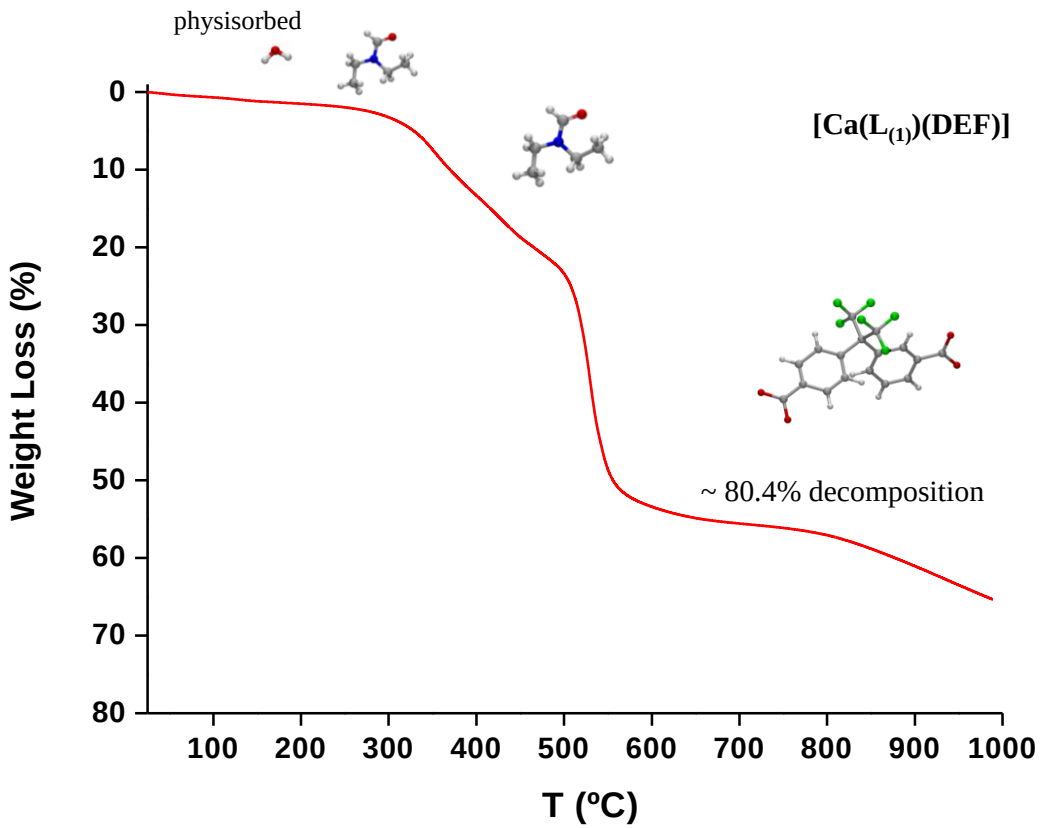

Figure 4.1.45. TGA profile for **Ca-AEPF-6** compound.

As it was above mentioned, DEF molecules block the large rhombic pores determined in **AEPF-6**. Taking into account the results coming from thermal gravimetric analyses, it was possible to determine that the loss of these DEF molecules, which are covalently bonded to calcium ions, implies the loss of the **AEPF-6** framework. Therefore, it was demonstrated that it is not possible to improve the accessible free space of this material through the application of thermal treatments.

4.1.2.2.

Ca-AEPF-7

As it was above explained, the rhombic large pores in **AEPF-6** are blocked due to the presence of DEF molecules. Taking into account this fact, the use of an organic molecule which can act as template (Py) was studied and a novel Ca-MOF (**AEPF-7**) with a similar framework to that determined in **AEPF-6** was successfully synthesized. In addition, the subsequently activation processes performed to clean the pores in **AEPF-7** was also studied.

4.1.2.2.1. Structural and topological description

The hydrothermal reaction between $H_2L_{(1)}$ and calcium acetate hydrate, using Py as base, gives rise to the **[Ca($L_{(1)}$)(H_2O)]·(Py)·(H_2O)$_{0.5}$** (**AEPF-7**), which crystallizes in the orthorhombic crystal system (*Pna2$_1$* space group). The cell parameters determined for this structure are: a = 27.8140(8) Å, b = 11.9487(4) Å, c = 6.9066(2) Å and V = 2295.35(12) Å^3. In **AEPF-7**, the asymmetric unit comprises one independent calcium ion, one deprotonated ligand ($L_{(1)}^{-2}$), one coordinated water molecule, one Py molecule and a hydration water molecule with occupancy factor ~0.5.

The ORTEP representation of **AEPF-7** asymmetric unit is shown in **Figure 4.1.46** and the main crystallographic and refinement data for this compound are shown in **Table 4.1.22**.

Table 4.1.22. Crystallographic and refinement data for **AEPF-7**.

Identification code	AEPF-7
Empirical formula	$C_{44}\ H_{32}\ Ca_2\ F_{12}\ N_2\ O_{11}$
Formula weight	1072.88
Temperature	296(2) K
Wavelength	1.54178 Å
Crystal system	Orthorhombic
Space group	*Pna2 1*
Unit cell dimensions	*a* = 27.8140(8) Å α = 90° *b* = 11.9487(4) Å β = 90° *c* = 6.9066(2) Å γ = 90º
Volume	2295.35(12) $Å^3$
Z	2
Density (calculated)	1.552 Mg/m^3
Absorption coefficient	3.158 mm^{-1}
F(000)	1092
Crystal size	0.15 x 0.05 x 0.05 mm^3
Theta range for data collection	3.18 to 58.74°
Index ranges	-30<=h<=30, -12<=k<=13, -7<=l<=4
Reflections collected	8380
Independent reflections	2062 [R(int) = 0.0324]
Completeness to theta = 58.74°	97.30%
Absorption correction	Semi-empirical from equivalents
Max. and min. Transmission	0.8581 and 0.6488
Refinement method	Full-matrix least-squares on F^2
Data / restraints / parameters	2062 / 6 / 338
Goodness-of-fit on F^2	1.018
Final R indices [I>2sigma(I)]	R_1 = 0.0292, wR_2 = 0.0764
R indices (all data)	R_1 = 0.0315, wR_2 = 0.0779
Absolute structure parameter	0.007(11)
Largest diff. peak and hole	0.207 and -0.217 $e.Å^{-3}$

In **AEPF-7**, Ca^{+2} ions are octa-coordinated to two μ_2-(H_2O) molecules and six oxygen atoms coming from $L_{(1)}^{-2}$ carboxylate groups of four different ligands that are bonded in a chelate-bridge mode, giving CaO_8 bicapped trigonal prisms (**Figure 4.1.47a**). These polyhedra, which can be considered as the primary inorganic building units (PBUs), have an average Ca-O distance of ~2.47 Å (**Table 4.1.23**). Moreover, it is worth mentioning that two kinds of Ca-O distances can be distinguished for $L_{(1)}^{-2}$

carboxylate groups: the shortest bond corresponds to the bridge mode (~2.34 Å) and the largest one corresponds to those oxygen atoms bonding in a chelate mode (~2.51 Å). Concerning the Ca-O bond to water molecules, they exhibit similar distances to those determined for oxygen atoms bonded in a bridge mode (~2.52 Å).

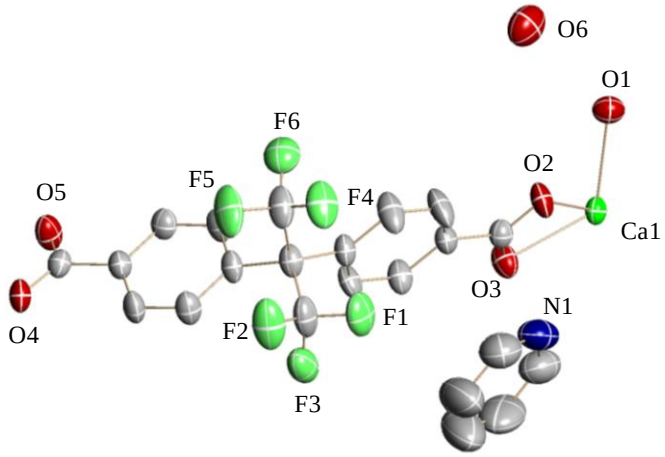

Figure 4.1.46. ORTEP representation of **AEPF-7** asymmetric unit. Ellipsoids are displayed at the 50% probability level. Hydrogen atoms were omitted for clarity.

Table 4.1.23. Interatomic distances in the coordination sphere of the CaO_8 polyhedra in **AEPF-7**.

Bond	Distance (Å)
Ca(1)-O(1)w	2.536(3)
Ca(1)-O(1)[1]w	2.494(3)
Ca(1)-O(2)c	2.550(3)
Ca(1)-O(2)[1]c	2.354(2)
Ca(1)-O(3)c	2.455(2)
Ca(1)-O(4)[2]c	2.335(2)
Ca(1)-O(4)[3]c	2.473(2)
Ca(1)-O(5)[3]c	2.543(2)

Symmetry transformations used to generate equivalent atoms:
[1] -x+1,-y+1,z+1/2
[2] -x+3/2,y+1/2,z+1/2
[3] x-1/2,-y+1/2,z

Ow: oxygen atom coming from a water molecule. Oc: oxygen atom coming from a carboxylate group.

As it is depicted in **Figure 4.1.47**, the CaO_8 polyhedra determined in **AEPF-7** are connected among them sharing their faces, leading to the formation of inorganic chains along *c* axis (**Figure 4.1.47b**). Junction of these chains is made through the $L_{(1)}^{-2}$ ligands, which act in a $\eta^2\mu_2$-$\eta^2\mu_2$ mode (**Figure 4.1.47c**), giving rise to a three-dimensional framework with rhombic shaped channels (**Figure 4.1.48a).**

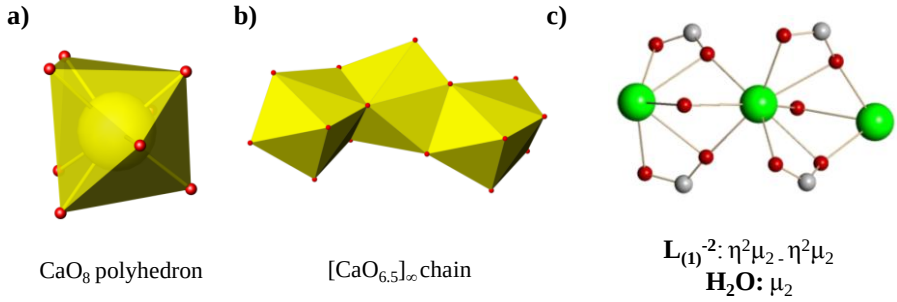

Figure 4.1.47. a) Inorganic PBUs in **AEPF-7**, **b)** detail of the CaO_8 chains that run along *c* axis, sharing faces and **c)** coordination mode of $L_{(1)}^{-2}$ linker and water molecules.

In **Figure 4.1.48**, different polyhedral views along the crystallographic axis are depicted, evidencing the three-dimensional covalent framework determined in **AEPF-7**.

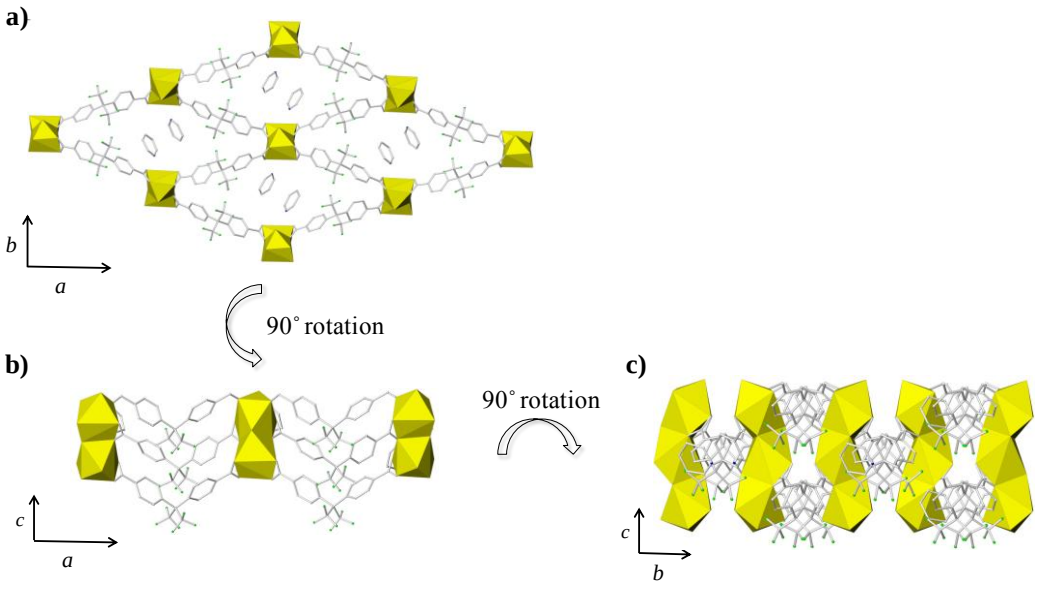

Figure 4.1.48. a) Polyhedral representation for **AEPF-7** along the *c* axis, **b)** along the *b* axis and **c)** along the *a* axis.

Moreover, as it was previously mentioned, two different types of water molecules were determined in **AEPF-7**. The presence of these water molecules in the compound allows the formation of strong hydrogen bonds interactions (**Table 4.1.24**). On one hand, coordinated water molecules establish one type of hydrogen bonds with Py molecules. On the other hand, a strong interaction was also found among hydration water molecules and one $L_{(1)}^{-2}$ carboxylate groups.

Table 4.1.24. Distances and angles of hydrogen bonds found in **AEPF-7** compound.

D-H···A[1]	D-H[2]	H···A[3]	D···A[4]	<D-H···A[5]
O(1)w-H(10B)w ··· N1 [1]	0.96(2)	1.73(2)	2.687(4)	172(4)
$O(6)w_h$-H(60B)w_h ··· O(5)c [2]	1.00(2)	1.76(3)	2.733(7)	163(8)

Symmetry operators codes

[1] -x+1, -y+1, z+1/2 [2] -x+3/2, y+1/2, z-1/2

D: donor atom, A: acceptor atom. [1]Names of donor, hydrogen and acceptor atoms involved in the hydrogen bond. [2] Distance D – A. [3]Distances H – A. [4]Distance D – A. [5] Angle D – H – A.

Oc: oxygen atom coming from a carboxylate group. Ow: oxygen atom coming from a coordinated water molecule. Ow_h: oxygen atom coming a hydration water molecule. Hw: hydrogen atom coming from a coordinated water molecule. Hw: hydrogen atom coming from a hydration water molecule.

As it was performed in the case of **AEPF-6** compound, the conformation of the organic linker was also analysed in **AEPF-7**. The values determined for the geometrical parameters **θ**, **ω** and **d** are listed in **Table 4.1.25**. Compared to the values obtained for **AEPF-6** (**Table 4.1.20**), subtle differences can be found in the conformation of the linker for both compounds. Thus, although both materials exhibit similar frameworks, in **AEPF-7** the linker exhibit a higher value of the torsion angle **ω** and the distance **d**.

Table 4.1.25. θ angle, **ω** dihedral angle and **d** distance values determined for $L_{(1)}^{-2}$ linker in **AEPF-7** compound.

θ (º)	ω (º)	d (Å)
112.78	74.82	9.994

To describe the topological features in this material, the inorganic chains found in **AEPF-7** consisting of CaO_8 polyhedra sharing faces, were simplified as rods using TOPOS,[4] taking into account the previously mentioned work of Yaghi and O'Keeffe.[23]

Thus, the inorganic SBU in **AEPF-7** can be defined as these infinite $(\text{-O-Ca-})_\infty$ rods with carboxylate O atoms completing the octa-coordination around Ca atoms to result in infinite rods of CaO_8 bicapped trigonal prisms sharing faces. In **Figure 4.1.49** the topological simplifications performed in the CaO_8 chains to build the inorganic SBU are shown.

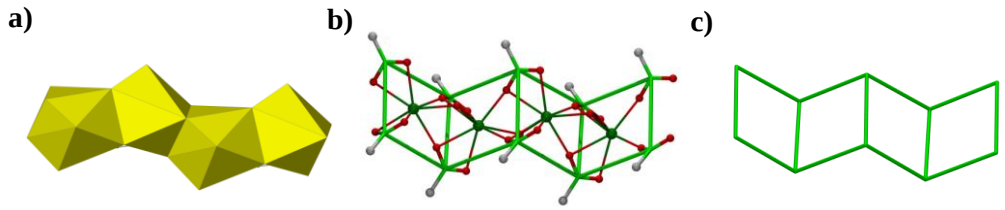

Figure 4.1.49. a) CaO_8 polyhedra chain. **b)** Topological simplifications performed to describe the $(\text{-O-Ca-})_\infty$ rods as the inorganic SBUs. **c)** Simplified inorganic SBU.

Considering the topological simplifications above mentioned, the **AEPF-7** net can be described as rods of quadrangles linked by sharing opposite edges (ladders). These ladders are linked with the rungs parallel to form a **sra** uninodal 4-connected net (point symbol $(4^2.6^3.8)$). The main simplification points, as well as the decorated and final simplified nets for **AEPF-7**, are shown in **Figure 4.1.50.**

Moreover, thanks to the topological studies performed in **AEPF-7** net, it was also possible to analyse the connection of the chains through the $L_{(1)}^{-2}$ organic linker. Thus, as it is depicted in **Figure 4.1.51**, the connection of the inorganic chains *via* de $L_{(1)}^{-2}$ ligands is made in a parallel way, being the channels of the **B**-type.[1]

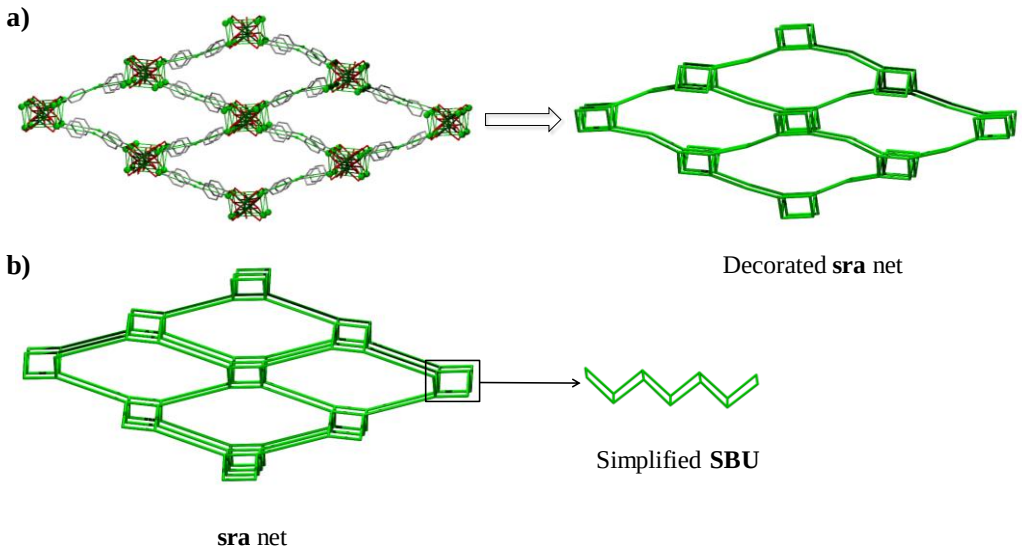

Figure 4.1.50. a) Depiction of the **AEPF-7** real net together with the decorated **sra** net. **b)** Simplified **sra** net described in **AEPF-7** and detail of the simplified inorganic SBU.

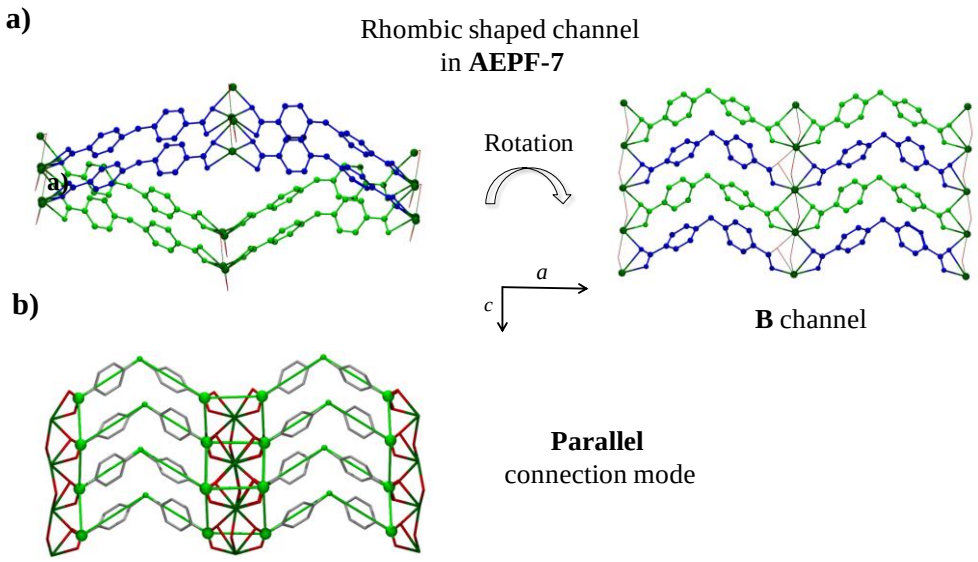

Figure 4.1.51. a) Different projections of the rhombic shaped channels in **AEPF-7**. **b)** Detail of the real net together with the decorated **sra** net, evidencing the parallel connection mode for $L_{(1)}^{-2}$ ligand. Hydrogen atoms and $-CF_3$ groups were omitted for clarity.

Additionally, a more profound topological study was performed in **AEPF-7** framework, in order to analyse the natural tiling that can be described for a **sra** net. For that purpose, in a first step, the idealisation of the **sra** net described in **AEPF-7** was performed in its maximum symmetry embedding (*Imma* space group), using Systre package.[28] In **Figures 4.1.52a-4.1.52b** both the real ($Pna2_1$ space group) and the idealised net (*Imma* space group) are shown. Thus, considering the idealised net, $[4^2.6^2.8^2]$ cages or tiles can be described (**Figure 4.1.52c**), which explain the natural tiling corresponding to a **sra** net.

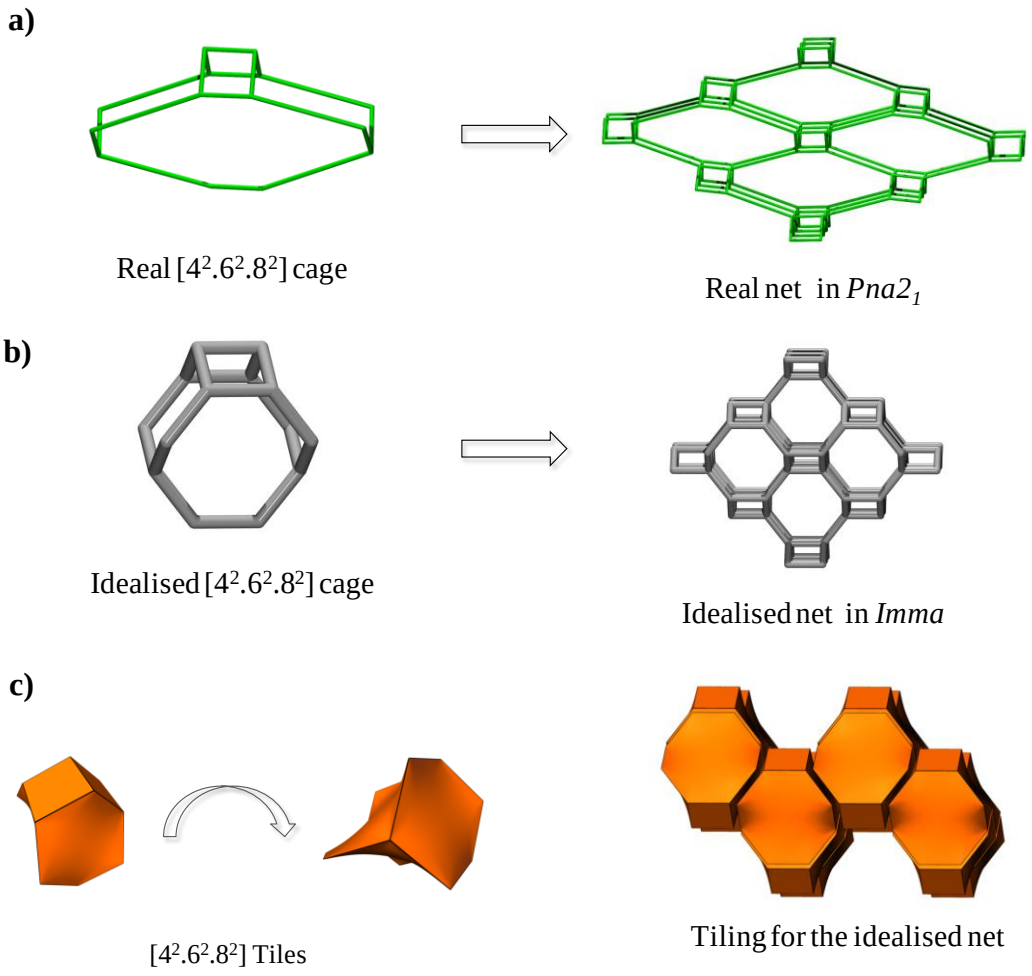

Figure 4.1.52. a) Real net and cage in $Pna2_1$ space group. **b)** Idealised net and cage in *Imma* space group. **c)** $[4^2.6^2.8^2]$ tile together with a tiling depiction corresponding to the idealised **sra** net described in **AEPF-7**.

4.1.2.2.2. Characterization

X-Ray Powder Diffraction

In order to check the purity of the bulk sample, a Pawley refinement[12] for **AEPF-7** compound was performed using Materials Studio software.[13] Pawley refinement profile and the main refinement values for **AEPF-7** are shown in **Figure 4.1.53** and **Table 4.1.26**, respectively.

Table 4.1.26. Crystal Data and Pawley profile refinement values for **AEPF-7.**

Compound	AEPF-7	
Crystal system	Orthorhombic	
Space group	$Pna2_1$	
Unit cell dimensions	a= 27.846(1) Å	α = 90˚
	b= 11.9682(3) Å	β = 90˚
	c= 6.9029(5) Å	γ = 90˚
Profile Function	Pseudo-Voigt	
U	0.07(3)	
V	0.007(6)	
W	0.0017(3)	
NA	0.73(3)	
NB	-0.004(2)	
Zero Point	0.0605(2)	
Asymmetry correction	Finger-Cox-Jephcoat	
H/L	0.01423(6)	
S/L	0.01423(6)	
Rwp	0.0422	
Rp	0.1115	

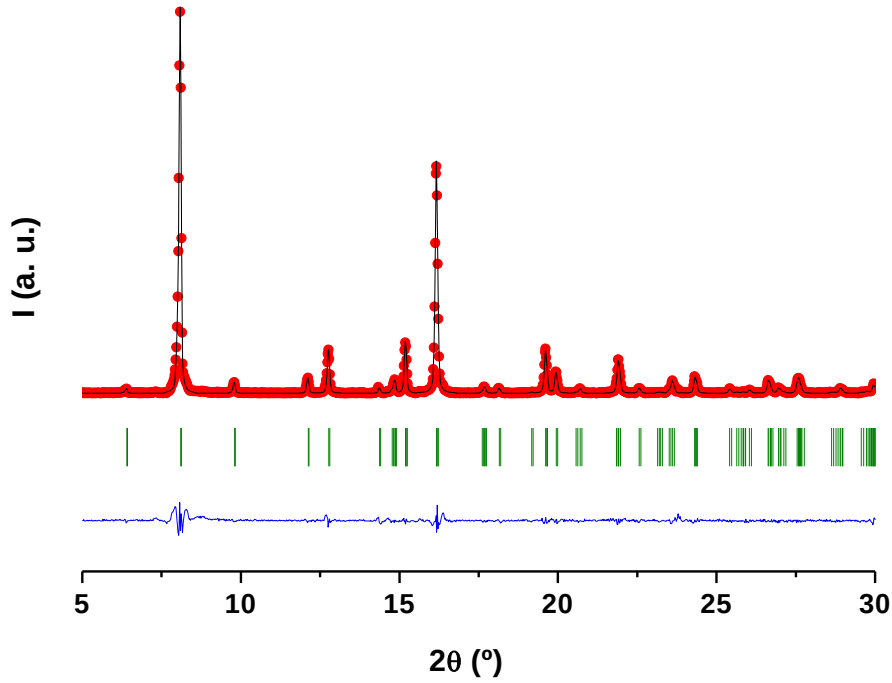

Figure 4.1.53. Pawley refinement for **AEPF-7**. Experimental data (red), simulated pattern (black) and difference (blue); observed reflections (green).

Infrared Spectroscopy

Infrared (IR) spectrum of **AEPF-7** shows the presence of bands corresponding to CO_2^- groups found at 1700-1500 (υ_{as}) and 1500-1300 (υ_s) cm^{-1}; and -OH stretching mode bands (3750-3200 cm^{-1}) which correspond to water molecules determined in this material. Due to the presence of Py molecules in channels, additional bands were determined in the region corresponding aromatic –C=N stretching mode (~1700 cm^{-1}).

Details of IR spectrum for **AEPF-7** in the areas corresponding to -OH and -CO_2^- stretching modes are given in **Figure 4.1.54**.

In -OH stretching mode region, two bands centred at ~3445 cm^{-1} and ~3360 cm^{-1} are observed (**Figure 4.1.54a**), which can be associated with the contribution of -OH stretching mode of both hydration and coordinated water molecules.

In -CO_2^- stretching mode zone five bands are observed at: ~1625 cm^{-1}, ~1610 cm^{-1}, ~1570 cm^{-1} and ~1560 cm^{-1} (υ_{as}); and ~1415 cm^{-1} (υ_s). In this region, a band centred at ~1693 cm^{-1} can be also determined, which corresponds to –C=N stretching mode of Py molecules.

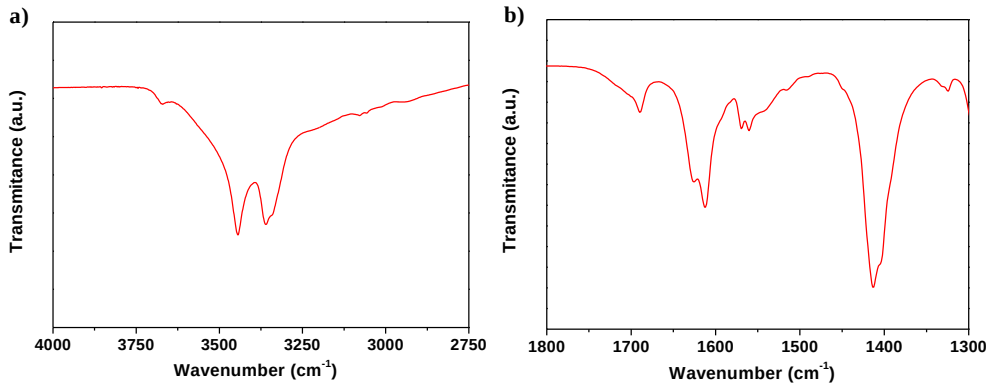

Figure 4.1.54. Details of IR spectrum in the: **a)**-OH stretching mode zone and **b)**–C=N and -CO_2^- stretching mode zone for **AEPF-7**.

Thermal Gravimetric Analyses

Thermal Gravimetric Analysis (TGA) curve for **AEPF-7** performed under nitrogen atmosphere is shown in **Figure 4.1.55**.

Thermogravimetric profile of **AEPF-7** (**Figure 4.1.55**) shows a first weight loss of ~ 4.2% which is determined between ~ 30-130 ºC, consistent with the loss of hydration and coordinated water molecules determined in **AEPF-7** (2.5 water molecules per Ca^{+2} centre, calc. 4.2%). The second loss of ~ 13.8% between ~ 250-405 ºC is consistent with the removal of Py molecules present in pores of **AEPF-7** (calc. 15.5%). Finally, at temperatures above 450 ºC, a total decomposition of the framework occurs giving rise to CaF_2 as a residual solid (found: 83.9%; calculated: 85.5%), confirmed by XRPD (JCPDS file No. 01-075-0097).

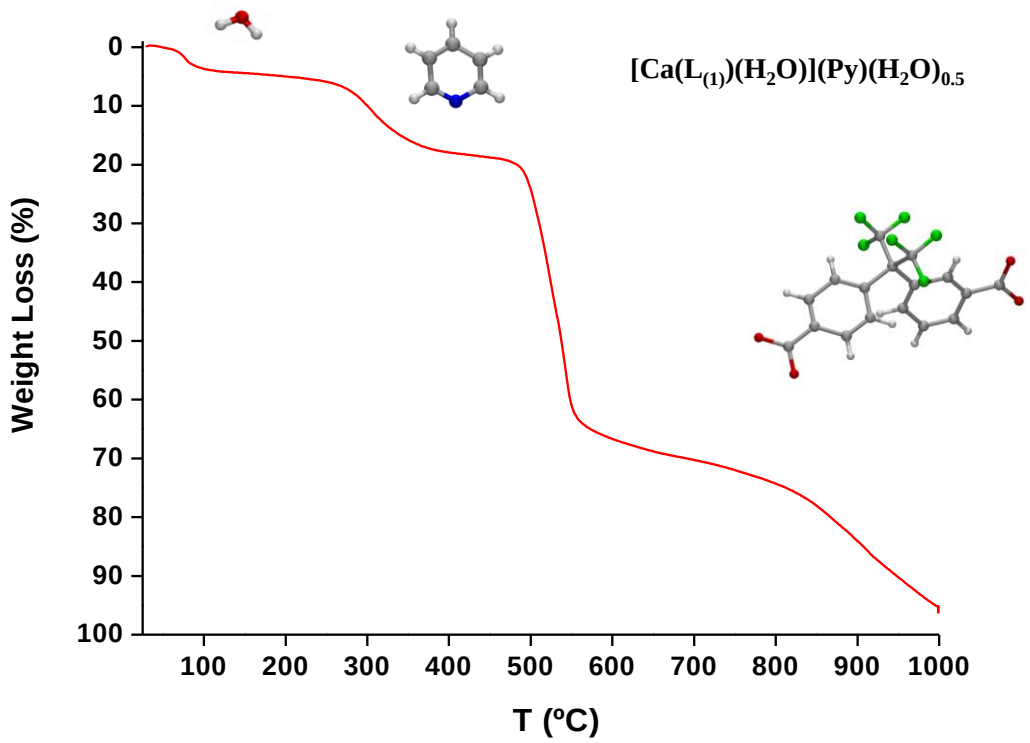

Figure 4.1.55. TGA profile for **AEPF-7**.

4.1.2.2.3. Study of AEPF-7 activation

To investigate the potential application of this material in adsorption, a detailed study of **AEPF-7** activation process was performed following both the loss of guest molecules from its pores (Py) and the interchange of guest molecules by other solvent molecules.

Activation by drying treatments

In the first step, different drying processes were performed in order to remove Py molecules from **AEPF-7** pores. Taking into account TGA data, **AEPF-7** samples were dried under vacuum at two different temperatures: 120 ºC and 250 ºC. **Figure 4.1.56** depicts the corresponding XRPD pattern for the as-synthesised sample and the dried samples, showing the robustness of **AEPF-7** crystalline phase after the drying treatments.

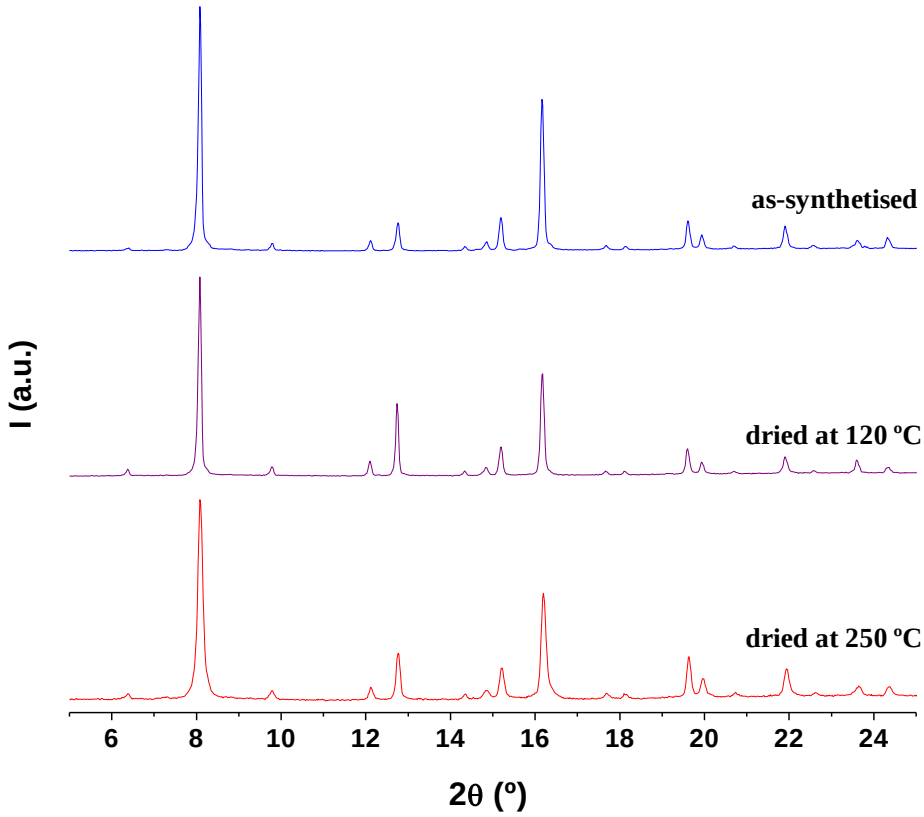

Figure 4.1.56. XRPD patterns for as-synthesised **AEPF-7** sample and the dried samples (at the two studied temperatures).

In the next step, the effectiveness of Py removal was checked following the variation of %N before and after the activation (**Table 4.1.27**). Thus, as it can be concluded with these results, the activation of **AEPF-7** compound by heating treatment was unsuccessful. As it is shown in **Table 4.1.27**, regarding the sample dried at 250 ºC, the presence of 0.8 Py molecules per calcium atom was found.

Table 4.1.27. %N found in **AEPF-7** after activation and the estimated amount of Py molecules per calcium atom.

Activation process	% N	Py molecules / Ca
as-synthesised sample	2.65	0.94
dried at 120 ˚C	2.40	0.92
dried at 250 ˚C	2.09	0.80

Activation by interchange treatments

As the results of thermal activation were unsatisfied, in the next step the activation by interchange treatments was proved. Thus, the interchange between Py molecules and other solvent molecules which can be easily removed by drying treatments was studied and the main results are presented in the following.

- **Interchange treatment with toluene**

In a first stage, **AEPF-7** activation by interchange treatments was tried using toluene, mainly due to the shape/size similarities between Py and toluene molecules. In a standard procedure, an **AEPF-7** powder sample (40 mg) was dispersed in toluene (30 ml) and vigorously stirred at 80 ºC during three days. The sample was then isolated by centrifugation and air-dried. As it is shown in **Table 4.1.28**, the **AEPF-7** sample after the activation with toluene contains ~1.38% N, which corresponds to ~0.53 Py molecules per calcium atom. The robustness of the crystalline phase was checked by means of XRPD, showing that the **AEPF-7** maintains the crystallinity after the activation process (**Figure 4.1.57**).

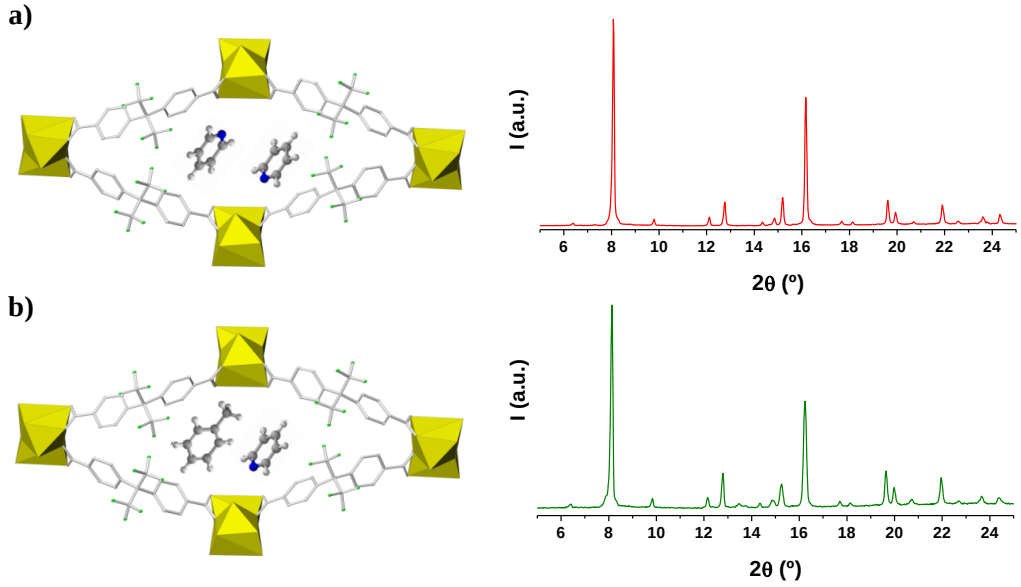

Figure 4.1.57. XRPD patterns for **AEPF-7** samples after the corresponding interchange treatment with: **a)** toluene and **b)** Py.

Table 4.1.28. %N found in **AEPF-7** after activation and the estimated amount of Py molecules per calcium atom.

Activation process	% N	% C	Py molecules / Ca
as-synthesised sample	2.40	49.21	0.92
activated with toluene at 80 ºC	1.38	49.33	0.53
activated with toluene at 80 ºC and dried at 275 ºC	1.35	47.81	0.52

In the next step, thermal gravimetric analyses were performed in order to evaluate the suitable temperature to remove guest molecules in the activated sample. A detail of TGA curve is depicted in **Figure 4.1.58a** for the activated **AEPF-7** sample. A first weight loss of ~ 5.1% is determined between ~ 30-110 ºC, consistent with the loss of coordinated and hydration water molecules determined in this compound (1.5 water molecules per Ca centre, calc. 5.0%). The second loss of ~ 12.6% occurred between ~ 250-400 ºC corresponds to the removal of guest molecules present in pores (calc. 15.9%, considering ~0.5 Py molecules and ~0.5 toluene molecules per Ca centre).

The activated sample was dried at 275 ºC under vacuum in order to check the structural stability of the material after the loss of guest molecules. However, as it is shown in **Figure 4.1.58b**, after the drying process the material does not retain the **AEPF-7** framework, as the XRPD pattern shows the presence of new no identified Bragg peaks.

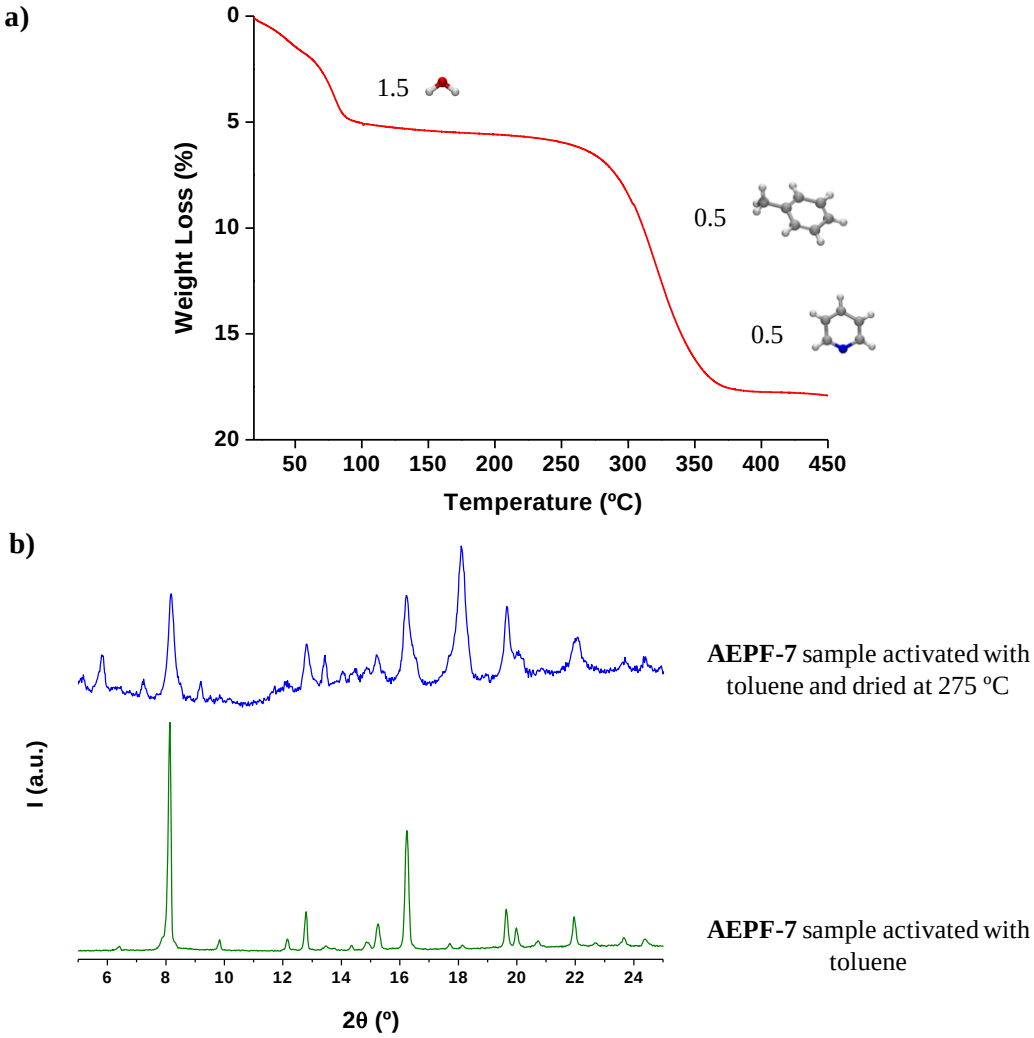

Figure 4.1.58. a) Detail of TGA curve for **AEPF-7** sample the activation treatment with toluene. **b)** XRPD patterns for as-synthesised **AEPF-7** sample and the activated **AEPF-7** sample (at the two studied temperatures).

- **Interchange treatment with acetonitrile**

As it was above shown, the guest interchange with toluene was unsuccessful due to the loss of crystallinity of **AEPF-7** after the evacuation of guest molecules after the activation process. For that reason, in a next step, **AEPF-7** activation by interchange treatments was performed using acetonitrile.

Several features were considered to choose acetronitrile to perform interchange treatments, which are going to be discussed point by point.

- Acetronitrile shows a similar **polarity** to that of pyridine, with polarity indexes of 5.8 and 5.3, respectively, which is a crucial factor to remove Py from pores by dispersion of **AEPF-7** in acetronitrile.

- Nitrogen atoms of Py molecules act as acceptor atoms of strong **hydrogen bonds** in **AEPF-7**. These supramolecular interactions play an important role in the stabilization the **AEPF-7** framework. In this sense, acetronitrile molecules, with nitrogen atoms apt to become acceptor atoms of hydrogen bonds, can play a similar stabilizing structural role.

- Finally, it is worth highlighting the high difference between Py and acetonitrile molecular volumes (104.5 and 43.1 $Å^3$, respectively). This fact is of great importance as Py molecules block large rhombic pores determined in **AEPF-7**. Thus, by replacing Py molecule with smaller guest molecules (like acetonitrile), the obtaining of a more porous **AEPF-7** framework can be achieved.

In a standard procedure, an **AEPF-7** powder sample (40 mg) was dispersed in acetonitrile (30 ml) and vigorously stirred at room temperature during 2 hours. The sample was then isolated by centrifugation. In order to ensure the effectiveness of the interchange process, this procedure was repeated three times. The sample was then isolated by centrifugation and air-dried. The effectiveness of the activation process with acetonitrile was followed by Infrared Spectroscopy. As it is shown in **Figure 4.1.59a**, the IR spectrum for as-synthesised **AEPF-7** sample shows a band at ~1695 cm^{-1}, which corresponds to aromatic –C=N stretching mode of Py molecules. Regarding the sample after the activation with acetonitrile, this band has clearly disappeared, assuring the replacement of the majority of pyridine molecules by acetonitrile (**Figure 4.1.59b)**.

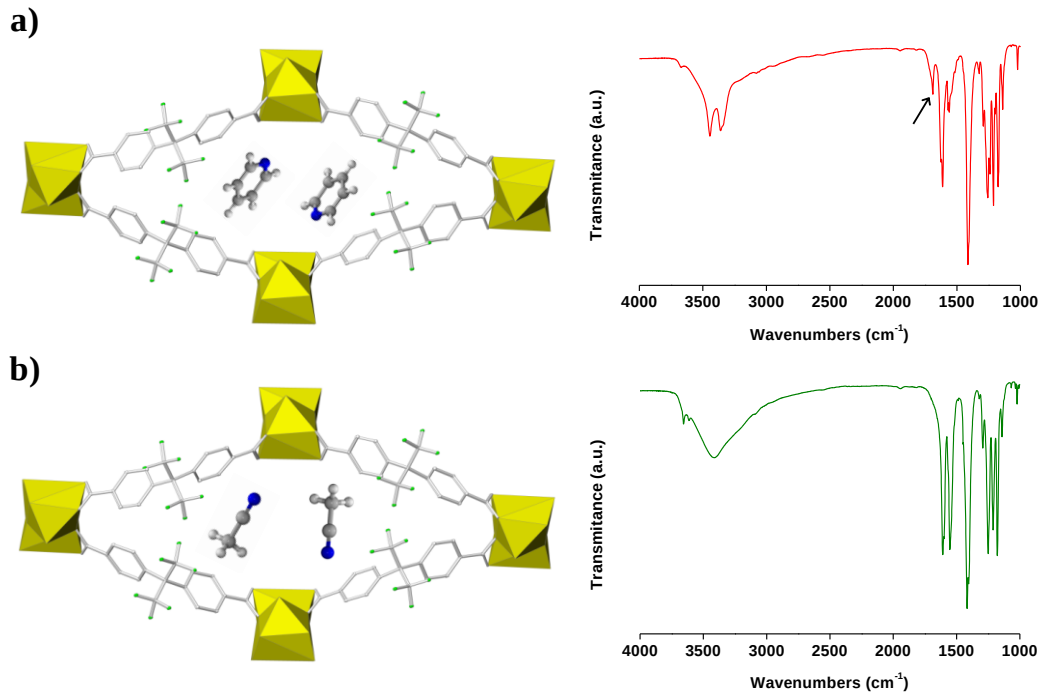

Figure 4.1.59. Details of IR spectra for: **a)** as-synthesised **AEPF-7** sample and **b) AEPF-7** sample activated with acetonitrile.

Due to the fact that the two studied guests are nitrogenated molecules, in this case both the % N and %C amounts for **AEPF-7** samples before and after the activation with acetonitrile were determined by Elemental Analyses (**Table 4.1.29**). For the as-synthesised **AEPF-7** sample the %N and %C amounts determined fit well with the presence of ~0.92 Py molecules per calcium atom. For the activated **AEPF-7** sample, the %N and %C determined (2.10% and 46.71%, respectively) can correspond to the presence of ~0.5 acetonitrile and ~0.25 Py molecules per calcium atom (calc. 2.15 % N and 47.30% C).

Thermal gravimetric analyses were performed in order to evaluate the suitable temperature to remove guest molecules in the activated sample. A detail of TGA curve is depicted in **Figure 4.1.60a** for the activated **AEPF-7** sample. Three consecutive weight losses of ~ 15.1% totally are determined between ~ 30-400 ºC, consistent with the removal of coordinated water molecules and guest molecules (calc.11.9%, taking into account approximately ~0.5 acetonitrile molecules and ~0.25 Py molecules per Ca centre).

Considering these data, the activated sample was dried at 180 ºC under vacuum in order to check the structural stability of the material after the loss of acetonitrile molecules. As it is shown in **Figure 4.1.60b**, after the drying treatment, the material retains the **AEPF-7** framework, although some amorphization is also determined.

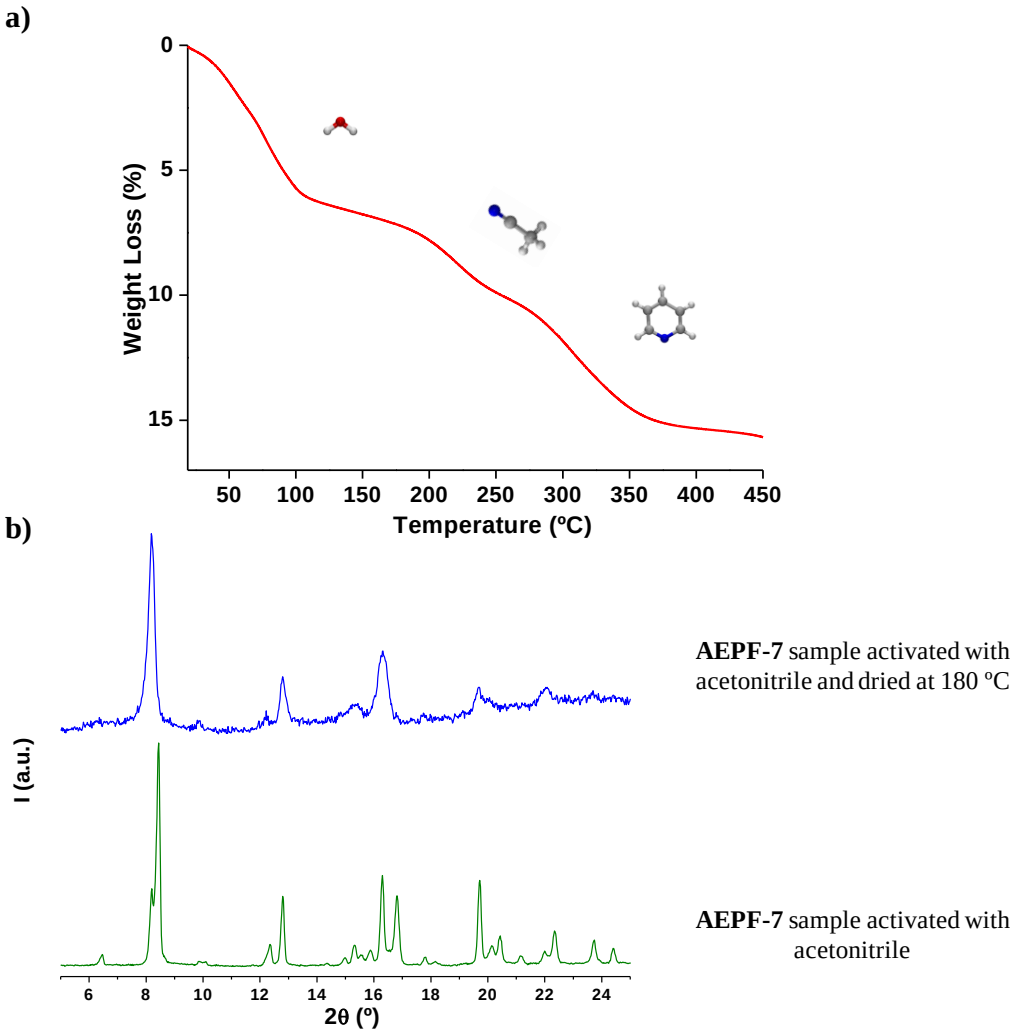

Figure 4.1.60. a) Detail of TGA curve for **AEPF-7** sample after the activation treatment with acetonitrile. **b)** XRPD patterns for as-synthesised **AEPF-7** sample and the activated **AEPF-7** sample dried at 180ºC under vacuum.

Finally, the %N was determined in the activated sample dried at 180ºC. As it is shown in **Table 4.1.29**, we can conclude that the activation of **AEPF-7** was successful due to the decrease in %N together with the retaining of the framework.

Table 4.1.29. The table shows the %N and %C found by Elemental Analyses and the corresponding estimated amount of *Py* or acetonitrile (CH_3CN) molecules per calcium atom.

Activation process	% N	% C	Py molecules / Ca	CH_3CN molecules / Ca
as-synthesised sample	2.40	49.21	0.92	-
activated with CH_3CN	2.10	46.71	0.25	0.50
activated with CH_3CN and dried at 180 ºC	0.80	45.11	0.20	-

4.1.2.2.4. Gas sorption studies

In order to evaluate the potential applications of **AEPF-7** in gas adsorption, the specific surface area for the activated sample was determined measuring the N_2 adsorption-desorption at 77 K (*see* Chapter 2, *Techniques*). Before adsorption measurements the sample was outgassed at 453 K in order to evacuate guest molecules from pores. Adsorption isotherms were performed in relative pressure range of 10^{-6} to 1 atm (**Figure 4.1.61**).

A BET surface area of 259 $m^2 \cdot g^{-1}$ was obtained for **AEPF-7** using the data points on the adsorption branch of the N_2 isotherm the range P/P_0 = 0.1-0.3.

Taking into account this result, it can be concluded that, after carrying out the activation processes by interchange treatment with acetonitrile in order to substitute Py from pores, **AEPF-7** certainly exhibits a porous framework.

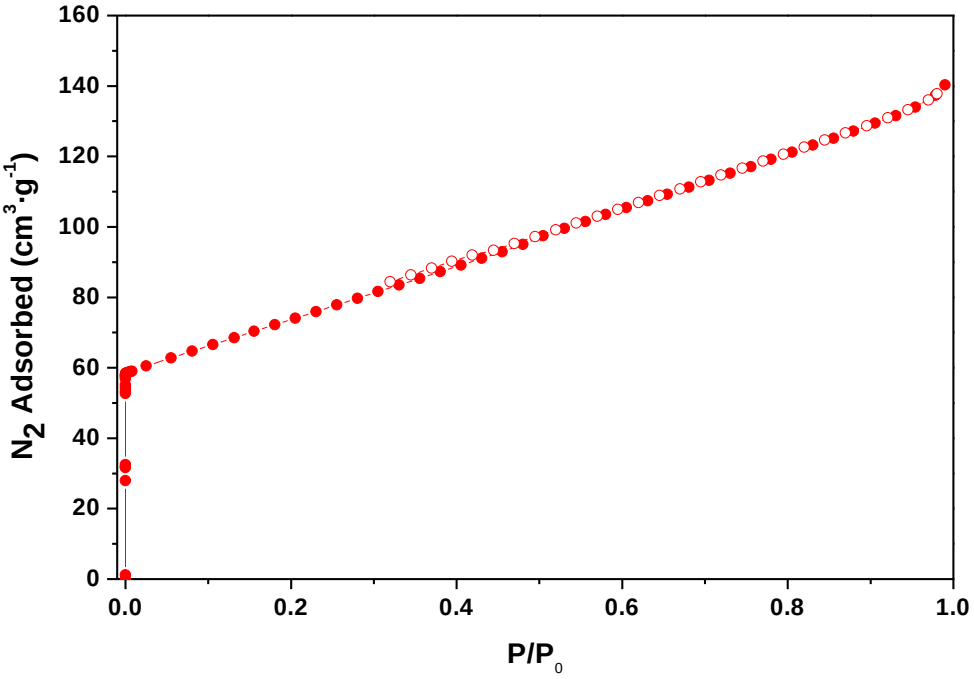

Figure 4.1.61. Nitrogen adsorption isotherm (filled points) and desorption isotherm (empty points) at 77 K for **AEPF-7**.

4.1.3.

Mg-AEPF-8 and Mg-AEPF-9

Taking into account the interesting materials obtained with calcium, in a next step we scope the use of other alkaline-earth elements in the obtaining of MOFs based on $H_2L_{(1)}$. In this section we present the structural and topological description of two new magnesium MOFs, which have been synthesised under solvothermal conditions using DEF as solvent.

Firstly, the **AEPF-8** compound was obtained, which exhibits a marked poor crystallinity. In spite of the experimental difficulties, after careful optimising the synthesis conditions, it was possible to obtain suitable **AEPF-8** single crystals for its structural determination by single-crystal XRD. It is worth highlighting that **AEPF-8** possesses an interesting three-dimensional open framework which is going to be discussed in the following. On the other hand, a novel compound named **AEPF-9**, which possesses a layered structure, was also obtained.

4.1.3.1.

Mg-AEPF-8: structural and topological description

The reaction between $H_2L_{(1)}$ and magnesium acetate hydrate under the optimized solvothermal conditions, using DEF as solvent, gives rise to the **[$Mg_{1.5}(L_{(1)})_{1.5}$(DEF)]** compound (**AEPF-8**) (*see* Chapter 2, *Synthesis procedures*). This compound crystallizes in the orthorhombic crystal system (*C2/c* space group). The cell parameters determined for this structure are: a = 37.225(2) Å, b = 14.3269(7) Å, c = 25.873(2) Å, β = 128.017(2) º and V = 10870.6(1) $Å^3$. The main crystallographic and refinement data for this compound are shown in **Table 4.1.30** and the ORTEP representation of **AEPF-8** asymmetric unit is shown in **Figure 4.1.62**.

Table 4.1.30. Crystallographic and refinement data for **AEPF-8**.

Identification code	AEPF-8
Empirical formula	$C_{61}\ H_{46}\ F_{18}\ Mg_3\ N_2\ O_{16}$
Formula weight	1477.93
Temperature	296(2) K
Wavelength	1.54178 Å
Crystal system	Monoclinic
Space group	*C2/c*
Unit cell dimensions	a = 37.225(2) Å α = 90° b = 14.3269(7) Å β = 128.017(2)° c = 25.873(2) Å γ = 90°
Volume	10870.6(1) $Å^3$
Z	4
Density (calculated)	0.903 Mg/m^3
Absorption coefficient	0.902 mm^{-1}
F(000)	3008
Crystal size	0.10 x 0.10 x 0.05 mm^3
Theta range for data collection	3.01 to 53.59°
Index ranges	-29<=h<=30, -14<=k<=10, -17<=l<=25
Reflections collected	17095
Independent reflections	3721 [R(int) = 0.0369]
Completeness to theta = 53.59°	57.4%
Absorption correction	Semi-empirical from equivalents
Max. and min. Transmission	0.9563 and 0.9152
Refinement method	Full-matrix least-squares on F^2
Data / restraints / parameters	3721 / 0 / 441
Goodness-of-fit on F^2	1.56
Final R indices [I>2sigma(I)]	R_1 = 0.1369, wR_2 = 0.3849
R indices (all data)	R_1 = 0.1805, wR_2 = 0.4028
Extinction coefficient	0.0013(2)
Largest diff. peak and hole	0.800 and -0.536 $e.Å^{-3}$

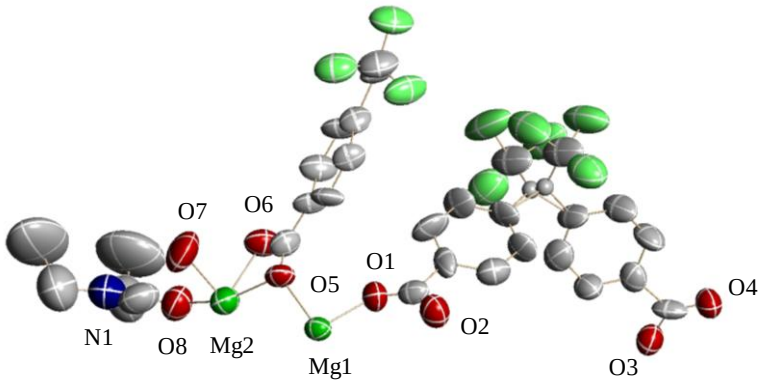

Figure 4.1.62. ORTEP representation of **AEPF-8** asymmetric unit. Ellipsoids are displayed at the 50% probability level. Hydrogen atoms were omitted for clarity.

In the **AEPF-8** asymmetric unit there are two independent Mg^{+2} ions, which show both hexa-coordinated environments. The two metallic centers are present forming two types of octahedra, which can be considered as the inorganic PBUs in the structure.

On one hand, Mg(1) centers are bonded to four oxygen atoms coming from bridge $L_{(1)}^{-2}$ carboxylate groups and to two oxygen atoms from chelate-bridge $L_{(1)}^{-2}$ carboxylate groups, giving regular MgO_6 regular octahedra with an average Mg-O distance of ~2.05 Å (**Table 4.1.31** and **Figure 4.1.63a**).

Concerning the Mg(2) centers, the magnesium ions are bonded to two oxygen atoms from chelate-bridge $L_{(1)}^{-2}$ carboxylate groups, two oxygen atoms coming from chelate-bridge $L_{(1)}^{-2}$ carboxylate groups, one oxygen atom from a DEF carbonyl group and one oxygen atom from a coordinated water molecule. It is worth mentioning that in this case two kinds of distances can be distinguished: a shorter distance with an average value of ~2.05 Å for oxygen atoms from the DEF molecule and the bridge $L_{(1)}^{-2}$ carboxylate groups; and a larger distance with ~2.16 Å for oxygen atoms from the water molecule and the chelate-bridge $L_{(1)}^{-2}$ carboxylate groups. These differences provoke a clear distortion in the octahedra found for Mg(2) centres (**Table 4.1.31** and **Figure 4.1.63a**).

Table 4.1.31. Interatomic distances in the coordination sphere of the MgO_6 polyhedra in **AEPF-8.**

Mg(1)

Bond	Distance (Å)
Mg(1)-O(1)c	2.03(1)
Mg(1)-O(1)[1]c	2.03(1)
Mg(1)-O(4)[2]c	2.00(1)
Mg(1)-O(4)[3]c	2.00(1)
Mg(1)-O(5)c	2.109(9)
Mg(1)-O(5)[1]c	2.109(9)

Symmetry transformations used to generate equivalent atoms:
[1]-x+1/2,-y+1/2,-z+1 [3]-x+1/2,y-1/2,-z+1/2
[2] x,-y+1,z+1/2

Mg(2)

Bond	Distance (Å)
Mg(2)-O(2)[1]c	2.01(1)
Mg(2)-O(3)[2]c	2.02(1)
Mg(2)-O(5)c	2.16(1)
Mg(2)-O(6)c	2.14(1)
Mg(2)-O(7)w	2.17(1)
Mg(2)-O(8)co	2.02(2)

Symmetry transformations used to generate equivalent atoms:
[1]-x+1/2,-y+1/2,-z+1 [2]-x+1/2,y-1/2,-z+1/2

Oc: oxygen atom coming from a carboxylate group. Od: oxygen atom coming from a DEF carbonyl group. Ow: oxygen atom coming from a water molecule.

The two kinds of MgO_6 polyhedra form sharing-vertex Mg_3O_{16} clusters, which can be considered as the inorganic secondary building units (SBUs) in **AEPF-8** (**Figure 4.1.63b**). As it is shown is **Figure 4.1.63c**, the formation of these trimers is due to the junction of one Mg(1) octahedron to other two Mg(2) octahedra *via* $L_{(1)}^{-2}$ carboxylate groups acting in a $\eta^2\mu_2$-$\eta^2\mu_2$ coordination mode. Moreover, DEF and water molecules are coordinated to Mg(2) centers completing their octahedral environment.

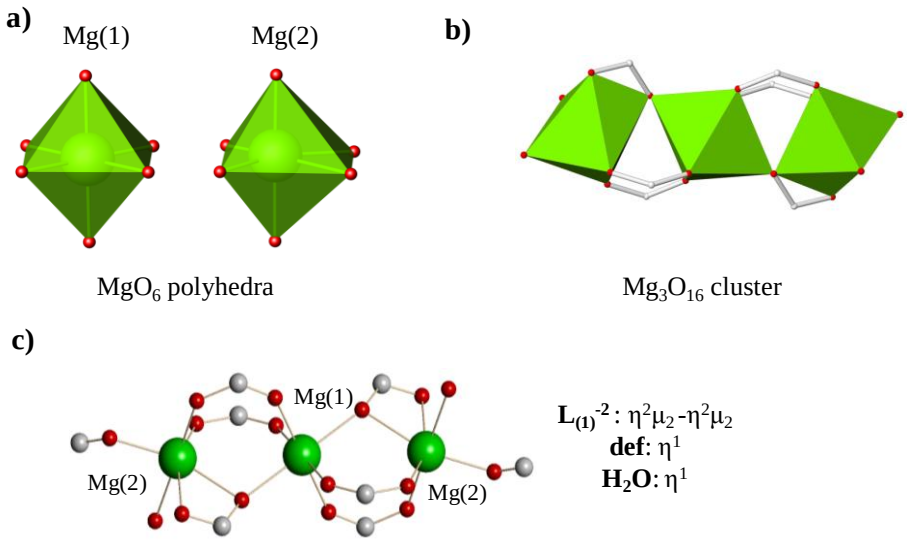

Figure 4.1.63. a) Inorganic PBUs in **AEPF-8**, **b)** Mg_3O_{16} cluster acting as inorganic SBU and **c)** coordination modes of $L_{(1)}^{-2}$ linker, DEF and water molecules.

The metallic clusters described in **AEPF-8** are linked in two different ways (**Figure 4.1.64a**). On one hand, these clusters are joint through one type of $L_{(1)}^{-2}$ linker (named $L_{(1)}^{-2}{}_{\mathbf{A}}$), which act in a $\eta^2\mu_2$(bridge)-$\eta^2\mu_2$(bridge) coordination mode (**Figure 4.1.63c**), forming layers with square shaped channels parallel to the *bc* plane. On the other hand, the channel layers are linked along the [1 0 0] direction through another $L_{(1)}^{-2}$ linker (named $L_{(1)}^{-2}{}_{\mathbf{B}}$), that acts in a $\eta^2\mu_2$(chelate-bridge)-$\eta^2\mu_2$(chelate-bridge) mode (**Figure 4.1.64c**). Moreover, two additional kinds of channels are found: large spherical channels that run along *c* axis (**Figure 4.1.64b**) and rhombic channels (similar to those determined in **Ca-AEPF-6** and **Ca-AEPF-7** compounds) along [101] direction (**Figure 4.1.64c**).

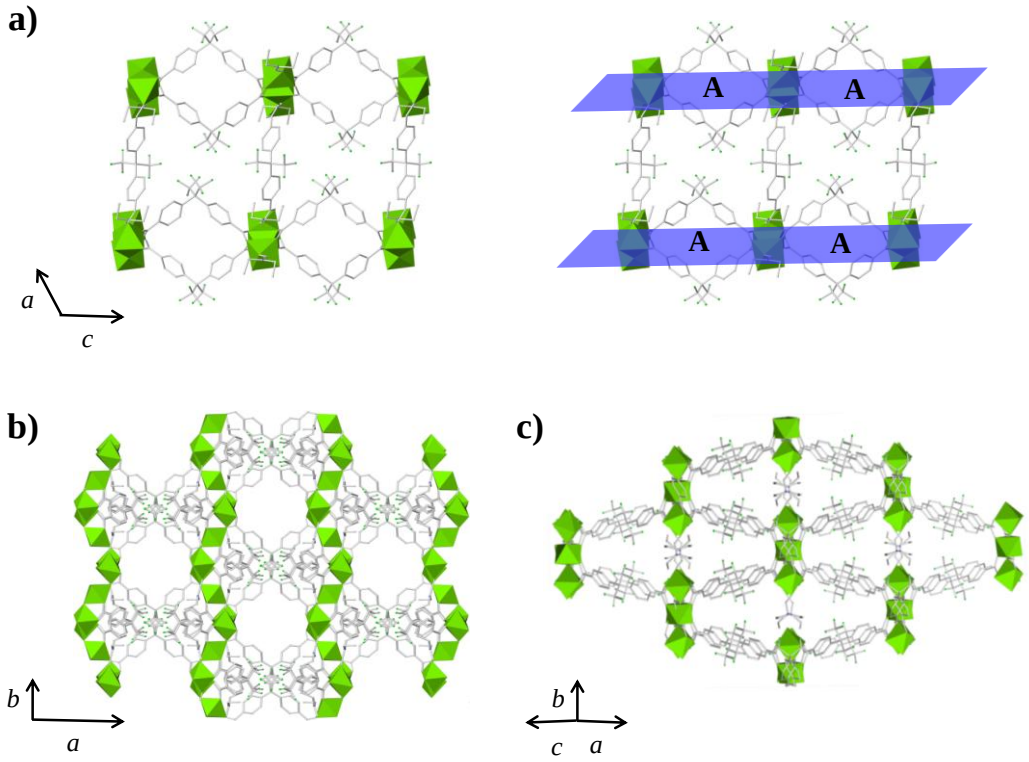

Figure 4.1.64. a) AEPF-8 polyhedral view along the *b* axis, showing the square-shaped channels layers**. b**) Polyhedral representation along the *c* axis and **c)** along the [101] direction.

Taking into account the interesting open framework determined for **AEPF-8**, the potential accessible voids present in its crystal structure were calculated using PLATON software[5] (SOLV mode). Thus, a potential free space was estimated as 49.1%, which corresponds to 5333.7 $Å^3$ per unit cell. This high porosity is explained by the presence of different spherical cavities, whose sizes are comprised between ~70-300 $Å^3$. These pores are connected among them, giving rise to the porous three-dimensional net of channels depicted in **Figure 4.1.65**.

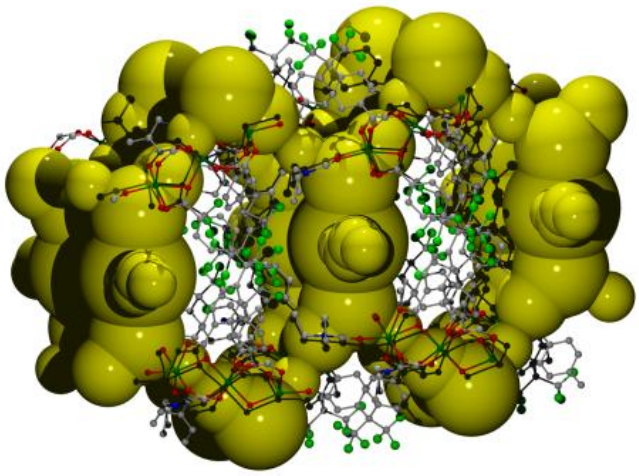

Figure 4.1.65. Depiction of the porous framework determined in **AEPF-8** compound (cavities, in yellow, were calculated using PLATON software).

In order to study the linker conformation in **AEPF-8**, the corresponding values of **θ** angle, **ω** angle and **d** distance are listed in **Table 4.1.32**. It is worth highlighting the difference observed between the **d** values for the two linker forms ($L_{(1)}{}^{-2}{}_{A}$ and $L_{(1)}{}^{-2}{}_{B}$), being the largest the one corresponding to the ligands which form the square shaped channels.

Table 4.1.32. θ angle, **ω** dihedral angle **d** distance values in **AEPF-8** for the two $L_{(1)}{}^{-2}$ linker forms determined in this compound.

Linker	θ (º)	ω (º)	d (Å)
$\mathbf{L_{(1)}{}^{-2}{}_{A}}$	112.00	71.16	9.609
$\mathbf{L_{(1)}{}^{-2}{}_{B}}$	113.68	63.01	9.158

In order to describe the topology of **AEPF-8** net using TOPOS[,4] the best simplification consists of analysing each cluster as a node (**Figure 4.1.66a**). Thus, after studying the connectivity of the clusters in this compound, they can be simplified as a unique hexa-coordinated node located in Mg(1). The **AEPF-8** framework can be then described as a uninodal hexa-conneted net, exhibiting a **pcu** topology (Point Symbol ($4^{12}.6^{3}$)). The main simplifications points, as well as the decorated and the final simplified nets for **AEPF-8**, are shown in **Figure 4.1.66**.

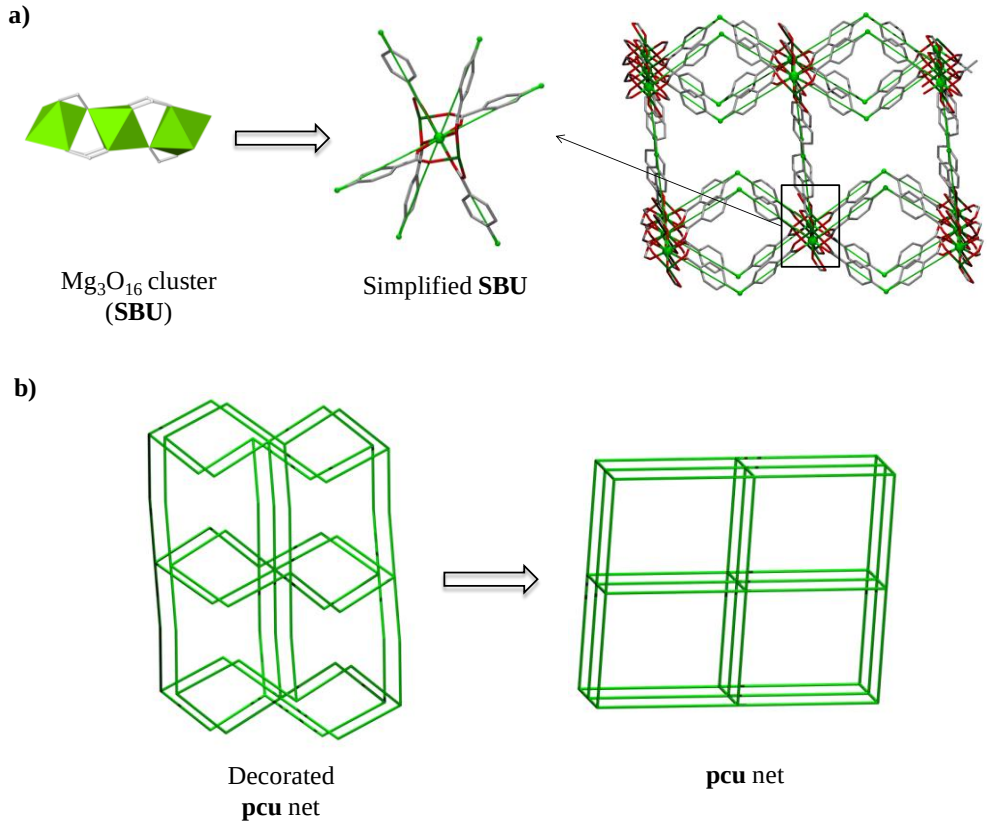

Figure 4.1.66. a) Depiction of the topological simplifications performed to describe the clusters. Hydrogen atoms and $-CF_3$ groups were omitted for clarity. **b)** Depiction of both decorated and simplified **pcu** net described for **AEPF-8**.

Additionally, a more profound topological study was performed in order to analyse the way in which the linker generates the square shaped channels in **AEPF-8**. As it is shown in **Figure 4.1.67**, in this structure the connections among the clusters are made in a parallel way, being thus of the **B**-type.[1]

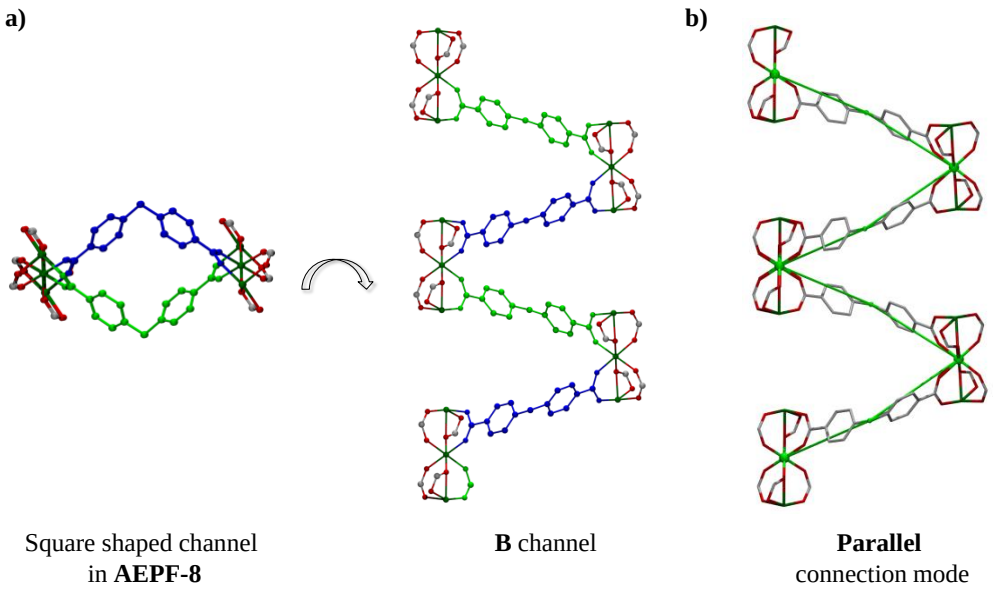

Figure 4.1.67. a) Different projections of the square-shaped channels in **AEPF-8**. **b)** Detail of the real net together with the decorated **pcu** net, showing the parallel mode for $L_{(1)}^{-2}$ ligand. Hydrogen atoms and $-CF_3$ groups were omitted for clarity.

4.1.3.2.

Mg-AEPF-9: structural and topological description

The reaction between $H_2L_{(1)}$ and magnesium acetate hydrate under the optimized solvothermal conditions, using DEF as solvent, gives rise to the **[Mg($L_{(1)}$)(DEF)]** compound (**AEPF-9**) (*see* Chapter 2, *Synthesis procedures*). This compound crystallizes in the orthorhombic crystal system ($P2_1/n$ space group). The cell parameters determined for this structure are: a = 16.725(2) Å, b = 7.1992(7) Å, c = 20.750(2) Å, β = 103.632(2)º and V = 2349.79(8) Å^3. The main crystallographic and refinement data for this compound are shown in **Table 4.1.33** and the ORTEP representation of **AEPF-9** asymmetric unit is shown in **Figure 4.1.68.**

Table 4.1.33. Crystallographic and refinement data for **AEPF-9**.

Identification code	AEPF-9
Empirical formula	$C_{22}\ H_{19}\ F_6\ Mg\ N\ O_5$
Formula weight	515.69
Temperature	296(2) K
Wavelength	0.71073 Å
Crystal system	Monoclinic
Space group	$P2_1/n$
Unit cell dimensions	a = 16.725(2) Å α = 90° b = 7.1992(7) Å β = 103.632(2)° c = 20.750(2) Å γ = 90°
Volume	2428.1(4) $Å^3$
Z	4
Density (calculated)	1.411 Mg/m^3
Absorption coefficient	0.152 mm^{-1}
F(000)	1056
Crystal size	0.30 x 0.15 x 0.05 mm^3
Theta range for data collection	1.41 to 25.02 °
Index ranges	-19<=h<=19, -8<=k<=8, -24<=l<=24
Reflections collected	15085
Independent reflections	4220 [R(int) = 0.0779]
Completeness to theta = 25.02°	98.3%
Absorption correction	Semi-empirical from equivalents
Max. and min. Transmission	0.9925 and 0.9559
Refinement method	Full-matrix least-squares on F^2
Data / restraints / parameters	4220 / 0 / 319
Goodness-of-fit on F^2	0.958
Final R indices [I>2sigma(I)]	R_1 = 0.0804, wR_2 = 0.2035
R indices (all data)	R_1 = 0.1745, wR_2 = 0.2560
Extinction coefficient	0.015(2)
Largest diff. peak and hole	2.279 and -0.450 e.$Å^{-3}$

In **AEPF-9**, Mg^{+2} ions are penta-coordinated to four oxygen atoms coming from $L_{(1)}^{-2}$ bridge carboxylate groups and one oxygen atom from a DEF carbonyl group, giving regular MgO_5 square prisms (**Figure 4.1.69a**). These polyhedra, which can be

considered as the inorganic PBUs in the structure, have an average Mg-O distance of ~1.99 Å (**Table 4.1.34**).

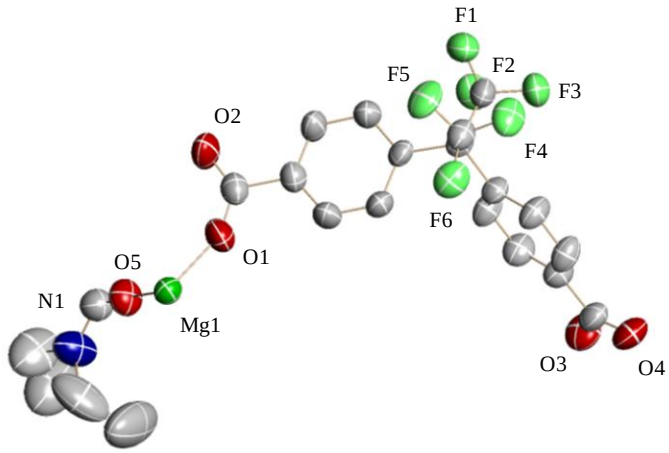

Figure 4.1.68. ORTEP representation of **AEPF-9** asymmetric unit. Ellipsoids are displayed at the 50% probability level. Hydrogen atoms were omitted for clarity.

The MgO_5 polyhedra determined in this material form chains that run along the *b* axis, *via* the $L_{(1)}^{-2}$ carboxylate groups (**Figure 4.1.69b**). These inorganic chains are joint through the $L_{(1)}^{-2}$ linker, which act in a $\eta^2\mu_2$-$\eta^2\mu_2$ coordination mode (**Figure 4.1.69c**), giving rise to covalent layers.

Table 4.1.34. Interatomic distances in the coordination sphere of the MgO_5 polyhedra in **AEPF-9**.

Bond	Distance (Å)
Mg(1)-O(1) c	1.986(5)
Mg(1)-O(2)[1] c	2.018(4)
Mg(1)-O(3)[2] c	1.972(5)
Mg(1)-O(4)[3] c	2.027(4)
Mg(1)-O(5) d	1.969(5)

Symmetry transformations used to generate equivalent atoms:

[1] -x+3/2,y+1/2,-z+1/2 [3] -x+1,-y+2,-z

[2] x+1/2,-y+3/2,z+1/2

Oc: oxygen atom coming from a carboxylate group. Od: oxygen atom coming from a DEF carbonyl group.

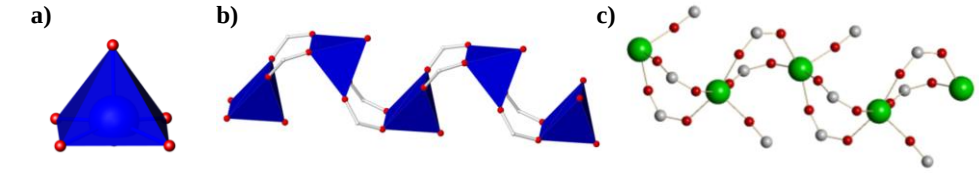

Figure 4.1.69. a) Inorganic PBUs in **AEPF-9**, **b)** detail of the MgO_5 chains that run along the *b* axis and **c)** coordination mode of $L_{(1)}^{-2}$ linker and DEF molecules.

In **Figure 4.1.70**, different polyhedral views along the crystallographic axes are depicted, evidencing the two-dimensional covalent framework determined in **AEPF-9.** As it is shown in **Figure 4.1.70a**, the presence of square shaped channels is also determined in this structure, giving rise to a free accessible space of 10.6% in its structure (calculated with PLATON,[5] SOLV mode).

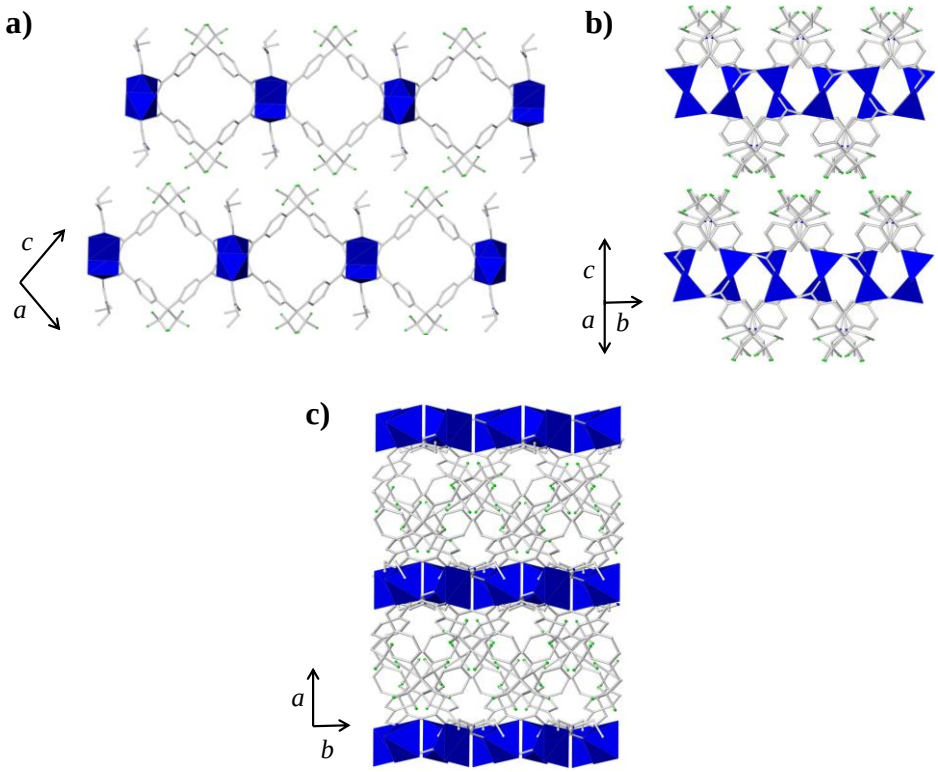

Figure 4.1.70. a) Depiction of **AEPF-9** square-shaped channels layers. **b)** Polyhedral representation along [1 1 1] direction and **c)** along the *c* axis.

In order to analyse the linker conformation in **AEPF-9**, the values for the three geometrical parameters **θ**, **ω** and **d** in this structure are listed in **Table 4.1.35**. In comparison with its counterpart **AEPF-8**, it was possible to conclude that the $L_{(1)}^{-2}$ linker in **AEPF-9** exhibits a similar conformation to that found for the $L_{(1)}^{-2}{}_{A}$ linker form determined in **AEPF-8** (**Table 4.1.32**).

Table 4.1.35. θ angle, **ω** dihedral angle **d** distance values in **AEPF-9** compound for the $L_{(1)}^{-2}$ linker.

θ (º)	ω (º)	d (Å)
110.83	72.29	9.566

In order to describe the topology of **AEPF-9** net using TOPOS,[4] the inorganic chains were simplified as rods, following the procedure proposed by Yaghi and O'Keeffe.[23] Thus, the MgO_5 chains formed *via* carboxylate groups were defined as infinite $(\text{-O-Mg-})_\infty$ rods. These rods, which are built with carboxylate oxygen atoms, can be assumed as the inorganic SBUs in **AEPF-9**. To clarify these topological features, in **Figure 4.1.71** the simplification performed in the MgO_5 chain to describe the inorganic SBU is shown.

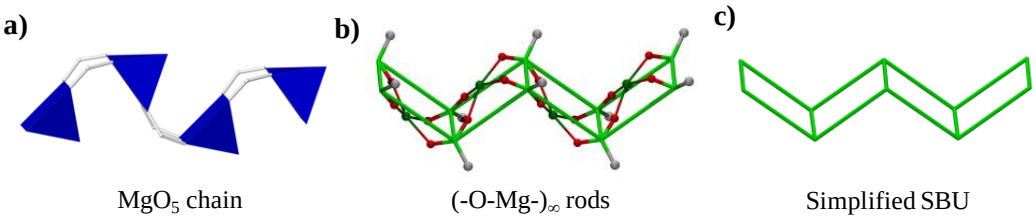

Figure 4.1.71. a) MgO_5 polyhedra chain. **b)** Topological simplifications performed to describe the $(\text{-O-Mg-})_\infty$ rods as the inorganic SBUs. **c)** Simplified inorganic SBU.

Considering the topological simplifications above mentioned, the **AEPF-9** net can be described as rods of quadrangles linked by sharing their opposite edges forming "ladders". These ladders are linked with the rungs parallel to form a **sql** uninodal 4-connected net, with Point Symbol $(4^4.6^2)$. The main simplification steps, as well as the decorated and final simplified nets for **AEPF-9**, are shown in **Figure 4.1.72.**

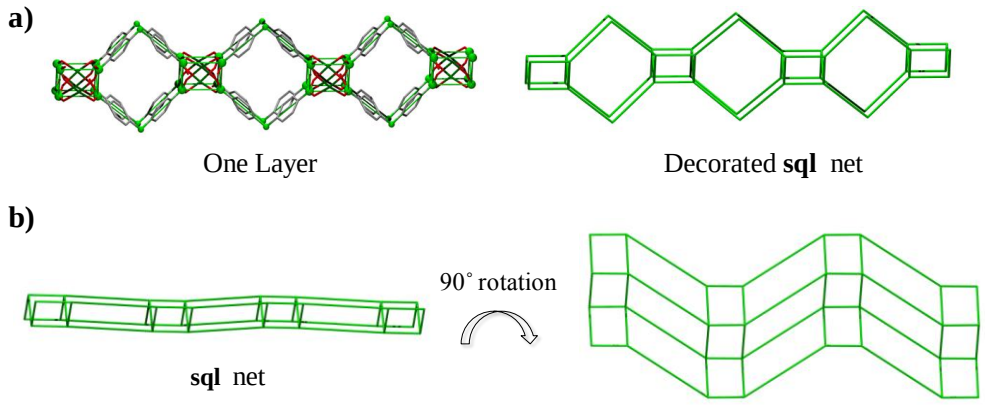

Figure 4.1.72. a) Depiction of a layer in the real net together with the decorated **sql** net, showing different orientations. Hydrogen atoms and $-CF_3$ groups were omitted for clarity. **b)** Representation of the simplified **sql** net in **AEPF-9**, showing different orientations.

As it was previously done for the other materials presented in this chapter, the square shaped channels were also analysed in detail (**Figure 4.1.73**). Thus, taking into account the topological simplifications performed in **AEPF-9** net, it was possible to describe the parallel way in which the linker generates the square shaped channels in this material, being thus of the **B**-type.[1]

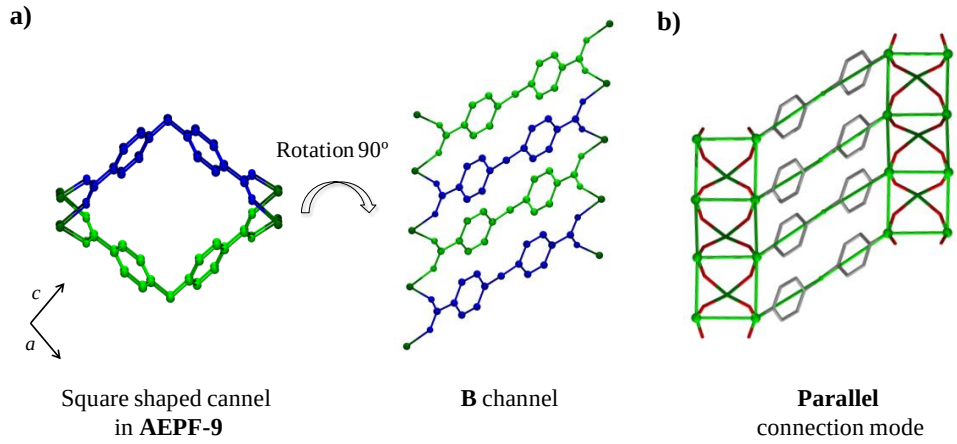

Figure 4.1.73. a) Different projections of the square shaped channels in **AEPF-9**. **b)** Detail of the real net together with the decorated **sql** net, showing the parallel connection mode of the linker. Hydrogen atoms and $-CF_3$ groups were omitted for clarity.

4.1.4.

Sr-AEPF-10

In this section, we present a novel strontium material based on $H_2L_{(1)}$ ligand named **AEPF-10**. Single crystals of this compound were obtained under solvothermal conditions using a mixture of water/n-hexane as solvent. In the following we present its structural and topological discussions.

The reaction between $H_2L_{(1)}$ and strontium acetate under the optimized solvothermal conditions, gives rise to the $[Sr_2(H_2L_{(1)})(HL_{(1)})_2(L_{(1)})]\cdot H_2O$ compound (**AEPF-10**) (*see* Chapter 2, *Synthesis procedures*). This compound crystallizes in the monoclinic crystal system (*C2* space group). The cell parameters determined for this structure are: a = 43.364(1) Å, b = 7.7459(2) Å, c = 20.3609(5) Å, β = 92.062(1)° and V = 6834.7(3) Å^3. The ORTEP representation of **AEPF-10** asymmetric unit is shown in **Figure 4.1.74** and the main crystallographic and refinement data for this compound are shown in **Table 4.1.36**.

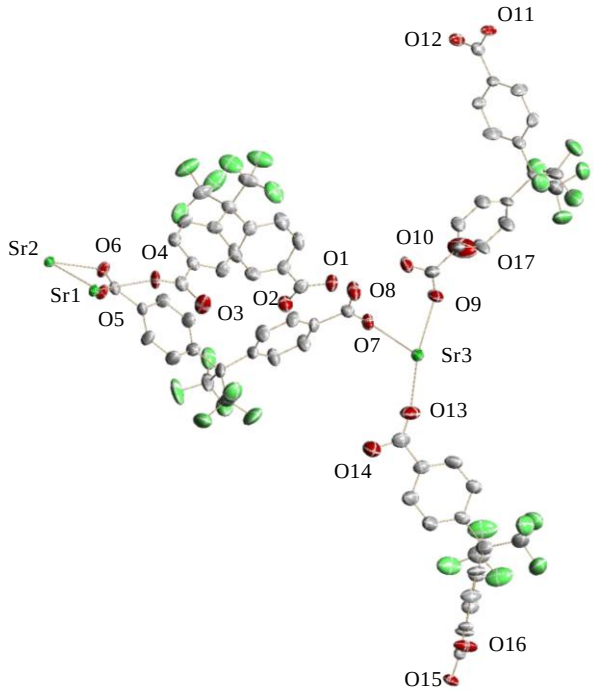

Figure 4.1.74. ORTEP representation of **AEPF-10** asymmetric unit. Ellipsoids are displayed at the 50% probability level. Hydrogen atoms were omitted for clarity.

Table 4.1.36. Crystallographic and refinement data for **AEPF-10**.

Identification code	AEPF-10
Empirical formula	$C_{68}\ H_{38}\ F_{24}\ O_{17}\ Sr_2$
Formula weight	1758.22
Temperature	296(2) K
Wavelength	1.54178 Å
Crystal system	Monoclinic
Space group	*C2*
Unit cell dimensions	a = 43.364(1) Å α = 90°
	b = 7.7459(2) Å β = 92.062(1)°
	c = 20.3609(5) Å γ = 90º
Volume	6834.7(3) $Å^3$
Z	4
Density (calculated)	1.709 Mg/m^3
Absorption coefficient	3.292 mm^{-1}
F(000)	3469
Crystal size	0.20 x 0.04 x 0.04 mm^3
Theta range for data collection	2.17 to 60.77º
Index ranges	-48<=h<=48, -5<=k<=8, -22<=l<=23
Reflections collected	23038
Independent reflections	8066 [R(int) = 0.0382]
Completeness to theta = 60.77°	98.1%
Absorption correction	Semi-empirical from equivalents
Max. and min. Transmission	0.8796 and 0.5589
Refinement method	Full-matrix least-squares on F^2
Data / restraints / parameters	8066 / 4 / 1006
Goodness-of-fit on F^2	1.089
Final R indices [I>2sigma(I)]	R_1 = 0.0524, wR_2 = 0.1338
R indices (all data)	R_1 = 0.0561, wR_2 = 0.1359
Absolute structure parameter	0.96(2)
Largest diff. peak and hole	2.279 and -0.450 e.$Å^{-3}$

In **AEPF-10**, there are three independent Sr^{+2} ions in the asymmetric unit (two of them with occupancy factor of 0.5), which show different coordination environments: hepta-coordinated and octa-coordinated (**Figure 4.1.75**). The hepta-coordinated Sr^{+2} ions are bonded to three oxygen atoms of one $HL_{(1)}^-$ carboxylate group in a chelate-bridge $\eta^2\mu_2$ mode, one oxygen atom of one $L_{(1)}^{-2}$ carboxylate group in a μ^2

mode, one oxygen atom of one $HL_{(1)}^-$ carbonyl group and one oxygen atom of one $H_2L_{(1)}$ carbonyl group, giving monocapped trigonal prisms (**Figure 1.59a**). Concerning the octa-coordinated centres, each Sr^{+2} ions is bonded to four oxygen atoms of two different $HL_{(1)}^-$ and $L_{(1)}^{-2}$ carboxylate groups in a chelate-bridge $\eta^2\mu_2$ mode and to two oxygen atoms of $H_2L_{(1)}$ carbonyl groups, giving two different types of SrO_8 bicapped trigonal prisms (**Figure 4.1.75a**).

The polyhedra determined in **AEPF-10**, which can be considered as the inorganic PBUs in the structure, are forming two different types of sharing-edges chains running along the *b* axis. The first type of chain is only built with Sr(1) hepta-coordinated polyhedra; however, the other type is formed by Sr(2) and Sr(3) octa-coordinated polyhedra in an alternated way (**Figure 4.1.75b**). Junction of these inorganic chains is made through the linker in two different ways: **i)** *via* $H_2L_{(1)}$ and $HL_{(1)}^-$ acting in a η^1-η^1 and η^1-$\eta^2\mu_2$ coordination modes, respectively; and **ii)** *via* $HL_{(1)}^-$ and $L_{(1)}^{-2}$ acting in a η^1-$\eta^2\mu_2$ and η^2-$\eta^2\mu_2$ coordination modes, respectively (**Figure 4.1.75c**).

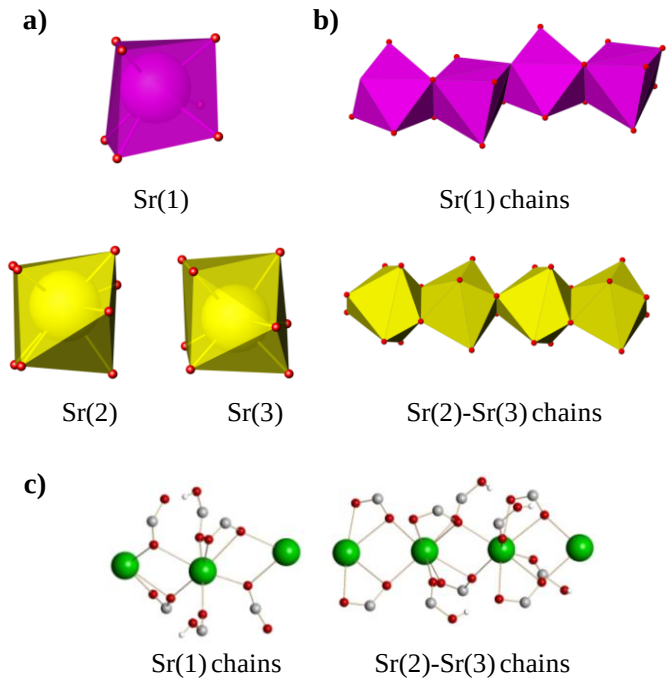

$H_2L_{(1)}$: η^1-η^1
$HL_{(1)}^-$: η^1-$\eta^2\mu_2$
$L_{(1)}^{-2}$: η^2-$\eta^2\mu_2$

Figure 4.1.75. a) Inorganic PBUs in **AEPF-10**, **b)** detail of the SrO_7 and SrO_8 chains that run along the *b* axis and **c)** coordination modes for the three different linker anions.

Analysing more profoundly the Sr-O bond for each kind of polyhedra, it is worth mentioning that different values for this distance are found for carboxylate groups depending on the coordination mode. Thus, in the case of carboxylate groups acting in a η^2 coordination mode, an average Sr-O distance of ~2.57 Å was determined. However, for those carboxylate groups that bond in a chelate-bridge $\eta^2\mu_2$ mode, two different kinds of Sr-O distances can be distinguished: a strong bond with an average Sr-O distance of ~2.47 Å and another weaker one (average Sr-O distance of ~2.62 Å). Moreover, in the case of carbonyl groups, which act in a η^1 coordination mode, an average Sr-O distance of ~2.58 Å was determined. These differences provoke a distortion in SrO_7 and SrO_8 polyhedra determined in **AEPF-10** (**Tables 4.1.37-4.1.38**).

Table 4.1.37. Interatomic distances in the coordination sphere of the SrO_7 polyhedra for Sr(1) in **AEPF-10**.

Bond	Distance (Å)
Sr(1)-O(1)[1] c	2.457(7)
Sr(1)-O(1)[2] c	2.652(7)
Sr(1)-O(2)[2]c	2.613(6)
Sr(1)-O(7) c	2.619(7)
Sr(1)-O(7)[1]c	2.523(7)
Sr(1)-O(9) co	2.589(6)
Sr(1)-O(13) co	2.522(6)

Symmetry transformations used to generate equivalent atoms:
[1] -x+1/2,y-1/2,-z+1
[2] x,y-1,z

Oc: oxygen atom coming from a carboxylate group. Oco: oxygen atom coming from a carbonyl group.

Table 4.1.38. Interatomic distances in the coordination sphere of the SrO_8 polyhedra for Sr(2) and Sr(3) in **AEPF-10**.

Sr(2)

Bond	Distance (Å)
Sr(2)-O(5) c	2.621(6)
Sr(2)-O(5)[1]c	2.621(6)
Sr(2)-O(6) c	2.589(5)
Sr(2)-O(6)[1]c	2.589(5)
Sr(2)-O(11)[2]c	2.456(6)
Sr(2)-O(11)[3]c	2.456(5)
Sr(2)-O(15)[4]co	2.591(6)
Sr(2)-O(15)[5]co	2.591(6)

Symmetry transformations used to generate equivalent atoms:

[1] -x+1,y,-z+2
[2] -x+1,y+1,-z+1
[3] x,y+1,z+1
[4] x+1/2,y+3/2,z
[5] -x+1/2,y+3/2,-z+2

Sr(3)

Bond	Distance (Å)
Sr(3)-O(4) c	2.598(6)
Sr(3)-O(4)[1]c	2.598(6)
Sr(3)-O(5)c	2.480(6)
Sr(3)-O(5)[1]c	2.480(6)
Sr(3)-O(11)[2]c	2.652(6)
Sr(3)-O(11)[3]c	2.652(6)
Sr(3)-O(12)[2]c	2.614(5)
Sr(3)-O(12)[3]c	2.614(5)

Symmetry transformations used to generate equivalent atoms:

[1] -x+1,y,-z+2
[2] -x+1,y,-z+1
[3] x,y,z+1

Oc: oxygen atom coming from a carboxylate group. Oco: oxygen atom coming from a carbonyl group.

In **Figure 4.1.76**, different polyhedral views of **AEPF-10** compound are depicted, showing the three-dimensional net determined for this compound.

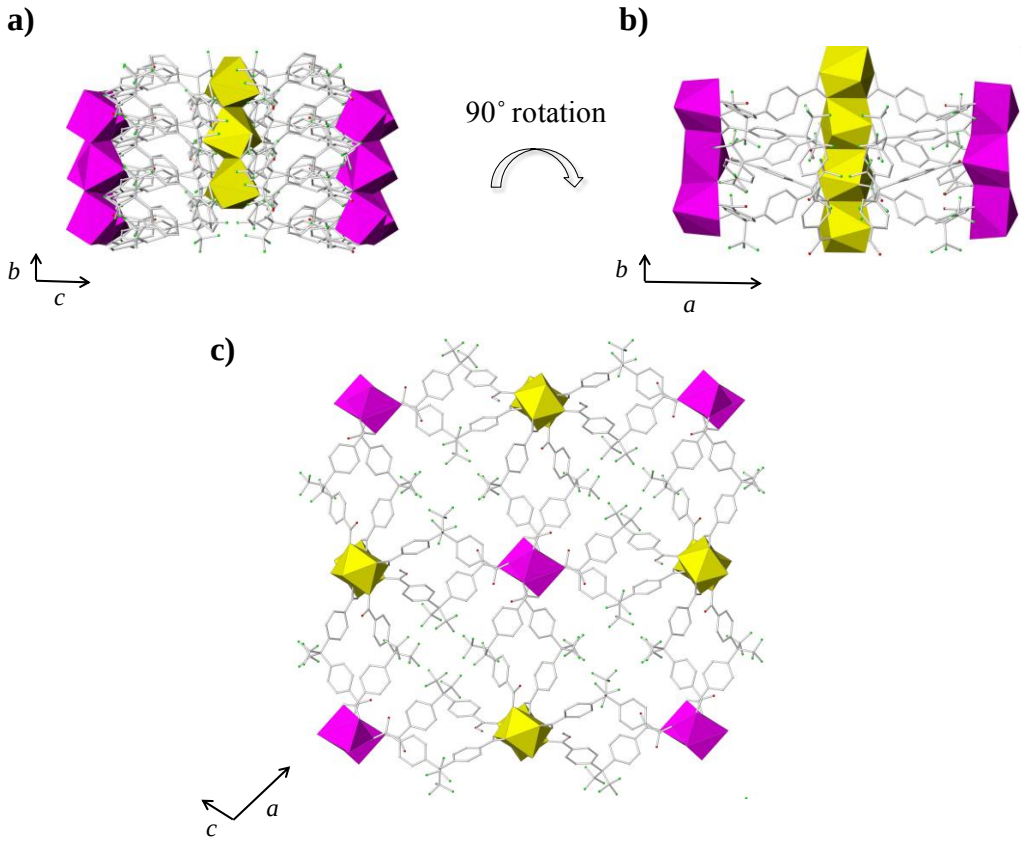

Figure 4.1.76. Polyhedral representation of **AEPF-10** along: **a)** the *a* axis projection, **b)** the *c* axis projection and **c)** the *b* axis projection.

As it was previously mentioned, the organic linker in **AEPF-10** exhibits different degrees of protonation ($H_2L_{(1)}$ and $HL_{(1)}^-$), giving rise to four different types of hydrogen bonds (**Table 4.1.39**). Thus, for those hydrogen bonds in which oxygen atoms of carboxylate groups are acceptors, the interactions are strong. In addition, a very weak interaction is present between one carboxylic group from the protonated ligand and one fluor atom from a $HL_{(1)}^-$ ligand. Finally, as it is shown in **Table 4.1.39**, hydration water molecules found in this structure establish one type of hydrogen bond in which oxygen atoms of $H_2L_{(1)}$ carboxylic groups act as acceptors.

Table 4.1.39. Distances and angles of hydrogen bonds found in **AEPF-10** compound.

D-H···A[1]	D-H[2]	H···A[3]	D···A[4]	<D-H···A[5]
O(3)c-H(3A)c ··· O(6)c[1]	0.82	1.88	2.59(1)	145.1
O(10)c-H(10A)c ··· O(8)c	1.01(2)	1.49(3)	2.494(8)	171(1)
O(14)c-H(14A)c ··· F(17)[2]	0.82	2.58	3.08(1)	116.8
O(16)c-H(16A)c ··· O(12)c[3]	0.82	1.74	2.559(9)	173.1
O(17)w-H(17B)w ··· O(14)c[2]	1.00	2.03	2.62(1)	115.7

Symmetry operators codes

[1] x, y-1, z

[2] -x+1/2, y+1/2, -z+1

[3] -x+1/2, y-3/2, -z+1

D: donor atom, A: acceptor atom. [1]Names of donor, hydrogen and acceptor atoms involved in the hydrogen bond. [2] Distance D – A. [3]Distances H – A. [4]Distance D – A. [5] Angle D – H – A.

In **AEPF-10**, the conformation of the linker was also analysed in detail (**Table 4.1.40**). In order to perform this kind of comparative studies, the two $HL_{(1)}^-$ linker forms are named as: $HL_{(1)}^-$**A** (a linker whose carbon atoms are labelled from C(1) to C(17)) and $HL_{(1)}^-$**B** (a linker whose carbon atoms are labelled from C(35) to C(51)). Thus, as it is shown in **Table 4.1.40**, both $H_2L_{(1)}$ and $HL_{(1)}^-$**B** exhibit similar conformations, with average values of: **θ**= 111.21º, **ω**= 73.8º and **d**= 9.556 Å. In the case of the $HL_{(1)}^-$**A** linker, the values for the three geometrical parameters are slightly higher (**θ**= 113.66º, **ω**= 75.45º and **d**= 9.626 Å. Finally, the conformation of the deprotonated linker is markedly different, for which the **ω** and **d** values are the highest (81.15º and 9.815 Å, respectively).

Table 4.1.40. θ angle, **ω** dihedral angle **d** distance values in **AEPF-10** for the four independent ligand anions.

Linker	θ (º)	ω (º)	d (Å)
$\mathbf{H_2L_{(1)}}$	111.42	74.21	9.527
$\mathbf{HL_{(1)}^-}$**A**	113.66	75.45	9.626
$\mathbf{HL_{(1)}^-}$**B**	110.99	73.39	9.585
$\mathbf{L_{(1)}^{-2}}$	112.62	81.15	9.857

To consider topological features, by simplification of the three-dimensional framework present in **AEPF-10** using TOPOS,[4] two types of six-connected nodes were found. One type of six-connected nodes corresponds to Sr(1) centres; in the case of Sr(2) and Sr(3), a unique six-connected node is defined for both metals. The found

three-dimensional binodal net has a point symbol $(4^6.6^7.8^2)(4^6.6^9)$ (**Figure 4.1.77**). This topological type does not appear in TOPOS or in the RCSR databases.

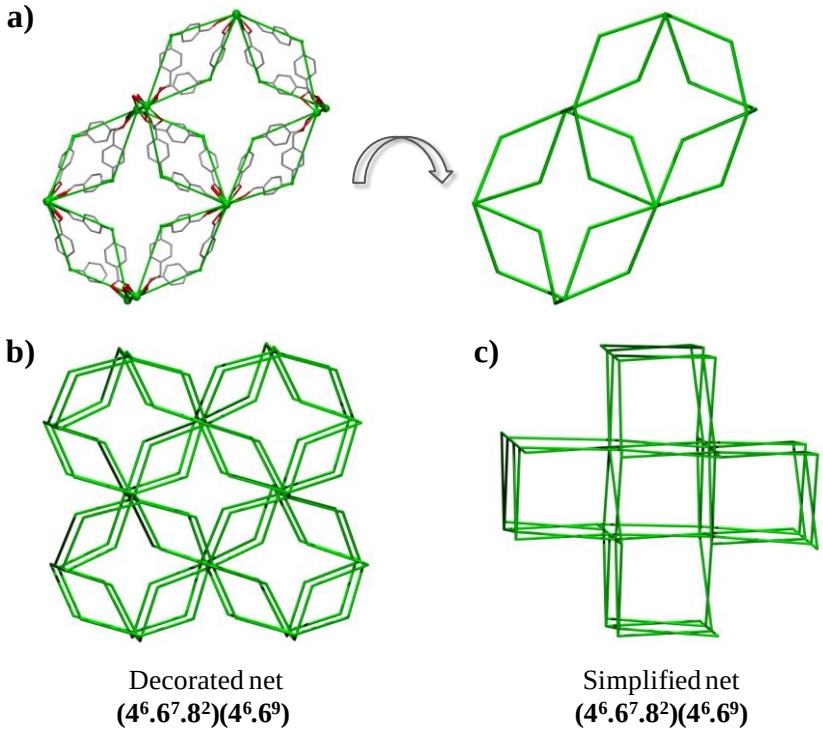

Figure 4.1.77. a) Depiction of one layer in the real net together with the decorated net in **AEPF-10**. Hydrogen atoms and $-CF_3$ groups were omitted for clarity. **b)** Representation of the decorated and simplified net described for **AEPF-10**.

Two kinds of square shaped channels are found in **AEPF-10** (named **A-** and **A'-**type channels).[1] On one hand, the **A** type channels are formed by $L_{(1)}^{-2}$ and $HL_{(1)}^{-}$**A** linkers, which are the linker anionic forms that exhibit the highest values of **d** (**Table 4.1.40**). On the other hand, the **A'** type channels are formed by $H_2L_{(1)}$ and $HL_{(1)}^{-}$**B**, showing both forms quite similar conformations (**Table 4.1.40**). Thus, the three-dimensional framework described in **AEPF-10** can be also described as two types of square shaped channel layers (**A** and **A'**), which are crossed among them with an angle of ~90º (**Figure 4.1.78**). Additionally, the crossing of these square shaped channels layers leads to the formation of a new star shaped type of channel (named **D**) (**Figure 4.1.78**).

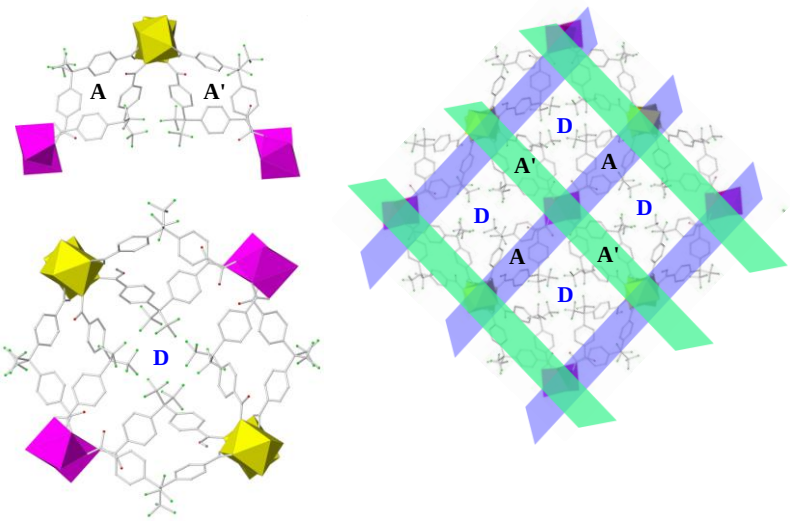

Figure 4.1.78. Depiction of the three types of square shape channels (**A** and **A'**) as well as the star shaped ones (**D**) described in **AEPF-10** material.

Additional topological study was performed in order to analyse the way in which the linker generates the square shaped channels in this structure. Thus, as it is shown in **Figure 4.1.79**, in **AEPF-10** this connection among the inorganic chains *via* the organic linker is made in a crossing way for both **A** and **A'** channels.

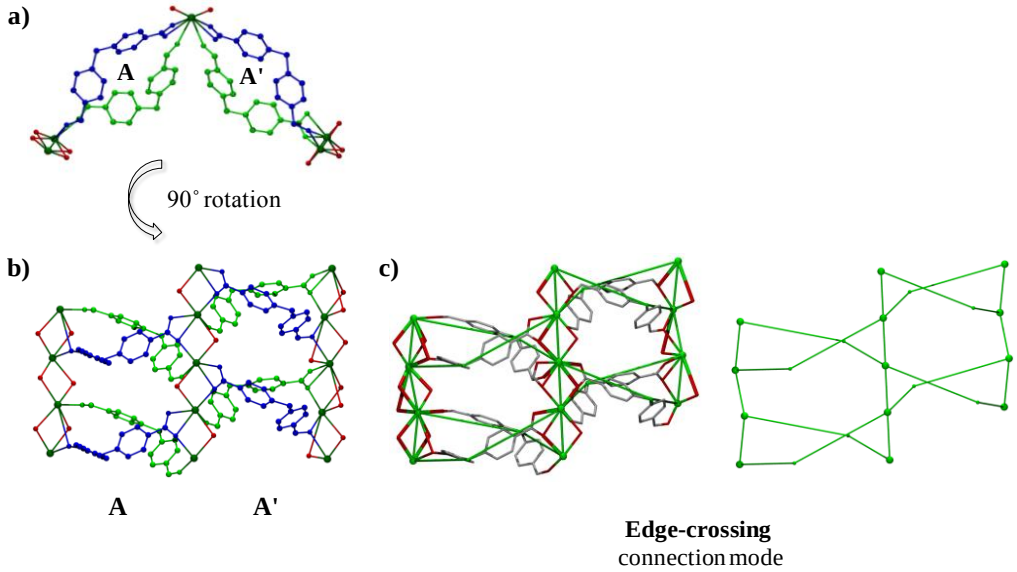

Figure 4.1.79. a) and **b) A** and **A'** square shaped channels described in **AEPF-10**, showing different projections. **c)** Detail of the real net together with the decorated net and **d)** decorated net, evidencing the edge crossing connection mode of the linker in both types of channels. Hydrogen atoms and $-CF_3$ groups were omitted for clarity.

Chapter 4.2

Diphenylmethane-4,4'-dicarboxylic acid ($H_2L_{(2)}$)

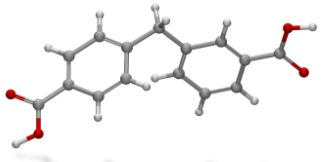

$H_2L_{(2)}$

Mg **Ca, Sr**

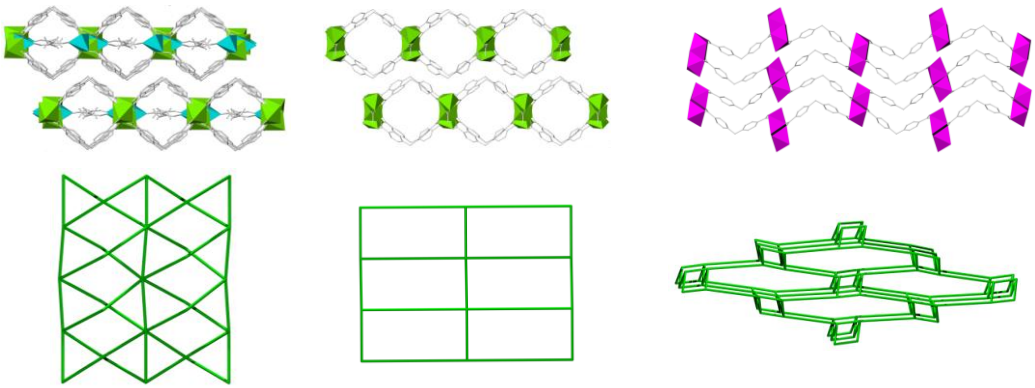

AEPF-11 **AEPF-12** **AEPF-13**

Abstract

Four new compounds based on alkaline-earth elements ions and diphenylmethane-4,4'-dicarboxylate ligand ($H_2L_{(2)}$) were obtained and characterized. These novel materials belong to three different structural types: **AEPF-11** (Mg), **AEPF-12** (Mg) and **AEPF-13** (Ca- and Sr-). While for the two magnesium containing compounds two-dimensional nets have been obtained, in the case of Ca^{+2} and Sr^{+2} a three-dimensional framework with a **sra** topology has been synthesised. The catalytic behaviour of these alkaline-earth materials in hydrogenation of alkenes under mild conditions has been investigated.

4.2.1.

Crystal structure description and topological analyses

Four new alkaline-earth materials based on the $H_2L_{(2)}$ ligand, which belong to three structural types, have been successfully synthesized and named **Mg-AEPF-11**, **Mg-AEPF-12** and **(Ca, Sr)-AEPF-13**. The aim of this section is to present a detailed structural description and the topological analyses performed to describe these materials

4.2.1.1.

Mg-AEPF-11

The solvothermal reaction between $H_2L_{(2)}$ and magnesium acetate tetrahydrate, using propan-1-amine as base (*n-prop*, from now on) and DEF as solvent, gives rise to the **[Mg($L_{(2)}$)$(DEF)_{0.5}$]** compound (**AEPF-11**) (*see* Chapter 2, *Synthesis procedures*).

During the structure determination of this compound, some problems related to the presence of DEF molecules coordinated to magnesium centres were found. Firstly, it is worth mentioning that the structure solution of **AEPF-11** using the software package SXELXTL 6.10,[24] leads to an orthorhombic crystal system (chiral space group $P2_12_12$). Even though that in this space group the refinement parameters values were quite satisfactory, when the structure model was carefully analysed, some problems concerning DEF molecule were found. As it is shown in **Figure 4.2.1a**, the presence of a 2-fold axis running along the Mg-O bond corresponding to a coordinated DEF molecule, gives rise to an incorrect geometry for this molecule. Therefore, the presence of this coordinated DEF molecule breaks the two-fold axis symmetry, leading to a pseudo-orthorhombic symmetry. For that reason, the structure solution process was repeated, but now forcing the solution in a monoclinic crystal system, which must be included in the $P2_12_12$ space group. The structure solution and refinement in $P2_1$ space group, lead to a right geometry for this DEF molecule, as well as reasonable refinement parameters (**Figure 4.2.1b**). To summarize, **AEPF-11** presents an orthorhombic pseudo-symmetry which is partially broken due to the presence of a DEF molecule (isotropically refined) bonded to a Mg^{+2} centre and giving rise to a monoclinic symmetry.

a)

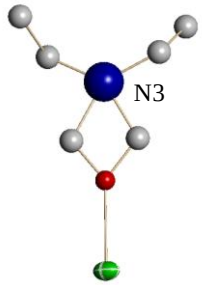

Orthorombic $P2_12_12$	
Goodness-of-fit on F^2	1.003
Final R indices [I>2sigma(I)]	$R_1 = 0.0800$, $wR_2 = 0.1844$
R indices (all data)	$R_1 = 0.1365$, $wR_2 = 0.2133$

b)

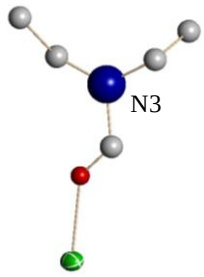

Monoclinic $P2_1$	
Goodness-of-fit on F^2	0.982
Final R indices [I>2sigma(I)]	$R_1 = 0.0784$, $wR_2 = 0.1707$
R indices (all data)	$R_1 = 0.1390$, $wR_2 = 0.2004$

Figure 4.2.1. Detail of **AEPF-11** structural model showing the studied DEF molecule in: **a)** $P2_1P2_12$ space group and **b)** $P2_1$ space group. The main refinement parameters are also shown for both space groups.

Taking into account these structural considerations, the **AEPF-11** compound crystallizes in the monoclinic crystal system ($P2_1$ space group). The cell parameters determined for this structure are: a = 11.049(3) Å, b = 20.781(7) Å, c = 20.875(7) Å, β = 90.239(5)°, V = 4793(3) Å^3. The **AEPF-11** asymmetric unit comprises six independent magnesium ions, six ligand anions ($L_{(2)}^{-2}$) and three DEF molecules. The ORTEP representation of **AEPF-11** asymmetric unit is depicted in **Figure 4.2.2** and the main crystallographic and refinement data for this compound are shown in **Table 4.2.1.**

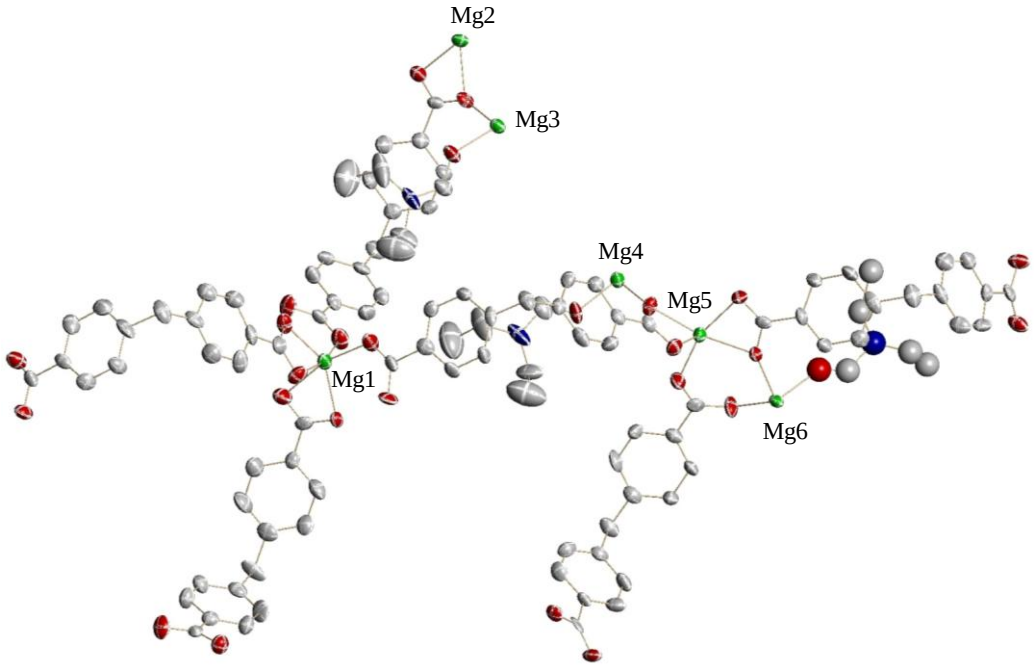

Figure 4.2.2. ORTEP representation of **AEPF-11** asymmetric unit. Ellipsoids are displayed at the 50% probability level.

As it was before mentioned, in the asymmetric unit of **AEPF-11** there are six independent Mg^{+2} ions, which show two different coordination environments: penta-coordinated and hexa-coordinated (**Figure 4.2.3a)**. The presence of these different Mg^{+2} centres gives rise to two kind of polyhedra, some of them distorted, which can be considered as the inorganic primary building units (PBUs) in the structure.

Table 4.2.1. Crystallographic and refinement data for **AEPF-11**.

Identification code	AEPF-11
Empirical formula	$C_{105}\ H_{93}\ Mg_6\ N_3\ O_{27}$
Formula weight	1974.68
Temperature	296(2) K
Wavelength	0.71073 Å
Crystal system	Monoclinic
Space group	$P2_1$
Unit cell dimensions	a = 11.049(3) Å α = 90°
	b = 20.781(7) Å β = 90.239(5)°
	c = 20.875(7) Å γ = 90º
Volume	4793(3) $Å^3$
Z	2
Density (calculated)	1.368 Mg/m^3
Absorption coefficient	0.133 mm^{-1}
F(000)	2064
Crystal size	0.15 x 0.10 x 0.05 mm^3
Theta range for data collection	1.95 to 25.05°
Index ranges	-13<=h<=13, -24<=k<=24, -24<=l<=24
Reflections collected	28626
Independent reflections	15003 [R(int) = 0.0709]
Completeness to theta = 25.05°	96.50%
Absorption correction	Semi-empirical from equivalents
Max. and min. Transmission	0.9934 and 0.9803
Refinement method	Full-matrix least-squares on F^2
Data / restraints / parameters	15003 / 1 / 1242
Goodness-of-fit on F^2	0.982
Final R indices [I>2sigma(I)]	R_1 = 0.0784, wR_2 = 0.1707
R indices (all data)	R_1 = 0.1390, wR_2 = 0.2004
Absolute structure parameter	0.1(3)
Largest diff. peak and hole	0.764 and -0.488 e.$Å^{-3}$

These MgO_5 and MgO_6 polyhedra form sharing vertex chains along the *b* axis (**Figure 4.2.3b**). Junction of these inorganic chains is made *via* the $L_{(2)}^{-2}$ linker, which acts in a $\eta^2\mu_2$-$\eta^2\mu_2$ coordination mode (**Figure 4.2.3c**), giving rise to layers perpendicular to the *c* axis and generating square shaped channels.

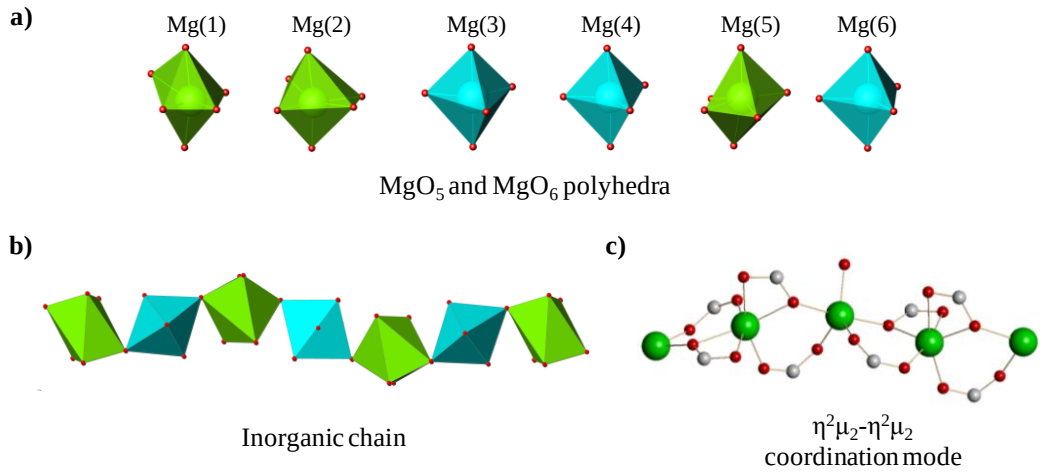

Figure 4.2.3. a) Inorganic PBUs in **AEPF-11**, **b)** detail of the MgO_5-MgO_6 chains that run along the *b* axis and **c)** coordination mode of $L_{(2)}^{-2}$ linker.

The penta-coordinated Mg^{+2} ions (Mg(3), Mg(4) and Mg(6)), are bonded to four oxygen atoms coming from $L_{(2)}^{-2}$ bridge carboxylate groups of two different ligands and one oxygen atom from a DEF carbonyl group, giving regular MgO_5 trigonal bipyramides (**Figure 4.2.3a**). It is worth mentioning that all penta-coordinated centres have one DEF molecule which is directly bonded. Thus, due to the steric impediment caused by the DEF molecules, the penta-coordinated environment is favoured instead of the octahedral one. The average Mg-O distance in these polyhedra is of ~2.01 Å (**Table 4.2.2**).

Concerning the hexa-coordinated centres (Mg(1), Mg(2) and Mg(5)), each Mg^{+2} ion is bonded to two oxygen atoms of two different $L_{(2)}^{-2}$ carboxylate groups in a bridge mode and four oxygen atoms of two different $L_{(2)}^{-2}$carboxylate groups in a chelate-bridge mode, forming the MgO_6 octahedra (**Figure 4.2.3a**). It is worth mentioning that these two kinds of oxygen atoms exhibit different average Mg-O distances: ~2.01 Å for bridge mode and ~2.17 Å for chelate-bridge mode. These differences provoke a marked distortion in the MgO_6 octahedra found in **AEPF-11** (**Table 4.2.3**).

Table 4.2.2. Interatomic distances in the coordination sphere of the MgO_5 polyhedra for Mg(3), Mg(4) and Mg(6) centres.

Mg(3)

Bond	Distance (Å)
Mg(3)-O(2)[1]c	1.959(5)
Mg(3)-O(3)[2]c	2.102(5)
Mg(3)-O(9)[2]c	1.950(6)
Mg(3)-O(12)c	2.047(5)
Mg(3)-O(13)d	1.994(5)

Symmetry transformations used to generate equivalent atoms:
[1] x-2,y,z
[2] x-1,y,z

Mg(4)

Bond	Distance (Å)
Mg(4)-O(6)[1]c	2.080(5)
Mg(4)-O(7)[2]c	1.972(5)
Mg(4)-O(15)[1]c	1.953(5)
Mg(4)-O(16)c	2.067(5)
Mg(4)-O(18)d	1.986(5)

Symmetry transformations used to generate equivalent atoms:
[1] x-1,y,z
[2] x-2,y,z

Mg(6)

Bond	Distance (Å)
Mg(6)-O(20)c	1.956(5)
Mg(6)-O(21)[1]c	2.070(6)
Mg(6)-O(23)d	1.992(6)
Mg(6)-O(24)c	2.069(5)
Mg(6)-O(26)[2]c	1.939(6)

Symmetry transformations used to generate equivalent atoms:
[1] x-1,y,z
[2] x+1,y,z

Od: oxygen atom coming from a DEF molecule. Oc: oxygen atom coming from a carboxylate group.

Table 4.2.3. Interatomic distances in the coordination sphere of the MgO_6 polyhedra for Mg(1), Mg(2) and Mg(5) centres.

Mg(1)

Bond	Distance (Å)
Mg(1)-O(3)c	2.137(6)
Mg(1)-O(4)c	2.210(5)
Mg(1)-O(5)c	2.199(5)
Mg(1)-O(6)c	2.164(5)
Mg(1)-O(10)c	2.021(6)
Mg(1)-O(14)c	2.006(5)

Mg(2)

Bond	Distance (Å)
Mg(2)-O(1)[1]c	1.989(6)
Mg(2)-O(11)c	2.172(5)
Mg(2)-O(12)c	2.131(5)
Mg(2)-O(21)[2]c	2.142(5)
Mg(2)-O(22)c	2.186(5)
Mg(2)-O(27)[3]c	2.015(6)

Symmetry transformations used to generate equivalent atoms:
[1] x-2,y,z
[2] x-1,y+1,z
[3] x+1,y+1,z

Mg(5)

Bond	Distance (Å)
Mg(5)-O(8)[1]c	2.001(6)
Mg(5)-O(16)c	2.131(5)
Mg(5)-O(17)c	2.181(5)
Mg(5)-O(19)c	2.026(5)
Mg(5)-O(24)c	2.153(5)
Mg(5)-O(25)c	2.168(5)

Symmetry transformations used to generate equivalent atoms:
[1] x-2,y,z

Oc: oxygen atom coming from a carboxylate group.

In **Figure 4.2.4**, different polyhedral views along the crystallographic axes are depicted, evidencing the two-dimensional covalent framework determined in **AEPF-11**. The potential accessible voids present in the crystal structure of **AEPF-11** were calculated using PLATON[5] software (SOLV mode). Due to the presence of DEF

coordinated molecules, which block the square shaped channels along the *a* direction (**Figure 4.2.4a**), this material does not possess any solvent accessible voids.

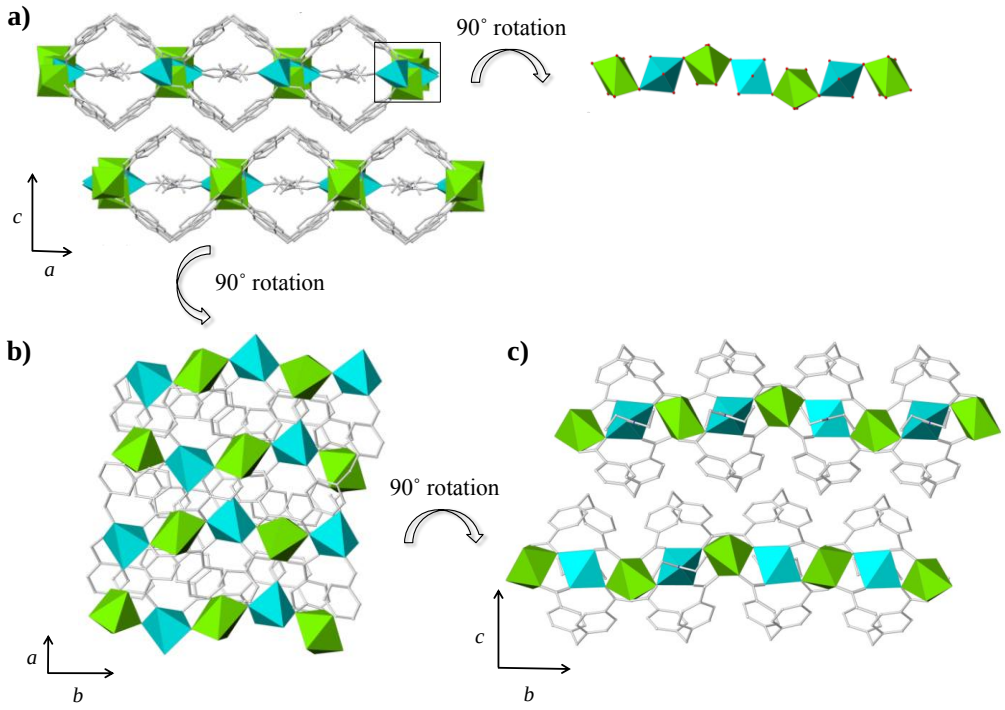

Figure 4.2.4. a) Depiction of **AEPF-11** layers perpendicular to *b* axis. **b)** Polyhedral representation along *c* axis and **c)** along *a* axis.

Taking into account the flexibility of the used organic linker, its conformation was analysed by describing some geometrical parameters (**θ** angle, **ω** dihedral angle and **d** distance) (**Figure 4.2.5**). Firstly, note that in order to perform this kind of comparative studies, the six $L_{(2)}^{-2}$ linker forms are named as: L_A (linker whose carbon atoms are labelled from C(1) to C(15)), L_B (linker whose carbon atoms are labelled from C(16) to C(30)), L_C (linker whose carbon atoms are labelled from C(31) to C(50)), L_D (linker whose carbon atoms are labelled from C(51) to C(70)), L_E (linker whose carbon atoms are labelled from C(71) to C(90)) and L_F (linker whose carbon atoms are labelled from C(91) to C(110)).

As it is shown in **Table 4.2.4**, three kinds of conformations can be defined for the linker forms present in **AEPF-11**. Thus, L_A and L_B linkers represent the first conformation type, for which the **ω** values are the highest (~78.08º) and the **d** values

the lowest (~9.037 Å). Contrary, L_E and L_F linkers represent the second conformation type, for which the **ω** values are the lowest (~76.18º) and the **d** values the highest (~9.205 Å). Finally, L_C and L_D containing linkers represent the third conformation type, with **ω** and **d** intermediate values (~72.67º and ~9.391 Å, respectively). It is worth mentioning that all these **d** distances are directly related with the distance that separates the inorganic chains in **AEPF-11** compound (**Figure 4.2.4a**).

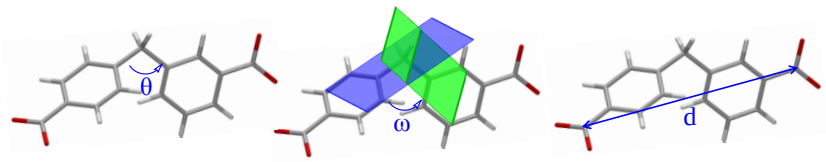

Figure 4.2.5. Definition of **θ** angle, **ω** dihedral angle and **d** distance to describe the linker conformation.

Table 4.2.4. θ angle, **ω** dihedral angle **d** distance values in the six independent $L_{(2)}^{-2}$ ligands for **AEPF-11** compound.

Linker	θ (º)	ω (º)	d (Å)
$\mathbf{L_A}$	110.66	78.04	9.043
$\mathbf{L_B}$	109.38	78.12	9.030
$\mathbf{L_C}$	111.21	72.56	9.384
$\mathbf{L_D}$	111.85	72.78	9.398
$\mathbf{L_E}$	110.77	76.00	9.198
$\mathbf{L_F}$	111.24	76.35	9.212

From the topological point of view, by simplification of the layers determined in **AEPF-11** compound using TOPOS,[4] one type of six-connected nodes were found, which correspond to those magnesium atoms with octahedral geometry. This two-periodic uninodal net exhibits a **SP 2-periodic net (4,4)IIb** topology (point symbol $(4^{13}.6^2)$). The main simplifications points, as well as the decorated and final simplified nets for **AEPF-11**, are shown in **Figure 4.2.6**.

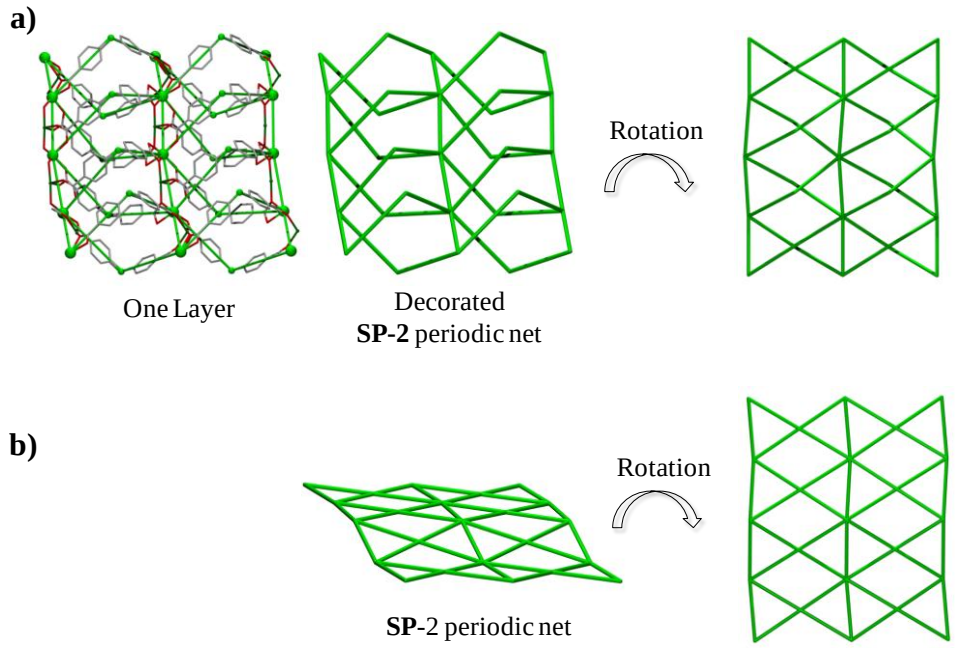

Figure 4.2.6. a) Depiction of the layer real net together with the decorated **SP**-2 periodic net, showing different orientations. Hydrogen atoms were omitted for clarity. **b)** Representation of the simplified **SP**-2 net in **AEPF-11**, showing different orientations.

Additionally, a more profound topological study was performed in order to analyse the way in which the linker generates the square shaped channels in this structure. As it is shown in **Figure 4.2.7**, in **AEPF-11** the connection among the inorganic chains *via* the $L_{(2)}^{-2}$ linker is made in a crossing way, being thus of the **A**-type.[1]

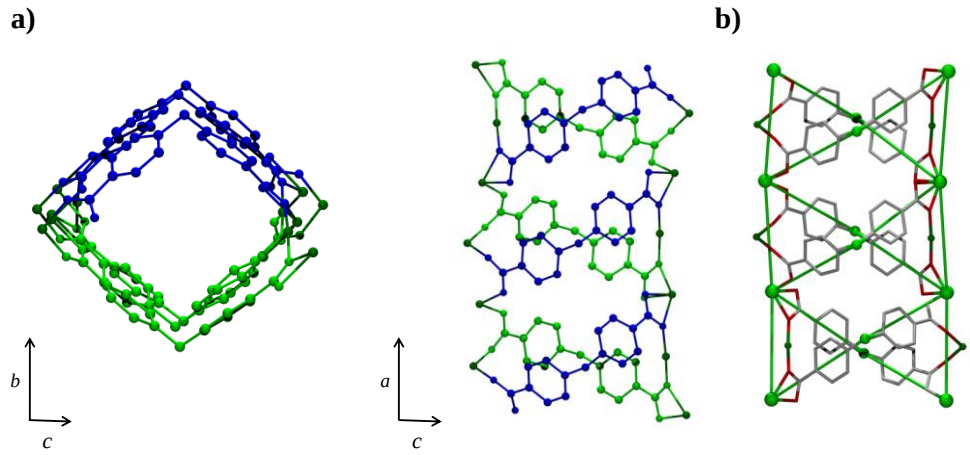

Figure 4.2.7. a) Different projections of the square shaped channels in **AEPF-11**. **b)** Detail of the real net together with the decorated **SP**-2 net, evidencing the **A**-type edge crossing mode for $L_{(2)}^{-2}$ ligand. Hydrogen atoms were omitted for clarity.

4.2.1.2.

Mg-AEPF-12

As it was before explained, in the structural discussion of **AEPF-11** structural type, the DEF molecules covalently bonded to Mg^{+2} ions block the pores present in the crystal structure of this material. Taking into account this fact, the synthesis conditions were optimized in order to obtain a porous material. Thus, when the reaction between $H_2L_{(2)}$ and magnesium acetate hydrate was performed using *n-prop* as base and dimethylformamide (DMF, from now on) as solvent, the **[$Mg_2(L_{(2)})(HL_{(2)})(CH_3CO_2)$]** compound was obtained (**AEPF-12**) (*see* Chapter 2, *Synthesis procedures*). This compound crystallizes in the orthorhombic crystal system (*Pna2₁* space group). The cell parameters determined for this structure are: a = 12.3582(7) Å, b = 22.940(1) Å, c = 12.8109(7) Å, V = 3631.9(3) $Å^3$). In **AEPF-12**, the asymmetric unit comprises two Mg^{+2} ions, one totally deprotonated ligand ($L_{(2)}^{-2}$), one partially deprotonaded ligand ($HL_{(2)}^{-}$) and one acetate group. Thus, the coordination sphere of Mg^{+2} centres is completed by one additional acetate group coming from magnesium salt, which forces

the presence of different degrees of protonation for the organic ligand. Besides, the DMF molecules do not coordinate to Mg^{+2} ions. The main crystallographic and refinement data for this compound are shown in **Table 4.2.5** and the ORTEP representation of **AEPF-12** asymmetric unit is shown in **Figure 4.2.8**.

Table 4.2.5. Crystallographic and refinement data for **AEPF-12**.

Identification code	AEPF-12
Empirical formula	$C_{32}\ H_{24}\ Mg_2\ O_{10}$
Formula weight	617.13
Temperature	296(2) K
Wavelength	0.71073 Å
Crystal system	Orthorhombic
Space group	*Pna2 1*
Unit cell dimensions	*a* = 12.3582(7) Å α = 90°
	b = 22.940(1) Å β = 90°
	c = 12.8109(7) Å γ = 90º
Volume	3631.9(3) $Å^3$
Z	4
Density (calculated)	1.129 Mg/m^3
Absorption coefficient	0.114 mm^{-1}
F(000)	1280
Crystal size	0.15 x 0.10 x 0.10 mm^3
Theta range for data collection	2.42 to 25.03°
Index ranges	-14<=h<=14, -27<=k<=26, -14<=l<=15
Reflections collected	23079
Independent reflections	6255 [R(int) = 0.0477]
Completeness to theta = 25.03°	99.30%
Absorption correction	Semi-empirical from equivalents
Max. and min. Transmission	0.9887 and 0.9831
Refinement method	Full-matrix least-squares on F^2
Data / restraints / parameters	6255 / 2 / 398
Goodness-of-fit on F^2	1.001
Final R indices [I>2sigma(I)]	R_1 = 0.0528, wR_2 = 0.1287
R indices (all data)	R_1 = 0.0690, wR_2 = 0.1359
Absolute structure parameter	0.6(3)
Largest diff. peak and hole	0.242 and -0.240 $e.Å^{-3}$

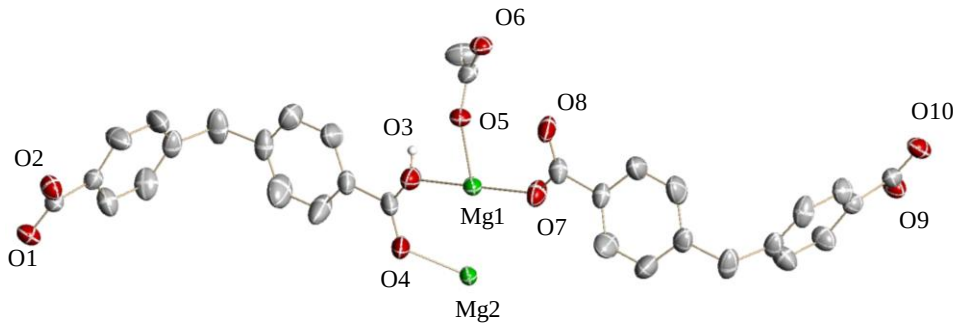

Figure 4.2.8. ORTEP representation of **AEPF-12** asymmetric unit. Ellipsoids are displayed at the 50% probability level. Hydrogen atoms were omitted for clarity.

In **AEPF-12**, Mg^{+2} ions are hexa-coordinated to two oxygen atoms coming from a $HL_{(2)}^{-}$ ligand, two oxygen atoms of $L_{(2)}^{-2}$ ligand and two oxygen atoms from the acetate group, giving MgO_6 octahedra (**Figure 4.2.9a**). These polyhedra, which can be considered as the inorganic PBUs in this structure, have an average Mg-O distance of ~2.08 Å in the case of Mg(1) and ~2.09 Å for Mg(2). It is worth mentioning that in the case of Mg(2) centres, the Mg-O distances corresponding to oxygen atoms from acetate groups are larger than those corresponding to carboxylate groups. These differences provoke a marked distortion in Mg(2) octahedra determined in **AEPF-12** (**Table 4.2.6**).

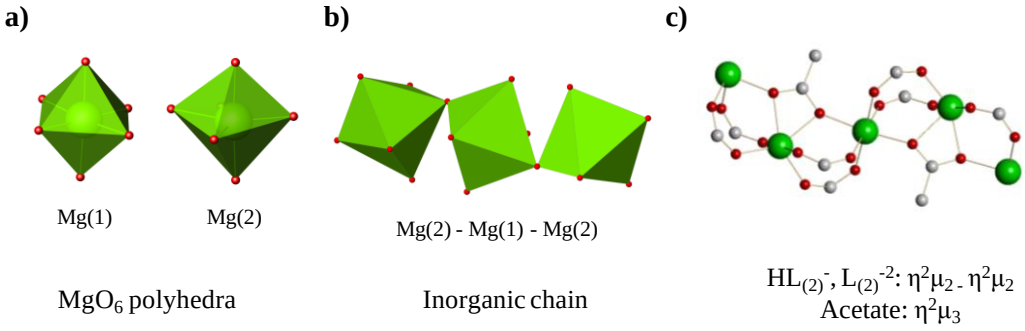

Figure 4.2.9. a) Inorganic PBUs in **AEPF-12**, **b)** detail of the MgO_6 chains that run along the *a* axis and **c)** coordination mode of $HL_{(2)}^{-}$, $L_{(2)}^{-2}$ linkers and acetate group.

As it is depicted in **Figure 4.2.9b**, the two types of MgO_6 octahedra determined in **AEPF-12** form sharing vertex chains that run along the *a* axis. Junction of these inorganic chains is made *via* both the $L_{(2)}^{-2}$ and $HL_{(2)}^{-}$ linkers, which act in a $\eta^2\mu_2$-$\eta^2\mu_2$ coordination mode (**Figure 4.2.9c**), giving rise to layers perpendicular to the *b* direction. Moreover, acetate groups, that coordinate to Mg^{+2} ions in a $\eta^2\mu_3$ coordination

mode (**Figure 4.2.9c**), are located parallel to *b* axis, not being involved in the layer formation.

Table 4.2.6. Interatomic distances in the coordination sphere of the MgO_6 octahedra for Mg(1) and Mg(2).

Mg(1)

Bond	Distance (Å)
Mg(1)-O(2)[1]c	2.068(3)
Mg(1)-O(3)c	2.076(3)
Mg(1)-O(5)a	2.073(2)
Mg(1)-O(6)[2]a	2.083(2)
Mg(1)-O(7)c	2.116(3)
Mg(1)-O(9)[3]c	2.056(3)

Symmetry transformations used to generate equivalent atoms:
[1] x,y,z+1
[2] x-1/2,-y+1/2,z
[3] x,y,z-1

Mg(2)

Bond	Distance (Å)
Mg(2)-O(1)[1]c	2.023(2)
Mg(2)-O(4)c	2.041(3)
Mg(2)-O(5)[2]a	2.230(2)
Mg(2)-O(6)[2]a	2.173(2)
Mg(2)-O(8)[2]c	2.053(3)
Mg(2)-O(10)[3]c	2.015(2)

Symmetry transformations used to generate equivalent atoms:
[1] x,y,z+1
[2] x-1/2,-y+1/2,z
[3] x-1/2,-y+1/2,z-1

Oa: oxygen atom coming from an acetate group. Oc: oxygen atom coming from a carboxylate group.

In **Figure 4.2.10**, different polyhedral views along the crystallographic axes are depicted, evidencing the two-dimensional covalent framework determined in **AEPF-12**.

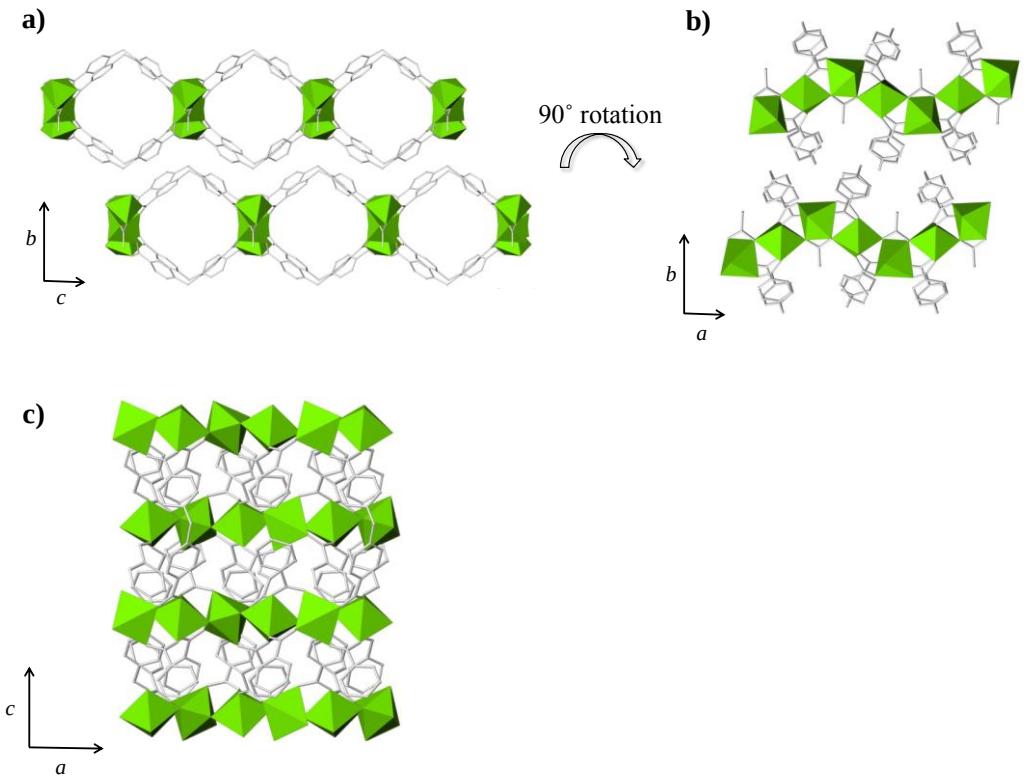

Figure 4.2.10. a) Depiction of **AEPF-12** layers perpendicular to *a* axis and **b)** along *c* axis. **c)** Polyhedral representation along the *b* axis.

As it was performed in the case of **AEPF-11** compound, the linker conformation in **AEPF-12** was also analysed by studying the geometrical parameters **θ** angle, **ω** dihedral angle and **d** distance (**Figure 4.2.5**). In this case, the study was focussed on the differences between $HL_{(2)}^{-}$ and $L_{(2)}^{-2}$ (**Table 4.2.7**). Thus, in the case of the partially deprotonated form, the linker presents a lower **ω** value and a higher **θ** value, in comparison with the totally deprotonated $L_{(2)}^{-2}$ one. These differences cause that the **d** distance determined in the $HL_{(2)}^{-2}$ ligand is slightly higher than the one defined for $L_{(2)}^{-2}$ ligand. Besides, these **d** distances are directly involved in the inorganic chains separation for **AEPF-12** compound.

Table 4.2.7. **θ** angle, **ω** dihedral angle and **d** distance values in **AEPF-12** for the deprotonated ligand ($L_{(2)}^{-2}$) and the partially deprotonaded ligand ($HL_{(2)}^{-}$).

Linker	θ (º)	ω (º)	d (Å)
$\mathbf{HL_{(2)}^{-}}$	111.89	77.08	9.225
$\mathbf{L_{(2)}^{-2}}$	110.54	86.84	9.191

AEPF-12 crystallizes with *n-prop* molecules in the channels. Despite the fact that several efforts have been done in order to obtain a structural model suitable for these molecules, it was not possible. For that reason, the SQUEEZE technique was applied, which is implemented in PLATON package.[5] The SQUEEZE procedure takes care of the contribution of a disordered solvent to the calculated structure factors by back-Fourier transformation of the continuous density found in a masked out region of the difference map. The masked region is defined as the solvent accessible region left unoccupied by the ordered part of the structure. Thus, it was possible to determine the presence of 132 electrons counts per unit cell in **AEPF-12**, which correspond to ~4 *n-prop* molecules per unit cell. Taking into account that Z=4 for this compound, a new formula considering these guest molecules can be defined as $[Mg_2(L_2)(HL_2)(CH_3CO_2)]\cdot(CH_3(CH_2)_2NH_2)$. As it is going to be explained in the following sections, these *n-prop* molecules can be quite easily evacuated by heating treatments. When considering the crystal structure without these molecules in pores, a potential accessible free space of 27.1% can be determined using PLATON (SOLV mode).[5] The porous structure in this material is explained by the presence of spherical cavities with ~9.6 Å diameter (**Figure 4.2.10a**).

From the topological point of view, by simplification of the layers present in **AEPF-12** using TOPOS,[4] one type of four-connected nodes were found, which correspond to Mg(2) centres. This two-periodic net exhibits a **sql** topological type, with point symbol ($4^4.6^2$). The main simplifications points, as well as the decorated and final simplified nets for **AEPF-12**, are shown in **Figure 4.2.11**.

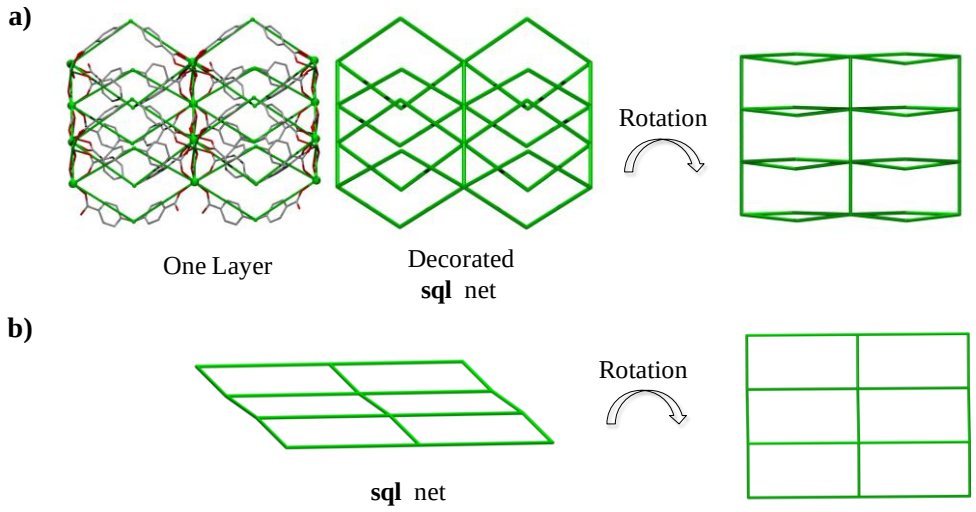

Figure 4.2.11. a) Depiction of one layer in the real net together with the decorated **sql** net, showing different orientations. Hydrogen atoms were omitted for clarity. **b)** Representation of the simplified **sql** net in **AEPF-12**, showing different orientations.

An additional topological study was performed in order to analyse the way in which the linker generates the square shaped channels in this structure. Thus, as it is shown in **Figure 4.2.12**, in **AEPF-12** the connections of metallic chains *via* $HL_{(2)}^{-}$ and $L_{(2)}^{-2}$ linkers is made in a parallel way, being thus of the **B**-type[1] (contrary to **AEPF-11**, for which **A**-type channels are described).

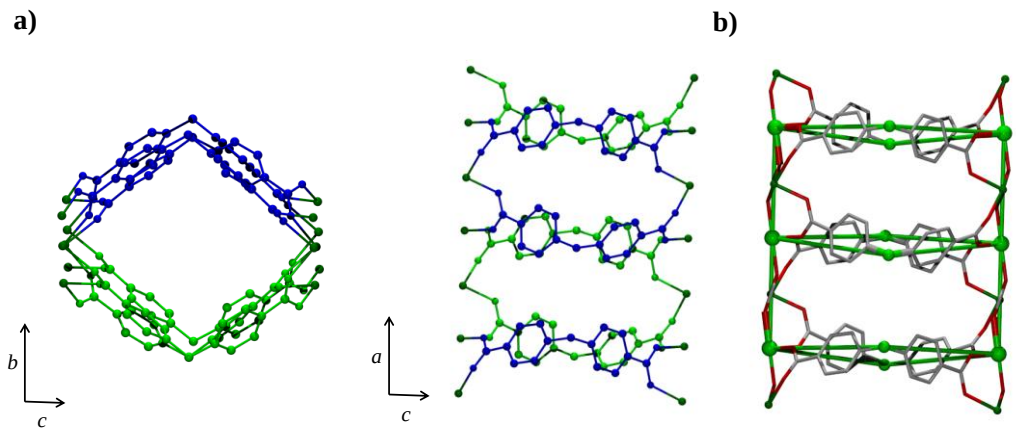

Figure 4.2.12. a) Different projections of the square shaped channels in **AEPF-12**. **b)** Detail of the real net together with the decorated **sql** net, evidencing the edge parallel mode for $HL_{(2)}^{-}$ and $L_{(2)}^{-2}$ ligand.

4.2.1.3.

(Ca, Sr)-AEPF-13

In the case of Ca and Sr, the hydrothermal reaction between $H_2L_{(2)}$ and the corresponding alkaline-earth acetate, using *n-prop* as base, gives rise to two isostructural **[M($L_{(2)}$)(H_2O)]** compounds (where M= Ca^{+2} or Sr^{+2}) (**AEPF-13**). Although for Ca^{+2} and Sr^{+2} ions, the compounds were synthesised as pure crystalline phases, single crystals could be only obtained in the case of Sr. Thus, the structure was determined for the Sr compound using single crystal X-Ray Diffraction data. **Sr-AEPF-13** crystallizes in the orthorhombic crystal system ($P2_1/c$ space group). The cell parameters determined for this structure are: a = 5.8667(1) Å, b = 25.3028(6) Å, c = 27.3046(7) Å, β = 92.383(1)°, V = 4049.7(2) Å^3. The asymmetric unit for this compound comprises three Sr^{+2} ions, three deprotonated ligands ($L_{(2)}^{-2}$) and three coordinated water molecules. The ORTEP representation of **Sr-AEPF-13** asymmetric unit is exposed in **Figure 4.2.13** and the main crystallographic and refinement data for this compound are shown in **Table 4.2.8**. In the case of **Ca-AEPF-13**, the compound was proved to be isostructural to **Sr-AEPF-13** by the application of Rietveld method, using X-Ray Powder Diffraction (XRPD) data.

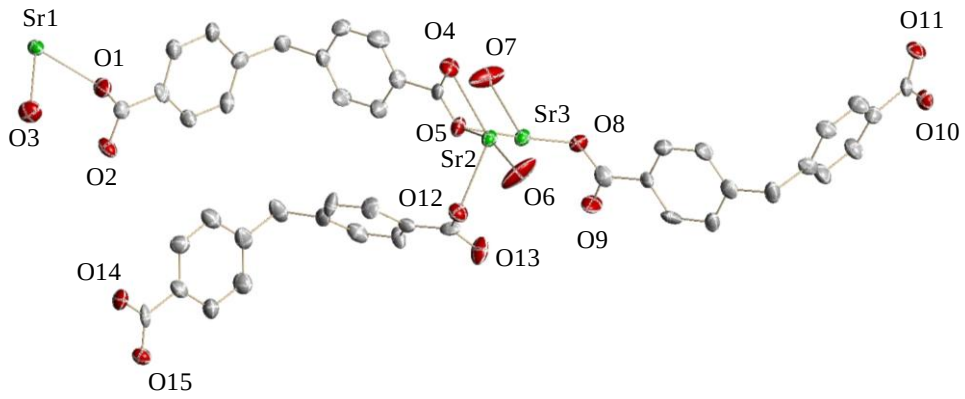

Figure 4.2.13. ORTEP representation of **Sr-AEPF-13** asymmetric unit. Ellipsoids are displayed at the 50% probability level. Hydrogen atoms were omitted for clarity.

Moreover, it is worth highlighting that **Sr-AEPF-13** crystallizes in the form of twin crystals, which have been carefully studied in order to obtain a good structural

model. For that purpose, in a first step, CELL_NOW[25] was used, which analyses a list of reflections to find cell parameters and orientation matrix despite of the presence of several twin domains. Once the two domains present in a **Sr-AEPF-13** twin crystal were identified, the whole data were integrated using SAINT,[26] which allows working with the both of them. The scaling and adsorption procedure were carried out with TWINABS,[27] which generates two different .hkl files. The structure was solved using the *de-twinned* HKLF4 file, and was refined with the twinned HKLF5 file. BASF parameter was refined to a final composition of the two domains in the twin equal to 15.4 % : 84.6%.

Table 4.2.8. Crystallographic and refinement data for **Sr-AEPF-13**.

Identification code	Sr-AEPF-13
Empirical formula	C_{45} H_{36} O_{15} Sr_3
Formula weight	1079.6
Temperature	296(2) K
Wavelength	1.54178 Å
Crystal system	Monoclinic
Space group	$P2_1/c$
Unit cell dimensions	a = 5.8667(1) Å α = 90° b = 25.3028(6) Å β = 92.383(1)° c = 27.3046(7) Å γ = 90°
Volume	4049.70(16) $Å^3$
Z	4
Density (calculated)	1.771 Mg/m^3
Absorption coefficient	5.742 mm^{-1}
F(000)	22160
Crystal size	0.15 x 0.10 x 0.05 mm^3
Theta range for data collection	2.38 to 65.32°
Index ranges	-6<=h<=3, -29<=k<=28, -32<=l<=31
Reflections collected	12529
Independent reflections	6603 [R(int) = 0.1215
Completeness to theta = 65.33°	95.30%
Absorption correction	Semi-empirical from equivalents
Max. and min. Transmission	0.7622 and 0.4797
Refinement method	Full-matrix least-squares on F^2
Data / restraints / parameters	6603 / 9 / 568
Goodness-of-fit on F^2	1.12
Final R indices [I>2sigma(I)]	R_1 = 0.0883, wR_2 = 0.2469
R indices (all data)	R_1 = 0.1122, wR_2 = 0.2877
Largest diff. peak and hole	1.728 and -1.548 e.$Å^{-3}$

In **Sr-AEPF-13**, each Sr^{+2} ion is hepta-coordinated to two oxygen atoms of one $L_{(2)}^{-2}$ carboxylate group in a bridge mode, four oxygen atoms of two different $L_{(2)}^{-2}$ carboxylate groups in a bridge-chelate-bridge mode and one oxygen of a coordinated water molecule, giving rise to three different SrO_7 monocapped trigonal prisms (**Figure 4.2.14a**). These polyhedra, which can be considered as the inorganic PBUs, are present in the compound forming two different types of chains running along the *a* axis, by sharing edges: the first one, which is the only built with Sr(1) polyhedra and the other one where Sr(2) and Sr(3) polyhedra are alternated (**Figure 4.2.14b**). Junction of these SrO_7 chains is made *via* the $L_{(2)}^{-2}$ ligands, which act in a $\eta^2\mu_2$-$\eta^2\mu_3$ coordination mode (**Figure 4.2.14c**), giving rise to a three-dimensional framework.

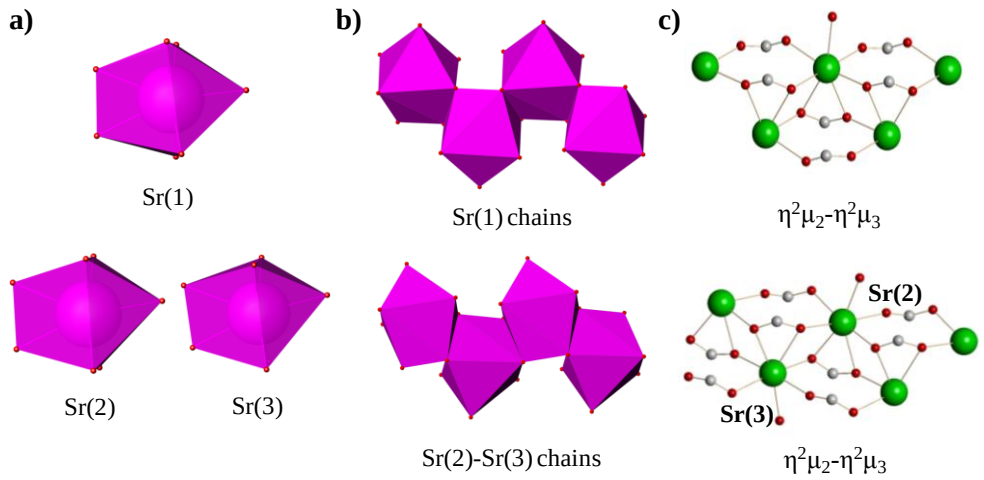

Figure 4.2.14. a) Inorganic PBUs in **Sr-AEPF-12**. **b)** Detail of the two different SrO_7 chains that run along the *a* axis. **c)** Coordination mode of $L_{(2)}^{-2}$ ligand in this compound.

In **Sr-AEPF-13**, $L_{(2)}^{-2}$ carboxylate groups exhibit different behaviour concerning their Sr-O distances. Thus, for those carboxylate groups that are bonded in a bridge mode, an average Sr-O distance of ~2.47 Å was determined. However, in the case bridge-chelate-bridge mode carboxylate groups, two different kinds of Sr-O distances can be distinguished: a strong bond with an average Sr-O distance of ~2.50 Å and another one weaker (average Sr-O distance ~2.70 Å). These differences are responsible for the SrO_7 polyhedra distortion (**Table 4.2.9**).

Table 4.2.9. Interatomic distances in the coordination sphere of the SrO_7 polyhedra for Sr(1), Sr(2) and Sr(3) in **Sr-AEPF-13**.

Sr(1)

Bond	Distance (Å)
Sr(1)-O(1)c	2.442(7)
Sr(1)-O(2)[1]c	2.511(6)
Sr(1)-O(3)w	2.555(7)
Sr(1)-O(10)[2]c	2.709(7)
Sr(1)-O(10)[3]c	2.493(6)
Sr(1)-O(11)[2]c	2.672(7)
Sr(1)-O(11)[4]c	2.499(6)

Symmetry transformations used to generate equivalent atoms:
[1] x+1,y,z
[2] -x+1,-y,-z+2
[3] x+2,y,z-1
[4] x+1,y,z-1

Sr(2)

Bond	Distance (Å)
Sr(2)-O(4)c	2.749(7)
Sr(2)-O(5)c	2.663(7)
Sr(2)-O(6) w	2.663(7)
Sr(2)-O(12)c	2.518(6)
Sr(2)-O(13)[1]c	2.403(6)
Sr(2)-O(14)[2]c	2.462(7)
Sr(2)-O(15)[3]c	2.529(6)

Symmetry transformations used to generate equivalent atoms:
[1] x+1,y,z
[2] x,-y+1/2,z+1/2
[3] x+1,-y+1/2,z+1/2

Sr(3)

Bond	Distance (Å)
Sr(3)-O(4)[1]c	2.483(6)
Sr(3)-O(5)c	2.513(6)
Sr(3)-O(7)w	2.537(7)
Sr(3)-O(8)c	2.510(7)
Sr(3)-O(9)[2]c	2.440(6)
Sr(3)-O(14)[3]c	2.799(8)
Sr(3)-O(15)[3]c	2.613(6)

Symmetry transformations used to generate equivalent atoms:
[1] x-1,y,z
[2] x+1,y,z
[3] x,-y+1/2,z+1/2

Oc: oxygen atom coming from a carboxylate group. Ow: oxygen atom coming from a coordinated water molecule.

The coordinated water molecules in **Sr-AEPF-13** give rise to the presence of four different types of interactions. As it is shown in **Table 4.2.10**, these supramolecular interactions are determined between coordinated water molecules and $L_{(2)}^{-2}$ carboxylate groups that coordinate in a bridge mode. However, while the water molecule bonded to Sr(1) centre establishes one hydrogen bond and a very weak interaction, in the case of Sr(2) and Sr(3) centres only one type of hydrogen bond is found.

Table 4.2.10. Distances and angles of hydrogen bonds found in **Sr-AEPF-13** compound.

D-H···A [1]	D-H [2]	H···A [3]	D···A [4]	<D-H···A [5]
O(3)w-H(3B)w ··· O(12)c [1]	1.01	1.83	2.817(9)	167.5
O(3)w-H(3B)w ··· O(13)c [1]	1.01	2.64	3.25(1)	119.4
O(6)w-H(6B)w ··· O(2)c [2]	0.99	2.18	2.77(1)	116.8
O(7)w-H(7B)w ··· O(8)c [3]	1	2.06	2.73(1)	123.6

Symmetry operators codes

[1] x+1, -y+1/2, z-1/2 [2] x, -y+1/2 z+1/2 [3] -x, -y, -z+2

D: donor atom, A: acceptor atom. [1]Names of donor, hydrogen and acceptor atoms involved in the hydrogen bond. [2] Distance D – A. [3]Distances H – A. [4]Distance D – A. [5] Angle D – H – A.

Oc: oxygen atom corresponding to a carboxylate group. Ow: oxygen atom corresponding to a coordinate water molecule. Hw: hydrogen atom corresponding to a coordinate water molecule.

In **Figure 4.2.15**, different polyhedral views along the crystallographic axes are depicted, evidencing the three-dimensional covalent framework determined in **AEPF-13**.

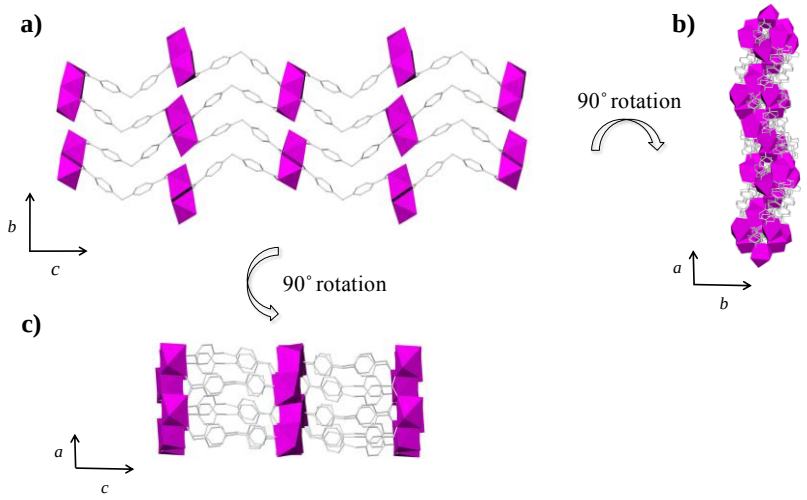

Figure 4.2.15. a) Polyhedral representation for **Sr-AEPF-13** along the *a* direction, **b)** along the *c* axis and **c)** along the *b* axis.

The same analysis of the linker conformation done before (see **Figure 4.2.5**, **Tables 4.2.4** and **4.2.7**) has been performed in **AEPF-13**, studying the **θ**, **ω** and **d** parameters. In order to perform these analyses, the three linker forms were named as: L_A^{-2} (linker molecule for which carbon atoms are labelled from C(1) to C(15)), L_B^{-2}(linker molecule for which carbon atoms are labelled from C(16) to C(30)) and L_C^{-2} (linker molecule for which carbon atoms are labelled from C(31) to C(50). In **Table 4.2.11,** the values of these parameters are listed for the three independent linkers determined in **AEPF-13**. Analysing these parameters, a general conclusion can be drawn: the linker conformations determined for **AEPF-13** are clearly different to those found in **AEPF-11** and **AEPF-12**. Thus, while in **AEPF-13** the **d** distances are clearly larger (average **d** value ~ 9.7 Å), in the case of **AEPF-11** and **AEPF-12** those distances are markedly shorter (average **d** value ~ 9.21 Å, for both compounds).

From these results it can be concluded that: *for those materials in which $L_{(2)}^{-2}$ ligand generates square shaped channels, **d** value is limited (around ~ 9.2 Å). Contrary, when the linker conformation exhibits larger **d** distances, the obtaining of other nets can be possible (as it was the case of Ca^{+2} and Sr^{+2}, for which **AEPF-13** nets were obtained).*

Table 4.2.11. θ angle, **ω** dihedral angle **d** distance values in the six independent $L_{(2)}^{-2}$ ligands for **Sr-AEPF-13** compound.

$L_{(2)}^{-2}$ linker	θ (º)	ω (º)	d (Å)
L_A	114.03	64.80	9.707
L_B	113.66	75.94	9.665
L_C	112.01	78.02	9.715

To consider topological features of **AEPF-13**, the simplifications were performed using TOPOS.[4] As it was previously commented in the discussion of **Sr-AEPF-13** structure, there are two kinds of inorganic chains parallel to the *a* axis (one built with alternated Sr(2)-Sr(3) polyhedra sharing edges, and the other one with only Sr(1) polyhedra sharing edges). As it was before done, the topological simplifications for **AEPF-13** were performed taking into account an interesting work of Yaghi and O'Keeffe, in which the authors carefully studied the rod-packing phenomenon in MOFs.[23] Thus, the topological simplifications were carried out considering the $(\text{-O-Sr-})_\infty$ rods determined in **AEPF-13** as the inorganic SBUs. These $(\text{-O-Sr-})_\infty$ rods are built

up from carboxylate O atoms completing the heptahedral coordination around Sr atoms to result in an infinite rod of SrO_7 monocapped trigonal prisms sharing edges. To exemplify, in **Figure 4.2.16** the simplifications performed in the Sr(2)-Sr(3) chains to build the inorganic SBU are shown (the same kind of simplifications were done for Sr(1) chains).

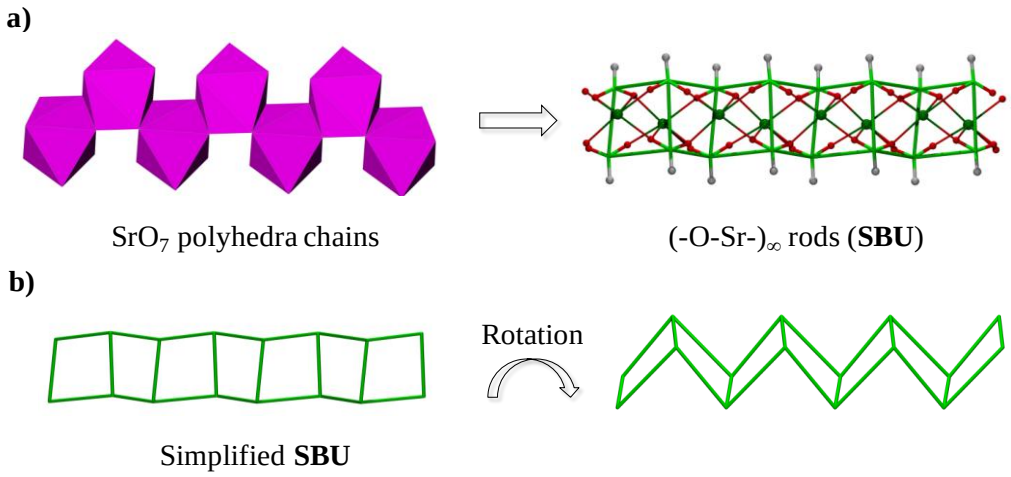

Figure 4.2.16. a) Representation of the topological simplifications performed in a Sr(2)-Sr(3) polyhedra chain. **b)** Simplified SBU in **AEPF-13**, showing different orientations.

Taking into account these topological considerations, the **AEPF-13** net can be explained as rods of quadrangles linked by sharing opposite edges (ladders). These ladders are linked with the rungs parallel to form a **sra** 4-connected net, with point symbol ($4^2.6^3.8$) (**Figure 4.2.17)**. It is worth highlighting that this net exhibits the same topology to that determined for ABW framework type in zeolites.

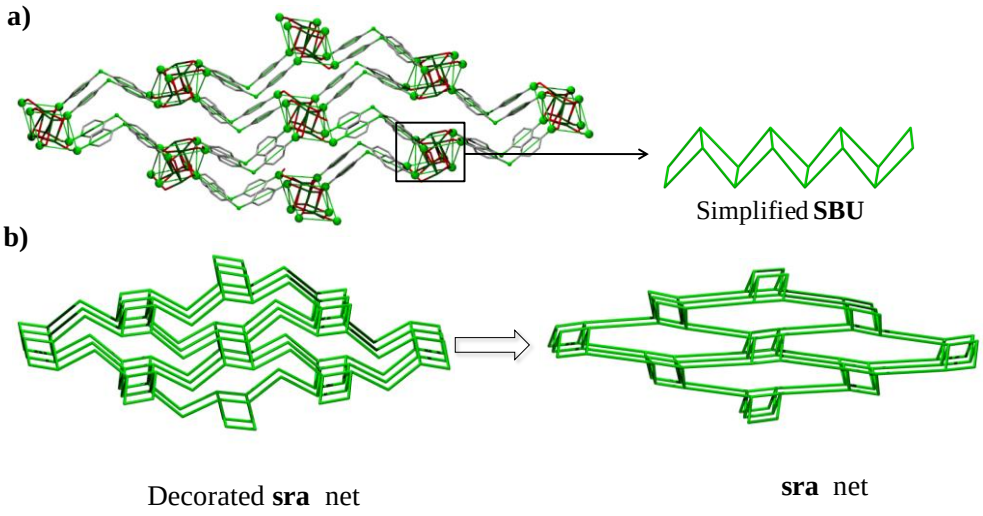

Figure 4.2.17. a) Depiction of the **AEPF-13** real net together with the decorated **sra** net and detail of the simplified SBU. **b)** Decorated and simplified **sra** net.

An additional topological study was performed in order to analyse the way in which the linker generates the distorted rhombic shaped channels in this structure. Thus, as it is shown in **Figure 4.2.18**, in **AEPF-13** the connections of metallic chains *via* the linker is made in a parallel way, being thus of the **B**-type.[1]

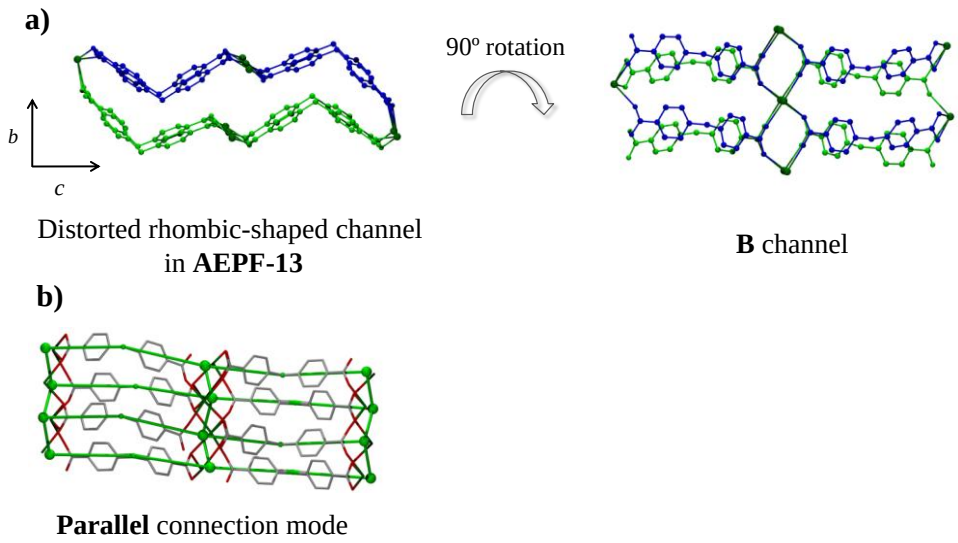

Figure 4.2.18. a) Different projections of the distorted rhombic shaped channels in **AEPF-13**. **b)** Detail of the real net together with the decorated **sra** net, evidencing the parallel connection mode of the linker.

Finally, a more profound topological study was performed for **AEPF-13** framework, in order to analyse the natural tiling that can be described for a **sra** net. For that purpose, in a first step, the idealisation of the **sra** net determined in **AEPF-13** was performed in its maximum symmetry embedding (*Imma* space group), using Systre package.[28] In **Figure 4.2.19a** and **4.2.19b** both the real ($P2_1/c$ space group) and the idealised net (*Imma* space group) for **AEPF-13** are shown. Thus, considering the idealised net, $[4^2.6^2.8^2]$ cages (*tiles*) can be described (**Figure 4.2.19c**), which explain the natural tiling corresponding to a **sra** net.

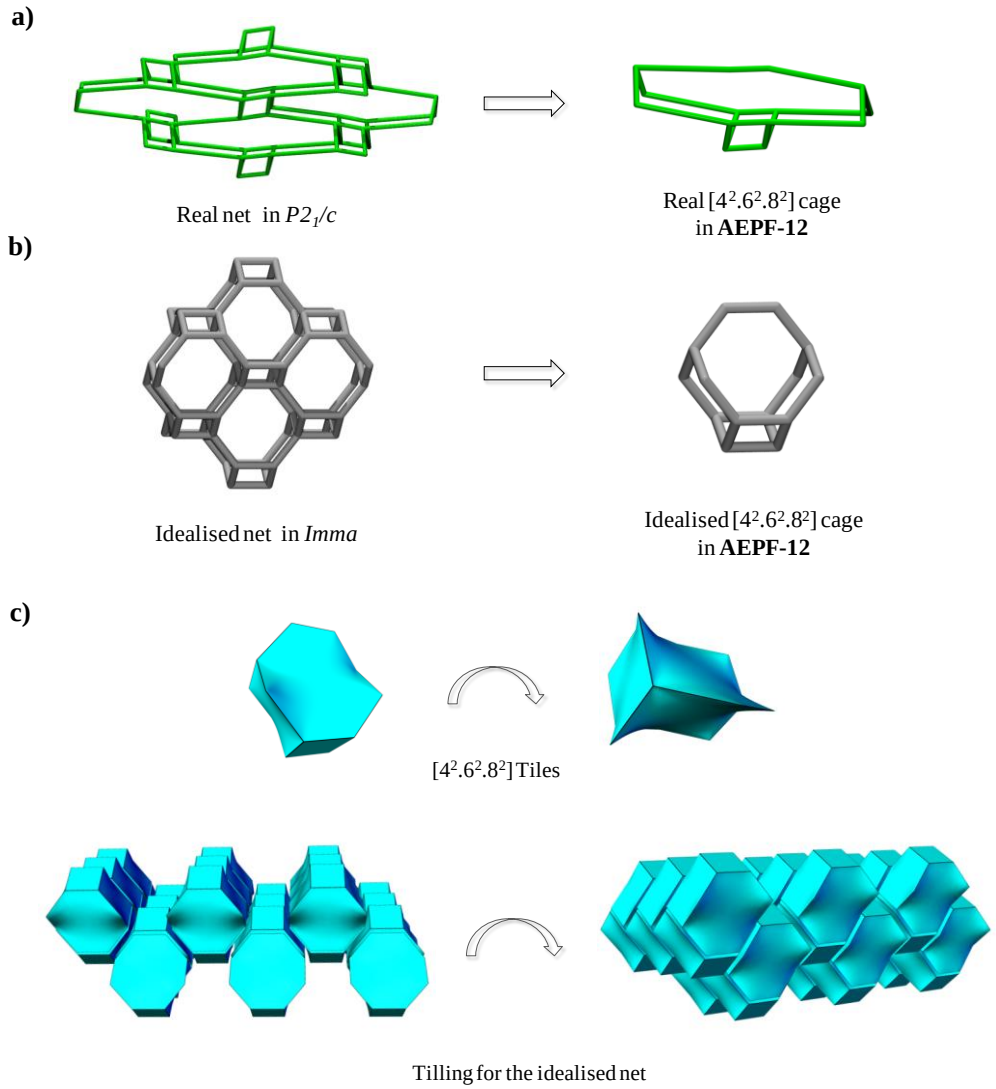

Figure 4.2.19. a) Real net and cage in $P2_1/c$ space group. **b)** Idealised net and cage in *Imma* space group. **c)** $4^2.6^2.8^2$ tile together with some views of the tiling corresponding to the idealised **sra** net descried in **AEPF-13**.

4.2.1.4.

Topological summary

To clarify all the structural information presented in this chapter, **Figure 4.2.20** summarizes the main topological simplifications obtained for the previous discussed materials based on alkaline-earth elements and $H_2L_{(2)}$ linker.

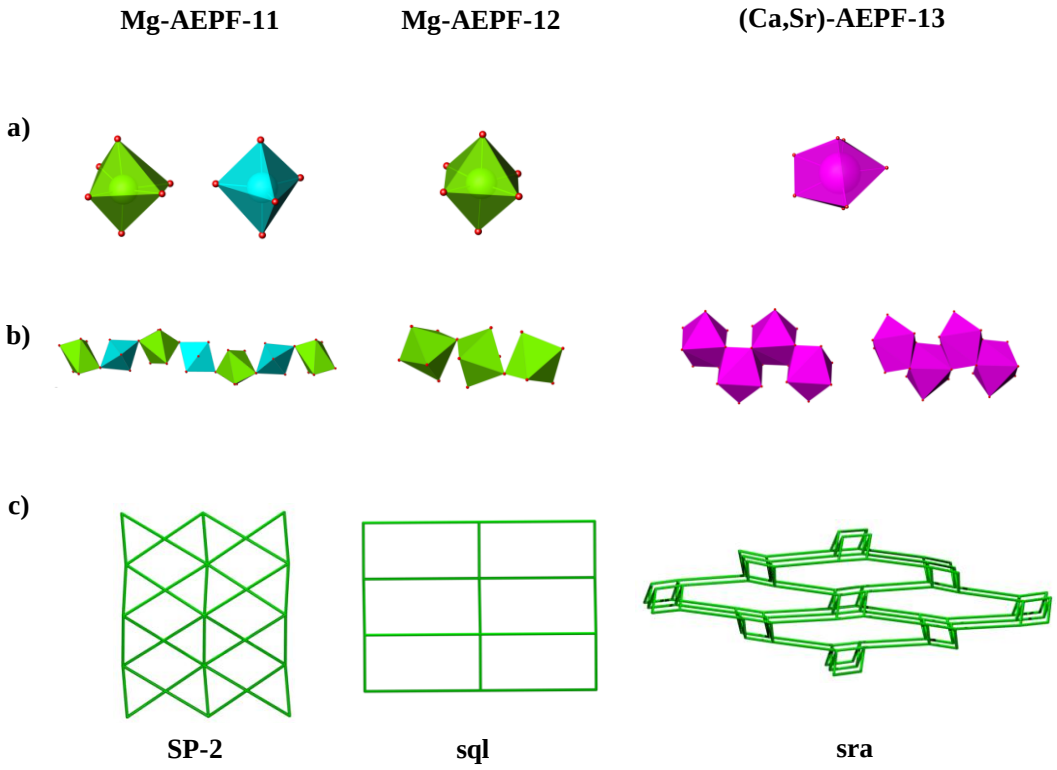

Figure 4.2.20. a) Inorganic PBUs and **b)** Inorganic chains determined for each compound. **c)** Topological net simplification for each compound.

4.2.2.

Characterization

4.2.2.1.

X-Ray Powder Diffraction

Pawley refinements[12] were performed using Materials Studio software[13] for the four compounds in order to check the purity of the bulk samples (*see* Chapter 2, *Techniques*). Pawley refinement profiles and the main refinement values for the **Mg-AEPF-11**, **Mg-AEPF-12** and **Sr-AEPF-13** (whose structural models were solved by Single-Crystal X-Ray Diffraction methods), are shown in **Tables 4.2.12-4.2.14** and **Figures 4.2.21-4.2.23**. All the crystalline phases show the high purity obtained for each compound.

Table 4.2.12. Crystal Data and Pawley profile refinement values for **AEPF-11**.

Compound	AEPF-11
Crystal system	Monoclinic
Space group	$P2_1$
Unit cell dimensions	a= 11.032(1) Å α = 90˚
	b= 20.777(2) Å β = 90.272(6)˚
	c= 20.890(1) Å γ = 90˚
Profile Function	Pseudo-Voigt
U	-0.5(1)
V	0.27(3)
W	-0.013(2)
NA	1.07(5)
NB	-0.033(3)
Zero Point	0.109(1)
Asymmetry correction	Finger-Cox-Jephcoat
H/L	0.0262(5)
S/L	0.0134(7)
Rwp	0.0790
Rp	0.1197

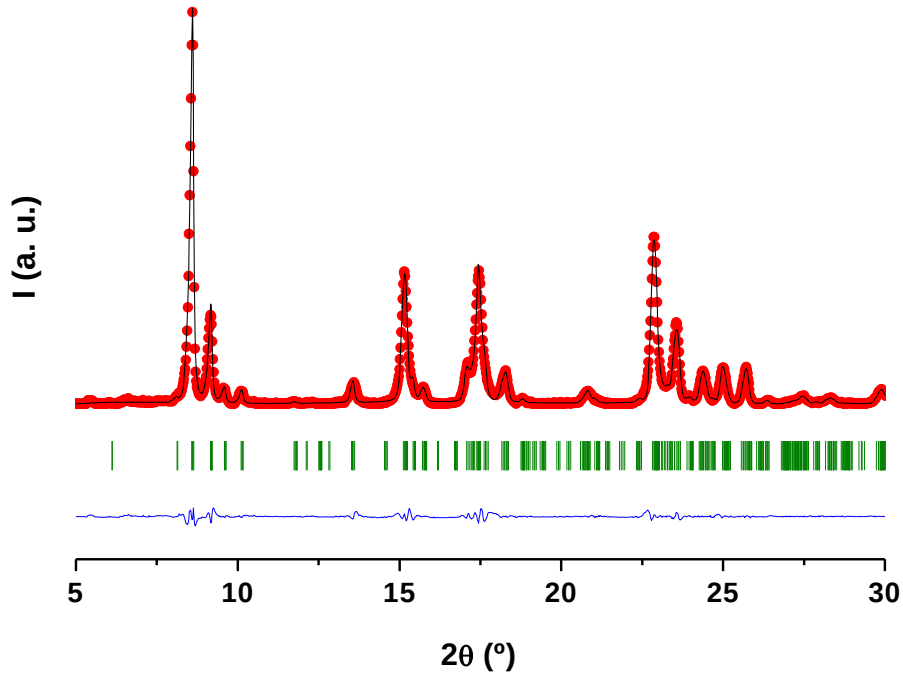

Figure 4.2.21. Pawley refinement for **AEPF-11**. Experimental data (red), simulated pattern (black) and difference (blue); observed reflections (green).

Table 4.2.13. Crystal Data and Pawley profile refinement values for **AEPF-12**.

Compound	AEPF-12	
Crystal system	Orthorhombic	
Space group	$Pna2_1$	
Unit cell dimensions	a= 12.2899(8) Å	α = 90˚
	b= 22.892(2) Å	β = 90˚
	c= 12.831(1)Å	γ = 90˚
Profile Function	Pseudo-Voigt	
U	-0.54(8)	
V	0.24(2)	
W	-0.011(1)	
NA	1.07(5)	
NB	-0.033(3)	
Zero Point	0.105(1)	
Asymmetry correction	Finger-Cox-Jephcoat	
H/L	0.0231(6)	
S/L	0.0129(7)	
Rwp	0.0789	
Rp	0.1332	

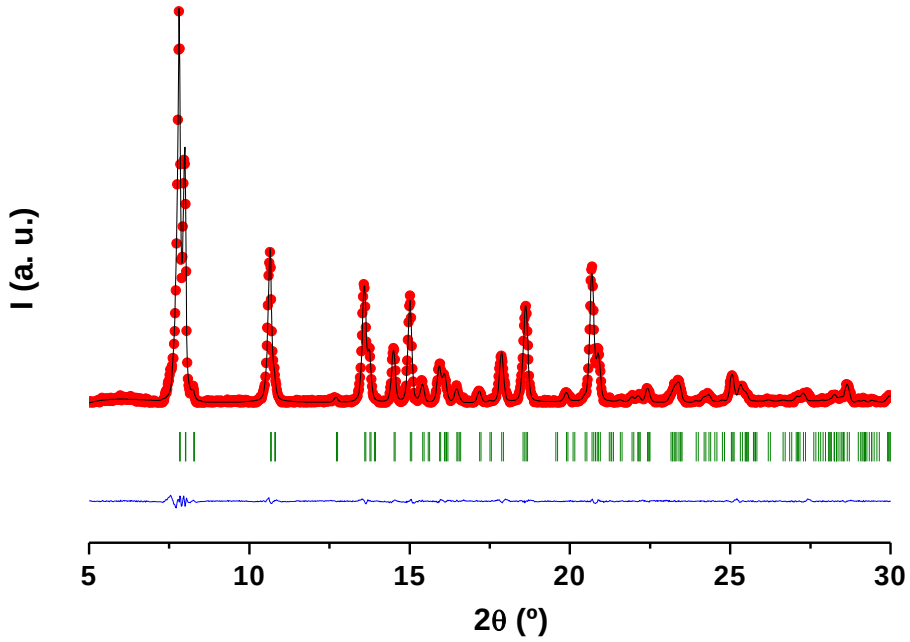

Figure 4.2.22. Pawley refinement for **AEPF-12**. Experimental data (red), simulated pattern (black) and difference (blue); observed reflections (green).

Table 4.2.14. Crystal Data and Pawley profile refinement values for **Sr-AEPF-13**.

Compound	Sr-AEPF-13
Crystal system	Monoclinic
Space group	$P2_1/c$
Unit cell dimensions	a = 5.8682(2) Å α = 90˚ b = 25.325(1) Å β = 92.320(2)˚ c = 27.336(2) Å γ = 90˚
Profile Function	Pseudo-Voigt
U	-0.02(4)
V	0.042(9)
W	-0.0005(4)
NA	0.92(4)
NB	-0.031(3)
Zero Point	0.1096(6)
Asymmetry correction	Finger-Cox-Jephcoat
H/L	0.01555(9)
S/L	0.01573(9)
Rwp	0.0887
Rp	0.0605

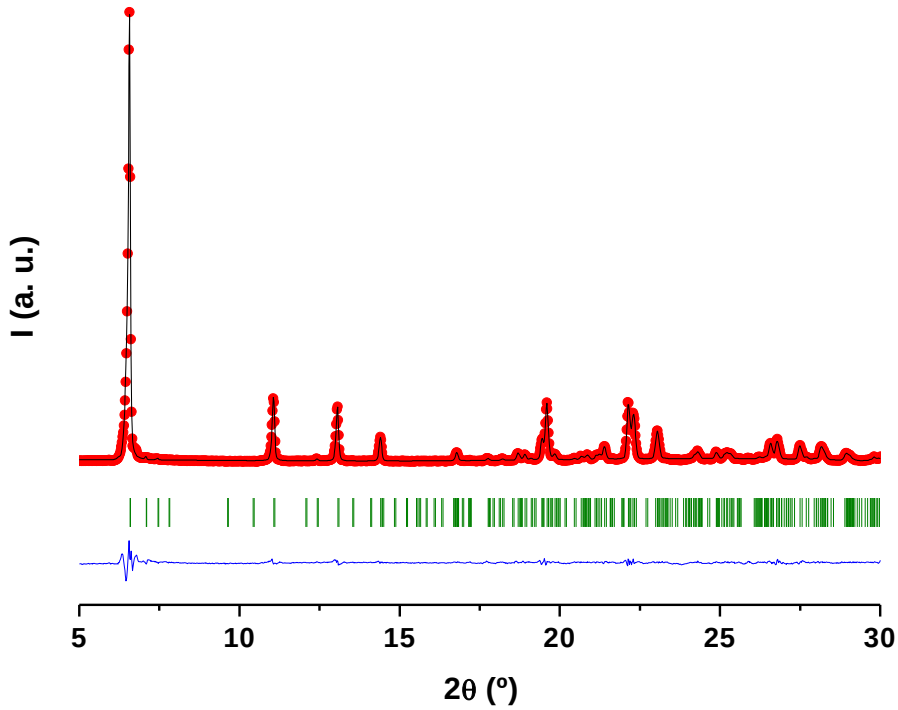

Figure 4.2.23. Pawley refinement for **Sr-AEPF-13**. Experimental data (red), simulated pattern (black) and difference (blue); observed reflections (green).

In the case of **Ca-AEPF-13**, it was not possible to obtain suitable single crystals for its structural solution by single crystal X-Ray Diffraction methods. For this reason, Rietlveld analyses were used to determine the structural parameters. Thus, in a first step, **Ca-AEPF-13** XRPD pattern was indexed by using DICVOL04 program[10,11] in a monoclinic unit cell with cell parameters: a = 4.6124 Å, b =27.0538 Å, c =24.7517 Å, β = 91.282˚ and V = 3087.79 Å^3(figures of merit M_{20}=10.3, F_{20}=18.6). In a next step, due to the similarities of this cell with that determined for **Sr-AEPF-13** (a = 5.8667(1) Å, b = 25.3028(6) Å, c = 27.3046(7) Å, β = 92.383(1)˚, V= 4049.7(2) Å^3), we chose as a structural model to perform the Rietveld refinements[16] that of **Sr-AEPF-13** compound, but replacing Sr atoms by Ca atoms. This model converged to R_{wp}=0.107 and R_p=0.2807 values, with refined cell parameters a = 5.646(1) Å, b = 25.054(3) Å, c = 27.393(5) Å, β = 90.24(2)˚ and V= 3874.8(2) Å^3 (**Table 4.2.15** and **Figure 4.2.24**).

Table 4.2.15. Crystal Data and Rietveld profile refinement values for **Ca-AEPF-13**.

Compound	Ca-AEPF-13
Crystal system	Monoclinic
Space group	$P2_1/c$
Unit cell dimensions	a= 5.646(1) Å α = 90˚
	b= 25.054(3) Å β = 90.24(2)˚
	c= 27.393(5) Å γ = 90˚
Profile Function	Pseudo-Voigt
U	0.1(1)
V	0.01(3)
W	0.002(2)
NA	0.58(5)
NB	-0.009(5)
Zero Point	0.1177(1)
Asymmetry correction	Finger-Cox-Jephcoat
H/L	0.0230(1)
S/L	0.0098(3)
Rwp	0.1076
Rp	0.2807

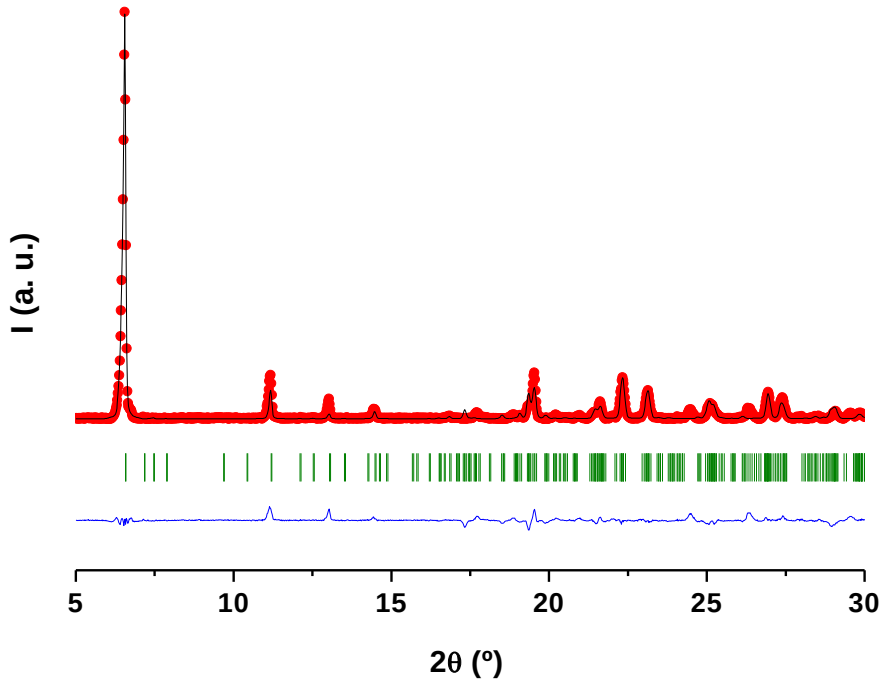

Figure 4.2.24. Rietveld refinement for **Ca-AEPF-13**. Experimental data (red), simulated pattern (black) and difference (blue); observed reflections (green).

4.2.2.2.

Infrared Spectroscopy

Infrared (IR) spectra of **Mg-AEPF-11**, **Mg-AEPF-12**, **Ca-AEPF-13** and **Sr-AEPF-13** show the presence of bands in the $-CO_2^-$ stretching mode zone (at ~1700-1500 (υ_{as}) and ~1500-1300 (υ_s) cm^{-1}), which correspond to the presence of carboxylate groups. Moreover, **Mg-AEPF-11**, additional bands were determined in the region corresponding to -NH and aromatic –CH stretching mode zone (~3500-3400 and ~3000 cm^{-1}, respectively).

Detail of **Mg-AEPF-11** IR spectrum of the region corresponding to CO_2^- and C=O stretching mode zone is given in **Figure 4.2.25**. Thus, for **Mg-AEPF-11**, CO_2^- stretching mode bands were observed at ~1625, ~1605, ~1555 and ~1590 cm^{-1} (υ_{as}); at ~1415 and ~1400 cm^{-1} (υ_s). Moreover, an additional band at ~1665 cm^{-1} was determined, which can be assigned to C=O stretching mode corresponding to carbonyl groups of DEF molecules coordinated to Mg^{+2} ions.

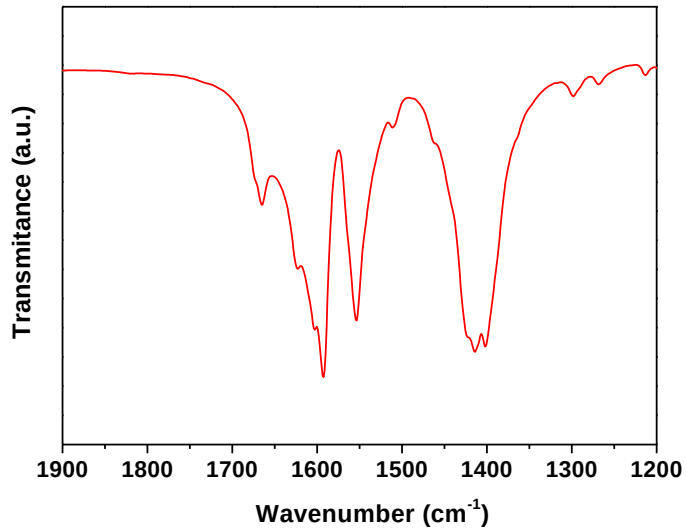

Figure 4.2.25. Detail of IR spectrum in the –C=O and $-CO_2^-$ stretching mode zone (1900-1200 cm^{-1}) for **AEPF-11**.

Details of IR spectrum for **Mg-AEPF-12** in the region corresponding to -NH and –CH stretching mode (4000-2250 cm^{-1}) and $-CO_2^-$ and -C=O stretching mode (1900-1200 cm^{-1}) zones are given in **Figure 4.2.26**.

In the first studied region (**Figure 4.2.26a**), a broad band centred at ~3415 cm^{-1} is observed, which can be explained by the contribution of -NH stretching mode of propan-1-amine and -OH stretching mode corresponding to physisorbed water molecules and $HL_{(2)}^-$ protonated carboxylic groups. Moreover, multiple weak bands are determined between ~3065-2930 cm^{-1} associated to –CH stretching mode of both aromatic groups and propan-1-amine molecules.

In the CO_2^- and C=O stretching mode zone (**Figure 4.2.26b**) bands are observed at: ~1555 and ~1605 cm^{-1}(υ_{as}); and ~1405 cm^{-1} (υ_s). Moreover, additional weak bands are found at ~1635 cm^{-1}, related to NH_2 scissoring mode of propan-1-amine molecules, and at ~1665 cm^{-1} related to C=O stretching of $HL_{(2)}^-$ protonated carboxylic groups.

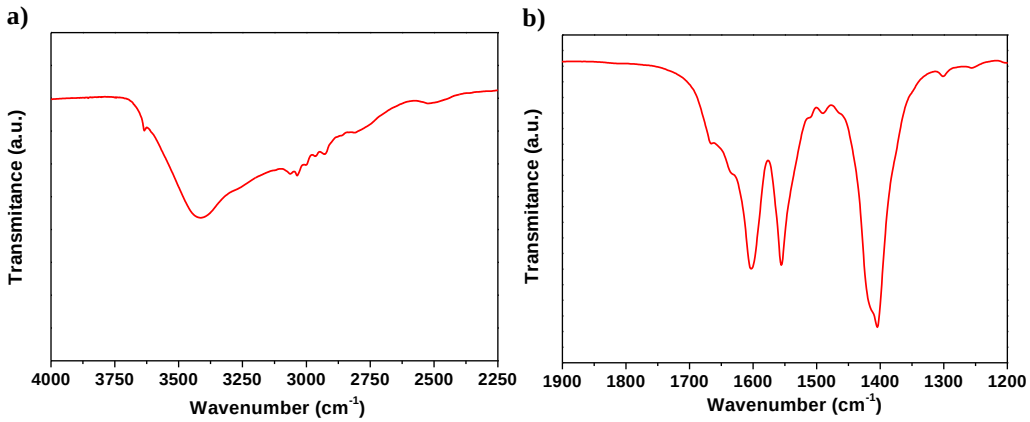

Figure 4.2.26. Details of IR spectrum for **Mg-AEPF-12** in the: **a)**-NH and –CH stretching mode zone (4000-2250 cm^{-1}) and **b)** –C=O and $-CO_2^-$ stretching mode zone (1900-1200 cm^{-1}).

Details of **Ca-AEPF-13** and **Sr-AEPF-13** IR spectra in the region corresponding to -OH and –CH stretching mode (4000-2250 cm^{-1}) and $-CO_2$ stretching mode (1900-1200 cm^{-1}) zones are given in **Figures 4.2.27-4.2.28**, respectively.

In the region corresponding to –OH and –CH stretching mode, for **Ca-AEPF-13** compound (**Figure 4.2.27a**) a broad band centred at ~3425 cm^{-1} is observed, which can be explained by the contribution of -OH stretching mode of those groups which establish hydrogen bonds. An additional sharp band at ~3585 cm^{-1} is observed, which can be assigned to the contribution of free –OH groups not involved in hydrogen bonds. In the case of **Sr-AEPF-13** compound (**Figure 4.2.27b**), a broad band is observed

centred at ~3345 cm^{-1}, showing the presence of several contributions (-OH groups involved in hydrogen bonds). Moreover, two sharp bands are observed at ~3565 and ~3595 cm^{-1} (-OH groups not involved in hydrogen bonds). The differences observed in this region between **Ca-AEPF-13** and **Sr-AEPF-13** compounds show that the two materials present subtle variances concerning hydrogen bonds interactions.

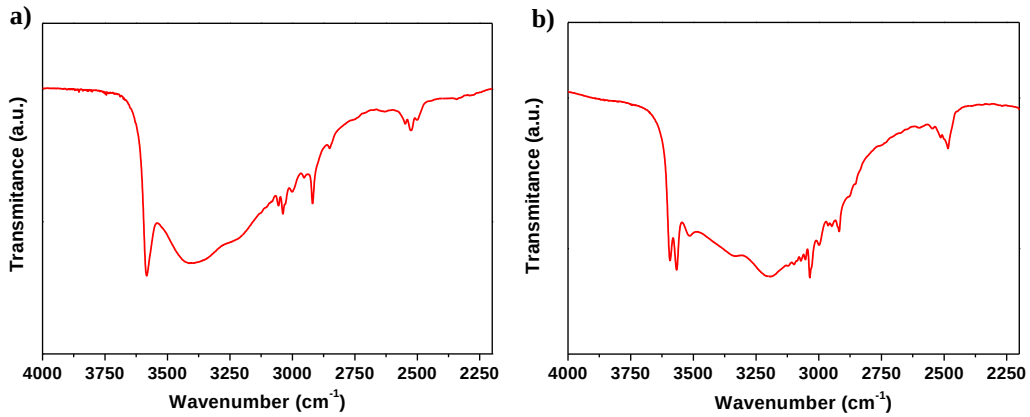

Figure 4.2.27. Details of IR spectra in the –OH stretching mode zone (4000-2250 cm^{-1}) for: **a) Ca-AEPF-13** and **b) Sr-AEPF-13**.

In the -CO_2^- stretching mode region (**Figure 4.2.28**), for **Ca-AEPF-13** bands were observed at: ~1605, ~1590, ~1550, ~1520 and ~1470 cm^{-1} (υ_{as}); and ~1425, ~1410 and ~1385 cm^{-1} (υ_s) (**Figure 4.2.28a**). In the case of this region for **Sr-AEPF-13** compound, in this region bands were observed at: ~1605, ~1590, ~1545, ~1520 and ~1475 cm^{-1} (υ_{as}); and ~1430, ~1415 and ~1390 cm^{-1} (υ_s) (**Figure 4.2.28b**).

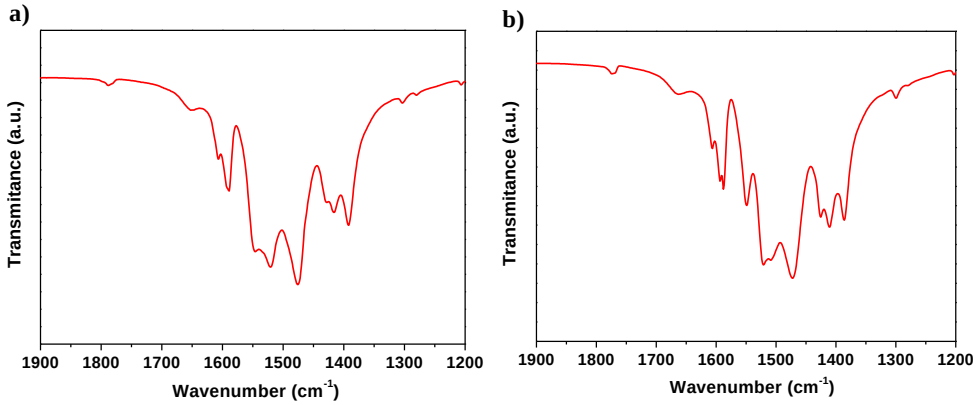

Figure 4.2.28. Details of IR spectra in the -CO_2^- stretching mode zone (1900-1200 cm^{-1}) for: **a) Ca-AEPF-13** and **b) Sr-AEPF-13**.

4.2.2.3.

Thermal Gravimetric Analyses

Thermal Gravimetric Analyses (TGA) curves for **Mg-AEPF-11**, **Mg-AEPF-12**, **Ca-AEPF-13** and **Sr-AEPF-13** are shown in **Figures 4.2.29-4.2.32**, respectively.

- Thermogravimetric profile of **Mg-AEPF-11** (**Figure 4.2.29**), shows a first weight loss of ~ 3.7% between ~ 30-220 ºC, consistent with the loss of physisorbed species (water, DEF molecules). The second weight loss of ~ 17.3% between ~ 220-445 ºC is consistent with the removal of the coordinated DEF molecules (calc. 15.3%). After these two initial weight losses of ~21%, the product gradually decomposes until a final weight loss of 69.7%, which indicates the partial loss of the organic linker $L_{(2)}^{-2}$ (~51.9% decomposition) (the decomposition percentage for organic linker was calculated considering MgO as the main residue). MgO phase was identified as a main residue by XRPD using the Joint Committee on Powder Diffraction Standards files (JCPDS file No.77-2179), together with an important amorphous contribution.

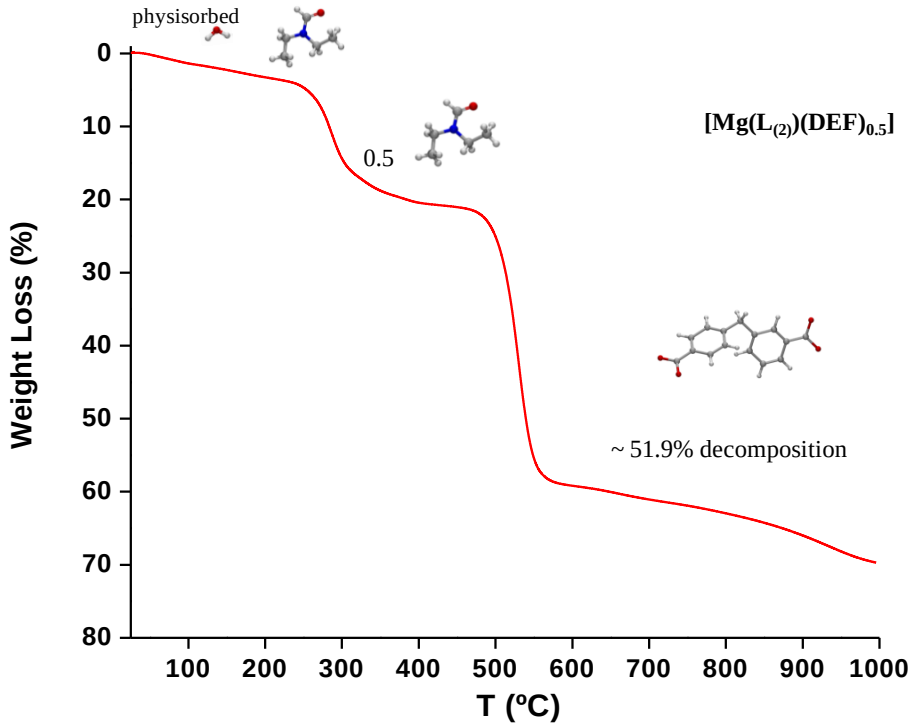

Figure 4.2.29. TGA profile for **Mg-AEPF-11**.

- Thermogravimetric profile of **Mg-AEPF-12** (**Figure 4.2.30**), shows a first weight loss of ~ 3.5% between ~30-115 ºC, consistent with the loss of physisorbed species (water, *n-prop* molecules, DMF molecules). Then, two consecutive processes can be seen between ~115-450 ºC with a unique weight loss of ~ 21.9%, consistent with the loss of *n-prop* molecules present in the pores and the acetate group (calc. 18.3%). Then, the compound gradually decomposes until a final mass loss of 69.7%, which indicates the partial loss of the organic linker (~74.5% decomposition) (the decomposition percentage for organic linker was calculated considering MgO as the main residue). MgO phase was identified as a main residue by XRPD (JCPDS file No.77-2179), together with an important amorphous contribution.

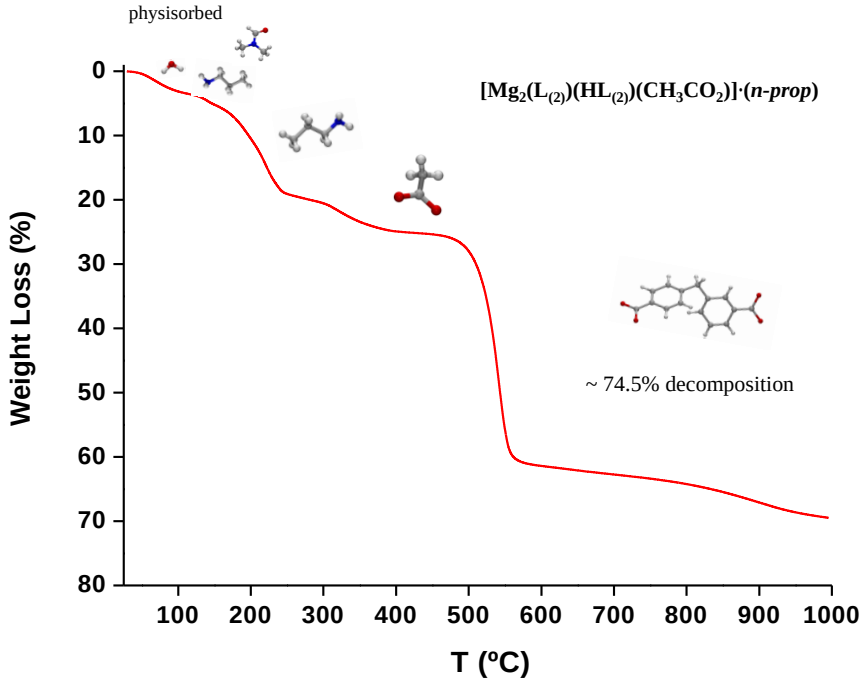

Figure 4.2.30. TGA profile for **Mg-AEPF-12**.

- Thermogravimetric profile of **Ca-AEPF-13** (**Figure 4.2.31**) shows a first weight loss of ~5.1% that starts at ~120 ºC consistent with the removal of coordinated water molecules (calc. 5.8%). The second weight loss of 55.0% at ~470 ºC corresponds to the partial decomposition of organic linker (~81.0% decomposition), which takes place in two successive processes (the decomposition percentage for organic linker was calculated considering $CaCO_3$ as the main residue). Although XRPD technique was

used to identify the residue, this was not possible due to the important contribution of an amorphous phase for the final product.

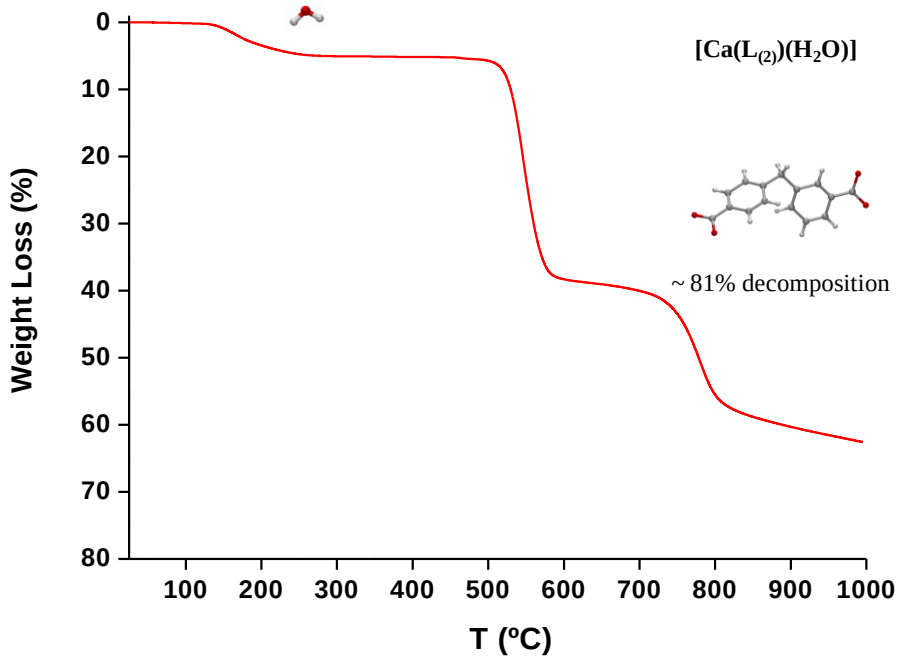

Figure 4.2.31. TGA profile for **Ca-AEPF-13**.

- Thermogravimetric profile of **Sr-AEPF-13** (**Figure 4.2.32**) shows a first weight loss of ~4.9% starting at ~120 ºC consistent with the removal of coordinated water molecules (calc. 5.0%). The second weight loss of 57.5% at ~425 ºC corresponds to the partial decomposition of organic linker (~97.5% decomposition), which takes place in two successive processes (the decomposition percentage for organic linker was calculated considering $SrCO_3$). The presence of some of the Bragg peaks which correspond to $SrCO_3$ phase (strontianite) were identified in the residue, compared with its standard JCPDS file (JCPDS file No. 05-0418).

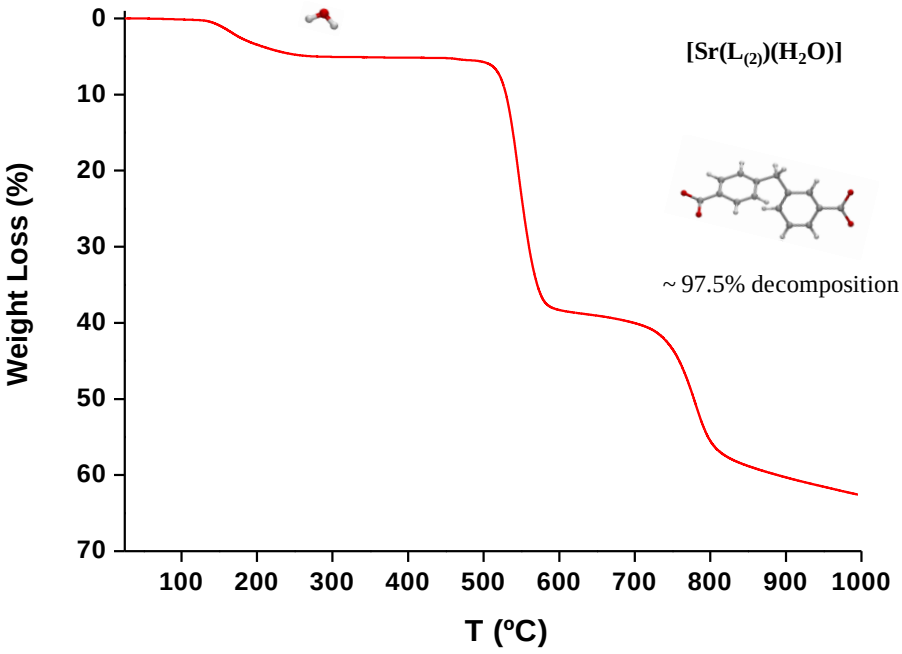

Figure 4.2.32. TGA profile for **Sr-AEPF-13**.

4.2.3.

Catalytic Experiments

The use of the $H_2L_{(2)}$ ligand as dicarboxylate linker has given rise to alkaline-earth MOFs with three different structural types. These materials were used as heterogeneous catalysts in the selective hydrogenation of styrene to ethylbenzene under mild conditions; the main results are shown in the following section.

Catalytic tests. Continuing with the catalytic studies performed with dicarboxylate **AEPFs** materials (*see* previous section), the catalytic properties of the four compounds presented in this chapter were also investigated. Thus, **Mg-AEPF-11**, **Mg-AEPF-12** and **AEPF-13** (**Ca-** and **Sr-**) were tested as catalysts for the hydrogenation of alkenes using styrene as substrate model under mild conditions (*see* Chapter 2 and **Scheme 4.2.1**).

Scheme 4.2.1. Scheme reaction of styrene reduction with H_2.

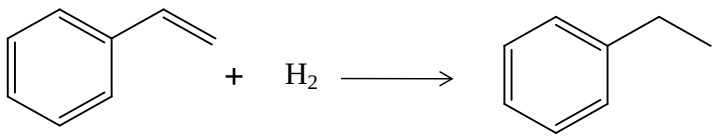

After optimising the catalytic conditions with the best catalyst to perform the styrene hydrogenation, the four catalysts were tested in the same conditions in order to compare their catalytic activity (323 K, 5 atm H_2, 1 mol% catalyst). **Mg-AEPF-11** and **Mg-AEPF-12** samples were heated at 150 ºC under vacuum overnight in order to evacuate the different physisorbed species determined by TGA in these materials (DMF, DEF, *n-prop*, among others). **AEPF-13** compounds, were heated at a higher temperature (170 ºC), in order to evacuate the coordinated water molecules. The obtained results are summarized in **Table 4.2.16** and **Figure 4.2.33**.

Table 4.2.16. Hydrogenation of styrene in toluene, at 323 K, 5 atm H_2, using 1 mol% catalyst.

Compound	Active Center	Time (min)	Conversion (%)	TOF (h^{-1})
AEPF-11	Mg^{+2}	45	100	221.1
AEPF-12	Mg^{+2}	45	100	167.5
Ca-AEPF-13	Ca^{+2}	90	100	207.2
Sr-AEPF-13	Sr^{+2}	30	100	365.1

As it is shown in **Table 4.2.16**, the best results were obtained with **Sr-AEPF-13**, for which the total and selective hydrogenation of styrene to ethylbenzene was achieved after 30 minutes (TOF= 365.1 h^{-1}). In all cases 100% selectivity was achieved toward ethylbenzene, in contrast with the data obtained for previously reported calcium and strontium homogeneous catalysts.[20,29] Moreover, in the studied conditions, 100% conversion was achieved in all cases: in 30 min for **Sr-AEPF-13**, 45 minutes for **Mg-AEPF-11** and **Mg-AEPF-12** and 90 minutes in the case of **Ca-AEPF-13**.

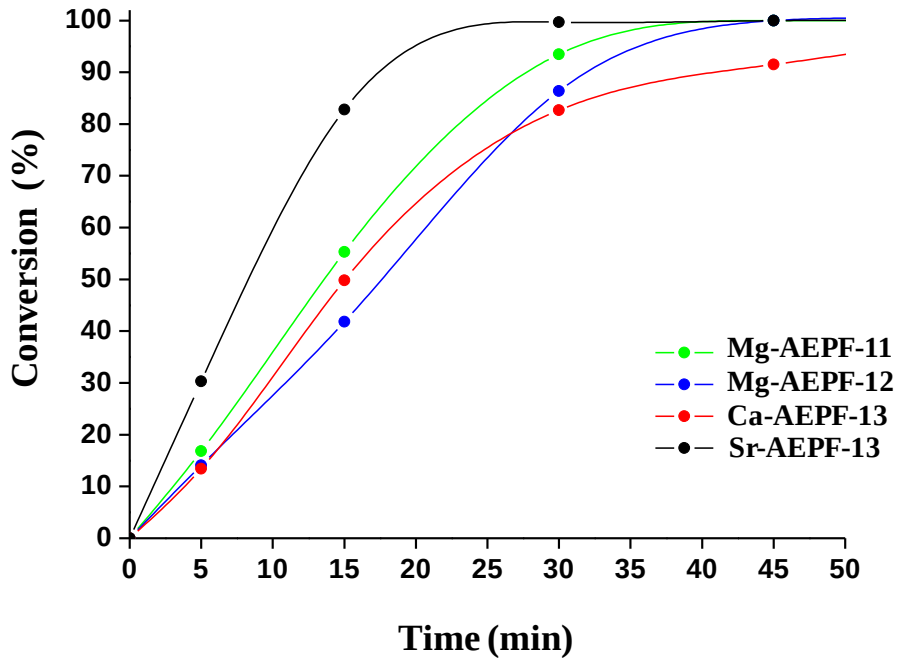

Figure 4.2.33. Kinetic profiles of styrene hydrogenation with **Mg-AEPF-11**, **Mg-AEPF-12** and **AEPF-13** (**Ca-** and **Sr-**) as catalysts, at 323 K, 5 atm H_2, using 1 mol%.

Taking into account the results obtained in the studied conditions, several conclusions can be drawn for each compound:

a) AEPF-11 and AEPF-12 structural types

As it was mentioned, in **Mg-AEPF-11** material DEF molecules are covalently coordinated to Mg^{+2} centers, blocking the potential pores in this material. On the other hand, in the case of **Mg-AEPF-12** a total accessible surface of 27.1% can be obtained after evacuating *n-prop* molecules from pores. However, contrary to what could be expected, the catalytic behaviour of both compounds is quite similar, with TOF values of 221.1 h^{-1} and 167.5 h^{-1}, for **Mg-AEPF-11** and **Mg-AEPF-12**, respectively. Therefore, it seems that the catalytic reaction for both compounds (**AEPF-11** and **AEPF-12**) may have taken place on the external surface.

b) AEPF-13 structural type

Concerning the **AEPF-13** structural type material, the best results were obtained when using Sr as metal center instead of Ca. Kinetic experiments were carried out to determine the apparent activation energy under the above described conditions (1% mol catalyst and 5 atm H_2), using different temperatures (333K, 323K, 313 K and 298K). Thus, taking into account the Arrhenius equation, the apparent E_a can be expressed as:

$$E_a = -RTlnv$$

where

E_a: Apparent activation energy ($J \cdot mol^{-1}$)
R: 8.314 $J \cdot K \cdot mol^{-1}$
T: Temperature (K)
v: Reaction rate

In **Figures 4.2.34** and **4.2.35**, the kinetic experiments performed to determine the E_a values for **Ca-AEPF-13** and **Sr-AEPF-13,** respectively, are shown. Together with the kinetic curves corresponding to each studied temperature, the representations of the natural logarithm of each kinetic curve rate (ln(*v*)) versus T^{-1} are depicted for both compounds. First of all, it is worth highlighting that the representation of ln(*v*) versus T^{-1} is lineal in both cases, which is in good agreement with a first order reaction. Thus, taking into account these analyses, the E_a values for styrene hydrogenation are: for **Ca-AEPF-13** ~5.4 $cal \cdot mol^{-1}$ and for **Sr-AEPF-13**, ~13.5 $cal \cdot mol^{-1}$.

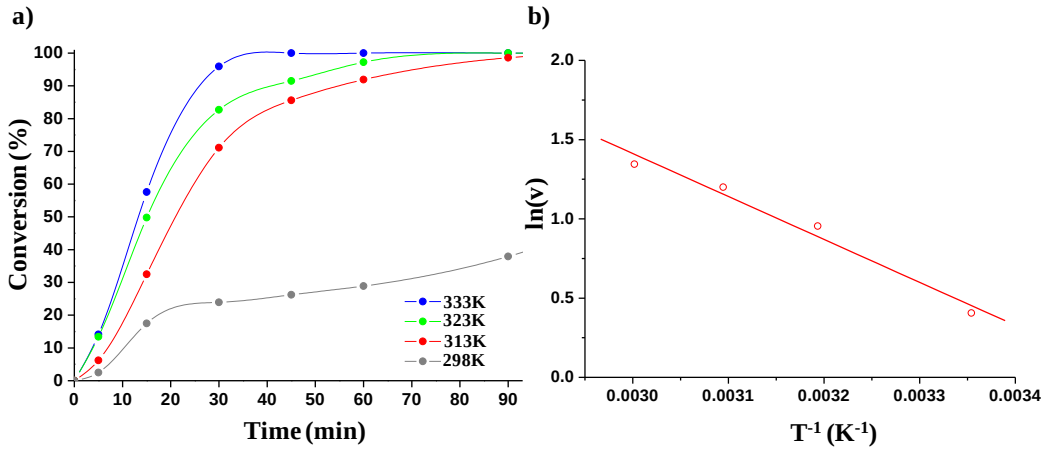

Figure 4.2.34. a) Kinetic profiles of styrene hydrogenation using **Ca-AEPF-13** as catalyst (at different temperatures, 5 atm H_2, using 1 mol%). **b)** Representation of ln(*v*) versus T^{-1} and the linear fit.

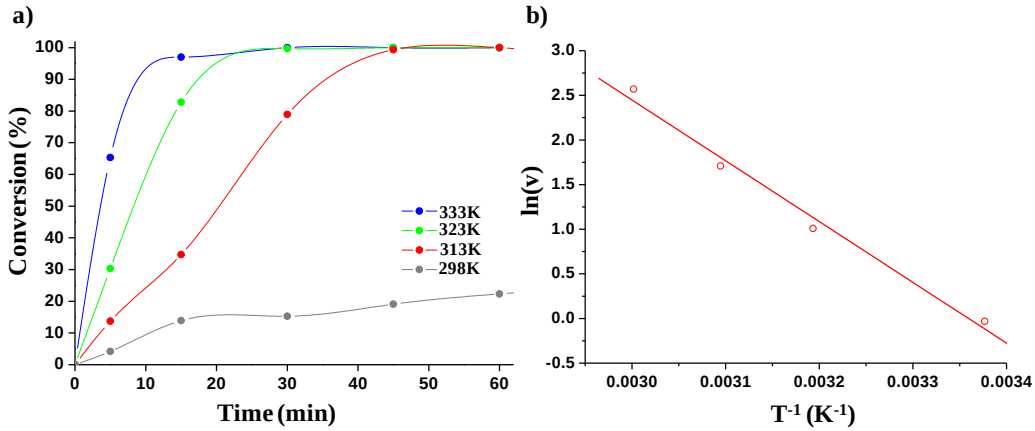

Figure 4.2.35. a) Kinetic profiles of styrene hydrogenation using **Sr-AEPF-13** as catalyst (at different temperatures, 5 atm H_2, using 1 mol%). **b)** Representation of ln(*v*) versus T^{-1} and the linear fit.

Recycling experiments. To investigate the lifetime, heterogeneity and the stability of the better catalyst (**Sr-AEPF-13**) in styrene hydrogenation, recycling experiments were performed employing the same catalyst in three consecutive reaction cycles. The observed activity is kept over the three cycles of reaction, although a slightly improvement in TOF value is observed in the second cycle (**Table 4.2.17** and **Figure 4.2.36**).

Table 4.2.17. Recycling experiments for styrene hydrogenation in toluene, at 313 K, 5 atm H_2, using 1 mol% **Sr-AEPF-13** as catalyst.

Cycle	TOF (h^{-1})	Time for total conversion (min)
1	165.1	45
2	226.5	45
3	175.9	60

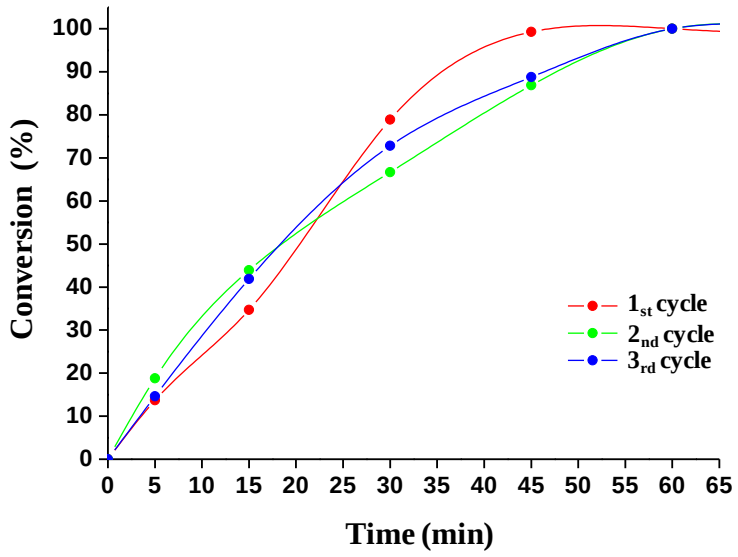

Figure 4.2.36. Kinetic profiles in three consecutive reaction cycles employing **Sr-AEPF-13** as catalyst.

Catalysts robustness. All catalysts employed in styrene hydrogenation were recovered by centrifugation, washed with toluene, and then characterized by X-ray powder diffraction (XRPD) to corroborate possible structural changes after reaction. Comparison of the XRPD patterns before and after the catalytic reactions confirms the robustness of the four compounds in the studied conditions (**Figures 4.2.37-4.2.40**). In the case of **Sr-AEPF-13**, the XRPD pattern after the third run (recycling experiments) is shown (**Figure 4.2.40**).

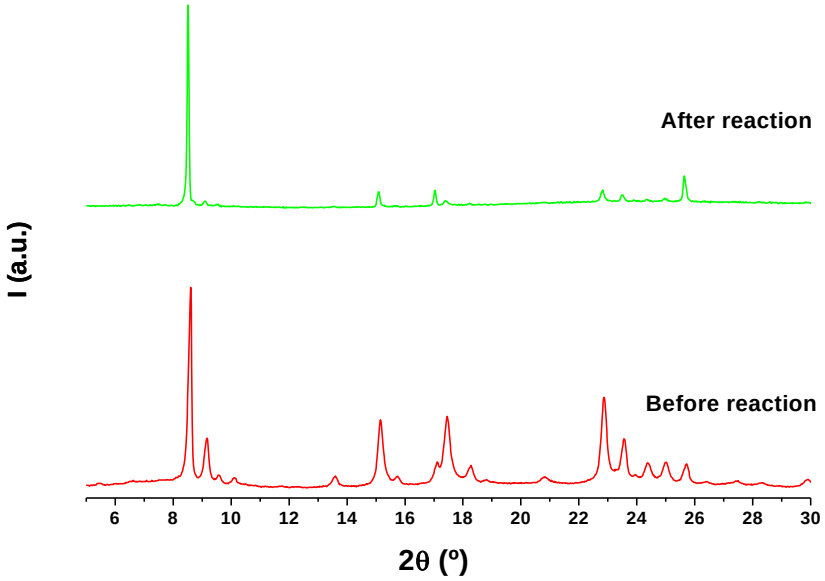

Figure 4.2.37. Comparison of the experimental XRPD pattern of **Mg-AEPF-11** after hydrogenation catalytic recycling experiments (green) with the pattern of the fresh sample before reaction (red).

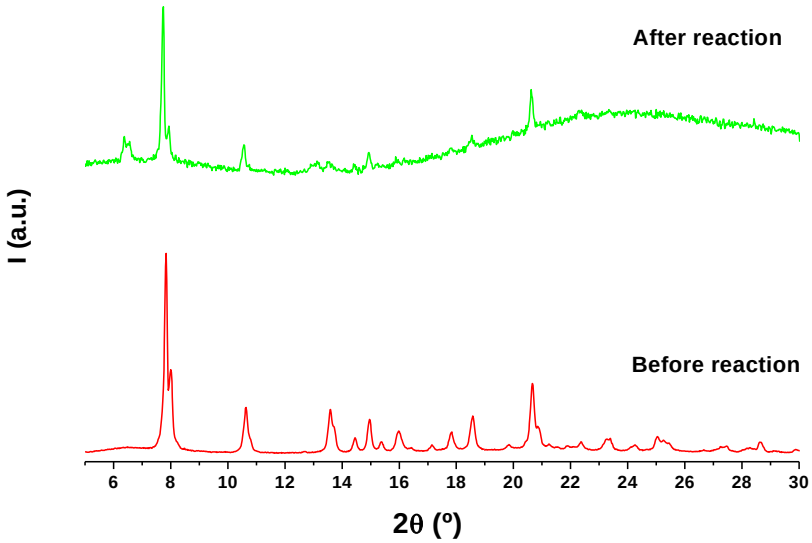

Figure 4.2.38. Comparison of the experimental XRPD pattern of **Mg-AEPF-12** after hydrogenation catalytic recycling experiments (green) with the pattern of the fresh sample before reaction (red).

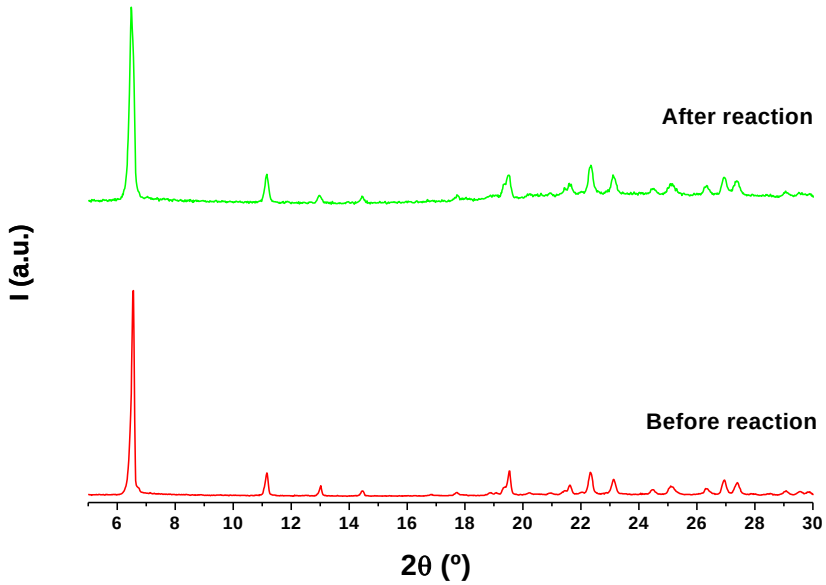

Figure 4.2.39. Comparison of the experimental XRPD pattern of **Ca-AEPF-13** after hydrogenation catalytic recycling experiments (green) with the pattern of the fresh sample before reaction (red).

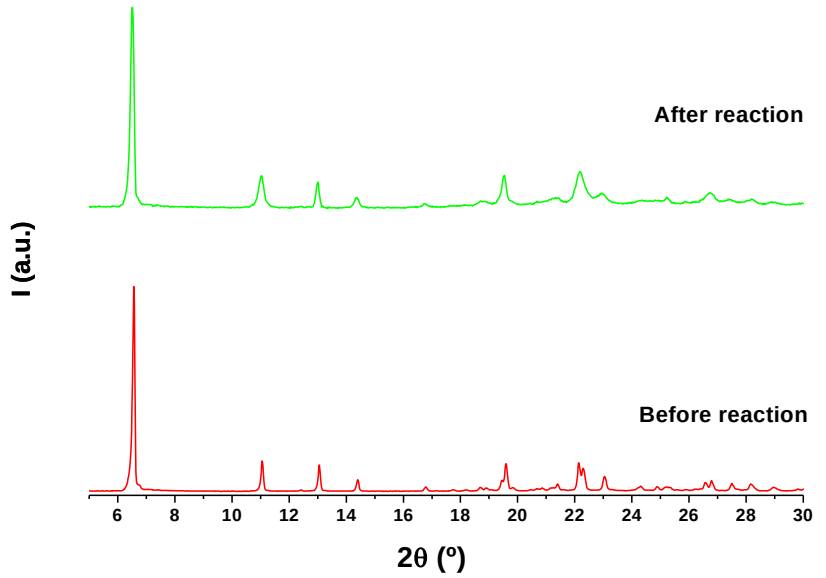

Figure 4.2.40. Comparison of the experimental XRPD pattern of **Sr-AEPF-13** after hydrogenation catalytic recycling experiments (green) with the pattern of the fresh sample before reaction (red).

References

1. Gándara, F.; Andrés, A. d.; Gómez-Lor, B.; Gutiérrez-Puebla, E.; Iglesias, M.; Monge, M. A.; Proserpio, D. M.; Snejko, N. *Cryst. Growth Des.*, **2008**, *8(2)*, 378.
2. Gándara, F.; Medina, M. E.; Snejko, N.; Gutiérrez-Puebla, E.; Proserpio, D. M.; Ángeles Monge, M. *CrystEngComm*, **2010**, *12*, 711.
3. Liu, Z.; Stern, C.; Lambert, J, B. *Organometallics*, **2009**, *28*, 84.
4. Blatov, V.A. *IUCrComput. Comm. Newslett.*, **2006**, *7*, 4. See also: http://www.topos.ssu.samara.ru.
5. Spek, A. L. *PLATON*: A multipurpose Crystallographic Tool, Utrecht University, Utrecht, Holland, **2005**.
6. Devic, T.; Horcajada, P.; Serre, C.; Salles, F.; Maurin, G.; Moulin, B.; Heurtaux, D.; Clet, g.; Vimont, A.; Grenéche, j. M.; Ouay, B. L.; Moreau, F.; Magnier, E.; Filinchuk, Y.; Marrot, J. M.; Lavalley, J. C.; Daturi, M.; Férey, F. *J. Am. Chem. Soc*., **2010**, *132(3)*, 1127-1136.
7. Volkringer, c.; Loiseau, T.;. Férey, G.; Warren, J. E.; Wragg, D. S.; Morris, R.E. *Solid State Sci.*, **2007**, *9*, 455.
8. Devautour-Vinot, S.; Maurin, G.; Henn, F.; Serre, C.; Devic. T.; Férey, G. *Chem. Commun.*, **2009**, 2733.
9. Apparent energy desorption value was calculated using the formula:

   $\Delta H_{des}=E_{AEPF-1}$ - ($E_{\text{AEPF-1(wo acetone)}}$ + E_{acetone}).

   where $E_{\text{AEPF-1(wo acetone)}}$=Energy of **AEPF-1** without acetone.
10. Lour, D.; Louer, M. J. *J. Appl. Crystallogr.*, **1972**, *5*, 271.
11. Boultif, A.; Louer, D. *J. Appl. Crystallogr.*, **1991**, *24*, 987.
12. Pawley, G. S. *J. Appl. Crystallogr.*, **1981**, *14*, 357.
13. Materials Studio Modelling 4.4, http://www.accelerys.com/mstudio/ms_modeling.
14. Favre-Nicolin, V.; Cerny, R. *J. Appl. Crystallogr.*, **2002**, *35*, 734.
15. Fox: Free Objects for Crystallography, http://objcryst.sourceforge.net.

16. Rietveld, H. M., *J. Appl. Crystallogr.* **1969**, *2*, 65.

17. Pan, L.; Olson, D. H.; Ciemnolonski, l. R.; Heddy, R.; Li, J. *Angew. Chem.*, **2006**, *118*, 632.

18. Pan, L.; Olson, D. H.; Ciemnolonski, l. R.; Heddy, R.; Li, J. *Angew. Chem. Int. Ed.*, **2006**, *45*, 616.

19. Spielmann, J.; Buch, F.; Harder, S. *Angew. Chem.*, **2008**, *120*, 9576.

20. Spielmann, J.; Buch, F.; Harder, S. *Angew. Chem. Int. Ed.*, **2008**, *47*, 9434.

21. Gauvin, r. M.; Buch,F.; Delevoye, L.; Harder, S. *Chem. Eur. J.*, **2009**, *15*, 4382.

22. Niu, S.; Hall, M. B. *Chem. Rev.*, **2000**, *100*, 353.

23. Rosi, N. L.; Kim, J.; Eddaoudi, M.; Chen, B.; O'Keeffe, M.; Yaghi, O. M. *J. Am. Chem. Soc.*, **2005**, *127(5)*, 1504-1518.

24. Sheldrick, G. M. *Acta. Crystallogr.*, **2008**, *A64*, 112-122.

25. Sheldrick, G. *Cell_Now*, Bruker-AXS, Inc., Madison, Wisconsin, USA, **2004**.

26. Bruker AXS Inc. *SAINTplus package*, Madison, Wisconsin, USA, **2007**.

27. Bruker AXS Inc. *TWINABS*, Madison, Wisconsin, USA, **2001**.

28. Delgado–Friedrichs, O.; O'Keeffe, M. *Acta. Crystallogr.*, **2003**, *B59*, 351.

29. Harder, S. *Chem. Rev.*, **2010**, *110(7)*, 3852.

Chapter 5

Effect of the introduction of chelating ancillary ligands

4,4'-(hexafluoroisopropylidene)*bis*(benzoic acid) ($H_2L_{(1)}$)

1,10-phenantroline (phen)

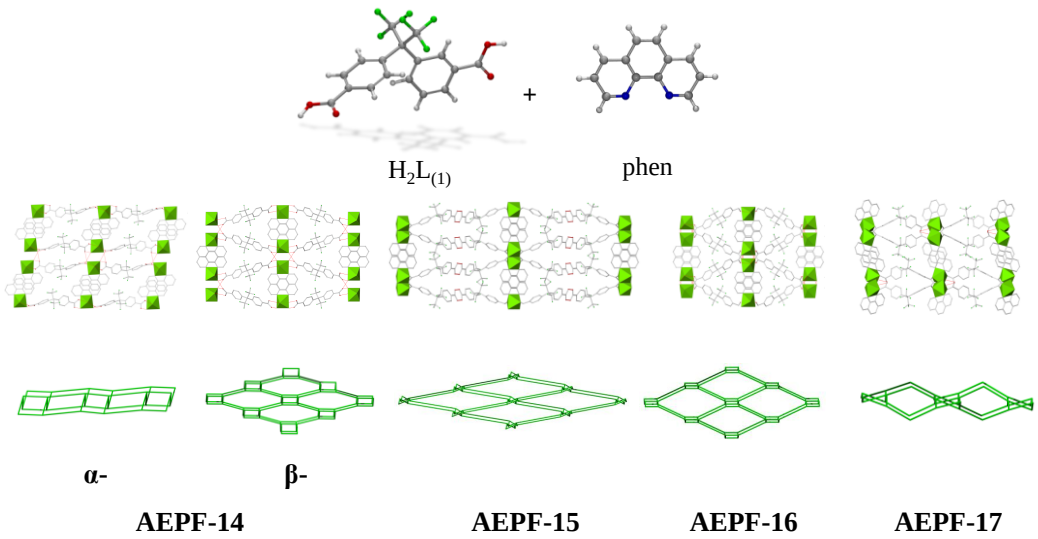

Abstract

Five new compounds based on Mg^{+2} ion, 4,4'-(hexafluoroisopropylidene)*bis*(benzoic acid) ($H_2L_{(1)}$) and 1,10-phenantroline (phen) ligands were obtained and characterized. These novel materials belong to five different structural types: **AEPF-14**, **AEPF-15**, **AEPF16** and **AEPF-17**. **AEPF-14** presents two polymorphic phases (**α-** and **β-**); **AEPF-15,** and **AEPF-16** are both 1D MOFs (**AEPF-16** owns a helical structure). Finally, **AEPF-17** is a layered material.

The hydrogen bond interactions found in the five compounds were taken into account to study the topology of their supramolecular nets. Then, in a next step, computational studies were performed to show the relative energy for the five obtained networks.

5.1.

Introduction

Concerning the MOFs design, the insertion of additional organic linkers in the synthesis media can have a crucial effect on the dimensionality of the resulting network, and therefore on its topology. In this context, the use of N-donor ligands as additional linkers to target a variety of networks architectures has been extensively studied. For instance, 4,4'-bipyridine (4,4-Bipy) possesses, at opposite ends of the molecule, monodentate donor nitrogen atoms, which coordinate in a linear ditopic manner similar to the shorter cyanide anion. Thus, 4,4'-Bipy can act as a longer linear spacer, and therefore extends the connections between nodes, resulting ideally in more open structures compared to analogous metal cyanides. On the other hand, a synthetic strategy that has been proved to be successful at controlling the metal coordination environment is the use of a terminal chelating ligand (ethylenediamine (en), 2,2'-bipyridine (2,2'-Bipy), 1,10-phenantroline (phen), among others) to cap sites of the metal to give a specific geometry. A classic example is the use of 4,4'-Bipy and en ligand to obtain Pd(II) molecular squares.[1]

The work presented in this chapter is addressed toward the use of the flexible fluoride dicarboxylate ligand 4,4'-(hexafluoroisopropylidene)*bis*(benzoic acid ($H_2L_{(1)}$) and an additional chelating aromatic N-donor ligand (phen) to obtain novel magnesium MOFs. On one hand, the use of $H_2L_{(1)}$ linker, which exhibits a bent geometry, has yet given rise to an interesting phenomenon of polymorphism in MOFs,[2] as well as very robust and promising materials with applications in heterogeneous catalysis and hydrogen storage.[3-4] On the other hand, the use of the phen ligand in the synthesis of magnesium MOFs can block sites of the typical octahedral geometry of Mg^{+2} ion, giving unexpected networks. Moreover, phen can induce supramolecular interactions such as π-π stacking.

This chapter encompasses five novel magnesium compounds, which exhibit 0D, 1D and 2D dimensionalities, and 2D and 3D supramolecular frameworks: a molecular magnesium material with polymorphism (named **AEPF-14**, **α-** and **β-** forms), a 1D MOF (**AEPF-15**), a 1D helical MOF (**AEPF-16**) and a 2D MOF (**AEPF-17**). The role that the synthesis conditions play in the obtaining of each phase has been

exhaustively studied. Moreover, a combination of topological comparative analyses with computational studies was performed to determine the relative energies for the five obtained networks.

5.2.

Effect of synthesis conditions

In the following sections of this chapter, five new magnesium compounds based on $H_2L_{(1)}$ and the ancillary phen ligand are going to be discussed both from the structural and the topological point of view. Thus, it has been proved that a wide variety of supramolecular frameworks can be obtained starting from the same primary building units (that is, octahedral Mg^{+2} ions as metallic centers and $H_2L_{(1)}$ and phen as ligands). The aim of this section is to emphasize the high influence of the synthetic procedure in the MOF structural design. The experiments performed during this investigation not only have led to isolate the highest number of compounds (in this case, all the compounds were obtained as pure phases unless **AEPF-15**), but also to understand which is the influence of the experimental variables that are implied in the obtaining of each magnesium material.

This study began with the observation that the hydrothermal reaction of magnesium acetate and $H_2L_{(1)}$ using phen as ancillary ligand at 160 ºC during 2 days gave rise to a non-homogenic crystalline sample (the composition of the reaction mixture was 1 Mg^{+2} / 1 phen / 1 $H_2L_{(1)}$ molar ratio). After careful analysis of this sample, several single crystals with different morphologies were identified, which were all of a size and quality suitable for their structure determination by single crystal X-Ray Diffraction experiments. In fact, three different crystal morphologies were observed, which corresponded to different novel magnesium compounds:

- **α-AEPF-14**, with formula **$[Mg(H_2O)_4(phen)]L_{(1)}$**
- **AEPF-15**, with formula **$[Mg(HL_{(1)})_2(phen)]$**
- **AEPF-16**, with formula **$[Mg(H_2O)_2(L_{(1)})(phen)]$**

From that moment on, the synthetic work was focussed on the rational optimization of **hydrothermal** synthesis conditions (**SC**) procedure to obtain these compounds as pure crystalline phases. In order to reach this objective, the effect of the

reaction temperature was systematically studied and the main results are going to be discussed in the following. In all cases, the composition of the reaction mixture was 1 Mg^{+2} / 1 phen / 1 $H_2L_{(1)}$ molar ratio (*see* Chapter 2, *Synthesis procedures*).

• **T= 160 ºC.** First of all, different experiments were performed at 160 ºC in order to study the effect of reaction time. As it is shown in **Table 5.1**, when the time of reaction was 1 hour, **α-AEPF-14** polymorph was isolated as a pure phase (**SC1**). When the time of reaction increased up to 2 and then to 3 hours (**SC2** and **SC3,** respectively), a mixture of **α-AEPF-14**, **AEPF-15** and **AEPF-16** was determined, in which **α-AEPF-14** was the principal component. After two days of reaction, **AEPF-15** compound became the principal component of the mixture (**SC4**).

• **T= 170 ºC.** The effect of increasing the temperature of reaction up to 170 ºC was then investigated. The main results are shown in **Table 5.1** (**SC5-SC8**). Thus, when the time of reaction was 1 hour, a mixture of **α-AEPF-14** and **AEPF-15** was found (**SC5**) (~50% of each phase was obtained). When the time of reaction increased up to 2 and then to 3 hours **(SC6** and **SC7**, respectively), the main component of the mixture was **AEPF-15,** together with traces of **AEPF-16**. The same results were obtained increasing the time of reaction up to 2 days **(SC8).**

Table 5.1. Effect of synthesis conditions used during the optimization under hydrothermal conditions at 160 ºC and 170ºC.

SC	T (ºC)	t (h)	Phase
1	160	1	**α–AEPF-14**
2	160	2	**α–AEPF-14 > AEPF-15, AEPF-16**
3	160	3	**α-AEPF-14 > AEPF-15, AEPF-16**
4	160	48	**AEPF-15 > α-AEPF-14, AEPF-16**
5	170	1	**α-AEPF-14, AEPF-15**
6	170	2	**AEPF-15 > AEPF-16**
7	170	3	**AEPF-15 > AEPF-16**
8	170	48	**AEPF-15 > AEPF-16**

• **T= 180 ºC.** Since it was proved that the reaction temperature had an important effect in this system, several experiments were then performed at 180 ºC and the effect of this variation was studied. In order to isolate **AEPF-15** and **AEPF-16,** and taking into account the tendencies observed at 160 ºC and 170 ºC, in this step the effect of the reaction time was studied exploring a longer interval of time (1, 5 and 10 days of

reaction). The main results are shown in **Table 5.2** (**SC9-SC11**). Under these hydrothermal conditions, when the time of reaction was 1 day, a mixture of **AEPF-16** and a new phase named **AEPF-17** was obtained (**SC9**) (~50% of each). Increasing the time of reaction up to 5 and 10 days (**SC10** and **SC11**, respectively), the contribution of **AEPF-17** in the mixture increased. However, it was not possible to obtain neither of the two compounds as pure phases.

At this point, the study of **pH** was also considered as an additional variable. Thus, in a next step the effect of the pH increasing up to 7 using a NaOH solution (0.1M) was investigated. The main results of these experiments are shown in **Table 5.2** (**SC12-SC14**). By comparison of the sample obtained after 1 day of reaction at pH=7 (**SC12**) to that obtained without varying of the pH (pH=6, **SC9**), it could be concluded that a higher pH value favours the formation of **AEPF-16** instead of **AEPF-17**. Finally, when the time of reaction is increased up to 5 days (**SC13**), pure **AEPF-16** was successfully isolated (the same result is obtained after 10 days, **SC14**).

Table 5.2. Effect of synthesis conditions used during the optimization under hydrothermal conditions at 180 ºC, at pH=6 and pH=7.

SC	T (ºC)	t (days)	pH	Phase
9	180	1	6	**AEPF-16, AEPF-17**
10	180	5	6	**AEPF-17 > AEPF-16**
11	180	10	6	**AEPF-17> AEPF-16**
12	180	1	7	**AEPF-16 > AEPF-17**
13	180	5	7	**AEPF-16**
14	180	10	7	**AEPF-16**

- **T= 200 ºC.** Once **AEPF-16** compound was obtained as a pure crystalline phase, the next aim was to isolate **AEPF-17**. In order to reach this objective, a series of experiments were carried out at 200 ºC and the obtained results are shown in **Table 5.3**. Using these hydrothermal conditions, when the time of reaction was 1 day, a mixture of **AEPF-16** as a major component and **AEPF-17** was obtained (**SC15**). Then, the same tendency than the one described at 180 ºC is observed; that is, **AEPF-17** becomes the major mixture component when the time of reaction is increased (**SC16-SC17**). However, yet under these conditions it was not possible to isolate **AEPF-17**.

Table 5.3. Effect of synthesis conditions used during the optimization under hydrothermal conditions at 180 ºC and 200ºC.

SC	T (ºC)	t (days)	Phase
9	180	1	**AEPF-16, AEPF-17**
10	180	5	**AEPF-17 > AEPF-16**
11	180	10	**AEPF-17 > AEPF-16**
15	200	1	**AEPF-16 > AEPF-17**
16	200	5	**AEPF-16, AEPF-17**
17	200	10	**AEPF-17 > AEPF-16**

Solvothermal conditions were also optimized in order to obtain **AEPF-17** as a pure crystalline phase. In our case a mixture of acetone (Me_2CO) and water was chosen as solvent media, using different ratios. It is worth mentioning that, although a wide variety of conditions were investigated during this work (the studied variables were: time, temperature and H_2O:Me_2CO volume ratio), at the beginning all the experiments resulted in the formation of oils or liquids.

Unexpectedly, during the development of this investigation it was observed that the heating rate played an important role. Up to the moment, all the experiments were performed using a fast heating treatment of the reactor up to the desired temperature. However, at this point, certain hydrothermal conditions were chosen (**SC16**) and the reaction was then repeated by using a slow heating treatment (**SC18**). Surprisingly, a new compound was determined (named **β-AEPF-14**, which is a polymorph of **α-AEPF-14**), together with an important amorphous contribution.

Taking into account this interesting result, the solvothermal optimisation procedure was then carried out using slow heating treatments (T= 200 ºC and 5 days reaction time). During the optimisation process under solvothermal conditions, the polarity of the reaction media (H_2O:Me_2CO volume ratio) was systematically changed and the main results are presented in **Table 5.4**. Thus, when the polarity of the reaction media was decreased (H_2O:Me_2CO volume ratios= 2:1 and 1:1), the **β-AEPF-14** polymorph was successfully obtained (**SC21** and **SC22**, respectively). In addition, at H_2O:Me_2CO volume ratio of 20:1, **AEPF-17** compound was successfully synthesised as a pure phase (**SC19**). Finally, when the mixture is principally or totally composed by Me_2CO (**SC23** and **SC24**, respectively), the solvothermal reactions resulted in the formation of oils which could not be characterized.

Table 5.4. Effect of synthesis conditions used during the optimization under solvothermal conditions.

SC	T (ºC)	t(days)	H_2O : Me_2CO	Phase	Heating
16	200	5	1:0	**AEPF-16, AEPF-17**	Fast
18	200	5	1:0	**β-AEPF-14,** Amorphous	Slow
19	200	5	20:1	**AEPF-17**	Slow
20	200	5	5:1	Amorphous	Slow
21	200	5	2:1	**β-AEPF-14**	Slow
22	200	5	1:1	**β-AEPF-14**	Slow
23	200	5	1:5	**-**	Slow
24	200	5	0:1	**-**	Slow

To summarize all mentioned above, after rational optimising the synthesis procedures:

1. Two **AEPF-14** polymorphs were obtained as pure crystalline phases under hydrothermal conditions (**α**-form, **SC1**) and solvothermal conditions (**β**-form, **SC21**).
2. In addition, **AEPF-16** compound was also isolated during the study of the effect of pH variations under hydrothermal conditions (**SC13**).
3. In the case of **AEPF-17** (as it occurs for **β-AEPF-14)** it was demonstrated the need to perform a slow heating treatment to isolate the compound under solvothermal conditions **(SC19).**
4. Unfortunately, it was not possible to synthesise **AEPF-15** as a pure phase as it was always mixed with **AEPF-16** compound.

5.2.1.

Summary of synthesis conditions

To clarify the information presented in this section, **Schemes 5.1-5.2** summarize the synthesis optimization procedures carried out under hydrothermal and solvothermal conditions, respectively.

Scheme 5.1. Summary of the hydrothermal conditions optimization.

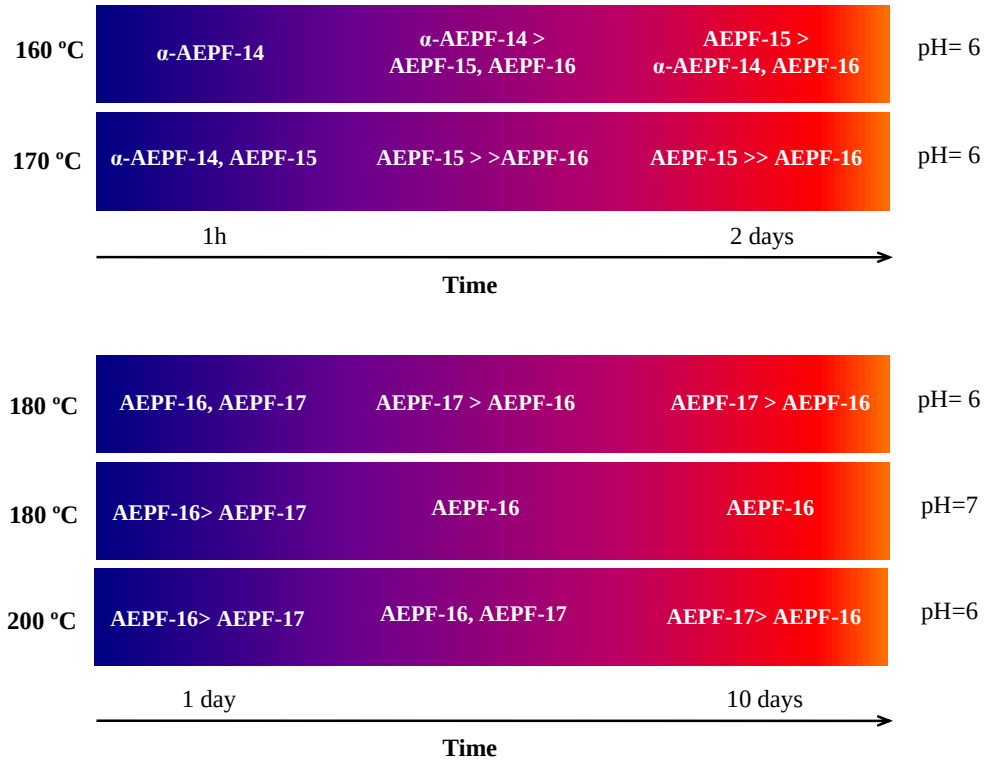

Scheme 5.2. Summary of the solvothermal conditions optimization.

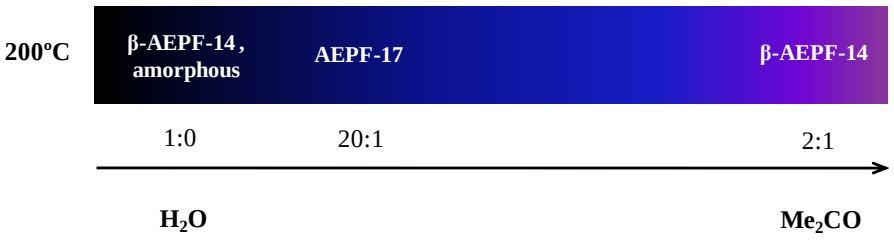

5.3.

Crystal structure description and topological analyses

As it was explained in the previous section of this chapter, after carefully optimizing the hydro- or solvothermal synthesis conditions, suitable single crystals were obtained for all the compounds presented in this chapter (**AEPF-14** (**α-** and **β-** polymorphs), **AEPF-15**, **AEPF-16** and **AEPF-17**). In the following, the structural features and the topological analyses for all of them are shown.

5.3.1.

Mg-AEPF-14

The reaction between $H_2L_{(1)}$ and magnesium acetate, using phen as an ancillary ligand, gives rise to the **[Mg(phen)(H_2O)$_4$]$L_{(1)}$** compound (**AEPF-14**). This compound presents two different polymorphs, named **α-** and **β-**, which have been isolated under optimized hydrothermal and solvothermal conditions, respectively.

The monoclinic **α-AEPF-14** polymorph crystallizes in the $P2_1/c$ space group. The cell parameters determined in its structure are: a = 13.2011(3) Å, b = 7.6121(2) Å, c = 31.0107(6) Å, β = 99.867(1) ° and V = 3070.1(1) Å^3. The orthorhombic **β-AEPF-14** polymorph crystallizes in the *Pnna* space group. The cell parameters determined in its crystal structure are: a = 7.306(2) Å, b = 32.602(1) Å, c = 12.544(4) Å and V = 2988.1(2) Å^3.

The ORTEP representations of **α-AEPF-14** and **β-AEPF-14** asymmetric units are shown in **Figures 5.1-5.2** and the main crystallographic and refinement data for both compounds are shown in **Tables 5.5-5.6**. As it is shown in the **α-AEPF-14** ORTEP representation, the asymmetric unit comprises one Mg^{+2} ion, one phen, one $L_{(1)}^{-2}$ and four coordinated water molecules. In the case of the **β-**polymorph the asymmetric unit consists of a half of the **α-**polymorph.

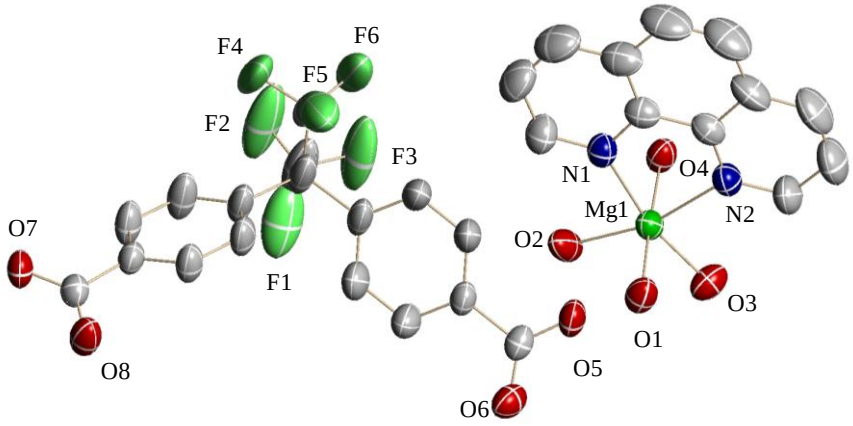

Figure 5.1. ORTEP representation of **α-AEPF-14** asymmetric unit. Ellipsoids are displayed at the 50% probability level. Hydrogen atoms were omitted for clarity.

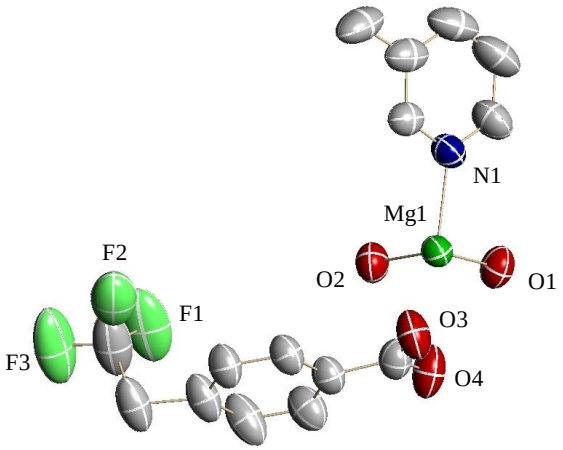

Figure 5.2.ORTEP representation of **β-AEPF-14** asymmetric unit. Ellipsoids are displayed at the 50% probability level. Hydrogen atoms were omitted for clarity.

Table 5.5. Crystallographic and refinement data for **α-AEPF-14** compound.

Identification code	α-AEPF-14
Empirical formula	$C_{29}H_{24}F_6MgN_2O_8$
Formula weight	666.81
Temperature	296(2) K
Wavelength	1.54178 Å
Crystal system	Monoclinic
Space group	$P2_1/c$
Unit cell dimensions	a = 13.2022(2) Å α = 90° b = 7.6135(1) Å β = 99.863(1)° c = 31.0128(5) Å γ = 90°
Volume	3071.18(8) $Å^3$
Z	4
Density (calculated)	1.442 Mg/m^3
Absorption coefficient	1.302 mm^{-1}
F(000)	1368
Crystal size	0.20 x 0.05 x 0.05 mm^3
Theta range for data collection	2.89 to 62.38°
Index ranges	-15<=h<=15, -5<=k<=8, -35<=l<=35
Reflections collected	23890
Independent reflections	4821 [R(int) = 0.0296]
Completeness to theta = 62.38°	98.6%
Absorption correction	Semi-empirical from equivalents
Max. and min. Transmission	0.9377 and 0.7807
Refinement method	Full-matrix least-squares on F^2
Data / restraints / parameters	4821 / 8 / 447
Goodness-of-fit on F^2	1.035
Final R indices [I>2sigma(I)]	R_1 = 0.0464, wR_2 = 0.1191
R indices (all data)	R_1 = 0.0650, wR_2 = 0.1322
Largest diff. peak and hole	0.323 and -0.392 e.$Å^{-3}$

Table 5.6. Crystallographic and refinement data for **β-AEPF-14** compound.

Identification code	β-AEPF-14
Empirical formula	$C_{29}H_{24}F_6MgN_2O_8$
Formula weight	666.81
Temperature	296(2) K
Wavelength	1.54178 Å
Crystal system	Orthorhombic
Space group	*Pnna*
Unit cell dimensions	a = 7.3064(2) Å α = 90° b = 32.6024(10) Å β = 90° c = 12.5442(4) Å γ = 90°
Volume	2988.11(16) $Å^3$
Z	8
Density (calculated)	1.482 Mg/m^3
Absorption coefficient	1.338 mm^{-1}
F(000)	1368
Crystal size	0.15 x 0.10 x 0.05 mm^3
Theta range for data collection	2.71 to 63.34°
Index ranges	-8<=h<=4, -36<=k<=37, -14<=l<=14
Reflections collected	20793
Independent reflections	2434 [R(int) = 0.0726]
Completeness to theta = 63.34°	99.3%
Absorption correction	Semi-empirical from equivalents
Max. and min. Transmission	0.9361 and 0.8245
Refinement method	Full-matrix least-squares on F^2
Data / restraints / parameters	2434 / 4 / 226
Goodness-of-fit on F^2	1.055
Final R indices [I>2sigma(I)]	R_1= 0.0460, wR_2= 0.1261
R indices (all data)	R_1= 0.0548, wR_2= 0.1329
Extinction coefficient	0.0031(3)
Largest diff. peak and hole	0.201 and -0.280 e.$Å^{-3}$

In both **AEPF-14** polymorphs, Mg^{+2} ions are hexa-coordinated to four oxygen atoms coming from water molecules and two nitrogen atoms of one phen ligand, giving MgN_2O_4 octahedra. These inorganic polyhedra, which can be considered as the inorganic primary building units (PBUs), do not directly coordinate to carboxylate groups of $L_{(1)}^{-2}$ ligand. The average distances Mg-O and Mg-N for these polyhedra are the same for both polymorphs: ~2.04 Å and ~2.23 Å, respectively (**Table 5.7**). These differences in the bond distances provoke a marked distortion in the inorganic octahedra found for **AEPF-14** compounds (**Figure 5.3a-5.3c**).

Table 5.7. Interatomic distances in the coordination sphere of the MgN_2O_4 polyhedra for **α-AEPF-14** and **β-AEPF-14**.

Bond	Distance (Å)
α - AEPF-14	
Mg(1)-O(1)w	2.044(2)
Mg(1)-O(2)w	2.031(2)
Mg(1)-O(3)w	2.007(2)
Mg(1)-O(4)w	2.050(2)
Mg(1)-N(1)p	2.224(2)
Mg(1)-N(2)p	2.240(2)
β- AEPF-14	
Mg(1)-O(1)w	2.043(8)
Mg(1)-O(1)^{1}w	2.028(9)
Mg(1)-O(2)w	2.017(7)
Mg(1)-O(2)^{1}w	2.057(8)
Mg(1)-N(1)p	2.223(9)
Mg(1)-N(1)^{1}p	2.238(9)

Symmetry transformations used to generate equivalent atoms:
^{1} -x+1/2,-y+1,z

Ow: oxygen atom coming from a water coordination molecule. Np: nitrogen atom coming from a phen ligand.

Concerning the structural differences between the two polymorphic forms of **AEPF-14**, it is worth highlighting that the supramolecular interactions determined for **α-** and **β-** forms are different. In both cases the main supramolecular interactions are hydrogen bonds between water coordination molecules and $L_{(1)}^{-2}$ carboxylate groups. While in **α-AEPF-14** eight different types of strong hydrogen bonds are determined, in the case of **β-AEPF-14** only three different types of strong hydrogen are found. In order

to clarify this point, which is crucial to understand the supramolecular nets that are described for the two polymorphs, the distances and angles of hydrogen bonds for **AEPF-14** compounds were analysed and presented in **Table 5.8.**

Table 5.8. Distances and angles of hydrogen bonds found in **AEPF-14** compounds.

D-H···A[1]	D-H[2]	H···A[3]	D···A[4]	<D-H···A[5]
α - AEPF-14				
O(1)w-H(1A)w ··· O(5)c	0.96(2)	1.80(2)	2.753(3)	170(3)
O(1)w-H(1B)w ··· O(7)c [1]	0.98(2)	1.80(2)	2.777(2)	172(3)
O(2)w-H(2A)w ··· O(6)c [2]	0.97(2)	1.73(2)	2.693(3)	171(3)
O(2)w-H(2B)w ··· O(7)c [3]	0.96(2)	1.88(2)	2.795(3)	159(4)
O(3)w-H(3A)w ··· O(8)c [1]	0.99(2)	1.62(2)	2.591(3)	167(4)
O(3)w-H(3B)w ··· O(6)c [4]	0.96(2)	1.76(2)	2.717(3)	173(3)
O(4)w-H(4A)w ··· O(5)c [2]	0.98(2)	1.74(2)	2.713(2)	177(3)
O(4)w-H(4B)w ··· O(7)c [5]	0.97(2)	1.83(2)	2.760(3)	161(3)
Symmetry operators codes				
[1] x, -y+1/2, z+1/2	[3] -x+2, y+1/2, -z+3/2		[5] x, -y+3/2, z+1/2	
[2] x, y+1, z	[4] -x+2, -y+1, -z+2			
β - AEPF-14				
O(3)w-H(3A)w ··· O(2)c [1]	0.98(2)	1.65(2)	2.625(2)	172(4)
O(3)w-H(3B)w ··· O(2)c [2]	0.96(2)	1.64(2)	2.596(2)	172(2)
O(4)w-H(4A)w ··· O(1)c [3]	0.99(2)	1.68(2)	2.671(2)	174(3)
Symmetry operators codes				
[1] -x+1/2, -y+1, z	[2] -x+1, -y+1, -z+1		[3] x-1, y, z	

D: donor atom, A: acceptor atom. [1]Names of donor, hydrogen and acceptor atoms involved in the hydrogen bond. [2] Distance D – A. [3]Distances H – A. [4]Distance D – A. [5] Angle D – H – A.

Ow: oxygen atom coming from a water coordination molecule. Oc: oxygen atom coming from a carboxylate group.

As it is depicted in **Figures 5.3b-5.3d**, if these hydrogen bond interactions are taken into account, MgN_2O_4 polyhedra are bridged *via* the carboxylate $L_{(1)}^{-2}$ linkers

giving rise to inorganic chains parallel to the *b* axis (for **α**-polymorph) and the *a* axis (for **β**-polymorph).

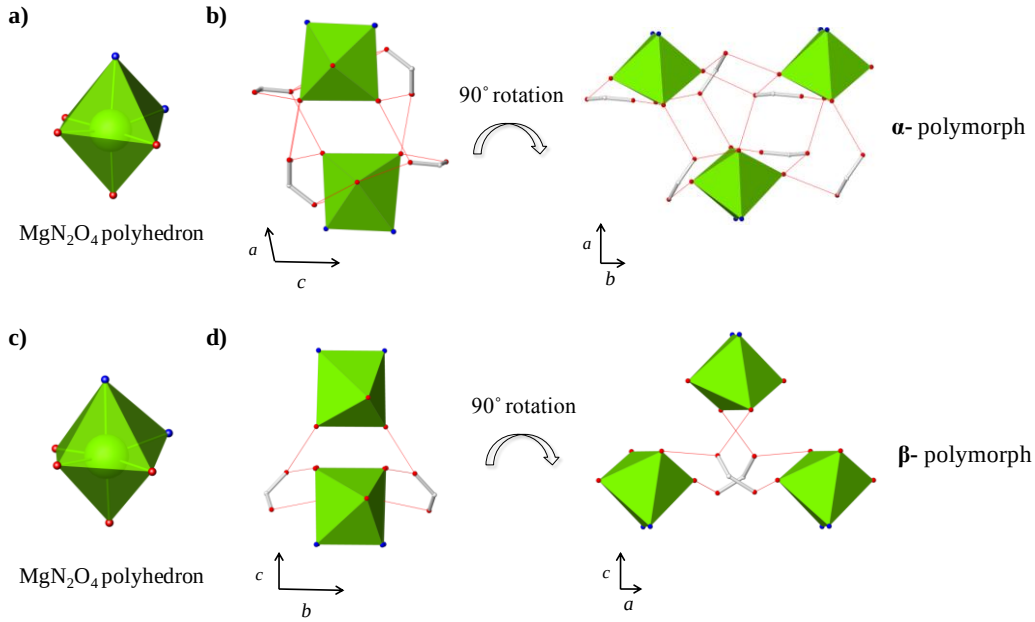

Figure 5.3. a) Inorganic PBUs and **b)** chains described when hydrogen bonds (in red) are taken into account for **α-AEPF-14**. **c)** Inorganic PBUs and **d)** chains described when hydrogen bonds (in red) are taken into account for **β-AEPF-14**.

Moreover, in the case of **α-AEPF-14** compound, each chain is joint to other two chains along the *c* axis via $L_{(1)}^{-2}$ linker, giving rise to layers. However, in the case of **β-AEPF-14** compound, a 3D net can be described, as each chain is linked to other four chains *via* the $L_{(1)}^{-2}$ ligand (**Figure 5.4**).

Besides, it is worth mentioning the presence of π-π stacking interactions along the *a* axis among $L_{(1)}^{-2}$ aromatic rings in **β-AEPF-14** (with distances among centroids of 3.655 Å). However, in the case of the **α-** form, the shorter distance between aromatic rings ~3.997 Å evidences the absence of this kind of interaction.

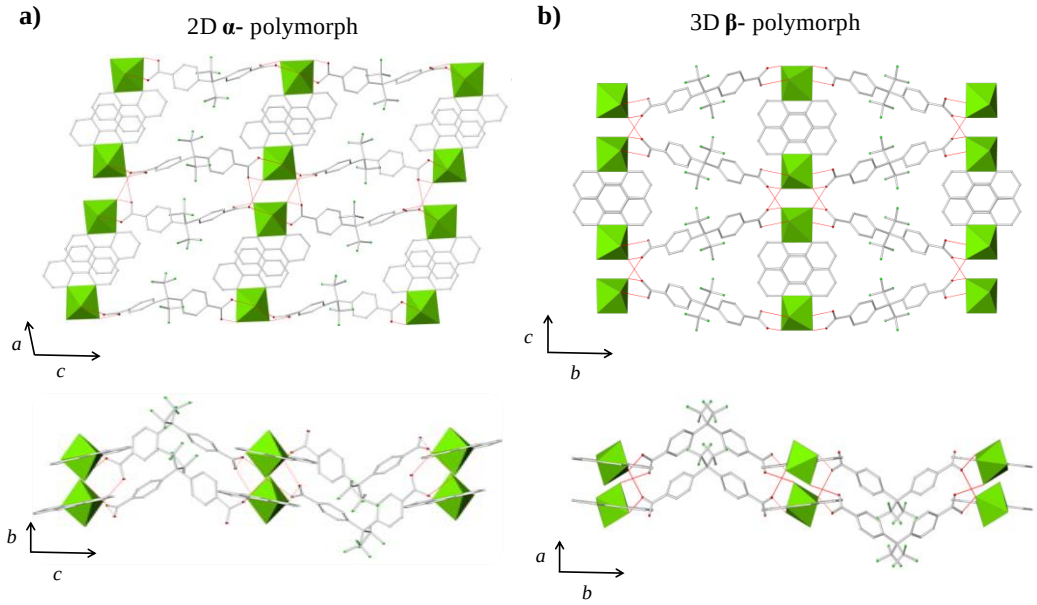

Figure 5.4. Details of the supramolecular nets built up from the junction of MgN_2O_4 polyhedra chains through hydrogen bonds for the two polymorphic forms of **AEPF-14** in different orientations: **a)** for **α**-form and **b)** for **β**-form.

Taking into account the flexibility of the organic linker, the two **AEPF-14** polymorphic forms have been also compared by analysing the conformation of $L_{(1)}^{-2}$ using some geometrical parameters (**θ** angle, **ω** dihedral angle and **d** distance) (**Figure 5.5).** Thus, as it is shown in **Table 5.9**, although the $L_{(1)}^{-2}$ conformations are quite similar in both polymorphs, the **α**-form has **θ** and **ω** values which are lower than in the case of the **β**-form, giving rise to a shorter **d** distance (d_α= 9.567 Å and d_β= 9.831 Å).

Figure 5.5. Definition of **θ** angle, **ω** dihedral angle and **d** distance used to describe the $L_{(1)}^{-2}$ linker conformation.

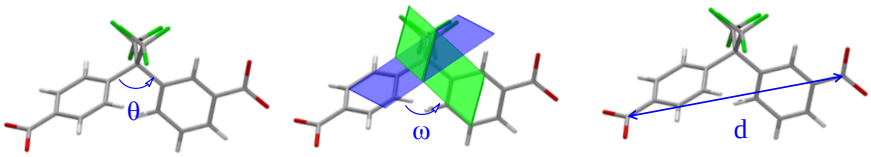

Table 5.9. **θ** angle, **ω** dihedral angle and **d** distance values determined for $L_{(1)}^{-2}$ linker in **AEPF-14** polymorphs.

Polymorph	θ (º)	ω (º)	d (Å)
α	109.4	69.35	9.567
β	112.0	72.56	9.831

Regarding the accessible free space of both **AEPF-14** polymorphs, it is worth mentioning that while the **β**-polymorph does not have any accessible free space in its structure, the **α**-polymorph has a 4.6% (140.4 $Å^3$ per unit cell), as computed by using PLATON[5] (SOLV mode).

To consider topological features of **AEPF-14**, the hydrogen bonds determined for both polymorphs are taken into account. The topological simplifications for **AEPF-14** polymorphs were performed taking into account the rod-packing phenomenon in MOFs.[6] Thus, the topological simplifications were carried out considering the infinite (-Mg-O···O-O···O-Mg-)$_\infty$ rods found in **AEPF-14** polymorphs as the inorganic secondary building units (SBUs) (the linker was simplified as O-O) (**Figures 5.6-5.7**).

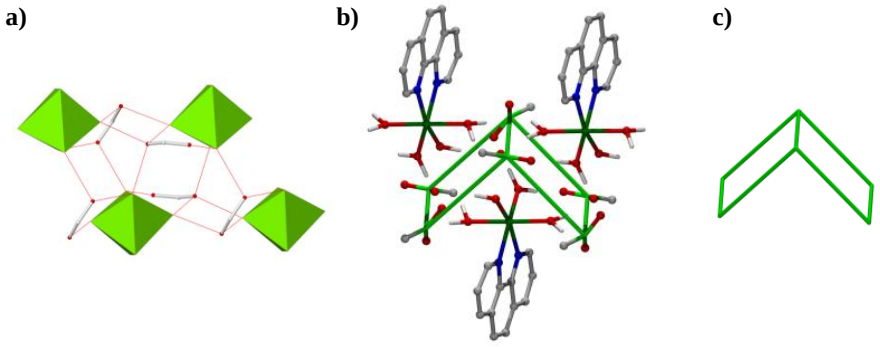

Figure 5.6. **a)** Detail of the MgN_2O_4 chains in **α-AEPF-14**, **b)** topological simplifications performed to describe the (-Mg-O···O-O···O-Mg-)$_\infty$ rods as the inorganic SBUs and **c)** simplified SBU in **α-AEPF-14**.

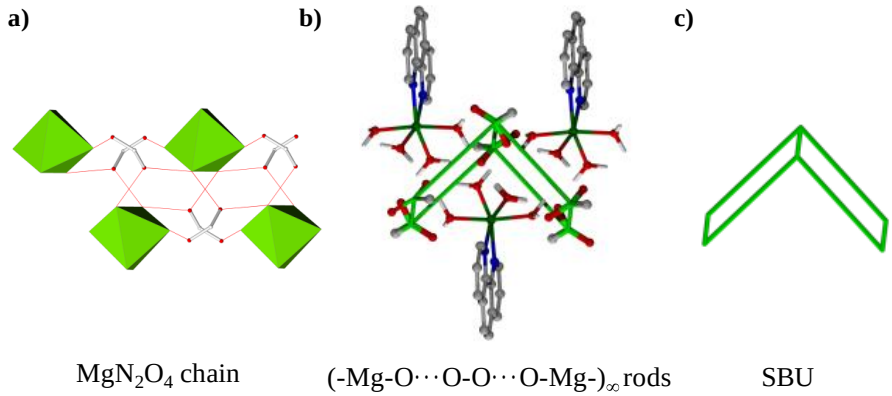

Figure 5.7. a) Detail of MgN_2O_4 chains in **β-AEPF-14**, **b)** topological simplifications performed to describe the (-O-Mg-)$_\infty$ rods as the inorganic SBUs and **c)** simplified SBU in **β-AEPF-14**.

Taking into account these topological considerations concerning the inorganic SBUs, by simplification of the supramolecular layers determined in **α-AEPF-14** using TOPOS,[7] only one type of four-connected nodes can be found. These nodes correspond to the C atoms of the carboxylate groups. This net exhibits a **sql** topology (point symbol ($4^4.6^2$). The main simplification points, as well as the decorated and final simplified nets for **α-AEPF-14** compound, are shown in **Figure 5.8**.

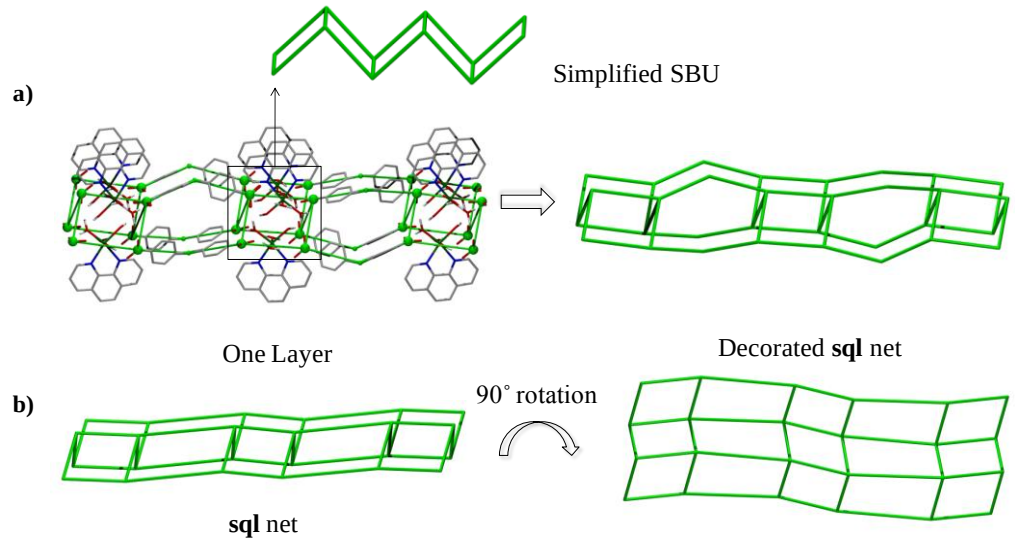

Figure 5.8. a) Depiction of the **α-AEPF-14** real net together with the decorated **sql** net. **b)** Detail of the simplified **sql** net in different orientations. Hydrogen atoms and $–CF_3$ groups were omitted for clarity.

In the case of **β-AEPF-14**, as it was before mentioned, the MgN_2O_4 chains are linked to other four chains through the $L_{(1)}^{-2}$ ligand *via* hydrogen bonds, giving rise to a three-dimensional net. Thus, taking into account these topological considerations concerning the inorganic SBUs, by simplification of the supramolecular net determined in **β-AEPF-14** using TOPOS,[7] only one type of four-connected nodes can be found, which correspond to the C atoms of the carboxylate groups (**Figure 5.9**). The supramolecular 3D net for this compound can be explained as rods of quadrangles linked by sharing opposite edges (ladders). These ladders are linked with the rungs parallel to form a **sra** four-connected net. The main simplifications points, as well as the decorated and final simplified nets for **β-AEPF-14**, are shown in **Figure 5.9**.

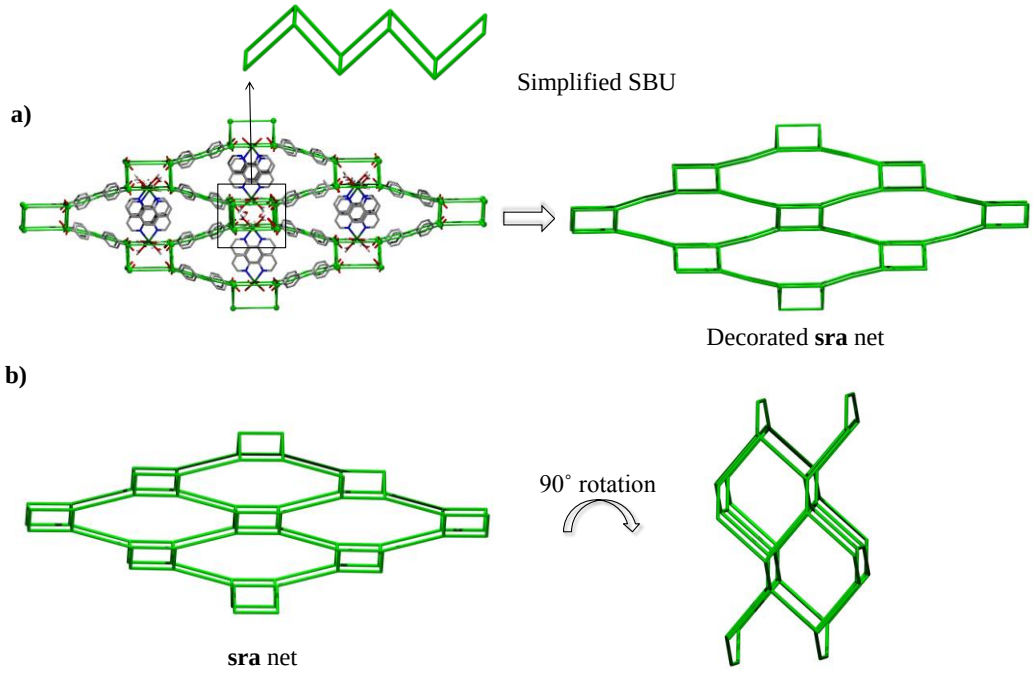

Figure 5.9. a) Depiction of the **β-AEPF-14** real net together with the simplified decorated **sra** net. **b)** Detail of the simplified **sra** net in different orientations. Hydrogen atoms and $–CF_3$ groups were omitted for clarity.

5.3.2.

Mg-AEPF-15

The hydrothermal reaction between $H_2L_{(1)}$ and magnesium acetate hydrate, using phen as ancillary ligand, gives rise to the **[Mg(HL$_{(1)}$)$_2$(phen)]** compound (**AEPF-15**), which crystallizes in the monoclinic crystal system (*C2/c* space group). The cell parameters determined for this structure are: a = 45.3030(8) Å, b = 10.6226(2) Å, c = 8.8701(2) Å, β = 90.215(1)º, and V = 4268.6(2) Å^3. In **AEPF-15**, the asymmetric unit comprises half independent magnesium ion, one partially deprotonated ligand ($HL_{(1)}^-$) and half phen molecule.

The ORTEP representation of **AEPF-15** asymmetric unit is shown in **Figure 5.10** and the main crystallographic and refinement data for this compound are shown in **Table 5.10**.

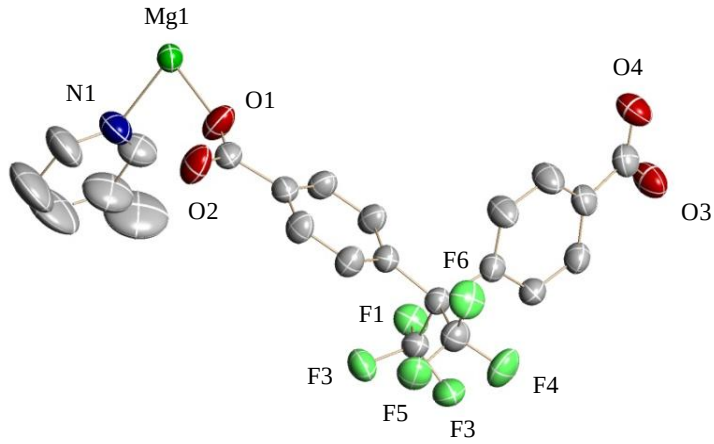

Figure 5.10. ORTEP representation of **AEPF-15** asymmetric unit. Ellipsoids are displayed at the 50% probability level. Hydrogen atoms were omitted for clarity.

In **AEPF-15** compound, Mg^{+2} ions are hexa-coordinated to four oxygen atoms coming from $HL_{(1)}^-$ carboxylate groups, and two nitrogen atoms coming from one phen ligand, giving rise to a MgN_2O_4 octahedra. The average Mg-O distance in this polyhedron is ~2.02 Å, which is shorter than the average Mg-N distance (~2.26 Å) (**Table 5.11**). These differences in the bond distances provoke the polyhedra distortion found in this compound **(Figure 5.11a**).

Table 5.10. Crystallographic and refinement data for **AEPF-15** compound.

Identification code	AEPF-15
Empirical formula	$C_{46}\ H_{26}\ F_{12}\ Mg\ N_2\ O_8$
Formula weight	987.0
Temperature	296(2) K
Wavelength	1.54178 Å
Crystal system	Monoclinic
Space group	*C2/c*
Unit cell dimensions	a = 45.3030(8) Å α = 90° b = 10.6226(2) Å β = 90.215(1)° c = 8.8701(2) Å γ = 90°
Volume	4268.6(2) $Å^3$
Z	8
Density (calculated)	1.536 Mg/m^3
Absorption coefficient	1.360 mm^{-1}
F(000)	2000
Crystal size	0.30 x 0.12 x 0.02 mm^3
Theta range for data collection	1.95 to 59.52°
Index ranges	-50<=h<=50, -11<=k<=11, -9<=l<=4
Reflections collected	14912
Independent reflections	3070 [R(int) = 0.0228]
Completeness to theta = 59.52°	98.6%
Absorption correction	Semi-empirical from equivalents
Max. and min. Transmission	0.9733 and 0.6857
Refinement method	Full-matrix least-squares on F^2
Data / restraints / parameters	3070 / 0 / 313
Goodness-of-fit on F^2	1.03
Final R indices [I>2sigma(I)]	R_1 = 0.0352, wR_2 = 0.0926
R indices (all data)	R_1 = 0.0409, wR_2 = 0.0969
Largest diff. peak and hole	0.186 and -0.178 $e.Å^{-3}$

Table 5.11. Interatomic distances in the coordination sphere of the MgN_2O_4 polyhedra for **AEPF-15**.

Bond	Distance (Å)
Mg(1)-O(1) c	2.048(1)
Mg(1)-O(1)[1]c	2.048(2)
Mg(1)-O(2)[2]c	1.988(2)
Mg(1)-O(3)[3]c	1.988(2)
Mg(1)-N(1) p	2.255(2)
Mg(1)-N(1)[1]p	2.255(2)

Symmetry transformations used to generate equivalent atoms:

[1] -x+2,y,-z+5/2 [3] -x+2,-y+1,-z+2

[2] x,-y+1,z+1/2

Oc: oxygen atom coming from a carboxylate group. Np: nitrogen atom coming from a phen ligand.

The MgN_2O_4 polyhedra observed in **AEPF-15** form chains along the *c* axis (**Figures 5.11b**). Junction of these inorganic chains is made *via* the $HL_{(1)}^-$ linker, which acts in a $\eta^2\mu_2$ coordination mode (**Figure 5.11c**).

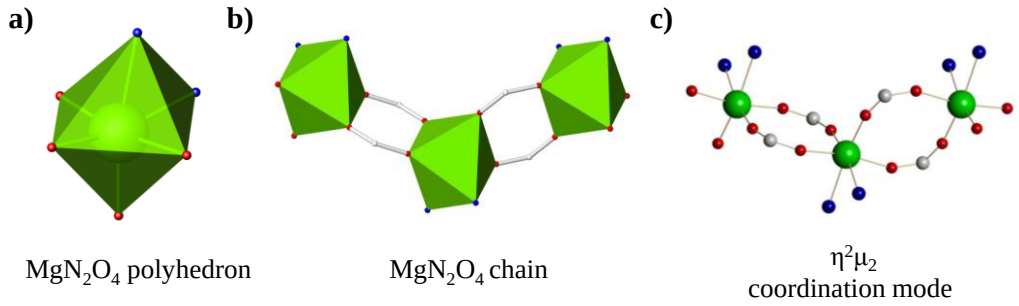

Figure 5.11. a) Inorganic PBUs in **AEPF-15**, **b)** detail of MgN_2O_4 chains found that run along the *c* axis and **c)** coordination mode of $HL_{(1)}^-$linker.

Thus, the covalent net in **AEPF-15** can be described as an extension of these magnesium chains, due to the coordination of phen and $HL_{(1)}^{-1}$ ligands (**Figure 5.12**). These metal-organic chains are joint to other four chains, *via* one type of strong hydrogen bond between the linker carboxylic groups (**Table 5.12**). The presence of these hydrogen bonds in **AEPF-15**, which link the metal-organic chains determined in

this compound (**Figure 5.13a**), allows the formation of a three-dimensional supramolecular net (**Figure 5.13b**).

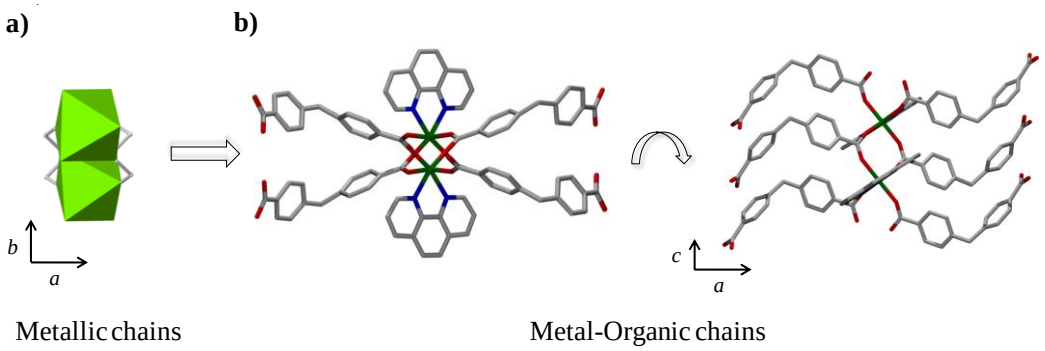

Figure 5.12. a) Metallic chains in **AEPF-15** and **b)** Metal-organic chains parallel to *c* axis.

Table 5.12. Distances and angles of hydrogen bonds found in **AEPF-15** compounds.

D-H···A[1]	D-H[2]	H···A[3]	D···A[4]	<D-H···A[5]
O(3)c-H(3A)c ··· O(4)co [1]	0.82	1.83	2.634(2)	167.4
Symmetry operators codes				
[1] -x+3/2, -y+1/2, -z+3				

D: donor atom, A: acceptor atom. [1]Names of donor, hydrogen and acceptor atoms involved in the hydrogen bond. [2] Distance D – A. [3]Distances H – A. [4]Distance D – A. [5] Angle D – H – A.

Oc: oxygen atom coming from a –OH of a carboxylic group. Hc: hydrogen atom coming from a –OH of a carboxylic group. Oco: oxygen atom coming from a carbonyl of a carboxylic group.

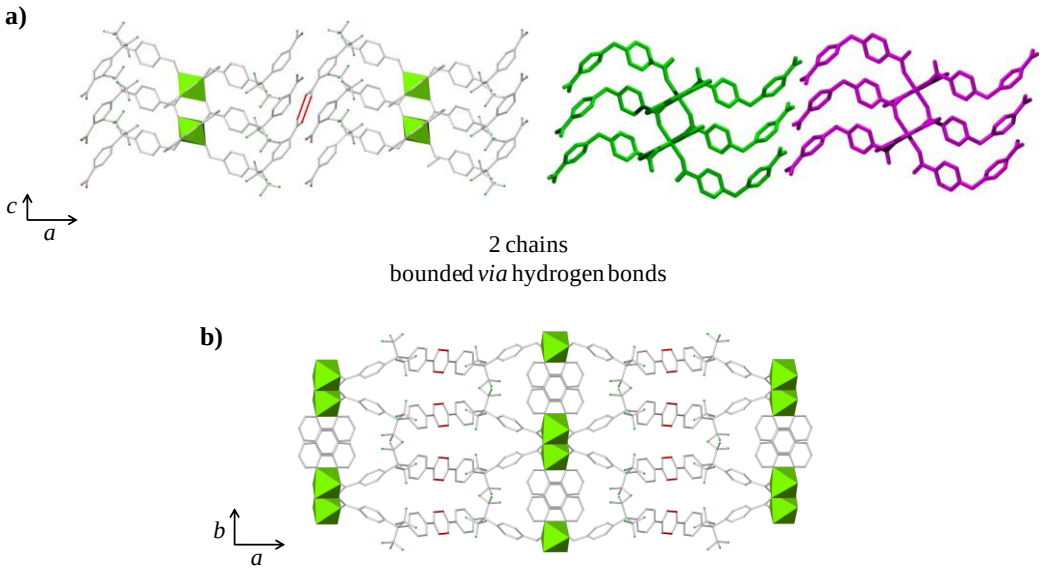

Figure 5.13. a) Depiction along the *b* axis of two **AEPF-15** metal-organic chains bounded *via* hydrogen bonds and **b)** polyhedral view of the supramolecular three-dimensional net determined in **AEPF-15** (hydrogen bonds in red).

As was previously discussed for **AEPF-14** polymorphs, the linker conformation was also analysed by means of three geometrical parameters (**θ**, **ω** and **d**, **Figure 5.5**). In **AEPF-15** the presence of hydrogen bonds between the $HL_{(1)}^-$ carboxylic groups forces a linker conformation which is quite similar to that found in **α-AEPF-14** polymorph, with similar values of **ω** angle and **d** distance (for **α-AEPF-14**: **ω** = 69.35º and **d** = 9.567 Å; for **AEPF-15: ω** = 69.35º and **d** = 9.567 Å) (**Table 5.13**).

Table 5.13. θ angle, **ω** dihedral angle and **d** distance values determined for $HL_{(1)}^-$ linker in **AEPF-15** compound.

θ (º)	ω (º)	d (Å)
111.8	66.36	9.469

Concerning the topology of the supramolecular net determined for **AEPF-15**, as it was done before for **AEPF-14** materials, the inorganic MgN_2O_4 chains can be simplified as rods, which can be considered as the inorganic SBUs. The topological simplifications were performed taking into account the previously mentioned work of Yaghi and O'Keeffe.[6] Thus, by simplification of these $(\text{-O-Mg})_\infty$ rods using TOPOS,[7] only one type of four-connected nodes can be found, which correspond to C atoms of $HL_{(1)}^-$ carboxylate groups (**Figure 5.14**).

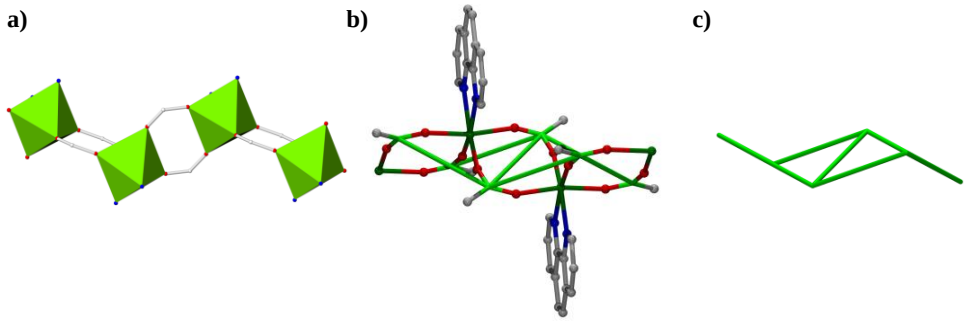

Figure 5.14. a) MgN_2O_4 polyhedra chain in **AEPF-15**. **b)** Topological simplifications performed to describe the $(\text{-O-Mg-})_\infty$ rods as the inorganic SBUs. **c)** Simplified SBU.

Considering the topological simplifications above mentioned, the **AEPF-15** supramolecular net can be described as rods of quadrangles linked by sharing opposite edges (ladders). These ladders are linked with the rungs at an angle to each other (*twisted* ladders), to form a three-dimensional **irl** 4-connected net (point symbol $(4^2.6^3.8)$). The main simplifications points, as well as the decorated and final simplified nets for **AEPF-15**, are shown in **Figure 5.15**.

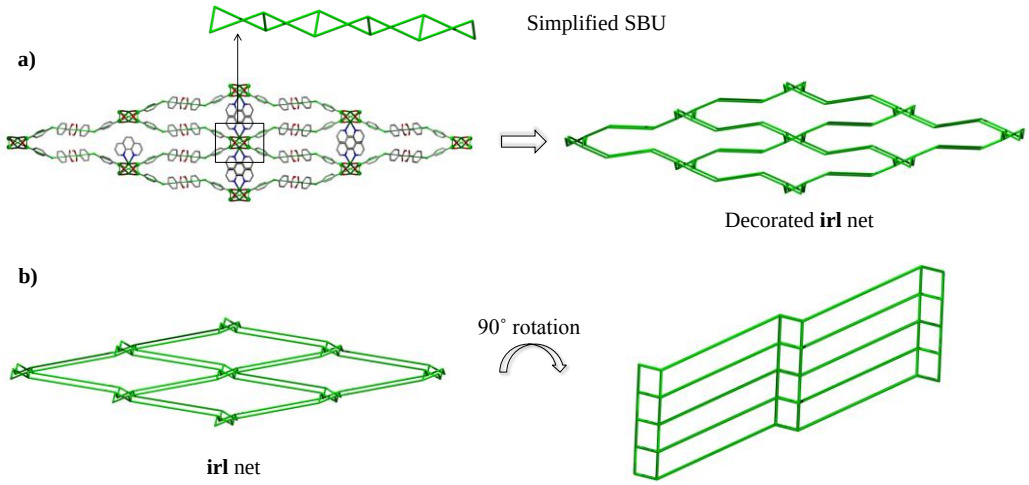

Figure 5.15. a) Depiction of the **AEPF-15** real net together with the decorated **irl** net. **b)** Detail of the simplified **irl** net in different orientations. Hydrogen atoms and $-CF_3$ groups were omitted for clarity.

5.3.3.

Mg-AEPF-16

The hydrothermal reaction between $H_2L_{(1)}$ and magnesium acetate tetrahydrate, using phen as a ancillary ligand and 0.1 M NaOH solution as base, gives rise to the formation of the novel compound **[Mg($L_{(1)}$)(phen)(H_2O)$_2$]** (**AEPF-16**). This material crystallizes in the orthorhombic crystal system (*Pnna* space group). The cell parameters determined for this structure are: a = 9.3105(3) Å, b = 26.8940(8) Å, c = 11.2146(3) Å, V = 2808.1(1) Å^3. The **AEPF-16** asymmetric unit comprises half of the molecular formula. The main crystallographic and refinement data for this compound are shown in **Table 5.14** and the ORTEP representation of **AEPF-16** asymmetric unit is shown in **Figure 5.16**.

Table 5.14. Crystallographic and refinement data for **AEPF-16** compound.

Identification code	AEPF-16
Empirical formula	$C_{29}H_{20}F_6MgN_2O_6$
Formula weight	630.76
Temperature	296(2) K
Wavelength	1.54178 Å
Crystal system	Orthorhombic
Space group	*Pnna*
Unit cell dimensions	a = 9.3105(3) Å α = 90° b = 26.8940(8) Å β = 90° c = 11.2146(3) Å γ = 90°
Volume	2808.1(1) $Å^3$
Z	4
Density (calculated)	1.492 Mg/m^3
Absorption coefficient	1.337 mm^{-1}
F(000)	1288
Crystal size	0.20 x 0.15 x 0.05 mm^3
Theta range for data collection	3.29 to 64.92°
Index ranges	-6<=h<=10, -31<=k<=30, -12<=l<=12
Reflections collected	22831
Independent reflections	2348 [R(int) = 0.0788]
Completeness to theta = 64.92°	98.1%
Absorption correction	Semi-empirical from equivalents
Max. and min. Transmission	0.9361 and 0.7758
Refinement method	Full-matrix least-squares on F^2
Data / restraints / parameters	2348 / 2 / 209
Goodness-of-fit on F^2	1.16
Final R indices [I>2sigma(I)]	R_1 = 0.0634, wR_2 = 0.1430
R indices (all data)	R_1 = 0.0654, wR_2 = 0.1452
Extinction coefficient	0.021(1)
Largest diff. peak and hole	0.385 and -0.610 e.$Å^{-3}$

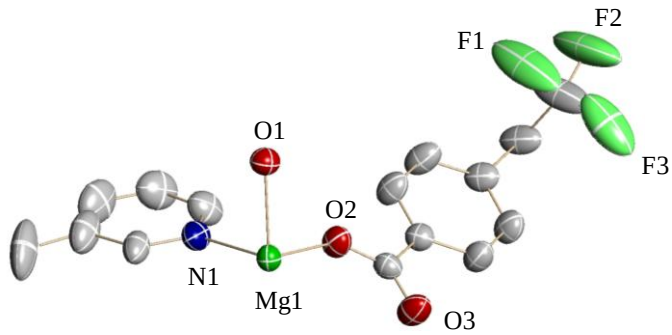

Figure 5.16. ORTEP representation of **AEPF-16** asymmetric unit. Ellipsoids are displayed at the 50% probability level. Hydrogen atoms were omitted for clarity.

In **AEPF-16** compound, Mg^{+2} ions are hexa-coordinated to two oxygen atoms coming from $L_{(1)}^{-2}$ carboxylate groups, two oxygen atoms of water molecules and two nitrogen atoms coming from one phen ligand, to give MgN_2O_4 octahedra. These polyhedra can be considered as the inorganic PBUs in this material. The average Mg-O distance in this polyhedron is ~2.06 Å, which is markedly shorter than the average Mg-N distance (~2.24 Å) (**Table 5.17**). Moreover, the Mg-O distance corresponding to $L_{(1)}^{-2}$ carboxylate group is shorter than the one corresponding to water molecules (**Table 5.17**). These differences cause a marked distortion in the coordination polyhedron found in **AEPF-16** (**Figure 5.17a**).

Table 5.17. Interatomic distances in the coordination sphere of the MgN_2O_4 polyhedra for **AEPF-16**.

Bond	Distance (Å)
Mg(1)-O(1) w	2.097(1)
Mg(1)-O(1)^{1}w	2.097(1)
Mg(1)-O(2) c	2.029(1)
Mg(1)-O(2)^{1}c	2.029(1)
Mg(1)-N(1) p	2.244(2)
Mg(1)-N(1)^{1}p	2.244(2)

Symmetry transformations used to generate equivalent atoms:
^{1}-x+1/2,-y+1,z

Ow: oxygen atom coming from a water coordination molecule. Oc: oxygen atom coming from a carboxylate group. Np: nitrogen atom coming from a phen ligand.

The inorganic PBUs in **AEPF-16** are connected through the deprotonated $L_{(1)}^{-2}$ ligand, which acts in a η^1- η^1 coordination mode (**Figure 5.17b**), giving rise to a 1-D helical magnesium material. Moreover, the supramolecular interactions in this compound are governed by hydrogen bonds, which are present between water coordination molecules and $L_{(1)}^{-2}$ carboxylate groups. Thus, three different types of hydrogen bonds are determined, one of them strong. The distances and angles of these interactions are present in **Table 5.18.**

Table 5.18. Distances and angles of hydrogen bonds found in **AEPF-16** compounds.

	D-H[2]	H···A[3]	D···A[4]	<D-H···A[5]
O(1)w-H(1B)w ··· O(3)c [1]	0.97(2)	1.76(2)	2.732(2)	178(3)
O(1)w-H(1A)w ··· O(3)c [2]	0.96(2)	2.50(3)	3.198(2)	129(3)
O(1)w-H(1A)w ··· O(2)c [3]	0.96(2)	2.32(3)	3.075(2)	135(3)

Symmetry operators codes

[1] x-1/2, y, -z+2 [2] -x+1/2, -y+1, z [3] -x, -y+1, -z+2

D: donor atom, A: acceptor atom. [1]Names of donor, hydrogen and acceptor atoms involved in the hydrogen bond. [2] Distance D – A. [3]Distances H – A. [4]Distance D – A. [5] Angle D – H – A.

Ow: oxygen atom coming from a water coordination molecule. Oc: oxygen atom coming from a carboxylate group.

As it is depicted in **Figure 5.17c**, when these hydrogen bonds are taken into account, MgN_2O_4 polyhedra are joint *via* $L_{(1)}^{-2}$ carboxylate groups, giving rise to the presence of inorganic chains.

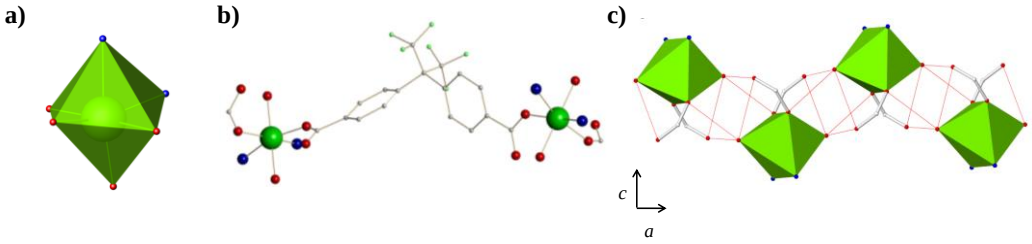

Figure 5.17. a) MgN_2O_4 polyhedron determined in **AEPF-16**, **b)** coordination mode of $L_{(1)}^{-2}$ linker and **c)** inorganic chains found in this compound, which are forming *via* the hydrogen bonds (in red).

The final supramolecular net that can be described for **AEPF-16** consists of double helical chains parallel to the *b* axis which are joint among them along the *c* direction (**Figure 5.18**), giving rise to a three-dimensional net (**Figure 5.19**).

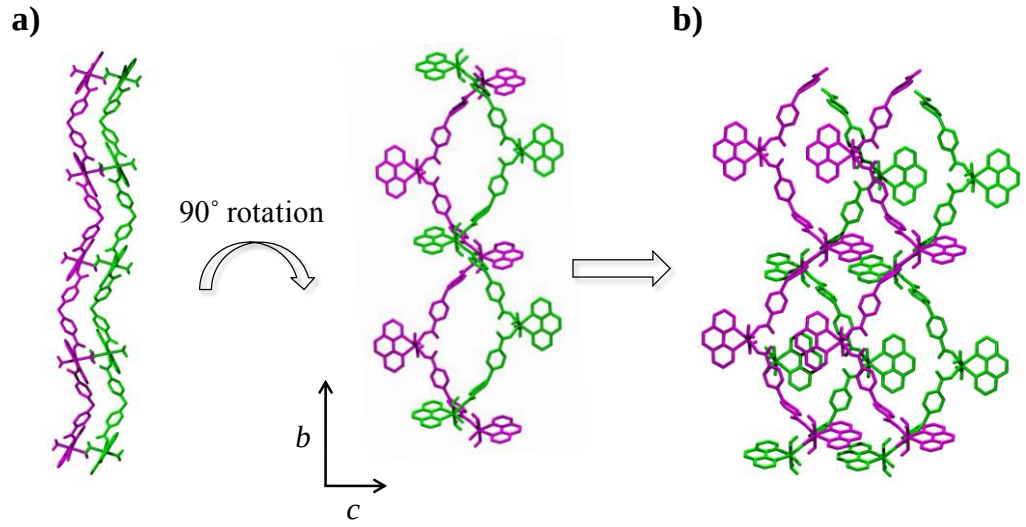

Figure 5.18. AEPF-16 supramolecular structure built up *via* hydrogen bonds. **a)** Double helical chains determined in this compound, showing different orientations. **b)** Junction of the double helical chains along the *c* axis.

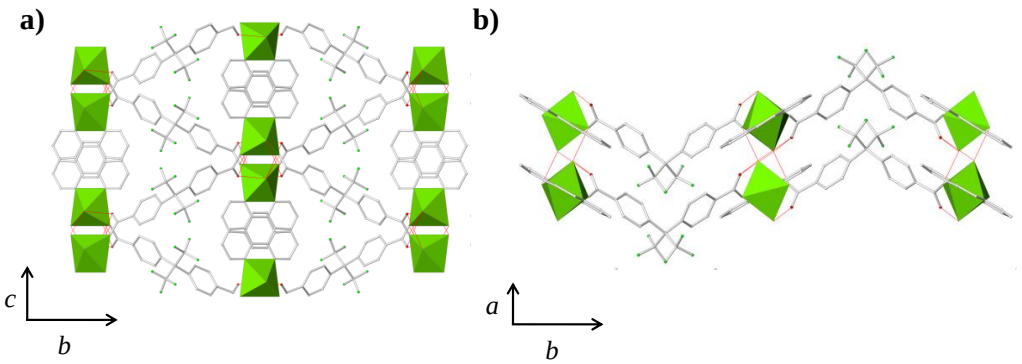

Figure 5.19. a) Polyhedral view of **AEPF-16** compound along the *a* axis and **b)** along the *c* axis.

In **AEPF-16**, the conformation of the linker is quite similar to that found for **β-AEPF-14**, but in this case the **d** distance is larger (for **β-AEPF-14**: **θ** = 112.0º, **ω** =72.56º and **d** = 9.831 Å; for **AEPF-16: θ** = 113.6º, **ω** = 72.75º and **d** = 10.129 Å) (**Table 5.19**).

Table 5.19. θ angle, **ω** dihedral angle and **d** distance values determined for $L_{(1)}^{-2}$ linker in **AEPF-16** compound.

θ (º)	ω (º)	d (Å)
113.6	72.75	10.129

To consider topological features of **AEPF-16**, the hydrogen bonds determined for this compound are considered. Thus, the inorganic MgN_2O_4 chains were simplified as rods, which can be considered the inorganic SBUs in this material. The topological simplifications were performed taking into account the previously mentioned work of Yaghi and O'Keeffe.[6] Thus, by simplification of these infinite $(\text{-O-Mg-})_\infty$ rods using TOPOS,[7] only one type of four-connected nodes can be determined, which corresponds to C atoms of $L_{(1)}^{-2}$ carboxylate groups (**Figure 5.20**). According to this simplification, the net can be explained as rods of quadrangles linked by sharing opposite edges (ladders). These ladders are linked with the rungs parallel to form a **sra** 4-connected net. The main simplification points, as well as the decorated and final simplified nets for **AEPF-16** are shown in **Figure 5.21**.

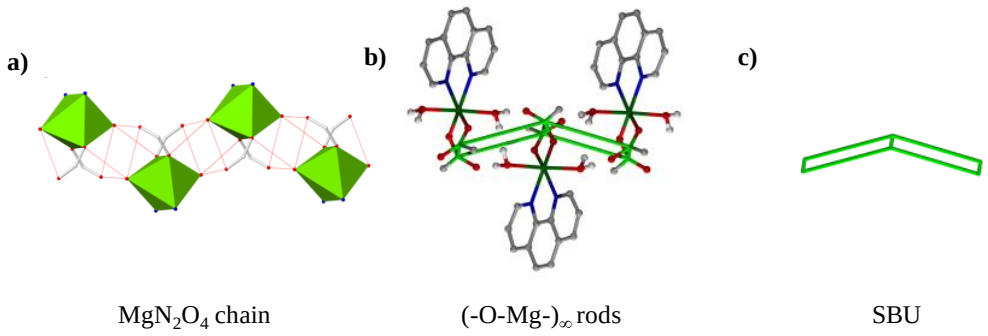

Figure 5.20. a) MgN_2O_4 polyhedra chain. **b)** Topological simplifications performed to describe the $(\text{-O-Mg-})_\infty$ rods as the inorganic SBUs. **c)** Simplified inorganic SBU.

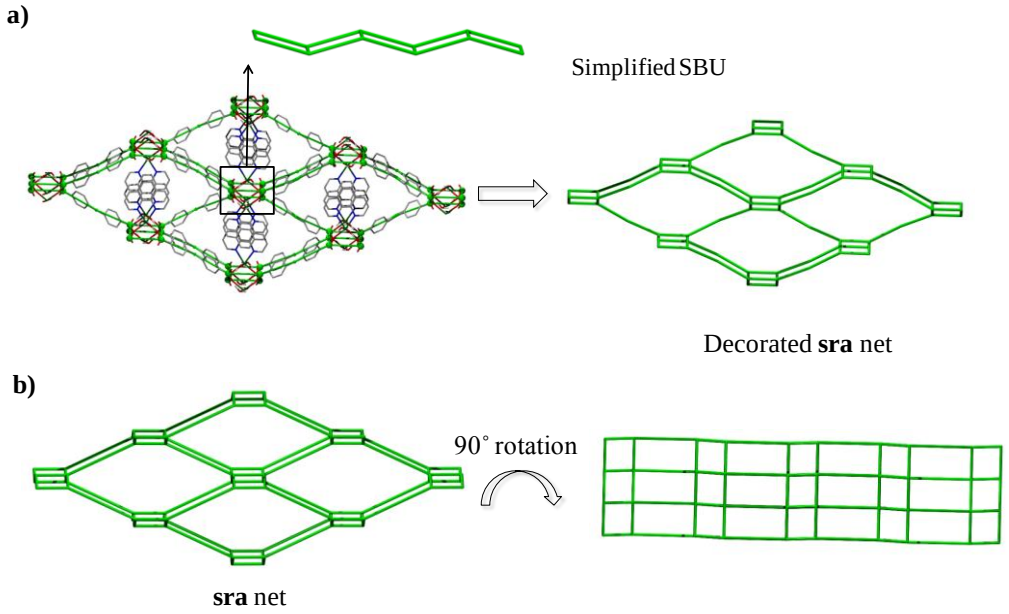

Figure 5.21. a) Depiction of the **AEPF-16** real net together with the simplified decorated **sra** net. **b)** Detail of the simplified **sra** net in different orientations. Hydrogen atoms and $-CF_3$ groups were omitted for clarity.

5.3.4.

Mg-AEPF-17

The solvothermal reaction between $H_2L_{(1)}$ and magnesium acetate tetrahydrate, using phen as an ancillary ligand, gives rise to the formation of a novel compound with formula **[Mg($L_{(1)}$)(phen)(H_2O)]** (**AEPF-17**). This material crystallizes in the orthorhombic crystal system (*Pbca* space group). The cell parameters determined for this structure are: a = 20.9727(5) Å, b = 9.3428(2) Å, c = 27.9724(6) Å, and V = 5481.0(2) $Å^3$. The **AEPF-17** asymmetric unit comprises half of the molecular formula. The main crystallographic and refinement data for this compound are shown in **Table 5.20** and the ORTEP representation of **AEPF-17** asymmetric unit is shown in **Figure 5.22**.

Table 5.20. Crystallographic and refinement data for **AEPF-17** compound.

Identification code	AEPF-17
Empirical formula	$C_{29}\ H_{18}\ F_6\ Mg\ N_2\ O_5$
Formula weight	612.76
Temperature	296(2) K
Wavelength	1.54178 Å
Crystal system	Orthorhombic
Space group	*Pbca*
Unit cell dimensions	a = 20.9727(5) Å α = 90° b = 9.3428(2) Å β = 90° c = 27.9724(6) Å γ = 90º
Volume	5481.0(2) $Å^3$
Z	8
Density (calculated)	1.485 Mg/m^3
Absorption coefficient	1.326 mm^{-1}
F(000)	2496
Crystal size	0.40 x 0.20 x 0.05 mm^3
Theta range for data collection	3.16 to 59.67°
Index ranges	-23<=h<=23, -5<=k<=10, -31<=l<=31
Reflections collected	34500
Independent reflections	3942 [R(int) = 0.0387]
Completeness to theta = 59.67°	97.6%
Absorption correction	Semi-empirical from equivalents
Max. and min. Transmission	0.9367 and 0.6191
Refinement method	Full-matrix least-squares on F^2
Data / restraints / parameters	3942 / 2 / 396
Goodness-of-fit on F^2	1.052
Final R indices [I>2sigma(I)]	R_1 = 0.0305, wR_2 = 0.0724
R indices (all data)	R_1 = 0.0425, wR_2 = 0.0789
Largest diff. peak and hole	0.191 and -0.150 e.$Å^{-3}$

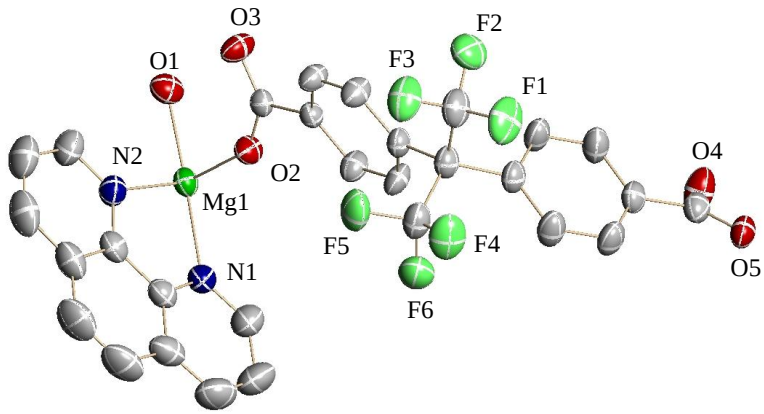

Figure 5.22. ORTEP representation of **AEPF-17** asymmetric unit. Ellipsoids are displayed at the 50% probability level. Hydrogen atoms were omitted for clarity.

In **AEPF-17** compound, Mg^{+2} ions are hexa-coordinated to three oxygen atoms coming from $L_{(1)}^{-2}$ carboxylate groups, one oxygen atom from a coordinated water molecule and to two nitrogen atoms coming from one phen ligand, to give MgN_2O_4 octahedra. These polyhedra can be considered as the inorganic PBUs in this material (**Figure 5.23a**). The average Mg-O distance in this polyhedron is ~2.05 Å, which is shorter than the average Mg-N distance (~2.24 Å) (**Table 5.21**). Moreover, the $L_{(1)}^{-2}$ linker exhibits a η^1-$\eta^2\mu_2$ coordination mode (**Figure 5.23b**), which provokes differences in the Mg-O bond distances that for correspond the $L_{(1)}^{-2}$ carboxylate groups. Thus, the carboxylate group which coordinates in a η^1 mode presents a larger Mg-O bond distance (Mg(1)-O(5)= 2.103(1) Å) than the one coordinating in a $\eta^2\mu_2$ mode (Mg(1)-O(2)= 2.041(1) Å and Mg(1)-O(3)= 2.012(1) Å) (**Table 5.21**). These differences cause a distortion in the coordination polyhedron found in this material.

Table 5.21. Interatomic distances in the coordination sphere of the MgN_2O_4polyhedra for **AEPF-17**.

Bond	Distance (Å)
Mg(1)-O(1)w	2.061(2)
Mg(1)-O(2)c	2.041(1)
Mg(1)-O(3)[1]c	2.012(1)
Mg(1)-O(5)[2]c	2.103(1)
Mg(1)-N(1) p	2.234(2)
Mg(1)-N(2) p	2.230(2)

Symmetry transformations used to generate equivalent atoms:
[1]-x+1/2,y+1/2,z [2] x,-y+3/2,z+1/2

Ow: oxygen atom coming from a water coordination molecule. Oc: oxygen atom coming from a carboxylate group. Np: nitrogen atom coming from a phen ligand.

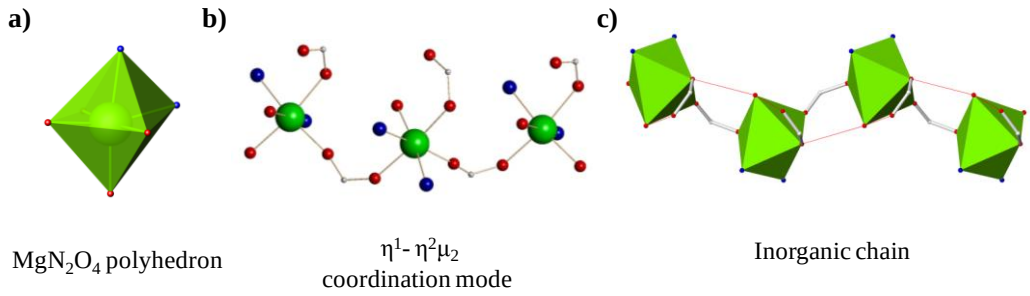

Figure 5.23. a) MgN_2O_4 polyhedron determined in **AEPF-17**, **b)** Coordination mode of $L_{(1)}^{-2}$ linker and **c)** Inorganic chains found in this compound, which are forming *via* $L_{(1)}^{-2}$ carboxylate groups (hydrogen bonds are depicted in red).

The inorganic PBUs in **AEPF-17** are connected through the deprotonated $L_{(1)}^{-2}$ ligand acting in a η^1-$\eta^2\mu_2$ coordination mode (**Figure 5.23c**), giving rise to MgN_2O_4 inorganic chains running along the *b* axis. Moreover, additional interactions are found among these polyhedra due to the presence of hydrogen bonds between coordinated water molecules and $L_{(1)}^{-2}$ carboxylate groups that act in a η^1 mode. It is worth mentioning that the strongest interaction is the one involving the non-coordinated oxygen atoms. The distances and angles of these hydrogen bonds are listed in **Table 5.22.**

Moreover, it is worth mentioning that the presences of π-π stacking interactions between phen aromatic rings are found, with a distance of 3.743 Å. This interaction is

slightly weaker than that found in **β-AEPF-14** compound, for which the distance is 3.655 Å.

Table 5.22. Distances and angles of hydrogen bonds found in **AEPF-17** compounds.

	D-H[2]	H···A[3]	D···A[4]	<D-H···A[5]
O(1)w-H(1A)w ··· O(5)c [1]	0.94(2)	2.03(2)	2.920(2)	157(3)
O(1)w-H(1B)w ··· O(4)c [2]	0.97(2)	1.65(2)	2.594(2)	163(2)
Symmetry operators codes				
[1] -x+1/2, -y+1, z+1/2	[2] x, -y+3/2, z+1/2			

D: donor atom, A: acceptor atom. [1]Names of donor, hydrogen and acceptor atoms involved in the hydrogen bond. [2] Distance D – A. [3]Distances H – A. [4]Distance D – A. [5] Angle D – H – A.

Ow: oxygen atom coming from a water coordination molecule. Oc: oxygen atom coming from a carboxylate group. Hw: hydrogen atom coming from a coordinated water molecule.

In the **AEPF-17**, each inorganic chain above described is bonded to other two chains *via* the $L_{(1)}^{-2}$ organic linker, giving rise to undulated layers perpendicular to the *a* axis (**Figure 5.24**).The hydrogen bonds described for **AEPF-17** are determined inside layers and do not contribute to increase the net dimensionality.

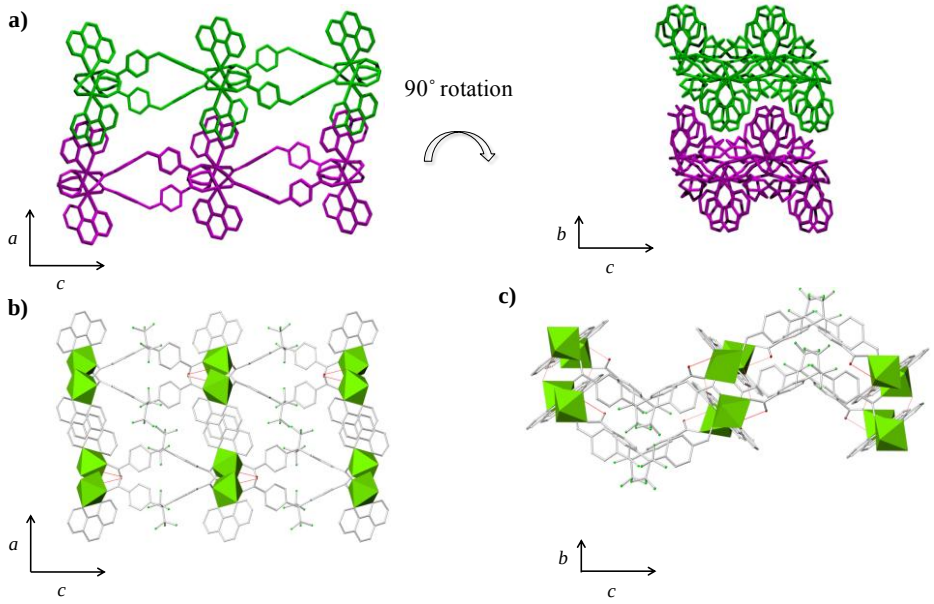

Figure 5.24. a) Depiction of two layers in **AEPF-17** showing different orientations, **b)** polyhedral view of two layers in **AEPF-17** layers along the *b* axis and **c)** detail of one layer along the *a* axis.

As was before done for the other materials presented in this chapter, the conformation of the $L_{(1)}^{-2}$ linker was analysed by describing some geometrical parameters (**Figure 5.5**). In **AEPF-17**, the conformation of the linker is quite similar to that found for **AEPF-15**, but in this case the **ω** value is higher (for **AEPF-15**: **θ** = 111.8º, **ω** = 66.36º and **d** = 9.469Å; for **AEPF-17: θ** = 110.47º, **ω** = 70.71º and **d** = 9.452 Å) (**Table 5.23**).

Table 5.23. θ angle, **ω** dihedral angle and **d** distance values determined for $L_{(1)}^{-2}$ linker in **AEPF-16** compound.

θ (º)	ω (º)	d (Å)
110.47	70.71	9.452

Concerning the topology of **AEPF-17** net, as was done for the other materials presented in this chapter, the inorganic MgN_2O_4 chains can be simplified as rods, which can be considered as the inorganic SBUs in this material. The topological simplifications were performed taking into account the previously mentioned work of Yaghi and O'Keeffe.[6] Thus, by simplification of these $(\text{-O-Mg})_\infty$ rods using TOPOS,[7] only one type of four-connected nodes can be found, which correspond to C atoms of $L_{(1)}^{-2}$ carboxylate groups (**Figure 5.25**).

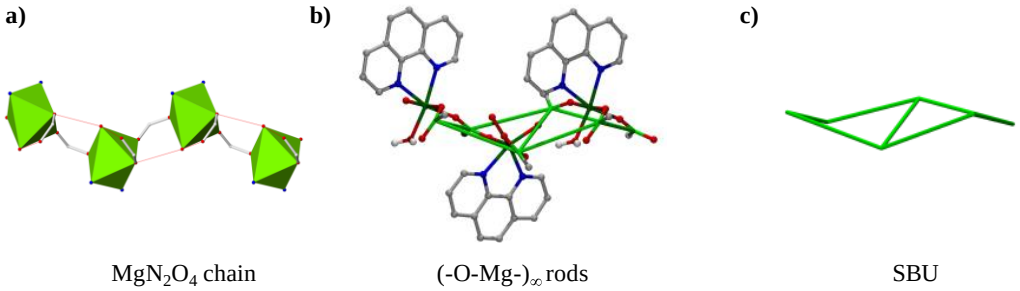

Figure 5.25. a) MgN_2O_4 polyhedra chain. **b)** Topological simplifications performed to describe the $(\text{-O-Mg-})_\infty$ rods as the inorganic SBUs. **c)** Simplified inorganic SBU.

Considering topological simplifications above mentioned, **AEPF-17** net can be described as rods of quadrangles linked by sharing opposite edges (ladders). These ladders are linked with the rungs to an angle to each other (*twisted* ladders), to form a **sql** 4-connected net. The main simplification points, as well as the decorated and final simplified nets for **AEPF-17**, are shown in **Figure 5.26**.

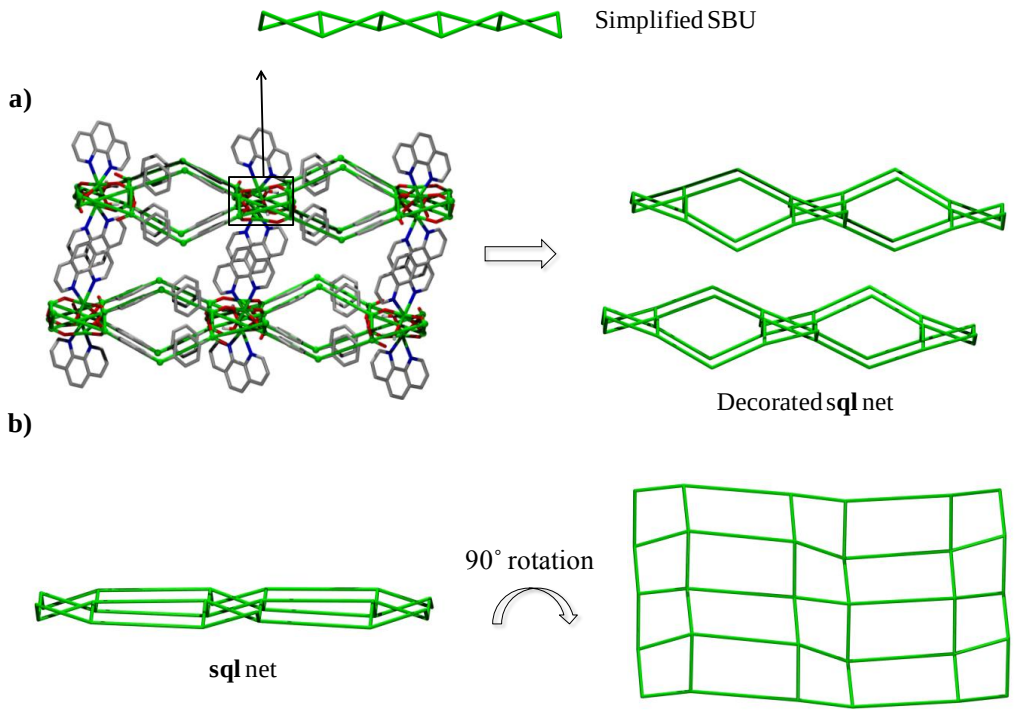

Figure 5.26. a) Depiction of the **AEPF-17** real net together with the simplified decorated **sql** net. **b)** Detail of the simplified **sql** net in different orientations. Hydrogen atoms and $-CF_3$ groups were omitted for clarity.

5.3.5.

Topological summary

To clarify all the structural information presented in this chapter, **Figure 5.27** summarizes the main topological simplifications obtained for the five magnesium compounds presented in this chapter.

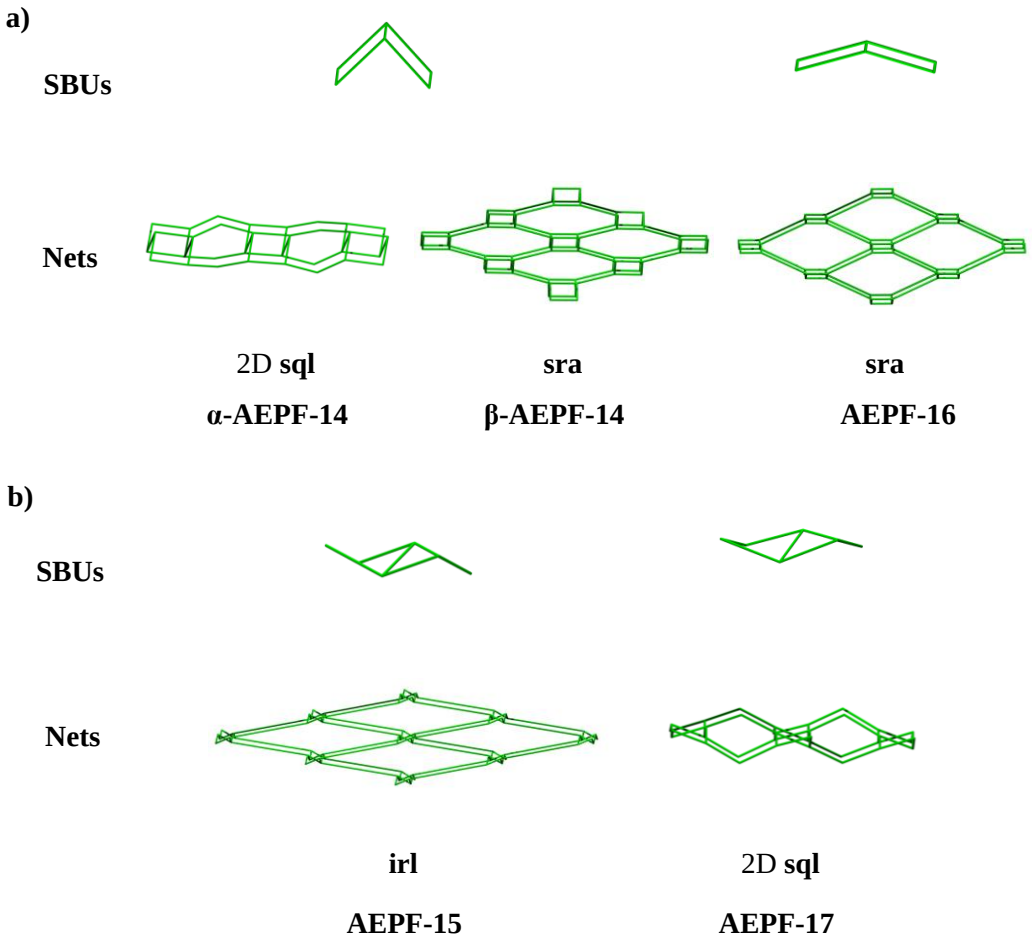

Figure 5.27. Simplified SBUs and described nets for: **a) AEPF-14** polymorphs and **AEPF-16** compound and **b) AEPF-15** and **AEPF-17** compounds.

5.4.

Characterization

5.4.1.

X-Ray Powder Diffraction

Pawley refinements[8] were performed, using Materials Studio[9] software, for the four compounds presented in this thesis that have been obtained as pure phases (*see* Chapter 2, *Synthesis procedures*). In the following, the Pawley refinement profiles and the main refinement values for **AEPF-14** (**α-** and **β-**), **AEPF-16** and **AEPF-17** compounds are shown in **Figures 5.28-5.31** and **Tables 5.24.-5.27**, respectively.

Table 5.24. Crystal Data and Pawley profile refinement values for **α-AEPF-14**.

Compound	α-AEPF-14	
Crystal system	Monoclinic	
Space group	$P2_1/c$	
Unit cell dimensions	a = 13.209(1) Å	α = 90˚
	b = 7.6132(7) Å	β = 99.818(6)˚
	c = 31.056(3) Å	γ = 90˚
Profile Function	Pseudo-Voigt	
U	0.48(5)	
V	-0.077(9)	
W	0.0046(5)	
NA	0.87(8)	
NB	0.004(4)	
Zero Point	0.035(2)	
Asymmetry correction	Finger-Cox-Jephcoat	
H/L	0.020(2)	
S/L	0.014(2)	
Rwp	0.0469	
Rp	0.0322	

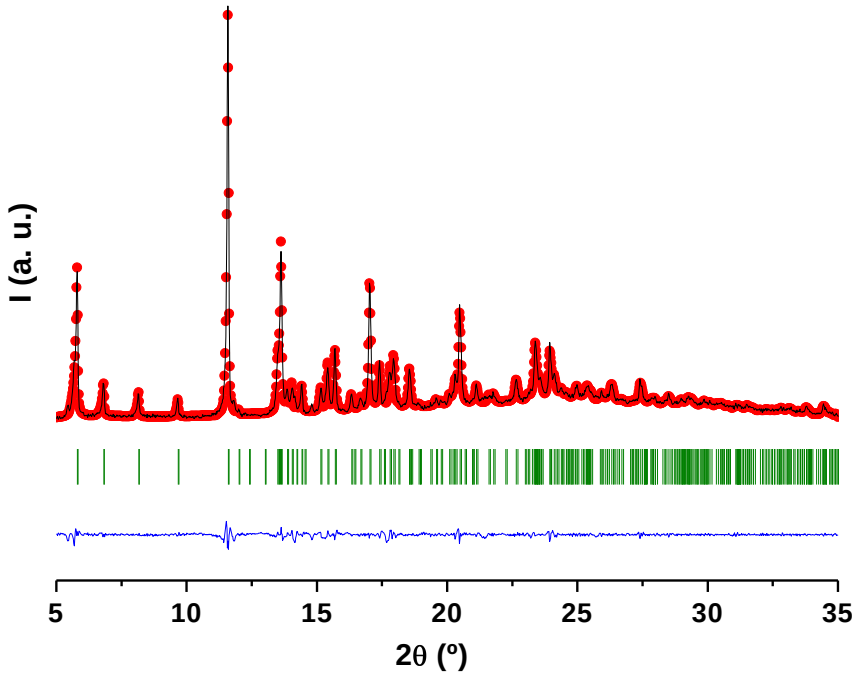

Figure 5.28. Pawley refinement for **α-AEPF-14**. Experimental data (red), simulated pattern (black) and difference (blue); observed reflections (green).

Table 5.25. Crystal Data and Pawley profile refinement values for **β-AEPF-14**.

Compound	β-AEPF-14	
Crystal system	Orthorhombic	
Space group	*Pnna*	
Unit cell dimensions	a = 7.3052(5) Å	α = 90˚
	b = 32.617(4) Å	β = 90˚
	c = 12.552(1) Å	γ = 90˚
Profile Function	Pseudo-Voigt	
U	0.65(7)	
V	-0.04(1)	
W	0.0030(6)	
NA	0.76(5)	
NB	0.005(3)	
Zero Point	0.040(1)	
Asymmetry correction	Finger-Cox-Jephcoat	
H/L	0.02(1)	
S/L	0.02(1)	
Rwp	0.0460	
Rp	0.0326	

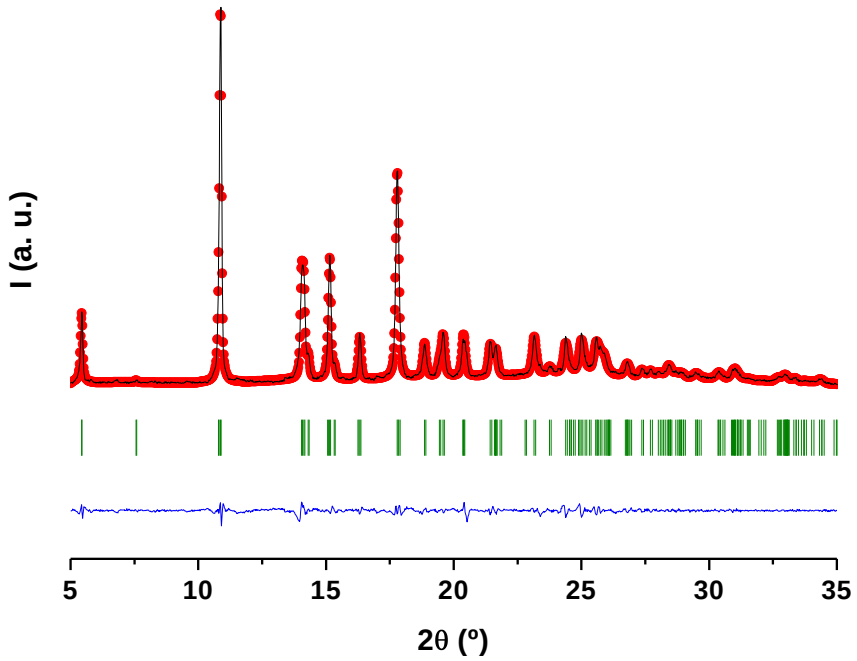

Figure 5.29. Pawley refinement for **β-AEPF-14**. Experimental data (red), simulated pattern (black) and difference (blue); observed reflections (green).

Table 5.26. Crystal Data and Pawley profile refinement values for **AEPF-16**.

Compound	AEPF-16	
Crystal system	Orthorhombic	
Space group	*Pnna*	
Unit cell dimensions	a= 9.313(1) Å	α = 90˚
	b= 26.911(4) Å	β = 90˚
	c= 11.225(2) Å	γ = 90˚
Profile Function	Pseudo-Voigt	
U	0.08(5)	
V	-0.03(2)	
W	0.021(1)	
NA	0.34(4)	
NB	0.009(2)	
Zero Point	0.119(5)	
Asymmetry correction	Finger-Cox-Jephcoat	
H/L	0.00001(3)	
S/L	0.003(7)	
Rwp	0.0739	
Rp	0.0505	

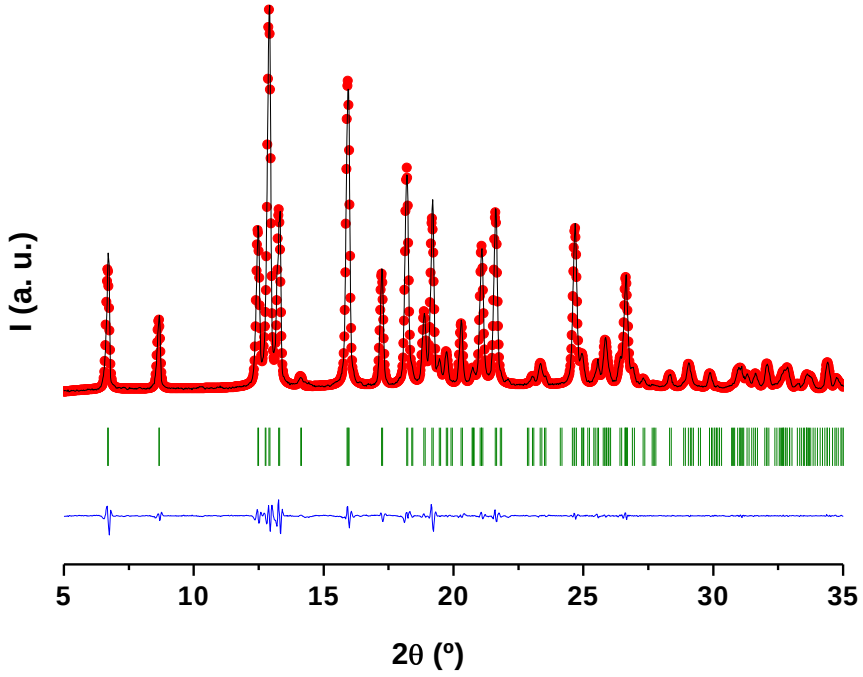

Figure 5.30. Pawley refinement for **AEPF-16**. Experimental data (red), simulated pattern (black) and difference (blue); observed reflections (green).

Table 5.27. Crystal Data and Pawley profile refinement values for **AEPF-17**.

Compound	AEPF-17	
Crystal system	Orthorhombic	
Space group	*Pbca*	
Unit cell dimensions	a = 21.006(39 Å	α = 90˚
	b = 9.365(1) Å	β = 90˚
	c = 27.991(4) Å	γ = 90˚
Profile Function	Pseudo-Voigt	
U	0.34(6)	
V	-0.05(1)	
W	0.007(1)	
NA	0.80(7)	
NB	0.0047(7)	
Zero Point	0.062(4)	
Asymmetry correction	Finger-Cox-Jephcoat	
H/L	0.02(1)	
S/L	0.01(1)	
Rwp	0.0205	
Rp	0.0148	

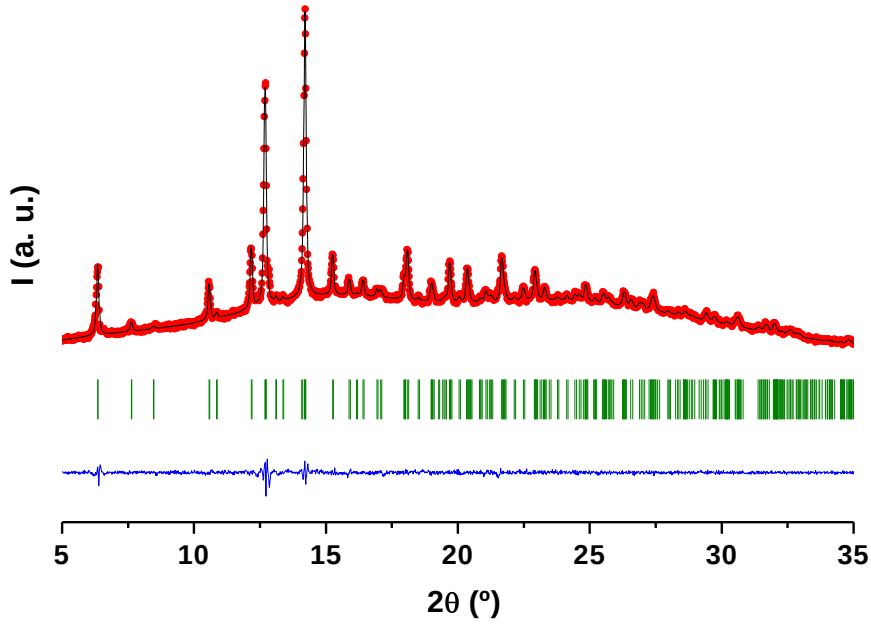

Figure 5.31. Pawley refinement for **AEPF-17**. Experimental data (red), simulated pattern (black) and difference (blue); observed reflections (green).

5.4.2.

Infrared Spectroscopy

Infrared (IR) spectra of **AEPF-14** (**α-** and **β-**), **AEPF-16** and **AEPF-17** show the presence of both υ_{as} and υ_{s} of the carboxylic groups found at 1700-1500 (υ_{as}) and 1500-1300 (υ_{s}) cm^{-1}. Moreover, additional bands in the –OH stretching mode region (3550-3200 cm^{-1}) which correspond to the coordinated water molecules present in these materials were also determined.

Details of **α-AEPF-14** and **β-AEPF-14** spectra of the region corresponding to –OH stretching mode zone (3550-3200 cm^{-1}) are given in **Figure 5.32**. In IR spectra of **α-AEPF-14** a broad band is observed in the IR spectrum centred at ~3390 cm^{-1}. For **β-AEPF-14**, two broad bands are observed in the IR spectrum at ~3395 cm^{-1} and ~3210 cm^{-1}. The differences observed for the two polymorphs are due to the different

contribution of hydrogen bonds in these materials (for **α**-polymorph eight strong hydrogen bonds are described, while in the case of the **β**-polymorph only three).

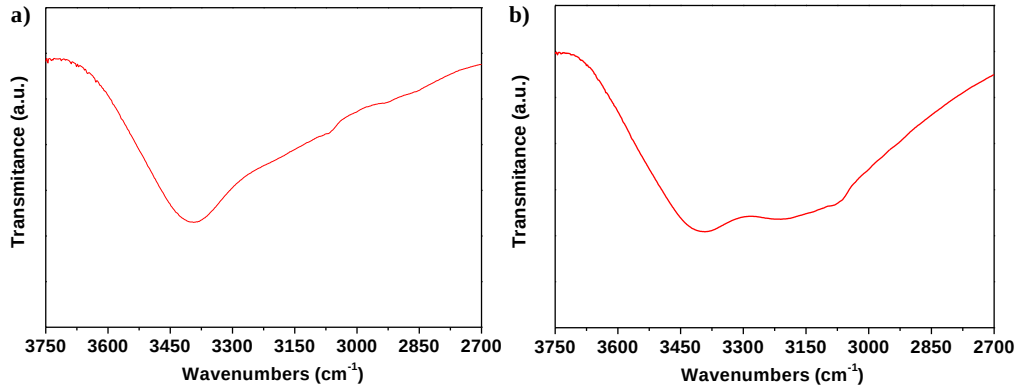

Figure 5.32. Details of IR spectra in the –OH stretching mode region (3750-3200 cm^{-1}) for: **a) α-AEPF-14** and **b) β-AEPF-14**.

Details of IR spectra for **AEPF-14** compounds in the region corresponding to CO_2^- stretching mode zone is given in **Figure 5.33**. Thus, for **α-AEPF-14**, bands were observed at: ~1595 cm^{-1}, ~1550 cm^{-1} and ~1520 cm^{-1} (υ_{as}); and ~1430 cm^{-1} and ~1390 cm^{-1} (υ_s). In the case of **β-AEPF-14**, bands were observed at: ~1595 cm^{-1}, ~1550 cm^{-1} and ~1520 cm^{-1} (υ_{as}); and ~1430 cm^{-1} and ~1380 cm^{-1} (υ_s). As well as for both **AEPF-14** polymorphs the presence of $L_{(1)}^{-2}$ linker molecules which are not covalently bonded to magnesium ions was determined. Therefore, this structural feature is in good agreement with the presence of the same CO_2^- stretching mode bands for the two **AEPF-14** polymorphs.

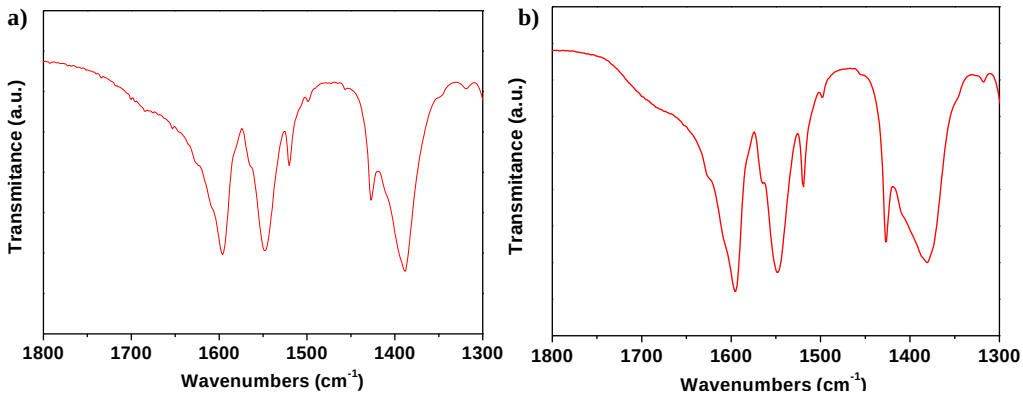

Figure 5.33. Details of IR spectrum in the -CO_2^- stretching mode zone (1900-1200 cm^{-1}) for: **a) α-AEPF-14** and **b) β-AEPF-14**.

Details of IR spectrum for **AEPF-16** are given in **Figure 5.34**. In the –OH and –CH stretching mode region, bands centred at ~3535 cm^{-1}, ~3405 cm^{-1} and ~3230 cm^{-1} are observed, which can be explained by the contribution of the coordinated water molecules in this compound. Besides, an additional band centred at ~3075 cm^{-1} is determined, which is associated to –CH stretching mode of $L_{(2)}^{-2}$ and phen aromatic groups (**Figure 5.34a**).

In the CO_2^- stretching mode zone, bands are observed at: ~1605(1620) cm^{-1}, ~1560(1570) cm^{-1} and ~1520 cm^{-1} (υ_{as}); and ~1425 cm^{-1} and ~1390 cm^{-1} (υ_s) (**Figure 5.34b**). Compared to the bands observed for **AEPF-14** polymorphs, some differences can be distinguished in the υ_{as} region. Thus, for **AEPF-16** compound, the bands in this region suffer a shift to higher wavenumbers values.

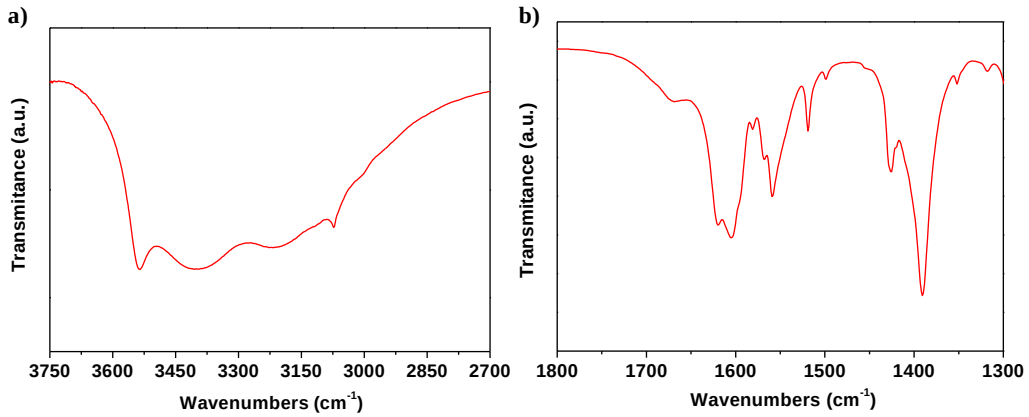

Figure 5.34. Details of IR spectrum in the: **a)** –OH and –CH stretching mode zone (3750-2700 cm^{-1}) and **b)** -CO_2^- stretching mode zone (1800-1300 cm^{-1}) for **AEPF-16**.

Details of IR spectrum for **AEPF-17** are given in **Figure 5.35**. In the –OH and –CH stretching mode region, a broad band centred at ~3435 cm^{-1} is determined, which corresponds to coordinated water molecules in this compound. Moreover, a weak band centred at ~3085 cm^{-1} is determined, which is associated to –CH stretching mode of $L_{(2)}^{-2}$ and phen aromatic groups (**Figure 5.35a**).

In the CO_2^- stretching mode zone, bands are observed at: ~1605(1645) cm^{-1}, ~1555 cm^{-1} and ~1515 cm^{-1} (υ_{as}); and ~1425 cm^{-1} and ~1395 cm^{-1} (υ_s) (**Figure 5.35b**). Compared to the bands observed for **AEPF-16** compound, for which $L_{(1)}^{-2}$ ligand bonds in a η^1-η^1 coordination mode, some differences can be mentioned in the υ_{as} region. Thus, in **AEPF-17** compound, for which the linker acts in a η^1-$\eta^2\mu^2$ coordination mode,

the bands observed in this region are centred at similar values to those found in **AEPF-16** (although a slight shift to lower wavenumbers values is observed).

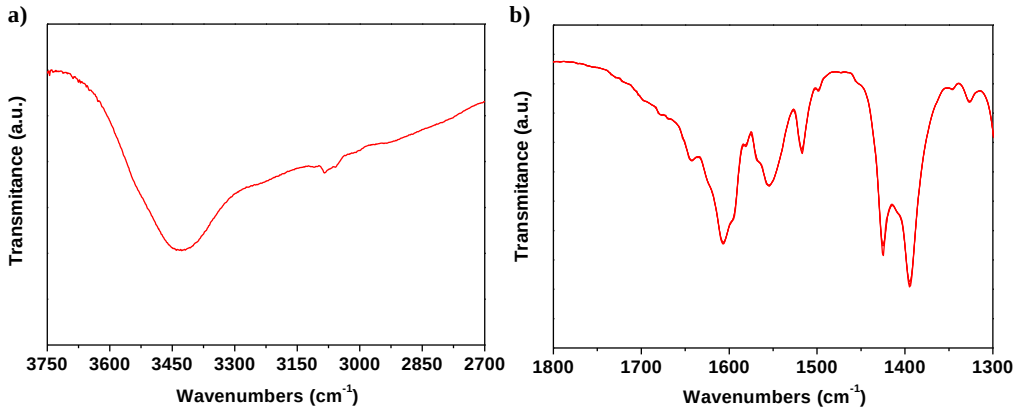

Figure 5.35. Details of IR spectrum in the: **a)** -OH and –CH stretching mode zone (3750-2700 cm^{-1}) and **b)** -CO_2^- stretching mode zone (1800-1300 cm^{-1}) for **AEPF-17**.

5.4.3.

Thermal Gravimetric Analyses

Thermal Gravimetric Analyses (TGA) curves for **AEPF-14** (**α-** and **β-** polymorphs), **AEPF-16** and **AEPF-17** are shown in **Figures 5.36-5.39**, respectively.

- Thermogravimetric profile of **α-AEPF-14** (**Figure 5.36**) shows a first weight loss between ~ 30-125 ºC of ~10.5% consistent with the removal of the water molecules present in the compound (calc. 10.8%). The second and third steps in the TGA curve are between ~275-495 ºC. These two consecutive weight losses of ~28.9% correspond to the removal of phen ligand (calc. 30.3%). Then, the compound decomposes gradually until a final mass loss of ~72.0%, which indicates the partial loss of the organic linker (~76.6% decomposition; the decomposition percentage for organic linker was calculated considering MgO as a main residue). MgO phase was identified as a main residue by XRPD (JCPDS file No.77-2179), together with an important amorphous contribution.

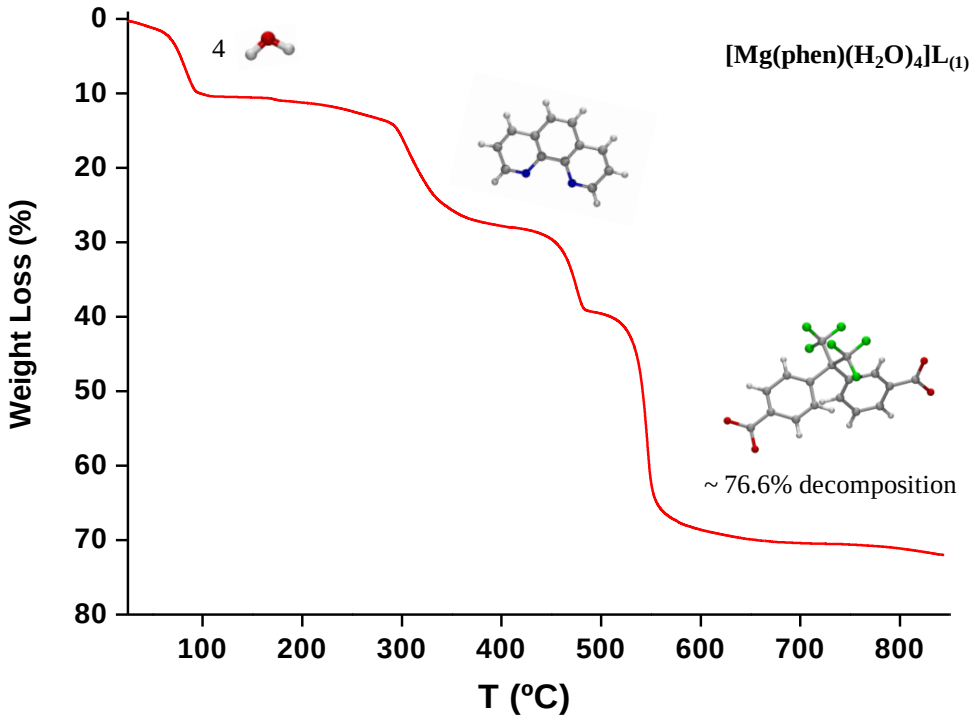

Figure 5.36. TGA profile for **α-AEPF-14**.

- Thermogravimetric profile of **β-AEPF-14** (**Figure 5.37**) shows a first weight loss between ~ 30-125 ºC of ~8.4% consistent with the removal of three water molecules (calc. 8.1%). The fourth coordinated water molecule determined in this compound is lost at ~ 160-200 ºC with a weight loss of ~2.6% (calc. 2.7%). A third weight loss of ~16.4% is found between ~220-305 ºC, with a sharp exothermic DTA signal; a fourth weight loss (~15.6%) is observed between ~430-505 ºC, with a broad exothermic DTA signal (not included). As in the case of the **α**-polymorph, these two weight losses of total 32% correspond to the removal of phen ligand (calc. 30.3%). Then, the compound decomposes gradually until a final mass loss of ~77.9 %, which indicates the partial loss of the organic linker (~82.9% decomposition, considering MgO as a main residue). MgO phase was identified as a main residue by XRPD (JCPDS file No.77-2179), together with an important amorphous contribution.

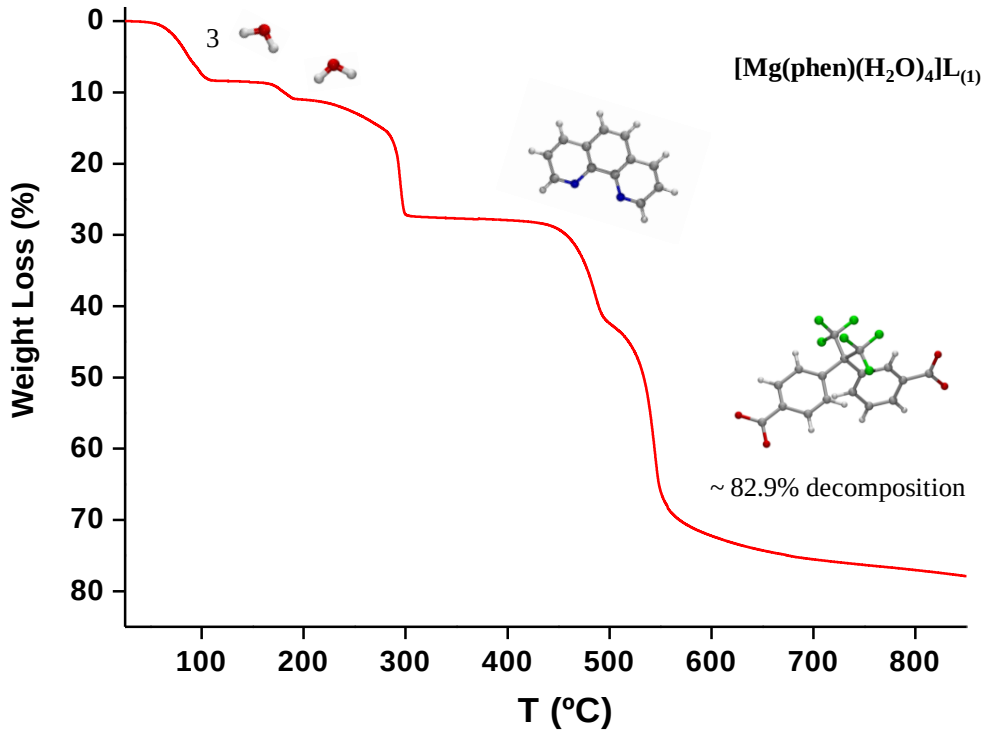

Figure 5.37. TGA profile for **β-AEPF-14**.

- Thermogravimetric profile of **AEPF-16** (**Figure 5.38**) shows a first weight loss between ~ 90-150 ºC of ~5.7% consistent with the removal of the coordinated water molecules determined in this compound (calc. 5.7%). The second and third steps in the TGA curve are determined between ~300-510 ºC. These two consecutive weight losses of ~31.3% correspond to the removal of phen ligand (calc. 30.3%). Then, the compound partially decomposes gradually until a final mass loss of ~71.9%, which indicates the partial loss of the organic linker (~76.8% decomposition). MgO phase was identified as a main residue by XRPD (JCPDS file No.77-2179), together with an important amorphous contribution.

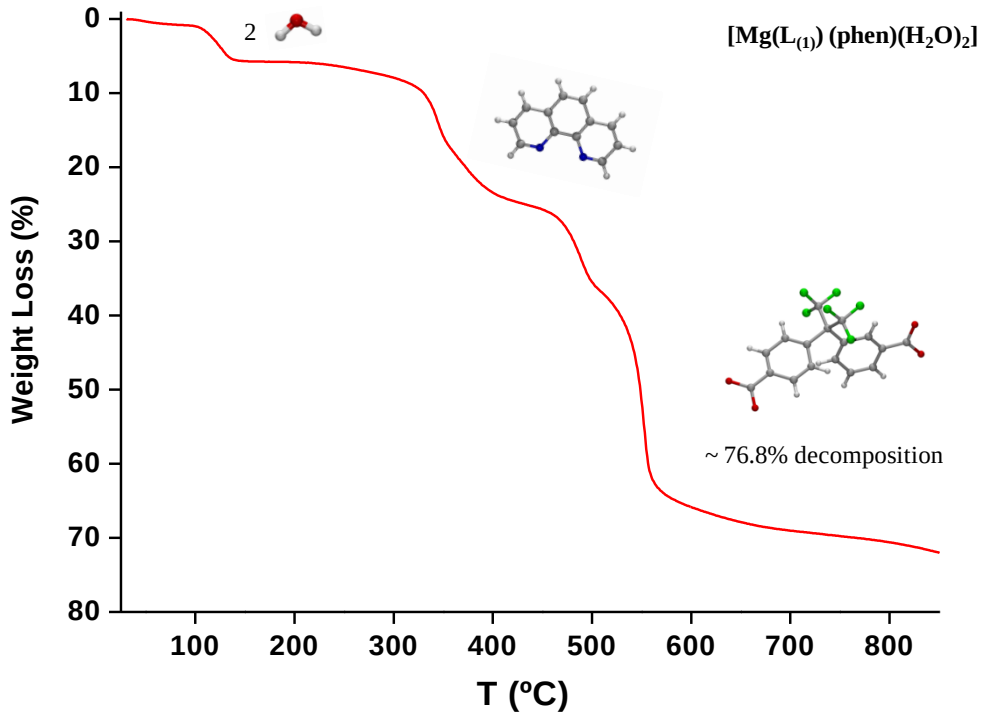

Figure 5.38. TGA profile for **AEPF-16**.

- Thermogravimetric profile of **AEPF-17** (**Figure 5.39**) shows a first weight loss of ~ 3.1% up to ~ 115 ºC, consistent with the loss of physisorbed water molecules. The second weight loss of ~3.0% is determined between ~ 115-215 ºC, consistent with the removal of the coordinated water molecules determined in this compound (calc. 2.9%). The third step in the TGA curve of ~35.9% is determined between ~215-370 ºC, corresponding to the removal of phen ligand (calc. 30.3%). The fourth step at ~435 ºC corresponds to the partial decomposition of the compound until a final mass loss of ~78.1%, which indicates the partial loss of the organic linker (~83.6% decomposition). MgO phase was identified as a main residue by XRPD (JCPDS file No.77-2179), together with an important amorphous contribution.

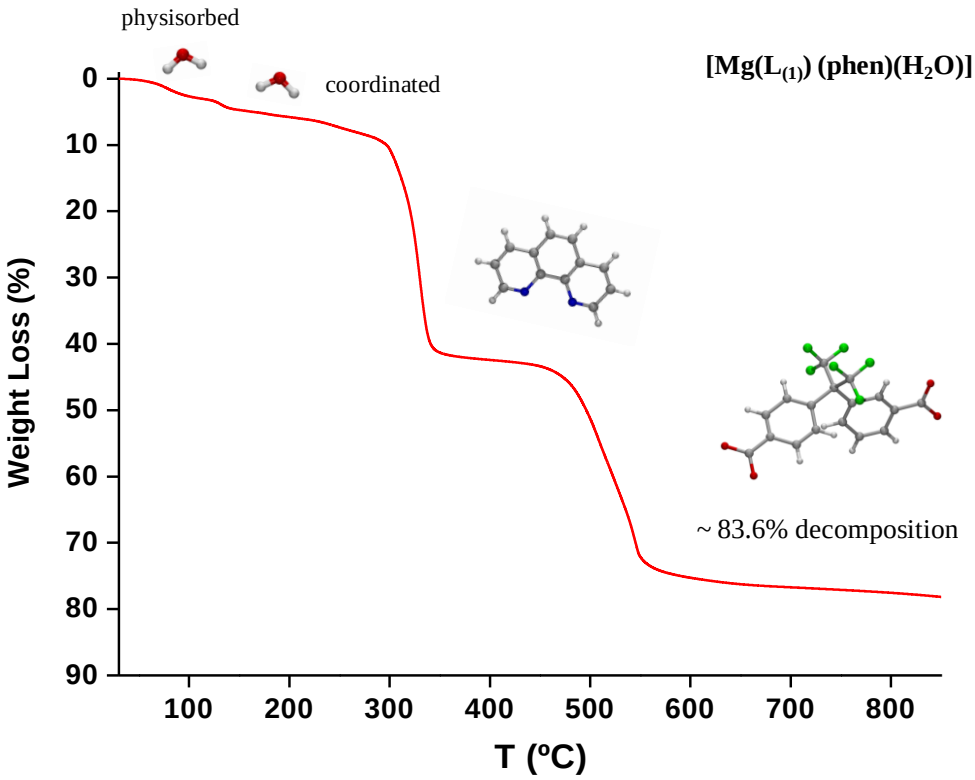

Figure 5.39. TGA profile for **AEPF-17**.

5.5.

Structural stability studies: Theoretical Calculations

In order to determine the structural stability of the magnesium compounds presented in this chapter and to deepen the understanding of their formation pathways, a series of theoretical DFT plane-wave based calculations were carried out. The apparent formation energies for the studied compounds were obtained using the VASP package (*see* Chapter 2, *Techniques*). In all cases, the geometry optimization converged to a stable structure with the same topology that the experimentally determined, even though no symmetry constraints were imposed.

On one hand, the polymorphism phenomenon found for **AEPF-14** compound was analysed in detail using computational studies. With that purpose, the relative energies for the two (**α-** and **β-**) **AEPF-14** polymorphs were determined by DFT based calculations. As it is shown in **Figure 5.40**, after comparing the relative energies for both networks, it can be concluded that the **β-**form is the most stable one. This fact is in good agreement with the higher dimensionality of the supramolecular net of this polymorph (3D).

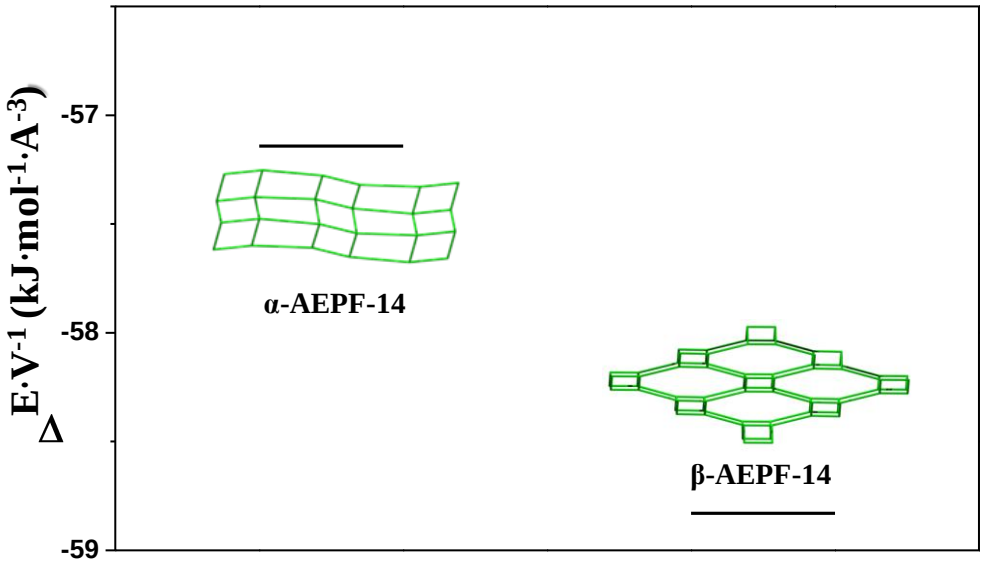

Figure 5.40. Energetic stabilities for both **AEPF-14** polymorphs.

In addition, in order to correlate the structural stability with the synthesis procedures (see *5.2. Effect of Synthesis conditions*), a series of computational studies were performed to determine the relative formation energies ($E_{Formation}$) for those compounds that coexist under certain conditions.

Regarding the hydrothermal reactions performed at lower temperatures (T = 160-170 ºC) and short reaction times (1 - 48 hours) (**Table 5.1**), the coexistence of **α-AEPF-14**, **AEPF-15** and **AEPF-16** compounds was observed. In addition, the ratio among these three phases varies through the time. Thus, while at 160 ºC **α-AEPF-14** is the principal component, when shorter reaction times are used, **AEPF-15** and **AEPF-16** become the principal components of the products mixture for longer reaction times. Taking into account the results coming from formation energies, several conclusions can be drawn. Firstly, **α-AEPF-14** presents the lowest $E_{Formation}$ among these three phases, what seems to indicate that, at shorter reaction times, thermodynamic processes govern the reaction. However, with the increasing of the reaction time and the temperature (170 ºC), **α-AEPF-14** dissolution processes may take place which lead to the formation of the less stable phases (**AEPF-15** and **AEPF-16**).

Concerning the hydrothermal reactions performed at higher temperatures (T= 180 and 200 ºC) and long reaction times (1-10 days) (**Table 5.3**), the coexistence of **AEPF-16** and **AEPF-17** compounds was observed. Moreover, the ratio among the phases varies through the time. Thus, at 180 ºC, after 1 day of reaction, **AEPF-16** and **AEPF-17** are found in a similar proportion; with the increase of the reaction time, **AEPF-17** becomes the principal phase. Taking into account the obtained $E_{Formation}$ values for these compounds (**Figure 5.41**), it can be concluded that at shorter reaction times, kinetic processes govern the reaction. However, when longer reaction times are used, the more stable **AEPF-17** compound is mainly obtained (thermodynamic control). At 200 ºC, an increase of the kinetically controlled phase (**AEPF-16**) is observed.

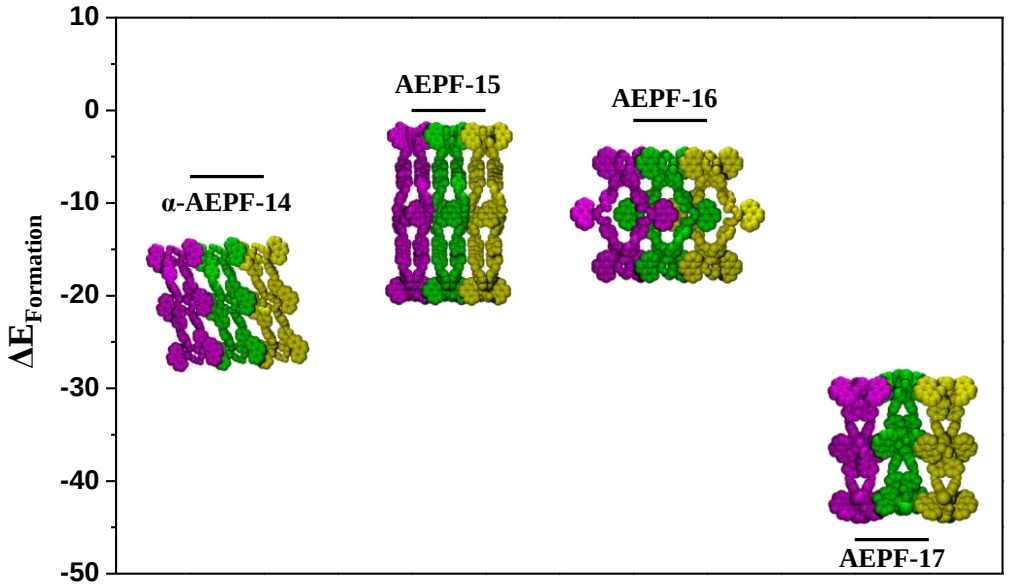

Figure 5.41. Calculated formation energies for **α-AEPF-14**, **AEPF-15**, **AEPF-16** and **AEPF-17** compounds.

5.6.

Dehydration processes: AEPF-14 polymorphs and AEPF-16

As it was above mentioned, both **β-AEPF-14** and **AEPF-16** compounds exhibit a supramolecular net with a **sra** topology. On the other hand, they present the same Mg/phen/$L_{(1)}$ ratio per molecular formula. In this context, we were interested in study of the dehydration processes of these compounds, in order to elucidate the possible transformation from **β-AEPF-14** to **AEPF-16**. This study was also extended to **α-AEPF-14** compound, to determine the possible structural transformations between both **AEPF-14** polymorphic forms.

Taking into account TGA results, both **AEPF-14** samples were heated under vacuum to ensure the removal of coordination water molecules (**α-AEPF-14** at 150ºC and **β-AEPF-14** at 180ºC). The dry samples were examined by XRPD in order to study the structural changes provoked by the dehydration. Although for both polymorphs an important loss of crystallinity was detected after this heating treatment, the indexation of their XRPD patterns could be performed using DICVOL04[10,11] software, implemented in FullProf package.[12] The cell parameters found for the dry samples, together with those determined by single-crystal X ray diffraction for as-synthesized compounds, are shown in **Table 5.28**.

Table 5.28. Cell parameters for **AEPF-14** polymorphs (**α-** and **β-**): for as-synthesised compounds (found by single crystal XRD) and after the dehydration process (found by XRPD).

	AEPF-14 polymorphs			
	α-	**dry α -**	**β-**	**dry β-**
a (Å)	13.2022(2)	11.0(1)	7.3064(2)	6.406(8)
b (Å)	7.6135(1)	9.11(2)	32.602(1)	27.40(2)
c (Å)	31.0128(5)	27.52(4)	12.5442(4)	11.75(1)
α (º)	90	90	90	90
β (º)	99.863(1)	97.6(7)	90	90
γ (º)	90	90	90	90
Volume (Å^3)	3071.18(8)	2735.3(2)	2988.1(2)	2062.0(1)
Figures of merit	-	M_{12}=12,F_{12}=19		M_{14}=10,F_{14}=12

In addition, in order to compare the obtained results, the same study was performed with **AEPF-16** compound (the sample was heated at 150ºC). The cell parameters found for the dry sample, together with those determined by single-crystal X ray diffraction for the as-synthesized compound, are shown in **Table 5.29**.

Table 5.29. Cell parameters for as-synthesised sample of **AEPF-16** (found by single crystal X Ray Diffraction) and for the sample after the dehydration process (found by XRPD).

	AEPF-16	dry AEPF-16
a (Å)	9.3105(3)	9.1736(8)
b (Å)	26.8940(8)	26.488(5)
c (Å)	11.2146(3)	11.057(3)
α (º)	90	90
β (º)	90	90
γ (º)	90	90
Volume (Å^3)	2808.1(1)	2686.8(2)
Figures of merit	-	M_{20}=35,F_{20}=68

Taking into account these results, several conclusions can be drawn: regarding the behaviour of **AEPF-16** during the dehydratation process, the compound suffers an isotropic contraction (~1.5%) of its cell parameters, giving rise to a reduction of 4.3% in its cell volume ($V_{AEPF-16}$= 2808.1 Å^3, $V_{dryAEPF-16}$= 2686.8 Å^3) (**Table 5.29**), retaining the orthorhombic crystal system and its crystallinity.

In the case of **AEPF-14,** both polymorphs exhibit different structural transformations when losing their coordinated water molecules, as it can be suspected considering the different topologies found in their supramolecular nets. Thus, while **β**-polymorph exhibits a double helical chains joint along the *a* and the *c* axes *via* hydrogen bonds (**sra** net), for **α**-polymorph only an undulating double chains jointed along the *b* axis can be found (**sql** layers). As it is shown in **Table 5.28**, after dehydration the orthorhombic **β**-polymorph retrains its crystal symmetry system although it suffers an important contraction of the *b* axis (~16%) (along which the 2_1 axis runs) and the *a* axis (~12%) (along which the π-π stacking runs). These results point out the first conclusion: *the similarities found between the cell parameters of* ***dry β-AEPF-14*** *and* ***dry AEPF-16*** *allows us to elucidate a transformation of both compounds to a similar orthorhombic phase with a double helical chains structure (Figure* ***5.42b*** *and* ***5.42c****). Considering the topological similarities between the two*

compounds, the structural transformation caused by the loss of coordinated water molecules can be explained as a subtle contraction of the 1D-helical structure.

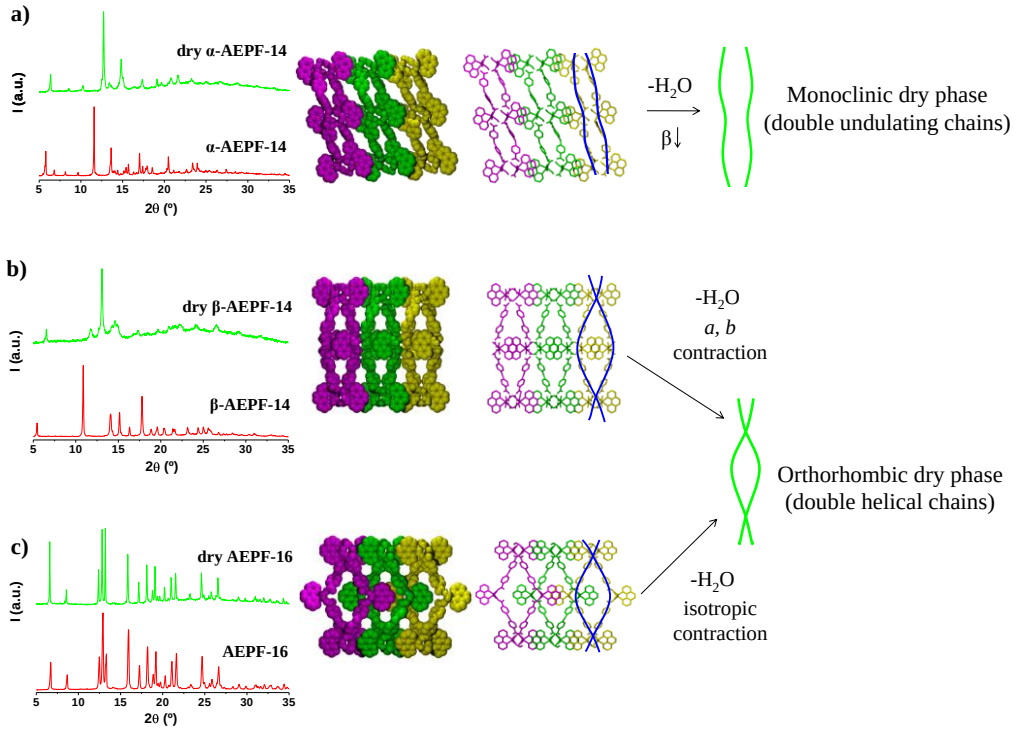

Figure 5.42. Structural study performed with dehydrated samples for: **a) α-AEPF-14**, **b) β-AEPF-14** and **c) AEPF-16**. On the left, comparison of XRPD patterns before and after the dehydration treatment is shown. On the right, stick and space filling representations of the double chain structures are depicted

In the case of the **dry α-AEPF-14** compound, its XRPD pattern was indexed to a monoclinic cell which exhibits similar cell parameter values with those of **dry AEPF-16** but a value of β~98º, which is far from the orthorhombic crystal system (**Table 5.28**). So, the second conclusion that can be drawn is: *starting from **α**-monoclinic polymorph, in which the double chains are not joint via inter-chain hydrogen bonds, the formation of 1D helical structure does not take place (Figure **5.42a**). Thus, the structural transformation that suffers **α-AEPF-14** after the dehydration treatment can be caused by little changes in the undulating packing of these layers.*

References

1. Fujita, M.; Tominaga, M.; Hori, A.; Therrien, B. *Acc. Chem. Res.*, **2005**, *38(4)*, 369.
2. Gándara, F.; de la Peña-O'Shea, V. A.; Illas, F.; Snejko, N.; Proserpio, D. M.; Gutiérrez-Puebla, E.; Monge, M. A. *Inorg. Chem.*, **2009**, *48*, 4707.
3. Gándara, F.; Gómez-Lor, B.; Gutiérrez-Puebla, E.; Iglesias, M.; Monge, M. A.; Proserpio, D. M.; Snejko, N. *Chem. Mater.*, **2007**, *20*, 72.
4. Pan, L.; Sander, M. B.; Huang, X.; Li, J.; Smith, M.; Bittner, E.; Bockrath, B.; Johnson, J. K. *J. Am. Chem. Soc.*, **2004**, *126*, 1308.
5. Spek, A. L. *PLATON*, A multipurpose Crystallographic Tool, Utrecht University, Utrecht, Holland, **2005**.
6. Rosi, N. L.; Kim, J.; Eddaoudi, M.; Chen, B.; O'Keeffe, M.; Yaghi, O. M. *J. Am. Chem. Soc.*, **2005**, *127(5)*, 1504.
7. Blatov, V.A. *IUCr Comput. Comm. Newslett.*, **2006**, *7*, 4; see also: http://www.topos.ssu.samara.ru.
8. Pawley, G. S. *J. Appl. Crystallogr.* **1981**, *14*, 357.
9. Materials Studio Modelling 4.4, http://www.accelerys.com/mstudio/ms_modeling.
10. Lour, D.; Louer, M. J. *J. Appl. Crystallogr.*, **1972**, *5*, 271.
11. Boultif, A.; Louer, D. *J. Appl. Crystallogr.*, **1991**, *24*, 987.
12. Rodriguez-Carvajal, J. *Physica B.* **1993**, *192*, 55.

Chapter 6

From coordinatively weak ability of constituents to very stable AEPFs

Anthraquinone-2,6-disulfonate ligand (2,6-AQDS)

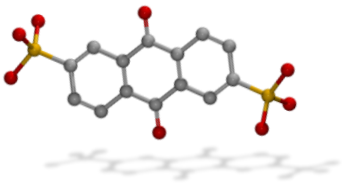

2,6-AQDS

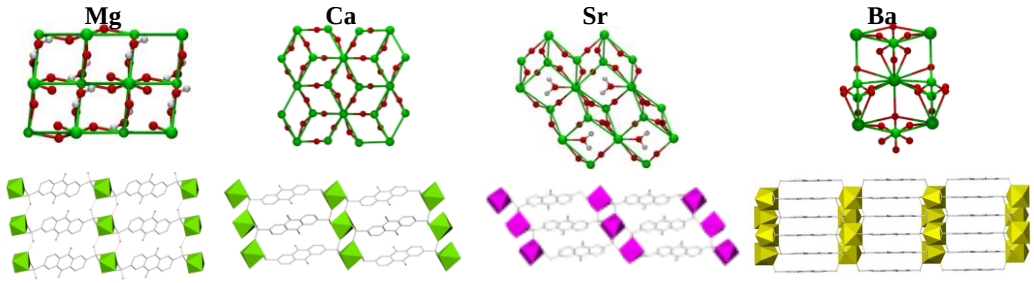

Abstract

Four new compounds based on alkaline-earth elements ions and anthraquinone-2,6-disulfonate (2,6-AQDS) ligand were obtained and characterized: **AEPF-2** is the first MOF Mg-based disulfonate, in which the ligand directly coordinates with Mg^{+2} ions to build a two-dimensional net; **AEPF-3**, **AEPF-4**, and **AEPF-5** for Ca^{+2}, Sr^{+2}, and Ba^{+2} ions, respectively, have different three-dimensional structural types and two new topologies. The catalytic behaviour of these alkaline-earth materials in alkenes hydrogenation and ketones hydrosilylation reactions makes them cheap and environmentally friendly promising catalysts: in all cases, 100% selectivity was achieved toward ethylbenzene, in contrast with the behaviour previously reported with calcium and strontium homogeneous catalysts. The high thermal stability (up to 500 ˚C) has to be emphasized for all these materials.

The results presented in this chapter have been published in Crystal Growth and Design, **2011**, *11 (5)*, 1750-1758.

6.1.

Introduction

As it happens with Metal-Organic Frameworks (MOFs) in which the organic linkers possess carboxylate groups, the majority of sulfonate MOFs reported up to the moment are based on transition metals and rare earth cations. However, the use of alkaline-earth metals have received much less attention,[1-5] probably because they are usually regarded as unsuitable metal centers to form such polymers. Two reasons prevent the use of s-blocks in the MOFs design: their unpredictable coordination numbers and geometries as no ligand field stabilization effects govern their coordinative bonding, and their tendency to form solvated metal centres, and thus, the formation of the typical alternating $[M(H_2O)_6]$ L organic-inorganic ionic layers or molecular compounds.

On the other hand, in the broad domain of MOFs synthesis, networks based on sulfonate ligation are relatively less studied despite of the fact that interesting materials with layered structures have been reported.[6,7] In this context, although some research groups have reported the synthesis of alkaline-earth MOFs using different dicarboxylate ligands,[8-14] notmany networks based on sulfonate coordination groups and alkaline-earth elements have been obtained. In fact, concerning the use of disulfonate ligands, only few examples of barium and strontium three-dimensional nets and just one layered calcium structure have been reported in the literature.[1-5]

Due to the weak coordination strength of the sulfonate functionality, many of them do not displace water from the primary coordination sphere. In the case of the Group 2 metals, only the larger alkaline-earth elements coordinate to both water molecules and sulfonate groups.[1] The supramolecular chemistry of the sulfonate group in extended solids was reviewed by Shimizu *et al.*,[15,16] and for the metal arenesulfonates, by J. Cai.*et al.*[17] Recently, a few systematic works have also shown that in the case of sulfonate ligands, hard metal ions remain highly hydrated and typically results in zero or one-dimensional structures.[2,3]

This chapter encompasses four novel 2D and 3D alkaline-earth polymeric frameworks (**AEPF**) belonging to different structural types (named **AEPF-2**, **AEPF-3**, **AEPF-4** and **AEPF-5**), in which the metal centers are coordinated to anthraquinone-

2,6-disulfonate (2,6-AQDS) ligands. The structure and properties of the four resulting compounds are discussed and the results of the catalytic activity of these materials in hydrogenation of alkenes and hydrosilylation of ketones reactions under mild conditions are also shown.

6.2.

Crystal structure description and topological analyses

As it was previously mentioned in Chapter 2 (see *Synthesis procedures)*, after carefully optimizing the solvothermal synthesis conditions, suitable single crystals were obtained for all the compounds presented in this chapter (**AEPF-2**, **AEPF-3**, **AEPF-4** and **AEPF-5**). In the following, the structural features and the topological analyses for **AEPF-2**, **AEPF-3**, **AEPF-4** and **AEPF-5** are shown.

6.2.1.

Mg-AEPF-2

The reaction between 2,6-AQDS and magnesium acetate tetrahydrate under the optimized solvothermal synthesis conditions (*see* Chapter 2, *Synthesis procedures*), gives rise to the **[Mg(2,6-AQDS)(H_2O)$_2$]** compound (**AEPF-2**), which crystallizes in the triclinic crystal system (*P-1* space group). The cell parameters determined for this structure are: a = 4.8682(5) Å, b = 5.7700(6) Å, c = 13.4652(15) Å, α = 94.500(2)˚, β = 90.517(2)˚, γ= 95.403(2)˚, and V= 375.34(7) Å^3.The main crystallographic and refinement data for this compound are shown in **Table 6.1** and the ORTEP representation of **AEPF-2** asymmetric unit is depicted in **Figure 6.1**.

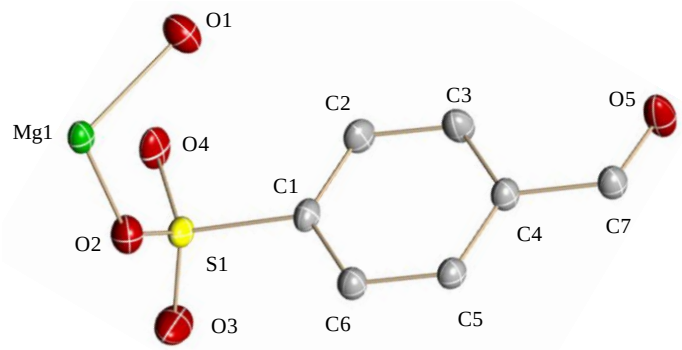

Figure 6.1. ORTEP representation of **AEPF-2** asymmetric unit. Ellipsoids are displayed at the 50% probability level. Hydrogen atoms were omitted for clarity.

It is worth mentioning that **AEPF-2** is the first reported magnesium-contained disulfonate MOF in which the SO_3^- groups directly coordinate the Mg^{+2} ions. The synthesis of this kind of magnesium materials entails several difficulties, which are inherent to the chemical properties of this alkaline-earth metal. All these synthetic difficulties were solved performing a careful study of the synthesis conditions. In this context, it should be highlighted that the solvent used in the synthesis of **AEPF-2** is crucial to avoid the formation of $[Mg(H_2O)_6]^{+2}$ species. In fact, when the reaction between 2,6-AQDS disulfonate ligand and magnesium salt is performed under hydrothermal conditions, Mg^{+2} ions were dissolved (due to the formation of $[Mg(H_2O)_6]^{+2}$ species) and only the precipitation of the 2,6-AQDS takes place. However, when a more non-polar solvent was added (like 1-butanol), the coordination of Mg^{+2} ions with sulfonate groups is favoured. Thus, after carefully optimising the solvothermal synthesis procedures, **AEPF-2** can be successfully synthesised using a suitable mixture of water and 1-butanol as solvent (see Chapter 2, *Synthesis procedures*).

Table 6.1. Crystallographic and refinement data for **AEPF-2**.

Identification code	**AEPF-2**
Empirical formula	C_{14} H_{10} Mg O_{10} S_2
Formula weight	426.67
Temperature	296(2) K
Wavelength	0.71073 Å
Crystal system	Triclinic
Space group	*P-1*
Unit cell dimensions	a = 4.8682(5) Å α = 94.500(2)° b = 5.7700(6) Å β = 90.517(2)° c = 13.465(2) Å γ = 95.403(2)°
Volume	375.34(7) $Å^3$
Z	1
Density (calculated)	1.888 Mg/m^3
Absorption coefficient	0.459 mm^{-1}
F(000)	218
Crystal size	0.15 x 0.10 x 0.04 mm^3
Theta range for data collection	3.04 to 25.03°
Index ranges	-5<=h<=5, -6<=k<=6, -15<=l<=15
Reflections collected	2682
Independent reflections	1292 [R(int) = 0.0179]
Completeness to theta = 25.03°	97.70%
Absorption correction	Semi-empirical from equivalents
Max. and min. Transmission	0.9819 and 0.9344
Refinement method	Full-matrix least-squares on F^2
Data / restraints / parameters	1292 / 2 / 132
Goodness-of-fit on F^2	1.093
Final R indices [I>2sigma(I)]	R_1 = 0.0295, wR_2 = 0.0749
R indices (all data)	R_1 = 0.0321, wR_2 = 0.0761
Largest diff. peak and hole	0.288 and -0.399 e.$Å^{-3}$

In **AEPF-2**, Mg^{+2} ion is hexa-coordinated to four oxygen atoms coming from two 2,6-AQDS ligands and to two oxygen atoms of water molecules, giving a regular MgO_6 octahedron (**Figure 6.2a**). These polyhedra, which can be considered as the inorganic primary building units (PBUs), have an average Mg-O distance of ~2.07 Å (**Table 6.2**). Moreover, those Mg-Ow bonds, which correspond to the coordination of water molecules, present the shorter distances.

Table 6.2. Interatomic distances in the coordination sphere of the MgO_6 octahedron.

Bond	Distance (Å)
Mg(1)-O(1)w	2.060(2)
Mg(1)-O(1)[1]w	2.060(2)
Mg(1)-O(4)[2]s	2.066(2)
Mg(1)-O(4)[3]s	2.066(2)
Mg(1)-O(2)s	2.072(2)
Mg(1)-O(2)[1]s	2.072(2)

Symmetry transformations used to generate equivalent atoms:
[1] -x,-y+1,-z+2
[2] x-1,y,z
[3] -x+1,-y+1,-z+2

Ow: oxygen atom coming from a water coordination molecule. Os: oxygen atom coming from a sulfonate group.

As it is depicted in **Figure 6.2**, the MgO_6 polyhedra determined in **AEPF-2** are connected *via* sulfonate groups, leading to the formation of chains along the *a* axis (**Figure 6.2b**). Junction of these chains is made through the complete linker, which acts in a $\eta^2\mu_2$-$\eta^2\mu_2$ coordination mode (**Figure 6.2c**). This coordination mode implies that 2,6-AQDS sulfonate groups do not exhibit their maximum coordination capability. In fact, each $–SO_3$ group presents one oxygen atom which is not covalently bounded to any metallic center. These non-coordinated oxygen atoms, which cause a lower dimensionality in the framework, are crucial in the formation of supramolecular interactions. Therefore, **AEPF-2** material can be described as a covalent framework consisting of layers perpendicular to the *b* direction (**Figure 6.3a**), in which the sulfonate linkers directly coordinate the magnesium atoms.

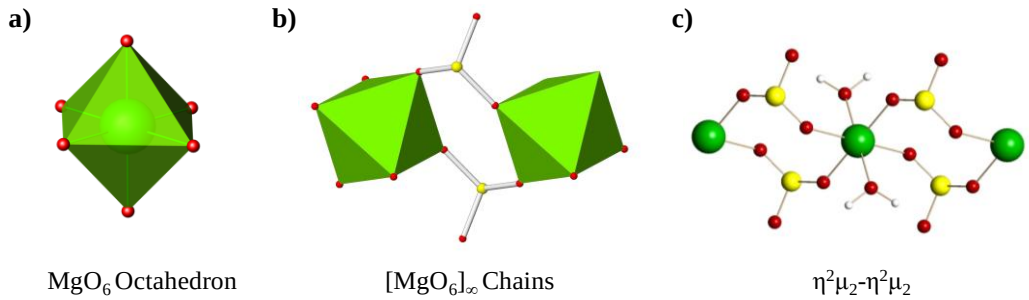

Figure 6.2. a) Inorganic PBUs in **AEPF-2, b)** detail of the MgO_6 chains that run along the *a* axis and **c)** coordination mode of 2,6-AQDS ligand.

Moreover, as it was previously mentioned, two water molecules are coordinated to each magnesium center, which give rise to the presence of three different types of hydrogen bonds. As it is shown in **Table 6.3**, these supramolecular interactions are determined between water molecules and non-coordinated oxygen atoms of 2,6-AQDS sulfonate groups.

Table 6.3. Distances and angles of hydrogen bonds found in **AEPF-2** compound.

D-H···A[1]	D-H[2]	H···A[3]	D···A[4]	<D-H···A[5]
O(1)w-H(1A)w...O(2)s[1]	0.94(2)	2.40(4)	3.060(2)	127(3)
O(1)w-H(1A)w...O(3)s[1]	0.94(2)	2.47(2)	3.355(3)	159(4)
O(1)w-H(1B)w...O(3)s[2]	0.94(2)	1.81(2)	2.748(2)	173(3)
Symmetry operators codes				
[1] x, y-1, z	[2] x-1, y-1, z			

D: donor atom, A: acceptor atom. [1]Names of donor, hydrogen and acceptor atoms involved in the hydrogen bond. [2]Distance D – A. [3]Distances H – A. [4]Distance D – A. [5] Angle D – H – A.

Os: oxygen atom corresponding to a sulfonate group. Ow: oxygen atom corresponding to a coordinated water molecule. Hw: hydrogen atom corresponding to a coordinated water molecule.

As it is depicted in **Figure 6.3b** and **6.3c**, the presence of these supramolecular interactions leads to the junction of the covalent layers among them, giving rise to a well-defined three-dimensional framework.

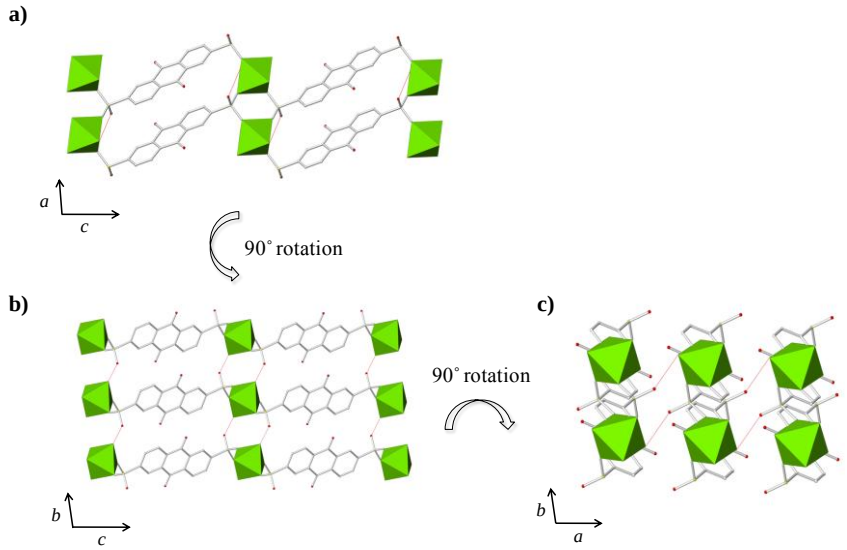

Figure 6.3. a) Layers perpendicular to the *b* direction, where the inorganic SBUs are forming chains along the *a* axis. **b)** View of interlayer hydrogen bonds (in red) along the *a* direction and **c)** along the *c* axis.

From the topological point of view, the net simplifications were performed considering S atoms from $–SO_3$ groups as nodes instead of analysing the whole 2,6-AQDS ligand as a unique node. After carefully studying these materials, it can be assumed that this kind of simplification is chemically clearer than other possibilities. Taking into account this, and by simplification of the covalent layers in **AEPF-2** using TOPOS,[19] two types of nodes are found: four-connected (Mg) and three-connected (S) nodes. This two-periodic net exhibits a **3,4L13** topology (point symbol $(4.6^2)_2(4^2.6^2.8^2)$) (**Figure 6.4a**). Moreover, as it is previously mentioned, the layers are bonded *via* hydrogen bonds formed by the coordinated water molecules and the 2,6-AQDS oxygen atoms. Taking into account these interactions, the supramolecular 3D net has the typical inorganic layered structure described previously for other materials based on this ligand.[18] By simplification of inorganic layers, two types of nodes can be found: eight-connected (Mg) and four-connected (S) nodes, giving rise to inorganic layers with point symbol $(4^{20}.6^8)(4^6)_2$ (**Figure 6.4b**). This layer type appears neither in TOPOS nor in the RCSR data bases. Joining of these layers through the four-connected nodes gives rise to a three-periodic net, which exhibits a **5,8T16** topology (point symbol $(4^{20}.6^8)(4^6.6^4)^2$) (**Figure 6.4c**).

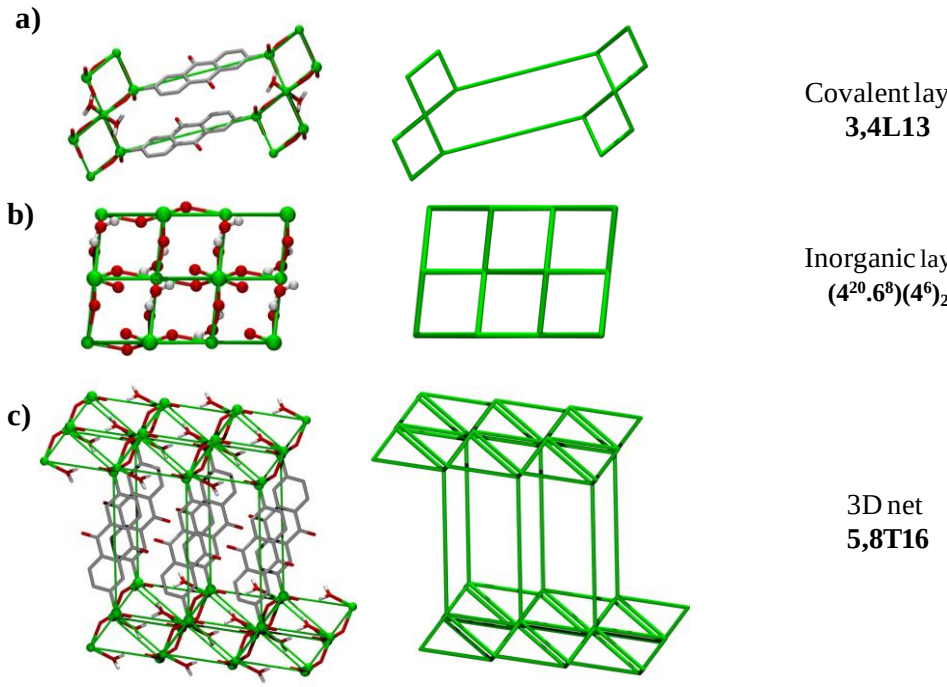

Figure 6.4. Topological simplifications performed in **AEPF-2** to describe the **a)** Covalent layers, **b)** Inorganic layers and **c)** 3D net.

6.2.2.

Ca-AEPF-3

As it occurs when magnesium is used as alkaline-earth metal center, in the case of calcium disulfonate materials, the control on the synthesis conditions is a critical point to obtain polymeric frameworks as pure phases. Thus, after careful optimizing the synthesis procedures, the solvothermal reaction between 2,6-AQDS disulfonate ligand and calcium acetate hydrate (*see* Chapter 2, *Synthesis procedures*), gives rise to a novel material with formula **[Ca(2,6-AQDS)]**(**AEPF-3**). This compound crystallizes in the monoclinic crystal system ($P2_1/c$ space group). The cell parameters determined for this structure are: a = 14.863(3) Å, b = 5.581(1) Å, c = 9.308(2) Å, β = 105.968(3)°, V = 742.2(3) Å^3.The ORTEP representation of **AEPF-3** asymmetric unit is shown in **Figure 6.5** and the main crystallographic and refinement data for this compound are shown in **Table 6.4**.

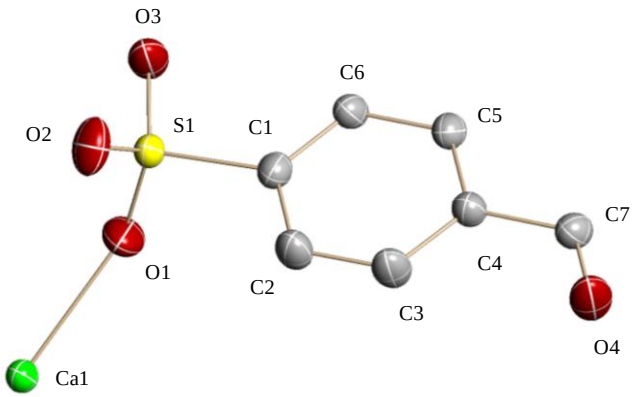

Figure 6.5. ORTEP representation of **AEPF-3** asymmetric unit. Ellipsoids are displayed at the 50% probability level. Hydrogen atoms were omitted for clarity.

In **AEPF-3**, Ca^{+2} ions are bonded to six oxygen atoms coming from 2,6-AQDS sulfonate groups. Thus, as it occurs in the case of **Mg-AEPF-2** compound, the alkaline-earth metal ions are occupying the centers of regular CaO_6 octahedra (**Figure 6a)**, with an average Ca-O distance of ~2.32 Å (**Table 6.5**). It is worth mentioning that the Ca-O distances corresponding to the three different types of bonds determined among sulfonate groups and calcium centers are quite different.

Table 6.4. Crystallographic and refinement data for **AEPF-3**.

Identification code	AEPF-3
Empirical formula	$C_{14}H_6CaO_8S_2$
Formula weight	406.41
Temperature	296(2) K
Wavelength	0.71073 Å
Crystal system	Monoclinic
Space group	$P2_1/c$
Unit cell dimensions	a = 14.863(3) Å α = 90° b = 5.581(1) Å β = 105.968(3)° c = 9.308(2) Å γ = 90°
Volume	742.2(3) $Å^3$
Z	2
Density (calculated)	1.818 Mg/m^3
Absorption coefficient	0.749 mm^{-1}
F(000)	412
Crystal size	0.20 x 0.10 x 0.05 mm^3
Theta range for data collection	1.43 to 28.26°
Index ranges	-19<=h<=19, -7<=k<=7, -12<=l<=12
Reflections collected	6281
Independent reflections	1796 [R(int) = 0.0376]
Completeness to theta = 25.03°	97.10%
Absorption correction	Semi-empirical from equivalents
Max. and min. Transmission	0.9635 and 0.8647
Refinement method	Full-matrix least-squares on F^2
Data / restraints / parameters	1796 / 0 / 115
Goodness-of-fit on F^2	1.058
Final R indices [I>2sigma(I)]	R_1 = 0.0499, wR_2 = 0.1376
R indices (all data)	R_1 = 0.0751, wR_2 = 0.1622
Largest diff. peak and hole	0.973 and -0.778 e.$Å^{-3}$

Moreover, as it is depicted in **Figure 6.6b**, each CaO_6 polyhedron, which can be considered as the inorganic PBU in **AEPF-3**, is bonded to other six octahedra *via* sulfonate 2,6-AQDS groups, which act in a hexa-topic $\eta^3\mu_3$-$\eta^3\mu_3$ coordination mode (**Figure 6.6c**). This kind of coordination mode gives rise to the presence of inorganic layers which are perpendicular to the *a* axis.

Table 6.5. Interatomic distances in the coordination sphere of the CaO_6 octahedron in **AEPF-3**.

Bond	Distance (Å)
Ca(1)-O(2)[1]s	2.292(2)
Ca(1)-O(2)[2]s	2.292(2)
Ca(1)-O(1)[3]s	2.319(2)
Ca(1)-O(1)s	2.319(2)
Ca(1)-O(3)[4]s	2.342(2)
Ca(1)-O(3)[5]s	2.342(2)

Symmetry transformations used to generate equivalent atoms:
[1] 2 -x+2,y+1/2,-z+3/2
[2] x,-y+1/2,z-1/2
[3] -x+2,-y+1,-z+1
[4] -x+2,-y,-z+1
[5] x,y+1,z

Os: oxygen atom coming from a sulfonate group.

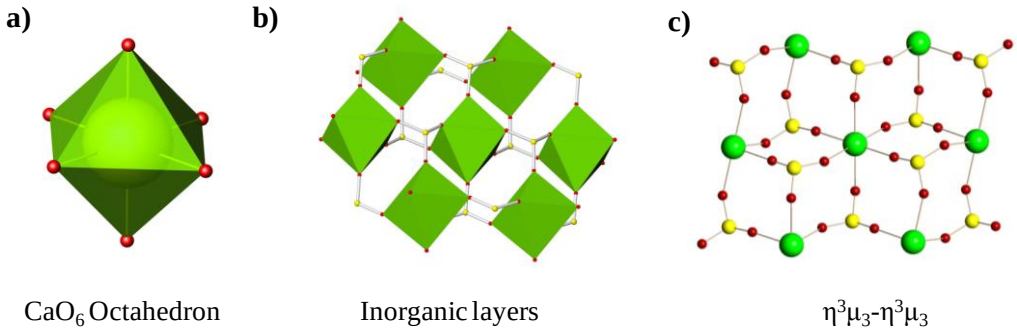

Figure 6.6.a) Inorganic PBUs, **b)** detail of the inorganic layers and **c)** coordination mode of 2,6-AQDS ligand in **AEPF-3**.

In **Figure 6.7**, different polyhedral views along the crystallographic axis are depicted, what evidences the three-dimensional covalent framework determined in **AEPF-3**. Moreover, it is worth mentioning that **AEPF-3** possesses inorganic layers perpendicular to the *a* axis, as it occurs in the case of **Mg-AEPF-2** (if hydrogen bonds are taken into account). However, for the calcium disulfonate material, the inorganic CaO_6 layers are covalently bounded among them through the 2,6-AQDS linker (**Figure 6.7c**).

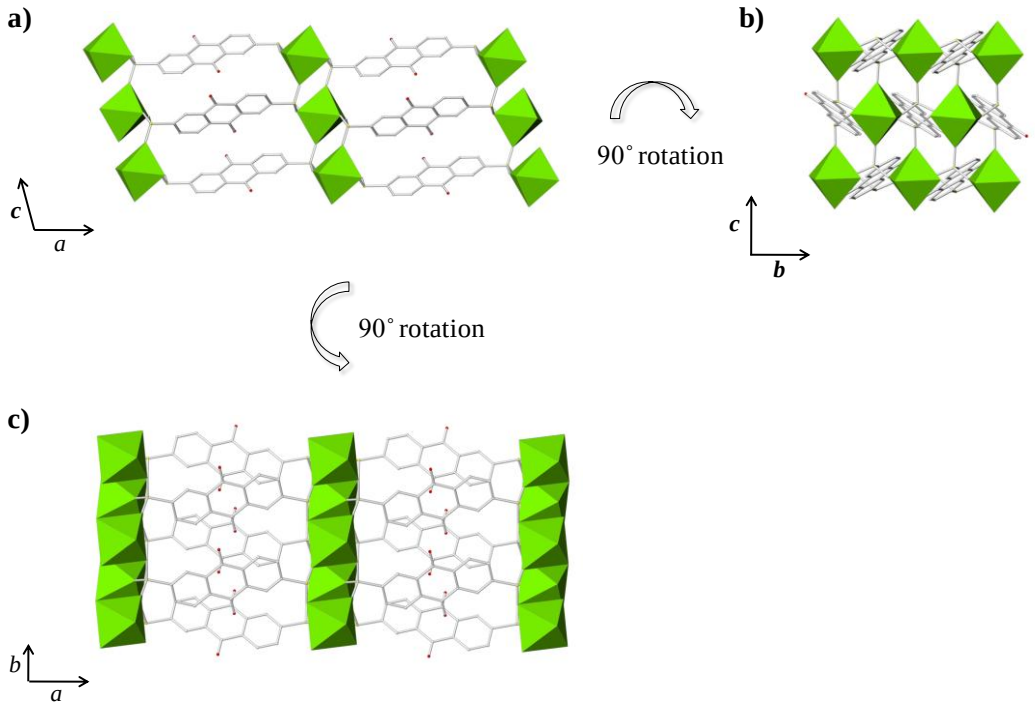

Figure 6.7. a) Polyhedral representation for **AEPF-3** along the *b* axis, **b)** along the *a* axis and **c)** depiction of inorganic layers perpendicular to the *a* axis.

From the topological point of view, by simplification of the inorganic layers in **AEPF-3** using TOPOS,[19] two types of nodes can be determined: six-connected (Ca) and three-connected (S) nodes. This two-periodic net belongs to the **kgd** topological type (point symbol $(4^3)_2(4^6.6^6.8^3)$) (**Figure 6.8a**). Joining of these layers through the three-connected nodes gives rise to an **fsh** three-dimensional net (point symbol $(4^3.6^3)_2(4^6.6^6.8^3)$) (**Figure 6.8b**).

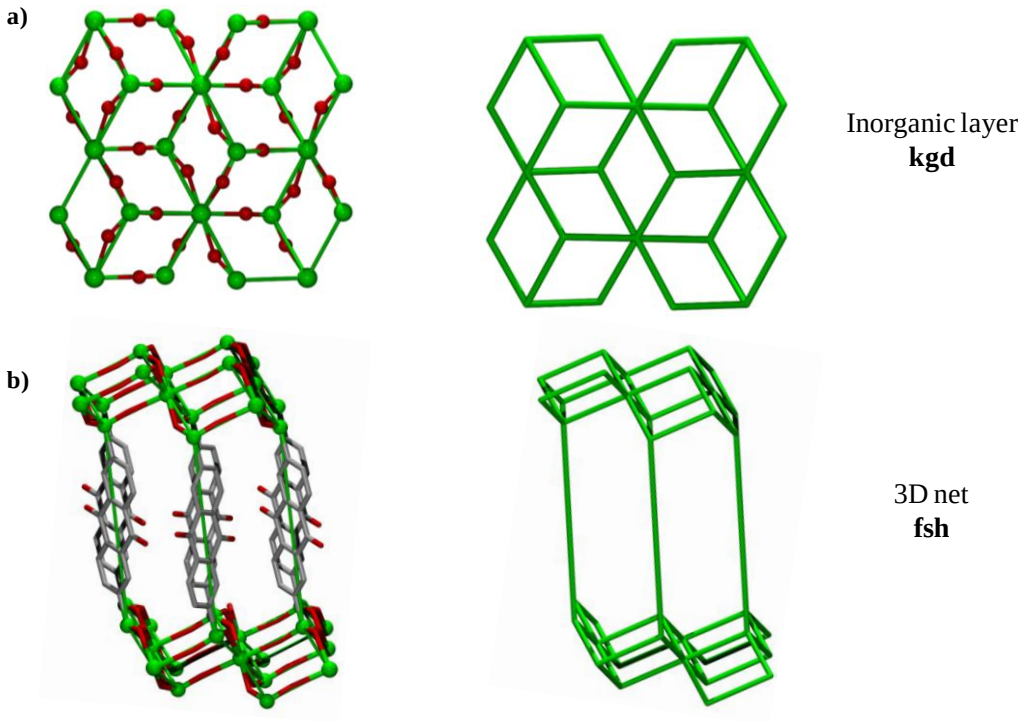

Figure 6.8. Depiction of the topological simplifications performed in **AEPF-3** to describe the **a)** inorganic layers and the **b)** 3D net.

Additionally, a deeper topological study was performed in **AEPF-3** framework, in order to analyse the natural tiling that can be described for an **fsh** net. For that purpose, in a first step, the idealisation of the **fsh** net determined in **AEPF-3** was performed in its maximum symmetry embedding (*R-3 m* space group), using Systre package.[20] In **Figures 6.9a** and **6.9b** both the real ($P2_1/c$ space group) and the idealised net (*R-3 m* space group) for **AEPF-3** are shown. Thus, considering the idealised net, $[4^3.6^3]$ cages or tiles can be described (**Figure 6.9c**), which explain the natural tiling corresponding to an **fsh** net.

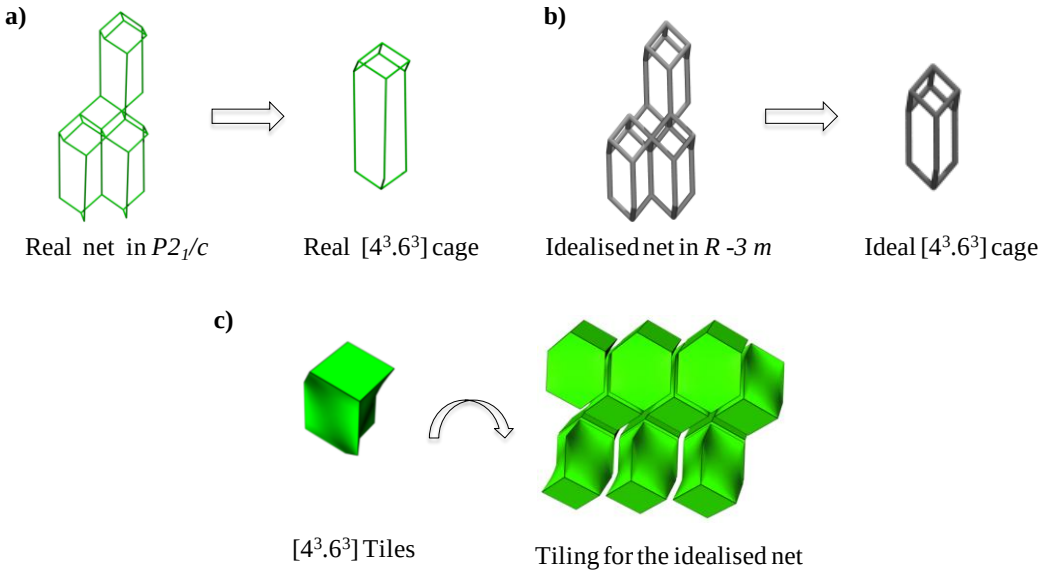

Figure 6.9. a) Real net and cage in $P2_1/c$ space group. **b)** Idealised net and cage in R-3m space group. **c)** $4^3.6^3$ tile and tiling corresponding to an **fsh** net described for**AEPF-3**.

6.2.3.

Sr-AEPF-4

The solvothermal reaction between 2,6-AQDS ligand and strontium acetate (*see* Chapter 2, *Synthesis procedures*) in the optimized synthesis conditions gives rise to a new disulfonate material with formula **[Sr(2,6-AQDS)(H_2O)]** (**AEPF-4**). This strontium compound crystallizes in the triclinic crystal system (*P-1* space group). The cell parameters determined in this structure are: a = 4.425(1) Å, b = 10.219(2) Å, c = 14.537(3) Å , α = 103.584(4), β = 99.853(4)˚, γ = 95.790(4)˚, and V = 763.4(3) Å^3. The ORTEP representation of **AEPF-4** asymmetric unit is shown in **Figure 6.10** and the main crystallographic and refinement data for this compound are shown in **Table 6.6**.

Table 6.6. Crystallographic and refinement data for **AEPF-4**.

Identification code	AEPF-4
Empirical formula	$C_{28}H_{16}O_{18}S_4Sr_2$
Formula weight	471.96
Temperature	296(2) K
Wavelength	0.71073 Å
Crystal system	Triclinic
Space group	*P-1*
Unit cell dimensions	a = 5.425(1) Å α = 103.584(4)°
	b = 10.219(2) Å β = 99.853(4)°
	c = 14.537(3) Å γ = 95.790(4)°
Volume	763.4(3) $Å^3$
Z	2
Density (calculated)	2.053 Mg/m^3
Absorption coefficient	3.857 mm^{-1}
F(000)	468
Crystal size	0.20 x 0.12 x 0.08 mm^3
Theta range for data collection	2.07 to 25.03°
Index ranges	-6<=h<=6, -11<=k<=12, -17<=l<=16
Reflections collected	5095
Independent reflections	2565 [R(int) = 0.0591]
Completeness to theta = 25.03°	94.60%
Absorption correction	Semi-empirical from equivalents
Max. and min. Transmission	0.7478 and 0.5126
Refinement method	Full-matrix least-squares on F^2
Data / restraints / parameters	2565 / 2 / 243
Goodness-of-fit on F^2	1.015
Final R indices [I>2sigma(I)]	R_1 = 0.0614, wR_2 = 0.1049
R indices (all data)	R_1 = 0.0981, wR_2 = 0.1152
Largest diff. peak and hole	0.754 and -0.573 $e.Å^{-3}$

In **AEPF-4**, Sr^{+2} ions are bonded to six oxygen atoms coming from 2,6-AQDS sulfonate groups and one oxygen atom from a coordinated water molecule. Thus, in this case the alkaline-earth metal ions are occupying the centers of SrO_7 monocapped trigonal prisms (**Figure 6.11a)**, with an average Sr-O distance of ~2.57 Å (**Table 6.7**). Moreover, those Sr-Ow bonds, which correspond to the coordination of water molecules, present the second larger distances in contrast to **AEPF-3** where this bond was the shorter one.

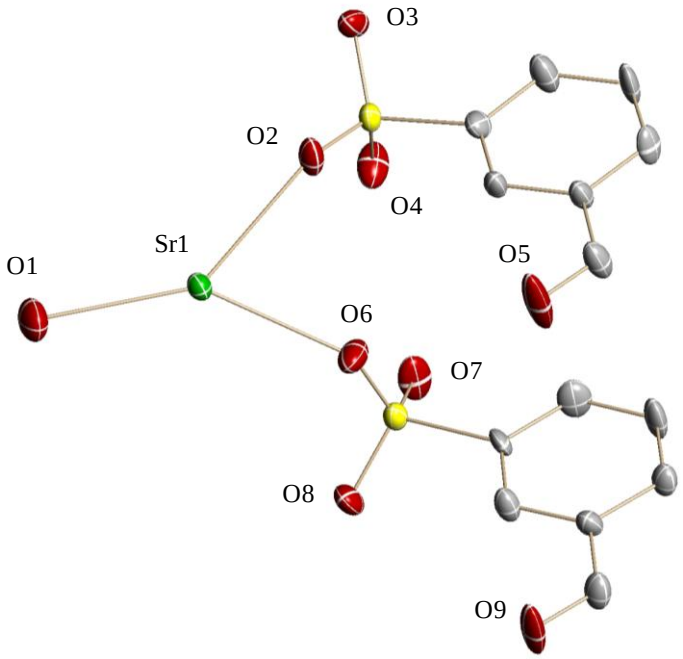

Figure 6.10. ORTEP representation of **AEPF-4** asymmetric unit. Ellipsoids are displayed at the 50% probability level. Hydrogen atoms were omitted for clarity.

Table 6.7. Interatomic distances in the coordination sphere of the SrO_7 monocapped trigonal prism in **AEPF-4**.

Bond	Distance (Å)
Sr(1)-O(1)w	2.591(5)
Sr(1)-O(2)s	2.607(5)
Sr(1)-O(3)[1]s	2.574(4)
Sr(1)-O(4)[2]s	2.459(5)
Sr(1)-O(6)s	2.564(5)
Sr(1)-O(7)[2]s	2.588(5)
Sr(1)-O(8)[3]s	2.529(5)

Symmetry transformations used to generate equivalent atoms:
[1]-x+1,-y+1,-z+2
[2]x,-y+1/2,z-1/2
[3]-x+1,-y+2,-z+2

Ow: oxygen atom coming from a water coordination molecule. Os: oxygen atom coming from a sulfonate group.

These SrO_7 polyhedra can be considered as the inorganic PBUs in this material. Moreover, as it is depicted in **Figure 6.11b**, each SrO_7 polyhedron is bonded to other six polyhedra *via* sulfonate groups of 2,6-AQDS linker, which acts in a hexatopic $\eta^3\mu_3$-$\eta^3\mu_3$ coordination mode (**Figure 6.11c**). As the coordination mode of sulfonate groups is the same that the found in the case of **AEPF-3**, in **AEPF-4** the presence of inorganic layers can be also determined.

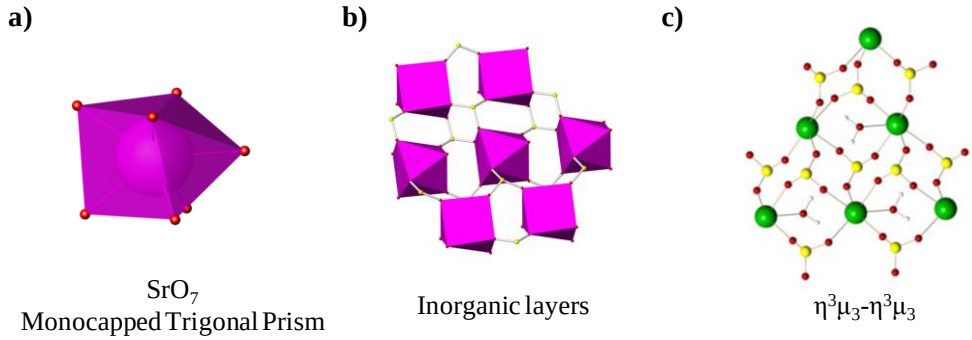

Figure 6.11. a) SrO_7 inorganic PBUs, **b)** inorganic layers and **c)** coordination mode of 2,6-AQDS linker in **AEPF-4**.

Besides, as it was previously mentioned, one water molecule is coordinated to each strontium center, which is located in the squared prism face of the SrO_7 polyhedron. The presence of these water molecules in **AEPF-4** leads to the formation of two types of hydrogen bonds. As it is shown in **Table 6.8**, these supramolecular interactions are determined between coordinated water molecules and oxygen atoms of 2,6-AQDS sulfonate groups.

Table 6.8. Distances and angles of hydrogen bonds found in **AEPF-4** compound.

D-H···A[1]	D-H[2]	H···A[3]	D···A[4]	<D-H···A[5]
O(1)w-H(1A)w...O(3)s[1]	0.99(2)	1.86(2)	2.845(7)	174(7)
O(1)w-H(1B)w...O(8)s[2]	1.00	2.39	3.090(7)	126.4

Symmetry operators codes

[1] -x, -y+1, -z+2 [2] -x, -y+2, -z+2

D: donor atom, A: acceptor atom. [1]Names of donor, hydrogen and acceptor atoms involved in the hydrogen bond. [2] Distance D – A. [3]Distances H – A. [4]Distance D – A. [5] Angle D – H – A.

Os: oxygen atom coming from a sulfonate group. Ow: oxygen coming from a coordinated water molecule. Hw: hydrogen coming from a coordinated water molecule.

It is worth mentioning that these supramolecular interactions are only located in the inorganic layer (**Figure 6.12**). Thus, as the $-SO_3$ groups exhibit the same hexa-topic coordination mode in **Ca-AEPF-3** and **Sr-AEPF-4** ($\eta^3\mu_3$-$\eta^3\mu_3$), the inorganic layers found in both materials are very similar. However, in the case of the strontium material, although water molecules do not participate in connectivity among metal centers, they are the main cause of the distortion found in the SrO_7 inorganic layer with regard to the more regular CaO_6 one.

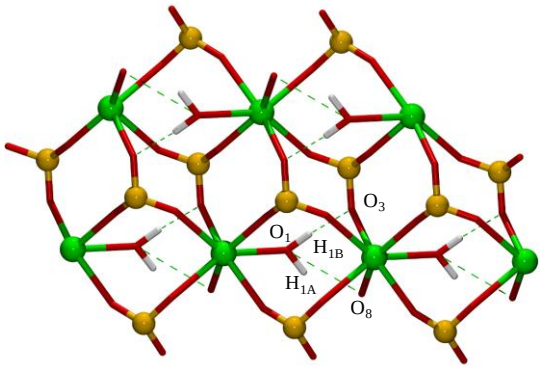

Figure 6.12. Hydrogen bonds determined in the inorganic layer for **AEPF-4**, among coordinated water molecules and sulfonate groups of 2,6-AQDS ligand.

In **Figure 6.13**, different polyhedral views along the crystallographic axis are depicted for **AEPF-4**, showing the three-dimensional covalent framework determined for this material. In **Figure 6.13c**, the presence of inorganic layers perpendicular to the *b* axis is shown.

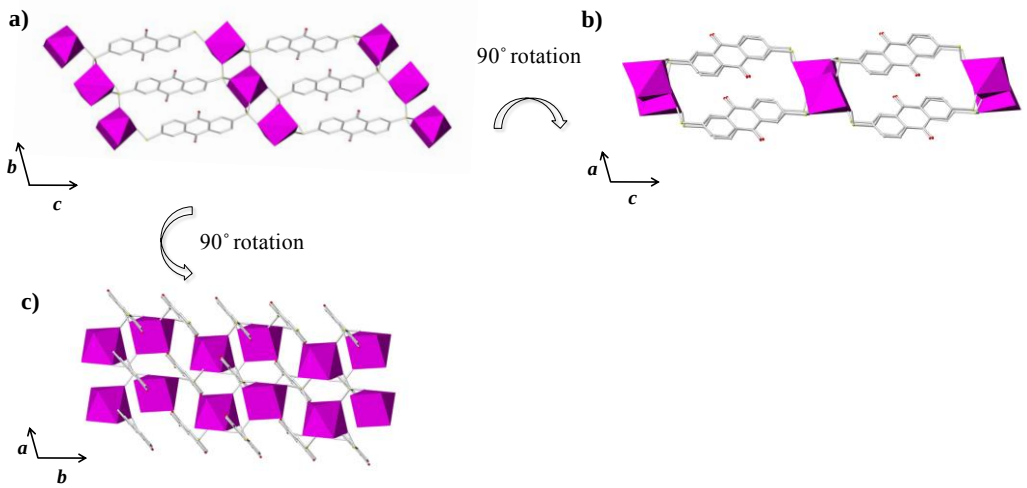

Figure 6.13.a) Polyhedral representation of **AEPF-4** along the *a* direction, **b)** along the *b* axis and **c)** representation of inorganic layers perpendicular to the *c* axis.

From the topological point of view, as it was before done for **Mg-AEPF-2** and **Ca-AEPF-3** materials, S atoms of 2,6-AQDS sulfonate groups were considered as nodes. Taking into account this fact, **AEPF-4** inorganic layers simplification, performed using TOPOS,[19] leads to the determination of two types of nodes: six-connected (Sr) and three-connected (S) nodes. As it can be suspected due to the similarities between the $-SO_3$ groups coordination mode in calcium and strontium materials, the inorganic layer in **Sr-AEPF-4** can also be described as a two-periodic net which exhibits a **kgd** topological type, with point symbol $(4^3)_2(4^6.6^6.8^3)$ (**Figure 6.14a**). Surprisingly, the joining of these layers through the three-connected nodes gives rise to a new topological type net with point symbol $(4^3.6^3)_2(4^6.6^7.8^2)$ (**Figure 6.14b**).

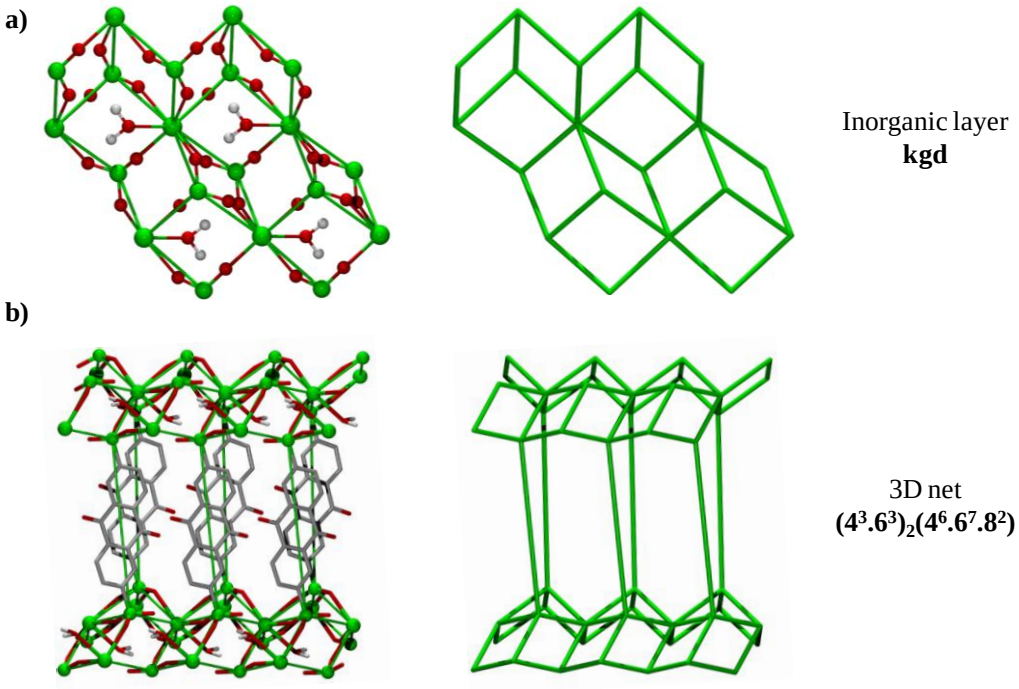

Figure 6.14. Depiction of the topological simplifications performed in **AEPF-4** to describe the **a)** inorganic layers (**kgd** topological type) and **b)** 3D net (point symbol $(4^3.6^3)_2(4^6.6^7.8^2)$).

Additionally, a deeper topological study was performed in order to give a tiling description for the **AEPF-4** net. For that purpose, in a first step, the idealization of the new net determined in **Sr-AEPF-4** was performed in its maximum symmetry embedding (*Cmcm* space group), using Systre package.[20] In this case, the new net

cannot be described with a natural tiling, but with two types of cages or tiles: $[4^5.6^4]$ + $[4+6^2]$. In **Figure 6.15** the two different cages are depicted for the real net (*P-1* space group) (**a**) and for the idealised one (*Cmcm* space group) (**b**). Thus, considering the idealised net, a tiling can be proposed with two types of tiles or cages ($[4^5.6^4]$ + $[4+6^2]$) (**Figure 6.15c**).

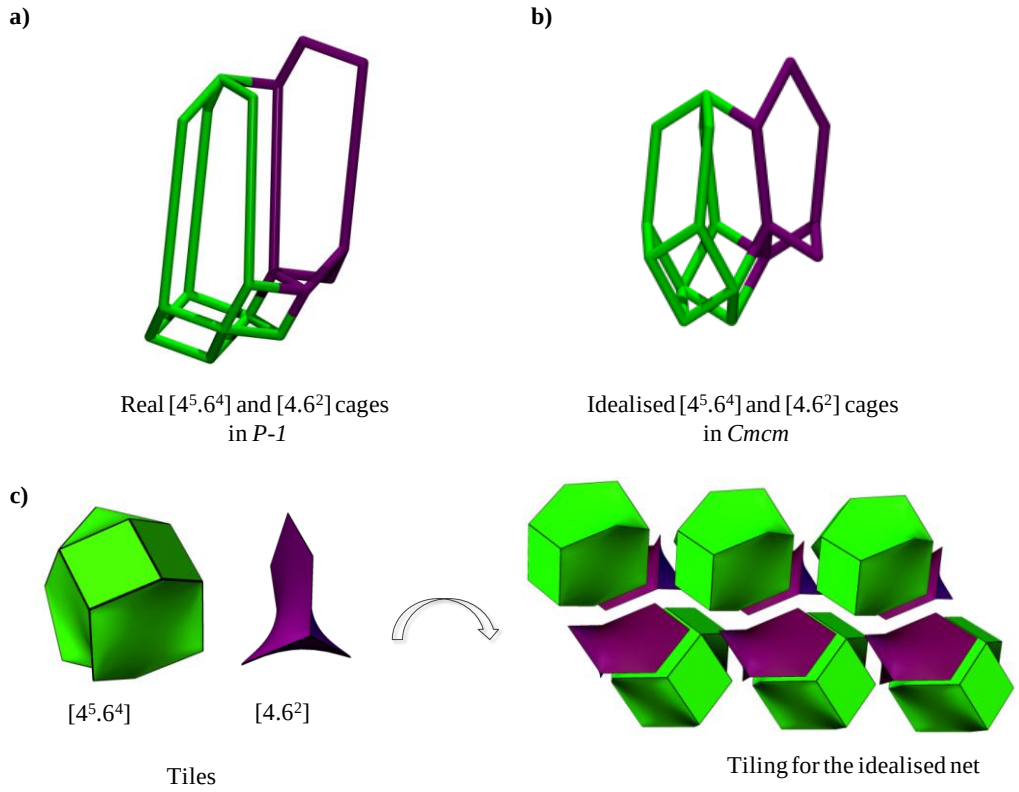

Figure 6.15. a) $[4^5.6^4]$ + $[4+6^2]$ cages in the real net (*P-1* space group) and **b)** the idealised one (*Cmcm* space group); **c)**$[4^5.6^4]$ + $[4+6^2]$ tiles and **c)** the resulting tiling found in **AEPF-4** net.

6.2.4.

Ba-AEPF-5

In the case of barium, we were successful in the obtaining of a material based on this metal and the 2,6-AQDS disulfonate linker. Thus, the solvothermal reaction with 2,6-AQDS and barium acetate under the optimized synthesis conditions (*see* Chapter 2, *Synthesis procedures*) gives rise to a new compound with formula **[Ba(2,6-AQDS)]** (**AEPF-5**). This material crystallizes in the orthorhombic crystal system (*Pnma* space group). The cell parameters observed in this structure are: a = 29.130(1) Å, b = 6.3329(3) Å, c = 7.8329(3) Å, and V = 1445.0(1) Å^3. The ORTEP representation of **AEPF-5** asymmetric unit is shown in **Figure 6.16** and the main crystallographic and refinement data for this compound are shown in **Table 6.9**.

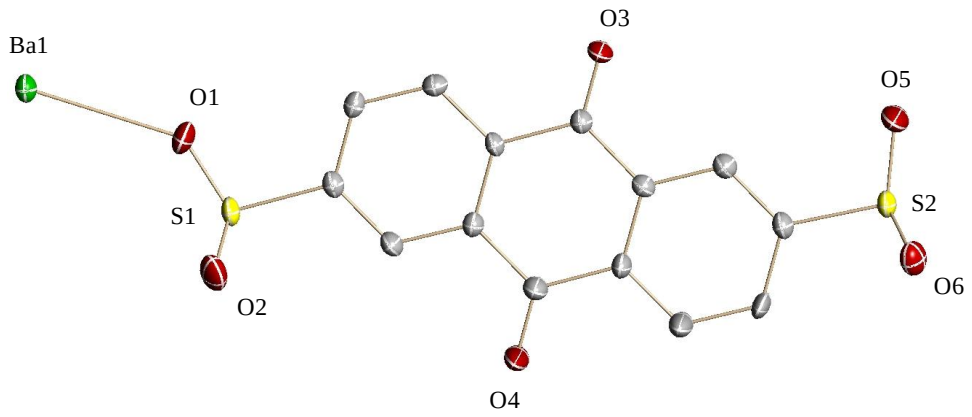

Figure 6.16. ORTEP representation of **AEPF-5** asymmetric unit. Ellipsoids are displayed at the 50% probability level. Hydrogen atoms were omitted for clarity.

In **AEPF-5**, Ba^{+2} ions are bonded to eight oxygen atoms coming from sulfonate groups of seven 2,6-$AQDS^{-2}$ anions. In this case the alkaline-earth metal ions are occupying the centers of a BaO_8 bicapped trigonal prisms (**Figure 6.17a)**, with an average Ba-O distance of ~2.84 Å (**Table 6.10**).

Table 6.9. Crystallographic and refinement data for **AEPF-5**.

Identification code	AEPF-5
Empirical formula	$C_{14}H_6BaO_8S_2$
Formula weight	503.66
Temperature	296(2) K
Wavelength	0.71073 Å
Crystal system	Orthorhombic
Space group	*Pnma*
Unit cell dimensions	a = 29.130(1) Å α = 90° b = 6.3329(3) Å β = 90° c = 7.8329(3) Å γ = 90°
Volume	1444.97(10) $Å^3$
Z	4
Density (calculated)	2.315 Mg/m^3
Absorption coefficient	3.083 mm^{-1}
F(000)	968
Crystal size	0.20 x 0.12 x 0.08 mm^3
Theta range for data collection	2.69 to 28.11°
Index ranges	-37<=h<=38, -8<=k<=8, -10<=l<=10
Reflections collected	11404
Independent reflections	1838 [R(int) = 0.0351]
Completeness to theta = 25.03°	95.40%
Absorption correction	Semi-empirical from equivalents
Max. and min. Transmission	0.7905 and 0.5775
Refinement method	Full-matrix least-squares on F^2
Data / restraints / parameters	1838 / 0 / 145
Goodness-of-fit on F^2	1.204
Final R indices [I>2sigma(I)]	R_1 = 0.0281, wR_2 = 0.0544
R indices (all data)	R_1 = 0.0334, wR_2 = 0.0557
Largest diff. peak and hole	0.482 and -0.926 e.$Å^{-3}$

Each one of these BaO_8 polyhedra, which can be considered as the inorganic PBUs, is bonded to other four by sharing vertexes, leading to the presence of inorganic layers (**Figure 6.17b)**. Moreover, given the capability of the Ba^{+2} ions to have different coordination numbers (mainly due to its high ionic radius value), the 2,6-AQDS linker exhibits in this material a hepta-topic $\eta^3\mu_4$-$\eta^3\mu_3$ coordination mode (**Figure 6.17c**).

Table 6.10. Interatomic distances in the coordination sphere of the BaO_8 bicapped trigonal prism in **AEPF-5**.

Bond	Distance (Å)
Ba(1)-O(1)s	2.730(3)
Ba(1)-O(2)[1]s	2.687(2)
Ba(1)-O(2)[2]s	2.687(2)
Ba(1)-O(5)[7]s	3.131(3)
Ba(1)-O(6)[3]s	2.737(2)
Ba(1)-O(6)[4]s	2.737(2)
Ba(1)-O(6)[5]s	2.993(2)
Ba(1)-O(6)[6]s	2.993(2)

Symmetry transformations used to generate equivalent atoms:

[1] -x+5/2,y+1/2,z-1/2
[2] -x+5/2,-y,z-1/2
[3] -x+2,-y,-z+1
[4] -x+2,y+1/2,-z+1
[5] x+1/2,-y+1/2,-z+3/2
[6] x+1/2,y,-z+3/2
[7] x+1/2,y,-z+1/2

Ow: oxygen atom coming from a water coordination molecule. Os: oxygen atom coming from a sulfonate group.

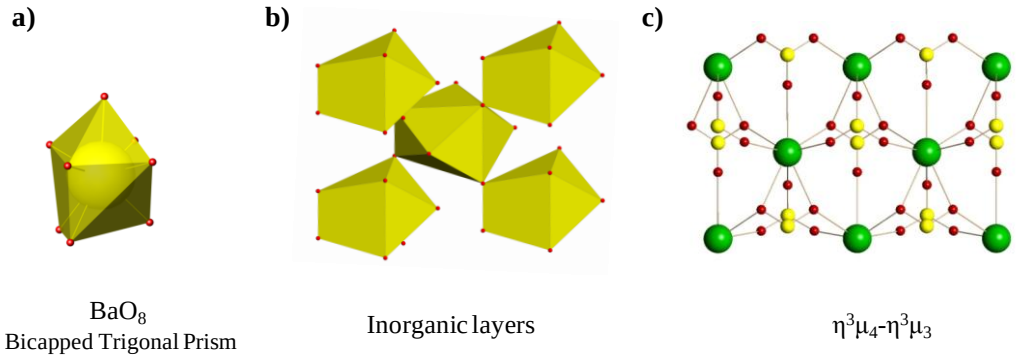

Figure 6.17. a) BaO_8 inorganic PBUs, **b)** Inorganic layers formed by BaO_8 polyhedra sharing vertexes and **c)** hepta-topic coordination mode of 2,6-AQDS linker in **AEPF-5**.

In **Figure 6.18**, different polyhedral views along the crystallographic axis are depicted for **AEPF-5**, showing the three-dimensional covalent framework determined for this material. As in the case of the other materials presented in this chapter, in **AEPF-5** inorganic layers can be also described, which are perpendicular to the *a* axis (**Figure 6.18c)**. Moreover, it is worth mentioning that 2,6-AQDS linkers are located in a parallel way along [010] direction, giving rise to the presence of π-π and π···O

stacking interactions among aromatic rings (distances of 3.15 Å and 3.76 Å, respectively).

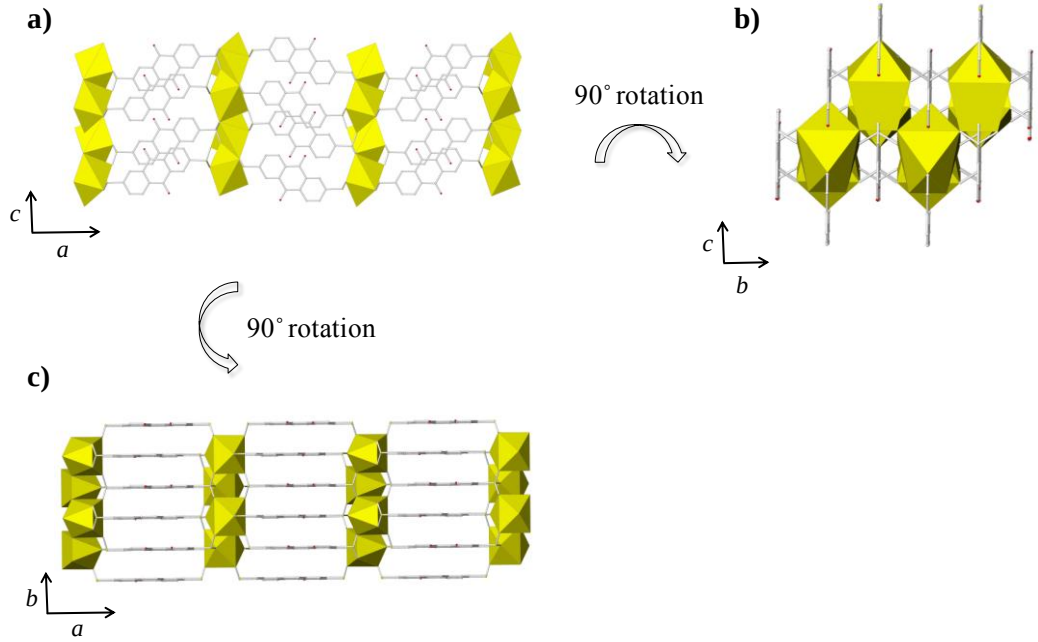

Figure 18. a) Polyhedral representation of **AEPF-5** along the *b* direction, **b)** along the *a* axis and **c)** representation of inorganic layers perpendicular to the *a* axis.

From the topological point of view, the inorganic layers in **AEPF-5** can be simplified, using TOPOS,[19] by three kinds of nodes: seven-connected (Ba), four-connected (S) and three-connected (S) nodes. This two-dimensional net has a point symbol $(4^{11}.6^{10})(4^{3})(4^{5}.6)$ (**Figure 6.19a**). Joining of these layers through the four- and three-connected nodes gives rise to three-dimensional net with point symbol $(4^{11}.6^{10})(4^{3}.6^{3})(4^{5}.6^{5})$ (**Figure 6.19b**). For this structure, the topological types of neither the inorganic layer nor the three-dimensional net appear in TOPOS or in the RCSR databases.

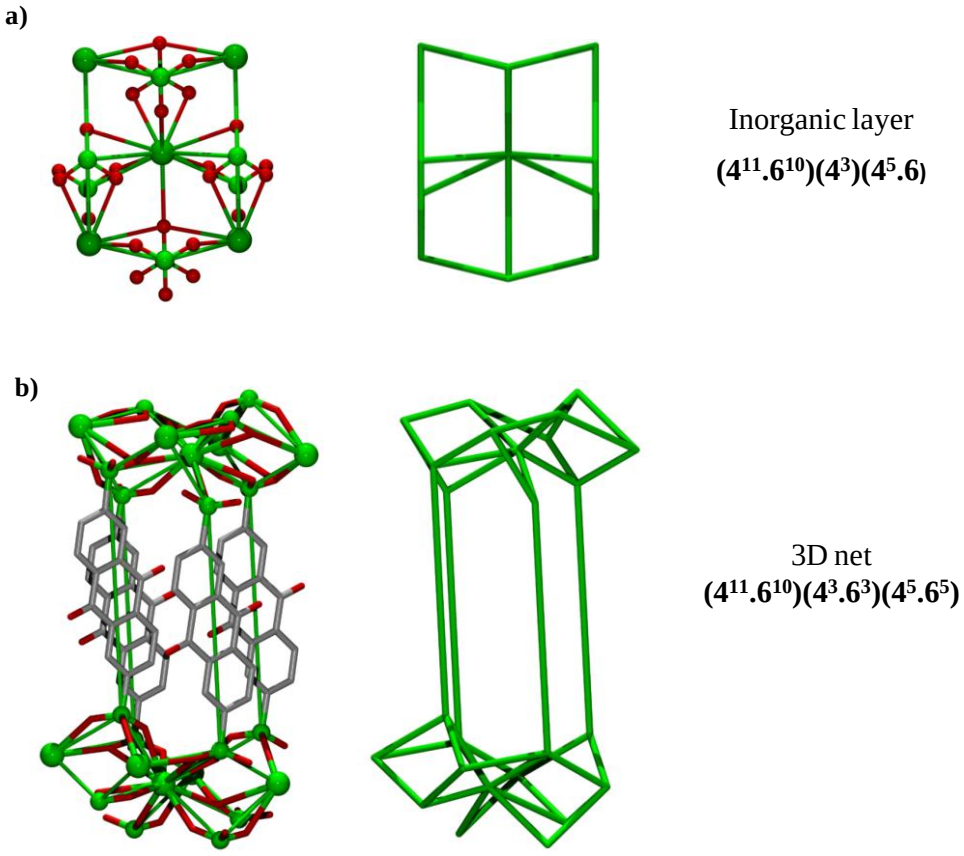

Figure 6.19. Depiction of the topological simplifications performed in **AEPF-5** to describe the **a)** inorganic layers (point symbol $(4^{11}.6^{10})(4^{3})(4^{5}.6)$) and **b)** 3D net (point symbol $(4^{11}.6^{10})(4^{3}.6^{3})(4^{5}.6^{5})$).

6.2.5.

Comparative topological considerations

As it was before discussed for **Ca-AEPF-3** and **Sr-AEPF-4**, the 2,6-AQDS linker coordinates the metallic centers in the same way for both materials: hexa-topic $\eta^3\mu_3$-$\eta^3\mu_3$ coordination mode. For that reason, as the inorganic layers are described by the metal centers and the sulfonate groups, the networks described for both materials have to be related. How can it be possible that, having the same connectivity in their inorganic layers (**kgd** net), the final 3D nets in **AEPF-3** and **AEPF-4** present different topological types? In order to find a suitable answer, a detailed topological comparative study between **AEPF-3** and **AEPF-4** was carried out to understand the subtle differences between the two nets.

The 2,6-AQDS linker coordinates in a hexa-topic way in both materials, giving rise the inorganic layers which exhibit a **kgd** topology. However, while in the case of **AEPF-3** the joining of these inorganic layers through the linker gives rise to a **fsh** net, in the case of **AEPF-4** a new net with point symbol $(4^3.6^3)_2(4^6.6^7.8^2)$ was found. In order to clarify this point, the idealization of both nets in their maximum symmetry embedding using Systre package[20] was performed. This analysis showed that the different found topologies can be explained in terms of the different distortions that present the inorganic layers for both compounds.

Thus, considering six member rings of the **kgd** net to describe the inorganic layers (**Figure 6.20a**), different conformations have been determined (**Figure 6.20b**): for **AEPF-3**, a "*chair*" conformation; for **AEPF-4**, a "*boat*" conformation. This fact explains the different packing modes of the **kgd** layers in the final structures (**Figure 6.20c**): A-A type packing (**fsh** net) in **AEPF-3** and A-B type packing (new topological type net with point symbol $(4_3.6_3)_2(4_6.6_7.8_2)$) in **AEPF-4**. Those differences are due to changes in the bond directionalities caused by the presence of a coordinated water molecule in the SrO_7 polyhedron. Besides, hydrogen bonds among the coordinated water molecules and the coordinated 2,6-AQDS oxygen atoms might also have some influence in the **AEPF-4** net distortion.

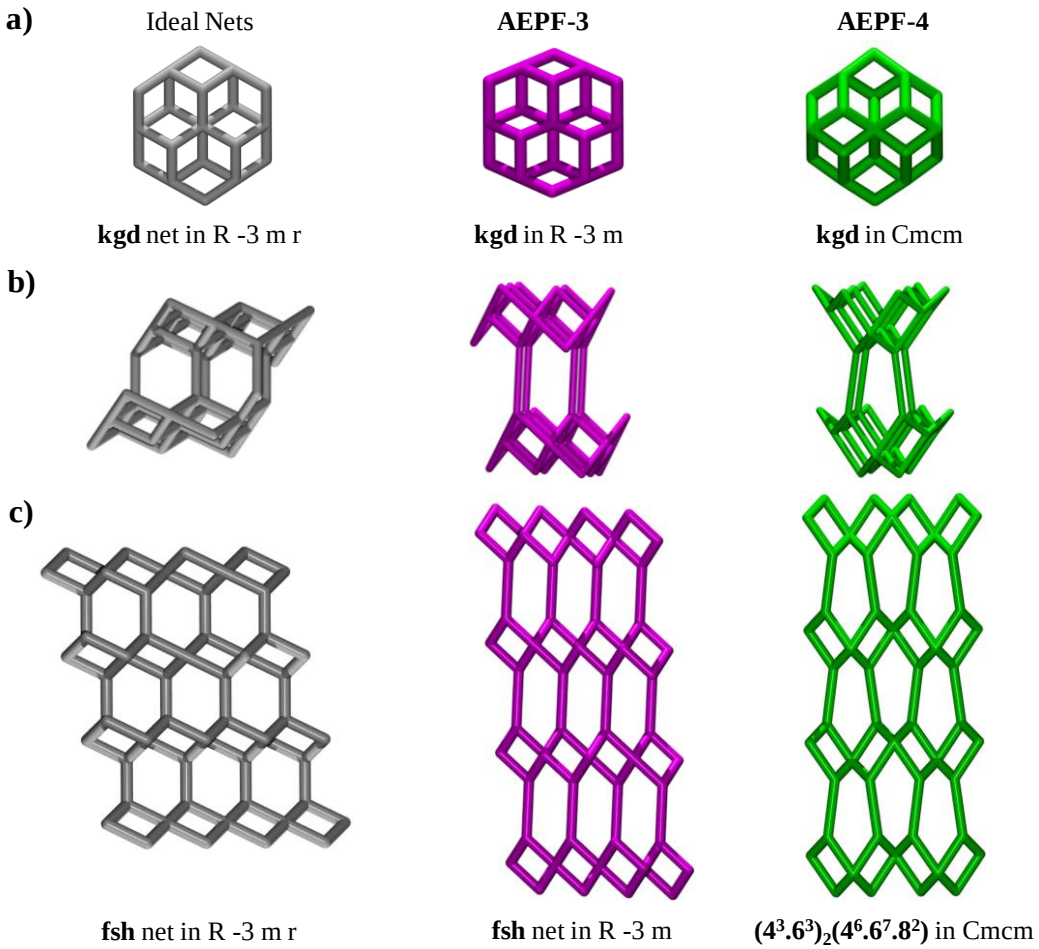

Figure 6.20. Comparative topological analysis performed for an **fsh** ideal net (left); and **AEPF-3** (middle) and **AEPF-4** (right) idealised nets: **a)** Six-member ring defined to describe the different **kgd** nets, **b)** Joining of two six-member rings, **c)** Different packing patterns: **fsh** net when "chair" conformation is found in the **kgd** layers of **AEPF-3** (left, middle); the new topological type net of **AEPF-4** with "boat" conformation (right).

6.2.6.

Topological summary

To clarify all the structural information presented in this chapter, **Figure 6.21** summarizes the main topological simplifications obtained for the four discussed materials based on alkaline-earth elements and 2,6-AQDS linker.

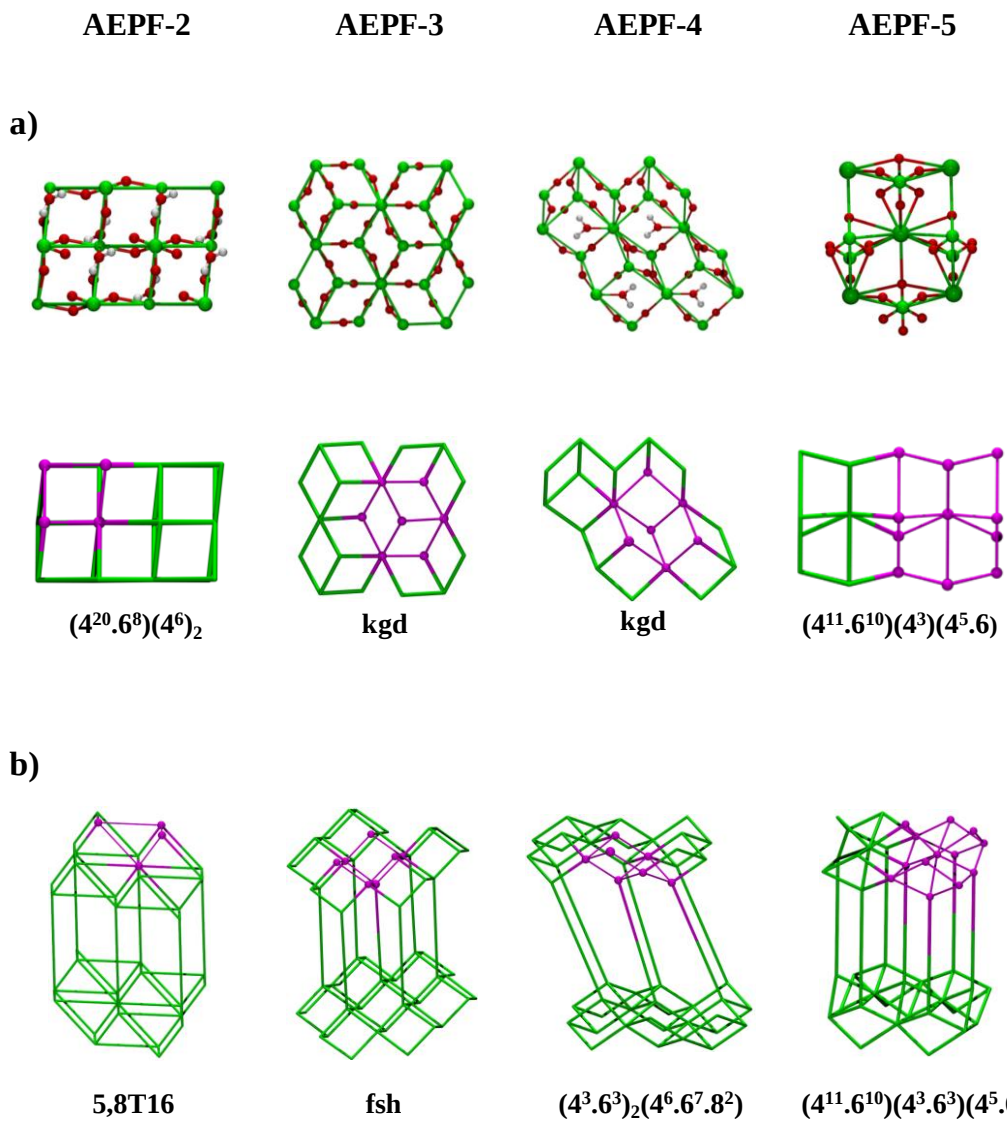

Figure 6.21. a) Inorganic layers for each compound and their topological simplification. **b)** Topological net simplification for each compound.

6.3.

Characterization

6.3.1.

X-Ray Powder Diffraction

Pawley refinements[21] were performed using Materials Studio[22] software for the four compounds presented in this chapter, in order to check the purity of bulk samples (see Chapter 2, *Techniques*). In the following, both the Pawley refinement profiles and the main refinement values for the **AEPF-2**, **AEPF-3**, **AEPF-4** and **AEPF-5** are shown in **Tables 6.11-6.14** and **Figures 6.22-6.25** and, respectively. All the crystalline phases show the high purity obtained in each synthetic procedure.

Table 6.11. Crystal Data and Pawley profile refinement values for **AEPF-2**.

Compound	AEPF-2
Crystal system	Triclinic
Space group	*P-1*
Unit cell dimensions	a= 4.8781(3) Å α = 94.499(4)˚
	b= 5.7837(1) Å β = 90.548(5)˚
	c= 5.7838(3) Å γ = 95.416(6)˚
Profile Function	Pseudo-Voigt
U	-0.06(2)
V	0.046(6)
W	-0.0004(3)
NA	0.46(4)
NB	0.012(2)
Zero Point	-0.032(3)
Asymmetry correction	Finger-Cox-Jephcoat
H/L	0.014(6)
S/L	0.016(6)
Rwp	0.0513
Rp	0.0383

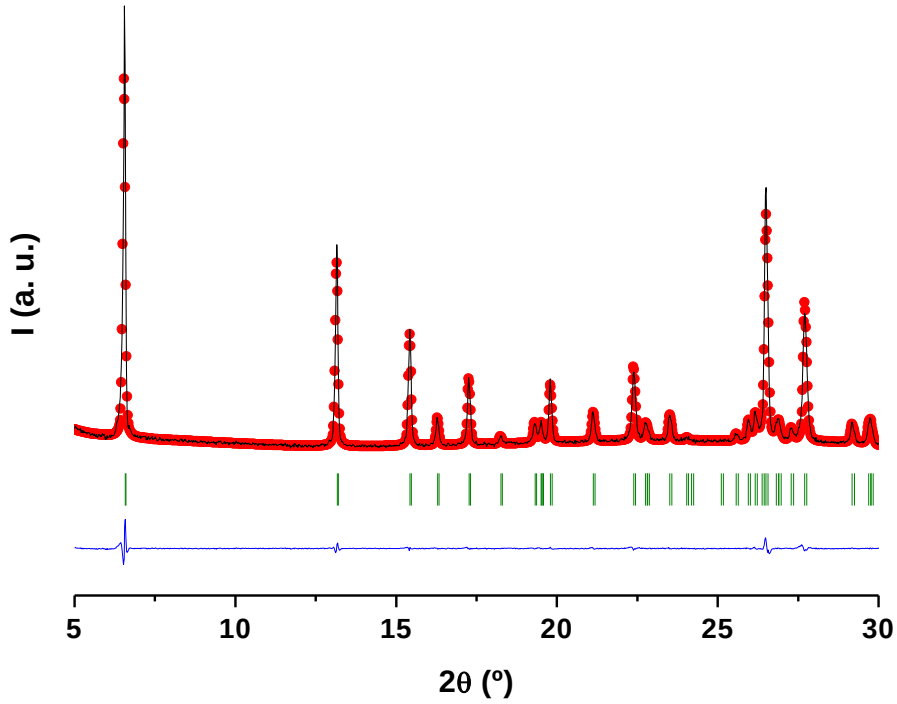

Figure 6.22. Pawley refinement for **AEPF-2**. Experimental data (red), simulated pattern (black) and difference (blue); observed reflections (green).

Table 6.12. Crystal Data and Pawley profile refinement values for **AEPF-3**.

Compound	AEPF-3
Crystal system	Monoclinic
Space group	$P2_1/c$
Unit cell dimensions	a= 14.8604(8) Å α = 90˚
	b= 5.5849(4) Å β = 105.952(7)˚
	c= 9.30589(6) γ= 90 ˚
Profile Function	Pseudo-Voigt
U	0.09(1)
V	-0.005(3)
W	0.0009(2)
NA	0.52(5)
NB	0.007(3)
Zero Point	0.0467(5)
Asymmetry correction	Finger-Cox-Jephcoat
H/L	0.013(3)
S/L	0.015(3)
Rwp	0.0841
Rp	0.0570

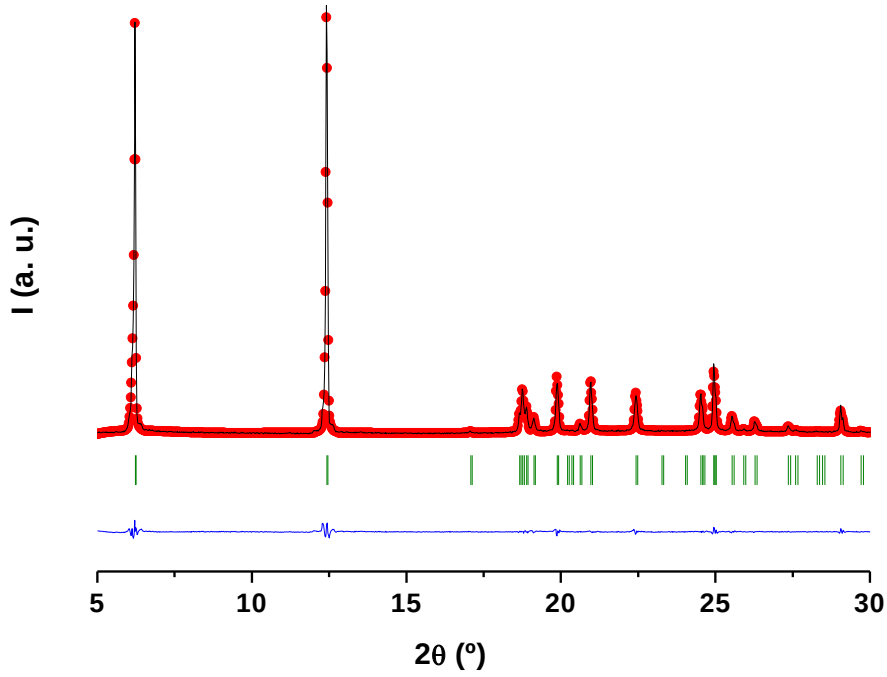

Figure 6.23. Pawley refinement for **AEPF-3**. Experimental data (red), simulated pattern (black) and difference (blue); observed reflections (green).

Table 6.13. Crystal Data and Pawley profile refinement values for **AEPF-4**.

Compound	AEPF-4
Crystal system	Triclinic
Space group	*P-1*
Unit cell dimensions	a= 5.43322(5) Å α = 103.588(8)˚
	b= 10.221(1) Å β = 99.834(7)˚
	c= 14.538(1) Å γ = 95.759 (6)˚
Profile Function	Pseudo-Voigt
U	0.81(4)
V	-0.128(8)
W	0.0070(4)
NA	0.56(4)
NB	0.006(2)
Zero Point	0.130(1)
Asymmetry correction	Finger-Cox-Jephcoat
H/L	0.018(2)
S/L	0.014(2)
Rwp	0.0824
Rp	0.0562

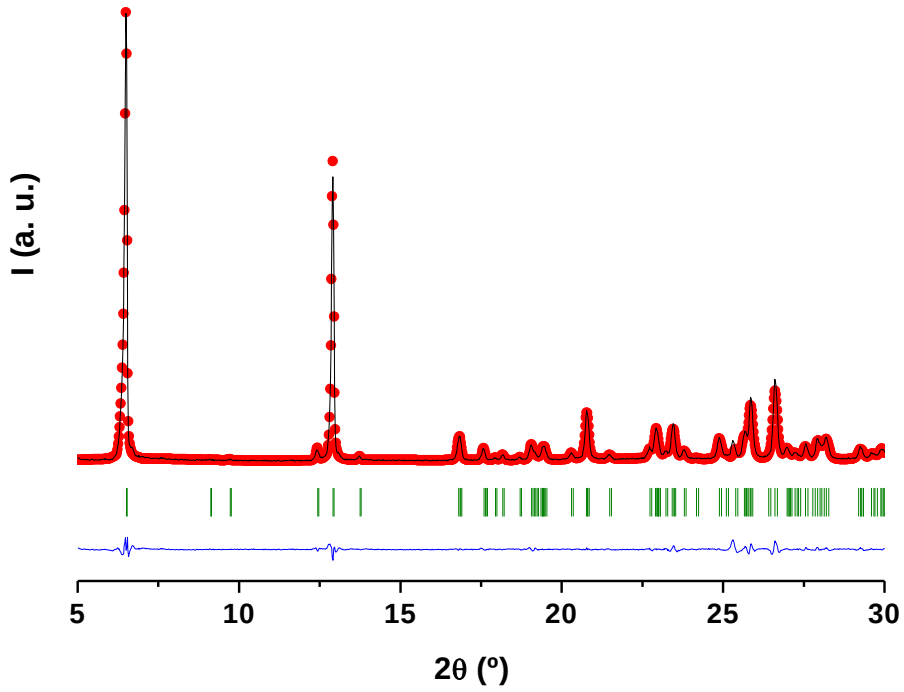

Figure 6.24. Pawley refinement for **AEPF-4**. Experimental data (red), simulated pattern (black) and difference (blue); observed reflections (green).

Table 6.14. Crystal Data and Pawley profile refinement values for **AEPF-5**.

Compound	AEPF-5	
Crystal system	Orthorhombic	
Space group	*Pnma*	
Unit cell dimensions	a = 29.172(3) Å	α = 90˚
	b = 6.3395(3) Å	β = 90˚
	c = 7.8455(5) Å	γ = 90˚
Profile Function	Pseudo-Voigt	
U	-0.13(4)	
V	0.070(9)	
W	-0.0007(5)	
NA	-0.20(5)	
NB	0.040(3)	
Zero Point	0.026(1)	
Asymmetry correction	Finger-Cox-Jephcoat	
H/L	0.0271(2)	
S/L	0.008(1)	
Rwp	0.0819	
Rp	0.0552	

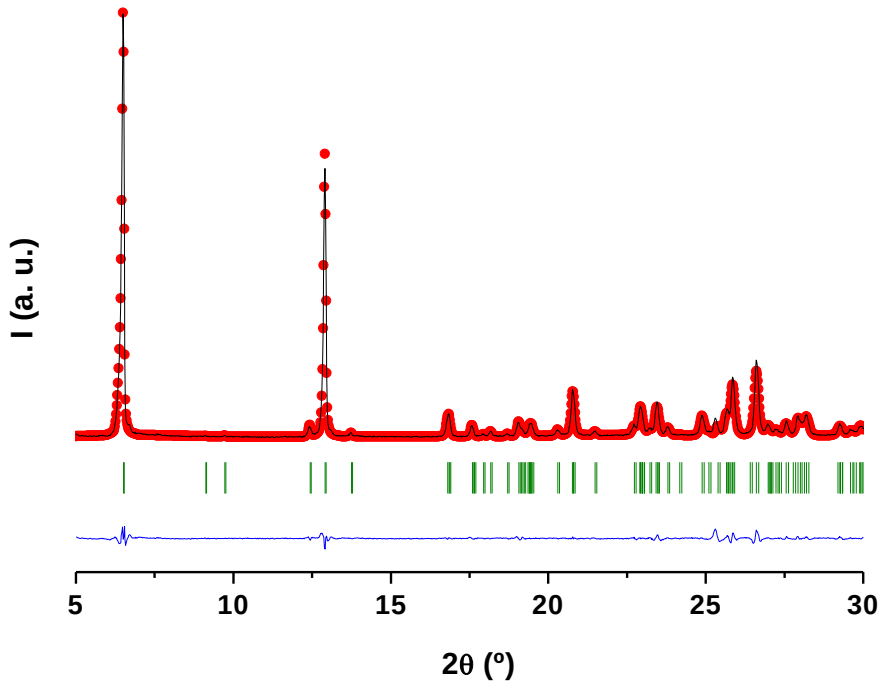

Figure 6.25. Pawley refinement for **AEPF-5.** Experimental data (red), simulated pattern (black) and difference (blue); observed reflections (green).

6.3.2.

Infrared Spectroscopy

Infrared (IR) spectra of **AEPF-2**, **AEPF-3**, **AEPF-4** and **AEPF-5** show the presence of both υ_{as} and $_{\upsilon s}$ of the SO_3^- groups found at ~1240-1180 (υ_{as}) and ~1100-1040 (υ_s) cm^{-1}. For **AEPF-2** and **AEPF-4**, additional bands in the -OH stretching mode region (~3750-3200 cm^{-1}) which correspond to the coordinated water molecules present in these materials were also determined.

Details of **Mg-AEPF-2** and **Sr-AEPF-4** IR spectra of the region corresponding to -OH stretching mode zone and aromatic C-H stretching mode zone are given in **Figure 6.26**. Thus, for **Mg-AEPF-2**, two broad bands are observed in the IR spectrum at ~3380 cm^{-1} and ~3575 cm^{-1} (**Figure 6.26a**). For **Sr-AEPF-4**, two broad bands are observed in the IR spectrum at ~3455 cm^{-1} and ~3595 cm^{-1} (**Figure 6.26b**). The shift to

lower wave number values in the case of **Mg-AEPF-2** is due to the strong hydrogen bonds present in the structure.

Details of IR spectra for the four compounds in the region corresponding to SO_3^- stretching mode zone are given in **Figure 6.27**. For **AEPF-2**, bands were observed at: ~1240, ~1200, ~1180 and ~1130 cm^{-1} (υ_{as}); and ~1085 and ~1060 cm^{-1}(υ_s) (**Figure 6.27a**). For **AEPF-3**, bands were observed at: ~1220, ~1180 and ~1134 cm^{-1} (υ_{as}); and ~1085 and ~1065 cm^{-1}(υ_s) (**Figure 6.27b**). For **AEPF-4**, bands were observed at: ~1230, ~1200, ~1175 and ~1130 cm^{-1} (υ_{as}); and ~1080 and ~1055 cm^{-1}(υ_s) (**Figure 6.27c**). For **AEPF-5**, bands were observed at: ~1230, ~1205, ~1180, ~1160 and ~1135 cm^{-1} (υ_{as}); and ~1080, ~1045 and ~1035 cm^{-1} (υs) (**Figure 6.27d**).

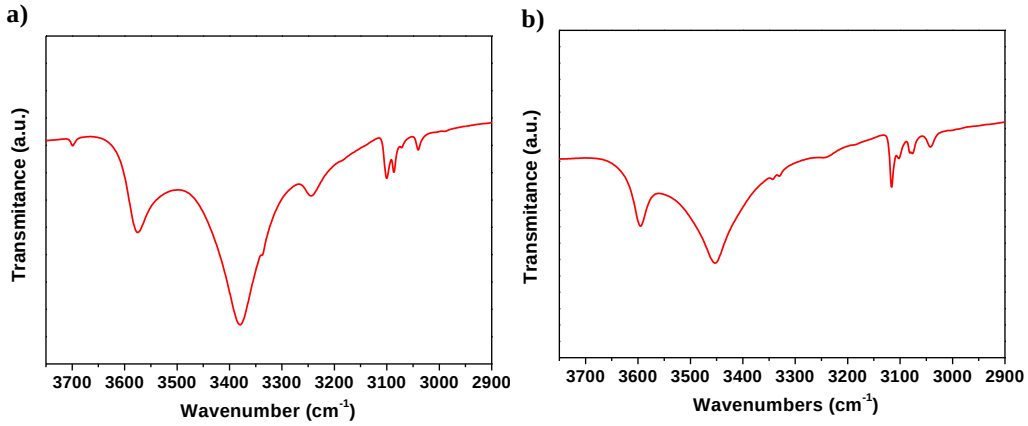

Figure 6.26. Details of IR spectra in the OH region (3750-3200 cm^{-1}) and the aromatic C-H stretching mode region (3100-3020 cm^{-1}) for: **a) AEPF-2** and **b) AEPF-4** compounds.

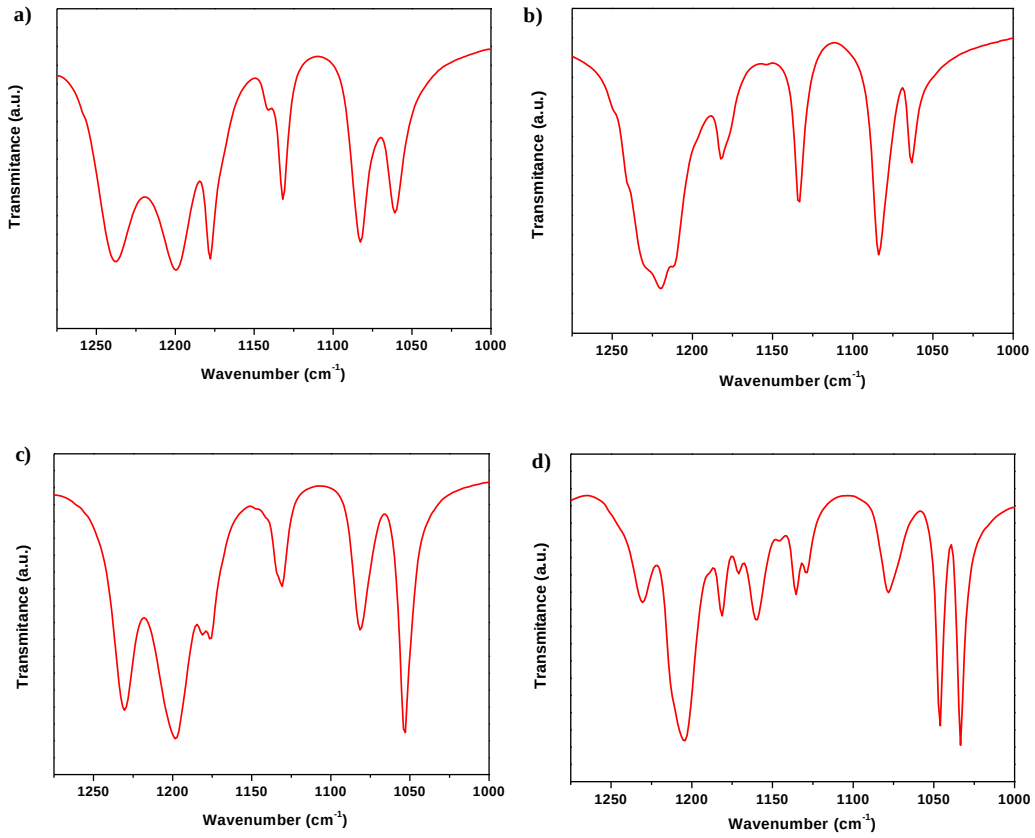

Figure 6.27. Details of IR spectra in the SO_3^- stretching mode zone (1240-1180 cm^{-1}(ν_{as}) and 1100-1040 cm^{-1}(ν_s)) for: **a) AEPF-2**, **b) AEPF-3**, **c) AEPF-4** and **d) AEPF-5**compounds.

6.3.3.

Thermal Gravimetric Analyses

Thermal Gravimetric Analyses (TGA) curves for **AEPF-2**, **AEPF-3**, **AEPF-4** and **AEPF-5** are shown in **Figures 6.28-6.31**, respectively. The exceptional thermal stability has to be emphasized for all four MOF materials. Thus, TGA results for the thermal decomposition for the four compounds reveal that their frameworks are stable up to ~ 500 ºC in air. Above this temperature the frameworks decompose completely.

- Thermogravimetric profile of **AEPF-2** (**Figure 6.28**) shows a first weight loss at ~180 ºC of ~8.5% consistent with the removal of the water molecules present in the compound (calc. 8.4%). The second step at ~500 ºC corresponds to the complete decomposition of the anhydrous compound. The calculated weight loss for the whole process (90.6%) is in good agreement with the experimental value of 88.5%. MgO phase was identified as a main residue by XRPD using the Joint Committee on Powder Diffraction Standards files (JCPDS file No.77-2179).

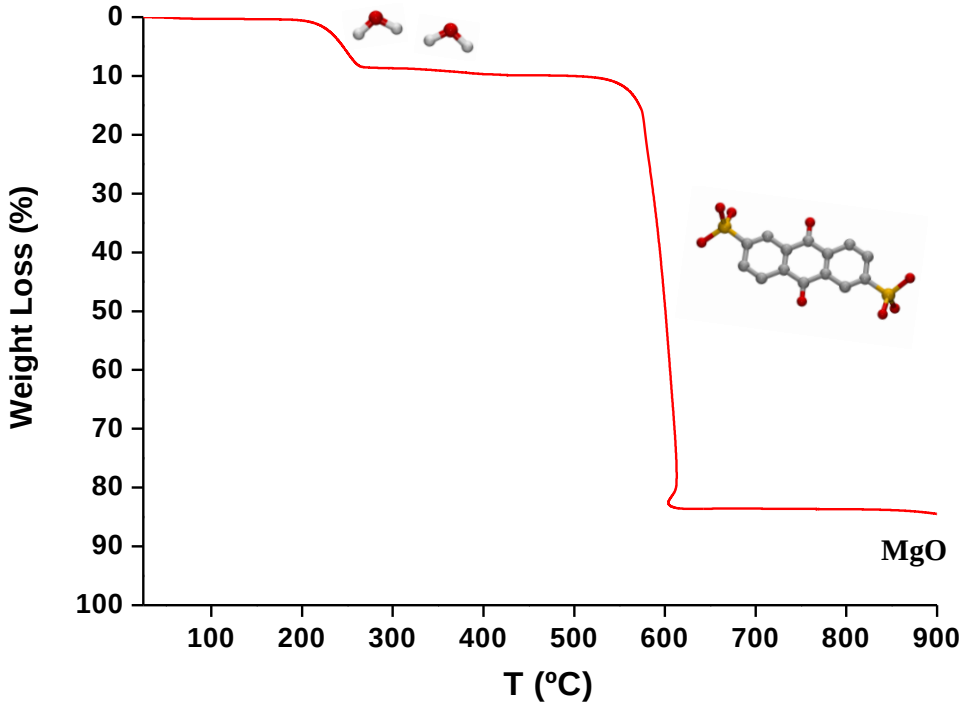

Figure 6.28. TGA profile for **AEPF-2** performed in air.

- Thermogravimetric profile of **AEPF-3** sample (**Figure 6.29**) shows that the complete decomposition of the compound proceeds in one step at ~500 ºC. The calculated weight loss for the whole process (66.5%) is in a good agreement with the experimental calculated value of 67%. $CaSO_4$ (anhydrite) phase was identified as a main residue by XRPD (JCPDS file No.20-0487).

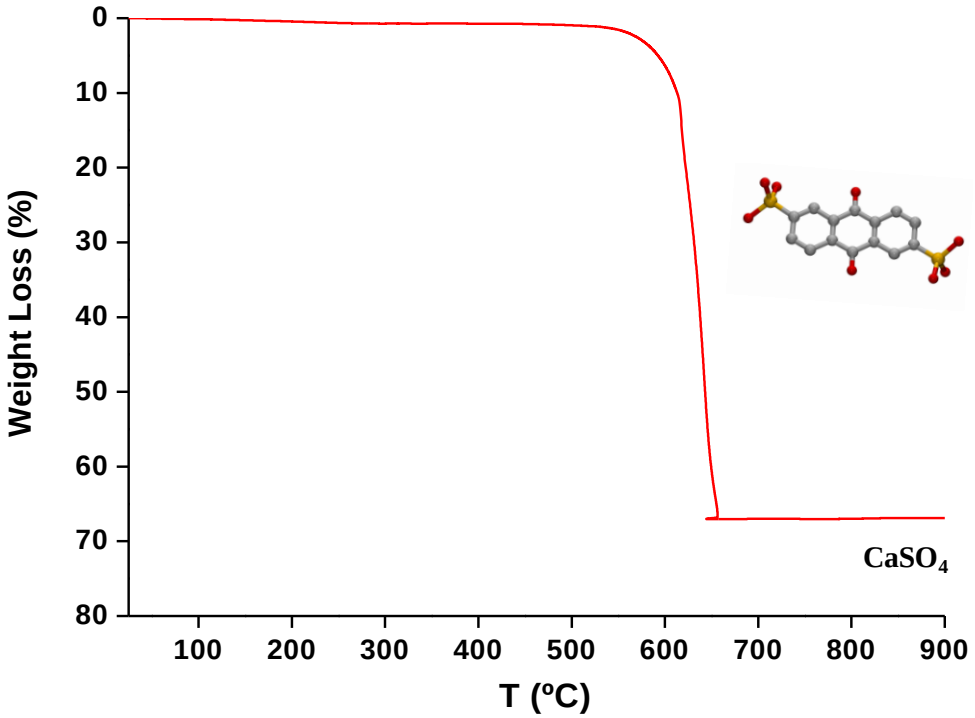

Figure 6.29. TGA profile for **AEPF-3** performed in air.

- Thermogravimetric profile of **AEPF-4** compound (**Figure 6.30**) shows a first stage at ~150 ºC, with a weight loss of ~4.0%, consistent with the coordination water removal (calc. 3.8%). The second step at ~490 ºC corresponds to the complete decomposition of the anhydrous compound. The calculated weight loss for the whole process (61.1%) is in a good agreement with the experimental value of 60.9%. A $SrSO_4$ (celestine) phase was identified as a main residue by XRPD (JCPDS file No. 05-0593).

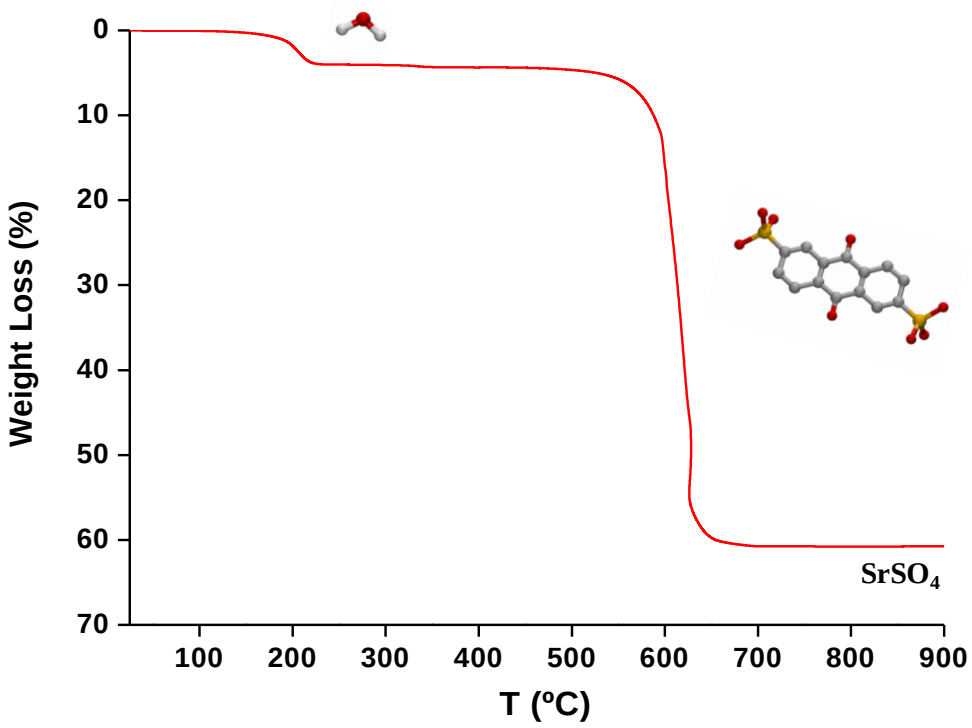

Figure 6.30. TGA profile for **AEPF-4** performed in air.

- Thermogravimetric profile of **AEPF-5** sample (**Figure 6.31**) shows that, the complete decomposition of the compound proceeds in one step at ~518 ºC.The calculated weight loss for the whole process (53.7%) is in a good agreement with the experimental value of 52.9%. A $BaSO_4$ (barite) phase was identified as a main residue by XRPD (JCPDS file No. 76-0217).

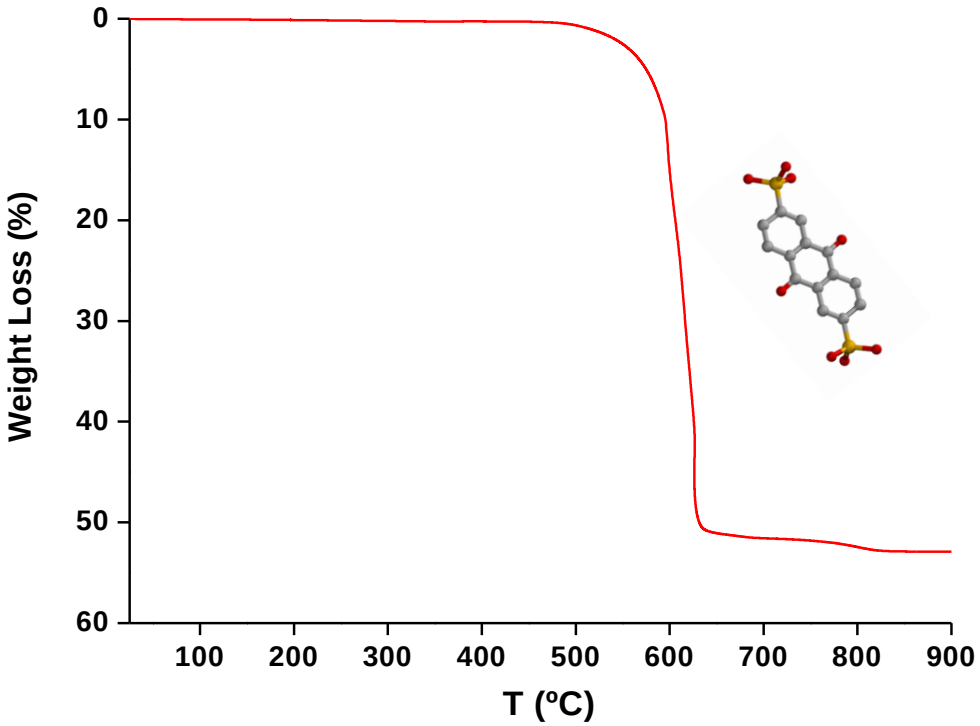

Figure 6.31. TGA profile for **AEPF-5** performed in air.

6.4.

Catalytic Experiments

As it was discussed in the structural section of this chapter, the use of the disulfonate 2,6-AQDS as ligand leads to the obtaining of robust alkaline-earth MOFs belonging to different structural types. Taking into account these novel results, the performance of these materials as heterogeneous catalysts was proved. In order to study the influence of both the structure and the metal center in the catalytic activity, two reactions were studied: **hydrogenation of alkenes** and **hydrosilylation of ketones.** The main obtained results are pointed out in the following.

6.4.1.

Hydrogenation of alkenes

Catalytic tests. Continuing with the catalytic studies performed with dicarboxylate MOFs (*see* previous chapters), the catalytic properties of the four disulfonate materials presented in this chapter were also investigated. Thus, **Mg-AEPF-2**, **Ca-AEPF-3**, **Sr-AEPF-4** and **Ba-AEPF-5** were tested as catalysts for the hydrogenation of alkenes using styrene as substrate model under mild conditions (*see* Chapter 2, *Techniques* and **Scheme 6.1**). The obtained results are summarized in **Table 6.15** and **Figure 6.32**).

Scheme 6.1. Scheme reaction of styrene reduction with H_2.

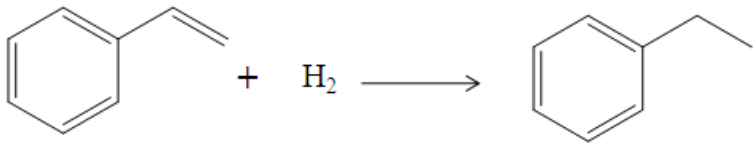

Table 6.15. Styrene hydrogenation in toluene, at 373 K, 5 atm H_2, using 1 mol% catalyst.

Compound	Active Center	Time (h)	Conversion (%)	TOF (h^{-1})
AEPF-2	Mg^{+2}	4	100	38.8
AEPF-3	Ca^{+2}	5	100	12.3
AEPF-4	Sr^{+2}	5	68.2	14.3
AEPF-5	Ba^{+2}	5	64.7	36.5

As it is shown in **Figure 6.32**, the best results were obtained with **Mg-AEPF-2**, for which the selective hydrogenation of styrene to ethylbenzene was achieved after 4 hours (TOF= 38.8 h^{-1}). It is worth highlighting that in all cases 100% selectivity was achieved toward ethylbenzene, in contrast with the behaviour of previously reported calcium and strontium homogeneous catalysts.[23,24] Moreover, in the studied conditions, a decrease in the catalytic activity as: **Mg-AEPF-2**>**Ca-AEPF-3**>**Sr-AEPF-4**>**Ba-AEPF-5** is observed. This tendency could be explained with the loss of Lewis Acidity order: Mg^{+2}> Ca^{+2}> Sr^{+2}> Ba^{+2}, confirming in that way that the catalytic process is metal mediated.

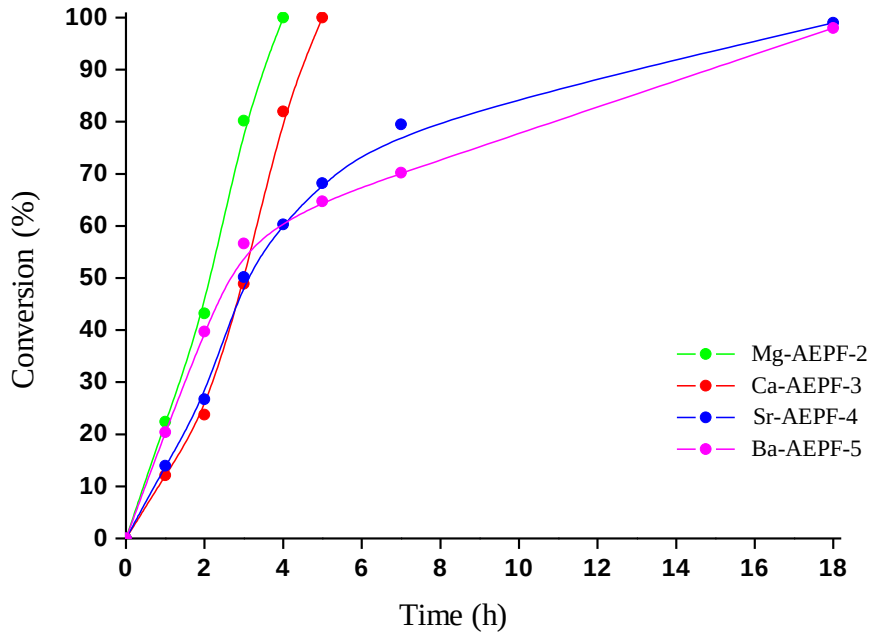

Figure 6.32. Kinetic profiles of styrene hydrogenation with **AEPF-2**, **AEPF-3**, **AEPF-4** and **AEPF-5** as catalysts.

Recycling experiments. To investigate the lifetime, heterogeneity and the stability of the better catalyst (**Mg-AEPF-2**) in styrene hydrogenation reaction, recycling experiments were performed employing the same catalyst in three consecutive reaction cycles. The observed activity is kept over the three cycles of reaction showing the robustness of this material (**Figure 6.33**).

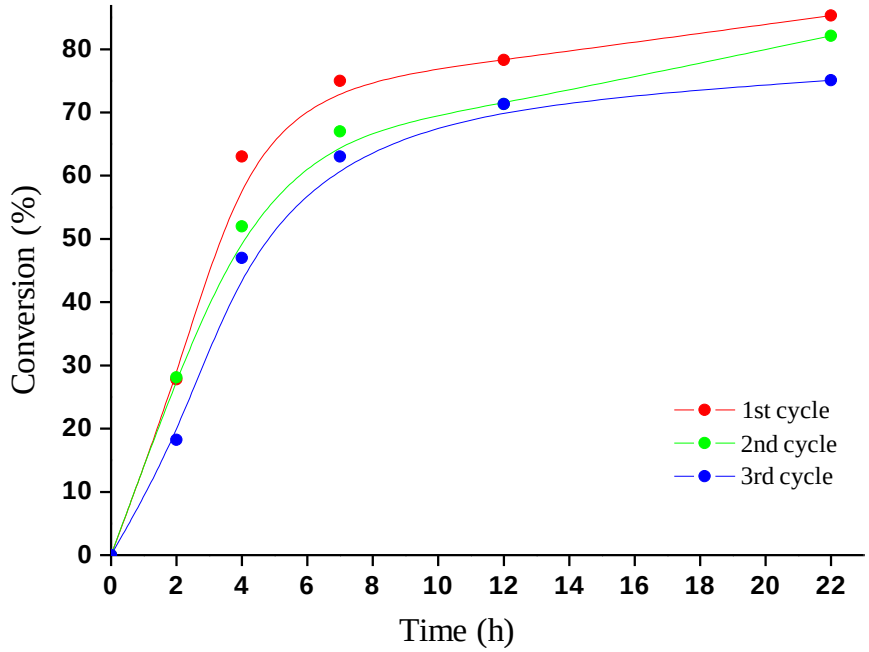

Figure 6.33. Kinetic profiles in three consecutive reaction cycles employing **Mg-AEPF-2** as catalyst.

Catalysts robustness. All catalysts employed in styrene hydrogenation were recovered by centrifugation, washed with toluene, and then characterized by X-ray powder diffraction (XRPD) to corroborate possible structural changes after reaction. The comparison of the XRPD patterns before and after the catalytic reaction confirms that the four catalysts remain unaltered after reaction in the studied conditions (**Figures 6.34-6.37**). In the case of **Mg-AEPF-2**, the XRPD pattern after the third run (recycling experiments) is shown (**Figures 6.34)**.

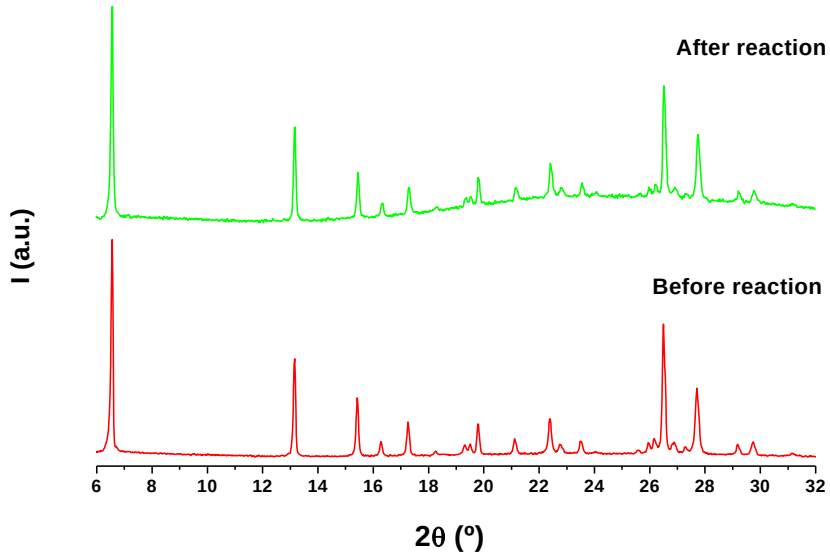

Figure 6.34. Comparison of the experimental XRPD pattern of **Mg-AEPF-2** after hydrogenation catalytic recycling experiments (green) with the pattern of fresh sample before reaction (red).

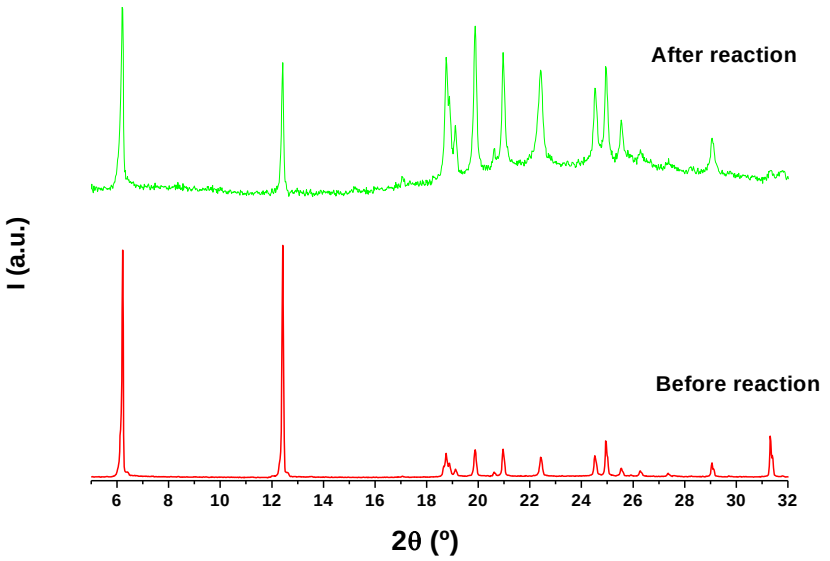

Figure 6.35. Comparison of the experimental XRPD pattern of **Ca-AEPF-3** after hydrogenation catalytic test experiments (green) with the pattern of fresh sample before reaction (red).

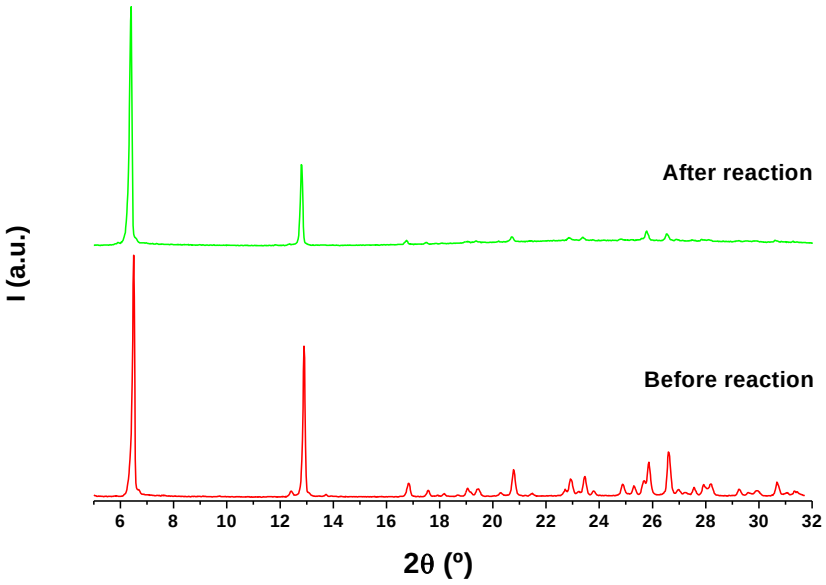

Figure 6.36. Comparison of the experimental XRPD pattern of **Sr-AEPF-4** after hydrogenation catalytic test experiments (green) with the pattern of fresh sample before reaction (red).

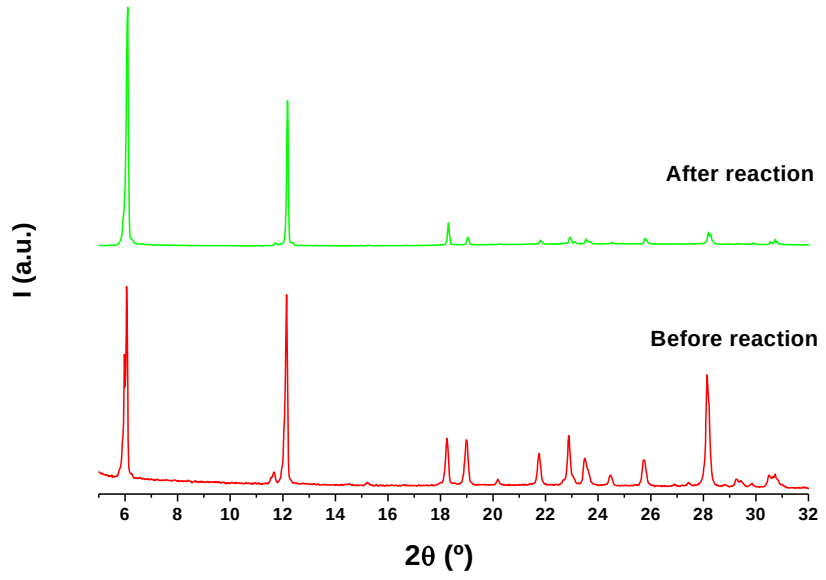

Figure 6.37. Comparison of the experimental XRPD pattern of **Ba-AEPF-5** after hydrogenation catalytic test experiments (green) with the pattern of fresh sample before reaction (red).

Structural comparative experiments. Finally, in order to compare the catalytic activity of the **Mg-AEPF-2** MOF to that of a simple magnesium salt (acetate), the styrene hydrogenation test was performed in the same conditions but now using magnesium acetate tetrahydrate as a catalyst. **Figure 6.38** shows a comparison between the catalytic performance of **Mg-AEPF-2** and the magnesium salt. After reaction, magnesium acetate tetrahydrate sample decomposes, as it was checked by XRPD, observing the appearance of unidentified Bragg peaks and an important amorphization of the sample. However, as it was previously mentioned, **Mg-AEPF-2** phase maintains its crystal structure after reaction.

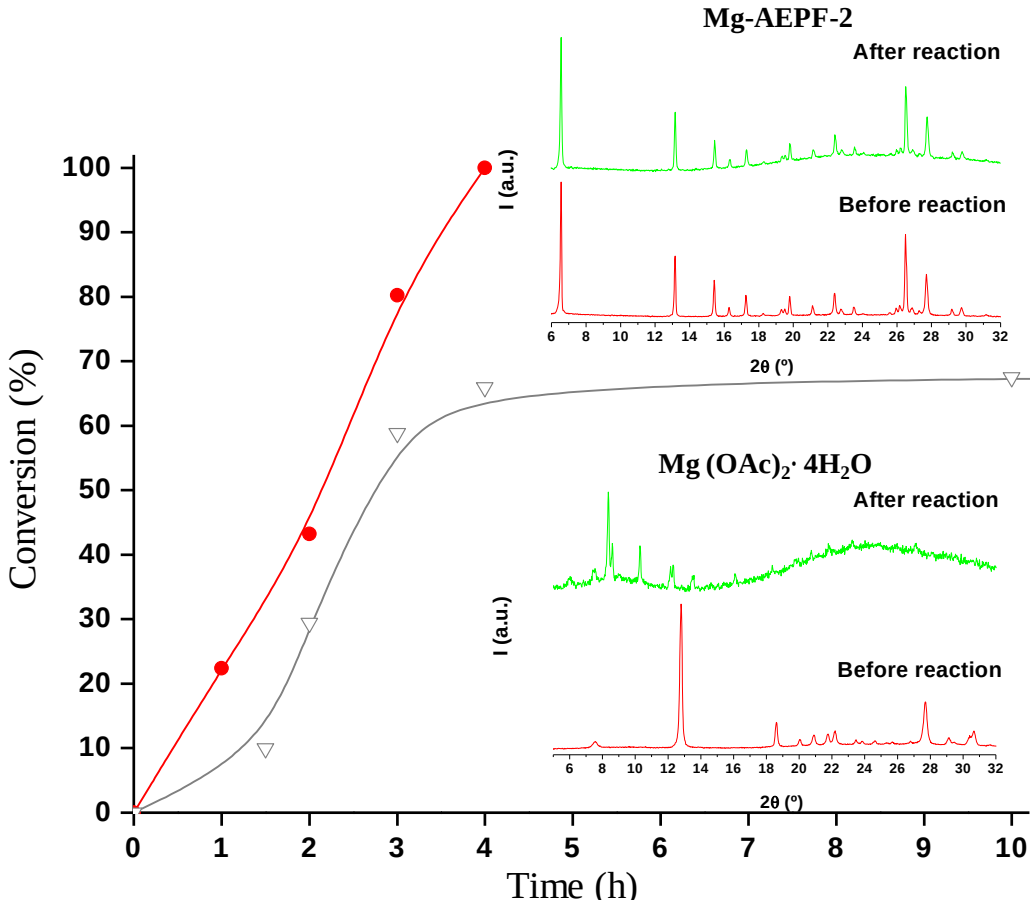

Figure 6.38. Conversionas a function of time for hydrogenation of styrene with H_2 in toluene at 373 K: Comparison between the performance of **Mg-AEPF-2** (in red) and magnesium acetate tetrahydrate (in grey). Robustness of both **Mg-AEPF-2** and the inorganic salt was checked by XRPD.

6.4.2.

Hydrosilylation of ketones

Catalytic tests. On the other hand, **Mg-AEPF-2**, **Ca-AEPF-3**, **Sr-AEPF-4** and **Ba-AEPF-5** were tested as heterogeneous catalysts for the hydrosilylation of benzaldehyde with diphenylsilane (*see* Chapter 2, *Techniques* and **Scheme 6.2**). The obtained results are shown in **Table 6.16** and **Figure 6.39**.

Scheme 6.2. Hydrosilylation of benzaldehyde with diphenylsilane.

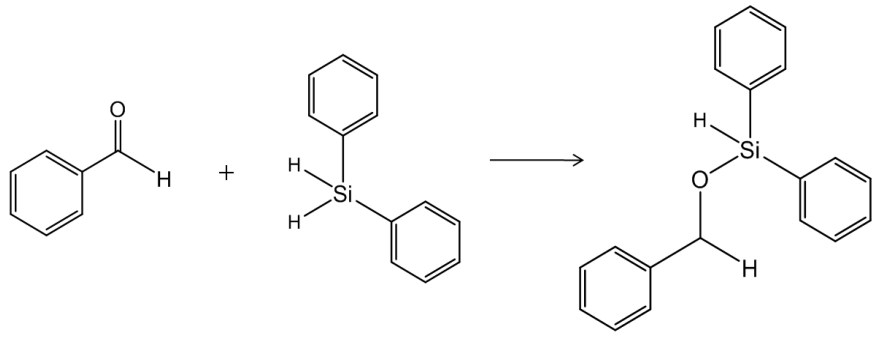

Table 6.16. Hydrosilylation of benzaldehyde with diphenylsilane in toluene, at 363 K, using 10 mol% catalyst.

Compound	Active Center	Time (h)	Conversion (%)	TOF (h^{-1})
AEPF-2	Mg^{+2}	22	34.6	0.21
AEPF-3	Ca^{+2}	22	85.3	1.52
AEPF-4	Sr^{+2}	22	65.5	1.41
AEPF-5	Ba^{+2}	22	39.5	0.24

As it is shown in **Figure 6.39**, the best result for the hydrosilylation of bezaldehyde was obtained with **Ca-AEPF-3** sample, for which silylated product yield was 85.3% after 22 hours (TOF= 1.52 h^{-1}). A similar behaviour was obtained with **Sr-AEPF-4** sample (silylated product yield 65.5% after 22 hours, TOF= 1.41 h^{-1}). However, in the case of both **Mg-AEPF-2** and **Ba-AEPF-5**, the catalytic activity was

clearly lower (silylated product yield lower than ~40% after 22 hours). Thus, in the studied conditions, the observed decrease in the catalytic activity **Ca-AEPF-3**>**Sr-AEPF-4**>**Ba-AEPF-5** could be explained with the loss of Lewis Acidity (Ca^{+2}>Sr^{+2}>Ba^{+2}).In the case of **Mg-AEPF-2**, the low activity could be explained in terms of the substrate steric impediment related to the Mg^{+2} ion size.

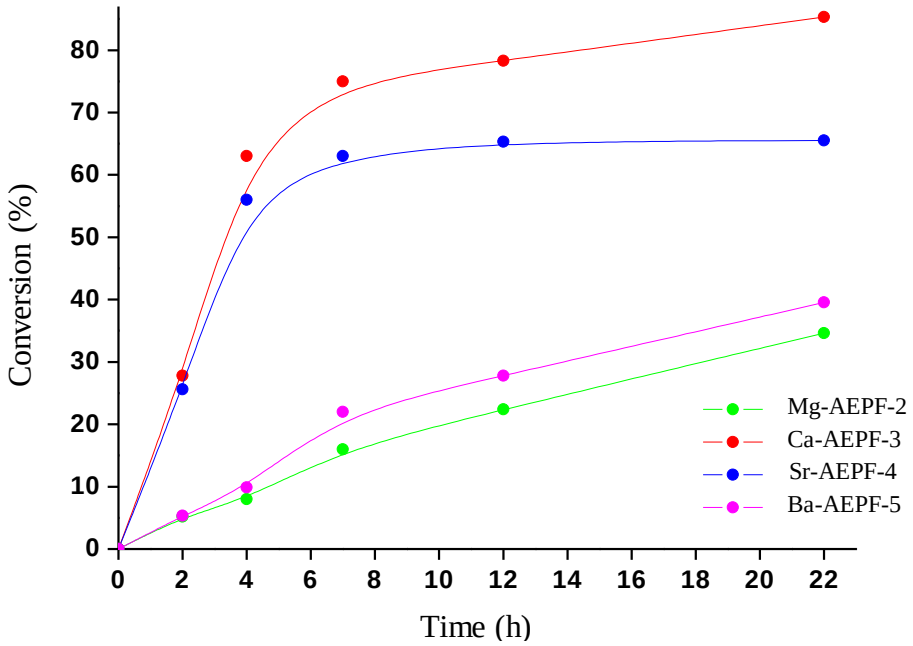

Figure 6.39. Kinetic profiles for hydrosilylation of benzaldehyde with diphenylsylane with **Mg-AEPF-2**, **Ca-AEPF-3**, **Sr-AEPF-4** and **Ba-AEPF-5** as catalysts.

Recycling experiments. To investigate the lifetime, heterogeneity and the stability of the best catalyst (**Ca-AEPF-3**), a recycling experiment was performed employing the recovered catalyst in three consecutive reaction cycles. The observed activity is kept over the three cycles of reaction, being slightly decreased in the third one (**Figure 6.40**).

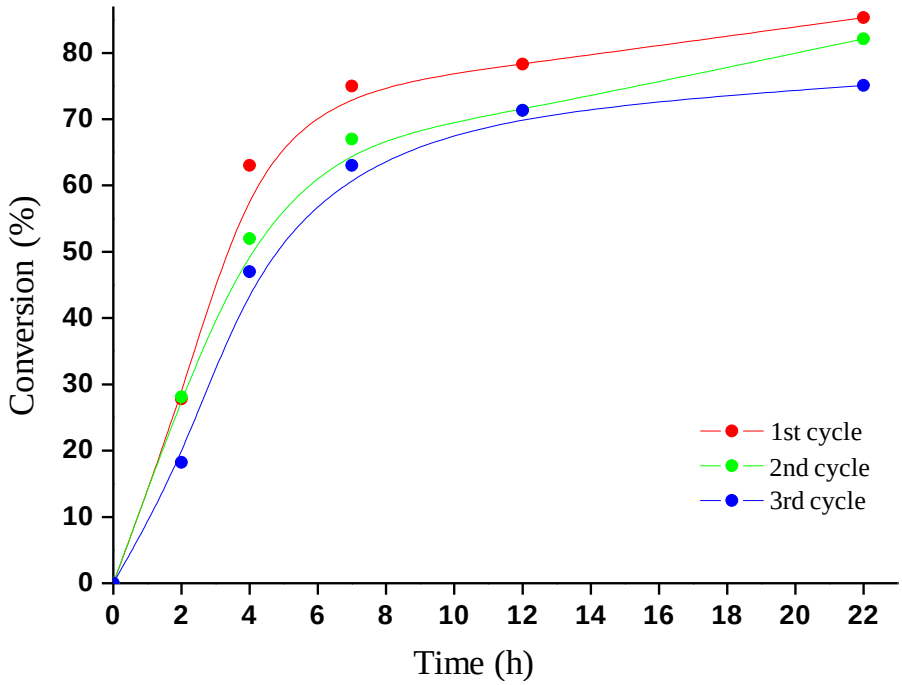

Figure 6.40. Kinetic profiles in three consecutive reaction cycles employing **Ca-AEPF-3** as catalyst.

Catalysts robustness. All catalysts employed in the hydrosilylation reactions were recovered as it was before explained and then characterized by X-ray powder diffraction (XRPD) to study possible structural changes after reaction. Comparison of the XRPD patterns before and after the catalytic reaction, confirm the robustness of the four compounds in the studied conditions (**Figures 6.41-44**). In the case of **Ca-AEPF-3**, the XRPD pattern after the third run (recycling experiments) is shown (**Figures 6.42)**.

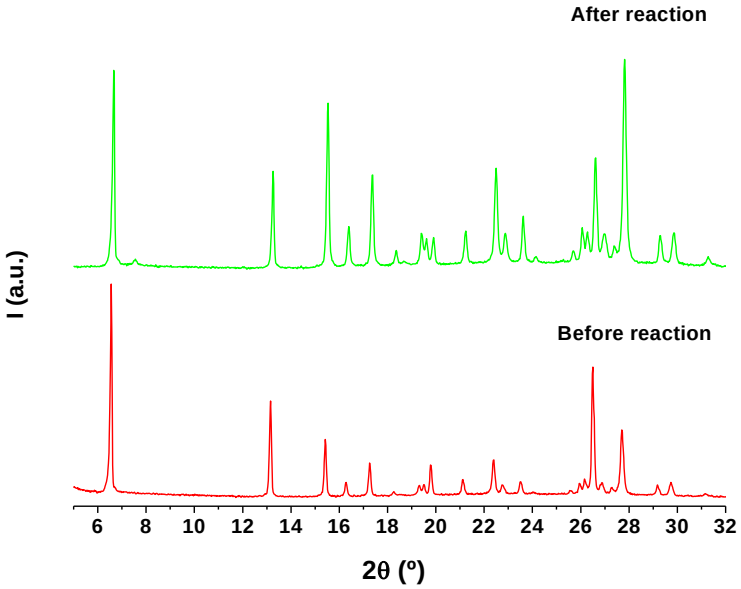

Figure 6.41. Comparison of the experimental XRPD pattern of **Mg-AEPF-2** after hydrogenation catalytic experiments (green) with the pattern of fresh sample before reaction (red).

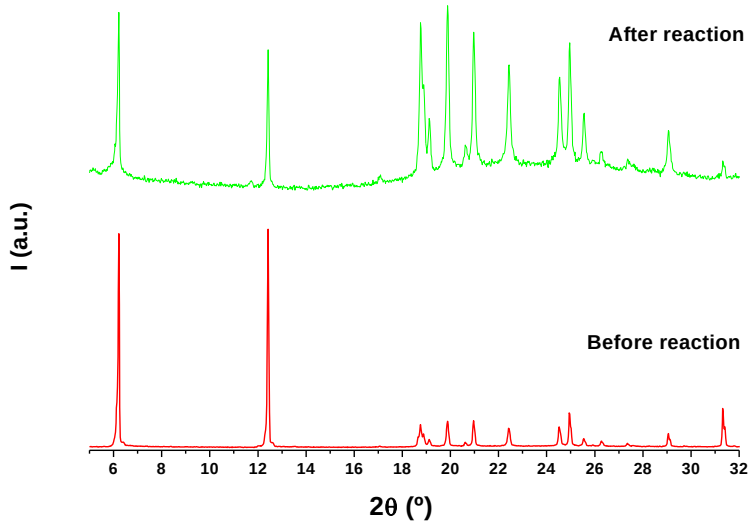

Figure 6.42. Comparison of the experimental XRPD pattern of **Ca-AEPF-3** after hydrogenation catalytic recycling experiments (green) with the pattern of fresh sample before reaction (red).

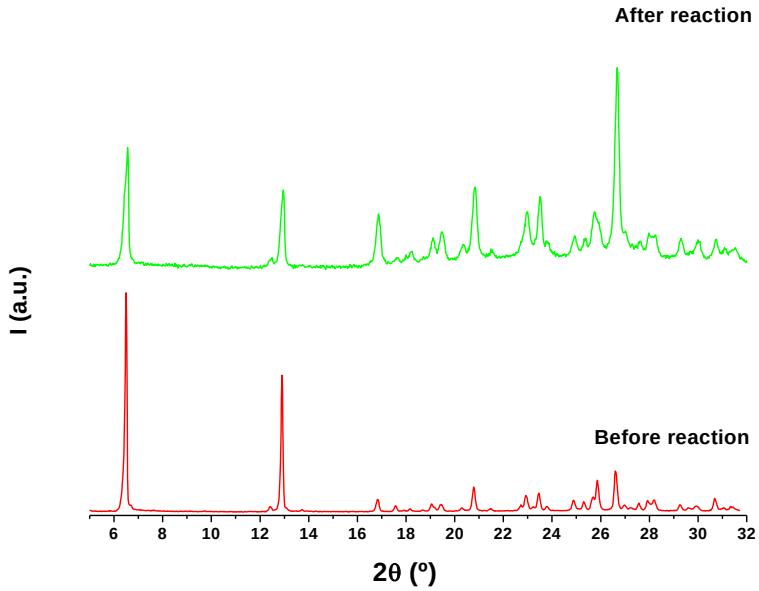

Figure 6.43. Comparison of the experimental XRPD pattern of **Sr-AEPF-4** after hydrogenation catalytic experiments (green) with the pattern of fresh sample before reaction (red).

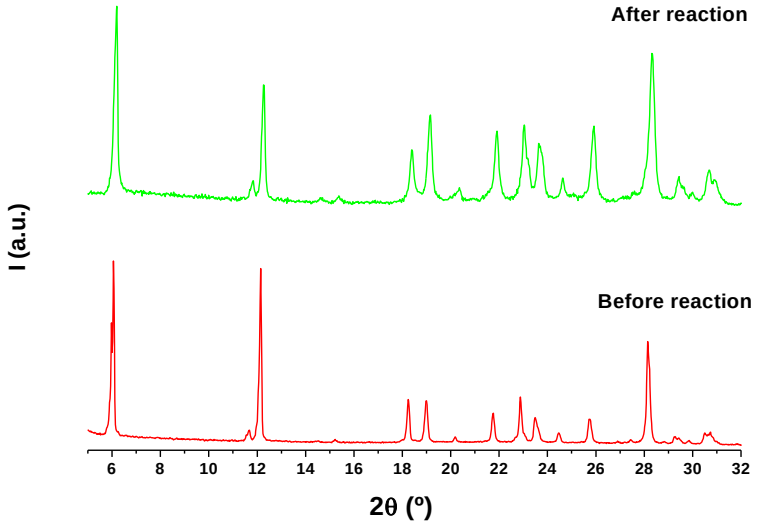

Figure 6.44. Comparison of the experimental XRPD pattern of **Ba-AEPF-4** after hydrogenation catalytic experiments (green) with the pattern of fresh sample before reaction (red).

References

1. Cai, J.; Chen, C.-H.; Liao, C.-Z.; Feng, X.-L.; Chen, X.-M. *Acta Crystallogr.*, **2001**, *B57(4)*, 520.
2. Côté,A.C.; Shimizu, G.K.H. *Chem. Eur. J.*, **2003**, *9(21)*, 5361.
3. Kennedy, A. R.; Kirkhouse, J. B. A.; McCarney, K. M.; Puissegur, O.; Smith, W. E.; Staunton, E.; Teat, S. J.; Cherryman, J. C.; James, R. *Chem. Eur. J.*, **2004**, *10(18)*, 4606.
4. Huo, L.-H.; Gao, S.; Xu, S.-X.; Zhao, H.; Ng, S. W. *Acta Crystallogr.*, **2004**, *E60(9)*, m1240.
5. Gao, S.; Zhu, Z.-B.; Huo, L.-H.; Ng, S. W. *Acta Crystallogr.*, **2005**, *E61(3)*, m528.
6. Russell, V. A.; Etter, M. C.; Ward, M. D. *J. Am. Chem. Soc.*, **2004**, *116*, 1941.
7. Pivovar, A. M.; Holman, K. T.; Ward, M. D. *Chem. Mater.* ,**2001**, *13(9)*, 3018.
8. Dincă, M.; Long, J. R. *J. Am. Chem. Soc.*, **2005**, *127(26)*, 9376.
9. deLill, D. T.; Bozzuto, D. J.; Cahill, C. L. *Dalton Trans.*, **2005**, *12*, 2111.
10. Birkedal Nielsen, R. K.; Kongshaug, K. O.; Fjellvåg, H. *Solid State Sciences*, **2006**, *8(10)*, 1237.
11. Davies, R. P.; Less, R. J.; Lickiss, P. D.; White, A. J. P. *Dalton Trans.*, **2007**, *24*, 2528.
12. Senkovska, I.; Fritsch, J.; Kaskel, S. *Eur. J. Inorg. Chem.*, **2007**, *35*, 5475.
13. Dietzel, P. D. C.; Blom, R.; Fjellvåg, H. *Eur. J. Inorg. Chem.*, **2008**, *23*, 3624.
14. Volkringer, C.; Marrot, J.; Férey, G.; Loiseau, T. *Cryst. Growth Des.*, **2008**, *8(2)*, 685.
15. Côte A.P.; Shimizu G.K.H. *Coord. Chem. Rev.*, **2003**, *245*, 49.
16. Shimizu G.K.H.; Vaidhyanathan R.; Taylor J.M. *Chem. Soc. Rev.*, **2009**, *38*, 1430.
17. Cai, J. *Coord. Chem. Rev.*, **2004**, *248*, 1061.
18. Gándara, F.; Puebla, E. G.; Iglesias, M.; Proserpio, D. M.; Snejko, N.; Monge, M. Á. *Chem. Mater.*, **2009**, *21(4)*, 655.

19. Blatov, V.A. *IUCrComput. Comm. Newslett.*, **2006**, **7**, 4. See also: http://www.topos.ssu.samara.ru.

20. Delgado–Friedrichs, O.; O'Keeffe, M. *Acta Crystallogr.*, **2003**, *B59*, 351.

21. G. S. Pawley, *J. Appl. Crystallogr.*, **1981**, *14*, 357.

22. *Materials Studio Modelling 4.4* software, http://www.accelerys.com/mstudio/ms_modeling

23. Spielmann, J.; Buch, F.; Harder, S. *Angew. Chem. In. Ed.*, **2008,** *47(49)*, 9434.

24. Harder, S. *Chem. Rev.*, **2010**, *110(7)*, 3852.

Chapter 7

Discussion and Conclusions

7.1.

Comparative Analyses

The work presented in this thesis has been focussed in the design of new architectures using alkaline-earth elements and different organic linkers. The careful design of reaction conditions has allowed the obtaining of eighteen novel alkaline-earth materials, belonging to seventeen different structural types. In the following, a detailed comparative study is presented in order to extract some conclusions about the structural features of these new materials.

7.1.1.

Chapter 4: $H_2L_{(1)}$ and $H_2L_{(2)}$ flexible dicarboxylate ligands

Mg MOFs. During the optimization of the reaction conditions to obtain new Mg MOFs, it was earlier shown that this element had to be considered as a "special" case. First of all, from the synthetic point of view, the solvent used to perform the reaction is a crucial point to avoid the formation of soluble $[Mg(H_2O)_6]^{+2}$ species. As it has been shown in this thesis, the formation of these soluble species can be avoided and therefore the coordination of Mg^{+2} ion to different organic linkers can be achieved under solvothermal conditions.

From the exhaustive synthetic study performed then under solvothermal conditions a wide variety of structural types have been obtained. Analysing these materials coming from Mg/H_2L/ancillary ligand systems, a nice conclusion can be drawn. Due to its low coordination numbers (normally 5 or 6), the dimensionality of the obtained frameworks strongly depends on the proportion of the ancillary ligand (**Table 7.1**). Moreover, due to the small ionic radius of this element (~0.65 Å), the inorganic SBUs consist of sharing-vertexes or C-bridge chains or clusters (**Table 7.1** and **Figure 7.1**).

Ca and Sr MOFs. Concerning calcium and strontium elements, as it is known, both of them exhibit variable and higher coordination numbers than Mg (typically from

6 to 8). Thus, analysing the obtained materials based on these elements, it can be concluded that the ancillary ligands do not have influence on the dimensionality of the frameworks, since all are 3D nets (**Table 7.2**). In addition, due to the higher ionic radius of these elements (~0.99 Å for Ca^{+2} and ~1.13 Å for Sr^{+2}), the inorganic SBUs consist of sharing-edges of sharing-faces chains or clusters (**Table 7.2** and **Figure 7.2**).

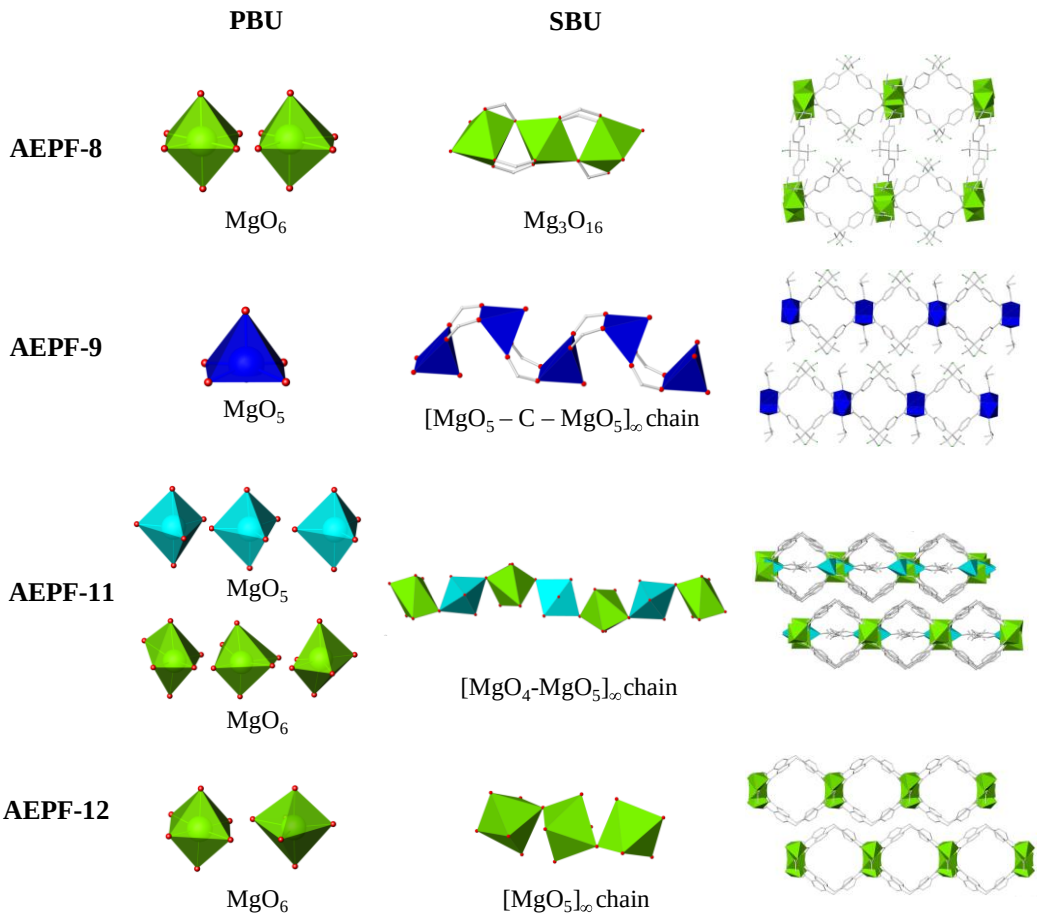

Figure 7.1. Structural summary of the magnesium materials based on dicarboxylate flexible ligands obtained in this thesis.

Table 7.1. Some structural features corresponding to the magnesium materials based on dicarboxylate flexible ligands obtained in this thesis.

		AE / H_2L / anc	PBU	SBU	Dimensionality
$H_2L_{(1)}$	**AEPF-8**	3/3/2	MgO_6	Mg_3O_{16} trimmers	3D
	AEPF-9	1/1/1	MgO_5	C-bridge-chains	2D
$H_2L_{(2)}$	**AEPF-11**	2/2/1	MgO_5 and MgO_6	sh-vert-chains	2D
	AEPF-12	2/2/1	MgO_6	sh-vert-chains	2D

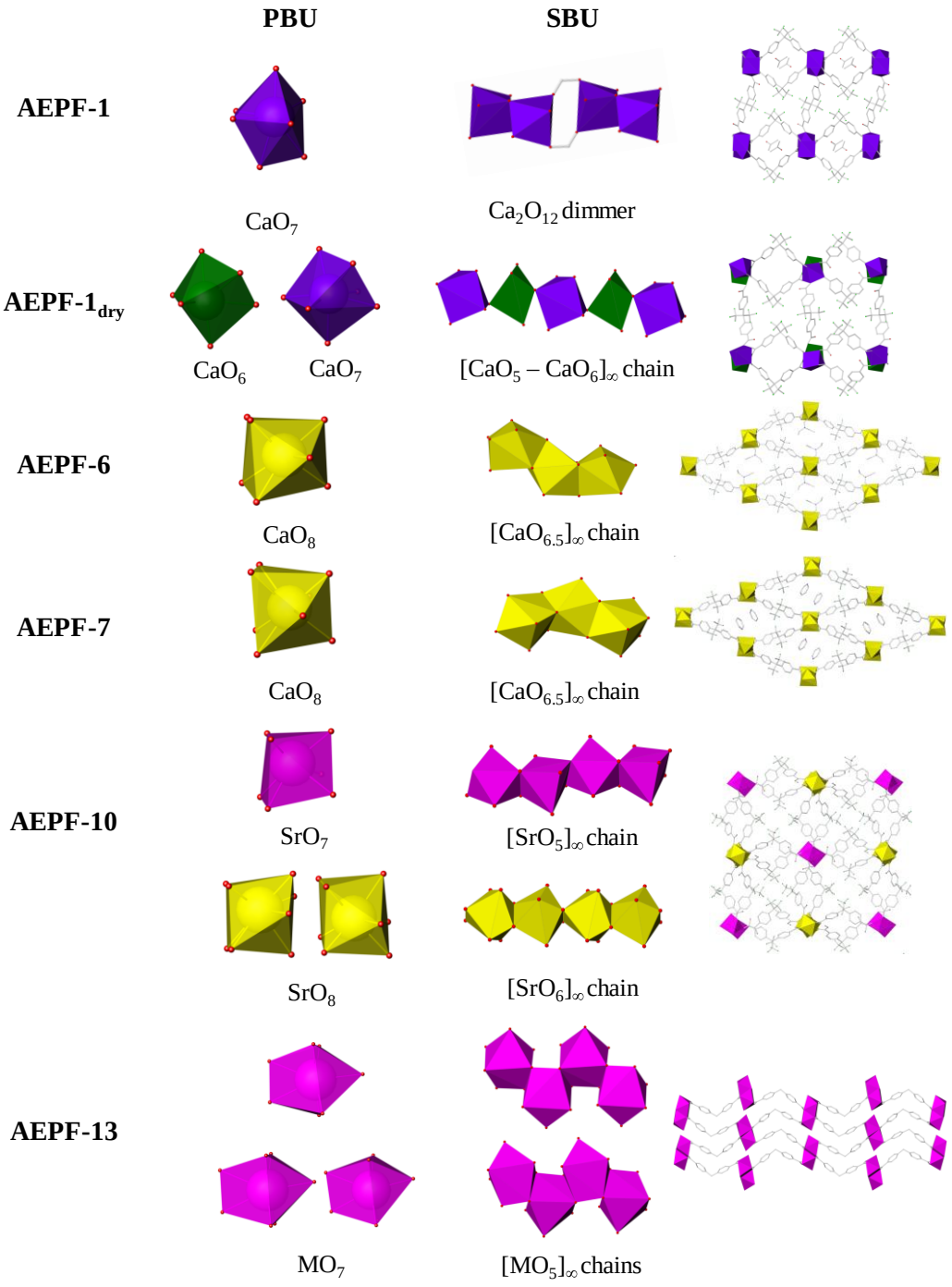

Figure 7.2. Some structural features corresponding to the calcium and strontium materials based on dicarboxylate flexible ligands obtained in this thesis.

Table 7.2. Some structural features corresponding to the magnesium materials based on dicarboxylate flexible ligands obtained in this thesis.

		AE / H_2L / anc	PBU	SBU	Dimensionality
$H_2L_{(1)}$	**Ca-AEPF-1**	3/2/3	CaO_7	Ca_2O_{12} dimmers	3D
	Ca-AEPF-1$_{dry}$	3/2/3	CaO_6 and CaO_7	sh-vert-chains	3D
	Ca-AEPF-6	1/1/1	CaO_8	sh-fac-chains	3D
	Ca-AEPF-7	1/1/1	CaO_8	sh-fac-chains	3D
	Sr-AEPF-10	1/3/0	SrO_7 and SrO_8	sh-edge-chains	3D
$H_2L_{(2)}$	**(Ca, Sr)-AEPF-13**	1/1/1	MO_7	sh-edge-chains	3D

To consider topological features of these materials, detailed analyses were performed to study the conformation of the two used flexible linkers ($H_2L_{(1)}$ and $H_2L_{(2)}$). On one hand, the way in which the linkers form the channels in these frameworks was carefully studied. As it was discussed in this thesis, the square or rhombic shaped channels can be named as **A** (crossing-edge mode) or **B** (parallel mode). Surprisingly, a new **D**-type channel, being star shaped, was found for the first time using $H_2L_{(1)}$ linker (**Sr-AEPF-10**). The different conformations of the channels determined for the obtained materials are listed in **Table 7.3**. Concerning the topological features of these nets, except for **AEPF-1** and **AEPF-1$_{dry}$** that own infrequent five-connected nets, all the other materials nets can be described with four- or six-connected nodes.

With regard to the role that play the non-binding groups in the two studied linkers, it is worth mentioning that the **d** distances for $H_2L_{(1)}$ (with $–CF_3$ groups) are clearly higher than those determined for $H_2L_{(2)}$ (with –H groups). In addition, in the case of **sra** nets found for both ligands, which exhibit rhombic pores, they are the nets for which the **d** distances are the largest (**Table 7.3**).

Table 7.3. Summary of structural and topological features determined for the materials obtained using $H_2L_{(1)}$ and $H_2L_{(2)}$.

		PBU	SBU	Net	PS	Nodes	Channel	d (Å)
$H_2L_{(1)}$	Ca-**AEPF-1**	CaO_7	Ca_2O_{12} dimmers	**hxg-d-5-Pbcn**	(6^{10})	5c	A	9.502
	Ca-**AEPF-1$_{dry}$**	CaO_6 and CaO_7	sh-vert-chains	**5/4/o13**	$(4^4.6^6)$	5c	A	9.693, 8.794
	Ca-**AEPF-6**	CaO_8	sh-fac-chains	**sra**	$(4^2.6^3.8)$	4c	B	9.896
	Ca-**AEPF-7**	CaO_8	sh-fac-chains	**sra**	$(4^2.6^3.8)$	4c	B	9.994
	Mg-**AEPF-8**	MgO_6	Mg_3O_{16} trimmers	**pcu**	$(4^{12}.6^3)$	6c	B	9.609
	Mg-**AEPF-9**	MgO_5	C-bridge-chains	**2D sql**	$(4^4.6^2)$	4c	B	6.566
	Sr-**AEPF-10**	SrO_7 and SrO_8	sh-fac-chains	**new type**	$(4^6.6^7.8^2)(4^6.6^9)$	6c, 6c	A, D	9.742, 9.556
$H_2L_{(2)}$	Mg-**AEPF-11**	MgO_5 and MgO_6	sh-vert-chains	**SP 2-periodic net (4,4)IIb**	$(4^{13}.6^2)$	6c	A	9.037, 9.205, 9.391
	Mg-**AEPF-12**	MgO_6	sh-vert-chains	**2D sql**	$(4^4.6^2)$	4c	B	9.208
	(Ca, Sr)-**AEPF-13**	MO_7	sh-edge-chains	**sra**	$(4^2.6^3.8)$	4c	B	9.696

7.1.2.

Chapter 5: $H_2L_{(1)}$ and phen ligands

The supramolecular frameworks of the obtained compounds using phen and $H_2L_{(1)}$ as linkers are formed by hydrogen bonds. Since in all cases the presence of $(Mg\text{-}O_x)_\infty$ rod is found, the inorganic SBUs for the five compounds can be described as rods of quadrangles linked by sharing opposite edges (*ladders*) (**Figure 7.3**). Analysing the simplified SBUs for the five materials, two kinds of ladders can be described. On one hand, in the case of **AEPF-14** polymorphs and **AEPF-16**, the rungs of these ladders are parallel among them, giving 2D **sql** and 3D **sra** networks. In contrast, in the case of **AEPF-15** and **AEPF-17** materials the corresponding SBUs described ladders with the rungs linked at an angle to each other (*twisted* ladders), what in the case of the 3D networks gives rise to a different topology (**irl**, instead of **sra**).

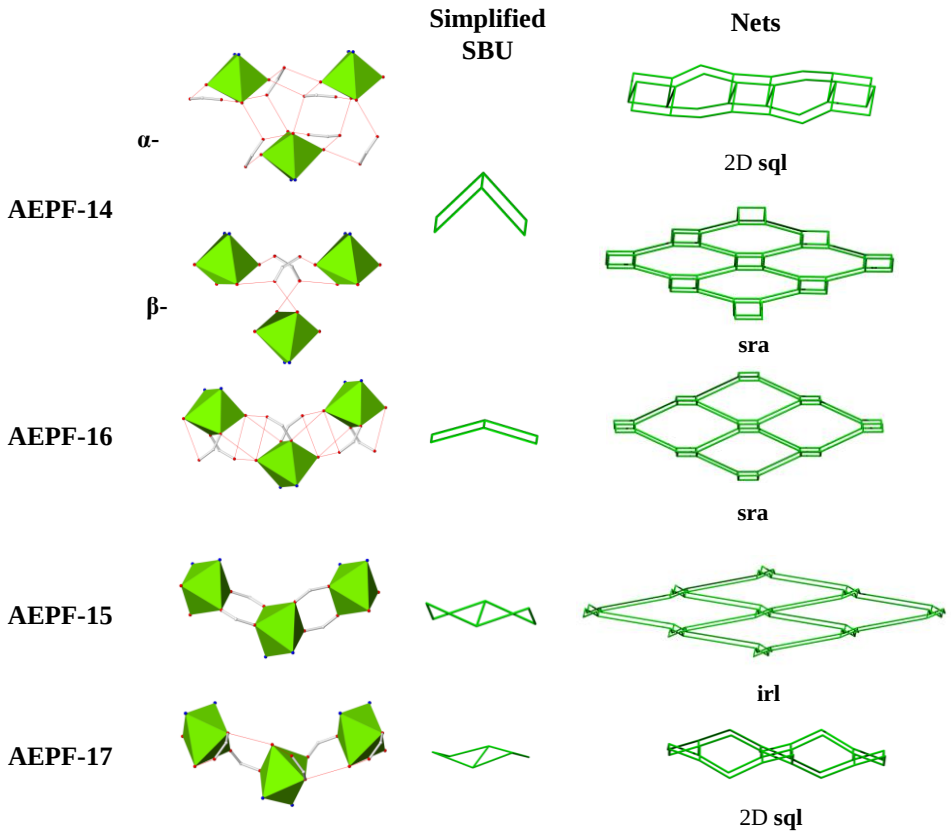

Figure 7.3. Topological summary of the obtained magnesium materials based on the chelating ligand phen and the dicarboxylate flexible ligand $H_2L_{(1)}$.

7.1.3.

Chapter 6: 2,6-AQDS ligand

Concerning the materials obtained using the 2,6-AQDS disulfonate linker, the main topological features can be understood analysing their inorganic layers. Thus, the linker can be considered as a simple spacer among these inorganic layers. A structural summary of the disulfonate materials presented in Chapter 6 is depicted in **Figure 7.4**.

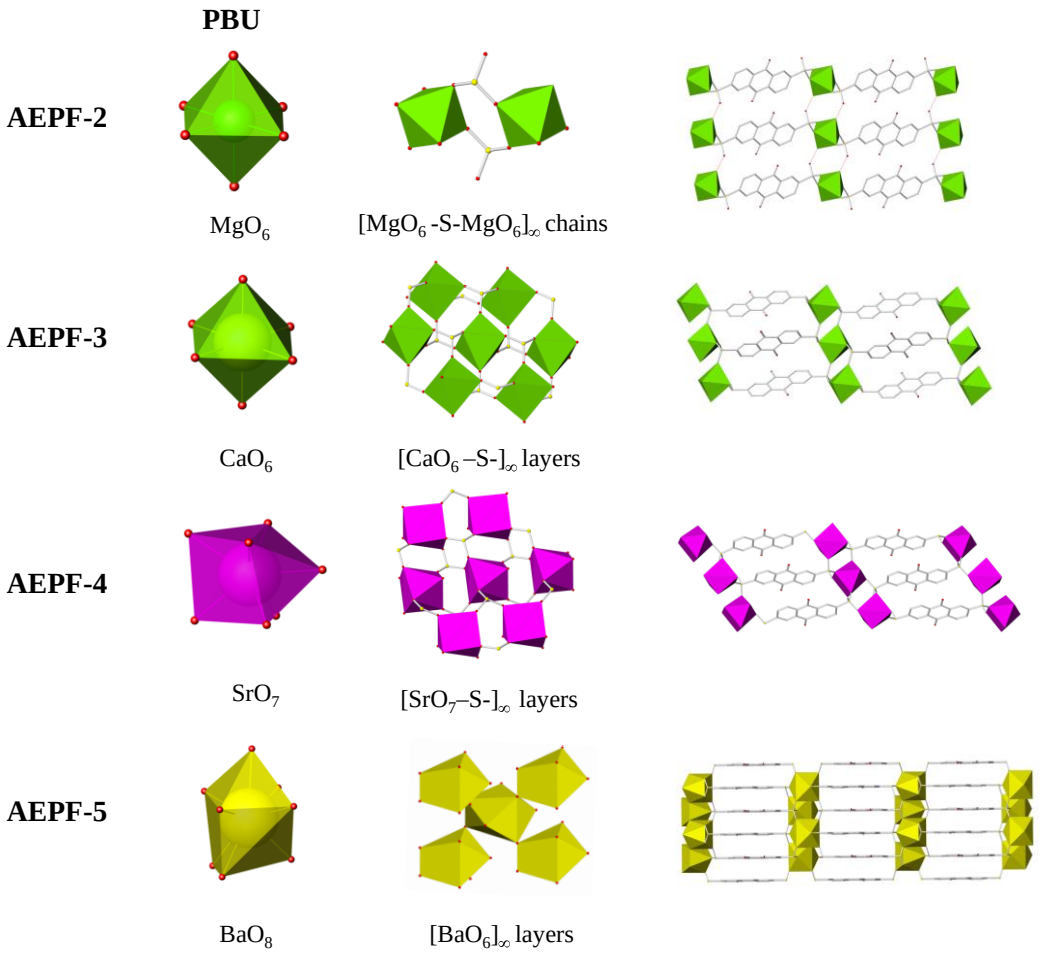

Figure 7.4. Some structural features corresponding to the alkaline-earth disulfonate materials based on the 2,6-AQDS.

First, in the case of magnesium, in **AEPF-2** the sulfonate groups do not exhibit their maximum coordination capability ($\eta^2\mu_2$-$\eta^2\mu_2$ coordination mode), giving rise to a layered material. With regard to calcium and strontium materials (**AEPF-3** and **AEPF-4**, respectively), the sulfonate groups are bonding in a $\eta^3\mu_3$-$\eta^3\mu_3$ coordination mode, determining the same type of inorganic layer for both compounds (**kgd** topological type). However, the presence of a coordinated water molecule in **AEPF-4** causes a subtle distortion of its inorganic layer, what explains the obtaining of a different 3D framework to that found in **AEPF-3**. Finally, when barium is used as a metal center (**AEPF-5**), due to the capability of these element to exhibit higher coordination numbers, the sulfonate groups bond in a hepta-topic $\eta^3\mu_4$-$\eta^3\mu_3$ coordination mode, giving a more complicate inorganic layers. In consequence of that, **AEPF-5** possesses a 3D frameworks for which a new topological type has been described (point symbol $(4^{11}.6^{10})(4^3.6^3)(4^5.6^5)$).

7.2.

Conclusions

In the present work the studies were focused on the obtaining of new MOFs using **alkaline-earth elements** as metal centers. Eighteen new compounds were obtained and studied in detail.

- The system **alkaline-earth element / H_2L / ancillary ligand** has been investigated, obtaining eleven new compounds. Seven of them, with 4,4'-(hexafluoroisopropylidene)*bis*(benzoic acid) (**$H_2L_{(1)}$**) as linker, belong to seven different structural types: **AEPF-1** and **AEPF-1$_{dry}$** (Ca), **AEPF-6** (Ca), **AEPF-7** (Ca), **AEPF-8** (Mg), **AEPF-9** (Mg) and **AEPF-10** (Sr). The other four, with diphenylmethane-4,4'-dicarboxylic acid ligand (**$H_2L_{(2)}$**), belong to three different structural types **AEPF-11** (Mg), **AEPF-12** (Mg) and **AEPF-13** (Ca, Sr).

- From the exploration of the system **alkaline-earth element / H_2L / ancillary ligand**, using the **$H_2L_{(1)}$** ligand, some conclusions can be drawn:

  - **AEPF-1** material (**$[Ca(L_{(1)})(H_2L_{(1)})_{0.5}(H_2O)]\cdot 0.5Me_2CO$**), which presents a reversible phase transition related to the loss of guest molecules to **AEPF-1$_{dry}$** (**$[Ca(L_{(1)})(H_2L_{(1)})_{0.5}(H_2O)]$**), is a good candidate for sorption and catalytic applications. The special structural properties of this Ca-based MOF lead to the selective sorption of different organic compounds depending on their size, shape and polarity in different mixtures. On the other hand, gas sorption studies show that gas adsorption through **AEPF-1** pores does not depend on the size of adsorbed molecules, but could be related with adsorption energy, being the lowest for H_2. In addition, this material has been proved to serve as an alternative to conventional precious metal-based alkene-hydrogenation catalysts. It is remarkable that both structures form uninodal five connected 3D nets belonging to the **hxg-d-5-Pbcn** (point symbol (6^{10})) and **5/4/o13** (point symbol ($4^4.6^6$)) topological types for **AEPF-1** and **AEPF-1$_{dry}$**, respectively.

- Following with the compounds based on the $\mathbf{H_2L_{(1)}}$ ligand, the Ca MOFs named **AEPF-6** (**[Ca($L_{(1)}$)(DEF)]**) and **AEPF-7** (**[Ca($L_{(1)}$)(H_2O)]·(Py)·0.5H_2O**) were also obtained. They are two porous materials that have been synthesised employing a strategy based on the incorporation of other smaller organic molecules into the system, with the purpose of studying their influence on the pore size. The strategy used was either the employing of an organic molecule (DEF) as candidate to coordinate to Ca centers in a η^1 coordination mode (replacing the role of coordinated water molecules), and favouring in that way the formation of an open-framework (**AEPF-6**); or the use of an aromatic organic molecule (Py) that can act as a template (**AEPF-7**). In both compounds, the Ca^{+2} ions are octa-coordinated, giving CaO_8 polyhedra (PBU) which form sharing-faces chains (SBU) joint together *via* the $L_{(1)}^{-2}$ linkers. Such arrangement gives rise to a three-dimensional framework with rhombic shaped channels, belonging to a **sra** topology. However, while in **AEPF-6** the Ca eighth coordination position is occupied by a DEF molecule, which obstructs the porous window and cannot be eliminated without the net collapse, in **AEPF-7** this coordination position is occupied by a removable water molecule. The channels are due, in this case, to the Py molecules that clearly acts as templates. Finally, taking into account the results about the **AEPF-7** activation process by which Py molecules are interchanged by acetonitrile molecules, and taking into account the results of **AEPF-7** specific surface area measurements, it can be concluded that after carrying out the activation processes **AEPF-7** certainly exhibits a porous framework.

- **AEPF-8** (**[$Mg_{1.5}$($L_{(1)}$)$_{1.5}$(DEF)]**) and **AEPF-9** (**[Mg($L_{(1)}$)(DEF)]**) compounds are obtained exploring the system Mg / $H_2L_{(1)}$ / DEF. The different proportions Mg/$H_2L_{(1)}$/DEF in the system (3/3/2 in the former and 1/1/1 in the latter) give rise to different 3D and 2D frameworks. In **AEPF-8** the DEF molecules only block the terminal positions of every Mg_3O_{16} cluster, what allows the formation of a 3D net with **pcu** topology. However, in **AEPF-9** these DEF molecules block one position of every polyhedron, forcing in that way the formation of a layered 2D framework with **sql** topology. Both structures bear square shaped channels of the **B**-type (parallel mode). Taking into account these results, it can be concluded that the net dimensionality can be changed by varying the proportion of the DEF ancillary ligand in the system Mg/$H_2L_{(1)}$/DEF.

- Finally, the Sr MOF **AEPF-10** (**[$Sr_2(H_2L_{(1)})(HL_{(1)})_2(L_{(1)})]\cdot H_2O$**) is obtained when a mixture of water/n-hexane is used as a solvent media. **AEPF-10** possesses an elegant 3D framework, which exhibits two kinds of channels: those square-shaped (**A**-type) similar to the other compounds and others star shape (**D**-type). The three-dimensional can be described as a binodal six-connected net with point symbol $(4^6.6^7.8^2)(4^6.6^9)$, which is new topological type and thus, does not appear in TOPOS or in the RCSR databases.

- From the exploration of the system **alkaline earth element/ L / ancillary ligand**, employing the less sterically impeding **$H_2L_{(2)}$** ligand, some conclusion can be deduced:

- **AEPF-11** (**[$Mg(L_{(2)})(DEF)_{0.5}$]**) and **AEPF-12** (**[$Mg_2(L_{(2)})(HL_{(2)})(CH_3CO_2)$]**) both exhibit frameworks built from sharing-vertex chains (SBU). However, while in the former they are formed by MgO_5 and MgO_6 polyhedra, in the latter all the polyhedra are MgO_6 octahedra. Due to the existence in both cases of ancillary ligands in the same proportion, the structures are 2D**.** Nevertheless, the frameworks can be simplified as a uninodal six-connected net with **SP 2-periodic net (4,4)IIb** topology (point symbol $(4^{13}.6^2)$) for **AEPF-11**; and as a uninodal four-connected net with **sql** topology (point symbol $(4^4.6^2)$) for **AEPF-12**. Once again, it is shown that for the same proportion of the ancillary ligand, the net dimensionality does not vary in the resulting MOF.

- Concerning the **AEPF-13** compounds (**[$M(L_{(2)})(H_2O)$]**, where M= Ca^{+2} or Sr^{+2}), these materials exhibit a 3D framework, whose SBUs are chains formed by sharing-edges MO_7 polyhedra. These frameworks can be described as uninodal 4-connected nets with a **sra** topology (point symbol $(4^2.6^3.8)$).

- From the Ca and Sr structures we can see that, due to the variable and high coordination number of these metals, the ancillary ligands do not have influence in the net dimensionality, since all the obtained are 3D nets, and except for **AEPF-1** that owns a very infrequent five connected nets, and **AEPF-10** that presents a new topology (point symbol $(4^6.6^7.8^2)(4^6.6^9)$), they are four-connected **sra** nets.

- The effect of the introduction of nitrogenated chelating ancillary ligands has been also explored, resulting in five new compounds, which exhibit 0D, 1D and 2D dimensionalities, and 2D and 3D supramolecular frameworks: a molecular magnesium material with polymorphism (named **AEPF-14**, **α-** and **β**-forms), a 1D MOF (**AEPF-15**), a 1D helical MOF (**AEPF-16**) and a 2D MOF (**AEPF-17**). The role that the synthesis conditions play in the obtaining of each phase has been exhaustively studied, deducing the following conclusions:

- The hydrogen bond interactions found in the five compounds were taken into account to study the topology of their supra-molecular nets, achieving nets with higher dimensionality in all the cases except for **AEPF-17**, where the chelating ligands hinder any interlayer hydrogen bond interaction.

- From the comparison of relative energies for the two **AEPF-14** polymorphs, it can be concluded that the **β**-form is the most stable one, which agrees with the higher dimensionality of the supramolecular net of this polymorph.

- From computational studies on relative formation energies ($E_{Formation}$) of **α-AEPF-14**, **AEPF-15**, and **AEPF-16** phases, which are together obtained at lower temperatures (T = 160-170 ºC) and short reaction times (1-48 hours), the following conclusions can be drawn. First, **α-AEPF-14** presents the lowest $E_{Formation}$ among these three phases, what seems to indicate that, at shorter reaction times, thermodynamic processes govern the reaction. However, increasing the reaction time and the temperature, **α-AEPF-14** dissolution processes may take place, leading to the formation of the less stable phases (**AEPF-15** and **AEPF-16**).

- Computational studies on relative formation energies ($E_{Formation}$) were also performed to analyse **AEPF-16**, and **AEPF-17** phases, which are together obtained at higher temperatures (T = 180 and 200 ºC) and long reaction times (1-10 days). Taking into account the obtained $E_{Formation}$ values for these compounds, it can be concluded that when longer reaction times are used, the more stable **AEPF-17** compound is mainly obtained (thermodynamic control). However, at shorter reaction times, kinetic processes govern the reaction, leading to a less

thermodynamically stable phase **AEPF-16**. At 200 ºC, an increase of the kinetically controlled phase (**AEPF-16**) is also observed.

- Finally, by exploring the system **alkaline-earth element / 2,6-AQDS ligand**, four new compounds were obtained and completely characterized. **AEPF-2 ([Mg(2,6-AQDS)(H_2O)$_2$])** is the first Mg-based disulfonate MOF, in which the ligand coordinates directly with Mg^{+2} ions to build a 2D net. **AEPF-3** (**[Ca(2,6-AQDS)]**), **AEPF-4** (**[Sr(2,6-AQDS)(H_2O)]**) and **AEPF-5** (**[Ba(2,6-AQDS)]**) are belong to different 3D structural types and exhibit two new topologies. In addition, it is worth highlighting the high thermal stability (up to 500 ºC) of all these materials. The catalytic behaviour of these alkaline-earth materials in hydrogenation of alkenes and hydrosilylation of ketones reactions makes these MOFs promising environmentally friendly cheap catalysts.

7.3.
Conclusiones

El trabajo realizado en esta tesis se ha centrado en la preparación de nuevos MOFs usando elementos alcalinotérreos como centros metálicos. Así, dieciocho nuevos compuestos han sido obtenidos y meticulosamente estudiados.

- El sistema **elemento alcalinotérreo / H_2L / ligando auxiliar** ha sido investigado, obteniéndose diez nuevos compuestos. Seis de ellos basados en el ligando (hexafluoroisopropylidene)*bis*(benzoicacid) (**$H_2L_{(1)}$**), pertenecen a siete tipos estructurales diferentes: **AEPF-1** and **AEPF-1$_{dry}$** (Ca), **AEPF-6** (Ca), **AEPF-7** (Ca), **AEPF-8** (Mg), **AEPF-9** (Mg) and **AEPF-10** (Sr). Los otros cuatro, basados en el ligando diphenylmethane-4,4'-dicarboxylic acid (**$H_2L_{(2)}$**), pertenecen a tres tipos estructurales diferentes: **AEPF-11** (Mg), **AEPF-12** (Mg) y **AEPF-13** (Ca, Sr).

- Del estudio del sistema **elemento alcalinotérreo / H_2L / ligando auxiliar**, usando el ligando **$H_2L_{(1)}$**, se pueden extraer las siguientes conclusiones:

  - El material **AEPF-1** (**[Ca($L_{(1)}$)($H_2L_{(1)}$)$_{0.5}$(H_2O)]·0.5Me_2CO**), el cual presenta una transición de fase reversible relacionada con la pérdida de moléculas huésped en los poros dando la fase **AEPF-1$_{dry}$** (**[Ca($L_{(1)}$)($H_2L_{(1)}$)$_{0.5}$(H_2O)]**), es un buen candidato para aplicaciones de sorción y catalíticas. Las especiales propiedades estructurales de este MOF de Ca dan lugar a la sorción selectiva de diferentes compuestos orgánicos, en función del tamaño, forma y polaridad de los mismos en diferentes mezclas. Además, gracias a los estudios de sorción de diferentes gases se ha podido determinar que la adsorción de gases a través de los poros presentes en **AEPF-1** no depende tanto del tamaño de las moléculas adsorbidas, sino de la correspondiente energía de adsorción, siendo ésta menor en el caso del H_2. Por otro lado, se han demostrado las potenciales aplicaciones catalíticas de este material, siendo una alternativa a los catalizadores convencionales de metales preciosos usados en hidrogenación de alquenos. Cabe destacar que las dos estructuras presentan redes tridimensionales penta-conectadas de tipo topológico **hxg-d-5-**

Pbcn (símbolo puntual (6^{10})) y **5/4/o13** (símbolo puntual ($4^4.6^6$)), para **AEPF-1** y **AEPF-1$_{dry}$**, respectivamente.

- Siguiendo con los compuestos basados en el ligando **$H_2L_{(1)}$**, se han obtenido también los MOFs de Ca **AEPF-6** (**[Ca($L_{(1)}$)(DEF)]**) y **AEPF-7** (**[Ca($L_{(1)}$)(H_2O)]·(Py)·0.5H_2O**). Se trata de materiales porosos que han sido obtenidos mediante estrategias sintéticas basadas en la incorporación de moléculas orgánicas pequeñas, a fin de estudiar su influencia en el tamaño de los poros del material. Así, la estrategia utilizada ha consistido o bien en el uso de una molécula orgánica (DEF) con capacidad de coordinar los centros de Ca en modo η^1 (remplazando así el papel de una molécula de agua coordinada), y favoreciendo además la formación de una estructura abierta (**AEPF-6**); o bien en el uso de una molécula orgánica aromática (Py) con capacidad de actuar como *template* (**AEPF-7**). En ambos casos, los iones Ca^{+2} se hallan octa-coordinados, formando cadenas en las que los poliedros inorgánicos comparten cara. La unión de estas cadenas inorgánicas mediante el ligando **$L_{(1)}^{-2}$** da lugar a la formación de una red tridimensional con canales rómbicos y topología de tipo **sra**. Sin embargo, mientras que en **AEPF-6** una posición de coordinación del Ca está ocupada por una molécula de DEF coordinada, la cual obstruye el poro y no puede ser eliminada sin colapsar la red, en **AEPF-7** esta posición de coordinación la ocupa una molécula de agua que puede ser fácilmente eliminada. En este último caso, la presencia de canales es debido a las moléculas de Py que claramente actúan como *templates*. Finalmente, con respecto a los procesos de activación llevados a cabo en **AEPF-7** mediante el intercambio de las moléculas de piridina por moléculas de acetonitrilo, y teniendo en cuenta los resultados de área superficial obtenidos, se puede concluir que efectivamente se ha conseguido eliminar la mayoría de moléculas de *template*, dando lugar así a una red porosa.

- **AEPF-8** (**[$Mg_{1.5}(L_{(1)})_{1.5}$(DEF)]**) y **AEPF-9** (**[Mg($L_{(1)}$)(DEF)]**) se han obtenido explorando el sistema Mg / $H_2L_{(1)}$ / DEF. Así, la diferente proporción en el sistema Mg/$H_2L_{(1)}$/DEF (3/3/2 en **AEPF-8** y 1/1/1 en **AEPF-9**) da lugar a redes de diferente dimensionalidad (2D y 3D). En el caso de **AEPF-8**, las moléculas de DEF sólo bloquean las posiciones terminales de los clúster Mg_3O_{16} determinados en este material, lo cual posibilita la formación de una red tridimensional de tipo

topológico **pcu**. Sin embargo, en el caso de **AEPF-9**, las moléculas de DEF bloquean una posición de cada poliedro inorgánico, forzando así la formación de una red bidimensional de tipo topológico **sql**. Ambas estructuras poseen canales de forma cuadrada de tipo **B** (modo paralelo). Teniendo en cuenta estos resultados, se puede concluir que la dimensional de la red puede ser cambiada variando la proporción del ligando auxiliar en este tipo de sistema estudiado.

- En el caso de **AEPF-10** (**[$Sr_2(H_2L_{(1)})(HL_{(1)})_2(L_{(1)})]\cdot H_2O$**), para cuya obtención se utiliza una mezcla de disolventes agua/n-hexano y en el cual el metal es Sr, se forma una elegante red tridimensional. Esta red posee dos tipos de canales: unos de forma cuadrada (tipo **A**) similares a los encontrados en otros compuestos y otros con forma de estrella (tipo **D**). La red tridimensional es binodal seis-conectada (grupo puntual $(4^6.6^7.8^2)(4^6.6^9)$). Este tipo topológico no se ha descrito previamente ni en las bases de datos del programa TOPOS ni en la RCSR.

- Del estudio del sistema **elemento alcalinotérreo / H_2L / ligando auxiliar**, usando el ligando **$H_2L_{(2)}$** que está menos impedido estéricamente, se deducen las siguientes conclusiones:

- **AEPF-11** (**[$Mg(L_{(2)})(DEF)_{0.5}$]**) y **AEPF-12** (**[$Mg_2(L_{(2)})(HL_{(2)})(CH_3CO_2)$]**) son materiales para los cuales la SBU se describe como cadenas de poliedros inorgánicos compartiendo vértices. Sin embargo, mientras que para **AEPF-11** estas cadenas se componen de dos tipos de poliedros (MgO_5 y MgO_6), en el caso de **AEPF-12** sólo se ha determinado la presencia de octaedros MgO_6. Debido a que para los dos compuestos la proporción de ligando auxiliar es la misma, en ambos casos se obtienen redes 2D. Sin embargo, cabe diferenciar que las redes poseen diferentes topologías: uninodal seis-conectada de tipo **SP 2-periodic net (4,4)IIb** (grupo puntual $(4^{13}.6^2)$) para **AEPF-11** y uninodal cuatro-conectada de tipo **sql** (grupo puntual $(4^4.6^2)$) para **AEPF-12**. Así, se ha demostrado que para la misma proporción de ligando auxiliar, la dimensionalidad de la red obtenida en el MOF no varía.

- Los compuestos **AEPF-13** (**[$M(L_{(2)})(H_2O)$]**, donde M= Ca^{+2}or Sr^{+2}) poseen una red tridimensional, para la cual la SBU se describe como cadenas de poliedros

MO_7 que comparten arista. La red determinada es uninodal cuatro-conectada, de tipo topológico **sra** (grupo puntual ($4^2.6^3.8$)).

- De las estructuras obtenidas de Ca y Sr se puede deducir que, debido a que estos metales poseen números de coordinación mayores y más variables, los ligandos auxiliares no tienen influencia en la dimensionalidad de la red obtenida. De hecho, todas las redes obtenidas con estos metales son tridimensionales y cuatro-conectadas de tipo topológico **sra**, salvo en el caso de **AEPF-1**, que posee una red penta-conectada poco frecuente; y en el caso de **AEPF-10**, para el cual se ha descrito una nueva topología (grupo puntual ($4^6.6^7.8^2$)($4^6.6^9$)).

- Se ha estudiado el efecto de la introducción de ligandos nitrogenados de tipo quelato, obteniéndose así cinco nuevos compuestos (los cuales exhiben estructuras 0D, 1D y 2D; y redes supramoleculares 2D y 3D): un material molecular con polimorfismo (**AEPF-14**, formas **α-** y **β-**), un MOF 1D (**AEPF-15**), un MOF helicoidal 1D (**AEPF-16**) y un MOF 2D (**AEPF-17**). Además, se ha estudiado exhaustivamente el papel que juegan las condiciones de síntesis en la obtención de cada fase, deduciendo las siguientes conclusiones:

- Los enlaces de hidrógeno determinados para los cinco compuestos han sido tenidos en cuenta para el estudio topológico de las redes supramoleculares de estos materiales. En todos los casos se obtienen redes de mayor dimensionalidad, excepto para **AEPF-17**, en el cual los ligandos aromáticos de tipo quelato se hallan impidiendo la formación de enlaces de hidrógeno entre capas.

- Gracias a los estudios computacionales realizados para analizar las energías relativas de los dos polimorfos del compuesto **AEPF-14**, se ha podido determinar que la forma **β** es la más estable. Este hecho está en acuerdo con la mayor dimensionalidad de la red supramolecular determinada para este polimorfo.

- De los estudios computacionales realizados para determinar las energías de formación relativas ($E_{Formation}$) de los compuestos **α-AEPF-14**, **AEPF-15** y **AEPF-16**, los cuales se obtienen conjuntamente a bajas temperaturas (T = 160-170 ºC) y

tiempos cortos de reacción (1-48 horas), se han obtenido las siguientes conclusiones. En primer lugar, **α-AEPF-14** presenta la menor energía de formación, lo que parece indicar que, a tiempos cortos de reacción, procesos termodinámicos rigen la reacción. Sin embargo, tanto al incrementar el tiempo de reacción como la temperatura, tienen lugar procesos de disolución del compuesto **α-AEPF-14**, dando lugar a la formación de las fases menos estables termodinámicamente (**AEPF-15** y **AEPF-16**).

- Finalmente, se han llevado a cabo estudios computacionales para determinar las energías de formación relativas ($E_{Formation}$) de **AEPF-16** y **AEPF-17**, los cuales se obtienen conjuntamente a mayores temperaturas (T = 180 y 200 ºC) y tiempos de reacción más largos (1-10 días). Teniendo en cuenta los valores de energías de formación obtenidos para estos compuestos, se puede concluir que para tiempos largos de reacción, se obtiene mayoritariamente la fase más estable **AEPF-17** (control termodinámico). Sin embargo, a tiempos cortos, los procesos cinéticos gobiernan la reacción, dando lugar a la fase menos estable termodinámicamente **AEPF-16**. A 200 ºC, se observa un incremento del control cinético (**AEPF-16**).

- Explorando el sistema **elemento alcalinotérreo / ligando 2,6-AQDS**, se han obtenido cuatro nuevos compuestos que han sido detalladamente caracterizados. **AEPF-2** (**[Mg(2,6-AQDS)(H_2O)$_2$]**) es el primer MOF disulfonato de Mg en el que el ligando orgánico coordina directamente con los iones Mg^{+2} para formar una red bidimensional. Los compuestos **AEPF-3** (**[Ca(2,6-AQDS)]**), **AEPF-4** (**[Sr(2,6-AQDS)(H_2O)]**) y **AEPF-5** (**[Ba(2,6-AQDS)]**) muestran redes tridimensionales y dos nuevas topologías. Además, cabe destacar la gran estabilidad térmica que muestran estos MOFs (hasta 500ºC). Finalmente, la potencial aplicación de estos compuestos como catalizadores heterogéneos se ha evaluado para la hidrogenación de alquenos y la hidrosililación de cetonas.

Appendix

1.

Topological terminology

A brief summary of the specific topological terminology used in this thesis is presented in this section. More detailed set of definitions is given by Delgado-Friedrichs and O'Keeffe.[1]

- **Graph.** A *graph* is a set of vertices or points, on which a *topology* is given as a set of ordered pairs of vertices; each pair determines an edge of a graph. In chemistry, the graph vertices and edges correspond to atoms and interatomic bonds, respectively. Taking into account this description, *topology* means nothing but the set of all interatomic bonds.

- **Net.** A *net* is a special kind of infinite graph, that is: *simple* (without loops, multiple or directed edges) and *connected* (any pair of vertices in a graph is connected by a chain of edges).

- **Node.** Vertices of the graph are called *nodes* of the net. The *coordination number or degree of a nod*e is the number of edges incident on the node. A net is *uninodal* (bi-, tri-, …, polynodal) if all its nodes are equivalent (or there are two, three, …, many inequivalent nodes).

- **Embedding.** *Embedding* of a net is a method of allocating nodes in the space. A net embedding has *collisions* if it contains coinciding nodes ad has crossing if some edges intersect.

- **Dimensionality.** The *dimensionality* of a net is equal to the dimensionality of the Euclidean space to which the net can be embedded without collisions. It is worth highlighting the net dimensionality can be larger than the net periodicity: for instance, double layers are 3D nets with 2-periodicity.

- **Cycle.** A *cycle* or circuit is a closed path beginning and ending at a node, characterized by a size equal to the number of edges in the path (three-circuit, four circuit, and so on).

- **Ring.** A *ring* is a n-membered cycle that represents the shortest possible path connecting all the (n(n-1)/2) pairs of nodes belonging to that circuit. That is, is not the sum of two smaller cycles.

2.

Single Crystal X-Ray Diffraction measurements

The experimental details corresponding to the Single-Crystal X-Ray Diffraction measurements performed to solve the structures of the compounds presented in this thesis are in **Table I**.

In a general procedure, diffraction data were collected exploring over a hemisphere of the reciprocal space in a combination of phi and omega scans to reach a good resolution (each exposure covered 0.5º in ω). Unit cell dimensions were determined by a least-squares fit of reflections with $I > 2\sigma(I)$.

Data were then integrated and scaled using SAINTplus[2] program. Semi-empirical absorption and scale corrections based on equivalent reflections were carried out using SADABS.[3] Space group determinations and tests for merohedral twining were carried out using XPREP.[4] The structures were solved using the Direct Methods program SHELXS.[4] The final cycles of refinement were carried out by full-matrix least-squares analyses with anisotropic thermal parameters for all non-hydrogen atoms. All hydrogen atoms were placed in geometrically calculated positions and subsequently refined using a riding model with $U_{iso}(H) = 1.2U_{eq}(C)$, except for those of water molecules, which were located from difference Fourier maps. The final structures were examined and tested using PLATON.[5]

Table I. Some experimental details corresponding to single-crystal X-Ray Diffraction measurements of each compound presented in this thesis .

	Instrument	Radiation	T (K)	Exposure time (s)	Crystal size (mm^3)
Ca-**AEPF-1**	four cicle kappa AXIOM	Cu Kα, microsource	123	10	0.14 x 0.10 x 0.10
Mg-**AEPF-2**	SMART CCD	Mo Kα, tube X-Ray source	296	20	0.15 x 0.10 x 0.04
Ca-**AEPF-3**	SMART CCD	Mo Kα, tube X-Ray source	296	20	0.20 x 0.10 x 0.05
Sr-**AEPF-4**	SMART CCD	Mo Kα, tube X-Ray source	296	20	0.20 x 0.12 x 0.08
Ba-**AEPF-5**	SMART CCD	Mo Kα, tube X-Ray source	296	20	0.20 x 0.12 x 0.08
Ca-**AEPF-6**	four cicle kappa AXIOM	Cu Kα, microsource	296	10	0.10 x 0.10 x 0.05
Ca-**AEPF-7**	four cicle kappa AXIOM	Cu Kα, microsource	296	2	0.15 x 0.05 x 0.05
Mg-**AEPF-8**	four cicle kappa AXIOM	Cu Kα, microsource	296	10	0.10 x 0.10 x 0.05
Mg-**AEPF-9**	SMART CCD	Mo Kα, tube X-Ray source	296	30	0.30 x 0.15 x 0.05
Sr-**AEPF-10**	four cicle kappa APEXII	Cu Kα, microsource	296	2	0.20 x 0.04 x 0.04
Mg-**AEPF-11**	SMART CCD	Mo Kα, tube X-Ray source	296	20	0.15 x 0.10 x 0.05
Mg-**AEPF-12**	SMART CCD	Mo Kα, tube X-Ray source	296	20	0.15 x 0.10 x 0.10
Sr-**AEPF-13**	four cicle kappa AXIOM	Cu Kα, microsource	296	10	0.15 x 0.10 x 0.10
Mg-**α-AEPF-14**	four cicle kappa AXIOM	Cu Kα, microsource	296	5	0.20 x 0.05 x 0.05
Mg-**β-AEPF-14**	four cicle kappa AXIOM	Cu Kα, microsource	296	10	0.15 x 0.10 x 0.05
Mg-**AEPF-15**	four cicle kappa APEXII	Cu Kα, microsource	296	3	0.30 x 0.12 x 0.02
Mg-**AEPF-16**	four cicle kappa AXIOM	Cu Kα, microsource	296	10	0.20 x 0.15 x 0.05
Mg-**AEPF-17**	four cicle kappa APEXII	Cu Kα, microsource	296	10	0.40 x 0.20 x 0.05

References

1. Delgado-Friedrichs, O.; O'Keeffe, M. *J. Solid State Chem.*, **2005**, *178*, 2480.
2. Bruker AXS Inc. *SAINTplus package*, Madison, Wisconsin, USA, **2007**.
3. Sheldrick, G. M. *SADABS program integrated in SAINTplus package*. Bruker AXS Inc., Madison, Wisconsin, USA.
4. Bruker (**2006**) *SHELXTL package*. Bruker AXS Inc., Madison, Wisconsin, USA.
5. Spek, A. L. (2005) PLATON, A multipurpose *Crystallographic Tool*, Utrecht University, Utrecht, Holland.

Published articles

With the results of the present thesis, the following articles have been published:

1. Cover Picture. Platero-Prats, A. E.; de la Peña-O'Shea, V. A.; Iglesias, M.; Snejko, N.; Monge, Á.; Gutiérrez-Puebla, E. "Heterogeneous Catalysis with Alkaline-Earth Metal-Based MOFs: A Green Calcium Catalyst". *ChemCatChem*, **2010**, 2, 113.

2. Platero-Prats, A. E.; de la Peña-O'Shea, V. A.; Iglesias, M.; Snejko, N.; Monge, Á.; Gutiérrez-Puebla, E. "Heterogeneous Catalysis with Alkaline-Earth Metal-Based MOFs: A Green Calcium Catalyst". *ChemCatChem*, **2010**, 2, (2), 147-149.

3. Platero-Prats, A. E.; de la Peña-O'Shea, V. A.; Snejko, N.; Monge, Á.; Gutiérrez-Puebla, E. "Dynamic Calcium Metal–Organic Framework Acts as a Selective Organic Solvent Sponge". *Chemistry – A European Journal*. **2010**, 16, (38), 11632-11640.

4. Platero-Prats, A.E.; Iglesias, M.; Snejko, N.; Monge, Á.; Gutiérrez-Puebla, E. "From coordinatively weak ability of constituents to very stable alkaline-earth sulfonate metal-organic frameworks". *Crystal Growth and Design*, **2011**, 11, 5, 4, 1750-1758.

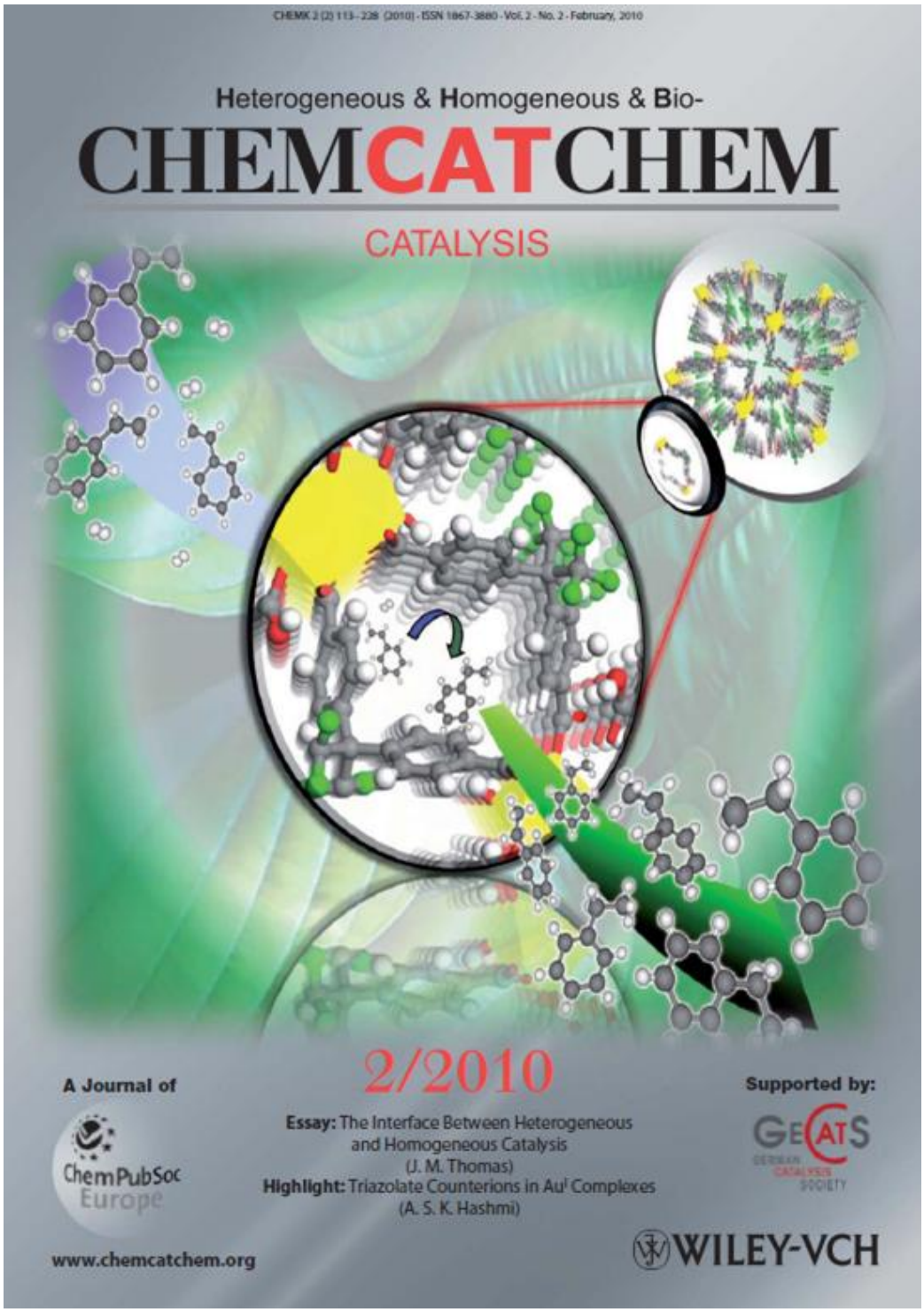
CHEMK 2 (2) 113 - 228 (2010) - ISSN 1867-3880 - Vol. 2 - No. 2 - February, 2010
Heterogeneous & Homogeneous & Bio-
CHEMCATCHEM
CATALYSIS
2/2010
A Journal of
ChemPubSoc Europe
Supported by:
GECATS
Essay: The Interface Between Heterogeneous and Homogeneous Catalysis (J. M. Thomas)
Highlight: Triazolate Counterions in Au[I] Complexes (A. S. K. Hashmi)
www.chemcatchem.org
WILEY-VCH

COMMUNICATIONS

DOI: 10.1002/cctc.200900228

Heterogeneous Catalysis with Alkaline-Earth Metal-Based MOFs: A Green Calcium Catalyst

Ana E. Platero Prats,[a] Víctor A. de la Peña-O'Shea,[b] Marta Iglesias,[a] Natalia Snejko,[a] Ángeles Monge,[a] and Enrique Gutiérrez-Puebla*[a]

A new class of hydrogenation catalysts is required to develop cheaper and environmentally friendly alternatives, in order to avoid the loss of the huge quantities of precious metals, such as Pd, Pt, Rh, Ir, Re, which are widely used to perform traditional heterogeneous hydrogenation[1] for the needs of pharmaceutical, petrochemical, food, soap and detergent, or plasticizer industries. Soluble rhodium and iridium complexes, such as Wilkinson's[2] and Crabtree's[3] catalysts, are elegant examples of homogeneous catalysts for these reactions. However, the complicated recovering and recycling processes of homogeneous catalysts have prevented many of them from being commercialized.[4] In this context, metal–organic frameworks (MOFs) can be expected to provide interesting alternatives. These materials are known to possess the capability for several important functionalities,[5] including gas storage,[6] catalysis,[7] and optical properties.[8] Usually, transition metals or rare earths are used to synthesize MOF materials, yet, in spite of the similarities[9] between rare-earth and alkaline-earth complexes, the use of the latter to build MOFs has been much less studied.[10] However, the high Lewis acidity of the alkaline-earth metal ions can provide catalysts with very active sites for alkene hydrogenation; strontium and calcium complexes have recently been used as homogeneous catalysts, both for hydrogenation[11] and polymerization of alkenes.[12] Taking into account these considerations, we present herein the synthesis and studies of the properties of a new MOF based on calcium, one of the most abundant and cheap elements. This environmentally friendly material could provide an alternative to traditional precious metal-based hydrogenation catalysts, owing to its low cost, easy fabrication, thermal stability, and robust framework. Previously, we have reported heterogeneous catalysts based on Ln, In, and Zn cations with 4,4′-(hexafluoroisopropylidene)bis(benzoic acid) (H_2hfipbb) as a ligand.[8] MOFs of H_2hfipbb with transition metals such as Cu and Co have also been studied.[8]

Solvothermal reaction of $Ca(CH_3CO_2)_2{\cdot}H_2O$ and H_2hfipbb in a water/acetone mixture[13] resulted in the formation of a new MOF with the formula $[Ca(hfipbb)(H_2hfipbb)_{0.5}(H_2O)]{\cdot}0.7C_3H_6O$, AEPF-1 (AEPF = alkaline earth polymeric framework) in approximately 70% yield.

In AEPF-1 calcium atoms are heptacoordinated to form monocapped octahedra, whose vertices are occupied by five oxygen atoms from completely deprotonated $hfipbb^{2-}$ ligands, one from a protonated H_2hfipbb ligand, and one water molecule (Figure 1). For every Ca^{2+} cation there is one

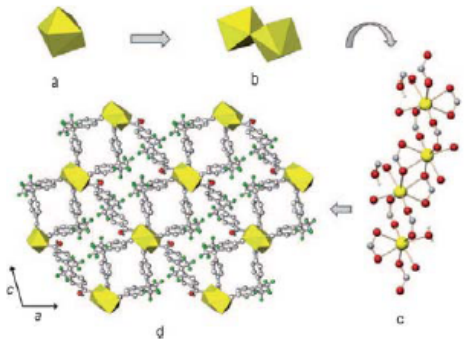

Figure 1. Polyhedral representation of the structure of AEPF-1: a) Coordination environment of the Ca center; b) Ca_2O_{12} dimeric units formed by edge sharing; c) chains of calcium polyhedra along the *b* direction, showing the three types of carboxylate bridges; d) view of the 3D structure along the *b* direction.

$hfipbb^{2-}$ anion that coordinates to four metal atoms in a $\eta^2\mu_3$–$\eta^2\mu_2$ (chelate-bridge–bridge) way, and half of a protonated ligand. This arrangement gives rise to the formation of Ca_2O_{12} edge-sharing dimeric units, linked by carboxylate bridges along the *b* direction. These chains are joined together by $hfipbb^{2-}$ anions along the *c* direction, leading to the formation of layers parallel to the crystallographic [−101] direction. As the linker is bent, these layers are nonplanar, and each layer is transversally crossed by square-shaped channels along the *b* direction. These layers are joined along the [101] direction through the protonated ligand, giving rise to a 3D framework. There are two types of cavity in AEPF-1: 1) an accessible free space of $V = 157$ Å^3 with an accessible window of 5.8 Å × 8.6 Å and a pore diameter of 6.9 Å, and 2) a microporous cavity with a free space of $V = 18.6$ Å^3 and a pore diameter of 3.3 Å.

The performance of AEPF-1 as a catalyst was tested for the hydrogenation of styrene to form ethyl benzene under rather mild conditions [373 K, 5 atm H_2 (1 atm = 101325 Pa)], using toluene as solvent and a 1:100 Ca/styrene molar ratio.[12]

[a] A. E. Platero Prats, Dr. M. Iglesias, Dr. N. Snejko, Prof. Á. Monge, Prof. E. Gutiérrez-Puebla
New Architectures in Materials Chemistry
Instituto de Ciencia de Materiales de Madrid (ICMM-CSIC)
C/Sor Juana de la Cruz 3, Cantoblanco, Madrid (Spain)
Fax: (+34) 913720623
E-mail: egutierrez@icmm.csic.es

[b] Dr. V. A. de la Peña-O'Shea
Thermochemical Processes
Instituto Madrileño de Estudios Avanzados en Energía IMDEA Energía
C/Tulipán s/n Móstoles, Madrid (Spain)

Supporting information for this article is available on the WWW under http://dx.doi.org/10.1002/cctc.200900228.

CHEMCATCHEM

Hydrogenation was completed, with 100% selectivity, after 2 h without the formation of byproducts (Figure 2). A blank run with calcium acetate replacing AEPF-1 was also carried out.

In addition, kinetics experiments were carried out under the above-described conditions (Table 1) with the activation

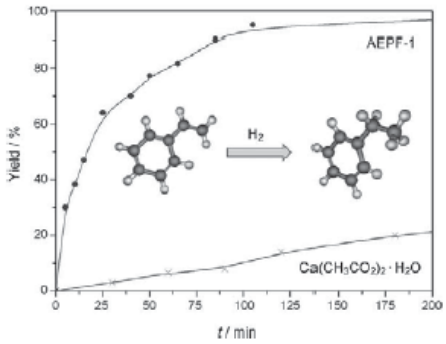

Figure 2. Yield as a function of time for hydrogenation of styrene with H_2 in toluene at 373 K: Comparison between the performance of AEPF-1 and calcium acetate monohydrate, used as a blank.

Table 1. Hydrogenation of styrene (182 μL) with H_2 (5 atm) in toluene (40 mL), using AEPF-1 (1 mol%).

Cycle	T [K]	t [h]	Conv. [%][a]	TOF [h^{-1}][b]
1	313	4	50	82
2	343	4	52	164
3	358	4	55	201
4	373	2	100	254

[a] Yield of ethylbenzene based on styrene conversion (in all cases 100% selectivity was achieved); [b] TOF calculated after 15 min.

energy $E_a = 8.8$ kcal mol^{-1}. To determine the influence of the substrate size and shape and their effect on the catalytic behavior of AEPF-1, experiments were performed using a bulkier alkene, α-methylstyrene, affording a lower yield (60%) after 2 h, but again giving 100% selectivity.[13] Although a significant part of the reaction may have taken place in the external surface, these experiments highlighted the shape selectivity of AEPF-1.

A mechanism for the calcium MOF-mediated hydrogenation, based on the H_2 heterolytic cleavage (Scheme 1), could be analogous to that reported for transition metals.[14] The catalytic behavior of AEPF-1 could be favored by the hepta-coordinated Ca environment, which aids coordination of the substrate and hydride formation, by increasing the calcium coordination number to eight. Furthermore, the acidity of AEPF-1, introduced by the protonated ligand, makes easier the heterolytic cleavage of the hydrogen molecule.

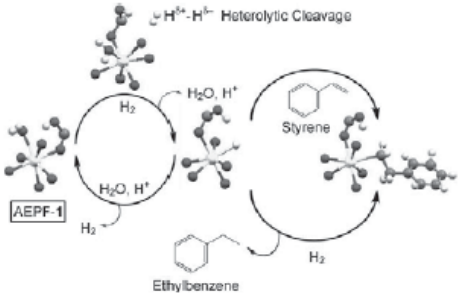

Scheme 1. Proposed catalytic cycle for styrene hydrogenation in the presence of AEPF-1 based on the heterolytic cleavage of H_2.

Preliminary investigations were also carried out into the catalytic activity of AEPF-1 for hydrosilylation reactions (see the Supporting Information, section S5). AEPF-1 showed an effective and robust catalytic behavior in the heterogeneous hydrosilylation of a variety of functionalities (aldehyde, ketone, alkene) with diphenylsilane.[13]

The reaction with styrene led to a 100% yield of the linear silane, probably influenced by the protonated ligand. For investigations with carbonyl compounds, the silylated product yields were 100% for benzaldehyde and 70% for the more voluminous acetophenone.

By comparing the AEPF-1 catalytic results with those of recently reported calcium complexes in solution[11a] or supported,[11b] we can conclude that the use of AEPF-1 as catalyst results in total conversion with 100% selectivity to the hydrogenated product in 2 h, by using 1 mol% of catalyst at 373 K and 5 atm H_2, whereas the reported homogeneous catalyst[11a] reached 100% conversion with 80% selectivity towards the alkane after 15 h with 5 mol% of catalyst at 293 K and 20 atm H_2. In the case of the silica-supported complex[11b] for the hydrosilylation of styrene, the existence of soluble calcium species and a lack of evidence as to whether catalysis proceeded in a homogeneous or heterogeneous mode have been reported. AEPF-1, thanks to its stable robust structure with all of the active calcium centers forming part of the framework, acts as a purely heterogeneous catalyst, which has been proven by experiments that demonstrated an absence of both active-site leaching and catalyst deactivation.

These results indicate that gas adsorption into AEPF-1 pores does not depend on the size of the adsorbed molecules, but could be related to the adsorption energy, which is lowest for H_2. This fact could explain the reactivity of H_2 molecules in AEPF-1, favoring the hydrogenation process.

In summary, the calcium MOF AEPF-1 has been obtained and studied. The main feature of this new material is its high catalytic activity in hydrogenation processes under mild conditions, which makes it a real candidate to provide an alternative to conventional precious metal-based alkene-hydrogenation catalysts, although further study is still required.[15]

Experimental Section

Synthesis of AEPF-**1**: A solution of H_2hfipbb (400 mg, 1 mmol) in acetone (9 mL) was added under continuous stirring to a solution of $Ca(CH_3CO_2)_2{\cdot}H_2O$ (178 mg, 1 mmol) in distilled water (10 mL). The resulting mixture was sealed in a Teflon-lined steel autoclave and heated at 170 °C under autogenous pressure for 72 h. The autoclave was allowed to cool to room temperature and the product was filtered and washed with distilled water (3×10 mL) and acetone (3×5 mL; 70% yield). Ground samples were used for analytical characterization, surface and catalytic studies. The phase purity of the bulk material was independently confirmed by X-ray diffraction, thermal gravimetric analysis, and elemental analysis.

CCDC 733398 contains the supplementary crystallographic data for this paper. These data can be obtained free of charge from The Cambridge Crystallographic Data Centre via www.ccdc.cam.ac.uk/data_request/cif. For more specific information about the characterization of AEPF-**1** and reaction procedures, see the Supporting Information.

Acknowledgements

This work has been supported by the Spanish MCYT Project Mat 2007-60822, CTQ 2007-28909-E/BQU, and Consolider-Ingenio CSD2006-2001. AEPP acknowledges JAE fellowship from CSIC and VAPO acknowledges financial support from the MCYT in the Ramón y Cajal research programme.

Keywords: calcium · coordination polymers · heterogeneous catalysis · hydrogenation · metal–organic frameworks

[1] a) G. Ertl, H. Knözinger, J. Weitkamp in *Handbook of Heterogeneous Catalysis, Vol. 5*, Wiley-VCH, Weinheim, **1997**; b) R. A. Sheldon, H. van Bekkum in *Fine Chemicals through heterogeneous catalysis, Vol. 5*, Wiley-VCH, Weinheim, **2001**.
[2] J. A. Osborn, F. H. Jardine, J. F. Young, G. Wilkinson, *J. Chem. Soc. A* **1966**, 1711–1732.
[3] R. H. Crabtree, P. C. Demou, D. Eden, J. M. Mihelcic, C. A. Parnell, J. M. Quirk, G. E. Morris, *J. Am. Chem. Soc.* **1982**, *104*, 6994–7001.
[4] D. J. Cole-Hamilton, *Science* **2003**, *299*, 1702–1706.
[5] a) J. L. C. Rowsell and O. M. Yaghi, *Microporous Mesoporous Mater.* **2004**, *73*, 3–14; b) G. K. H. Shimizu, *J. Solid State Chem.* **2005**, *178*, 2519–2526; c) C. Janiak, *Dalton Trans.* **2003**, 2781–2804; d) S. Kitagawa, R. Kitaura, S. Noro, *Angew. Chem.* **2004**, *116*, 2388–2430; *Angew. Chem. Int. Ed.* **2004**, *43*, 2334–2375; e) A. Y. Robin, K. M. Fromm, *Coord. Chem. Rev.* **2006**, *250*, 2127–2157.
[6] a) M. Eddaoudi, H. Li, O. M. Yaghi, *J. Am. Chem. Soc.* **2000**, *122*, 1391–1397; b) R. Matsuda, R. Kitaura, S. Kitagawa, Y. Kubota, R. V. Belosludov, T. C. Kobayashi, H. Sakamoto, T. Chiba, M. Takata, Y. Kawazoe, Y. Mita, *Nature* **2005**, *436*, 238–241; c) S. Noro, S. Kitagawa, M. Kondo, K. Seki, *Angew. Chem.* **2000**, *112*, 2161–2164; *Angew. Chem. Int. Ed. Engl.* **2000**, *39*, 2081–2084.
[7] a) F. Gándara, B. Gomez-Lor, E. Gutiérrez-Puebla, M. Iglesias, M. A. Monge, D. M. Proserpio, N. Snejko, *Chem. Mater.* **2008**, *20*, 72–76; b) B. Gómez-Lor, E. Gutierrez-Puebla, M. Iglesias, M. A. Monge, C. Ruiz-Valero, N. Snejko, *Chem. Mater.* **2005**, *17*, 2568–2573; c) L. Alaerts, E. Seguin, H. Poelman, F. Thibault-Starzyk, P. A. Jacobs, D. E. De Vos, *Chem. Eur. J.* **2006**, *12*, 7353–7363; d) J. J. Y. Lee, O. K. Farha, J. Roberts, K. A. Scheidt, S. B. T. Nguyen, J. T. Hupp, *Chem. Soc. Rev.* **2009**, *38*, 1450.
[8] a) F. Gándara, A. d. Andrés, B. Gómez-Lor, E. Gutiérrez-Puebla, M. Iglesias, M. A. Monge, D. M. Proserpio, N. Snejko, *Cryst. Growth Des.* **2008**, *8*, 378–380; b) R. J. Hill, D. L. Long, P. Hubberstey, M. Schroder, N. R. Champness, *J. Solid State Chem.* **2005**, *178*, 2414–2419; c) C. A. Bauer, T. V. Timofeeva, T. B. Settersten, B. D. Patterson, V. H. Liu, B. A. Simmons, M. D. Allendorf, *J. Am. Chem. Soc.* **2007**, *129*, 7136–7144.
[9] W. Maudez, M. Meuwly, K. M. Fromm, *Chem. Eur. J.* **2007**, *13*, 8302.
[10] a) K. M. Fromm, *Coord. Chem. Rev.* **2008**, *252*, 856–885; b) C. A. Williams, A. J. Blake, C. Wilson, P. Hubberstey, M. Schroeder, *Cryst. Growth Des.* **2008**, *8*, 911–922; c) C. Volkringer, T. Loiseau, G. Férey, J. E. Warren, D. S. Wragg, R. E. Morris, *Solid State Sci.* **2007**, *9*, 455–458.
[11] a) J. Spielmann, F. Buch, S. Harder, *Angew. Chem.* **2008**, *120*, 9576–9580; *Angew. Chem. Int. Ed.* **2008**, *47*, 9434–9438; b) R. M. Gauvin, F. Buch, L. Delevoye, S. Harder, *Chem. Eur. J.* **2009**, *15*, 4382–4393.
[12] A. F. Halasa, W. L. Hsu, J. R. Zuppo, US7087549, **2006**.
[13] See the Supporting Information.
[14] S. Niu, M. B. Hall, *Chem. Rev.* **2000**, *100*, 353–406.
[15] This work is covered under the patent: A. E. Platero-Prats, E. Gutiérrez-Puebla, Á. Monge, N. Snejko, M. Iglesias, B. Gómez-Lor, V. A. de la Peña-O'Shea, ES1641.453, **2009**.

Received: August 31, 2009
Revised: October 23, 2009
Published online on December 23, 2009

CHEMISTRY
A EUROPEAN JOURNAL

DOI: 10.1002/chem.201001218

Dynamic Calcium Metal–Organic Framework Acts as a Selective Organic Solvent Sponge

Ana E. Platero-Prats,[a] Víctor A. de la Peña-O'Shea,[b] Natalia Snejko,[a] Ángeles Monge,[a] and Enrique Gutiérrez-Puebla*[a]

Abstract: Herein, we present a Ca-based metal–organic framework named AEPF-1, which is an active and selective catalyst in olefin hydrogenation reactions. AEPF-1 exhibits a phase transition upon desorption of guest molecules. This structural transformation takes place by a crystal to crystal transformation accompanied by the loss of single-crystal integrity. Powder diffraction methods and computational studies were applied to determine the structure of the guest-free phase. This work also presents data on the exceptional adsorption behavior of this material, which is shown to be capable of separating polar from nonpolar organic solvents, and is a good candidate for selective solvent adsorption under mild conditions.

Keywords: crystal engineering · crystal transformations · dynamic porous materials · host–guest systems · metal–organic frameworks

Introduction

During recent years, great attention has been paid to the design and synthesis of porous metal–organic frameworks (MOFs) due to their high versatility, and their many potential applications in areas such as gas storage and separation, sensors, heterogeneous catalysis, and drug delivery.[1–7] Within this field, one of the main challenges is the synthesis and the study of dynamic MOFs, the so-called third-generation compounds, which exhibit interesting properties on response to stimuli (heat, pressure, light, external molecules, etc.).[8,9] Some interesting porous MOFs have been reported[10,11] that can change their porosity in various ways; for example, by reversible collapse and recovery of pores, or through structural changes. This dynamic structural behavior is of great importance, because these flexible materials can exhibit high selectivity for guest inclusion, selective molecular recognition, or drug-delivery properties, among others, as mentioned above.[12,13]

A suitable guest can induce the formation of a specific framework, thereby playing an important role in the dynamic changes in the framework. Guest removal can also lead to structural changes in the host framework, which normally gives rise to phase transitions. On the other hand, the original structure can often be restored by exposing the dry material to the guest again. These structural transformations can take place as 1) single-crystal to single-crystal transformations[14,15] or 2) crystal to crystal (CC) (losing the single crystal integrity) transformations. To appreciate the structural features of these guest-induced transformations, X-ray powder diffraction (XRPD) methods and computational methods need to be applied.[16]

MOFs based on alkaline-earth metals remain a scientific challenge because of the inherent difficulties concerning the formation and crystallization of these MOFs.[17] In fact, few examples of rigid MOFs based on calcium have yet been reported.[18–20] However, flexible materials based on alkaline-earth metals could represent a comparatively cheap, nontoxic, green alternative to conventional transition-metal-based dynamic MOFs.

Recently, we have prepared a Ca-MOF named AEPF-1 (in which AEPF = alkaline-earth polymer framework), based on the organic linker 4,4′-(hexafluoroisopropylidene)-

[a] A. E. Platero-Prats, Dr. N. Snejko, Prof. Á. Monge, Prof. E. Gutiérrez-Puebla
New Architectures in Materials Chemistry
Instituto de Ciencia de Materiales de Madrid (ICMM-CSIC)
C/Sor Juana de la Cruz 3, Cantoblanco, Madrid (Spain)
Fax: (+34) 913720623
E-mail: egutierrez@icmm.csic.es

[b] Dr. V. A. de la Peña-O'Shea
Thermochemical Processes Group
Instituto Madrileño de Estudios Avanzados en Energía (IMDEA Energía), C/Tulipán s/n Móstoles
Madrid (Spain)

Supporting information for this article is available on the WWW under http://dx.doi.org/10.1002/chem.201001218.

bis(benzoic acid) (H_2hfipbb = $C_{17}H_{10}O_4F_6$), in which an sp^3 carbon atom joins the two benzoic moieties, rendering it flexible. Our preliminary catalytic tests showed that AEPF-1 is an active and selective catalyst in olefin hydrogenation and hydrosilylation reactions.[21] The catalyst is an economical and environmentally friendly alternative to conventional catalysts based on precious metals. Herein, we report a summary of the synthesis, structure, and catalytic activity of this new Ca-MOF, as well as new results based on its reversible structural CC transformation, the new structure of the AEPF-1 dry-phase (AEPF-1_{dry}) solved by XRPD and computational studies, and the application of AEPF-1 as a selective absorbent of organic solvents under mild conditions.

Results and Discussion

The three-dimensional framework of AEPF-1 was synthesized from the solvothermal reaction of [$Ca(CH_3CO_2)_2{\cdot}H_2O$] and H_2hfipbb in a water/acetone mixture, which resulted in the formation of single crystals of a new MOF with formula [Ca(hfipbb)(H_2hfipbb)$_{0.5}$(H_2O)]·0.5C_3H_6O, (in which hfipbb is the deprotonated form of H_2hfipbb) in around 70% yield. The structure has been solved by single-crystal X-ray diffraction experiments, which showed that it consists of a monocapped octahedral calcium polyhedron that forms Ca_2O_{12} edge-sharing dimeric units, which are linked by the dibenzoic carboxylate ligand along the *b* direction. These chains are joined through the whole deprotonated linker $hfipbb^{2-}$, forming layers with square-shaped channels along the [101] direction, and joined along the [−101] direction through the protonated linker H_2hfipbb (see Figure 3 and Table S1 and Figure S1 in the Supporting Information). This arrangement gives rise to a 3D framework. Three characteristics of this calcium-based MOF are noteworthy: 1) it has a porous structure, possessing cavities with an accessible free space of $V = 157$ Å^3 and a pore-size diameter of 6.9 Å (calculated with PLATON, taking into account the van der Waals radii);[22] 2) the results of our previous tests (Figure S14 in the Supporting Information) showed that AEPF-1 is an active catalyst: total conversion of styrene proceeds, with 100% selectivity, to the hydrogenated product ethyl benzene in 2 h, by using 1 mol% of catalyst at 373 K and 5 atm H_2;[21] 3) AEPF-1 contains acetone as guest molecules, which are held inside pores through soft interactions, and can be removed by heating (Figure S2 in the Supporting Information). Hence, the reversible uptake–release behavior of guest molecules in AEPF-1 would demonstrate the potential application of this material as an absorber, or as an organic-molecule sensor. Such studies have been reported for transition-metal-based MOFs,[16] but not for alkaline-earth-metal MOFs.

Study of AEPF-1 activation: To investigate the potential application of this material for adsorption, a detailed study of AEPF-1 activation processes was performed following the loss of guest molecules from its pores, as follows: A thermal study of AEPF-1 was carefully performed in the temperature range 20–200°C by using thermogravimetric analysis (TGA) combined with mass spectrometry (TGA-MS) and differential scanning calorimetry (DSC). Within the temperature range explored, the weight loss was attributed to 1) physisorbed water and acetone molecules (up to 75°C), and 2) guest molecules from pores (up to 200°C), corresponding to two acetone molecules per unit cell (Figure S4 in the Supporting Information). Above this temperature, the material is stable up to 400°C (see the Supporting Information). A change in the weight-loss rate was observed at around 75°C. This weight-loss rate reflects the departure of acetone from pores. It continues up to around 105°C (T_c), where the weight-loss rate changes again. These results are in accordance with recent studies,[18] which show a two-step departure of acetone molecules that could be associated with structural changes in the framework. Furthermore, DSC has been used as a complementary tool to explore the energetic processes involved in the acetone departure from the pores in AEPF-1 (see Figure S4 in the Supporting Information for details). A single peak centered at 105°C (T_c) is observed. This process is composed of two simultaneous steps: 1) acetone loss from the pores; and 2) structural changes in the AEPF-1 framework.[23]

To determine the intrinsic energy involved in the guest removal process, a series of computational studies was performed by using the AEPF-1 atomic coordinates determined by single-crystal XRD. All structural models were optimized by using plane wave density functional calculations (PWDF) (see the Experimental Section). Geometry optimization of AEPF-1 converged to the same structure as determined by X-ray crystallography, which confirms the accuracy of the calculation method. These theoretical calculations allowed the guest desorption apparent energy to be estimated at 25.5 kJ mol^{-1}.[24]

Taking into account the results of the activation process of AEPF-1, along with those of our previous studies, a detailed structural study was performed to elucidate the effect on the crystal structure on the guest removal process. This entailed a series of experiments using variable-temperature optical microscopy (VTOM), variable-temperature diffuse reflectance Fourier-transform infrared spectroscopy (VT-DRIFTS), and X-ray powder thermodiffraction (XRPTD).

Variable-temperature optical microscopy: To study the variations in crystallinity accompanying the guest removal process in AEPF-1, VTOM experiments were performed (see the Experimental Section and the Supporting Information, Section S3). Thus, a single crystal of AEPF-1 was heated from room temperature to 150°C. At around 75°C the crystal began to decay, which corresponds to removal of guest molecules from the pores (Figure 1B), as described above. Subsequent temperature increase to 105°C causes the total loss of single-crystal integrity, although the crystal retains its shape (Figure 1F), a phenomenon that gives rise to typical microcrystalline X-ray diffraction diagrams. These results confirm that possible structural changes related to the guest

bis(benzoic acid) (H_2hfipbb = $C_{17}H_{10}O_4F_6$), in which an sp^3 carbon atom joins the two benzoic moieties, rendering it flexible. Our preliminary catalytic tests showed that AEPF-1 is an active and selective catalyst in olefin hydrogenation and hydrosilylation reactions.[21] The catalyst is an economical and environmentally friendly alternative to conventional catalysts based on precious metals. Herein, we report a summary of the synthesis, structure, and catalytic activity of this new Ca-MOF, as well as new results based on its reversible structural CC transformation, the new structure of the AEPF-1 dry-phase (AEPF-1_{dry}) solved by XRPD and computational studies, and the application of AEPF-1 as a selective absorbent of organic solvents under mild conditions.

Results and Discussion

The three-dimensional framework of AEPF-1 was synthesized from the solvothermal reaction of $[Ca(CH_3CO_2)_2{\cdot}H_2O]$ and H_2hfipbb in a water/acetone mixture, which resulted in the formation of single crystals of a new MOF with formula $[Ca(hfipbb)(H_2hfipbb)_{0.5}(H_2O)]{\cdot}0.5C_3H_6O$, (in which hfipbb is the deprotonated form of H_2hfipbb) in around 70% yield. The structure has been solved by single-crystal X-ray diffraction experiments, which showed that it consists of a monocapped octahedral calcium polyhedron that forms Ca_2O_{12} edge-sharing dimeric units, which are linked by the dibenzoic carboxylate ligand along the *b* direction. These chains are joined through the whole deprotonated linker $hfipbb^{2-}$, forming layers with square-shaped channels along the [101] direction, and joined along the [−101] direction through the protonated linker H_2hfipbb (see Figure 3 and Table S1 and Figure S1 in the Supporting Information). This arrangement gives rise to a 3D framework. Three characteristics of this calcium-based MOF are noteworthy: 1) it has a porous structure, possessing cavities with an accessible free space of $V = 157$ Å^3 and a pore-size diameter of 6.9 Å (calculated with PLATON, taking into account the van der Waals radii);[22] 2) the results of our previous tests (Figure S14 in the Supporting Information) showed that AEPF-1 is an active catalyst: total conversion of styrene proceeds, with 100% selectivity, to the hydrogenated product ethyl benzene in 2 h, by using 1 mol% of catalyst at 373 K and 5 atm H_2;[21] 3) AEPF-1 contains acetone as guest molecules, which are held inside pores through soft interactions, and can be removed by heating (Figure S2 in the Supporting Information). Hence, the reversible uptake–release behavior of guest molecules in AEPF-1 would demonstrate the potential application of this material as an absorber, or as an organic-molecule sensor. Such studies have been reported for transition-metal-based MOFs,[16] but not for alkaline-earth-metal MOFs.

Study of AEPF-1 activation: To investigate the potential application of this material for adsorption, a detailed study of AEPF-1 activation processes was performed following the loss of guest molecules from its pores, as follows: A thermal study of AEPF-1 was carefully performed in the temperature range 20–200°C by using thermogravimetric analysis (TGA) combined with mass spectrometry (TGA-MS) and differential scanning calorimetry (DSC). Within the temperature range explored, the weight loss was attributed to 1) physisorbed water and acetone molecules (up to 75°C), and 2) guest molecules from pores (up to 200°C), corresponding to two acetone molecules per unit cell (Figure S4 in the Supporting Information). Above this temperature, the material is stable up to 400°C (see the Supporting Information). A change in the weight-loss rate was observed at around 75°C. This weight-loss rate reflects the departure of acetone from pores. It continues up to around 105°C (T_c), where the weight-loss rate changes again. These results are in accordance with recent studies,[18] which show a two-step departure of acetone molecules that could be associated with structural changes in the framework. Furthermore, DSC has been used as a complementary tool to explore the energetic processes involved in the acetone departure from the pores in AEPF-1 (see Figure S4 in the Supporting Information for details). A single peak centered at 105°C (T_c) is observed. This process is composed of two simultaneous steps: 1) acetone loss from the pores; and 2) structural changes in the AEPF-1 framework.[23]

To determine the intrinsic energy involved in the guest removal process, a series of computational studies was performed by using the AEPF-1 atomic coordinates determined by single-crystal XRD. All structural models were optimized by using plane wave density functional calculations (PWDF) (see the Experimental Section). Geometry optimization of AEPF-1 converged to the same structure as determined by X-ray crystallography, which confirms the accuracy of the calculation method. These theoretical calculations allowed the guest desorption apparent energy to be estimated at 25.5 kJ mol^{-1}.[24]

Taking into account the results of the activation process of AEPF-1, along with those of our previous studies, a detailed structural study was performed to elucidate the effect on the crystal structure on the guest removal process. This entailed a series of experiments using variable-temperature optical microscopy (VTOM), variable-temperature diffuse reflectance Fourier-transform infrared spectroscopy (VT-DRIFTS), and X-ray powder thermodiffraction (XRPTD).

Variable-temperature optical microscopy: To study the variations in crystallinity accompanying the guest removal process in AEPF-1, VTOM experiments were performed (see the Experimental Section and the Supporting Information, Section S3). Thus, a single crystal of AEPF-1 was heated from room temperature to 150°C. At around 75°C the crystal began to decay, which corresponds to removal of guest molecules from the pores (Figure 1B), as described above. Subsequent temperature increase to 105°C causes the total loss of single-crystal integrity, although the crystal retains its shape (Figure 1F), a phenomenon that gives rise to typical microcrystalline X-ray diffraction diagrams. These results confirm that possible structural changes related to the guest

CHEMISTRY
A EUROPEAN JOURNAL

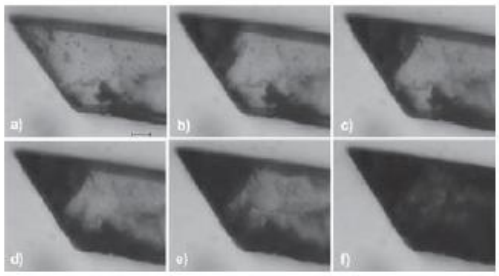

Figure 1. Optical microphotographs of a single crystal of AEPF-1 at a) room temperature, b) 75°C, c) 82°C, d) 90°C, e) 97°C, f) 105°C. (For details, see the Supporting Information, Section S3.) Scale bar is 20 μm.

removal process cannot be followed by single-crystal diffraction studies for AEPF-1.

X-ray powder thermodiffraction: To accurately follow the structural changes accompanying the acetone removal process in AEPF-1, XRPTD experiments were performed (see the Experimental Section). These studies show that when the temperature reaches 75°C, new peaks corresponding to an unknown crystalline phase (named AEPF-1_{dry}) appear together with those peaks associated with the AEPF-1 phase. As the temperature is further increased, the intensity of the AEPF-1 peaks decreases, whereas that of the AEPF-1_{dry} peaks increases; these two phases coexist up to 95°C. Finally, at temperatures above 100°C only the peaks of the AEPF-1_{dry} phase could be observed. These experiments confirm that the host material exhibits a structural transformation due to the loss of guest molecules (Figure 2A and 2B), which gives rise to AEPF-1_{dry} with formula $[CaC_{25.5}F_9O_6H_{15}]_\infty$, as determined by elemental analysis (see the Experimental Section).

Variable-temperature diffuse reflectance Fourier-transform infrared spectroscopy: VT-DRIFTS studies were carried out at temperatures up to 130°C (see the Experimental Section). At room temperature, typical υ_{CO} vibrations corresponding to the carbonyl groups of free acetone (present in the pores of the framework) are observed at 1715 cm^{-1}. As the temperature is raised, a slight blueshift of the acetone band is observed (1720 cm^{-1}), while its intensity decreases (Figure 2C). Finally, above 120°C, no band corresponding to

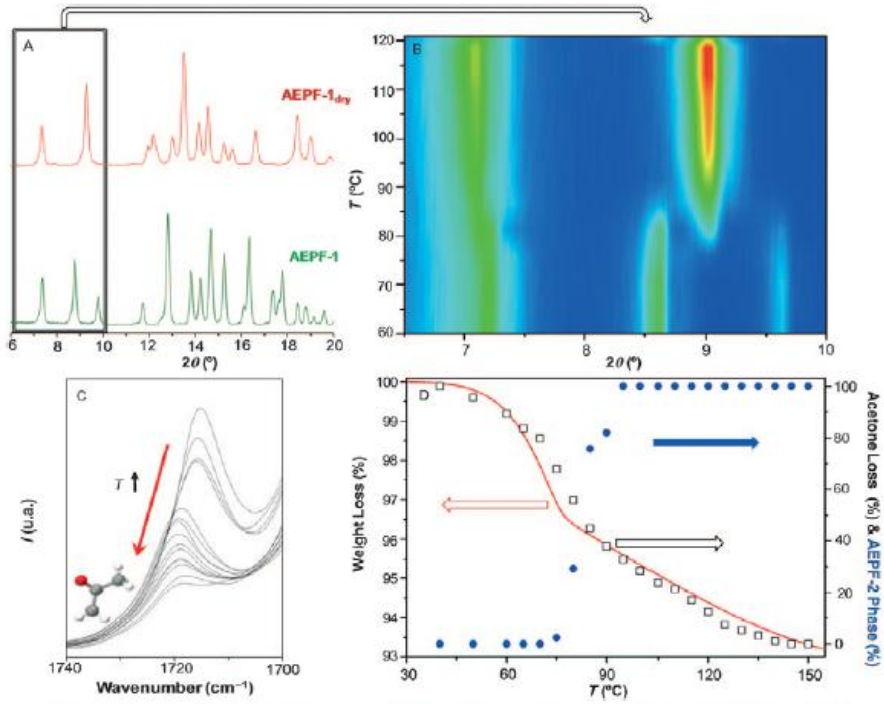

Figure 2. A) XRPD patterns of AEPF-1 (red) and AEPF-1_{dry} (green). B) XRPTD experiments that show the transformation of AEPF-1 to AEPF-1_{dry} increases with the temperature. C) Change in the IR spectrum of AEPF-1 versus temperature, in the region of υ_{CO} for free acetone, due to the acetone loss. D) Plot of the ratio of AEPF-1_{dry} (blue), acetone loss (black), and weight loss (red) versus temperature.

acetone is observed. This variation was used to calculate the loss of acetone in AEPF-1 (Figure 2C). At room temperature, the bands corresponding to the υ_{CO} vibrations of the carboxylate groups of AEPF-1 were observed at 1687, 1609 (1595) ($\eta^2\mu_3$ mode), and 1562 (1547) cm^{-1} ($\eta^2\mu_2$ mode), which is consistent with the coordination modes of the carboxylate groups determined by single-crystal XRD. Upon increasing the temperature, the bands in this range are observed at 1682, 1662, 1611, and 1566 cm^{-1}. These results confirm that structural changes take place during guest removal (see the Supporting Information, Figure S5).

To summarize the variable-temperature studies results, a plot of the ratio of AEPF-1_{dry} (calculated from XRPD data), the acetone loss (calculated from IR data), and the weight loss (calculated from TGA data) versus temperature are shown in Figure 2. A clear relationship between the weight loss due to acetone removal and the phase transition from AEPF-1 to AEPF-1_{dry} is observed.

Structure determination of AEPF-1_{dry}: Because guest removal caused single-crystal decay, the structure of AEPF-1_{dry} was determined by XRPD and computational methods. The XRPD pattern of AEPF-1_{dry} shows clear peak overlap and a lack of peaks at high Bragg angles. Nevertheless, the pattern was indexed by using the DICVOL04 program[25,26] in an orthorhombic unit cell with $a=31.55$, $b=24.64$, and $c=7.37$ Å, and $V=5731.7$ Å^3 (figures of merit $M_{20}=10$, $F_{20}=24$). However, after carefully studying the systematic absences, the monoclinic system was chosen with β angle close to 90° and the space group was determined to be $P2/c$ ($Z=4$). A matrix transformation was then applied to obtain the correct monoclinic unit cell with $a=24.64$, $b=7.37$, and $c=31.55$ Å, and $\beta=90°$.

First, a Pawley profile fitting procedure,[27] which employed the Materials Studio software,[28] was used to refine the cell and peak-profile parameters, as well as those of the background, peak asymmetry, and zero shift. Then, a crystal-structure model could be obtained by using the direct-space global optimization algorithms implemented in the computer program FOX.[29,30] Since the unit cell volume of AEPF-1_{dry} ($V_{AEPF\text{-}1dry}$) is, approximately, twice that of the unit cell volume of AEPF-1 ($V_{AEPF\text{-}1}$), a valid chemical model consisting of two AEPF-1 asymmetric units was used. The best of the AEPF-1_{dry} models generated by FOX was then optimized by Rietveld refinement[31] (considering molecules as rigid bodies) with energy optimization (Pareto optimization), using the Reflex module of the Materials Studio software. This method tries to balance matching the simulated pattern with the experimental diffraction data and then to minimize the potential energy of the structure.

Then, subsequent Rietveld refinements were performed by using only gradually relaxed constraints (some torsion angles were relaxed) to keep the model chemically sensible. Finally, hydrogen atoms were geometrically situated to complete the model. Refinement of this model converged with the R values $R_{wp}=0.186$ and $R_p=0.263$. Finally, to determine a chemically consistent structure of the dry phase PWDF calculations were carried out (see the Experimental Section). The initial coordinates of AEPF-1_{dry} were taken from the final refined structural model obtained by XRPD.

A structure minimization calculation was performed in the space group $P1$ by keeping the cell parameters fixed. The newly obtained structural model was then optimized, as mentioned above, by using Rietveld methodology. Refinement of this model converged with R values $R_{wp}=0.115$ and $R_p=0.156$. The final refined cell parameters are $a=24.644$, $b=7.382$, and $c=31.578$ Å, with $\beta=90.17°$. This study has given rise to a structural model of the dry phase that is chemically consistent and consistent with the crystal structure, despite the complexity of the structure. Details of the unit cell and the refinement of AEPF-1_{dry} are given in Table S2 (see also the Experimental Section).

The structural model of AEPF-1_{dry} contains two independent calcium atoms: one is hepta-coordinated, and forms a monocapped octahedron, as it does in AEPF-1; however, the other calcium center is hexa-coordinated, forming a monocapped trigonal bipyramidal distorted polyhedron, the vertices of which are occupied by four oxygen atoms; two from completely deprotonated hfipbb^{2-} ligands, one from a protonated H_2hfipbb ligand, and one from a water molecule. It is remarkable that the coordination modes of carboxylate groups from deprotonated hfipbb^{2-} ligands in AEPF-1_{dry} ($\eta^2\mu_3$ (chelate bridge), $\eta^2\mu_2$ (bridge), and $\eta^1\mu_1$ (monodentate)) are different from those in AEPF-1 ($\eta^2\mu_3$ (chelate bridge) and $\eta^2\mu_2$ (bridge)). Moreover, a hydrogen bond between a coordinated water molecule and the monodentate carboxylate group is found (with $d_{O10\text{-}O2}=2.688$ Å) for AEPF-1_{dry}. It was also found that the loss of acetone molecules involves changes in the torsion angles of the organic ligand: along the c direction, all ligands have the same orientation (for AEPF-1 the torsion angle is C_{21}-C_{22}-C_{25}-C_{22}= 44.23°; for AEPF-1_{dry}, it is C_{46}-C_{45}-C_{42}-C_{40}=134.29°), whereas along the a direction, the ligands forming the square-shaped channels in AEPF-1_{dry} show alternating conformations (for AEPF-1 the torsion angle is C_{12}-C_{11}-C_8-C_5= 146.06°; for AEPF-1_{dry} the alternating torsion angles are C_{29}-C_{28}-C_{25}-C_{24}=49.79° and C_{12}-C_{11}-C_8-C_7=17.11°), as shown in Figure 3C.

These observations suggest that, when a guest molecule enters into a fully open A′ channel (Figure 3C, right), a conformational change occurs, giving the A-type partially open channel (Figure 3C, left) and opening the closed channel A″ (Figure 3C, right), which would be then accessible to other guest molecules. These changes could thus facilitate the migration of each guest molecule to the neighboring unit cell along the channel. Propagation of this process could effectively pump the solvent molecules along the channels throughout the crystal.

Topological study: The networks of both AEPF-1 and AEPF-1_{dry} can be simplified as rods of Ca atoms, running along the b axis, with the organic ligands acting as linkers between Ca nodes from different chains. Connections between them along the [−101] direction are made by two

CHEMISTRY
A EUROPEAN JOURNAL

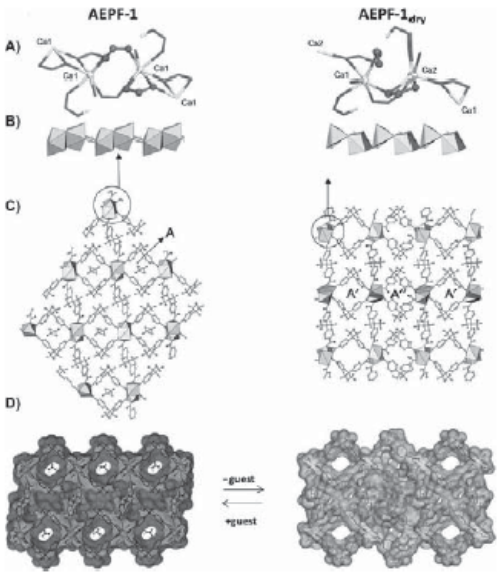

Figure 3. A) Coordination environments for the calcium center of AEPF-1 and AEPF-1_{dry}. B) Polyhedron representation along the *b* direction. C) Structures of both compounds showing the different channels along the *b* direction. D) Connolly surface representation (effectively the inverse of the solvent-accessible surface) for both materials.

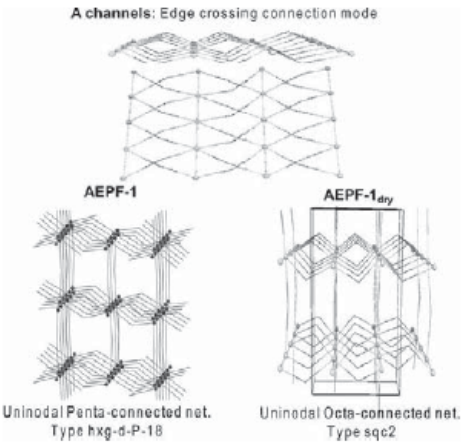

Figure 4. Square-channel and net topology for AEPF-1 and AEPF-1_{dry}.

linkers, above and below the chains, which then gives rise to the typical square channels that appear when using this ligand as a linker.[32-35] These connections exist in both compounds in an edge-crossing manner, similar to those of the LnPF-4 γ-polymorph (A-type channels).[36] However, the ligand can exhibit various torsion angles; when the channels are occupied by the solvent (AEPF-1) all the channels have the same configuration (A type), whereas after extracting the solvent (AEPF-1_{dry}), two kinds of alternated configurations appear (A′ and A″).

The 3D framework for AEPF-1 is a uninodal pentaconnected net, with Schläfli symbol 610 of the type hxg-d-P-18 (vertex symbol [63.63.63.63.63.63.64.65.65.67]) (Figure 4). The AEPF-1_{dry} framework is an uninodal octaconnected net, in which each node is directly joined to two others in the same chain, to four other chains in the *ab* plane, through linkers, and along the *c* direction to two others (Figure 4). The net has a point symbol (425.63) and code sqc2.[37]

Computational studies: In addition to the diffraction experiments, a computational study was also performed to determine the energetic balance between the intrinsic stability of AEPF-1 and the new AEPF-1_{dry} phase. As discussed above, PWDF calculations predicted an accurate 3D structure for AEPF-1_{dry}. Due to the fact that the unit cell volume of AEPF-1_{dry} ($V_{AEPF\text{-}1dry}$) is approximately twice that of AEPF-1 ($V_{AEPF\text{-}1}$), the starting configuration of AEPF-1 was based on a new cell twice as big as the original unit cell. This calculation showed that AEPF-1 is more thermodynamically stable than AEPF-1_{dry}, and allowed us to estimate the energy required for the phase transition ($E_{AEPF\text{-}1}-E_{AEPF\text{-}1dry}$) as 283.9 kJ mol^{-1}.

AEPF-1 phase recovery: The structural analyses described above show that the transformation of AEPF-1 into AEPF-1_{dry} with the loss of acetone guests leads to a new 3D structure. The next step was to investigate the reversibility of this process. Treatment of AEPF-1_{dry} in acetone at room temperature for 2 h (see the Experimental Section), gave the recovered phase named AEPF-1′. This shows that AEPF-1_{dry} can reabsorb acetone guests. To confirm the phase transition, the bulk samples were analyzed by XRPD. As shown in Figure 5, the observed patterns match the simulated ones for AEPF-1 and AEPF-1_{dry}. Note that sample AEPF-1′ shows a pattern closely resembling that of AEPF-1, in accordance with the reversibility of the AEPF-1 to AEPF-1_{dry} phase transition. The differences in relative intensities observed for the Bragg peak centered at 7.2° can be attributed to preferential adsorption of acetone molecules through the plane (101) in AEPF-1′ (Figure 5). Further evidence for readsorption of the guest was obtained by TGA-MS. The TGA curve of AEPF-1′ shows a weight loss of around 5.6 wt% from 75 to 200 °C, which corresponds to the loss of 2.5 acetone molecules per unit cell.

Adsorption by immersion in organic solvents: To investigate whether or not AEPF-1_{dry} can act as an absorber of other organic solvents, experiments were performed by suspending AEPF-1_{dry} samples in a number of different liquids with variable polarity and molecular size/shape (acetone, acetonitrile, 1-butanol, isopropyl alcohol, toluene, benzene, *n*-

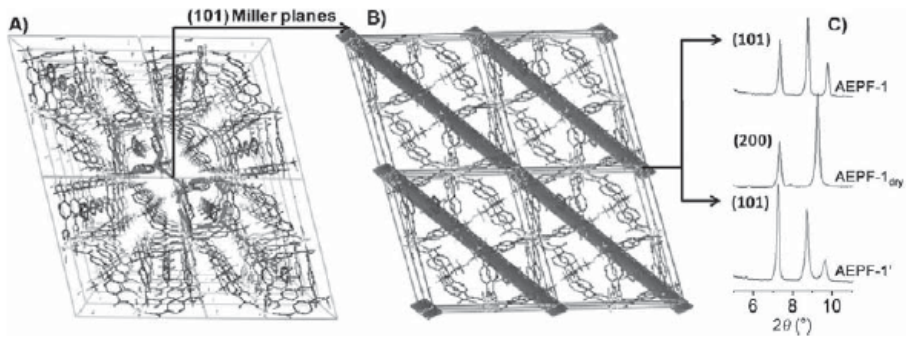

Figure 5. A) AEPF-1 net representation. B) (101) Miller plane representation in AEPF-1. C) Comparison of the X-ray patterns of AEPF-1, AEPF-1_{dry} and AEPF-1′.

hexane, and isooctane). All these solvents possess a molecular volume that is lower than the pore volume, and should theoretically fit into the cavities of AEPF-1 (Table 1).

Table 1. Sorption properties of AEPF-1_{dry} at 25°C.

Solvent	Molecular volume[a] [Å^3]	Sorption (molar) [%]	Sorption [wt%]	Solvent molecules per unit cell
toluene	91	16	2.2	1.4[b]
benzene	81	22	2.7	2.3[b]
isopropyl alcohol	64	41	3.8	1.6
1-butanol	79	62	7.1	2.5
acetone	57	70	6.2	2.8
acetonitrile	26	90	5.7	3.6

[a] Approximate volume for each molecule calculated from the van der Waals surface. [b] Number of solvent molecules per unit cell of AEPF-1 according to XRPD data.

AEPF-1_{dry} samples were suspended in each solvent at room temperature for 2 h and then dried in air (see the Experimental Section). TGA-MS was used to evaluate the presence of solvent guest molecules after the treatment (Figure 6A). These studies showed that AEPF-1_{dry} exhibits a huge adsorption capacity in the cases of acetonitrile, acetone, and 1-butanol (ca. 90, ca. 70, and ca. 62 mol% adsorbate, respectively). Note that the linear 1-butanol is strongly adsorbed despite its high molecular volume (see Table 1).

The aromatic solvents (benzene and toluene) were less strongly adsorbed (Figure 6). The nonpolar aliphatic organic solvents (*n*-hexane, isooctane) were not adsorbed at all. These experiments demonstrate the selectivity of AEPF-1_{dry} for small polar organic solvent molecules. The opposite behavior, with selective adsorption of nonpolar organic solvents, was previously reported for a Cu-based MOF.[38]

XRPD was used to check the recovery of the AEPF-1′ phase for AEPF-1_{dry} samples after the treatment. The XRPD patterns corresponding to samples immersed in each solvent are depicted in Figure 6C and D. For polar organic solvents complete recovery of AEPF-1′ is observed (Figure 6C), whereas the sorption behavior for aromatic solvents clearly entails a partial phase conversion (Figure 6D). A profile fitting of XRPD data for each AEPF-1′ sample was performed to determine the structural changes produced in the organic solvent sorption experiments (see the Supporting Information, Section S6).

Selective adsorption by immersion in mixtures of organic solvents: The selective adsorption behavior of AEPF-1_{dry} and AEPF-1′ was examined in four equimolar mixtures of organic solvents: A) acetone/acetonitrile, B) acetone/1-butanol, C) acetone/toluene, and D) acetone/hexane (see the Experimental Section). TGA-MS analyses were performed on AEPF-1_{dry} samples after immersion treatments to evaluate the selectivity of the adsorption process (see Figure 7). For the mixture A, the thermogravimetric profile of AEPF-1′ shows a weight loss of around 6.1 wt% up to 250°C, which corresponds to the loss of 2.60 acetone molecules and 0.40 acetonitrile molecules per unit cell. For the mixture B, the sample shows a weight loss of around 5.9 wt% up to 250°C, which corresponds to the loss of 2.10 acetone molecules and 0.50 1-butanol molecules per unit cell. For the mixture C, AEPF-1′ shows a weight loss of around 5.4 wt% up to 275°C, which corresponds to the loss of 2.48 acetone molecules and 0.05 toluene molecules per unit cell. Finally, for the mixture D, only acetone adsorption is observed, with a weight loss of around 4.9 wt% , which corresponds to the loss of 2.19 acetone molecules per unit cell.

XRPD was used to examine the recovery of all samples of AEPF-1′ (see the Supporting Information, Section S7), which showed that AEPF-1_{dry} not only selectively adsorbs polar organic solvents, but can also selectively separate organic solvents according to their size, shape, or polarity. Such behavior could be important for potential applications of this Ca-based MOF as an adsorbent and/or sensor of organic compounds.

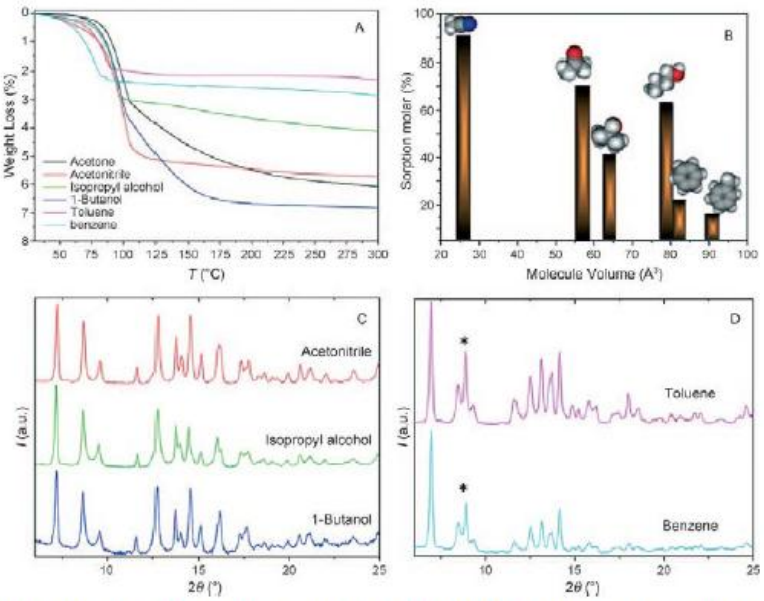

Figure 6. A) TGA under Ar for AEPF-1_{dry} samples after each sorption treatment. B) Plot of molar sorption for each solvent (calculated from TGA-MS) versus molecular volume. C) Comparison of the X-ray patterns for samples after sorption of polar organic solvents. D) Comparison of the X-ray patterns for samples after sorption of aromatic solvents. * denotes the most intense diffraction peak of AEPF-1_{dry}

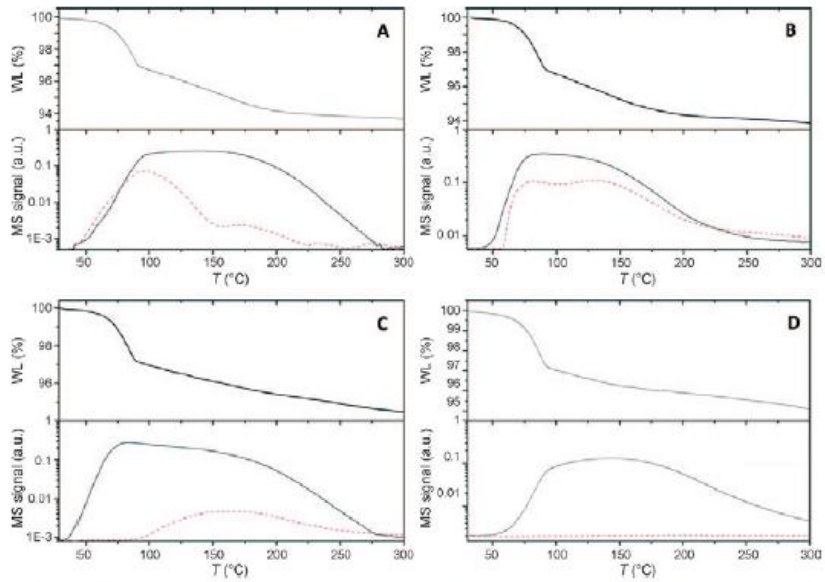

Figure 7. TGA-MS for solvent mixtures: A) acetone (——)/acetonitrile (-----), B) acetone (——)/1-butanol (-----), C) acetone (——)/toluene (-----), and D) acetone (——)/hexane (-----). WL = weight loss.

Conclusion

AEPF-1, a Ca-based MOF, has been synthesized with acetone as a guest molecule. A structural transformation occurs when guest removal takes place (this new phase was named AEPF-1_{dry}) by a crystal to crystal transformation without retention of single-crystal integrity. XRPD and computational studies were applied to determine the structure of the AEPF-1_{dry} phase.

Detailed guest-exchange studies using TGA-MS and XRPD revealed that recoverable guest release/uptake occurs quickly at room temperature, which shows that these structural changes are reversible. Moreover, the special structural properties of this Ca-based MOF lead to the selective adsorption of various organic compounds based on their size, shape, and polarity. This behavior makes AEPF-1 a good candidate for selective solvent adsorption under mild conditions.

Experimental Section

Synthesis: AEPF-1 was synthesized according to published procedures.[21] In brief, a solution of H_2hfipbb (400 mg, 1 mmol) in acetone (9 mL) was added under continuous stirring to a solution of $Ca(CH_3CO_2)_2{\cdot}H_2O$ (178 mg, 1 mmol) in distilled water (10 mL). The resulting mixture was sealed in a Teflon-lined steel autoclave and heated at 170 °C under autogenous pressure for 72 h. The autoclave was then cooled to room temperature, and the product was filtered and washed with distilled water and acetone. The phase purity of the bulk material was independently confirmed by XRPD, TGA, and elemental analysis (see the Supporting Information).

Elemental analysis: Quantitative elemental analyses for AEPF-1 indicated that the C and H ratios were equal to 47.3 and 2.85%, respectively (calcd (%) for AEPF-1: C 48.0, H 2.8). Quantitative elemental analyses for AEPF-1_{dry} indicated that the C and H ratios were equal to 48.27 and 1.97 %, respectively (calcd (%) for AEPF-1_{dry}: C 48.67, H 2.39).

Thermogravimetry: TGA was performed by using a Mettler–Toledo apparatus coupled with a mass spectrometer. The experiments were carried out between 25 and 1000 °C in argon (flow rate 50 mL min^{-1}) and at variable heating rates (between 2 and 10 °C min^{-1}). For more information see the Supporting Information.

Infrared spectroscopy: Spectra were recorded in the range 1900–1000 cm^{-1} on a Perkin–Elmer Spectrometer. The spectra of AEPF-1 clearly show the presence of the vibrational bands at around 1650 and 1500 cm^{-1}, characteristic for framework carboxylate groups. A band at 1715 cm^{-1} characteristic for free carbonyl groups is also observed for AEPF-1, which is in agreement with the presence of acetone molecules within the pores of this framework. Variable-temperature experiments were carried out at a heating rate of 2 °C min^{-1}.

Differential scanning calorimetry: DSC was performed at atmospheric pressure by using a Perkin–Elmer DSC-7 calorimeter; 4.7 mg of the sample was placed in a sealed aluminum capsule, and this was heated at 2 °C min^{-1} until melting was observed.

Variable-temperature optical microscopy: A Linkam THMSG-600 stage mounted to a Nikon Eclipse 50iPol Microscope was used to performed VTOM experiments. The sample was placed on a 7 mm quartz coverslip and encased within a pure Ag lid so that it was heated uniformly. The equipment also included a liquid nitrogen cooling system and a TMS94 temperature controller. Images were captured with a Nikon Digital Camera DXM1200F and processed with NIS-Elements Software.

Crystal structure determination: A colorless parallelepiped-shaped crystal of AEPF-1 of dimension 0.14 × 0.10 × 0.10 mm^3 was selected under a polarizing optical microscope and mounted on a polyimide micromounts (MiTeGen) with perfluoropolyether oil (Fomblin, Aldrich). Data were collected on a Bruker four circle kappa-diffractometer equipped with a Cu microsource operated at 30 W power (45 kV, 0.60 mA) to generate $Cu_{K\alpha}$ radiation (λ = 1.54178 Å), with a Bruker AXIOM area detector (microgap technology) at 123 K using an Oxford N-HELIX device (Oxford Cryosystem). Structure resolution details can be found elsewhere.[16] A summary of the main crystallographic data is given in Table S1 (see the Supporting Information).

X-ray powder diffraction: XRPD measurements were performed with a Bruker D8 diffractometer in the θ–θ mode using nickel-filtered $Cu_{K\alpha}$1,2 (λ = 0.15418 nm) radiation. The best counting statistics were achieved by using a scanning step of 0.02° between 5 and 80° Bragg angles with an exposure time of 0.5 s per step.

Variable-temperature XRPD: Measurements were performed with a Philips X'Pert diffractometer in the θ–θ mode using nickel-filtered $Cu_{K\alpha}$ 1,2 (λ = 0.15418 nm) radiation. A scanning step of 0.02° was used between 4 and 40° Bragg angles with 1 s per step. To perform in situ XRPD thermodiffraction studies, the diffractometer was equipped with an Anton-Paar chamber. The sample was dispersed on the steel sample holder and heated slowly to 100 °C under vacuum. Each pattern was recorded between 4 and 40° Bragg angles with a scanning step of 0.02° at 1 s per step. The heating rate between temperatures was 2 °C min^{-1}. A final pattern of AEPF-1_{dry} was recorded at 383 K between 4 and 40° Bragg angles with a scanning step of 0.0093° at 1 s per step.

DFT calculations: Periodic DFT calculations were carried out by using a plane wave basis set and the VASP package.[39,40] The initial unit cell parameters and atom positions were taken from the experimental single-crystal and powder X-ray analyses. The data obtained were then fully optimized by using the PW91 implementation of the GGA exchange correlation function[41,42] through the spin-interpolation formula of Vosko–Wilk–Nusair.[43,44] For AEPF-1 and AEPF-1_{dry}, the unit cells contain 251 and 460 atoms, respectively. The effect of the core electrons on the valence electron density was described by the projector augmented wave method[45] implemented by Kresse and Joubert.[46] The valence one-electron Kohn–Sham states have been expanded on a plane wave basis with a cutoff of 415 eV for the kinetic energy. The total energy threshold defining self-consistency of the electron density was set to 10^{-4} eV. The convergence criterion for structural optimization was set to less than 10^{-3} eV, for the difference of total energy from consecutive geometries. Thus, forces on all atoms were ensured to be less than 0.3 eV nm^{-1}. A Gaussian smearing technique with a 0.2 eV width has been applied to enhance convergence. However, all energies presented in the following have been obtained by extrapolating to zero smearing (0 K). Integration in the reciprocal space was carried out by using the Monkhorst–Pack[47] sampling of the Brillouin zone. Several meshes of special k points were used to obtain the desired accuracy in the calculated energies. The apparent energy desorption value was calculated by using a previously published formula.[24] Structural energy transformation was calculated by using the unit cell of AEPF-1_{dry} (twice the unit cell for AEPF-1). In this case both systems have the same number of atoms.

Solvent sorption experiments: Acetone (Cor Química, 99.6%), isopropyl alcohol (Scharlau, 99.5%), acetonitrile (Scharlau, 99.7%), toluene (Riedel de Haen, 99.7%), 1-butanol (Merck, 99%), *n*-hexane (Merck, 99%), isooctane (Scharlau, 99.5%), benzene (Scharlau, 99%), and cyclohexane (Scharlau, 99.7%) were used to determine the selectivity and adsorption capability of AEPF-1_{dry} for various common solvents (polar and nonpolar). A series of post-synthesis treatments of AEPF-1 were performed:

1) Activation. The AEPF-1 was dried (vacuum, 383 K) to remove the extra framework species (acetone molecules) to yield AEPF-1_{dry}. The completeness of conversion of AEPF-1 to AEPF-1_{dry} was tested by means of XRPD data.
2) Solvent sorption experiments. A powder sample of AEPF-1_{dry} was dispersed in various common solvents in a glass holder and vigorously stirred for 4 h at 298 K. The sample was then isolated by centrifugation, and air-dried.

CHEMISTRY
A EUROPEAN JOURNAL

3) Structural and thermogravimetric studies. First, XRPD was performed on the AEPF-1_{dry} sample after sorption experiments (denoted as AEPF-1′) to evaluate structural transformations. Then, TGA-MS was performed to study the desorption process of acetone inside the pores of AEPF-1′.

CCDC-733398 (AEPF-1) and 771413 (AEPF-1_{dry}) contain the supplementary crystallographic data for this paper. These data can be obtained free of charge from The Cambridge Crystallographic Data Centre via www.ccdc.cam.ac.uk/data_request/cif.

Acknowledgements

This work has been supported by the Spanish MCYT Project Mat 2007-60822, CTQ 2007-28909-E/BQU, and Consolider-Ingenio CSD2006-2001. A.E.P.P. acknowledges a JAE fellowship from CSIC and Fondo Social Europeo from EU. V.A.P.O. acknowledges financial support from the MCYT in the Ramón y Cajal research program. A.E.P.P. thanks the group of Prof. Cuevas-Diarte at the University of Barcelona for the valuable help and support in VTOM experiments. The authors thank Dr. Gándara for help with the topological analysis. Computational time has been provided by the Centre de Supercomputació de Catalunya (CESCA).

[1] G. Férey, *Chem. Soc. Rev.* **2008**, *37*, 191.
[2] O. M. Yaghi, M. O'Keeffe, N. W. Ockwig, H. K. Chae, M. Eddaoudi, J. Kim, *Nature* **2003**, *423*, 705.
[3] S. Kitagawa, R. Kitaura, S. I. Noro, *Angew. Chem.* **2004**, *116*, 2388; *Angew. Chem. Int. Ed.* **2004**, *43*, 2334.
[4] X. Lin, X. , J. Jia, P. Hubberstey, M. Schröder, N. R. Champness, *CrystEngComm* **2007**, *9*, 438.
[5] M. B. Duriska, S. M. Neville, J. Lu, S. S. Iremonger, J. F. Boas, C. J. Kepert, S. R. Batten, *Angew. Chem. Int. Ed.* **2009**, *48*, 8919.
[6] M. J. Zaworotko, *Nat. Chem.* **2009**, *1*, 267.
[7] L. Sbircea, N. D. Sharma, W. Clegg, R. W. Harrington, P. N. Horton, M. B. Hursthouse, D. C. Apperley, D. R. Boyd, S. L. James, *Chem. Commun.* **2008**, 5538.
[8] F. Salles, A. Ghoufi, G. Maurin, R. G. Bell, C. Mellot-Draznieks, G. Férey, *Angew. Chem.* **2008**, *120*, 8615; *Angew. Chem. Int. Ed.* **2008**, *47*, 8487.
[9] K. W. Chapman, G. J. Halder, P. J. Chupas, *J. Am. Chem. Soc.* **2009**, *131*, 17546.
[10] S. Kitagawa, K. J. Uemura, *Chem. Soc. Rev.* **2005**, *34*, 109.
[11] R. Kitaura, K. Seki, G. Akiyama, S. Kitagawa, *Angew. Chem.* **2003**, *115*, 444; *Angew. Chem. Int. Ed.* **2003**, *42*, 428.
[12] G. Férey, C. Serre, *Chem. Soc. Rev.* **2009**, *38*, 1380.
[13] P. Horcajada, T. Chalati, C. Serre, B. Gillet, C. Sebrie, T. Baati, J. F. Eubank, D. Heurtaux, P. Clayette, C. Kreuz, J. S. Chang, Y. K. Hwang, V. Marsaud, P. N. Bories, L. Cynober, S. Gil, G. Ferey, P. Couvreur, R. Gref, *Nat. Mater.* **2010**, *9*, 172.
[14] Z. Chun-Feng, Z. Jianyong, W. Qing, C. Zhao-Hua, F. Dieter, S. Cheng-Yong, *Chem. Eur. J.* **2009**, *15*, 7578.
[15] M. C. Das, P. K. Bharadwaj, *J. Am. Chem. Soc.* **2009**, *131*, 10942.
[16] T. Devic, P. Horcajada, C. Serre, F. Salles, G. Maurin, B. Moulin, D. Heurtaux, G. Clet, A. Vimont, J. M. Grenéche, B. L. Ouay, F. Moreau, E. Magnier, Y. Filinchuk, J. M. Marrot, J. C. Lavalley, M. Daturi, G. Férey, *J. Am. Chem. Soc.* **2009**, *131*, 1127.
[17] K. M. Fromm, *Coord. Chem. Rev.* **2008**, *252*, 856–885.
[18] C. Volkringer, T. Loiseau, G. Férey, J. E. Warren, D. S. Wragg, R. E. Morris, *Solid State Sci.* **2007**, *9*, 455.
[19] C. Volkringer, J. Marrot, G. Férey, T. Loiseau, *Cryst. Growth Des.* **2007**, *7*, 685.
[20] C. A. Williams, A. J. Blake, C. Wilson, P. Hubberstey, M. Schröder, *Cryst. Growth Des.* **2008**, *8*, 911.
[21] A. E. Platero-Prats, V. A. de La Peña-O'Shea, M. Iglesias, N. Snejko, Á Monge, E. Gutiérrez-Puebla, *ChemCatChem* **2010**, *2*, 2, 147.
[22] PLATON, A multipurpose Crystallographic Tool, A. L. Spek, Utrecht University, Utrecht, **2005**.
[23] S. Devautour-Vinot, G. Maurin, F. Henn, C. Serre, T. Devic, G. Ferey, *Chem. Commun.* **2009**, 2733.
[24] Apparent energy desorption value was calculated using the formula: $\Delta H_{des} = E_{AEPF\text{-}1} - (E_{AEPF\text{-}1\,(evacuated)} + E_{acetone})$. $E_{AEPF\text{-}1\,(evacuated)}$ = Energy of AEPF-1 without acetone.
[25] D. Louër, M. J. Louer, *J. Appl. Crystallogr.* **1972**, *5*, 271.
[26] A. Boultif, D. Louer, *J. Appl. Crystallogr.* **1991**, *24*, 987.
[27] G. S. Pawley, *J. Appl. Crystallogr.* **1981**, *14*, 357.
[28] Materials Studio Modelling 4.4, http://www.accelerys.com/mstudio/ms_modeling.
[29] V. Favre-Nicolin, R. Cerny, *J. Appl. Crystallogr.* **2002**, *35*, 734.
[30] FOX, Free Objects for Crystallography, http://objcryst.sourceforge.net.
[31] H. M. Rietveld, *J. Appl. Crystallogr.* **1969**, *2*, 65.
[32] L. Pan, M. B. Sander, X. Huang, J. Li, M. Smith, E. Bittner, B. Bockrath, J. K. Johnson, *J. Am. Chem. Soc.* **2004**, *126*, 1308.
[33] A. Monge, N. Snejko, E. Gutierrez-Puebla, M. Medina, C. Cascales, C. Ruiz-Valero, M. Iglesias, B. Gómez-Lor, *Chem. Commun.* **2005**, 1291.
[34] F. Gándara, B. Gómez-Lor, E. Gutiérrez-Puebla, M. Iglesias, M. A. Monge, D. M. Proserpio, N. Snejko, *Chem. Mater.* **2007**, *19*, 72.
[35] F. Gándara, A. de Andrés, B. Gómez-Lor, E. Gutiérrez-Puebla, M. Iglesias, M. A. Monge, D. M. Proserpio, N. Snejko, *Cryst. Growth Des.* **2008**, *8*, 378.
[36] F. Gándara, V. A. de La Peña-O'Shea, F. Illas, N. Snejko, D. M. Proserpio, E. Gutiérrez-Puebla, Á. Monge, *Inorg. Chem.* **2009**, *48*, 4707.
[37] EPINET: Euclidean Patterns in Non-Euclidean Tilings, S. J. Ramsden, V. Robins, S. T. Hyde, S. Hungerford, The Australian National University, 2005–2009, http://epinet.anu.edu.au/.
[38] L. Pan, D. H. Olson, L. R. Ciemnolonski, R. Heddy, J. Li, *Angew. Chem.* **2006**, *118*, 632; *Angew. Chem. Int. Ed.* **2006**, *45*, 616.
[39] G. Kresse, J. Furthmüller, *Comput. Mater. Sci.* **1996**, *6*, 15.
[40] G. Kresse, J. Hafner, *Phys. Rev. B* **1993**, *47*, 558.
[41] J. P. Perdew, Y. Wang, *Phys. Rev. B* **1992**, *45*, 13244.
[42] J. P. Perdew, J. A. Chevary, S. H. Vosko, K. A. Jackson, M. R. Pederson, D. J. Singh, C. Fiolhais, *Phys. Rev. B* **1992**, *46*, 6671.
[43] Y. Zhang, W. Yang, *Phys. Rev. Lett.* **1998**, *80*, 890.
[44] S. H. Vosko, L. Wilk, M. Nusair, *Can. J. Phys.* **1980**, *58*, 1200.
[45] P. E. Blöchl, *Phys. Rev. B* **1994**, *50*, 17953.
[46] G. Kresse, D. Joubert, *Phys. Rev. B.* **1999**, *59*, 1758.
[47] H. J. Monkhorst, J. D. Pack, *Phys. Rev. B* **1976**, *13*, 5188.

Received: May 6, 2010
Published online: August 30, 2010

CRYSTAL GROWTH & DESIGN

ARTICLE

pubs.acs.org/crystal

From Coordinatively Weak Ability of Constituents to Very Stable Alkaline-Earth Sulfonate Metal−Organic Frameworks

Ana E. Platero-Prats, Marta Iglesias, Natalia Snejko, Ángeles Monge,* and E. Gutiérrez-Puebla

Instituto de Ciencia de Materiales de Madrid, ICMM-CSIC, Madrid, Spain

Supporting Information

ABSTRACT: Four new compounds based on alkaline-earth elements ions and anthraquinone-2,6-disulfonate (2,6-AQDS) ligand were obtained and characterized: **AEPF-2** is the first metal−organic framework (MOF) Mg-based disulfonate, in which the ligand directly coordinates with Mg^{2+} ions to build a two-dimensional net; **AEPF-3**, **AEPF-4**, and **AEPF-5** for Ca(II), Sr(II), and Ba(II) ions, respectively, have different three-dimensional structural types and two new topologies. The catalytic behavior of these alkaline-earth materials in alkenes hydrogenation and ketones hydrosilylation reactions makes them cheap and environmentally friendly promising catalysts: in all cases, 100% selectivity was achieved toward ethylbenzene, in contrast with the behavior previously reported with calcium and strontium homogeneous catalysts. The high thermal stability (up to 500 °C) is to be emphasized for all these materials.

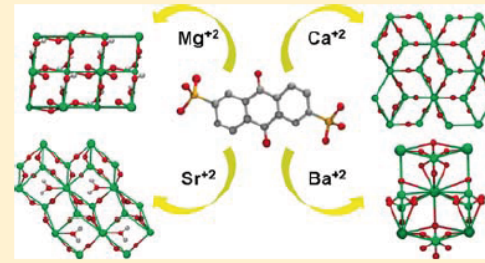

INTRODUCTION

The immense majority of coordination polymers concerns transition metals, and, more recently, rare earth cations; however, s-blocks metals have received relatively less attention,[1] probably because as it happened with lanthanide elements, they are usually regarded as unsuitable metal centers to form such polymers. Two reasons prevent the use of s-blocks in the metal−organic frameworks (MOFs) design: their unpredictable coordination numbers and geometries as no ligand field stabilization effects govern their coordinative bonding, and their tendency to form solvated metal centers, and thus, the formation of the typical alternating $[M(H_2O)_6]$ L organic−inorganic ionic layers.

On the other hand, in the broad domain of MOFs research, networks based on sulfonate ligation are much less studied, despite the fact that interesting materials with layered structures have been reported.[2] Because of the weak coordination strength of the sulfonate functionality, many of them do not displace water from the primary coordination sphere. In the case of the Group 2 metals, only the larger alkaline-earth elements coordinate to both water molecules and sulfonate groups.[3] Although some research groups have published MOF-type alkaline earth-based carboxylates,[3−5] not many networks based on sulfonate coordination have been reported.[1] The supramolecular chemistry of the sulfonate group in extended solids was reviewed by Côte and Shimizu,[6] and that of the metal arenesulfonates, by Cai.[7] Structures of compounds of Group 1 and Group 2 metal ions with 1,5-naphthalenedisulfonate (1,5-NDS) are also found;[2] recently, a new review by Shimizu et al. shows that for sulfonates, hard metal ions remain highly hydrated and typically results in zero- or one-dimensional (0D or 1D) structures.[8−10] In our ongoing studies of arene-sulfonate groups[11−13] as linkers in the search of multifunctional materials, we report here four novel two- and three-dimensional (2D and 3D) alkaline-earth polymeric frameworks (**AEPF**) belonging to four different structural types, in which the metal centers are coordinated to anthraquinone-2,6-disulfonate (2,6-AQDS) ligands. The structure and properties of the four resulting compounds are discussed, and the results of the catalytic activity of these materials in alkenes hydrogenation and ketones hydrosilylation reactions under mild conditions are also reported.

EXPERIMENTAL SECTION

General Information. All reagents were purchased (AR grade) from Aldrich and used without further purification. IR spectra were recorded from KBr pellets in the range 4000−400 cm^{-1} on a Perkin-Elmer spectrometer. Thermal gravimetric analyses (TGA) were performed using a Mettler−Toledo apparatus, between 25 and 1000 °C in air (flow rate 50 mL min^{-1}, heating rate 10 °C min^{-1}).

Synthesis. The compounds were synthesized under hydrothermal conditions, by heating the reactant mixture at 170 °C for 72 h in a Teflon-lined stainless steel autoclave. After that time, the autoclave was cooled to room temperature; the product was filtered and washed with distilled water and acetone. Typically, 0.24 mmol of 2,6-AQDSNa_2 and 0.24 mmol of alkaline-earth acetate were dissolved in a mixture of 5 mL of water (278.8 mmol) and 5 mL of 1-butanol (54.6 mmol). In all cases, the products were isolated as pure phases: yellow crystals in all cases were obtained (**AEPF-2** (65% yield), **AEPF-3** (70% yield), **AEPF-4**

Received: December 17, 2010
Revised: February 14, 2011
Published: March 14, 2011

Table 1. Crystallographic Data

	AEPF-2	AEPF-3	AEPF-4	AEPF-5
formula	$C_{14}H_{10}MgS_2O_{10}$	$C_{14}H_6CaS_2O_8$	$C_{14}H_8SrS_2O_9$	$C_{14}H_6BaS_2O_8$
formula weight	426.67	406.41	471.96	503.66
temperature (K)	296(2)	296(2)	296(2)	296(2)
wavelength (Å)	0.71073	0.71073	0.71073	0.71073
crystal system	triclinic	monoclinic	triclinic	orthorhombic
space group	$P\bar{1}$	$P2(1)/c$	$P\bar{1}$	*Pnma*
a/Á	4.8682(5)	14.863(3)	5.4254(13)	29.1296(11)
b/Á	5.7700(6)	5.5805(11)	10.219(2)	6.3329(3)
c/Á	13.4652(15)	9.3076(18)	14.537(3)	7.8329(3)
α/°	94.500(2)	90.00	103.584(4)	90.00
β/°	90.517(2)	105.968(3)	99.853(4)	90.00
γ/°	95.403(2)	90.00	95.790(4)	90.00
volume /Å^3	375.34(7)	742.2(3)	763.4(3)	1444.97(10)
Z	1	2	2	4
calc density/g cm^{-3}	1.888	1.818	2.053	2.315
μ/mm^{-1}	0.459	0.749	3.857	3.083
dimensions (mm)	0.15 × 0.10 × 0.04	0.20 × 0.10 × 0.05	0.20 × 0.12 × 0.08	0.20 × 0.12 × 0.08
limiting indices *h*	$-5 < h < 5$	$-19 < h < 19$	$-6 < h < 6$	$-37 < h < 38$
k	$-6 < k < 6$	$-7 < k < 7$	$-11 < k < 12$	$-8 < k < 8$
l	$-15 < l < 15$	$-12 < l < 12$	$-17 < l < 16$	$-23 < l < 23$
F(000)	218	412	468	968
reflections collected/unique with $I > 2\sigma(I)$	2682/1292	6281/1796	5095/2565	11404/1838
refined parameters	132	115	243	145
goodness-of-fit on F^2	1.093	1.058	1.015	1.204
R_1	0.0295	0.0499	0.0614	0.0281
wR_2	0.0749	0.1376	0.1049	0.0544

(62% yield), AEPF-5 (65% yield)). The purity of the products was tested by comparing the experimental and simulated powder X-ray diffraction (PXRD) patterns (see Supporting Information, Section S5) and through the elemental CHNS analyses. Calculated for AEPF-2: C, 39.41; H, 2.35; S, 15.03. Found: C, 38.69; H, 2.46; S, 14.49. Calculated for AEPF-3: C, 41.37; H, 1.48; S, 15.78. Found: C, 41.43; H, 1.64; S, 15.02. Calculated for AEPF-4: C, 35.63; H, 1.70; S, 13.56. Found: C, 35.49; H, 1.73; S, 13.25. Calculated for AEPF-5: C, 33.38; H, 1.19; S, 12.71. Found: C, 33.38; H, 1.23; S, 12.25.

Powder X-ray Diffraction. PXRD measurements were performed with a Bruker D8 diffractometer in the $\theta-\theta$ mode using nickel-filtered Cu K$\alpha_{1,2}$ (λ = 1.5418 Å) radiation. The best counting statistics were achieved by using a scanning step of 0.02° taken between 5 and 30° Bragg angles with an exposure time of 0.5 s per step.

Structure Determination by Single Crystal X-ray Diffraction. A summary of the main crystal and refinement data for the four compounds is given in Table 1. Data for single crystals of AEPF-2, AEPF-3, AEPF-4, and AEPF-5 were collected in a Bruker SMART CCD diffractometer equipped with a normal focus, 2.4 kW sealed tube X-ray source (MoKα radiation = 0.71073 Å). Data were collected over a hemisphere of the reciprocal space by a combination of three sets of exposures. Each exposure of 20 s covered 0.3° in ϕ. Unit cell dimensions were determined by a least-squares fit of 60 reflections with $I > 2\sigma(I)$. Main crystallographic data are given in Table 1. The structures were solved by direct methods. The final cycles of refinement were carried out by full-matrix least-squares analyses with anisotropic thermal parameters for all non-hydrogen atoms. All hydrogen atoms were placed in geometrically calculated positions and subsequently refined using a riding model with $U_{iso}(H) = 1.2U_{eq}(C)$, except in the case of coordinated water molecules, for which hydrogen atoms were located from difference Fourier maps. Calculations were carried out with SMART software for data collection and data reduction and SHELXTL.[14] CCDC reference numbers 804863, 804864, 804865, 804866 contain the supplementary crystallographic data for this paper. These data can be obtained free of charge from the Cambridge Crystallographic Data Center.

Topological Analyses. Topological analyses were performed using TOPOS software.[15] For AEPF-3 and AEPF-4, whose nets have an equilibrium placement with no vertex collisions, it was possible to idealize them in their maximum symmetry embedding using Systre software.[16,17]

Catalytic Activity Experiments. For both Lewis-acidic catalytic reactions, time-over-frequency (TOF) values were calculated from first reaction run data points in the batch experiments (after 15 reaction minutes).

(i) **Alkenes Hydrogenation.** The catalytic properties of these materials in the hydrogenation of styrene to form ethyl benzene (see Supporting Information, Scheme S1) were examined under mild conditions (toluene, 373 K, 5 atm H_2) using 1 mol % amount of catalyst. Reaction mixture was monitored by gas chromatography (GC) using a Hewlett-Packard 5890 II, coupled with a mass detector, and a methylsilicone (ov-1701) and permethylcyclodextrine column. (ii) **Ketones Hydrosilylation.** The catalytic properties of these materials in the hydrosilylation of benzaldehyde with diphenylsilane (see Supporting Information, Scheme S2) were examined using 10% mol amount of catalyst and an optimal ratio of carbonyl/diphenylsilane (1:2) under mild conditions (toluene, 363 K, nitrogen atmosphere). The reaction mixture was analyzed by GC using a KONIK HRGC 40000B chromatograph equipped with an FID detector and a KAP-120212 column.

Recycling Experiments. The best catalyst for each studied reaction was chosen to perform recycling experiments. Thus, AEPF-2 was reused in three consecutive styrene hydrogenation cycles and AEPF-3, in benzaldehyde hydrosilylation. Before reuse, the solid was separated from

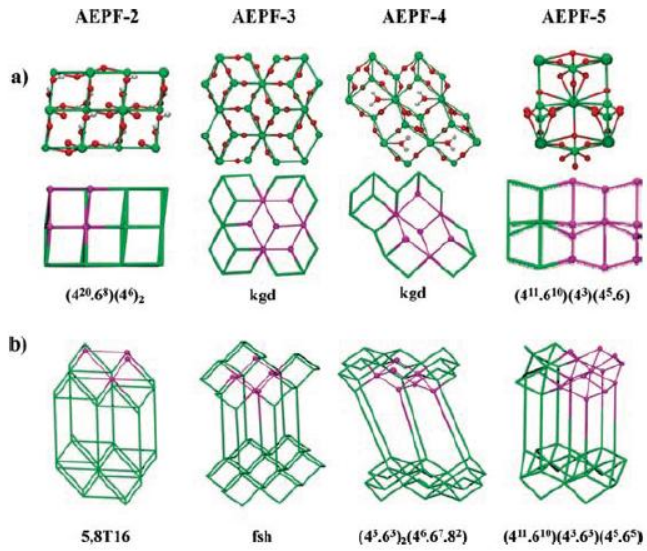

Figure 1. (a) Inorganic layer for each compound and its topological simplification. (b) Topological net simplification for each compound.

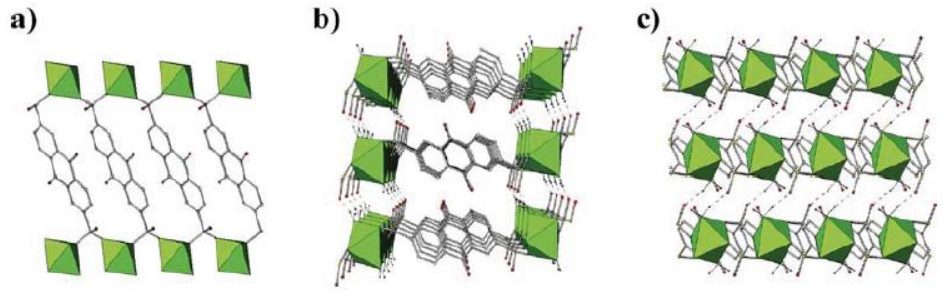

Figure 2. Polyhedral representation for (AEPF-2): (a) Layers perpendicular to the *b* direction, where MgO_6 octahedra form chains along the *a* direction; (b) representation of interlayer hydrogen bonds along the *a* direction; and (c) representation of interlayer hydrogen bonds along the *c* direction.

the reaction medium by centrifugation, washed with toluene, and dried at 120 °C under a vacuum; then fresh substrates and solvent were added, in three consecutive experiments. To verify the heterogeneous nature of the catalytic reaction, the residual activity of the supernatant solution after separation of the catalyst was studied. To rule out a potential leaching, the liquid phase of the first run was separated from the catalyst. New fractions of reagents were added to the clear filtrate, and the composition of the homogeneous reaction was determined by GC. This mixture was used in a standard catalytic experiment. After 3 h, the mixture composition was checked and no reaction was observed for each experiment, which excluded the presence of active catalytic species in solution.

■ RESULTS AND DISCUSSION

Crystal Structure Description and Topological Analyses. Details of the unit cells, data collection, and refinement for the four compounds are given in Tables S1−S4, Supporting Information. Figure 1 summarizes the topological analyses performed. Details of topological analyses performed for the four compounds are shown in Figures S5−S8, Supporting Information. The molecular formulas of the four compounds are [Mg-(2,6-AQDS)$(H_2O)_2$] (**AEPF-2**), [Ca(2,6-AQDS)] (**AEPF-3**), [Sr(2,6-AQDS)(H_2O)] (**AEPF-4**), and [Ba(2,6-AQDS)] (**AEPF-5**).

In [Mg (2,6-AQDS) $(H_2O)_2$] (**AEPF-2**), Mg^{2+} ion is hexacoordinated to four oxygen atoms coming from two (2,6-AQDS) linkers, and to two oxygen atoms of two different water molecules to give MgO_6 octahedra, which are connected through the S atoms forming chains along the *a* direction (Figure 2). Junction among chains is made via the complete linker, which acts in a $\eta^2\mu_2$-$\eta^2\mu_2$ coordination mode giving rise to layers perpendicular to the *b* direction and thus to a 2D structure. From the topological point

Crystal Growth & Design ARTICLE

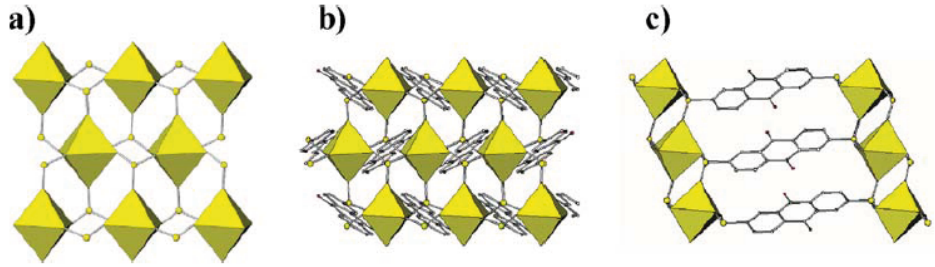

Figure 3. Polyhedral representation for AEPF-3: (a) inorganic layer; (b, c) three-dimensional net.

of view, S atoms were considered as three-connected nodes instead of analyzing the whole ligand as a unique node. We think that this kind of simplification, which has been applied for the four compounds, is chemically clearer than other possibilities. Thus, by simplification of the layers, two types of nodes can be found: four-connected (Mg) and three-connected (S) nodes. This two-periodic net exhibits a 3,4L13 (point symbol $(4.6^2)_2(4^2.6^2.8^2)$) topology (see Supporting Information, Figure S5b). The layers are bonded through three types of hydrogen bonds among the coordinated water molecules and the 2,6-AQDS oxygen atoms (one strong: *d*: $O_1-O_3 = 2.748(2)$ Å, $O_3\cdots H_{1B} = 1.81(2)$ Å; two weak: *d*: $O_1-O_2 = 3.060(2)$ Å, $O_2\cdots H_{1A} = 2.40(4)$ Å; *d*: $O_3-O_1 = 3.355(3)$ Å, $O_3\cdots H_{1A} = 2.47(2)$ Å), along the *b* direction. Taking into account these interactions, the supramolecular structure would be 3D, exhibiting now the typical inorganic layer described in this kind of compound. By simplification of these inorganic layers, two types of nodes can be found: eight-connected (Mg) and four-connected (S) nodes, giving rise to inorganic layers with point symbol $(4^{20}.6^8)(4^6)_2$ (Figure 4a). Surprisingly, this layer type does not appear in TOPOS nor in the RCSR databases. Joining of these layers through the three-connected nodes gives rise to a three-periodic net, which exhibits a 5,8T16 topology (point symbol $(4^{20}.6^8)(4^6.6^4)_2$) (Figure 1b).

This is, to the best of our knowledge, the first MOF-type Mg-based disulfonate, in which the ligand directly coordinates with Mg^{2+} ion to build a 2D net.

In [Ca(2,6-AQDS)] (**AEPF-3**), Ca^{2+} ions also occupy the centers of regular CaO_6 octahedra, but in this case no water molecules are coordinated, and each Ca atom is bonded to six sulfonate oxygen atoms. The sulfonate linker acts in a hexatopic $\eta^3\mu_3$-$\eta^3\mu_3$ coordination mode (Figure 3). The inorganic layer is formed by six-connected (Ca) and three-connected (S) nodes, to give rise to a 2D net of the type **kgd** (Figure 1a). Joining of these layers through the three-connected nodes gives rise to an **fsh** type 3D net with point symbol $(4^3.6^3)_2(4^6.6^6.8^3)$ (Figure 1b).

[Sr(2,6-AQDS)(H_2O)] (**AEPF-4**). The Sr coordination polyhedron is a monocapped trigonal prism. The water molecule is situated in one of the prism squared faces. In this compound, the ligand also acts in a hexatopic $\eta^3\mu_3$-$\eta^3\mu_3$ coordination mode (Figure 4). Since the water molecule does not participate in connectivity, the inorganic layer is quite similar to that of **AEPF-3**. It is again of the type **kgd** formed by six-connected (Sr) and three-connected (S) nodes, but some subtle differences appear when connecting them through the three-connected nodes to give rise to the 3D net. In fact, contrary to **AEPF-3** with a **fsh** net topology,

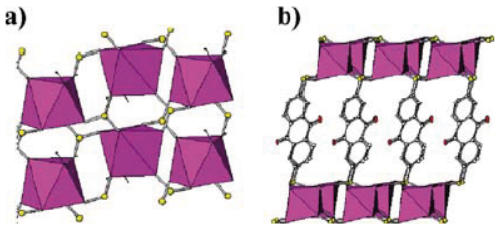

Figure 4. Polyhedral representation for compound (**AEPF-4**) (a) inorganic layer and (b) three-dimensional net.

joining of the inorganic **kgd** layers in **AEPF-4** gives rise to a new net with point symbol $(4^3.6^3)_2(4^6.6^7.8^2)$. In order to clarify this point, we performed the idealization of both nets with Systre software (see Experimental Section).[16] Once both structures were idealized in their maximum symmetry embedding, comparative topological studies were performed to understand the observed structural differences in their nets. Our analyses showed that the different topologies found can be explained in terms of the different distortions present in the inorganic layers for both compounds. Considering a six-member ring of the **kgd** net to describe the inorganic layers (Figure 5a), we determined different "conformations" (Figure 5b): for **AEPF-3**, a "chair" conformation; for **AEPF-4**, a "boat" conformation. This explains the different packing modes of the **kgd** layers in the final structures (Figure 5c): A-A type packing (**fsh** net) in **AEPF-3**, and A-B type packing (new topological type net with point symbol $(4^3.6^3)_2(4^6.6^7.8^2)$) in **AEPF-4**. Those differences are due to the change in the bond directionalities because of the presence of a coordinated water molecule in the Sr coordination polyhedron. Hydrogen bonds among the coordinated water molecules and the coordinated 2,6-AQDS oxygen atoms (*d*: $O_1-O_3 = 2.845(7)$ Å, $O_3\cdots H_{1A} = 1.86(2)$ Å) and ($O_1-O_8 = 3.090(7)$ Å, $O_8\cdots H_{1B} = 2.39$ Å) (Figure 6) might also have some influence in the **AEPF-4** net distortion.

[Ba(2,6-AQDS)] (**AEPF-5**) exhibits a 3D net, with the $AQDS^{2-}$ anions coordinated to the Ba atoms (Figure 7). Different from the former compounds and given the capability of the Ba cation to have different coordination numbers and ways of coordination, the alkaline-earth ion in **AEPF-5** is octa-coordinated to oxygen atoms, belonging to sulfonate groups, giving a BaO_8 triangulated dodecahedron. It is worth noticing that in this compound the 2,6-AQDS ligand acts as a hepta-topic $\eta^3\mu_4$-$\eta^3\mu_3$ linker, since one sulfonate oxygen atom is shared by two Ba^{2+}

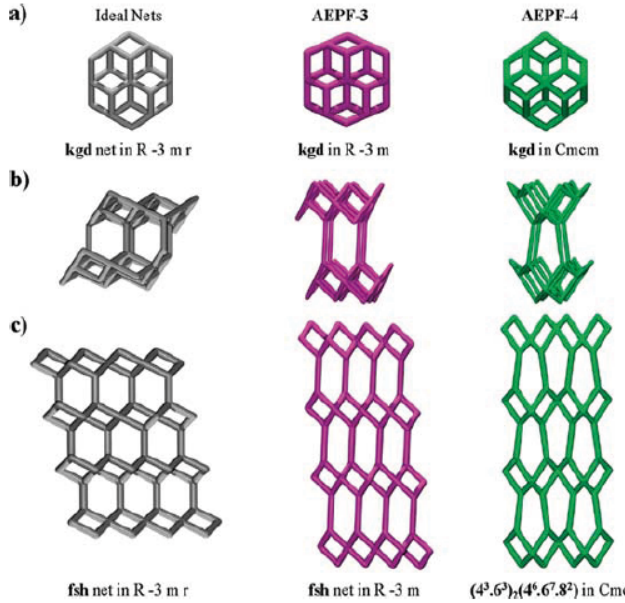

Figure 5. The figure depicts a comparative topological analysis for both **fsh** ideal net (left) and for **AEPF-3** (middle) and **AEPF-4** (right) idealized nets. (a) Six-member ring defined to describe the different **kgd** nets found in **fsh** net, **AEPF-3** and **AEPF-4**; (b) joining of two six-member rings; (c) different packing patterns: **fsh** net when "chair" conformation is found in the **kgd** layers of **AEPF-3** (left, middle); the new topological type net of **AEPF-4** with "boat" conformation (right).

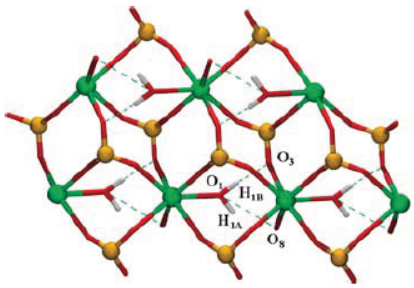

Figure 6. Hydrogen bonds in of **AEPF-4** between coordinated water molecules, and the coordinated 2,6-AQDS oxygen atoms.

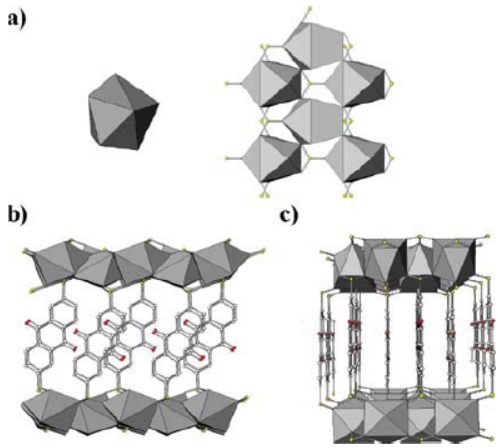

Figure 7. Polyhedral representation for **AEPF-5**: (a) (Left) BaO_8 triangulated dodecahedron and inorganic layer; (b, c) three-dimensional net.

cations. The inorganic layer is formed by seven-connected (Ba), four-connected (S), and three-connected (S) nodes, to give rise to inorganic layers with point symbol $(4^{11}.6^{10})(4^3)(4^5.6)$ (Figure 1). Joining of these layers through the four- and three-connected nodes gives rise to a 3D net with point symbol $(4^{11}.6^{10})(4^3.6^3)(4^5.6^5)$. For this structure, the topological types of neither the inorganic layer nor the 3D net appear in TOPOS or in the RCSR databases.

Role of the Alkaline-Earth Ion. As it has been previously shown for this kind of alkaline-earth disulfonate, different degrees of dimensionality are obtained depending on the metal used.[9,10] This fact can be explained as follows. First, moving down Group 2, the alkaline-earth ions form fewer bonds with water and more with SO_3^- groups, which can be rationalized in terms of hard−soft acid−base principles. On the other hand, an alternative explanation can be based on electronegativities. Thus, moving down Group 2, as the metals become more ionic in

character, the interactions with SO_3^- groups are favored over the interactions with water molecules.

Mg^{2+} ion (hexa-coordinated), which can be considered as a hard acid ion, is normally present as a 0D hexaaquo species that forms charge-assisted hydrogen bonds with sulfonate ligands.[2−10] However, by using solvothermal conditions, we were able to obtain the first MOF-type Mg based disulfonate, in which the ligand directly coordinates with Mg^{2+} ions to build a 2D net (**AEPF-2**).

For Ca^{2+} (hexa-coordinated) and Sr^{2+} (hepta-coordinated) ions, 3D nets with related topologies were obtained (**AEPF-3** and **AEPF-4**, respectively) (Figures 4 and 7). The increase in the net dimensionality is explained on the basis of the decrease in the charge/radius ratio. It is worth mentioning that both ions present different coordination numbers: 6 for Ca^{2+} and 7 in the case of Sr^{2+}, the latter additionally coordinating to one water molecule decorating the net. Thus, in **AEPF-4** the presence of coordinated water molecules changes the bond directionalities in the inorganic layer, giving rise to a new net with point symbol $(4^3.6^3)_2$-$(4^6.6^7.8^2)$.

For Ba^{2+} (octa-coordinated) ion, a 3D net has been obtained (**AEPF-5**) (Figures 6 and 7). The remarkable increase in the polarizability and atomic radius for Ba^{2+} ion results in an increase in its number of coordination. **AEPF-5** exhibits a more complicated net with point symbol $(4^{11}.6^{10})(4^3.6^3)(4^5.6^5)$, which corresponds, as in the case of **AEPF-4**, to a new topological type. On the other hand, the presence of a hepta,- tetra-, and three-connected three-nodal inorganic layer in **AEPF-5** forces the aromatic rings to be much closer than in the other compounds, giving rise to $\pi-\pi$, and $\pi\cdots O$ stacking interactions, along the (010) direction (distances of 3.15 and 3.76 Å, respectively).

Infrared Spectroscopy Studies. IR spectra of **AEPF-2**, **AEPF-3**, **AEPF-4**, and **AEPF-5** show the presence of both υ_{as} and υ_s of the SO_3 groups found at 1240−1180 (υ_{as}) and 1100−1040 (υ_s) cm^{-1}, the aromatic C−H stretching mode being situated in the area of 3100−2860 cm^{-1} (see Supporting Information, Figures S9−10). For **AEPF-2** and **AEPF-4**, IR spectra show additional bands in the −OH stretching mode region (3750−3200 $cm^{-}1$), which correspond to the coordinated water molecules present in these materials (see Supporting Information, Figure S9).

Thermal Behavior. TGA curves for **AEPF-2**, **AEPF-3**, **AEPF-4**, and **AEPF-5** are shown in Supporting Information (Figures S15−S16). The exceptional thermal stability is to be emphasized for all four MOF materials. Thus, TGA results for the thermal decomposition for the four compounds reveal that their frameworks are stable up to ∼500 °C in air; above this temperature the frameworks decompose completely.

AEPF-2. Dehydration proceeds in one stage with a weight loss of ∼8.5% at ∼180 °C consistent with the removal of the water molecules present in the compound (calc. 8.4%). The second step at ∼500 °C corresponds to the complete decomposition of the anhydrous compound. The calculated weight loss for the whole process (90.6%) is in good agreement with the experimental value of 88.5%. The PXRD pattern shows magnesium oxide as a main final product (PDF = 45-946).

AEPF-3. The complete decomposition of the compound proceeds in one step at ∼500 °C. The calculated weight loss for the whole process (66.5%) is in good agreement with the experimental value of 67%. The PXRD pattern shows calcium sulfate (anhydrite) as a main final product (PDF = 37-1496).

AEPF-4. Dehydration proceeds in one stage with a weight loss of ∼4.0% at ∼150 °C consistent with the removal of the water molecules present in the compound (calc. 3.8%). The second step at ∼490 °C corresponds to the complete decomposition of the anhydrous compound. The calculated weight loss for the whole process (61.1%) is in good agreement with the experimental value of 60.9%. PXRD pattern shows strontium sulfate (celestine) as a main final product (PDF = 5-593).

AEPF-5. The complete decomposition of the compound proceeds in one step at ∼518 °C. The calculated weight loss for the whole process (53.7%) is in good agreement with the experimental value of 52.9%. The PXRD pattern shows barium sulfate (Barite) as a main final product (PDF = 24-1035).

Catalytic Activity Tests. Alkenes Hydrogenation. The catalytic hydrogenation of unsaturated compounds represents one of the earliest examples in heterogeneous as well as homogeneous catalysis.[18] However, because of its high industrial potential, this particular conversion is even currently intensively investigated.[19] Nowadays, a new class of hydrogenation catalysts is required to develop cheap and environmentally friendly alternatives, because traditional hydrogenation catalysts are based on precious metals (Pt, Pd, Rh, Ir, Re).[20] In fact, non-transition metal catalysts such as NaH, KH, MgH_2, or $LiAlH_4$ are industrially used, although they need forcing conditions (150−225 °C, 60−100 bar H_2) and give predominantly oligomeric or polymeric subproducts.[21] In this way, the possibility to use alkaline-earth elements based catalysts in hydrogenation processes has been recently reviewed by Harder.[22] Two years earlier, the good performance of calcium and strontium homogeneous catalysts in alkenes hydrogenation has been also shown.[23]

Continuing with our previous studies on the catalytic activity of alkaline-earth MOFs, in which we showed the high catalytic activity in hydrogenation processes under mild conditions of a flexible calcium MOF,[24,25] **AEPF-2**, **AEPF-3**, **AEPF-4**, and **AEPF-5** were tested as catalysts for the hydrogenation of alkenes using styrene as substrate model under mild conditions (see Experimental Section, Section S6). The obtained results are summarized in Figure 8 and Table 2. The best results were obtained with **AEPF-2**, for which the total and selective hydrogenation of styrene to ethylbenzene was achieved after 4 h (TOF = 38.8 h^{-1}). It is worth highlighting that in all cases 100% selectivity was achieved toward ethylbenzene, in contrast with the behavior of previously reported calcium and strontium homogeneous catalysts.[23]

All catalysts employed in styrene hydrogenation were recovered by centrifugation, washed with toluene, and then characterized by PXRD. Comparison of the PXRD patterns before and after the catalytic reaction confirm the robustness of the four compounds in the studied conditions (see Supporting Information, Figures S19−S22).

A mechanism for the alkaline-earth MOF-mediated hydrogenation, based on the H_2 heterolytic cleavage, could be analogous to that proposed by Harder et al. for soluble calcium hydride complexes,[22,23] in which the catalytic activity is explained by the formation of Ca-hydride intermediate species. Taking this into account, the observed decrease in the catalytic activity in the **AEPF-2** > **AEPF-3** > **AEPF-4** > **AEPF-5** direction can be explained by the loss of Lewis acidity in the Mg(II) > Ca(II) > Sr(II) > Ba(II) direction (Figure 8 and Table 2).

Recycling Experiments. Alkenes Hydrogenation. To investigate the lifetime and the stability of the better catalyst in styrene hydrogenation (**AEPF-2**), a recycling experiment was

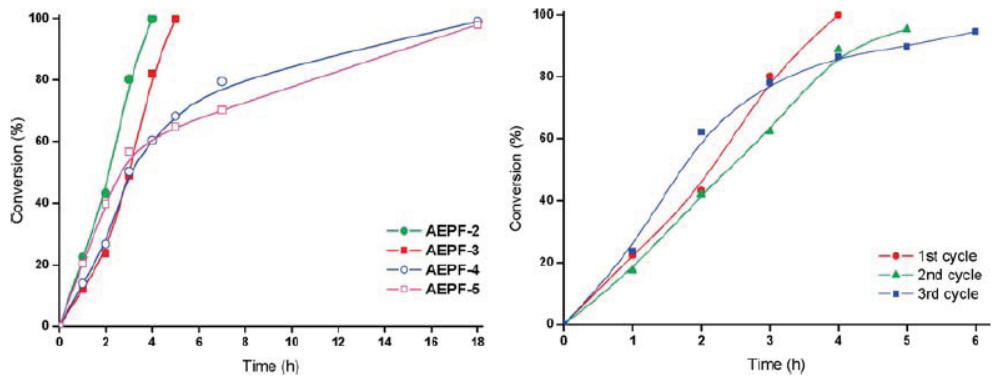

Figure 8. (Left) Kinetic profiles of styrene hydrogenation with AEPF-2, AEPF-3, AEPF-4, and AEPF-5 as catalysts. (Right) Kinetic profiles in three consecutive reaction cycles employing AEPF-2 as catalyst.

Table 2. Styrene Hydrogenation in Toluene, at 373 K, 5 atm H_2, Using 1 mol % Catalyst

compound	active center	time (h)	conversion (%)	TOF (h^{-1})
AEPF-2	Mg(II)	4	100	38.8
AEPF-3	Ca(II)	5	100	12.3
AEPF-4	Sr(II)	5	68.2	14.3
AEPF-5	Ba(II)	5	64.7	36.5

Table 3. Benzaldehyde Hydrosilylation with Diphenylsilane in Toluene, at 363 K, Using 10 mol % Catalyst

compound	active center	time (h)	conversion (%)	TOF (h^{-1})
AEPF-2	Mg(II)	22	34.6	0.21
AEPF-3	Ca(II)	22	85.3	1.52
AEPF-4	Sr(II)	22	65.5	1.41
AEPF-5	Ba(II)	22	39.5	0.24

performed employing it in three consecutive reaction cycles. The observed activity is kept over the three cycles of reaction (Figure 8 right). A blank run with magnesium acetate tetrahydrate replacing AEPF-2 was also carried out, in order to compare both activity and robustness (Figure S23, Supporting Information).

The catalyst employed in the three consecutive cycles of reaction was recovered as explained before, and then characterized by PXRD. The comparison of the PXRD patterns of the catalyst before and after the recycling allows us to confirm that the compound is unaltered after the three cycles of reaction (see Supporting Information, Figure S19).

Catalytic Activity Tests. Ketones Hydrosilylation. Hydrosilylation reactions are considered as a highly atom-efficient key transformation, which has great importance for the silicon industry and organic synthesis, dendrimer, and polymer chemistry.[26] In particular, catalytic hydrosilylation of ketones is a convenient one-step procedure to prepare protected alcohols. The mechanism is similar to that of the hydrogenation reaction, and generally similar catalysts are employed for the two catalytic processes. Recently, main group metal homogeneous catalysts have been introduced for this reaction.[22]

Continuing with our previous work,[24] AEPF-2, AEPF-3, AEPF-4, and AEPF-5 were tested as ketones hydrosilylation catalysts in the hydrosilylation of benzaldehyde with diphenylsilane (see Experimental Section). The obtained results are shown in Table 3, Figure 9 left. The best result was obtained with AEPF-3, for which the silylated product yield was 85.3% after 22 h (TOF = 1.52 h^{-1}). A similar behavior was obtained with AEPF-4 (silylated product yield 65.5% after 22 h, TOF = 1.41 h^{-1}). However, in the case of both AEPF-2 and AEPF-5, the catalytic activity was clearly lower (silylated product yield lower than ~40% after 22 h).

All the catalysts employed in hydrosilylation of benzaldehyde with diphenylsilane were recovered as explained before and then characterized by PXRD. The comparison of the PXRD patterns of the catalysts before and after the reaction allows us to confirm the robustness of the four compounds in the studied conditions (see Supporting Information, Figures S24–S27).

The mechanism proposed for ketones hydrosilylation usually assumes the intermediacy of a metal complex that contains a hydride, a silyl ligand (R_3Si), and the ketone substrate.[22,23] Taking into account this type of mechanism, two different kinds of requirements are needed: (i) Lewis acidity, that favors the formation of hydride intermediate species and (ii) capability of the catalytically active alkaline-earth center to increase its coordination number and give rise to the metal complex intermediate species. Thus, in the studied conditions, the observed decrease in the catalytic activity in the AEPF-3 > AEPF-4 > AEPF-5 direction can be explained with the loss of Lewis acidity in the Ca(II) > Sr(II) > Ba(II) direction. For AEPF-2, in which Mg(II) is the active center, the low activity is explained in terms of the substrate steric impediment related to the Mg ion size.

Recycling Experiments. Ketones Hydrosilylation. To investigate the lifetime and the stability of the better catalyst in benzaldehyde hydrosilylation with diphenylsilane (AEPF-3), a recycling experiment was performed employing it in three consecutive reaction cycles. The observed activity is kept over the three cycles of reaction, being slightly decreased in the third one (Figure 9).

The catalyst employed in the three consecutive cycles of reaction was recovered as explained before, washed with

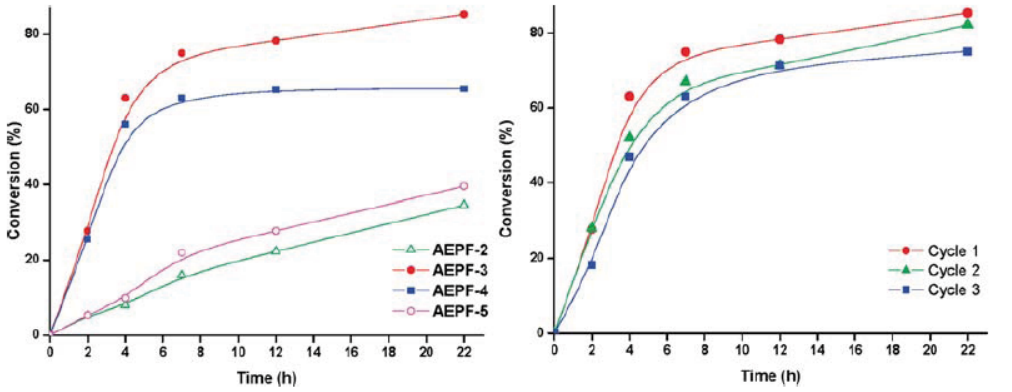

Figure 9. (Left) Kinetic profiles for bezaldehyde hydrosilylation with diphenylsylane with AEPF-2, AEPF-3, AEPF-4, and AEPF-5 as catalysts. (Right) Kinetic profiles in three consecutive reaction cycles employing AEPF-3 as catalyst.

toluene, and then characterized by PXRD. The comparison of the PXRD patterns of the catalyst before and after the recycling allows us to confirm that the compound is unaltered after the three cycles of reaction (see Supporting Information, Figure S25).

CONCLUSIONS

In summary, by using appropriate solvothermal conditions, the four new compounds, based on coordinatively "weak" alkaline-earth elements cations and anthraquinone-2,6-disulfonate (2,6-AQDS) anions, were obtained and characterized. In the novel first MOF-type Mg-based disulfonate, **AEPF-2**, the ligand coordinates directly with hexa-coordinated Mg^{2+} ion to build a layered 2D structure; these layers are bonded through hydrogen bonds giving 3D supramolecular structure. In **AEPF-3**, **AEPF-4**, and **AEPF-5** for Ca^{2+}, Sr^{2+}, and Ba^{2+} ions respectively, the structures possess different 3D structural types and represent two new topologies (for **AEPF-4** and **AEPF-5**).

The exceptional thermal stability (up to 500 °C) is to be emphasized for all these MOF compounds. On the other hand, and although these frameworks do not allow the substrate accessibility to the interior, and thus the catalytic reactions take place on the surface, the new compounds exhibit activity as alkene hydrogenation and ketones hydrosilylation heterogeneous catalysts in mild conditions, **AEPF-2** being the best one for the hydrogenation of styrene. It is worth highlighting that in all cases 100% selectivity was achieved toward ethylbenzene, in contrast with the behavior previously reported for calcium and strontium homogeneous catalysts. **AEPF-3** is the most active catalyst for benzaldehyde hydrosilylation with diphenylsilane.

ASSOCIATED CONTENT

Supporting Information. Structural analyses by single crystal X-ray diffraction, topological analyses, infrared spectroscopy analyses, thermal gravimetric analyses, Pawley refinements, and catalytic studies for **AEPF-2**, **AEPF-3**, **AEPF-4**, and **AEPF-5**. This material is available free of charge via the Internet at http://pubs.acs.org.

AUTHOR INFORMATION

Corresponding Author
*E-mail: amonge@icmm.csic.es.

ACKNOWLEDGMENT

This work has been supported by the Spanish MCYT Project Mat 2007-60822, Mat 2010-17571, CAM S2009/MAT-1756/CAM, and Consolider-Ingenio CSD2006−2010. A.E.P.P. acknowledges the JAE fellowship from CSIC and Fondo Social Europeo from EU. The authors thank Prof. Davide M. Proserpio and Dr. Felipe Gándara for their help with the topological analysis.

REFERENCES

(1) Côté, A. C.; Shimizu, G. K. H. *Chem.—Eur. J.* **2003**, *9*, 5361–5370 and references therein.
(2) (a) Russell, V. A.; Etter, M. C.; Ward, M. D. *J. Am. Chem. Soc.* **2004**, *116*, 1941–1952. (b) Pivovar, A. M.; Holman, K. T.; Ward, M. D. *Chem. Mater.* **2001**, *13* (9), 3018–3031.
(3) Cai, J. W.; Chen, C. H.; Liao, C. Z.; Feng, X. L.; Chen, X. M. *Acta Crystallogr.* **2001**, *B57*, 520–530.
(4) (a) Dincă, M.; Long, J. R. *J. Am. Chem. Soc.* **2005**, *127* (26), 9376–9377. (b) Davies, R. P.; Less, R. J.; Lickiss, P. D.; White, A. J. P. *Dalton Trans.* **2007**, *24*, 2528–2535. (c) Senkovska, I.; Fritsch, J.; Kaskel, S. *Eur. J. Inorg. Chem.* **2007**, *35*, 5475–5479. (d) Dietzel, P. D. C.; Blom, R.; Fjellvåg, H. *Eur. J. Inorg. Chem.* **2008**, *23*, 3624–3632.
(5) (a) de Lill, D. T.; Bozzuto, D. J.; Cahill, C. L. *Dalton Trans.* **2005**, *12*, 2111–2115. (b) Birkedal Nielsen, R. K.; Kongshaug, K. O.; Fjellvåg, H. *Solid State Sci.* **2006**, *8* (10), 1237–1242. (c) Volkringer, C.; Marrot, J.; Férey, G.; Loiseau, T. *Cryst. Growth Des.* **2008**, *8* (2), 685–689.
(6) Côte, A. P.; Shimizu, G. K. H. *Coord. Chem. Rev.* **2003**, *245*, 49–64.
(7) Cai, J. *Coord. Chem. Rev.* **2004**, *248*, 1061–1083 and references therein.
(8) Shimizu, G. K. H.; Vaidhyanathan, R.; Taylor, J. M. *Chem. Soc. Rev.* **2009**, *38*, 1430–1449.
(9) Côté, A. P.; Shimizu, G. K. H. *Chem.—Eur. J.* **2003**, *9* (21), 5361–5370.
(10) Kennedy, A. R.; Kirkhouse, J. B. A.; McCarney, K. M.; Puissegur, O.; Smith, W. E.; Staunton, E.; Teat, S. J.; Cherryman, J. C.; James, R. *Chem.—Eur. J.* **2004**, *10* (18), 4606–4615.

(11) Gándara, F.; Fortes-Revilla, C.; Snejko, N.; Gutiérrez-Puebla, E.; Iglesias, M.; Monge, M. A. *Inorg. Chem.* **2007**, *46*, 3475–3484.
(12) Gándara, F.; Perles, J.; Snejko, N.; Iglesias, M.; Gómez-Lor, B.; Gutiérrez-Puebla, E.; M. Monge., M. A. *Angew. Chem. Int. Ed.* **2006**, *45*, 7998–8001.
(13) Gándara, F.; Puebla, E. G.; Iglesias, M.; Proserpio, D. M.; Snejko, N.; Monge, M. Á. *Chem. Mater.* **2009**, *21* (4), 655–661.
(14) *Software for the SMART System V5.04 and SHELXTL V 5.1*; Bruker-Siemens Analytical X-ray Instrument Inc.: Madison, WI, 1998.
(15) Blatov, V. A. *IUCr Comput. Comm. Newslett.* **2006**, *7*, 4–38; see also http://www.topos.ssu.samara.ru.
(16) Delgado−Friedrichs, O.; O'Keeffe, M. *Acta Crystallogr.* **2003**, *B59*, 351–360.
(17) Ramsden, S. J.; Robins, V.; Hyde, S. T.; Hungerford, S. EPINET: Euclidean Patterns in Non-Euclidean Tilings. The Australian National University: Canberra, Australia, 2005−2009; http://epinet.anu.edu.au/.
(18) (a) Sabatier, P. *La Catalyse en Chimie Organique*; Librairie Polytechnique: Paris, 1913. (b) Sabatier, P.; Nye, M. J. *Chem. World* **2004**, *1* (12), 46–49. (c) Wilkinson, G. *Bull. Soc. Chim. Fr.* **1968**, *12*, 5055–5058.
(19) de Vries, J. G.; Elsevier, C. J. *The Handbook of Homogeneous Hydrogenation*; Wiley-VCH: Weinheim, 2007.
(20) (a) Ertl, G.; Knçzinger, H.; Weitkamp, J. *Handbook of Heterogeneous Catalysis*; Wiley-VCH: Weinheim, 1997; Vol. 5. (b) Sheldon, R. A.; Van Bekkum, H. *Fine Chemicals through Heterogeneous Catalysis*; Wiley-VCH: Weinheim, 2001; Vol. 5.
(21) (a) Haenel, M. W.; Narangerel, J.; Richter, U.-B.; Rufińska, A. *Angew. Chem. In. Ed.* **2006**, *45* (7), 1061–1066. (b) Slaugh, L. H. *Tetrahedron.* **1966**, *22* (6), 1741–1746.
(22) Harder, S. *Chem. Rev.* **2010**, *110* (7), 3852–3876.
(23) Spielmann, J.; Buch, F.; Harder, S. *Angew. Chem. In. Ed.* **2008**, *47* (49), 9434–9438.
(24) Platero-Prats, A. E.; de la Peña-O'Shea, V. A.; Iglesias, M.; Snejko, N.; Monge, Á.; Gutiérrez-Puebla, E. *ChemCatChem* **2010**, *2*, 147–149.
(25) Platero-Prats, A. E.; de la Peña-O'Shea, V. A.; Snejko, N.; Monge, Á.; Gutiérrez-Puebla, E. *Chem.—Eur. J.* **2010**, *16* (38), 11632–11640.
(26) Ojima, I.; Li, Z.; Zhu, J. *The Chemistry of Organosilicon Compounds*; Rappoport, Z., Apeloig, Y., Eds.; John Wiley: New York, 1998; Vol 2, p 1687.